AD-A164 205 KALMAN FILTER DESIGN FOR THE LONG RANGE INTERCEPT FUNCTION OF THE F-4E/G F..(U) AIR FORCE INST OF TECH WRIGHT-PATTERSON AFB OH SCHOOL OF ENGI.. R C HALBERT 1/4

UNCLASSIFIED DEC 85 AFIT/GE/ENG/85D-20 F/G 17/9 NL

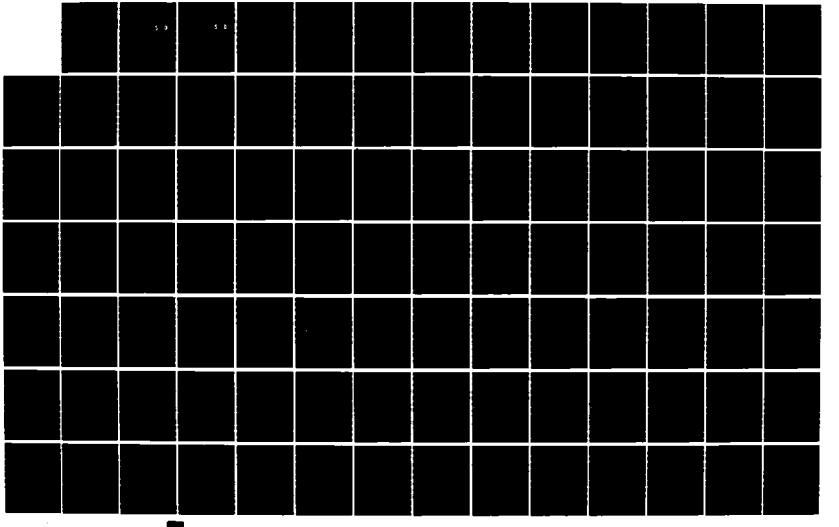

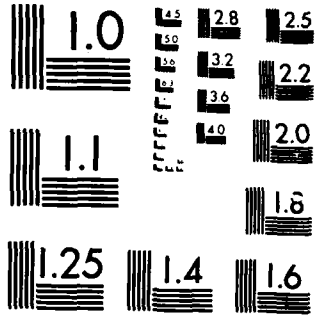

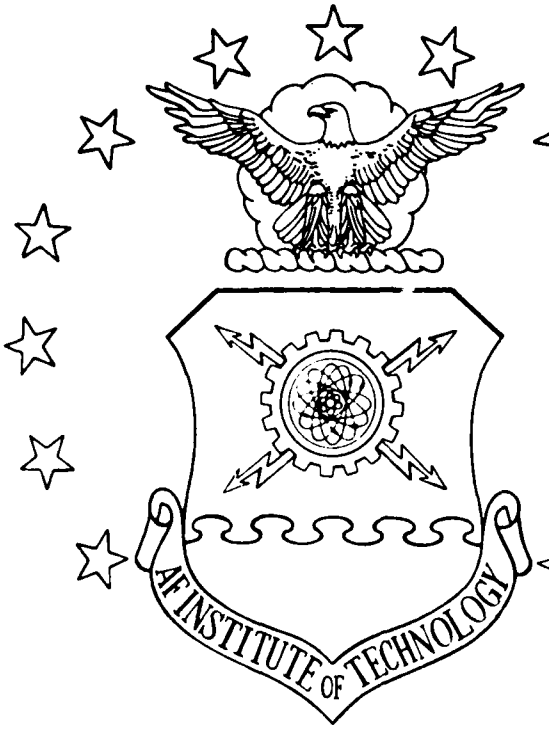

KALMAN FILTER DESIGN FOR THE LONG RANGE INTERCEPT FUNCTION OF THE F-4E/G FIRE CONTROL SYSTEM

THESIS

Robert C. Halbert
Captain, USAF

AFIT/GE/ENG/85D-20

DEPARTMENT OF THE AIR FORCE
AIR UNIVERSITY
AIR FORCE INSTITUTE OF TECHNOLOGY

Wright-Patterson Air Force Base, Ohio

AFIT/GE/ENG/85D-20

KALMAN FILTER DESIGN FOR THE LONG RANGE INTERCEPT FUNCTION OF THE F-4E/G FIRE CONTROL SYSTEM

THESIS

Robert C. Halbert
Captain, USAF

AFIT/GE/ENG/85D-20

AFIT/GE/ENG/85D-20

KALMAN FILTER DESIGN FOR THE LONG RANGE INTERCEPT FUNCTION OF THE F-4E/G FIRE CONTROL SYSTEM

THESIS

Presented to the Faculty of the School of Engineering

of the Air Force Institute of Technology

Air University

In Partial Fulfillment of the

Requirements for the Degree of

Master of Science in Electrical Engineering

Robert C. Halbert, B.S.

Captain, USAF

December 1985

Approved for public release; distribution unlimited

Acknowledgements

Many people have assisted me in the accomplishment of this thesis. I would like to thank my advisor, Major William H. Worsley for his guidance, and for his patience during many difficult periods. I would also like to thank Dr. Peter S. Maybeck for his many valuable suggestions during the course of this project. Dr. Maybeck's influence is also reflected in the bibliography, which lists his books as three primary sources. Other sources are listed in the order they are referenced in the text. I am also indebted to Mr. Stan Musick for his help with SOFE on several occasions. Special appreciation goes to the personnel of OO-ALC/MMECB at Hill AFB, Utah who sponsored this project. Mr. Hugh Hougaard, Mr. Bob Beal, Captain Chuck Strickler, and Captain Rob Crombie contributed many hours to telephone consultations and personal travel in support of my research. Finally, I would like to thank Captain Ross Anderson, whose work on the sister project to this thesis was an invaluable source of inspiration. Ross contributed ideas, sources, and helpful critiques throughout the entire project. His support made it possible to broaden the scope of this thesis significantly.

Table of Contents

List of Figures

List of Tables

Symbols and Abbreviations

Symbol	Meaning
ACM	Air Combat Maneuvering
A/D	Analog-to-Digital
AI	Airborne intercept (type of radar)
APQ-120	Designator for F-4E/G radar and its associated fire control system
CADC	Central Air Data Computer
CV	Constant Velocity model
EKF	Extended Kalman Filter
fps	feet per second
GMA	Gauss-Markov Acceleration model
INS	Inertial Navigation System
KOPS	1000 Operations per second
los	line-of-sight
LRI	Long Range Intercept function
LRU	Line Replaceable Unit
OFP	Operational Flight Program
TAS	True Airspeed

Abstract

This study examines reduced-order Kalman filters designed to improve performance of the F-4E/G long range air-to-air missile capability (LRI function). Operational requirements dictate a high degree of accuracy and constraints imposed by existing hardware mandate minimal complexity. Two linear dynamics models are proposed, one based on constant target velocity, and the other based on time-correlated target acceleration. Both are defined in inertial Cartesian coordinates aligned with north, east, and down. A nonlinear model is developed for measurements available in the existing F-4E/G hardware, including range, range rate, radar antenna gimbal angles, and radar antenna rates. The models are implemented in extended Kalman filter formulations employing linear propagation equations to avoid on-line numerical integration. Performance evaluations are performed on three test trajectories using Monte Carlo analysis. Filter tuning, error budgets, adaptive techniques, and observability issues are addressed during filter evaluation. Results of the evaluation indicate the filter designs can meet the requirements of the F-4E/G fire control system. Recommendations are made for continued testing and for operational implementation.

KALMAN FILTER DESIGN FOR THE LONG RANGE INTERCEPT FUNCTION OF THE F-4E/G FIRE CONTROL SYSTEM

I. Introduction

Background

Fruitful applications of Kalman filtering in the area of airborne target tracking are well documented in current technical literature (1,4). Extensive research has been conducted in this area since the advent of Kalman filter theory in the early 1960s, and today, fully developed systematic design procedures are available (1:341). Nevertheless, engineers involved in specific implementations face recurring difficulties associated with the limited speed, memory, and wordlength of the small on-line computers used to implement real time filters. This thesis is an attempt to build on the results of previous research by applying established Kalman filtering techniques to a highly specific problem, estimating the velocity of long range targets under the contraints imposed by hardware in the fire control system of the F-4E/G aircraft.

The F-4E/G's fire control system uses an onboard radar, the APQ-120, to track airborne targets prior to launching air-to-air missiles (9,11,21). A multifunction microprocessor controls the fire control system through associated

software, designated the Operational Flight Program (OFP). One function of the OFP is to combine radar target data with F-4E/G ownship attitude and velocity data to obtain accurate estimates of target velocity and acceleration. These estimates are then used to determine when the target is within an envelope for successfully launching a missile. Currently, the OFP uses a Wiener-Hopf filter to estimate target velocity and acceleration for use in computing the maximum and minimum lethal ranges of a missile under current flight conditions. The output of the OFP then drives a steering dot and a maximum missile range indicator in the cockpit. These instruments provide the pilot with the information needed to set up a successful attack against distant targets (the long range intercept, or LRI, function) and closer air combat maneuvering targets as well (the ACM function). Ideally, the pilot should be able to maneuver the aircraft by following the steering dot and to launch a missile successfully when the range indicator shows the target is within range. However, pilots have complained that the steering dot becomes unstable and the maximum missile range indicator temporarily goes to zero whenever the F-4E/G performs high roll rate combat maneuvers (5,8,9).

The steering dot instability stems from two sources, an increased noise level in the radar's rate gyro outputs during aircraft maneuvers and the tendency of the Wiener-Hopf filter to amplify this noise (5:1). Improvements might be achieved by replacing either the radar or the filter. However,

replacing the APQ-120 radar is a costly and uncertain fix at best, and no funds are available for this option. The second alternative, replacing the Wiener-Hopf filter, could be accomplished at much lower cost by reprogramming the OFP. For this reason, it is proposed to design a Kalman filter to replace the current Wiener-Hopf filter. If such a Kalman filter could be feasibly implemented in the constrained hardware of the F-4E/G fire control system, it could optimally process the poor quality radar data in such a way as to eliminate the steering dot instability without sacrificing performance.

Problem Statement

The purpose of this study is to determine the feasibility of implementing a suitable Kalman filter in the F-4E/G fire control system under the constraints imposed by current hardware. It is well established that higher order Kalman algorithms can achieve improved estimation performance over filters of the Wiener-Hopf type, providing that sufficient memory and computational speed are available from the computer (4, 6:157). In this respect, the F-4E/G's computer imposes severe constraints. It operates at 300,000 operations per second (300 KOPS), which is slow compared to state-of-the-art microprocessors for real time avionics. For instance, the fire control system in the F-16 currently operates at 700 KOPS (7). A maximum filter cycle time is specified as 40 msec by OFP software engineers (8). This is

actually a current requirement of the Wiener-Hopf filter needed to produce estimates of the desired accuracy and still leave time for other steering and range computations required to update the steering dot and range indicators in the cockpit at a 10 Hz rate (every 100 msec). The 10 Hz update of the cockpit indicators is considered a hard specification, but some minor flexibility might be available for the 40 msec filter execution time. Assuming 40 msec as worst case allows a maximum of 12000 computer operations on the F-4E/G's 300 KOPS fire control computer for a filter algorithm. Another limitation of this computer is that it has only 8K words of memory available for a Kalman filter algorithm and supporting auxillery calculations.

The Kalman filter implemented in this constrained memory must satisfy both the LRI and ACM functions. Unfortunately, these two functions operate under different target assumptions. LRI assumes a non-maneuvering target and requires filter estimates of target velocity only, while ACM assumes a highly dynamic target and requires filter estimates of target acceleration as well as velocity (9,10). Additionally, the noise content of the radar measurements is partially a function of target range and differs significantly between ACM measurements, taken within 8 nautical miles (nm), and LRI measurements, taken from 8 to 30 nm (9). As a result of these different operating conditions, inherent differences exist between the two functions and a filter designed for LRI might not prove suitable for ACM. In the

past, the Wiener-Hopf algorithm was implemented as two separate filters, one dedicated to ACM and the other for LRI. However, a significant portion of the filter computations are common to both functions. By carefully accounting for the differences discussed above, a single combined filter algorithm is designed to run in either ACM or LRI mode in the latest version of the OFP. The combined function filter conserves overall memory usage but exacts a cost in processing time because the more complex combined filter requires longer processing time than either single function filter alone. Regardless of whether separate or combined filters are implemented, the double constraint of memory space and processing time limits the complexity of the proposed Kalman filter. To cope with this constraint, reduced order and constant gain Kalman filters are investigated in this study. A third constraint imposed by the computer is its 16-bit wordlength. Short wordlength is a frequent contributor to numerical instability in Kalman filter applications, a problem which strongly motivates the use of square root or U-D filter formulations (1:368-369).

Besides the constraints imposed by computer hardware, the Kalman filter designer must also consider the constraints imposed by the F-4E/G sensor group. As explained earlier, it is not economically feasible at present to replace or upgrade the APQ-120 radar or other onboard sensors which supply measurements to the OFP for fire control purposes. These include the central air data computer

(CADC) and inertial navigation system (INS). The measurements provided by these instruments and the errors associated with them must be taken as givens for the purpose of this work.

The above constraints place severe limitations on a Kalman filter application for the F-4E/G. Such a limited Kalman filter might not perform accurately enough to meet the needs of the fire control system in a combat environment. To judge its adequacy, the performance of the filter must be measured against explicit criteria. In the case of LRI, the filter must produce target velocity estimates whose overall magnitude error has a maximum standard deviation of 30 feet per second (8). This accuracy is required by the current OFP to generate cockpit indications which meet the combat requirement of less than 10% out-of-boundary launches and less than 10% missed opportunities to attack (10:3-1).

To warrant implementation, the Kalman filter must continue to meet all performance criteria during any maneuvers required by LRI attack. Currently, the Wiener-Hopf filter's calculation of target velocity is adequate during straight and level flight, but is virtually useless during F-4E/G maneuvering (9). The radar azimuth and elevation positions as well as the outputs of the radar's rate gyros lag behind fighter maneuvers and oscillate. The Wiener-Hopf filter amplifies this problem so that during maneuvers, the lag and oscillation of the radar's outputs become so severe that the missile range estimate collapses

to zero and the pilot's steering dot in the cockpit bounces erratically across the screen.

To overcome this problem and to minimize pilot distraction, a postfilter is included in the present software. The postfilter essentially puts the fire control system into memory mode during fighter maneuvers by ignoring the amplified radar noise and by smoothing the output to the steering dot and range indicator using past values of rate gyro measurements. This arrangement provides a non-distracting display but fails to provide useful information to aid the pilot in successfully attacking the target. The problem is described in aircrew technical orders as follows:

> "When the aircraft rolls to center the aim dot, APQ-120 rate gyro transients make the steering dot jump. To make the dot stable, the computer uses the rate gyro outputs it received prior to roll until the fighter roll angle is established and the transients settle." (11:1-82)

Correcting this problem and eliminating the need for postfilter data processing are the essential benefits which could be derived from this research. Thus, the desired end product of this thesis effort is a Kalman algorithm which will generate target velocity estimates of the accuracy cited above, regardless of F-4E/G combat maneuvering, and which can be implemented in the onboard computer within the cited constraints of computer memory and execution time.

Scope and Assumptions

Although integration with the ACM function is a major consideration, this study deals directly with filter design

for LRI only. Filter algorithms are tested in a computer simulation using a Kalman filter analysis package called the Simulation for Optimal Filter Evaluation, or SOFE, and a complementary data postprocessor and plotting program called SOFE Plotter, or SOFEPL (13,28). The Fortran 77 language is used for the simulation and no attempt is made to implement the filters in F-4E/G machine language. This study does not include flight testing, but recommendations are included to assist the incorporation of the filters designed into the OFP for bench and flight testing.

Although many different Kalman filter configurations are possible for this application, only two filters are initially developed. Performance evaluations are then used to tune these filters for best possible performance. If further performance improvements are still required after tuning, filter modifications are possible. These modifications include constant gain, adaptive gain, or the augmentation of additional states to represent originally unmodelled effects.

Both of the initially proposed filter models are nonlinear in their measurement equations. This precludes use of conventional Kalman filter formulations. The extended Kalman filter (EKF) is used instead for these reasons:

(1) its proven superior performance over linearized Kalman filters in cases where a nominal state trajectory is not known a priori (2:42,52 to 55, 12:38)

(2) its computational simplicity when compared to higher order estimators (2:221,235), and

(3) its compatibility with the available performance evaluation tool, SOFE (12:38)(13).

Use of the EKF entails approximations of model nonlinearities in some aspects of the algorithm, and explicit evaluation of nonlinearities in other aspects, as explained in Chapter IV. It is important to note that the approximations inherent in the EKF formulation might not be adequate in cases where the nonlinearities are extremely harsh (2:224). The nonlinear models developed in this thesis are assumed to be sufficiently benign to allow use of the EKF. The validity of the dynamics models themselves for representing physical reality is another implicit assumption necessary for computer simulation studies. The models developed in Chapter II are assumed adequate based on their successful application in previous tracking problems.

In addition to the fundamental assumptions above, several specific assumptions allow the simplification of complex effects which have relatively minor influence on overall system behavior. The simplification of non-dominant effects permits this study to emphasize filter design and evaluation.

For LRI, the target is assumed to be a non-maneuvering point mass, while ACM assumes that targets are maneuvering. Both modes treat the F-4E/G as a three dimensional vehicle,

but the acknowledged velocity and acceleration discrepancies of different locations on the airframe during nonzero attitude rates are assumed neglible for LRI. Here, "attitude rate" refers to any combination of heading, pitch, or roll rate. Although yaw rates have an admitted effect, they are not calculated in the F-4E/G OFP (8). Flight without sideslip is assumed in this study. The OFP calculates fighter attitude rates by using the incremental INS angles of pitch, roll, and heading. The angles and angle rates derived from them are corrupted by sensor and approximation errors. These errors are expected to be much smaller than the errors committed by the filter, and are assumed neglible. Although this assumption may not be completely justifiable, the limited memory and speed of the fire control computer preclude the inclusion of a complex INS error model in the OFP.

The APQ-120 antenna is pointed at the target by a closed loop control system. The response time of this system is assumed to be very fast in comparison with the filter cycle time. For the short time required to take a measurement, the antenna is assumed to be space-stabilized. This allows simplification of the measurement equations since the antenna rates do not have to be integrated to determine antenna angle. The errors associated with antenna angle include true pointing error caused by the control system as well as measurement errors deriving from resolvers and other sensors. In this study, these errors are combined

and quantified as a total measurement error. Measurement assumptions are detailed in Chapter III.

Methodology

Having identified the problem, defined limitations, and proposed a Kalman filter as a solution, the goal of this study is to demonstrate the feasibility of the proposed solution. This section describes the logical approach used for this purpose and relates each step to the remaining chapters of the report. Conceptually, the study can be broken into the following steps:

(1) Model development (Chapters II and III),

(2) Filter implementation (Chapter IV),

(3) Performance evaluations of filters (Chapter V),

(4) Results of performance evaluations (Chapter VI),

(5) Conclusions and recommendations (Chapter VII).

These areas are expanded below.

The most crucial element of Kalman filter design is the selection of adequate models as a basis for the filter (1). In Chapter II, several dynamics models for air-to-air tracking are examined and two are selected using the criteria of adequacy to represent reality, computational simplicity, and compatibility with the existing F-4E/G fire control system. The measurements available to the filter are a fixed function of existing F-4E/G hardware. The mathematical modelling of these measurements is dependent on

the dynamics models chosen. For this reason, Chapter III begins with an examination of the available F-4E/G sensor group and then expresses the measurements produced by these sensors in terms of the state variables defined for both models in Chapter II.

Chapter IV develops the equations for an extended Kalman filter based on the models developed in Chapters II and III. This filter is evaluated using standard Monte Carlo analysis techniques explained in Chapter V. That chapter includes the development of a trajectory generation program used as a standard of comparison, or "truth model", for filter performance.

Finally, the results of the performance evaluations are analyzed in Chapter VI and recommendations concerning further study or actual implementation are summarized in Chapter VII.

II. Dynamics Models

Model Selection Process

This chapter describes practical dynamics models used to derive a Kalman filter for the F-4E/G fire control system. As discussed in Chapter I, the crux of the Kalman filter design problem is obtaining an adequate mathematical model upon which to base the filter (1:289). For this reason, considerable time and thought has been spent on acquiring appropriate dynamics models for this study.

The general case of airborne target tracking by radar has been researched extensively in the past and numerous mathematical models already exist for this purpose (4,12, 33,34,35). These models typically involve state variables defined in terms of target position, velocity, and acceleration. Table II-1 lists several well established dynamics models for target tracking and gives references for each.

TABLE II-1

Target Tracking Dynamics Models

Model	References
Constant Velocity	1,4
Constant Acceleration	4,15
Gauss-Markov Acceleration	4,34
Constant Turn Rate	12,33
Acceleration Perpendicular to Planform	36,37

Variations of the models listed in Table II-1 may include states defined in Cartesian, spherical, or cylindrical coordinates and aligned with inertial, line-of-sight, or other reference frames. Additionally, the target's position, velocity, and acceleration states may be defined as total parameters referenced to a fixed inertial point, or alternately, as relative parameters referenced to another system element, often the tracker. Each model variation entails different assumptions, approximations, and definitions. These differences can lead to vastly different Kalman filter implementations.

For the specific case of the F-4E/G fire control system, the initial problem is to select which variations of the above models are most appropriate for this particular application. In this study, the model selection process addresses three issues:

1. adequacy of the model to describe the physical behavior of the system,
2. complexity of the model, and
3. compatibility of the model with existing F-4E/G fire control system hardware and software.

The first consideration is the adequacy of the proposed models to describe the actual physical behavior of anticipated airborne targets. In reality, the F-4E/G's targets are various types of military aircraft. Such targets undergo unpredictable accelerations with resulting changes in

velocity and position. The accelerations, although unpredictable in both direction and magnitude, are bounded by the structural g-limitations of the particular aircraft type. Small, highly maneuverable fighter aircraft are capable of higher frequency variations of acceleration over a larger range of extremes than large, less maneuverable bomber or transport aircraft. Either type of target is well described by band-limited random acceleration modelled as a first order Gauss-Markov process (6:157):

$$\frac{d\underline{a}}{dt} = -\frac{1}{\tau}\underline{a} + \underline{w} \qquad (2\text{-}1)$$

where $\underline{a}$ is the target acceleration vector, τ is a time constant of target acceleration change associated with the type of aircraft, and $\underline{w}$ is a zero-mean, white Gaussian noise vector. Other models besides the Gauss-Markov model can accurately describe the motion of randomly accelerating aircraft targets. Constant turn rate and planform-dependent acceleration models are examples (12,33,36). Conversely, constant velocity or constant acceleration models are not usually good models for randomly accelerating targets because they assume a target with either zero acceleration or a steady maneuver. However, in the case of the F-4E/G LRI function, the effect of extended target range is that random accelerations caused by target maneuvers are obscured by system noise. Indeed, the current LRI function assumes a non-maneuvering target and does not use filter-computed estimates of target acceleration (10). For this reason,

constant velocity or acceleration models might be adequate for the LRI function, but are not acceptable for ACM.

A second consideration in selecting an appropriate dynamics model for the F-4E/G filter is model complexity. Complexity becomes an issue when hardware constraints limit the amount of computer memory available for filter implementation and computer speed restricts the amount of computation possible during real time operation. As discussed in Chapter I, these constraints are severe in the F-4E/G fire control system computer. The possible 8K words of memory available for the LRI filter shrink significantly when space is reserved for complex coordinate transformations, residual monitoring algorithms, adaptive estimation techniques, or decision logic for activating either ACM or LRI filters. Using Fig. 2-1 as a guide, the maximum number of states possible for a Kalman filter implementation in the available F-4E/G computer memory is estimated to be between 12 and 15. The combination of slow speed (300 KOPS) and limited time available for each filter recursion imposes an even more severe constraint and restricts the number of filter states to the lower end of this range. In final analysis, the severe constraints of the F-4E/G fire control system hardware dictate the choice of the simplest filter possible which meets performance specifications. This situation is not uncommon in engineering applications and is often espoused as a general design philosophy in textbooks (1:290,356).

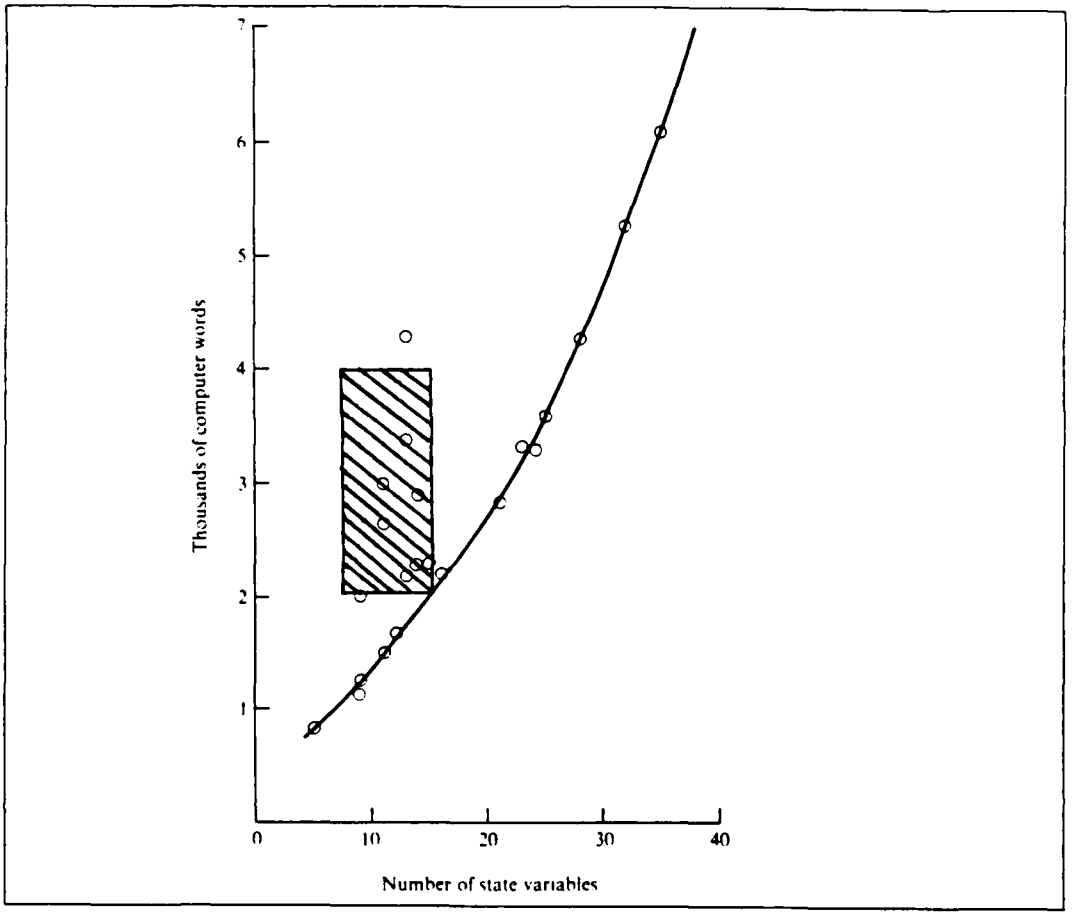

(1:355)

Fig. 2.1. Kalman Filter Computer Memory Requirements

In general, the complexity of a given Kalman filter implementation is both model dependent and geometry dependent. The choice of a particular dynamics model often determines the number of filter states required. For instance, a constant velocity model typically uses fewer states than a model which includes several acceleration states. Although the number of states is an important determinant, filter complexity is also a function of model nonlinearities

and required auxiliary computations such as coordinate transformations. These factors are closely related to the coordinate reference used to define the filter states. For example, a Gauss-Markov acceleration model results in linear dynamics equations when implemented in inertial Cartesian coordinates. The same model defined in a Cartesian line-of-sight reference has nonlinear dynamics (15,16). The increased complexity and computational burden resulting from model nonlinearity is discussed in greater detail in Chapter IV.

Given the discussion to this point, a constant velocity model defined in a reference frame which yields simple linear dynamics would be a good choice for the F-4E/G's LRI filter because it is the simplest model of those postulated as adequate. However, a third issue must be addressed before the final choice is made. The LRI function does not operate in isolation, but in conjunction with the total OFP. The LRI filter must be compatible with the ACM function and other OFP components. Also, it must make use of the existing measurements from the available F-4E/G sensor group, as will be discussed in Chapter III. The ACM function does not share the LRI assumption of a non-maneuvering target. Instead, it assumes a highly dynamic target at close range and requires filter computed estimates of the target's acceleration (10). Thus, the ACM filter demands a more complex dynamics model than LRI alone and any combined ACM/LRI filter implementation for the F-4E/G OFP must take this into account.

Using the criteria of adequacy, simplicity, and compatibility as discussed above, two candidate filters are initially proposed, one based on a constant velocity (CV) model and the other based on a Gauss-Markov acceleration (GMA) model. These models are developed in the following sections.

Constant Velocity (CV) Model

A six-state constant velocity model defined in Cartesian inertial coordinates is proposed as the basis of an acceptable LRI filter. This filter represents a solution of minimal complexity and is chosen based on the philosophy of using the simplest possible filter that yields adequate results (1:290, 6:159, 17:423). In addition to minimal state dimension, this model has the advantage of linear, time-invariant dynamics equations. These equations lead to a constant-valued state transition matrix in the filter implementation, assuming the filter measurement interval is constant. This greatly simplifies filter propagation, as explained in Chapter IV.

The major drawback of the CV model is that it does not model the target acceleration, which is a requirement for ACM. In the F-4E/G OFP, a CV-based filter would either be implemented as a separate LRI filter or integrated into a more complex ACM filter. In the context of this study, the CV filter serves as an initial demonstration of feasibility, as well as a viable LRI-only filter.

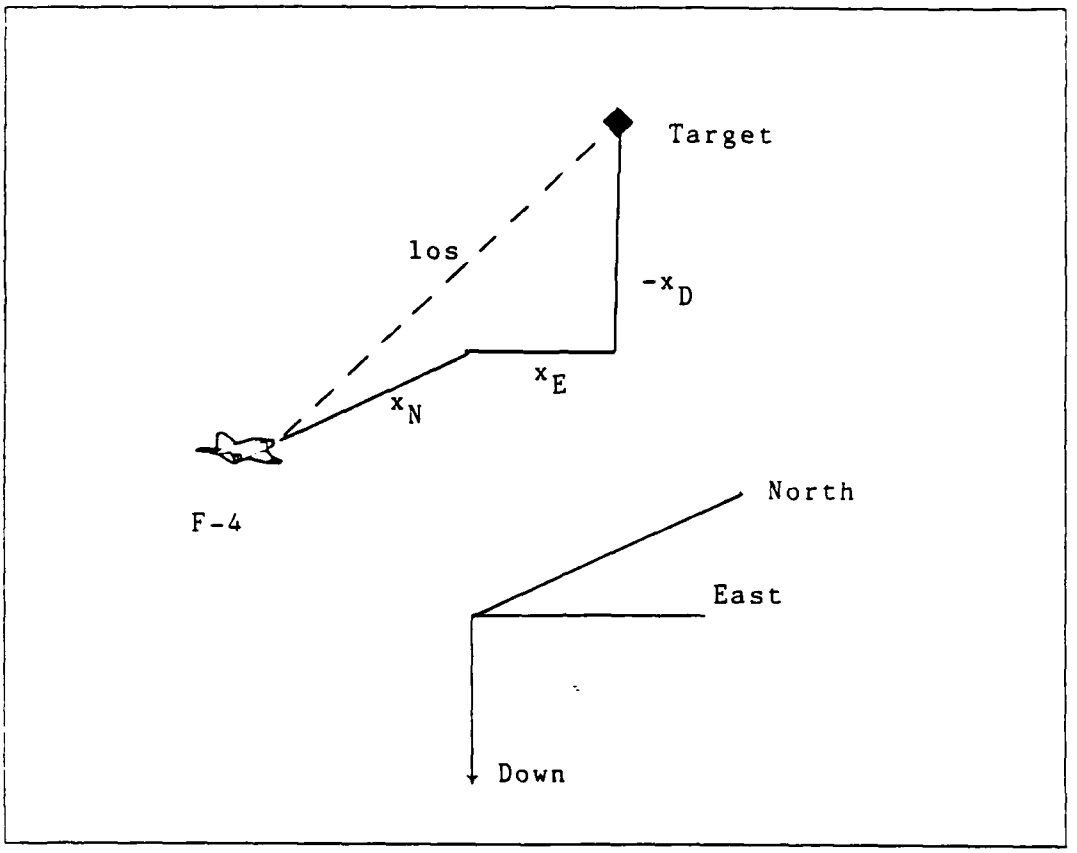

Fig. 2.2. Geographic Inertial Reference Frame

The state variables for the CV model are defined as the relative position of the target with respect to the F-4E/G tracker and the total velocity of the target with respect to an inertial reference. For this study, the inertial reference is a geographic frame fixed to the earth's surface. The three Cartesian reference axes for this frame are oriented to north, east, and down as depicted in Fig. 2.2. The effect of earth rotation is assumed neglible for the short duration encounters (1-2 minutes) and comparatively short distances (8-20 miles) anticipated in the LRI combat environment.

Two considerations motivate the choice of relative target position states. First, relative position states are limited in magnitude to the value of the target's actual range from the tracker, whereas total position states can exhibit much larger magnitudes in an earth fixed reference frame. Table II-2 contains typical values for comparison.

TABLE II-2

Maximum Magnitudes of Relative vs. Total States

State	Relative	Total
Position (feet)	182,400[a]	4,152,640[b]
Velocity (fps)	1520[c]	760[c]

[a] based on 30 nm required LRI tracking range (9)

[b] based on 683 nm combat radius (20:375)

[c] based on nominal 760 feet per second (fps) combat airspeed (10:3-417)

Numerical stability of the derived filter is improved by keeping the magnitudes of the position states as small as possible, since small differences of large numbers are a common source of numerical instability in Kalman filters (1:256). Keeping the magnitudes of the states small reduces the likelihood of this type of instability. Excessive reduction of state magnitudes, though, may result in filter outputs which lack sufficient precision. Such is the case when very large units are used in an attempt to reduce the

position state magnitudes. Target position estimates expressed in miles, for instance, are insufficiently precise for F-4E/G fire control system functions. For this reason, the OFP uses feet as the standard unit of distance. Expressing position in feet requires 14 bits to represent the largest relative position state magnitude in Table II-2 to within eight foot precision. It requires 18 bits to represent the largest total position state to the same precision (see Appendix A). Consequently, relative states produce position magnitudes which achieve the best compromise between numerical stability and precision. Note that in a computer simulation, the magnitude of total position states could be sufficiently limited by initializing the attacker at an inertial origin each time and limiting the simulation time to very short periods. However, this is not practical for the real world environment and thus, relative position states are again desirable.

A second, more important reason to use relative position states is the nature of the available F-4E/G target measurements. Radar measurements are inherently relative and require the incorporation of attacker ownship inertial position in order to generate measurements of the target's inertial position. Using relative target position states eliminates the need for F-4E/G ownship position. Since ownship position information is not available to the OFP in the F-4E/G fire control system, relative position states are, in fact, necessary.

Although similar considerations affect the choice of velocity states, the driving factor here is the enhancement of the modelling assumptions. As with position states, it is desirable from a numerics standpoint to limit the magnitudes which the velocity states can realize. Neglecting wind, inertial target velocity is limited by the target's maximum airspeed capability. Using relative velocities essentially doubles this range of values, with extremes occurring in cases of directly opposed trajectories. Table II-2 gives typical values for relative and total velocities. In this case, 7 bits achieve a 4 fps precision for the maximum total velocity value of 760 fps, while 8 bits achieve similar precision for the maximum relative velocity of 1520 fps (see Appendix A). Since it requires only one additional bit to obtain similar precision, the effect of using either of these velocity ranges is essentially the same.

A more critical consideration is again compatibility with existing OFP software. The F-4E/G's LRI function is presently designed to use total target velocity estimates from the filter. This fact in itself provides a strong incentive to use total velocity states. Further, in the CV model, the velocity states are assumed constant. The LRI function assumes a non-manuevering target, which supports the model of constant target inertial velocity. However, the F-4E/G itself must be assumed to be maneuvering into an optimal attack position. Since the attacker maneuvers, the

relative velocity is not constant and the validity of the CV model is degraded by using relative target velocity states.

Clearly, the use of relative position and total velocity states is viable, but this combination does give rise to some complicating factors. One consequence of using total target velocity states in the same model as relative position states is that the F-4E/G's ownship velocity must be calculated and subtracted from the position state dynamics equations and certain measurement equations. Fortunately, this does not create a problem in the F-4E/G because ownship velocity is already calculated in the current OFP from true airspeed and angle-of-attack inputs.

Using the states developed above, the CV model state vector is:

$$\underline{x}(t) = \begin{bmatrix} x_1(t) \\ x_2(t) \\ x_3(t) \\ x_4(t) \\ x_5(t) \\ x_6(t) \end{bmatrix} \qquad (2\text{-}2)$$

where $x_1(t)$, $x_3(t)$, and $x_5(t)$ in (2-2) are defined as the components of target position relative to the F-4E/G tracker in the north, east, and down directions respectively, (labeled x_N, x_E, and x_D in Fig. 2.2); and x_2, x_4, and x_6 are the respective north, east, and down components of the target's total inertial velocity.

The following set of differential equations governs the dynamics of the CV state vector:

$$\dot{x}_1(t) = x_2(t) - V^I_{FN}(t) \tag{2-3}$$

$$\dot{x}_2(t) = 0 + w_N(t) \tag{2-4}$$

$$\dot{x}_3(t) = x_4(t) - V^I_{FE}(t) \tag{2-5}$$

$$\dot{x}_4(t) = 0 + w_E(t) \tag{2-6}$$

$$\dot{x}_5(t) = x_6(t) - V^I_{FD}(t) \tag{2-7}$$

$$\dot{x}_6(t) = 0 + w_D(t) \tag{2-8}$$

where $\underline{V}^I_F(t)$ is a vector containing F-4E/G ownship inertial velocity at time t. Superscript I and subscript F denote inertial F-4E/G quantities, while the subscripts N, E, and D indicate north, east, and down components, respectively. The vector $\underline{w}(t)$ contains the north, east, and down components of zero-mean, white, Gaussian driving noise which are included to account for inherent modelling errors.

Errors exist in all models, especially highly simplified versions such as the CV model. These errors exist because all factors which affect the dynamics of a real world system are not included in the simple model. A reduced order model typically includes only the dominant

factors which affect the system. To account for the uncertainty introduced by modelling errors, the components of the driving noise vector, $\underline{w}(t)$, are added to the model equations. The strength of this noise, $Q(t)$, is a function of the various approximations and unmodelled effects associated with a given model.

In the CV model, target velocity is assumed constant, yet all real targets undergo some acceleration and velocity fluctuations. Even an aircraft attempting to fly straight and level at constant airspeed experiences minor velocity variations caused by complex aircraft dynamics and a variety of atmospheric conditions. At distant ranges, these small fluctuations are virtually undetectable and suggest that the terms of $Q(t)$ are small. For closer ranges or a maneuvering target, the terms of $Q(t)$ might be changed to account for greater uncertainty in the model.

Another unmodelled effect is earth rotation. Assumed neglible for brief encounters at short ranges, earth rotation becomes an increasingly significant source of error as target range and tracking time increase. Accordingly, the value of $Q(t)$ due to this effect increases with range and tends to offset the error described above.

A third source of error in the CV model is the error associated with F-4E/G ownship velocity. Mathematically, the velocity $\underline{V}_F^I(t)$ required in (2-3), (2-5), and (2-7) is the inertial velocity of the tracking radar in the nose of the aircraft. Realistically, the $\underline{V}_F^I(t)$ supplied to the OFP

is an approximation based on noise-corrupted measurements of true airspeed and angle-of-attack. There are measurement errors associated with the instruments which measure true airspeed and angle-of-attack, but within the limits of these errors, the approximation for F-4E/G inertial velocity is valid for any point on the aircraft, providing the F-4E/G has no attitude rate. When an attitude rate is present, the approximation is still valid for points lying along the aircraft's instantaneous axis of rotation, but becomes increasingly erroneous at points further from this axis. Since the F-4E/G tracking radar is located well forward of the aircraft's usual attitude rotation axis, it is reasonable to assign increased error to $\underline{V}_F^I$ during nonzero F-4E/G attitude rates and to adjust Q(t) accordingly. Correction factors for the errors in $\underline{V}_F^I(t)$ caused by F-4E/G attitude rates add significant complexity to the dynamics model. These factors are not included in this study because the constraints of the F-4E/G fire control computer require minimal complexity.

The above errors are combined into a single vector stochastic process, $\underline{w}(t)$. By virtue of the central limit theorem, $\underline{w}(t)$ is a zero-mean, white, Gaussian process, regardless of the probability distributions of the component errors (1:109). Q(t) is then expressed by the covariance

$$E\{\underline{w}(t)\underline{w}(t+\tau)^T\} = Q(t)\,\delta(\tau) \qquad (2\text{-}9)$$

Actual values for Q(t) are difficult to determine a priori. For this study, a nominal value of 5000 ft^2/sec^3 is chosen as a reasonable first guess for the diagonal elements of Q(t). This value can be increased or decreased to improve filter performance, as discussed in Chapter V. Several weaknesses in this noise model exist. First, noise strengths are assumed constant in this model. This is not true in reality because resolving target velocity into north, east, and down components yields noise strengths which are dependent on changing angular rates and accelerations. Additionally, the components of the driving noise are modelled as independent of each other and the off-diagonal terms of Q(t) are assumed zero. This aspect of the noise model is questionable because some degree of correlation among the noise components is unavoidable. These issues are not resolved in this study and provide an area for further investigation if the performance of the basic CV model does not meet the criteria outlined in Chapter I for the LRI function.

If the LRI function were the only function of the OFP requiring filtered estimates of target parameters, the CV model alone might represent an adequate filter using minimal memory and processing time. However, as discussed earlier, the F-4E/G OFP also has a requirement for target estimation in the ACM environment and this needs a more complex model than the simple CV model. For this reason, a Gauss-Markov acceleration model is also proposed.

Gauss-Markov Acceleration (GMA) Model

A nine-state Gauss-Markov acceleration model defined in Cartesian inertial coordinates is proposed as an adequate filter model for both ACM and LRI functions. This GMA model represents a modest increase in complexity when compared to the CV model, but still has an acceptably low state dimension for OFP implementation (see Fig. 2.1). The state variables chosen for the GMA model are total target acceleration, total target velocity, and target position relative to the F-4E/G tracker. All states are coordinatized in the geographic inertial coordinate system depicted in Fig. 2.2, which is identical to the frame used in the CV model. As in the CV model, the use of this non-rotating coordinate frame leads to linear, time-invariant dynamics equations and the resultant filter has benefits as described earlier, provided the time step between filter iterations is constant.

The GMA state vector is expressed as:

$$\underline{x}(t) = \begin{bmatrix} x_1(t) \\ x_2(t) \\ x_3(t) \\ x_4(t) \\ x_5(t) \\ x_6(t) \\ x_7(t) \\ x_8(t) \\ x_9(t) \end{bmatrix} \qquad (2\text{-}10)$$

where $x_1(t)$, $x_4(t)$, and $x_7(t)$ are the respective north, east, and down components of target position relative to the F-4E/G tracker (x_N, x_E, and x_D in Fig. 2.2); $x_2(t)$, $x_5(t)$, and $x_8(t)$ are north, east, and down components of target inertial velocity; and $x_3(t)$, $x_6(t)$, and $x_9(t)$ are north, east, and down components of target inertial acceleration.

The GMA model is based on the assumption that the time history of total target acceleration is well modelled by the first order Gauss-Markov process expressed in (2-1). This model has been used effectively for target tracking problems similar to the F-4E/G fire control problem (4, 6, 12). Previous work also indicates that this model is better suited for modelling total target acceleration than for describing the relative acceleration between a target and airborne tracker (15, 18, 19). For this reason, total target acceleration states are used for the GMA filter.

Total velocity states are also a logical choice for the GMA filter. As discussed in the CV model section, total velocity states enhance filter numerics slightly and also have the advantage of being in a form which is directly usable in other OFP functions. The enhancement of the CV modelling assumption is not a factor here, but total velocity is consistent with the GMA model of total acceleration. Using total velocity states with total acceleration states eliminates the need to correct for ownship acceleration in the GMA differential velocity equations, (2-12), (2-15), and (2-18) below. This is advantageous since forthcoming

versions of the OFP will phase out calculations of ownship acceleration (8). Finally, total velocity states facilitate the comparison of CV and GMA model performance for the purpose of this study.

Relative position states are used in the GMA model for the identical reasons that relative states are used in the CV model. As discussed earlier, relative position states enhance numerical stability and are compatible with available radar measurements and the available F-4E/G ownship velocity terms needed as correction factors in the differential position equations, (2-11), (2-14), and (2-17) below.

For the GMA dynamics model, the differential equations which follow from the above definitions are:

$$\dot{x}_1(t) = x_2(t) - V^I_{FN}(t) \qquad (2\text{-}11)$$

$$\dot{x}_2(t) = x_3(t) \qquad (2\text{-}12)$$

$$\dot{x}_3(t) = -\frac{1}{\tau} x_3(t) + w_N(t) \qquad (2\text{-}13)$$

$$\dot{x}_4(t) = x_5(t) - V^I_{FE}(t) \qquad (2\text{-}14)$$

$$\dot{x}_5(t) = x_6(t) \qquad (2\text{-}15)$$

$$\dot{x}_6(t) = -\frac{1}{\tau} x_6(t) + w_E(t) \qquad (2\text{-}16)$$

$$\dot{x}_7(t) = x_8(t) - V_{FD}^I(t) \tag{2-17}$$

$$\dot{x}_8(t) = x_9(t) \tag{2-18}$$

$$\dot{x}_9(t) = -\frac{1}{\tau} x_9(t) + w_D(t) \tag{2-19}$$

where $\underline{V}_F^I(t)$ is vector ownship velocity, $\underline{w}(t)$ is a vector of zero-mean, white, Gaussian driving noise, and τ is a time constant associated with target acceleration capability. The velocity $\underline{V}_F^I(t)$ is identical to the ownship velocity in the CV model. The strength of the driving noise is dependent on the modelling errors peculiar to the GMA model. Some errors such as the effect of earth rotation and attitude rate induced errors associated with $\underline{V}_F^I(t)$ are the same as in the CV model. However, structural differences in the two models lead to different strengths of driving noise. The GMA model accounts for target accelerations and thus allows changing target velocity. How close the GMA model characterizes target acceleration capability is determined largely by the accuracy of the time constant of target maneuver, τ. The value of τ is a function of the type of target aircraft and of changing flight conditions such as true airspeed and altitude. Since the value of τ varies with different targets and different conditions, the selection of any fixed value for τ leads to some degree of error. For aircraft, τ falls into a fairly narrow range, though,

and can be approximated accurately for various classes of targets. Highly maneuverable military fighter aircraft typically exhibit τ values on the order of 0.5 seconds (15), which is the value used in this study. Less maneuverable transport aircraft may have τ values of 2-3 seconds (15). For some applications, the values of τ associated with the different axes of a Cartesian coordinate system may not be identical. In this study, however, τ is given the same value for each direction because the target is assumed capable of any flight attitude and therefore equally capable of acceleration in any direction.

The value of τ is an important consideration in determining a reasonable value of Q(t) for the GMA model. As in the CV model, however, initial estimates of Q(t) are difficult to evaluate with certainty. A nominal value of 5000 ft^4/sec^5 is used as the initial value of Q(t) in this study. This value is not directly comparable to the value chosen for the CV model because $\underline{w}(t)$ represents different effects in the two models. Additionally, the units are different from those used for noise entering at the velocity level, as in the CV model. Both values of Q(t) are considered nominal starting points for the filter tuning procedure discussed later.

The GMA-based filter is expected to produce target velocity and acceleration estimates which meet the performance criteria detailed in Chapter I. If its actual performance does not meet this criteria in the computer simulation,

other models might be considered, including higher order models.

Summary

This chapter has defined dynamics models for a Kalman filter suitable for the F-4E/G fire control system. Each model described has well defined state variables. In the next chapter, the available measurements on the F-4E/G are examined and mathematically modelled in terms of the state variables just defined.

III. Measurement Models

Measurement Feedback in Kalman Filters

Real world estimators based on simplified mathematical models require feedback to control uncertainties associated with those models. Each dynamics model developed in the previous chapter potentially provides a basis for an open loop estimator of F-4E/G target parameters. Such an estimator would rapidly accumulate large errors caused by random inputs from the environment and by inherent deficiencies of the model itself. To prevent errors from growing unbounded, practical estimators employ feedback of measured quantities from the real dynamic system (7:421). In Kalman filter algorithms, the feedback of measurements is implemented in a predictor-corrector structure. Available measurements are modelled mathematically in terms of state variables from the dynamics equations. This model is included in the filter algorithm and produces a prediction of the measurement vector for each measurement time. The predicted measurements are subtracted from the actual measurements to form a residual (innovation) which is in turn multiplied by an optimal weighting matrix to form a correction factor. This factor is applied to the current output of the dynamics model to produce a corrected state estimate (1:217,218).

Deriving an accurate measurement model requires extensive knowledge of the physical nature of available measurements.

In the F-4E/G, the available measurements are limited to those produced by existing equipment in the fire control system. Consequently, this chapter's discussion of measurement models begins with a survey of the hardware comprising the available F-4E/G sensor group. The measurements produced by this set of existing sensors are analyzed and catalogued. The section following this hardware survey then develops the actual equations used to model each measurement in terms of CV or GMA state variables. Finally, the chapter concludes with a characterization of the errors associated with each measurement.

Available F-4E/G Sensor Group

The F-4E/G fire control computer receives inputs from several onboard sources. These inputs include discrete system controls as well as digital measurement data obtained through analog-to-digital (A/D) conversion of sensor signals. The measurements of primary importance to the target tracking filter originate in the radar, INS, and CADC subsystems. Fig. 3.1 illustrates the interrelationships of these and other fire control subsystems.

The APQ-120 radar is a complex multipurpose radar system with numerous configurations and operating modes. The only operating mode of interest for this study is the air-to-air tracking mode. In this mode, the radar functions as a typical conical scan airborne intercept (AI) radar capable of both range and angle tracking (21:2-1, 2-150). The tracker

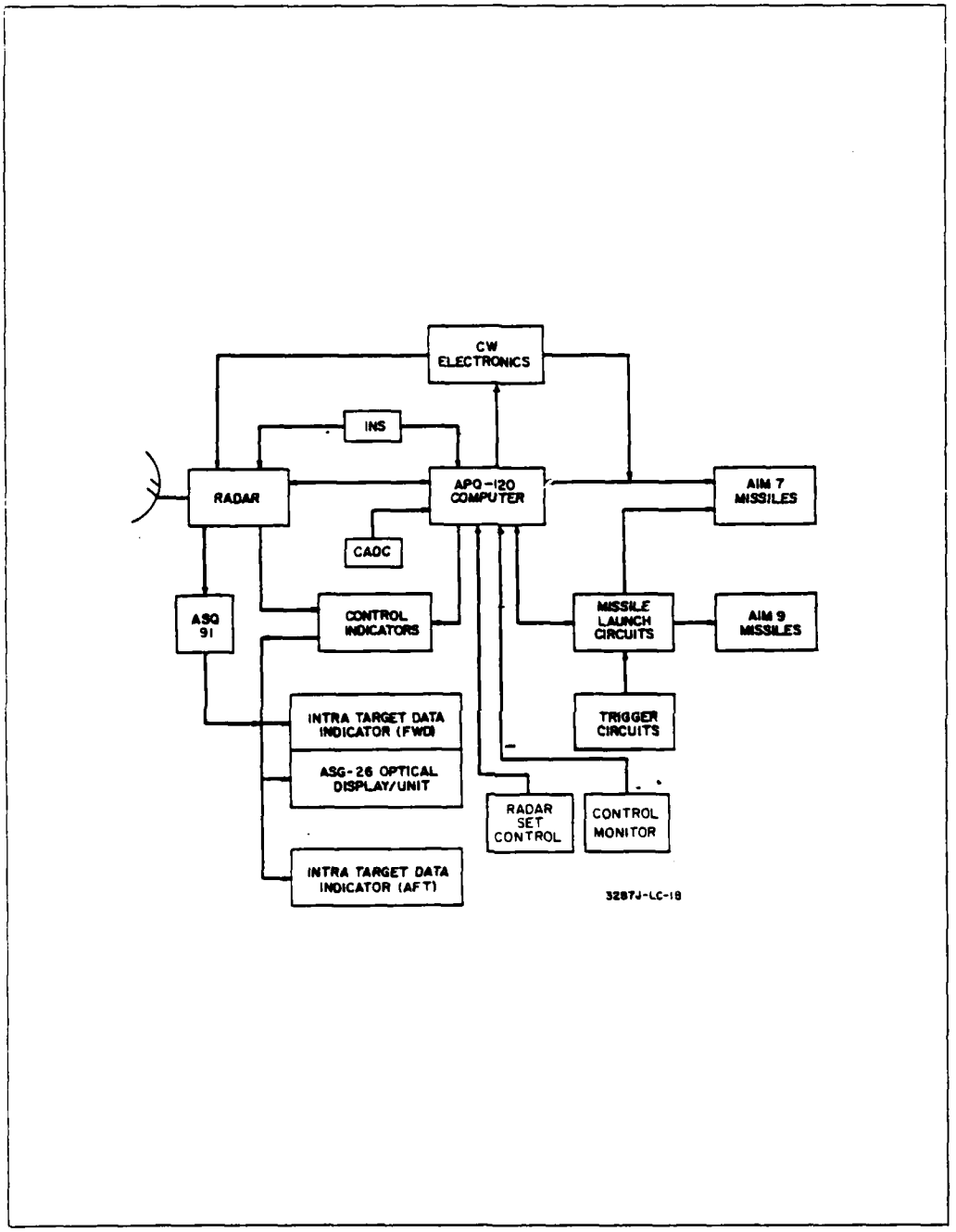

(20:2-3)

Fig. 3.1. APQ-120 Fire Control System Block Diagram

antenna is gimbal mounted, allowing ± 60° of travel in both azimuth and elevation. The radar has two pulse repetition rates (prf), one for long range, low resolution operation, and the other for short range, high resolution operation. These and other detailed performance specifications are given in Reference 21, Section 2.

The radar subsystem consists of over 20 separate components, designated as line replaceable units (LRU's). A full listing of radar LRU's is available in Reference 21, Section 5. Table III-1 lists important LRU's which produce or process radar measurements.

TABLE III-1

APQ-120 Radar Line Replaceable Units

LRU Number	Description
1	Digital ACM computer[a]
4	Gyro-stabilized platform
7	Antenna control (servo assembly)
16	Antenna, including gimbal assembly, feedhorn, reflector, and rate gyros
17	Electrical synchronizer

[a]Although not strictly a radar component, the fire control computer performs radar control functions in some modes and is included as a radar LRU. These control functions are not related to the filter function of the computer (20, 21).

Various LRU's produce different measurements, a fact that has significant implications for error models. For example, a single circuit in the electrical synchronizer (LRU 17)

produces both the range (R) and range rate ($\dot{R}$) measurements (21:2-19, 2-143). This leads to correlated noise corruption between R and $\dot{R}$ measurements as discussed subsequently in this chapter. Conversely, separate sets of induction potentiometers and resolvers in the antenna gimbal assembly produce the antenna azimuth and elevation angle signals, λ_a and λ_e. Also, separate rate gyros measure the antenna spatial rate components, ω_k, azimuth rate, and ω_j, elevation rate (21:2-19,3-341). Although common power plant and mechanical interconnection contribute some noise correlation, these devices are assumed sufficiently separated to produce four measurements which are independent of each other and of the range and range rate signals as well.

The F-4E/G INS is primarily a navigation device, but also provides measurements of aircraft pitch (θ), roll (Φ), and heading (Ψ) angles to the fire control system. These angles do not directly provide target information, but allow radar measurements made in radar reference (i_o, j_o, k_o) coordinates to be transformed to geographic (N,E,D) coordinates (see Appendix C). The CADC uses inputs from the F-4E/G pitot-static system and angle-of-attack sensors to calculate altitude, true airspeed (TAS), and stall warning signals for the cockpit. The CADC TAS and true angle-of-attack (α) measurements also provide the OFP with the ownship velocity aiding terms required in the Kalman filter dynamics models, Equations (2-3), (2-5), (2-7) and (2-11), (2-14), (2-17).

In addition to the measurements above, the radar, INS, CADC, and other aircraft systems send and receive numerous measurements and control signals to the fire control computer. Fig. 3.2 shows the overall flow of information in the fire control system. Most of these signals are of peripheral interest in this study and are included here only to provide context. The focus remains on the measurements already described.

The format in which the computer processes and stores these measurements is important. Prior to storage, the analog sensor signals are conditioned by buffering, prescaling, multiplexing, and A/D conversion. Each of these operations is an additional source of measurement noise corruption, as explained later. The conditioned measurements leave the A/D converter appropriately scaled and are loaded directly into core memory (20:2-50,2-66). Some measurements are given two different scalings and stored as two separate values. Range, for instance, is stored in one location as Coarse Range with a least significant bit (LSB) value of 232 feet per bit (air-to-air mode), and stored in another location as Fine Range with a LSB valued at 58.4 feet per bit (20:2-279). All angle measurements (λ_a, λ_e, θ, ϕ, Ψ) are also stored as two separate measurements, one representing the sine of the angle and the other the cosine. Table III-2 lists all measurements available to the fire control computer as they are actually stored in the computer memory.

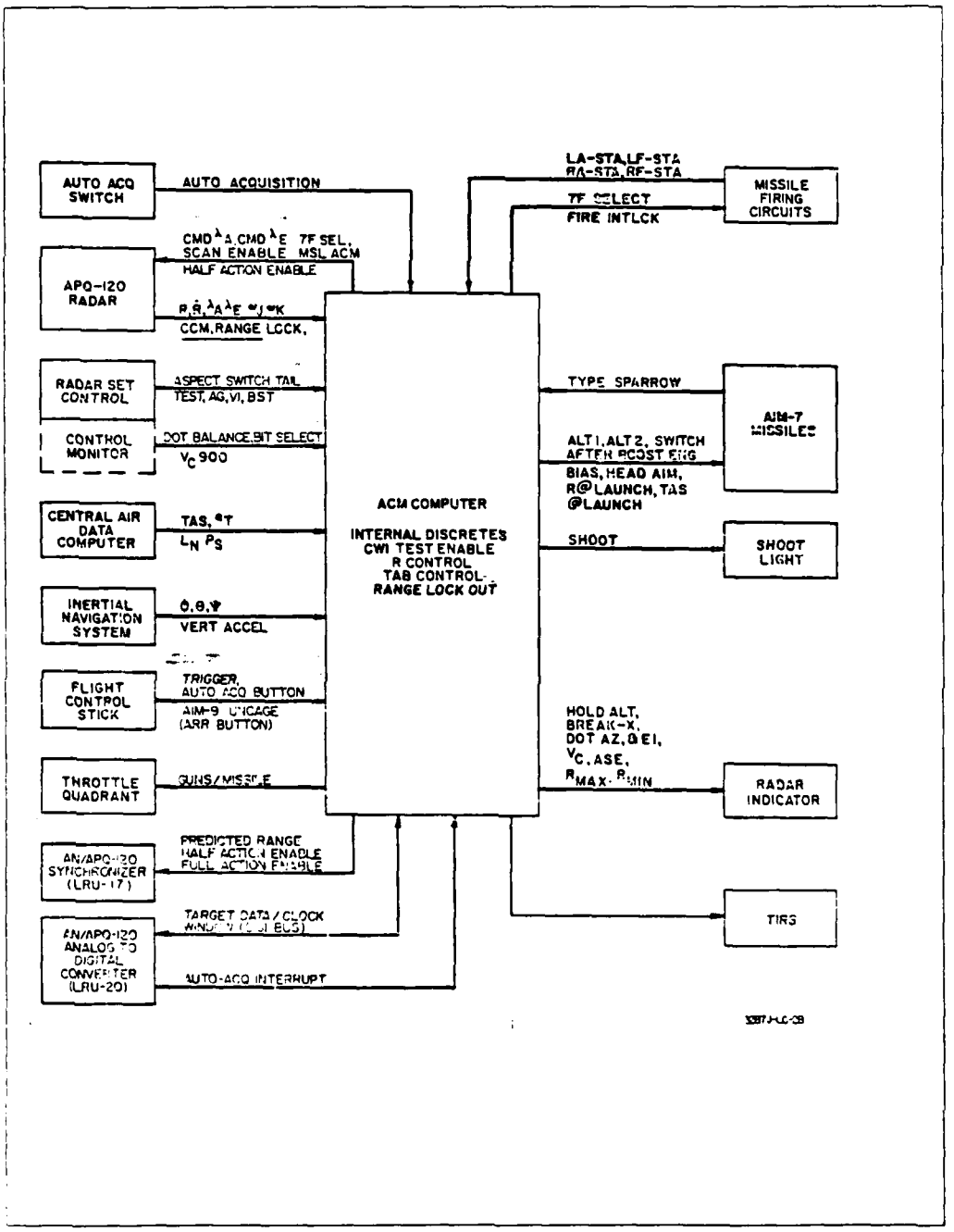

(20:2-5)

Fig. 3.2. Computer Inputs and Outputs

TABLE III-2 (sheet 1 of 2)

Measurement Storage in Computer Memory

DMA LOCATION (OCTAL)	DESCRIPTION	INPUT SOURCE
000	Clock	
001	Discrete Inputs	--
002	Discrete Inputs	--
003	Spare	
004	Spare	
005	Spare	
006	Spare	
007	Spare	
010	Spare	
011	Spare	
012	Spare	
013	Spare	
014	Pitch Cosine Component	INS Synchro Receiver
015	Pitch Sine Component	INS Synchro Receiver
016	Roll Cosine Component	INS Synchro Receiver
017	Roll Sine Component	INS Synchro Receiver
020	Antenna Rate Azimuth	Radar
021	Antenna Rate Elevation	Radar
022	Range Fine	Radar
023	Range Coarse	Radar
024	Spare	
025	Range Rate Fine	Radar
026	True Airspeed	CADC
027	Vertical Acceleration	INS
030	Log of Pressure Coarse	CADC
031	Spare	
032	Spare	
033	Log of Pressure Fine	CADC
034	Cosine Antenna Azimuth Angle	Radar Antenna
035	Sine Antenna Azimuth Angle	Radar Antenna
036	Cosine Antenna Elevation Angle	Radar Antenna
037	Sine Antenna Elevation Angle	Radar Antenna

(23:A7-6)

TABLE III-2 (sheet 2 of 2)

Measurement Storage in Computer Memory

DMA LOCATION (OCTAL)	DESCRIPTION	INPUT SOURCE
040	Range Rate Coarse	Radar
041	Aspect Switch	Radar Set Control Unit
042	Spare	
043	Spare	
044	Spare	
045	Spare	
046	Spare	
047	Spare	
050	Spare	
051	Spare	
052	Spare	
053	Spare	
054	Spare	
055	Spare	
056	Yaw Cosine Component	INS Synchro Receiver
057	Yaw Sine Component	INS Synchro Receiver
060	Spare	
061	Spare	
062	Spare	
063	Spare	
064	Spare	
065	Spare	
066	Spare	
067	Spare	
070	Spare	
071	Spare	
072	Spare	
073	Spare	
074	A.C. Reference Voltage	Computer Power Supply
075	Angle of Attack	CADC
076	Spare	
077	Spare	

(23:A7-7)

These measurements form a fixed set of information available to a Kalman filter. In the next section, measurements selected from this set are mathematically modelled in terms of the state variables defined by the dynamics models of Chapter II.

Measurement Model Equations

In the previous section, the entire list of available measurements produced by the existing F-4E/G sensor group was examined. From this group, six radar measurements are now selected as Kalman filter inputs. These six are range (R), range rate ($\dot{R}$), sine of the antenna azimuth gimbal angle (sin λ_a), sine of the antenna elevation gimbal angle (sin λ_e), azimuth component of antenna spatial rate (ω_k), and elevation component of antenna spatial rate (ω_j). The fine scaling for R and $\dot{R}$ is used since this is the normal scale for airborne targets inside 50 miles (21:2-38). In the case of antenna gimbal angles, the cosine information is discarded since the sine completely specifies any angle in the allowable range of ± 60°. This section develops equations to model each of the above measurements.

In terms of the position states defined in Fig. 2.2, the range from the radar to the target is given by

$$R = (x_N^2(t) + x_E^2(t) + x_D^2(t))^{\frac{1}{2}} \qquad (3-1)$$

where N, E, and D can be replaced by 1, 3, and 5 for the CV model or 1, 4, and 7 for the GMA model. Taking the time

deriviative yields the expression for range rate. Deleting time arguments for compactness, $\dot{R}$ is expressed in terms of CV states as

$$\dot{R} = \frac{x_1\dot{x}_1 + x_3\dot{x}_3 + x_5\dot{x}_5}{(x_1^2 + x_3^2 + x_5^2)^{\frac{1}{2}}} \tag{3-2}$$

Substituting (2-3), (2-5), (2-7), and (3-1) yields

$$\dot{R} = \frac{x_1(x_2 - V_{FN}^I) + x_3(x_4 - V_{FE}^I) + x_5(x_6 - V_{FD}^I)}{R} \tag{3-3}$$

For mathematical compatibility, the ownship velocity terms in (3-3) must be expressed in the same coordinate system as the state vector. Thus, $\underline{V}_F^I$ must be expressed in the geographic (N,E,D) inertial reference. In this study, superscript G implies quantities that are expressed in this specific inertial frame. Initially, the F-4E/G velocity vector is available to the OFP in radar reference coordinates (superscript R), as shown in Appendix C, transformation 1:

$$\underline{V}_F^R = \begin{bmatrix} \text{TAS } \cos(\alpha) \\ 0 \\ \text{TAS } \sin(\alpha) \end{bmatrix} \tag{3-4}$$

Obtaining the correct velocity components requires a coordinate transformation from radar reference (i_o, j_o, k_o) coordinates to geographic (N,E,D) coordinates given by

$$\underline{V}_F^G = [T_R^G]\ \underline{V}_F^R \tag{3-5}$$

where $[T_R^G]$ is the required transformation matrix (see Appendix C, transformation 2).

There is some ambiguity in the available F-4E/G documentation concerning the angles λ_a and λ_e. This study assumes that they are the actual radar gimbal angles illustrated in Fig. 3.3. Azimuth gimbal angle, λ_a, is defined as the angle between the radar reference i_o-axis and the projection of the line-of-sight (los) vector on the i_o-j_o plane. Elevation gimbal angle, λ_e, is the angle between the los and its projection on the i_o-j_o plane. Antenna pointing error is ignored, so the antenna boresight line coincides with the los. These definitions are consistent with References 10 and 20. However, Reference 14 describes azimuth and elevation space angles, A_s and E_s, used in the fire control system. These angles are defined in space (x,y,z) coordinates as shown in Fig. 3.4. Aircraft pitch (θ) and roll (ϕ) relate space coordinates to aircraft body (l,m,n) coordinates. A two degree offset angle between the body l-axis and the radar reference i_o-axis is described in Reference 10, but is left ambiguous in the discussion of A_s and E_s in Reference 14. This study includes the two degree angle in coordinate transformations, as shown in Appendix C.

The A_s and E_s signals are used exclusively to generate space stabilized cockpit displays. Pitch and roll signals from the INS are sent to the gyro-stabilized platform (LRU 4) where they are used to convert λ_a and λ_e to A_s and E_s. A_s and E_s are then sent to the control indicator

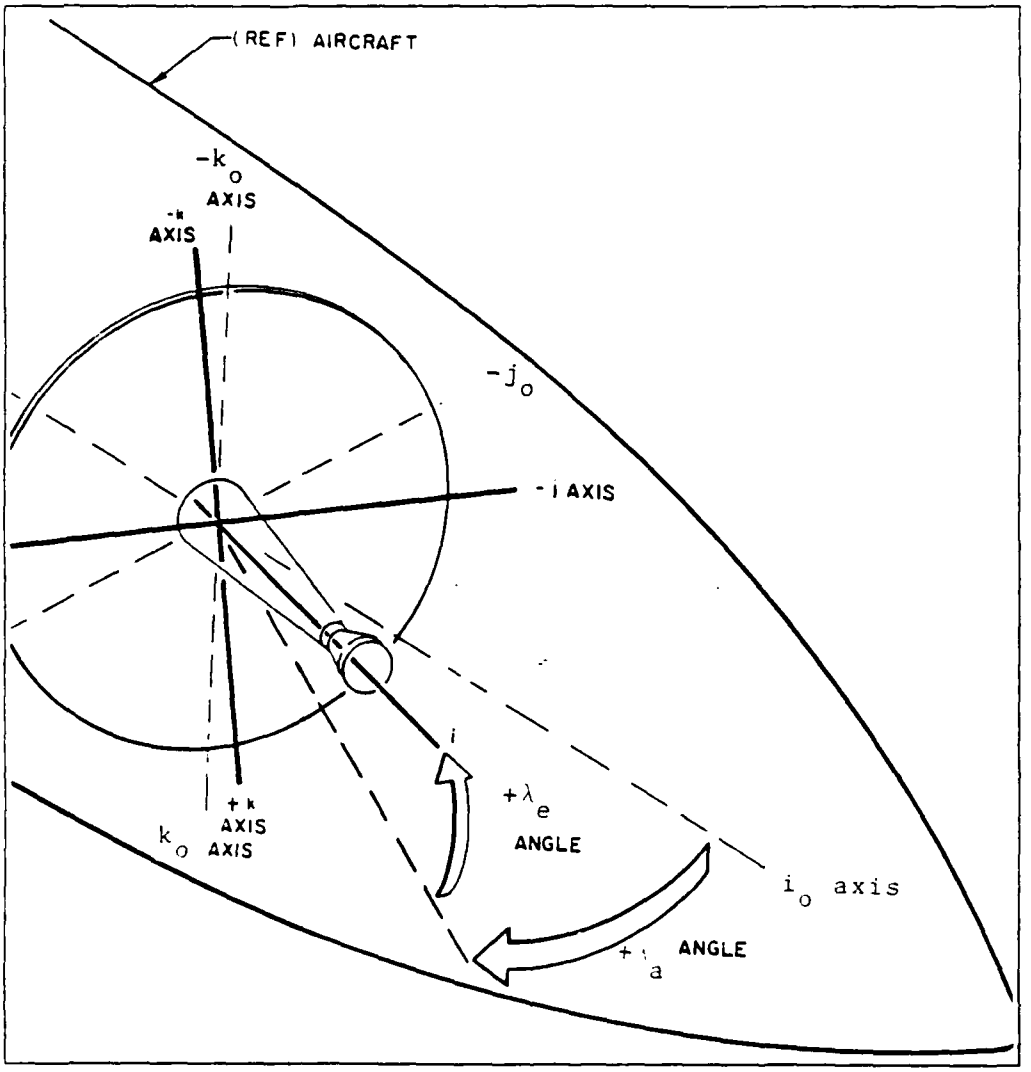

Adapted from (14:2-18)

Fig. 3.3. Antenna Gimbal Angles in Radar Reference Frame

(LRU 11) where they are used to produce a space stabilized horizon line and sweep display on cockpit radar scopes. They are not used by the computer (LRU 1), which receives its angle signals from the electrical synchronizer (LRU 17) (14:2-13,2-20, 21:2-130,2-131). For this reason, the A_s and

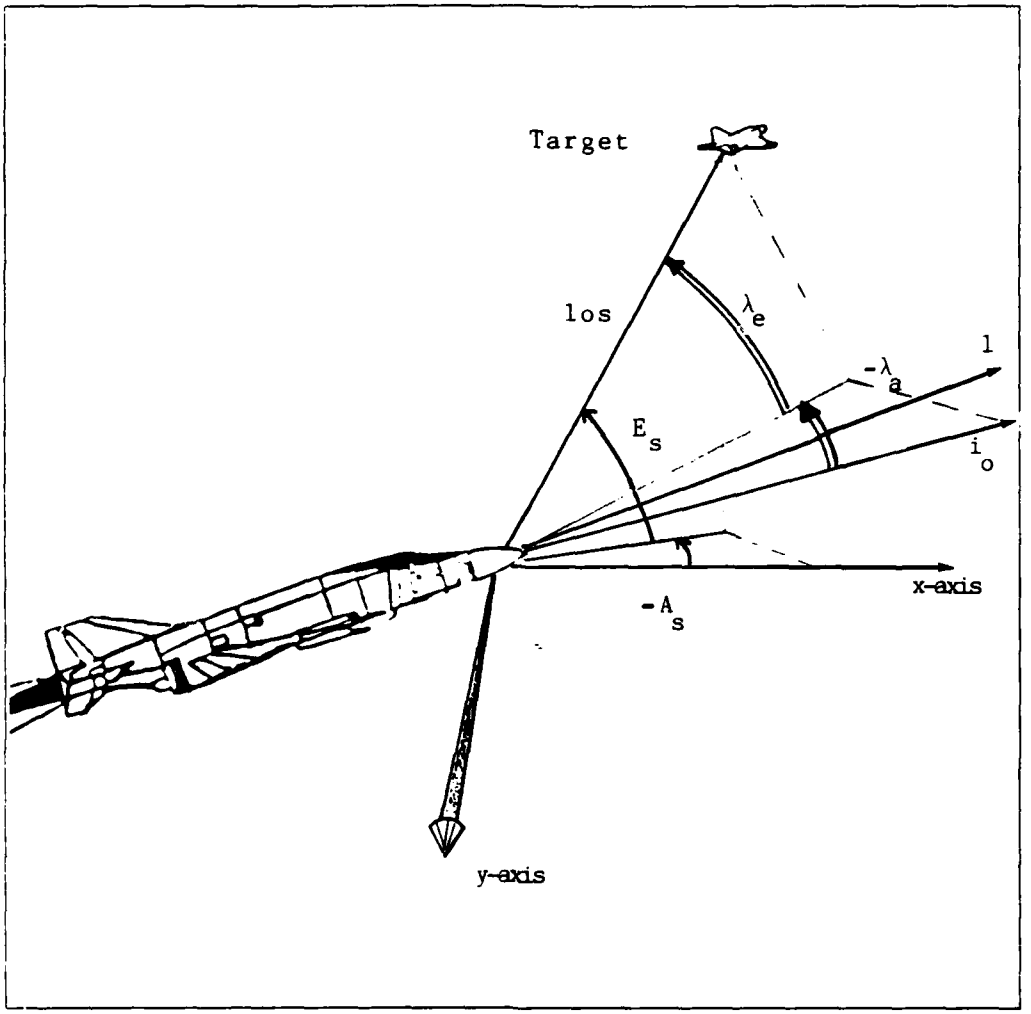

Fig. 3.4. Space and Gimbal Angles

E_s angles are not used in this study. The angles available to the F-4E/G fire control computer are assumed to be the antenna gimbal angles defined with respect to the radar reference (i_o, j_o, k_o) coordinate frame, as shown in Fig. 3.3.

Measurement model equations for the gimbal angles are obtained from trigometric relationships. If antenna pointing error is ignored, the i_o, j_o, and k_o components of the

los vector can be used in right triangle relationships to express the sine of either gimbal angle. Next, the i_o, j_o, and k_o components are expressed in terms of CV or GMA state variables by applying the inverse of the $[T_R^G]$ coordinate transformation used earlier. In radar reference coordinates, the trigometric relation for the sine of the antenna azimuth angle is given by

$$\sin \lambda_a = \frac{x_{jo}}{(x_{io}^2 + x_{jo}^2)^{\frac{1}{2}}} \tag{3-6}$$

The required transformation is illustrated in Fig. 3.5 and is expressed as

$$\begin{bmatrix} x_{io} \\ x_{jo} \\ x_{ko} \end{bmatrix} = [T_G^R] \begin{bmatrix} x_N \\ x_E \\ x_D \end{bmatrix} \tag{3-7}$$

Replacing x_{io} and x_{jo} in (3-6) with N, E, and D terms obtained in (3-7) yields

$$\sin \lambda_a = \frac{T_{21}x_N + T_{22}x_E + T_{23}x_D}{\{(T_{11}x_N+T_{12}x_E+T_{13}x_D)^2 + (T_{21}x_N+T_{22}x_E+T_{23}x_D)^2\}^{\frac{1}{2}}} \tag{3-8}$$

where T_{mn} is the m,n-th element of the transformation matrix described in Appendix C, transformation 3. Substituting the indices 1, 3, 5 or 1, 4, 7 for N, E, D gives the respective CV or GMA expressions.

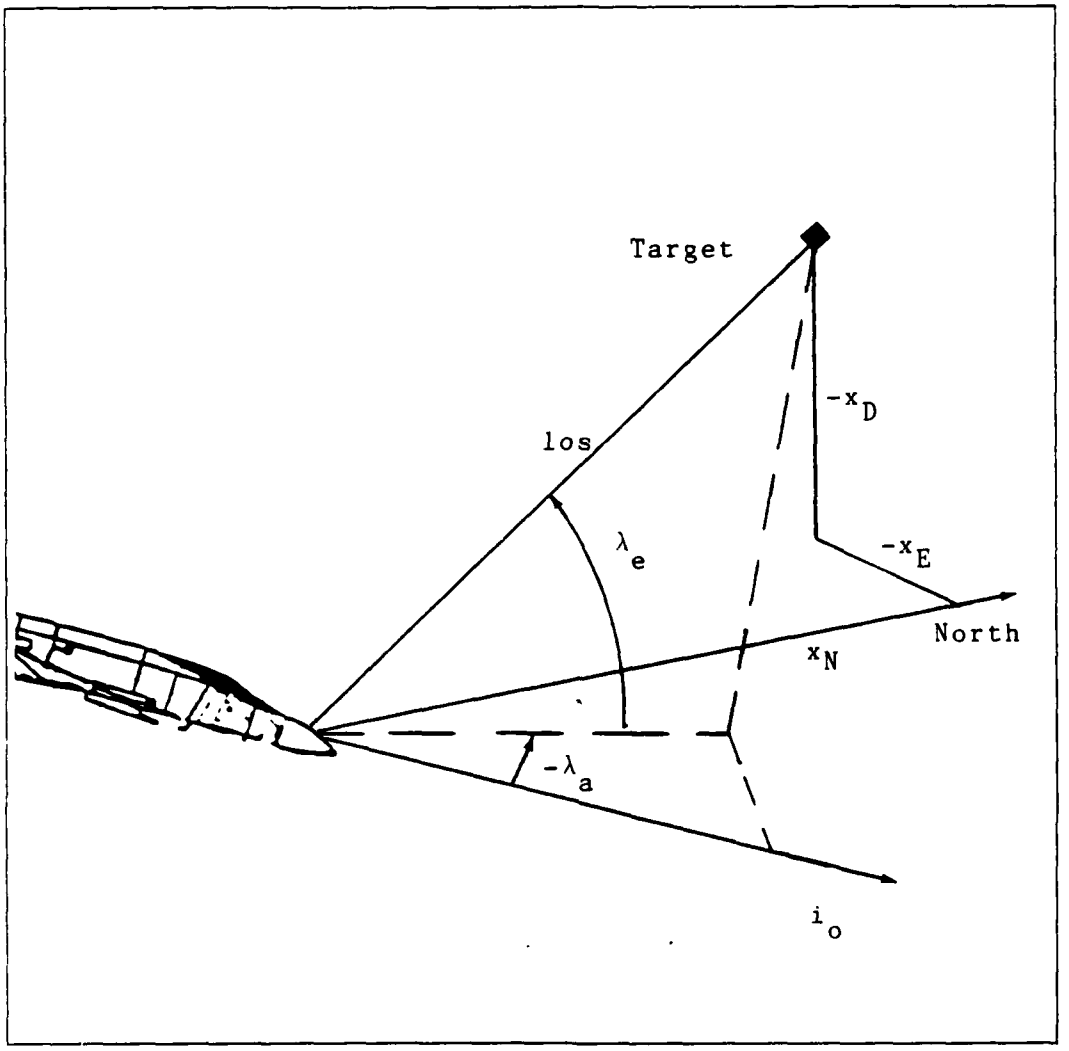

Fig. 3.5. Radar Reference and Geographic Coordinates

In an analagous manner, the sine of the antenna elevation angle is described by

$$\sin \lambda_e = \frac{-(T_{31}x_N + T_{32}x_E + T_{33}x_D)}{(x_N^2 + x_E^2 + x_D^2)^{\frac{1}{2}}} \qquad (3\text{-}9)$$

T_{mn} terms are not required in the denominator of (3-9) because the magnitude of the los vector is the same

regardless of coordinate frame. The previously defined range equation, (3-1), defines this quantity.

The remaining radar measurements are the outputs of two antenna-mounted rate gyros. The gyros measure two orthogonal components of the antenna's angular rate in inertial space, or spatial rate. Expressed in antenna (i,j,k) coordinates, the total antenna rate is represented by the vector, $\underline{\omega}_A^A$, where subscript A denotes antenna spatial rate and superscript A indicates the rates are expressed in antenna coordinates. One rate gyro is mounted so that it measures the component of $\underline{\omega}_A^A$ about the k-axis, ω_k, and the other gyro measures the component of $\underline{\omega}_A^A$ about the j-axis, ω_j. Fig. 3.6 illustrates these two measurements. Note that the third component, ω_i, is meaningless for a point target lying on the i-axis. The target will always lie on the antenna i-axis under the assumption of negligible pointing error, and thus, ω_j and ω_k completely characterize $\underline{\omega}_A^A$. Since the above assumption implies that the antenna i-axis and the target los are coincident, the measured antenna rate also approximates the instantaneous los rate. This approximation can be used to model the antenna rate measurements.

Using ω_j and ω_k as approximate los rate components, the target's relative velocity vector can be expressed in antenna (i,j,k) coordinates by

$$\underline{V}_{rel}^A = \begin{bmatrix} \dot{R} \\ R\omega_k \\ -R\omega_j \end{bmatrix} \qquad (3\text{-}10)$$

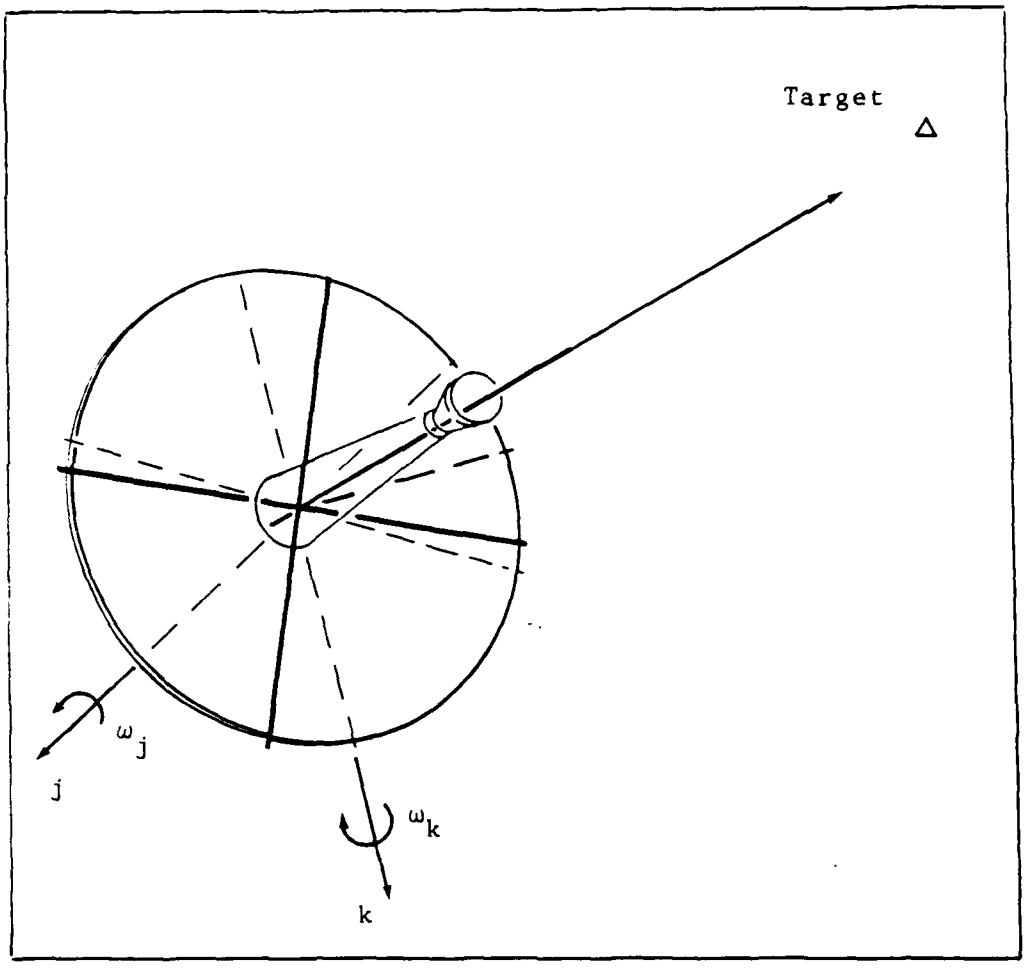

Fig. 3.6. Antenna Motion Through Space Measured in Antenna Coordinates

where R and $\dot{R}$ are the available range and range rate measurements (10:3-412). The same velocity vector can be expressed in geographic (N,E,D) coordinates using velocity states from the dynamics model and previously calculated ownship velocity terms. Expressed in CV model states, the vector is

$$\underline{V}^G_{rel} = \begin{bmatrix} x_2 - V^G_{FN} \\ x_4 - V^G_{FE} \\ x_6 - V^G_{FD} \end{bmatrix} \tag{3-11}$$

Since $\underline{V}^A_{rel}$ and $\underline{V}^G_{rel}$ represent the same vector in different coordinates, they can be related by a coordinate transformation defined by aircraft attitude angles provided by the INS, and the antenna gimbal angles. This coordinate transformation is expressed as

$$\begin{bmatrix} \dot{R} \\ R\omega_k \\ -R\omega_j \end{bmatrix} = [T^A_G] \begin{bmatrix} x_4 - V^G_{FN} \\ x_4 - V^G_{FE} \\ x_6 - V^G_{FD} \end{bmatrix} \tag{3-12}$$

where $[T^A_G]$ is now the matrix for transforming geographic coordinates to antenna coordinates (Appendix C, transformation 4). Equating terms and dividing through by R yields the desired measurement equations.

$$\omega_j = -\frac{T_{31}(x_2 - V^G_{FN}) + T_{32}(x_4 - V^G_{FE}) + T_{33}(x_6 - V^G_{FD})}{R} \tag{3-13}$$

$$\omega_k = \frac{T_{21}(x_2 - V^G_{FN}) + T_{22}(x_4 - V^G_{FE}) + T_{23}(x_6 - V^G_{FD})}{R} \tag{3-14}$$

Note that an equation for range rate also results.

$$\dot{R} = T_{11}(x_2 - V^G_{FN}) + T_{12}(x_4 - V^G_{FE}) + T_{13}(x_6 - V^G_{FD}) \qquad (3\text{-}15)$$

This equation could conceivably replace the range rate equation expressed by (3-3), but is not used in this study. The previously described range rate equation is superior for practical implementation, since [T] matrix elements, a potential source of error in finite wordlength computers are not required. A comparison of (3-3) and (3-15) also reveals an alternate method of calculating the first row of the [T] matrix, by equating coefficients of common terms.

The complete measurement models for both CV and GMA filters are now summarized. The selected measurements have been deterministically expressed as functions of both the state vector and independent functions of time. The six measurements are now combined into a single vector of functions denoted by $\underline{h}[\underline{x}(t),t]$ and defined as

$$\underline{h}[\underline{x}(t),t] = \begin{bmatrix} R \\ \dot{R} \\ \sin \lambda_a \\ \sin \lambda_e \\ \omega_j \\ \omega_k \end{bmatrix} \qquad (3\text{-}16)$$

This definition is not adequate because it fails to describe the effect of the random environmental disturbances which corrupt all physical measurements. To account for these uncertainties, additive noise is included in the measurement model. The vector of sampled-data measurements can then be expressed as

$$\underline{z}(t_i) = \underline{h}[\underline{x}(t_i), t_i] + \underline{v}(t_i) \tag{3-17}$$

where $\underline{v}(t_i)$ is a vector of zero-mean, white Gaussian noise included to account for the random disturbances which corrupt the measurements. Substituting the expressions previously derived into (3-17) and using CV state variables yields the following measurement equations, where time arguments are implicit:

$$z_1 = (x_1^2 + x_3^2 + x_5^2)^{\frac{1}{2}} + v_1 \tag{3-18}$$

$$z_2 = \frac{x_1(x_2 - V_{FN}^G) + x_3(x_4 - V_{FE}^G) + x_5(x_6 - V_{FD}^G)}{(x_1^2 + x_3^2 + x_5^2)^{\frac{1}{2}}} + v_2 \tag{3-19}$$

$$z_3 = \frac{T_{21}x_1 + T_{22}x_3 + T_{23}x_5}{(T_{11}x_1 + T_{12}x_3 + T_{13}x_5)^2 + (T_{21}x_1 + T_{22}x_3 + T_{23}x_5)^2)^{\frac{1}{2}}} + v_3 \tag{3-20}$$

$$z_4 = \frac{-(T_{31}x_1 + T_{32}x_3 + T_{33}x_5)}{(x_1^2 + x_3^2 + x_5^2)^{\frac{1}{2}}} \tag{3-21}$$

$$z_5 = - \frac{T_{31}(x_2 - V_{FN}^G) + T_{32}(x_4 - V_{FE}^G) + T_{33}(x_6 - V_{FD}^G)}{(x_1^2 + x_3^2 + x_5^2)^{\frac{1}{2}}} + v_5 \tag{3-22}$$

$$z_6 = \frac{T_{21}(x_2 - V_{FN}^G) + T_{22}(x_4 - V_{FE}^G) + T_{23}(x_6 - V_{FD}^G)}{(x_1^2 + x_3^2 + x_5^2)^{\frac{1}{2}}} + v_6 \tag{3-23}$$

Measurement equations for the GMA model are identical to (3-18) through (3-23) with the state variables appropriately renumbered. The nature of the noise corruption terms, $\underline{v}(t_i)$, and values associated with them are discussed in the next section.

Error Sources in Radar Measurements

The final consideration needed to complete the Kalman filter measurement model is a mathematical characterization of measurement noise. As mentioned earlier, all real measurements of physical quantities include noise, which is the combined result of several different physical effects. Although each separate effect may not individually possess a Gaussian distribution, the combined effect of several small scale effects can be modelled in terms of Gaussian random variables by virtue of the central limit theorem. It is the fact that measurement noise stems from a variety of independent sources that allows it to be adequately modelled as a zero-mean, white Gaussian process. In the Kalman filter context, the measurements form an m-vector, $\underline{v}(t_i)$, which

embodies the above properties in the statistics

$$E\{\underline{v}(t_i)\} = \underline{0} \tag{3-24}$$

$$E\{\underline{v}(t_i)\underline{v}^T(t_j)\} = [R]\,\delta_{ij} \tag{3-25}$$

where E{*} is the expectation operation and [R] is an m x m matrix. The diagonal terms of [R] correspond to the noise variances of the six measurements in the measurement vector. In the case of independent measurements, the off-diagonal elements of [R] are all zero. However, any measurements which exhibit correlated noise properties as a result of physical interrelationship produce non-zero cross terms in [R] matrix row/column intersections common to both measurements. The range and range rate measurements produced by the F-4E/G fire control system are examples of such cross correlated measurements. They are both processed by a single pair of cascade integrators in the electrical synchronizer (LRU 17), and share the thermal noise level present in that circuit. The noise correlation is not total because noise sources other than circuit thermal noise independently corrupt these measurements.

Actual values of [R] matrix terms can be determined by theoretical analysis of the sensor devices or by statistical reduction of experimental data. Both techniques are used in this study. Engineers at Hill, AFB, Utah provided recommended variances for range, range rate, gimbal angle, and angle rate measurements based on actual flight tests (24).

This information is augmented by data from a computer experiment used to determine variances for sin λ_a and sin λ_e. Typical values of conical scan AI radar accuracies listed in standard textbooks and F-4E/G maintenance manuals are also compared during filter tuning (14, 21, 25). Table III-3 summarizes the actual variance values used for both the CV and GMA measurement models.

TABLE III-3

Measurement Noise Variances for F-4E/G LRI Filter

Measurement	1-Sigma	Variance
Range	67 feet	4489
Range Rate	16 fps	256
Sin λ_a	1.05×10^{-3}	1.10×10^{-6}
Sin λ_e	1.05×10^{-3}	1.10×10^{-6}
ω_j	3.49×10^{-3} rad/s	1.22×10^{-5}
ω_k	3.49×10^{-3} rad/s	1.22×10^{-5}

An additional consideration in determining appropriate [R] matrix values for this study is the constrained wordlength of OFP measurements. Although the LRU-1 computer itself has 16-bit wordlength, the A/D converter which processes the measurements prior to storage in the computer allows only 10-bit wordlength. This restriction can affect the variance of measurement error under certain conditions.

For example, at maximum LRI ranges, the A/D converter's wordlength restriction causes the least significant bit of the range measurement to have a value of 256 feet. This is effectively a 3-sigma value for the range measurement and corresponds to a variance of 7282, or about twice the range variance listed in Table III-3.

The above quantification of measurement noise completes the development of models needed to form the basis of a Kalman filter. The implementation of these models in an extended Kalman filter format is the subject of the next chapter.

IV. Filter Implementation

Extended Kalman Filter

Model nonlinearities are an intrinsic characteristic of the air-to-air tracking problem. As discussed in Chapter II, the state variables of the CV, GMA, and other dynamics models can be defined as total or relative states and referenced to any of several inertial or line-of-sight coordinate frames. Regardless of the state variable definitions and reference frame used, each formulation leads to nonlinearities in either the dynamics model, the measurement model, or both (15,16). It is these inherent nonlinearities of the tracking problem which preclude exclusive use of conventional linear Kalman filter techniques in this study. Possible substitutes include linearized Kalman filters, extended Kalman filters, second-order filters, or other forms of state estimators such as maximum likelihood estimators (2:24,212). The extended Kalman filter (EKF) is selected as the most suitable implementation based on the three reasons explained in the introductory chapter: proven performance, computational tractability, and compatibility with available evaluation tools. The enhanced tractablility of the EKF results from linearizing the models about nominal points on the estimated state trajectory, although some portions of the algorithm still require the explicit evaluation of nonlinearities. The EKF maintains accuracy by repeatedly

relinearizing the filter about each new state estimate, in effect providing a new nominal trajectory for each successive filter operation.

This chapter explains EKF formulations for the models developed in preceding chapters. Filter propagation between measurement times is developed first. Both extended and conventional formulations are discussed in the filter propagation section because the preservation of linear dynamics in the CV and GMA filters allows the exploitation of linear techniques to simplify propagation. The next section discusses the EKF measurement update equations required by nonlinearities in the measurement models of both filters. The chapter's final section describes an EKF algorithm for the F-4E/G OFP and the evaluation of several key parameters. The actual EKF equations and their equivalent discrete versions are listed without proof. A detailed derivation is available in Reference 2, Chapter 9.

Filter Propagation

In the current context, the term propagation refers to the manner in which the states of a given process change, or evolve, in time. Applied to the sampled data Kalman estimator, propagation provides a description of the time evolution of the states during the periods of time between measurements. A Kalman filter propagates both the vector of state estimates, $\hat{\underline{x}}(t_i)$, and its associated covariance matrix, $P(t_i)$.

The Kalman filter's internal dynamics model governs filter propagation. For the extended Kalman filter formulation, system dynamics are modelled in the general form

$$\dot{\underline{x}}(t) = \underline{f}[\underline{x}(t),\underline{u}(t),t] + G(t)\underline{w}(t) \qquad (4\text{-}1)$$

where

$\underline{x}(t)$ is the state vector,

$\underline{f}[\underline{x}(t),\underline{u}(t),t]$ is a vector of functions describing state dynamics (not necessarily linear),

$\underline{u}(t)$ is a vector of deterministic inputs,

$G(t)$ is a coefficient matrix defining which states are driven by linearly additive noise terms,

and

$\underline{w}(t)$ is a vector of zero-mean white Gaussian noise of strength $Q(t)$ as defined by (2-9).

Defining an initial condition for (4-1) as a random vector $\underline{x}(t_o)$ with mean $\hat{\underline{x}}_o$ and covariance P_o completes the time domain description of the system of interest.

Given discrete time measurements up to and including time t_i, the propagated state estimate at any subsequent time t prior to the next sample time is denoted $\hat{\underline{x}}(t/t_i)$ and is obtained by integrating the equation

$$\dot{\hat{\underline{x}}}(t/t_i) = \underline{f}[\hat{\underline{x}}(t/t_i),\underline{u}(t),t] \qquad (4\text{-}2)$$

forward to time t from the initial condition

$$\hat{\underline{x}}(t_i/t_i) = \hat{\underline{x}}(t_i^+) \qquad (4\text{-}3)$$

where $\hat{\underline{x}}(t_i^+)$ describes the result of the previous

measurement update at time t_i. Superscript + indicates estimates immediately after the incorporation of measurements. If the recursion begins with a propagation, the initial condition for the first propagation is

$$\underline{\hat{x}}(t_o/t_o) = \underline{\hat{x}}_o \tag{4-4}$$

The propagated error covariance matrix of the estimated state vector is calculated similarly. Integrating the equation

$$\dot{P}(t/t_i) = F[t;\underline{\hat{x}}(t/t_i)]P(t/t_i) + P(t/t_i)F^T[t;\underline{\hat{x}}(t/t_i)] + G(t)Q(t)G^T(t) \tag{4-5}$$

forward to time t from the initial condition

$$P(t_i/t_i) = P(t_i^+) \tag{4-6}$$

yields the newly propagated state covariance matrix $P(t_{i+1}^-)$, where superscripts - and + respectively denote quantities before and after measurement update. The initial condition, defined above by (4-6), is obtained from the filter's previous measurement update or from the values in P_o in the case of the initial recursion. The matrix $F[t;\underline{\hat{x}}(t/t_i)]$ in (4-5) represents the Jacobian of the newly relinearized dynamics model and is defined by

$$F[t;\underline{\hat{x}}(t/t_i)] = \left.\frac{\partial \underline{f}[\underline{x},\underline{u}(t),t]}{\partial \underline{x}}\right|_{\underline{x}=\underline{\hat{x}}(t/t_i)} \tag{4-7}$$

where $\underline{\hat{x}}(t/t_i)$ is the current state estimate obtained by integrating (4-1).

For computer implementations, a discrete-time form of filter propagation is required. In this form, a newly propagated state estimate for time t_{i+1} is obtained by integrating (4-1) to yield:

$$\underline{\hat{x}}(t_{i+1}^-) = \underline{\hat{x}}(t_{i+1}/t_i) \tag{4-8}$$

This result is used to evaluate the current F matrix, expressed in (4-7), which is needed in the covariance propagation equation, defined by (4-5). The relinearized covariance propagation equation is integrated next to yield the propagated state covariance matrix at time t_{i+1}:

$$P(t_{i+1}^-) = P(t_{i+1}/t_i) \tag{4-9}$$

This completes the EKF propagation from t_i^+ to t_{i+1}^-.

If the function $\underline{f}[\underline{x}(t),\underline{u}(t),t]$ is nonlinear, as implied by a nonlinear dynamics model, solving the propagation equations, (4-1) and (4-5), requires some form of numerical integration in the computer implementation. The computational load of this requirement is severe. However, the propagation equations can be simplified if system dynamics are modelled using linear, time-invariant differential equations. If the dynamics model is linear, (4-1) can be expressed in matrix form as

$$\dot{\underline{x}}(t) = F(t)\underline{x}(t) + B(t)\underline{u}(t) + G(t)\underline{w}(t) \tag{4-10}$$

where F(t) is the plant matrix and B(t) is called the input matrix. The solution to (4-10) is given by

$$\underline{x}(t_{i+1}) = \Phi(t_{i+1},t_i)\underline{x}(t_i) + \int_{t_i}^{t_{i+1}} \Phi(t_{i+1},\tau)B(\tau)\underline{u}(\tau)d\tau$$

$$+ \int_{t_i}^{t_{i+1}} \Phi(t_{i+1},\tau)G(\tau)d\underline{\beta}(\tau) \qquad (4\text{-}11)$$

where $\Phi(t_{i+1},t_i)$ is the state transition matrix which propagates the solution from time t_i to time t_{i+1}, and $\underline{x}(t_i)$ is the initial condition for (4-10). The second integral term in (4-11) is a stochastic integral representing discrete-time white Gaussian noise, derived from a Brownian motion process, $\underline{\beta}(t)$. Reference 1, Chapter 4 explains the details of this derivation. If the system is time-invariant, F(t) is a constant matrix and $\Phi(t_{i+1},t_i)$ is a function of the time difference, $[t_{i+1} - t_i]$. If the propagation interval is constant, as is the case when the time between measurements is equal, the state transition matrix is a constant matrix which can be precomputed for all time. A Kalman filter operating under the above conditions propagates state and covariance estimates from time t_i^+ to time t_{i+1}^- by the equations

$$\underline{x}(t_{i+1}^-) = \Phi(\Delta t)\underline{x}(t_i^-) + B_d(t_i)\underline{u}(t_i) \qquad (4\text{-}12)$$

$$P(t_{i+1}^-) = \Phi(\Delta t)P(t_i^-)\Phi^T(\Delta t) + Q_d(t_i) \qquad (4\text{-}13)$$

where

$$\Delta t = t_{i+1} - t_i \ , \qquad (4\text{-}14)$$

$$B_d(t_i) = \int_{t_i}^{t_{i+1}} \Phi(t_{i+1},\tau)B(\tau)d\tau, \qquad (4\text{-}15)$$

$$Q_d(t_i) = \int_{t_i}^{t_{i+1}} \Phi(t_{i+1},\tau)G(\tau)Q(\tau)G^T(\tau)\Phi^T(t_{i+1},\tau)d\tau \ , \qquad (4\text{-}16)$$

and $\underline{u}(t_i)$ is an input vector approximated as constant over each sample period. The constant state transition matrix $\Phi(\Delta t)$ can be evaluated in closed form using Laplace transform theory:

$$\Phi(\Delta t) = L^{-1}[sI-F]^{-1} \Big|_{\Delta t} \qquad (4\text{-}17)$$

A filter propagation scheme which employs (4-12) and (4-13) can be implemented computationally by straightforward matrix addition and multiplication. Herein lies the great advantage of preserving linear, time-invariant dynamics models and incorporating measurements taken at equal intervals. Propagation under these conditions avoids the EKF requirements for the computationally expensive numerical integration and recursive evaluation of $F[t;\hat{\underline{x}}(t/t_i)]$.

As discussed in Chapter II, linear, time-invariant dynamics are intentionally preserved in the CV and GMA filter designs. Additionally, the APQ-120 takes measurements at a constant rate, every 0.01 second, and the OFP can be programmed to incorporate measurements at any multiple of this period (8). Thus, both models satisfy the prerequisites for propagation by means of (4-12) and (4-13).

For the CV model, putting the dynamics equations, (2-3) through (2-8), into the form of (4-10) results in

$$\begin{bmatrix} \dot{x}_1(t) \\ \dot{x}_2(t) \\ \dot{x}_3(t) \\ \dot{x}_4(t) \\ \dot{x}_5(t) \\ \dot{x}_6(t) \end{bmatrix} = [F] \begin{bmatrix} x_1(t) \\ x_2(t) \\ x_3(t) \\ x_4(t) \\ x_5(t) \\ x_6(t) \end{bmatrix} + [B] \begin{bmatrix} V_{FN}^I(t) \\ V_{FE}^I(t) \\ V_{FD}^I(t) \end{bmatrix} + [G] \begin{bmatrix} w_N(t) \\ w_E(t) \\ w_D(t) \end{bmatrix} \tag{4-18}$$

where

$$F = \begin{bmatrix} 0 & 1 & 0 & 0 & 0 & 0 \\ 0 & 0 & 0 & 0 & 0 & 0 \\ 0 & 0 & 0 & 1 & 0 & 0 \\ 0 & 0 & 0 & 0 & 0 & 0 \\ 0 & 0 & 0 & 0 & 0 & 1 \\ 0 & 0 & 0 & 0 & 0 & 0 \end{bmatrix}, \qquad B = \begin{bmatrix} -1 & 0 & 0 \\ 0 & 0 & 0 \\ 0 & -1 & 0 \\ 0 & 0 & 0 \\ 0 & 0 & -1 \\ 0 & 0 & 0 \end{bmatrix},$$

and

$$G = \begin{bmatrix} 0 & 0 & 0 \\ 1 & 0 & 0 \\ 0 & 0 & 0 \\ 0 & 1 & 0 \\ 0 & 0 & 0 \\ 0 & 0 & 1 \end{bmatrix}$$

Calculating the state transition matrix for $\Delta t = 0.04$ seconds yields

$$\Phi(\Delta t) = \begin{bmatrix} 1 & 0.04 & 0 & 0 & 0 & 0 \\ 0 & 1 & 0 & 0 & 0 & 0 \\ 0 & 0 & 1 & 0.04 & 0 & 0 \\ 0 & 0 & 0 & 1 & 0 & 0 \\ 0 & 0 & 0 & 0 & 1 & 0.04 \\ 0 & 0 & 0 & 0 & 0 & 1 \end{bmatrix} \tag{4-19}$$

as shown in Appendix B.

Evaluating (4-15) and (4-16) for the 0.04 measurement interval yields the discrete-time input and driving noise matrices,

$$B_d = \begin{bmatrix} -0.04 & 0 & 0 \\ 0 & 0 & 0 \\ 0 & -0.04 & 0 \\ 0 & 0 & 0 \\ 0 & 0 & -0.04 \\ 0 & 0 & 0 \end{bmatrix} \tag{4-20}$$

and

$$Q_d = \begin{bmatrix} 0 & 0 & 0 & 0 & 0 & 0 \\ 0 & 0.04q_N & 0 & 0 & 0 & 0 \\ 0 & 0 & 0 & 0 & 0 & 0 \\ 0 & 0 & 0 & 0.04q_E & 0 & 0 \\ 0 & 0 & 0 & 0 & 0 & 0 \\ 0 & 0 & 0 & 0 & 0 & 0.04q_D \end{bmatrix} \tag{4-21}$$

where q_N, q_E, and q_D in (4-21) are constant noise strengths associated respectively with $w_N(t)$, $w_E(t)$, and $w_D(t)$, the elements of the driving noise vector.

The determination of $\Phi(\Delta t)$, B_d, and Q_d completes the linear, time-invariant version of the recursive propagation expressions, (4-12) and (4-13), as applied to the CV model. To begin the recursion, the filter requires initial conditions $\underline{\hat{x}}_o$ and P_o. For this study, the initial state estimate is

$$\underline{\hat{x}}_o = \underline{0} \tag{4-22}$$

Values for the initial covariance matrix P_o are first selected as reasonable estimates of the filter's initial state uncertainty. However, these values can be adjusted during the filter tuning process to improve the initial convergence performance of the filters.

The propagation equations for the GMA model are found by a similar process. Modelling the dynamics equations, (2-11) through (2-19), in the form of (4-10) yields

$$\begin{bmatrix} \dot{x}_1(t) \\ \dot{x}_2(t) \\ \dot{x}_3(t) \\ \dot{x}_4(t) \\ \dot{x}_5(t) \\ \dot{x}_6(t) \\ \dot{x}_7(t) \\ \dot{x}_8(t) \\ \dot{x}_9(t) \end{bmatrix} = [F] \begin{bmatrix} x_1(t) \\ x_2(t) \\ x_3(t) \\ x_4(t) \\ x_5(t) \\ x_6(t) \\ x_7(t) \\ x_8(t) \\ x_9(t) \end{bmatrix} + [B] \begin{bmatrix} V_{FN}^I(t) \\ V_{FE}^I(t) \\ V_{FD}^I(t) \end{bmatrix} + [G] \begin{bmatrix} w_N(t) \\ w_E(t) \\ w_D(t) \end{bmatrix} \qquad (4\text{-}23)$$

where

$$F = \left[\begin{array}{ccc|ccc|ccc} 0 & 1 & 0 & 0 & 0 & 0 & 0 & 0 & 0 \\ 0 & 0 & 1 & 0 & 0 & 0 & 0 & 0 & 0 \\ 0 & 0 & -\frac{1}{\tau} & 0 & 0 & 0 & 0 & 0 & 0 \\ \hline 0 & 0 & 0 & 0 & 1 & 0 & 0 & 0 & 0 \\ 0 & 0 & 0 & 0 & 0 & 1 & 0 & 0 & 0 \\ 0 & 0 & 0 & 0 & 0 & -\frac{1}{\tau} & 0 & 0 & 0 \\ \hline 0 & 0 & 0 & 0 & 0 & 0 & 0 & 1 & 0 \\ 0 & 0 & 0 & 0 & 0 & 0 & 0 & 0 & 1 \\ 0 & 0 & 0 & 0 & 0 & 0 & 0 & 0 & -\frac{1}{\tau} \end{array}\right] \qquad (4\text{-}24)$$

The input and noise coefficient matrices for the GMA model are

$$B = \begin{bmatrix} -1 & 0 & 0 \\ 0 & 0 & 0 \\ 0 & 0 & 0 \\ 0 & -1 & 0 \\ 0 & 0 & 0 \\ 0 & 0 & 0 \\ 0 & 0 & -1 \\ 0 & 0 & 0 \\ 0 & 0 & 0 \end{bmatrix} \quad \text{and} \quad G = \begin{bmatrix} 0 & 0 & 0 \\ 0 & 0 & 0 \\ 1 & 0 & 0 \\ 0 & 0 & 0 \\ 0 & 0 & 0 \\ 0 & 1 & 0 \\ 0 & 0 & 0 \\ 0 & 0 & 0 \\ 0 & 0 & 1 \end{bmatrix}$$

In Appendix B, the state transition matrix is calculated for $\tau = 0.5$ and $\Delta t = 0.04$ seconds:

$$\Phi(\Delta t) = \left[\begin{array}{c|c|c} {}^{*}\underline{3x3} & \underline{0}_{3x3} & \underline{0}_{3x3} \\ \hline \underline{0}_{3x3} & {}^{*}\underline{3x3} & \underline{0}_{3x3} \\ \hline \underline{0}_{3x3} & \underline{0}_{3x3} & {}^{*}\underline{3x3} \end{array}\right] \qquad (4\text{-}25)$$

where

$${}^{*}\underline{3x3} = \begin{bmatrix} 1 & 0.04 & 0.0007791 \\ 0 & 1 & 0.0384418 \\ 0 & 0 & 0.9231163 \end{bmatrix}$$

B_d and Q_d are calculated using (4-15) and (4-16). Initial conditions $\hat{\underline{x}}_o$ and P_o are chosen in the same manner as in the CV model, but with additional terms for the acceleration states. Using $\Phi(\Delta t)$, B_d, Q_d, $\hat{\underline{x}}_o$, and P_o just described, the GMA filter can be propagated by the linear Kalman filter equations, (4-12) and (4-13).

This completes the description of time propagation in the CV and GMA filters. In these models, linear,

time-invariant dynamics lead to simplified calculation of state and covariance estimates, providing the estimates are propagated over equal time intervals between measurements. The next section describes the EKF equations for incorporating measurements into the state estimate at each measurement time t_i.

Measurement Update for Extended Kalman Filters

At each measurement time t_i, the EKF receives information from sensors in the form of a discrete time measurement vector $\underline{z}(t_i)$. Chapter III developed a mathematical model of the measurements available to the F-4E/G fire control computer. This model expresses $\underline{z}(t_i)$ as the sum of nonlinear functions of state variables and zero-mean white Gaussian noises:

$$\underline{z}(t_i) = \underline{h}[\underline{x}(t_i),t_i] + \underline{v}(t_i) \tag{4-26}$$

which is in the form of (3-17). This model governs the EKF update. For each update cycle, the filter algorithm evaluates the measurement function vector $\underline{h}[*,*]$ using the current propagated state estimate $\hat{x}(t\bar{i})$. This represents the filter's best prediction of what each measurement should be at time t_i:

$$\hat{\underline{z}}(t_i^-) = \underline{h}[\underline{x}(t_i^-),t_i] \tag{4-27}$$

When the actual noise-corrupted measurements from the environment, $\underline{z}_i$, become available, the EKF calculates the

difference between the actual and predicted values. The difference, or residual, is multiplied by an optimal weighting matrix $K(t_i)$ to produce a correction term for the state estimate. In this manner, the EKF incorporates measurement information into the current propagated state estimate $\hat{\underline{x}}(t_i^-)$ to produce an updated state estimate for the current time, $\hat{\underline{x}}(t_i^+)$. In equation form this is

$$\hat{\underline{x}}(t_i^+) = \hat{\underline{x}}(t_i^-) + K(t_i)\{\underline{z}_i - \underline{h}[\hat{\underline{x}}(t_i^-), t_i]\} \tag{4-28}$$

where $\underline{z}_i$ is the vector of actual measurements. The optimal weighting matrix $K(t_i)$ is found by

$$K(t_i) = P(t_i^-)H^T(t_i)\{H(t_i)P(t_i^-)H^T(t_i) + R(t_i)\}^{-1} \tag{4-29}$$

where $R(t_i)$ is the measurement noise matrix described in Chapter III and $H(t_i)$ is a partial deriviative matrix defined by

$$H[t_i;\hat{\underline{x}}(t_i^-)] = \left.\frac{\partial \underline{h}[\underline{x},t_i]}{\partial \underline{x}}\right|_{\underline{x} = \hat{\underline{x}}(t_i^-)} \tag{4-30}$$

The covariance is updated by

$$P(t_i^+) = P(t_i^-) - K(t_i)H(t_i)P(t_i^-) \tag{4-31}$$

where $K(t_i)$ and $H(t_i)$ are defined respectively by (4-29) and (4-30).

The measurement function vector $\underline{h}[*,*]$, as defined by (3-16), is physically the same for both the CV and GMA models. As illustrated below, this results in mathematical

similarities in the H matrix of both models. The only differences are attributable to the different dimensionality and the state variable numbering conventions of the two models. Calculating the partial deriviative matrix indicated by (4-30) in terms of the CV state vector yields

$$H = \begin{bmatrix} H_1 & 0 & H_2 & 0 & H_3 & 0 \\ H_4 & H_5 & H_6 & H_7 & H_8 & H_9 \\ H_{10} & 0 & H_{11} & 0 & H_{12} & 0 \\ H_{13} & 0 & H_{14} & 0 & H_{15} & 0 \\ H_{16} & H_{17} & H_{18} & H_{19} & H_{20} & H_{21} \\ H_{22} & H_{23} & H_{24} & H_{25} & H_{26} & H_{27} \end{bmatrix} \tag{4-32}$$

where individual elements are defined by the following equations. Zero valued elements are not listed.

$$H_1 = \frac{x_1}{(x_1^2 + x_3^2 + x_5^2)^{\frac{1}{2}}} \tag{4-33}$$

$$H_2 = \frac{x_3}{(x_1^2 + x_3^2 + x_5^2)^{\frac{1}{2}}} \tag{4-34}$$

$$H_3 = \frac{x_5}{(x_1^2 + x_3^2 + x_5^2)^{\frac{1}{2}}} \tag{4-35}$$

$$H_4 = \frac{(x_3^2 + x_5^2)(x_2 - V_{FN}^G) - x_1 x_3 (x_4 - V_{FE}^G) - x_1 x_5 (x_6 - V_{FD}^G)}{(x_1^2 + x_3^2 + x_5^2)^{3/2}} \tag{4-36}$$

$$H_5 = \frac{x_1}{(x_1^2 + x_3^2 + x_5^2)^{\frac{1}{2}}} \tag{4-37}$$

$$H_6 = \frac{(x_1^2 + x_5^2)(x_4 - V_{FE}^G) - x_1x_3(x_2 - V_{FN}^G) - x_3x_5(x_6 - V_{FD}^G)}{(x_1^2 + x_3^2 + x_5^2)^{3/2}} \tag{4-38}$$

$$H_7 = \frac{x_3}{(x_1^2 + x_3^2 + x_5^2)^{\frac{1}{2}}} \tag{4-39}$$

$$H_8 = \frac{(x_1^2 + x_3^2)(x_6 - V_{FD}^G) - x_1x_5(x_2 - V_{FN}^G) - x_3x_5(x_4 - V_{FE}^G)}{(x_1^2 + x_3^2 + x_5^2)^{3/2}} \tag{4-40}$$

$$H_9 = \frac{x_5}{(x_1^2 + x_3^2 + x_5^2)^{\frac{1}{2}}} \tag{4-41}$$

$$H_{10} = \frac{[-|M_{33}|x_3 - |M_{32}|x_5]\ (T_{11}x_1 + T_{12}x_3 + T_{13}x_5)}{[(T_{11}x_1 + T_{12}x_3 + T_{13}x_5)^2 + (T_{21}x_1 + T_{22}x_3 + T_{23}x_5)^2]^{3/2}} \tag{4-42}$$

$$H_{11} = \frac{[|M_{33}|x_1 - |M_{31}|x_5]\ (T_{11}x_1 + T_{12}x_3 + T_{13}x_5)}{[(T_{11}x_1 + T_{12}x_3 + T_{13}x_5)^2 + (T_{21}x_1 + T_{22}x_3 + T_{23}x_5)^2]^{3/2}} \tag{4-44}$$

$$H_{12} = \frac{[|M_{32}|x_1 - |M_{31}|x_3]\ (T_{11}x_1 + T_{12}x_3 + T_{13}x_5)}{[(T_{11}x_1 + T_{12}x_3 + T_{13}x_5)^2 + (T_{21}x_1 + T_{22}x_3 + T_{23}x_5)^2]^{3/2}} \tag{4-45}$$

In (4-43), (4-44), and (4-45), T_{ij} are elements of [T3], Transformation 3 in Appendix C, and $|M_{ij}|$ represents the determinant of the ij^{th} minor of [T3]. For example, M_{33} is found by deleting the third row and third column of [T3],

$$M_{33} = \begin{bmatrix} T3_{11} & T3_{12} \\ T3_{21} & T3_{22} \end{bmatrix}$$

and,

$$|M_{33}| = (T3_{11}T3_{22} - T3_{21}T3_{12}) \tag{4-46}$$

$$H_{13} = \frac{-T3_{31}(x_3^2 + x_5^2) + T3_{32}x_1x_3 + T3_{33}x_1x_5}{(x_1^2 + x_3^2 + x_5^2)^{3/2}} \tag{4-47}$$

$$H_{14} = \frac{-T3_{32}(x_1^2 + x_5^2) + T3_{31}x_1x_3 + T3_{33}x_3x_5}{(x_1^2 + x_3^2 + x_5^2)^{3/2}} \tag{4-48}$$

$$H_{15} = \frac{-T3_{33}(x_1^2 + x_3^2) + T3_{31}x_1x_5 + T3_{32}x_3x_5}{(x_1^2 + x_3^2 + x_5^2)^{3/2}} \tag{4-49}$$

The remaining H terms require [T4], Transformation 4 in Appendix C.

$$H_{16} = \frac{x_1[T4_{31}(x_2 - V_{FN}^G) + T4_{32}(x_4 - V_{FE}^G) + T4_{33}(x_6 - V_{FD}^G)]}{(x_1^2 + x_3^2 + x_5^2)^{3/2}} \tag{4-50}$$

$$H_{17} = \frac{T4_{31}}{(x_1^2 + x_3^2 + x_5^2)^{\frac{1}{2}}} \tag{4-51}$$

$$H_{18} = \frac{x_3[T4_{31}(x_2 - V_{FN}^G) + T4_{32}(x_4 - V_{FE}^G) + T4_{33}(x_6 - V_{FD}^G)]}{(x_1^2 + x_3^2 + x_5^2)^{3/2}} \tag{4-52}$$

$$H_{19} = \frac{T4_{32}}{(x_1^2 + x_3^2 + x_5^2)^{\frac{1}{2}}} \tag{4-53}$$

$$H_{20} = \frac{x_5[T4_{31}(x_2 - V_{FN}^G) + T4_{32}(x_4 - V_{FE}^G) + T4_{33}(x_6 - V_{FD}^G)]}{(x_1^2 + x_3^2 + x_5^2)^{3/2}} \tag{4-54}$$

$$H_{21} = \frac{T4_{33}}{(x_1^2 + x_3^2 + x_5^2)^{\frac{1}{2}}} \tag{4-55}$$

$$H_{22} = \frac{-x_1[T4_{21}(x_2 - V_{FN}^G) + T4_{22}(x_4 - V_{FE}^G) + T4_{23}(x_6 - V_{FD}^G)]}{(x_1^2 + x_3^2 + x_5^2)^{3/2}} \tag{4-56}$$

$$H_{23} = \frac{T4_{21}}{(x_1^2 + x_3^2 + x_5^2)^{\frac{1}{2}}} \tag{4-57}$$

$$H_{24} = \frac{-x_3[T4_{21}(x_2 - V_{FN}^G) + T4_{22}(x_4 - V_{FE}^G) + T4_{23}(x_6 - V_{FD}^G)]}{(x_1^2 + x_3^2 + x_5^2)^{3/2}} \tag{4-58}$$

$$H_{25} = \frac{T4_{22}}{(x_1^2 + x_3^2 + x_5^2)^{\frac{1}{2}}} \tag{4-59}$$

$$H_{26} = \frac{-x_5[T4_{21}(x_2 - V_{FN}^G) + T4_{22}(x_4 - V_{FE}^G) + T4_{23}(x_6 - V_{FD}^G)]}{(x_1^2 + x_3^2 + x_5^2)^{3/2}} \tag{4-60}$$

$$H_{27} = \frac{T4_{23}}{(x_1^2 + x_3^2 + x_5^2)^{\frac{1}{2}}} \tag{4-61}$$

For the GMA model, the H_i terms are identical to those of the CV model except that the state variables are renumbered to correspond with the appropriate GMA states. Applying (4-30) to the GMA model yields:

$$H = \begin{bmatrix} H_1 & 0 & 0 & H_2 & 0 & 0 & H_3 & 0 & 0 \\ H_4 & H_5 & 0 & H_6 & H_7 & 0 & H_8 & H_9 & 0 \\ H_{10} & 0 & 0 & H_{11} & 0 & 0 & H_{12} & 0 & 0 \\ H_{13} & 0 & 0 & H_{14} & 0 & 0 & H_{15} & 0 & 0 \\ H_{16} & H_{17} & 0 & H_{18} & H_{19} & 0 & H_{20} & H_{21} & 0 \\ H_{22} & H_{23} & 0 & H_{24} & H_{25} & 0 & H_{26} & H_{27} & 0 \end{bmatrix} \quad (4\text{-}62)$$

Algorithm for OFP Implementation

This section provides a step-by-step procedure which can be used as a framework for programming the EKF implementations discussed in this chapter. The three basic steps are filter initialization, propagation, and update. These steps are expanded below.

(1) The following vectors and matrices are initialized at program start.

(a) Noise matrices. Initial driving noise strength, Q(t), is discussed in Chapter II. The equivilent discrete noise matrix, Q_d, needed for this algorithm is given by (4-16), with an example calculation in Appendix B. Chapter III discusses measurement noise strengths. Final noise strengths are obtained during the tuning process, as described in Chapters V and VI.

(b) State transition matrix. This matrix is calculated by applying (4-17) to a linear, time-invariant dynamics model. It is constant for a given measurement interval. Appendix B contains sample calculations.

(c) Input matrix. B_d is calculated using (4-15). An example is in Appendix B.

(d) Initial conditions. The initial state estimate and covariance matrix are discussed in the filter propagation section. For P_o, the values are often adjusted during filter tuning. The final P_o values in this study are:

$$\begin{bmatrix} 10000 & 0 & 0 & 0 & 0 & 0 & 0 & 0 \\ 0 & 900 & 0 & 0 & 0 & 0 & 0 & 0 \\ 0 & 0 & 0 & 0 & 0 & 0 & 0 & 0 \\ 0 & 0 & 0 & 10000 & 0 & 0 & 0 & 0 \\ 0 & 0 & 0 & 0 & 900 & 0 & 0 & 0 \\ 0 & 0 & 0 & 0 & 0 & 0 & 0 & 0 \\ 0 & 0 & 0 & 0 & 0 & 10000 & 0 & 0 \\ 0 & 0 & 0 & 0 & 0 & 0 & 900 & 0 \\ 0 & 0 & 0 & 0 & 0 & 0 & 0 & 0 \end{bmatrix}$$

(e) Initial F-4E/G attitude angles are needed to calculate transformation matrices and velocity aiding terms for the initial propagation.

(2) Propagation.

(a) Calculate the propagated state estimate, using (4-12).

(b) Calculate the propagated covariance matrix, using (4-13).

(3) Update.

When each new set of measurement data becomes available, the following steps are accomplished in the order given:

(a) Calculate transformation matrix elements based on the new aircraft attitude angles.

(b) Calculate current ownship velocity components in north, east, and down coordinates.

(c) Calculate the predicted measurement vector, (4-27), using the result from step (2a) above.

(d) Calculate the partial deriviative matrix, (4-30), evaluated at $\underline{\hat{x}}(t_i^-)$, the result from step (2a).

(e) Calculate the Kalman filter gain, (4-29).

(f) Calculate the updated state estimate, (4-28).

(g) Calculate the updated covariance matrix, (4-31).

(4) Begin the next propagation cycle and continue the recursion.

The above algorithm is designed to implement an operational extended Kalman filter in the F-4E/G fire control system. A method of evaluating this filter's performance without actually implementing it on an aircraft is described in the next chapter.

V. Method of Evaluation

Introduction

An important advantage of Kalman filtering is its suitablity for computer testing and evaluation. Computer simulation allows repetitive evaluation of filters without the expense of constructing multiple prototypes. For this reason, the filters developed in this study are evaluated in a computer simulation. This chapter discusses the structure of the simulation software and the methods employed to evaluate filter performance using this simulation. The first section introduces a dedicated software package designed specifically for the evaluation of extended Kalman filters. A second section describes a computer program acquired from F-4E/G software engineers at Hill AFB, Utah and modified to provide a standard of comparison for filter performance. This standard, or truth model, augments the basic Kalman filter evaluation software to form a complete simulation package for testing the CV and GMA filters. The final section discusses the general procedures followed in using the simulation package for successive evaluations, improvements, and re-evaluations of filter performance.

SOFE

A number of software packages currently exist for the purpose of evaluating Kalman filter designs. One such program is SOFE, a general purpose Monte Carlo simulation, and

a companion data postprocessor and plotting program, SOFEPL (13,28). Monte Carlo analysis is a method of calculating a statistical description of a stochastic process and requires repeated runs of a computer simulation to generate many samples of the stochastic process. Each sample varies under the influence of a random number generator used as the source of realized pseudo-random effects within the process. Mean and variance statistics are calculated for each time these statistics are needed throughout the simulation by averaging data generated over the entire set of samples. If the number of samples is sufficiently large, the process statistics from the Monte Carlo study closely approximate the statistics of the real world process (1:329). In using the Monte Carlo technique, the analyst must address the issue of how many samples are sufficient to characterize the process statistics adequately. Previous studies suggest 20 runs as adequate for many applications (12:65,27:59). In this study, 5 run studies are used to examine general trends, and 20 run studies are used to fully characterize process statistics in the simulation.

In the present case, the stochastic process to be statistically characterized is a vector error process consisting of the errors committed by a reduced-order Kalman filter as it estimates target position, velocity, and acceleration values in the F-4E/G OFP. The filter's true errors are the differences between the filter-computed values and the true values of target position, velocity, and

acceleration in a real world scenario. In actual air combat, the true values of these quantities are not known. In a computer simulation, however, the true values of target position, velocity, and acceleration can be approximated by a mathematical model. Additionally, models can approximate true measurements which emulate the response of an APQ-120 radar operating under conditions associated with specific F-4E/G combat maneuvers. A mathematical model which closely approximates the true values of variables of interest within a dynamic system is called a truth model. A truth model must be the most accurate and complete model available because the validity of the filter's performance evaluation, and ultimately, the operational success of the filter, depend on the adequacy of the truth model to represent reality (1:326). Using a suitable truth model, a sample of the filter's error process can be generated by subtracting the outputs of the truth model from the corresponding outputs of the filter at each discrete time of a simulation run. Additional samples are generated in the same way, but remain independent of other samples through the use of a non-repetitive random number generator. Each sample associates a vector of error states with each discrete time of the simulation. For each of these discrete times, summing the corresponding components of the error state vectors associated with that time and dividing by the number of samples yields a mean error state vector for that particular time. Similarly, the error variance for each discrete time is also

calculated directly from the data generated by the samples. When these calculations are done for all times in the simulation, the completed Monte Carlo study characterizes the time history of the mean and variance of the error process associated with each component of the filter state vector. The following discussion illustrates Monte Carlo analysis in the context of the SOFE program.

Since SOFE is a general purpose Monte Carlo simulation, it can be adapted to a variety of Kalman filter applications. The user defines a specific problem by supplying both the filter structure and the truth model. User-specified input variables determine the number of filter states, the number of measurements, the measurement time increment, and other parameters which govern the dimensions of the models, program control, and input/output timing. The actual filter dynamics and measurement equations are implemented in user-written subroutines appended to the basic SOFE software. The basic SOFE code itself provides the overall Monte Carlo structure, control for event timing, and computational tools for propagating and updating a Kalman filter state vector and its associated covariance matrix (13).

The SOFE user provides a truth model in one of two ways. It can be implemented in user-written subroutines, a method which allows SOFE to propagate the truth states over each time step in parallel with the filter states, or alternately, the truth model can be supplied by means of an

external state trajectory. The latter configuration requires a separate data file that contains a time history of truth state values and/or true measurements. This file can consist of actual data recorded during operational tests of the physical system. Frequently, however, the physical system is not yet built or, as is the case in this study, not readily available. In this case, a separate computer program serves as the truth model and generates the external trajectory data a priori for storage in the data file. SOFE accesses and interpolates data from this file as necessary during the course of each Monte Carlo run. The external trajectory truth model configuration is particularly well suited to target tracking problems and is the choice for this study (29). The actual program used is covered later in this chapter.

The basic SOFE code includes subroutines which propagate and update both truth and filter states. SOFE accomplishes filter propagation by means of a fifth-order Kutta-Merson numerical integration routine. The simulation propagates filter estimates by this method regardless of the linearity or nonlinearity of the dynamics model. The time interval between measurements is subdivided into adjustable length subintervals. SOFE integrates the propagation equations for both the state vector and covariance matrix over each subinterval using the results from the previous subinterval integration as initial conditions. Also, the state estimate obtained by integrating over the previous subinterval

AD-A164 205 KALMAN FILTER DESIGN FOR THE LONG RANGE INTERCEPT FUNCTION OF THE F-4E/G F.. (U) AIR FORCE INST OF TECH WRIGHT-PATTERSON AFB OH SCHOOL OF ENGI.. R C HALBERT 2/4

UNCLASSIFIED DEC 85 AFIT/GE/ENG/85D-20 F/G 17/9 NL

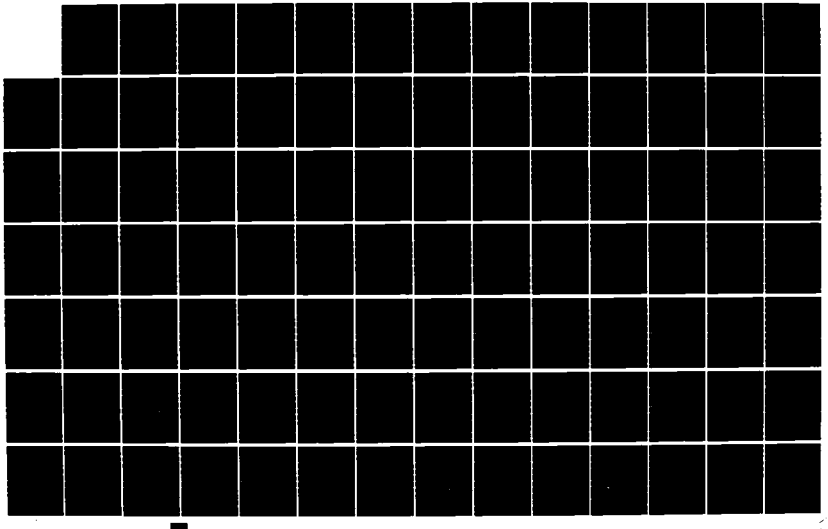

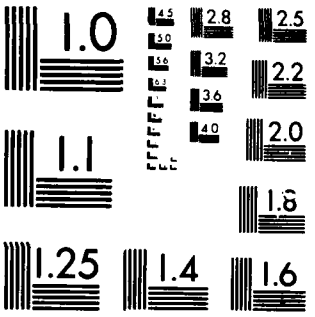

is used to evaluate the F matrix, defined by (4-7), which is needed to propagate the covariance over the current subinterval. SOFE automatically adjusts the size of each subinterval to maintain integration errors within user-defined tolerances while minimizing computer execution time (30:747). As propagation progresses, SOFE monitors the current time and compares it to the next scheduled measurement time. When a calculated subinterval reaches or exceeds the next measurement time, SOFE truncates that subinterval at the measurement time and terminates the propagation cycle at the end of that subinterval. At that point, SOFE updates the filter state estimates and covariance by means of a sequential Carlson square root algorithm, an update method with well established numerical stability (1:385,13:26). The Carlson method allows vector measurements to be incorporated sequentially as scalars. This capability allows SOFE users to omit some measurements during certain Monte Carlo studies in order to determine the effect of specific measurements on filter performance. When all desired measurement updates are complete, SOFE resumes the propagation cycle. Propagation and update cycles continue to alternate until the end of each Monte Carlo run.

As SOFE accomplishes each Monte Carlo run, it stores truth states, filter states, filter variances, residuals, and residual variances for each incremental filter time on an external interface file (28:5). Following the completion of all runs, the postprocessing and plotting program,

SOFEPL, reads the interface file and calculates averages of each of the five variables above for each time stored in the file (28:6). SOFEPL can also calculate the mean and variance of additional variables which represent the difference between two variables in the file. For example, the difference between a truth state and its corresponding filter state is an error state. SOFEPL can calculate the mean and variance of all error states for each measurement time. These statistics can be calculated over the entire Monte Carlo study or over a user-defined subset of runs.

Finally, SOFEPL displays the statistics on computer-generated plots. A number of different types of plots are available from SOFEPL. Two of these plots are of primary interest in this study and are discussed below.

The first plot contains five curves which display several statistics associated with a single error state averaged over an entire Monte Carlo study. Three of the five curves depict the actual mean-error of the filter state, the mean-error plus one standard deviation of the actual error, σ_{error}, and the mean-error minus σ_{error}. The other two curves show the one standard deviation bounds of the error state as computed by the filter. These latter bounds have the same values as the positive and negative square roots of the appropriate diagonal element of the filter covariance matrix and are thus labelled as ± square roots of $P_{jj}(t_i)$. Fig. 5.1 illustrates this type of plot.

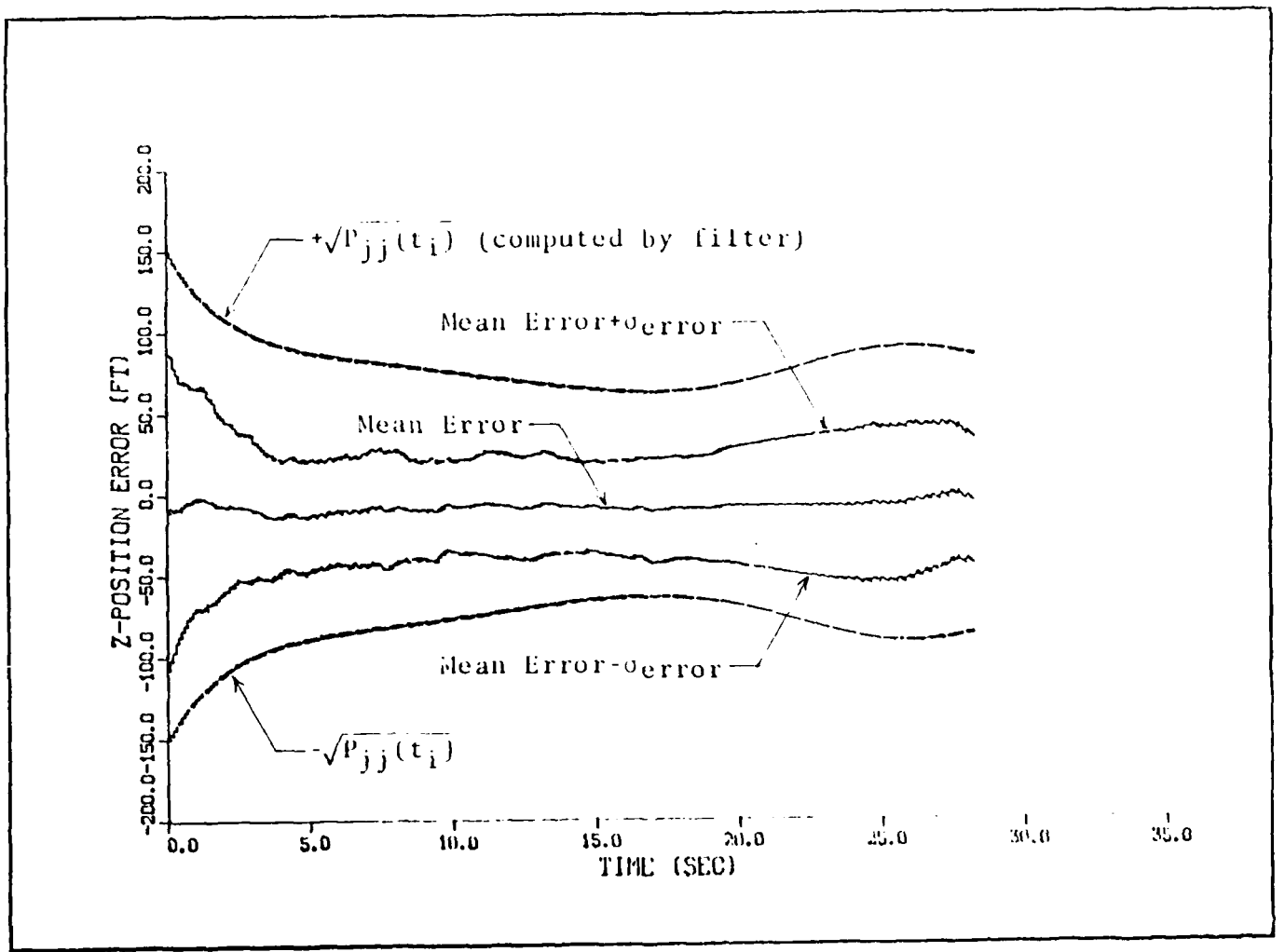

(27:60)

Figure 5.1. Sample SOFEPL Plot

Several advantages motivate the use of this plot. It enables the analyst to quickly assess overall filter performance by making filter divergence or bias in any state immediately apparent. Peak error magnitudes, settling time, and time-averaged error magnitudes are easily estimated from this plot. Additionally, causal relationships are often visible. For example, sudden changes in error magnitude or bias might be associated with specific events in the trajectory, such as a fighter roll maneuver. Finally, the inclusion of the filter-computed covariance curves allows the analyst to compare the filter's actual error variance for each state with its internally calculated representation of the error variance for that state. This information provides valuable insights regarding the filter's relative weighting of measurement information versus information from the dynamics model (1:337-339).

Another valuable SOFEPL plot displays the mean and one standard deviation bounds of a measurement residual. Residual plots provide valuable insights for the implementation of adaptive filtering techniques. For instance, a sudden increase in residual values during a fighter maneuver might motivate a shift in the relative weighting of measurement and dynamics information for the duration of the maneuver. Such a shift could be achieved by decreasing the strength of the process driving noise or by increasing the strength of measurement noise. Fig. 5.2 illustrates a typical SOFEPL residual plot.

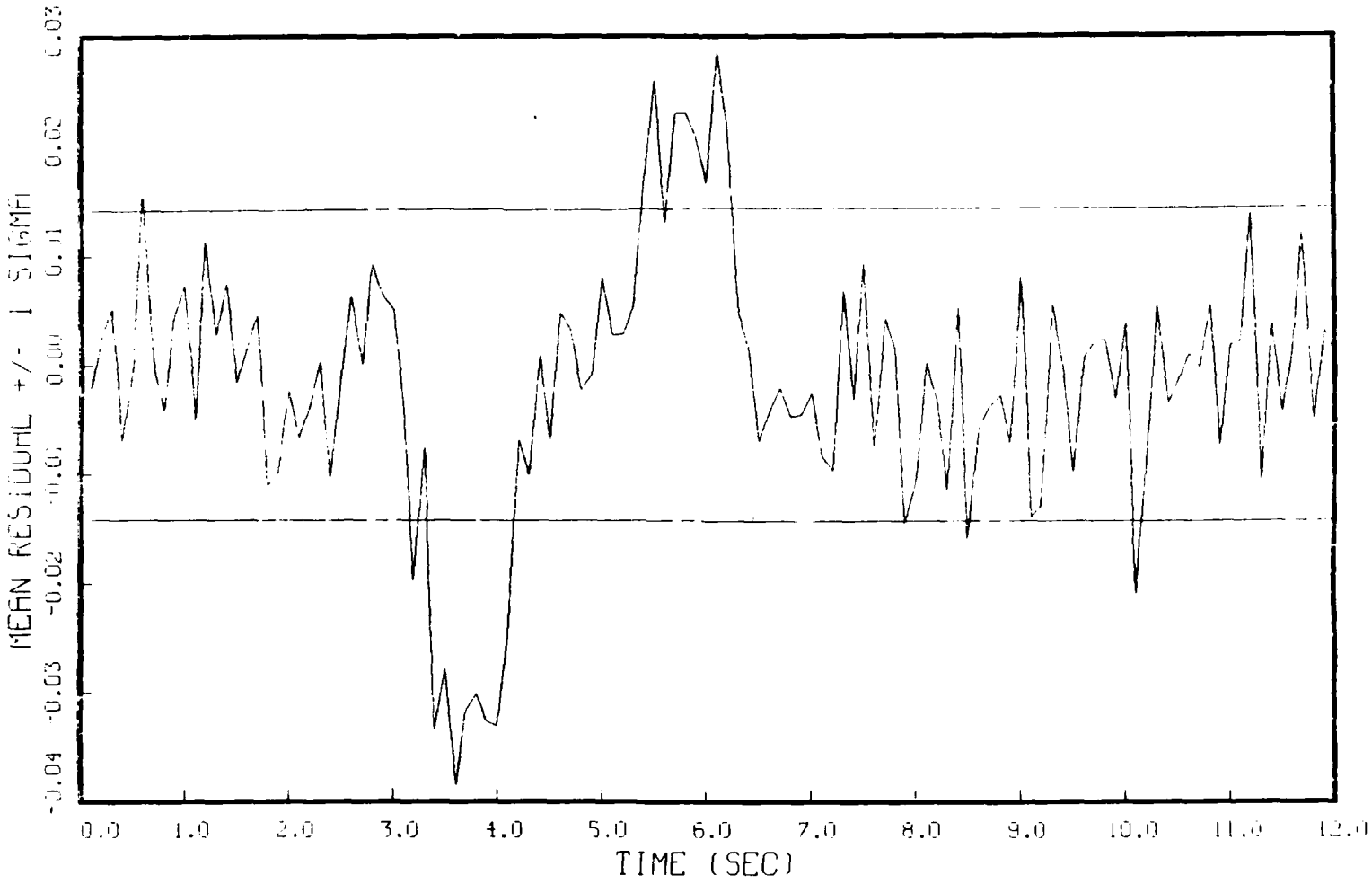

Fig. 5.2. Typical SOFEPL Residual Plot

Full descriptions of the two plots presented above and other plots generated by SOFEPL are available in Reference 28. Additionally, the interested reader is referred to References 13, 30, and 31 for a more detailed discussion of the mechanics of SOFE and SOFEPL. SOFE and SOFEPL provide only the overall Monte Carlo structure for this study. Completing the simulation requires an additional computer program to serve as truth model for the F-4E/G problem.

Truth Model

As explained in the previous section, the validity of a Monte Carlo analysis for any Kalman filter application is highly dependent on the quality of the truth model used as the standard of comparison for filter performance. Obtaining a suitable truth model for this study proved to be one of the most demanding challenges and a significant limiting factor in filter evaluation. Although a sophisticated computer model of the APQ-120 radar is available, its adaptation for use in the Kalman filter evaluation presents numerous difficulties. Resolving these difficulties requires extensive analysis and modification of the radar model software. Most of the required modifications are related to the following fundamental problems:

(1) The original truth model source code contained non-ANSI Fortran features and other defects which made it impossible to compile the program on the available computer, a CDC Cyber 74.

(2) The program was not designed for Kalman filter analysis and did not directly calculate relative target position, target acceleration, and other quantities needed from the truth model.

(3) The program only accommodated two dimensional trajectories for the attacker and target aircraft, a deficiency which led to observability problems in the three dimensional filters.

Modifying the truth model software to overcome these problems required considerably more effort than originally estimated. However, no better model was available. This fact made program modifications unavoidable.

The overall goal of the modified program is to produce realistic position, velocity, and acceleration histories for typical LRI combat trajectories and to preserve the modelling of dynamic lags in the APQ-120 gimbal angle and angle rate measurements which result from such trajectories. Additionally, the truth model must generate ownship attitude and airspeed information for the maneuvering F-4E/G. Although produced by a two dimensional model, all variables must be oriented in the three dimensional geometry of the Kalman filters under evaluation. Finally, the entire set of time-tagged truth states, radar measurements, airspeed values, and deterministic attitude angles must be written into an unformatted external trajectory file compatible with the SOFE simulation.

Following the modification and verification of the truth model program, three standard trajectories were developed for Kalman filter evaluations. All three trajectories incorporate an F-4E/G roll maneuver as a critical performance test. Each trajectory presents a target located at an initial range of 100,000 feet and constrained to the same altitude as the F-4E/G. To remain consistent with the LRI target assumptions discussed in Chapter II, the target maintains a non-maneuvering flight path and constant velocity of 800 feet per second. The trajectories vary according to the aspect and velocity which the target presents relative to the F-4E/G.

The first scenario, labelled the beam trajectory, simulates a westbound target crossing right to left in front of a northbound F-4E/G. The target's initial position is northeast of the F-4E/G on a line 45 degrees to the right of the attacker's nose. The F-4E/G maintains a constant velocity of 800 feet per second. This is slightly more than the nominal combat airspeed of 760 feet per second listed in Table II-2, but is used in this simulation to provide data for comparison with other studies conducted using that airspeed (8,32). After three seconds of straight and level flight, the F-4E/G begins a one radian per second roll to the right. At four seconds, the aircraft stabilizes its roll angle and holds a constant bank turn until five seconds. At that time, the fighter initiates a one radian per second rollout maneuver which achieves wings level flight at

approximately six seconds total time elapsed. The F-4E/G maintains the resulting heading and does not maneuver for the remainder of the 20 second trajectory. Fig. 5.3 illustrates the beam trajectory.

The second, or tailchase, trajectory simulates a target fleeing to the northeast with the F-4E/G maneuvering for pursuit, as shown in Fig. 5.4. Initial target position is in front of the northbound attacker, but bearing five degrees to the right of the attacker's nose. The airspeed of the F-4E/G is again constant, but set at 850 feet per second in this trajectory to permit the attacker to achieve a slight closure rate on the target. This prevents the range from exceeding LRI limits. The F-4E/G remains wings level northbound for five seconds before initiating a one radian per second right roll and stabilizing in a constant bank right turn one second later. This turn is held for 12 more seconds before the attacker rolls out to resume wings level flight in a position almost directly astern the target and at a heading which diverges slightly to the left (north) of the target's heading. This flight path is held for the remainder of the 20 second trajectory time.

The final test trajectory simulates a head-on attack profile. The target approaches from the northeast, heading 185 degrees. The northbound F-4E/G maintains a constant 800 feet per second airspeed and duplicates the maneuver described in the beam trajectory; a right roll at three seconds, constant bank at four seconds, and rollout to wings

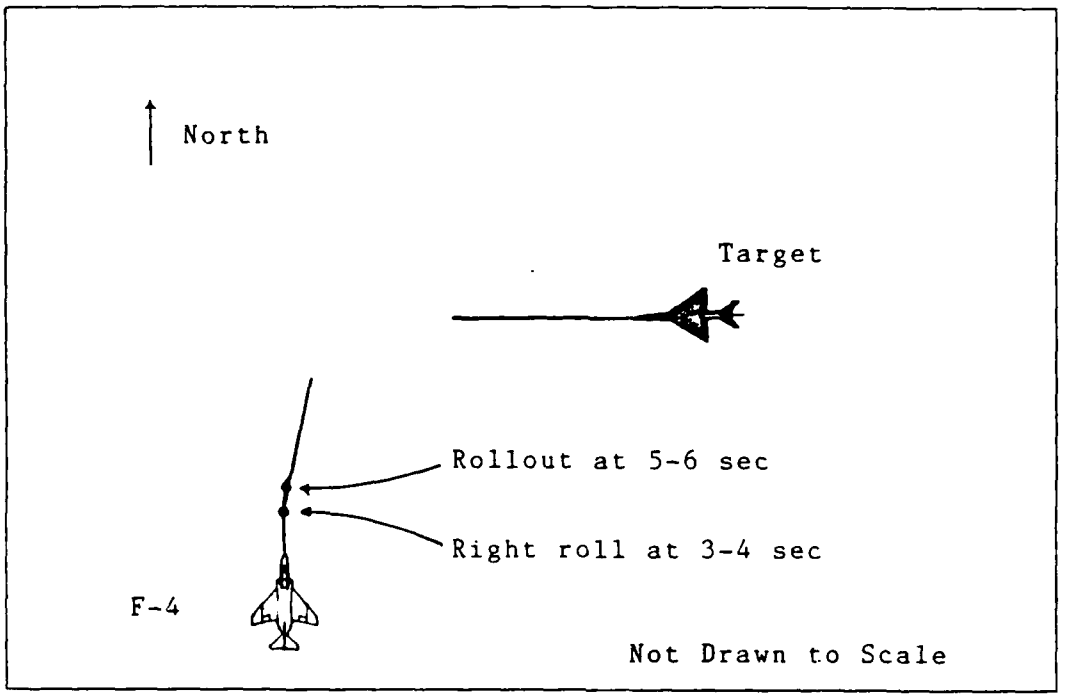

Fig. 5.3. Beam Trajectory

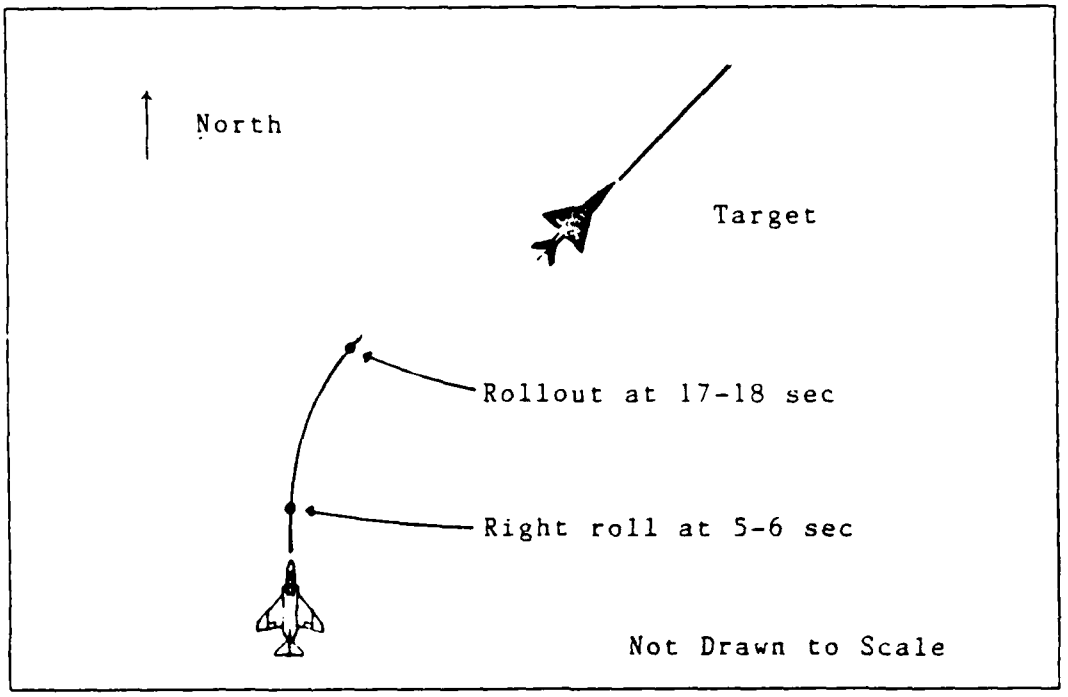

Fig. 5.4. Tailchase Trajectory

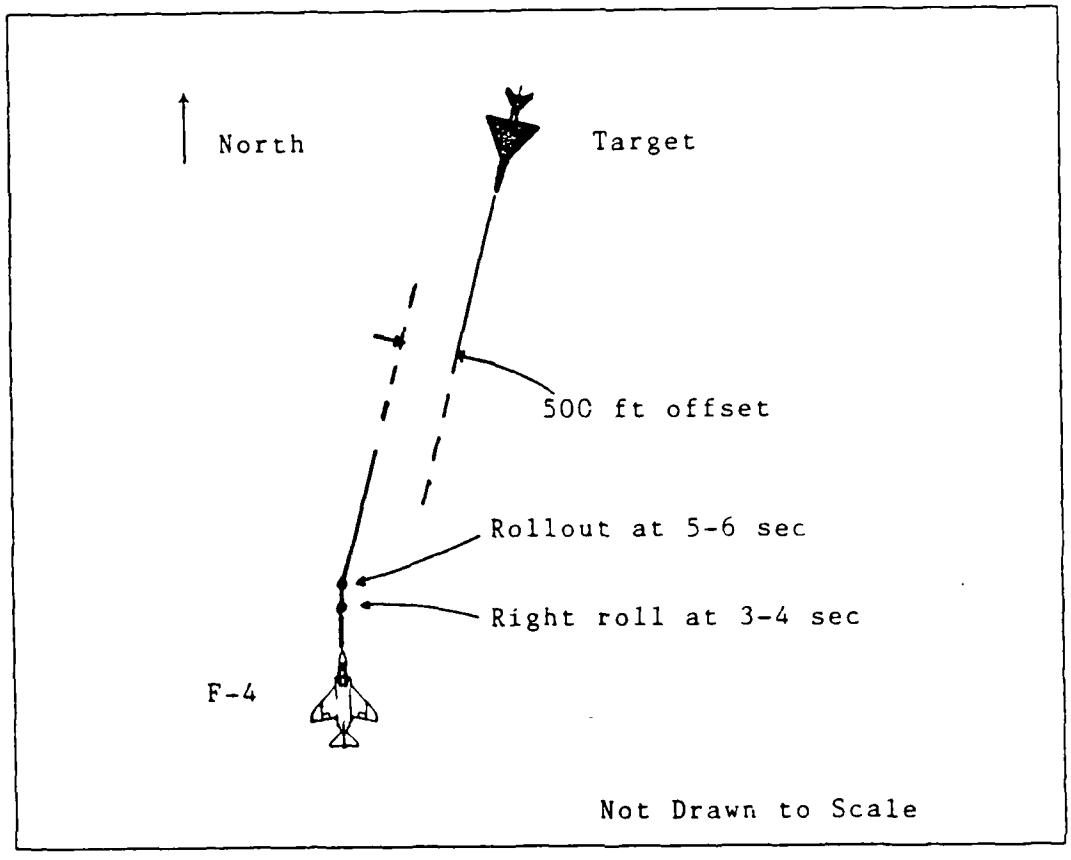

Fig. 5.5. Head-On Attack Trajectory

level at five seconds. This maneuver places the target and attacker on reciprocal headings with a 500 foot lateral offset as shown in Fig. 5.5. Both aircraft maintain heading for the 14 remaining seconds of this test.

The generation of the above truth state trajectories includes the calculation of corresponding time histories for radar measurements, ownship attitude angles, and ownship airspeed. These trajectories complete the software tools needed to conduct a Monte Carlo analysis of the CV and GMA filters. The next section discusses general procedures for using these tools.

General Evaluation Procedures

The preceding sections of this chapter explain the theoretical basis of Monte Carlo analysis and describe the structure of an actual Monte Carlo simulation program designed to evaluate the extended Kalman filters developed in this study. This section discusses methods of actually using the above simulation program to perform the desired evaluation. All of the methods presented are iterative procedures which, in their most fundamental sense, have the following form:

(1) Perform a Monte Carlo study on a candidate filter to obtain a statistical characterization of filter performance.

(2) Critically examine the filter performance from the previous step by comparing it to (a) the performance of other candidate filters operating under identical conditions, (b) performance of the same filter with varying noise strengths, time constants, or other variable parameters, and (c) predetermined standards of filter performance.

(3) Using insights gained from the previous step, adjust the values of filter parameters or change elements of the filter structure with the goal of improving filter performance.

(4) Repeat the above steps until satisfactory performance is obtained.

In order to perform meaningful comparisons of the type suggested in Step 2 of the above procedure, some metric or yardstick of filter performance is necessary. For this study, the following three figures of merit are used:

(1) peak error magnitude for each position and velocity state,

(2) settling time, defined as the time between the onset of an F-4E/G maneuver and the time filter error states stabilize within five per cent of peak values,

and,

(3) time-averaged error magnitude for each position and velocity state estimated over the length of a given trajectory. This value has little meaning except in relation to a specific trajectory and is used only to compare performance among filter versions operating over identical trajectories.

The above figures of merit are chosen because they characterize filter performance in terms consistent with the performance criteria for an adequate LRI filter as identified in Chapter I. Additionally, these figures of merit are also easily obtained from available SOFEPL plots. Acceleration states are not included in the figures of merit because they provide very little information in the benign trajectories associated with LRI targets, and are not available in the case of the CV model. Acceleration states are examined,

however, for evidence of filter divergence and/or observability problems, as discussed in Chapter VI.

The above figures of merit can be used in several ways to provide insights for improving filter performance over a succession of Monte Carlo studies. During the initial phase of filter evaluation, for instance, the filter designer seeks to validate filter models and the software which implements these models. One way of doing this is to use comparisons of figures of merit to establish consistency in the baseline performance of the filters under evaluation. In this sense, consistency implies that several similarly structured filters or filter variations are likely to exhibit the same general performance patterns when tested on the same trajectory. When comparing filter performance patterns, the analyst expects variations in peak error and other figures of merit. If the figures of merit vary in a consistent manner, overall confidence in the filter simulation is enhanced. However, inconsistencies in filter performance often point to serious modelling errors or mistakes in computer code.

As an example, consider two Monte Carlo studies of the GMA filter operating in the beam trajectory scenario. The first study incorporates only four of the available measurements; range, range rate, and the sines of the azimuth and elevation angles. The second study differs only in that it incorporates all six measurements into the state estimates. Comparing the results of these two studies, the analyst

finds a close resemblence in the general patterns of filter performance and perhaps notes a modest decrease in peak error magnitude for the second filter, indicating that the additional measurements improve filter performance in that respect. A series of consistent results of this nature lends confidence to the GMA model and its computer implementation. However, if results of the two studies show stable convergent performance in the first case, and several rapidly diverging states in the second case, then a problem exists which the analyst must investigate. This problem is likely related to the angle rate measurements, but might be in the form of a mismodelled measurement, a sign error in a filter measurement equation, an error in the truth model, a typographical error in the computer code, or some combination of these. Examples of each of these errors were actually uncovered during preliminary Monte Carlo studies for the F-4E/G problem.

Other examples of filter evaluation procedures include filter "tuning" and the determination of an error budget. Brief descriptions of these activities are given below. More detailed examples of their use and the results of their application in this study are discussed in Chapter VI.

Filter "tuning" describes the process of iteratively adjusting the value of a single filter parameter based on results of successive Monte Carlo studies. Commonly, the parameter chosen for adjustment is Q(t), the strength of dynamics driving noise, since its value is seldom known with

great certainty. By repeating Monte Carlo studies and using different values of Q(t), the filter analyst can find driving noise strenths which result in lower peak errors, shorter settling times, or other desirable qualities as measured by figures of merit. Similarly, a series of Monte Carlo studies can be conducted by leaving Q(t) constant and varying another parameter, such as measurement noise strengths or, in the case of the GMA model, the target acceleration time constant, τ.

An error budget is a technique used to determine the effect of separate sources of error on filter performance (1:339). If each known source of error is modelled separately in the truth model, it is posssible to turn on the error sources one at a time for a series of Monte Carlo studies. Using the figures of merit as metrics, the analyst compares the results of these Monter Carlo studies and assesses the relative contribution of each separate error source to the overall filter error. By identifying the largest contributors to filter error, the analyst determines areas in which adjustments or changes in filter design are most likely to yield significant performance improvements.

Conceptually, the above filter evaluation procedures can be separated into distinct activities and discussed in a logical sequence. In practice, however, these activities are strongly interdependent and are frequently accomplished iteratively or in parallel. For example, an error budget is typically constructed using a filter which has already been

validated and tuned. However, the results of the error budget may mandate filter changes which require re-validation and retuning of the modified filter. In turn, another error budget may be justified. The intricacies of the filter evaluation process vary from application to application and are best understood in the context of a specific problem. The next chapter discusses evaluation procedures as applied to the proposed F-4E/G LRI filters and presents the results from each stage of the filter evaluation process.

VI. Results

Introduction

This chapter presents the results of Monte Carlo studies conducted to evaluate the performance of the CV and GMA filters for the three test trajectories defined in the previous chapter. Initial Monte Carlo studies, which are used to identify and correct flaws in the simulation software, are not included here because they do not provide an accurate portrayal of actual filter performance. Later studies, conducted after the establishment of a credible simulation package, provide a better representation of filter performance and are used for filter tuning and other evaluation procedures. These studies are presented sequentially as follows:

(1) Baseline filter comparisons and validation

(2) Filter tuning using driving noise

(3) Error budget studies

(4) Filter tuning using measurement noise

(5) Filter adaptation to F-4E/G roll rate

(6) Filter comparisons on three trajectories

As emphasized in the previous chapter, filter evaluation procedures are highly interrelated. Most of the above studies are repeated several times in response to the outcomes of related studies. In most cases, the results tabulated in this chapter are the culmination of repetitive

testing. Furthermore, the order of the above activities does not imply their exact order of accomplishment.

Baseline Filter Comparisons and Validation

One of the early goals of the filter evaluation process is to obtain side-by-side comparisons of the CV and GMA filters operating under comparable conditions. To attain this goal, a five-run Monte Carlo study is conducted for each filter using the beam trajectory. The beam trajectory is considered the worst case trajectory because the los rates in this trajectory caused lags in the antenna angle and angle rate measurements which produced larger errors than in the other two trajectories. The beam trajectory is also the primary test case used for filter tuning and other evaluation procedures. The baseline comparison studies use the initial strengths of driving noise derived in Chapter II for the CV and GMA filters. Initial measurement noise strengths were provided by F-4E/G software engineers at Hill AFB, Utah, as discussed in Chapter III.

Although 0.04 second is the original update interval specified in Chapter I, allowance is made for longer update intervals. The maximum allowable interval is 0.1 second, a constraint imposed by the 10 Hz rate required for cockpit instrumentation updates. In terms of filter accuracy, the 0.1 second update rate is considered the most severe condition since it incorporates the least measurement information and allows propagation error to grow uncorrected for the

longest period of time. For this reason, 0.1 second is the measurement interval used for all filter evaluation studies. Theoretically, an actual filter implementation which uses a faster update rate could achieve improved performance after recalculation of Q_d, as given by (4-16).

The results of the baseline filter comparisons are illustrated in Appendix E. In studies using all six measurements, both filters performed well until the initiation of the F-4E/G roll maneuver, when both filters produced large errors in position and velocity states. The GMA filter converged to pre-maneuver accuracy in all states within six seconds after the end of the maneuver. The CV filter produced errors an order of magnitude greater than the GMA filter and failed to converge in all states after the maneuver ended. These results are illustrated by SOFEPL plots in Appendix E, Figs. E.1 through E.15. Table VI-1 summarizes the results.

A second set of studies compared CV and GMA filter performance using only four measurements; range, range rate, and the two gimbal angles. Again, both filters committed unacceptably large position and velocity errors during ownship maneuvers, but in this case, both filters exhibited errors of similar magnitudes and displayed settling times of 7-12 seconds in all states. Table VI-2 summarizes these studies. Full performance plots are shown in Figs. E.16 through E.20. Since the peak total velocity errors committed by both filter in these initial studies are two orders

TABLE VI-1

Baseline Comparison of CV and GMA Filters on Beam Trajectory
(6 Measurements)

State	Peak Error Magnitude		Settling time	
	CV	GMA	CV	GMA
Position				
North	65000 ft	980 ft	none	10.5 sec
East	61000 ft	980 ft	none	12.0 sec
Down	35000 ft	3500 ft	none	11.6 sec
Velocity				
North	41000 fps	590 fps	10.0 sec	10.5 sec
East	35000 fps	710 fps	9.0 sec	10.3 sec
Down	27000 fps	2800 fps	9.0 sec	11.0 sec

TABLE VI-2

Baseline Comparison of CV and GMA Filters on Beam Trajectory
(4 Measurements)

State	Peak Error Magnitude		Settling time	
	CV	GMA	CV	GMA
Position				
North	1250 ft	1125 ft	7.3 sec	10.2 sec
East	1270 ft	1100 ft	11.5 sec	10.0 sec
Down	4400 ft	3300 ft	7.3 sec	11.5 sec
Velocity				
North	1090 fps	475 fps	8.8 sec	10.2 sec
East	1250 fps	780 fps	9.0 sec	11.9 sec
Down	3900 fps	2520 fps	9.6 sec	11.0 sec

of magnitude higher than desired, filter tuning is required. An examination of the above data reveals that the GMA filter with four measurements committed the lowest peak total

velocity error, 2680 fps. For this reason most filter evaluation procedures after this point use only four measurements; range, range rate, and gimbal angle sines.

Comparison of CV and GMA filter performance using four measurements supports the expected result that the GMA filter provides improved estimation over the CV model. Peak position errors were 10-25 % lower and peak velocity errors were 35-56 % lower for the GMA filter as compared to the CV filter. The relatively large errors in the vertical channel are attributed to a lack of observability in that dimension, a consequence of the two-dimensional truth model. Settling times were slightly longer for the GMA model, but remained less than 12 seconds. Time-averaged error is not used for this portion of the evaluation because it provides little useful information when peak error magnitudes are very large.

Filter Tuning Using Driving Noise

This series of Monte Carlo studies sought to improve baseline performance of the GMA filter by adjusting the strength of dynamic driving noise. Several studies were conducted using the GMA filter with the four measurements discussed in the previous section. These studies indicate that filter performance improves as Q(t) is decreased from the baseline value. Table VI-3 summarizes a series of simulations in which Q(t) is lowered by factors of 10 and compared with baseline filter performance. Appendix F contains performance plots for these studies.

TABLE VI-3

Effect of Changing Driving Noise Strength on GMA Filter
(4 Measurements)

Q(t): (ft^4/sec^5)	5000	1000	100	10
Position:	Peak Error Magnitude (ft)/Settling time (sec)			
North	1125/10.2	1000/12.0	970/13.5	950/*
East	1100/10.0	990/12.5	980/15.0	900/17.0
Down	3300/11.5	2800/12.5	2450/13.0	2400/*
Velocity:	Peak Error Magnitude (fps)/Settling time (sec)			
North	475/10.2	360/12.3	265/17.0	250/*
East	780/11.9	365/12.5	250/16.5	240/*
Down	2520/11.0	1450/12.0	770/13.5	710/*

* Greater than 20 sec

Two trends are apparent in Table VI-3. As Q(t) is decreased, peak error magnitudes decrease and settling times increase. A value of 100 ft^4/sec^5 is chosen as a good value of Q(t), since it results in reasonable values for both peak error and settling time. This value is used in the remaining filter evaluations.

Error Budget Studies

Although the truth model used for filter evaluation does not model individual error sources in the dynamic system, it is possible to investigate the effect of different measurement noise sources by running the filter with different combinations of one, two, or three measurements. One complicating factor that results from testing the filter with fewer than four measurements is that the system is no

longer completely observable. In Monte Carlo studies using the GMA filter with three or fewer measurements, it is difficult to separate the effect of unobservable states from other effects, such as the effect of an improperly modelled measurement. However, useful insights can be obtained by this technique and it is used extensively in this study.

Three general performance patterns result from Monte Carlo studies using less than a full complement of four measurements. Those studies using only range, range rate, or both are completely insensitive to ownship maneuver. Mean errors remain close to zero in all states, but filter-computed covariances increase without bound. In Appendix G, Figs. G.1 through G.9 illustrate this performance pattern. A different pattern results from using only gimbal angle measurements. The filter error is extremely sensitive to ownship maneuvers. As seen in Figs. G.10 through G.18, the overall performance of filters using only angle measurements resembles the general pattern of performance with four measurements, but with larger peak errors and longer settling times in position and velocity states. A third general pattern of performance emerges from studies using only angle rate measurements. In these, several GMA states diverge rapidly after ownship maneuver, as illustrated in Figs. G.19 through G.27. This result gives additional impetus to continue testing without using angle rate measurements.

In order to further investigate the effect of dynamic lags in the gimbal angle measurements, the truth model is modified to remove these lags. This allows a critical source of error to be turned on and off in the truth model. A Monte Carlo study is performed using the GMA filter with range, range rate, and gimbal angle measurements with the lags removed. The results show peak error improvements of an order of magnitude or greater in all states, as can be seen by comparing Figs. G.28 through G.36 with Figs. F.10 through F.18. Table VI-4 summarizes this comparison.

TABLE VI-4

Effect of Removing Dynamic Lags from Angle Measurements (GMA model, 4 measurements, Q = 100)

	With Lags	Without Lags
Position:	Peak Error Magnitude (ft)/Settling time (sec)	
North	970/13.5	30/0.0
East	980/15.0	30/0.0
Down	2450/13.0	35/0.0
Velocity:	Peak Error Magnitude (fps)/Settling time (sec)	
North	265/17.0	8/0.0
East	250/16.5	8/0.0
Down	770/13.5	14/0.0

The results displayed in Table VI-4 suggest that the dynamic lags in the angle measurements contribute significantly to GMA filter error. One way to improve filter performance is to model the lags in the filter dynamics

equations. Another way is to adjust the value of measurement noise associated with angle measurements, as discussed in the next section.

Filter Tuning Using Measurement Noise

The results of the error budget studies discussed in the previous section suggest that the angle and angle rate measurements make the largest contributions to overall filter error. The lags in the antenna angle measurements are isolated and shown specifically to be an important source of filter error. These results motivate the next series of Monte Carlo studies, in which the strengths of the measurement noise associated with the angle and angle rate measurements are increased. The first study, illustrated in Appendix H, Figs. H.1 through H.13, evaluates the GMA filter using four measurements and a driving noise strength of 100 ft^4/sec^5. This allows direct comparison with the filter performance study shown in Figs. F.10 through F.18, in which the original angle measurement noise strength of 1.1×10^{-6} is used for both angle measurements. In the new study, measurement noise strengths for the two angle measurements are increased to 2.0×10^{-4}, as discussed below. The increase in measurement noise yields improvements of 76.4 to 80.8 % in the position states and improvements of 87.5 to 91.9 % in the velocity states. Settling times increase 2 to 4 seconds in position states, but decrease a similar amount in the velocity states. Table VI-5 summarizes these results.

TABLE VI-5

Effect of Increasing Measurement Noise Strengths Associated With Antenna Angle Measurements

(GMA model, 4 measurements, Q = 100)

Angle Measurement Noise Strength:	1.1×10^{-6}	2.0×10^{-4}
Position:	Peak Error Magnitude (ft)/Settling time (sec)	
North	970/13.5	230/15.0
East	980/15.0	230/19.0
Down	2450/13.0	470/13.0
Velocity:	Peak Error Magnitude (fps)/Settling time (sec)	
North	265/17.0	33/14.3
East	250/16.5	29/13.0
Down	770/13.5	62/13.0

The value of angle *measurement noise* strength in the right column Table VI-5 was selected after several earlier Monte Carlo studies indicated that higher values did not produce significant improvements in filter performance. The lowest possible value is desirable because the filter essentially ignores a measurement if its associated measurement noise strength is too large. The value of 2.0×10^{-4} also agreed closely with a computer experiment in which the truth model was adapted to calculate the variance of the sine of the angle errors during an F-4E/G roll maneuver.

Another group of Monte Carlo studies investigates the performance of the GMA filter with six measurements after increasing the noise strength of the angle rate measure-

ments. The results of this study, shown in Figs. H.14 through H.28, indicate that no performance advantage is gained by incorporating the angle rate measurements. Peak error statistics duplicate the right column of Table VI-5 except for an 8-10 % reduction in the vertical channel position and velocity states. Settling times increase in the six measurement simulation, and exceed the 20 second simulation time for the vertical channel states. For these reasons, no further evaluations are conducted using six measurements. Other techniques for improving GMA filter performance are discussed in the next section.

Filter Adaptation to F-4E/G Roll Rate

Adaptive filtering techniques are investigated in an attempt to further improve filter performance. Although adaptive filtering is typically based on residual monitoring schemes (2:69), a more direct method is chosen for this study. Since the most serious filter errors occur in response to F-4E/G maneuvers, a simple attitude rate detector can be used to trigger filter adaptations. Two studies are conducted on the GMA model using this approach. In the first, a roll detector increases the value of gimbal angle measurement noise whenever ownship roll rates exceed a threshold of 0.05 radians per second. In the second study, the value of Q(t) is decreased to 1 ft^4/sec^5 when roll rate exceeds the threshold. Both studies produced disappointing results. The adaptive Q(t) filter shows little change in

performance, while the adaptive measurement noise filter commits peak errors four times larger than the same filter without adaptation. In both cases, performance plots indicate that adaptations occur at the desired times but do not produce the desired effects. Appendix I contains performance plots for these studies.

Filter Comparisons on Three Trajectories

As a final demonstration of the feasibility of a Kalman filter for the F-4E/G LRI function, the tuned GMA filter is compared in all three trajectories discussed in Chapter V. The comparisons involve 20-run Monte Carlo simulations of the GMA filter using four measurements. The results indicate similar performance for the beam and tailchase trajectories. Performance improves significantly in the head-on attack profile. Appendix J contains performance plots of these studies, which are summarized in Table VI-6.

With the exception of the head-on attack profile, the final evaluations continue to display vertical channel errors approximately twice as large as errors in the other channels. As stated earlier, this is attributed to a lack of observability resulting from the two dimensional truth model trajectories. An attempt was made to evaluate GMA filter performance while masking the lack of observability in the vertical channel. This was done by repeating the 20-run Monte Carlo studies of each trajectory discussed above and artificially suppressing the errors in all three

TABLE VI-6

GMA Filter Performance on Three Trajectories
(4 measurements)

	BEAM	TAILCHASE	HEAD-ON
Position:	Peak/Time-averaged Error Magnitudes (ft)		
North	175/75	190/50	10/9
East	175/78	203/60	65/30
Down	345/90	500/100	50/25
Velocity:	Peak/Time-averaged Error Magnitudes (fps)		
North	24/8	23/5	2/0
East	23/10	25/5	8/2
Down	45/4	58/12	7/3

vertical channel states. The results of this ad hoc procedure were inconclusive. North and east channels produced approximately the same peak errors and settling times observed without vertical channel supression. In some states, peak errors were 2-5 % larger than in full state performance. Appendix K contains plots of these studies.

An analysis of the target velocity errors in Table VI-6 shows peak total velocity error values of 55.9 fps for the beam trajectory, 67.2 fps for the tailchase, and 10.8 fps for the head-on attack. If these values are considered to be three-sigma values of total velocity error, the one standard deviation values of velocity error are 18.6, 22.4, and 3.6 fps, respectively. In each case this is lower than the 30 fps benchmark established in Chapter I, and suggests

TABLE VI-7

Comparison of Tuned CV and GMA Filters
(4 measurements, 20 runs, Beam Trajectory)

	CV	GMA
Position:	Peak/Time-averaged Error Magnitudes (ft)	
North	180/80	175/75
East	180/90	175/78
Down	350/50	345/90
Velocity:	Peak/Time-averaged Error Magnitudes (fps)	
North	28/10	24/8
East	26/11	23/10
Down	50/20	45/4

that the GMA filter with four measurements can exceed Wiener-Hopf filter performance.

A final validation of the CV filter is also accomplished using four measurements and noise values obtained from the previous filter evaluations. A 20-run Monte Carlo analysis of CV filter performance on the beam trajectory is illustrated in Appendix D, Figs. D.1 through D.6 and summarized in Table VI-7. The overall standard deviation of velocity error for the CV filter is 21.0 fps in this study, which establishes this filter as a viable alternative for use in the F-4E/G LRI function.

VII. Conclusions and Recommendations

As stated in the introductory chapter, the purpose of this study is to determine the feasibility of improving the LRI function of the F-4E/G fire control system by replacing the existing Wiener-Hop filter with a Kalman filter. To warrant implementation, the proposed Kalman filter must produce target velocity estimates which meet LRI accuracy criteria regardless of F-4E/G combat maneuvering. Additionally, the Kalman filter must operate under the severe constraints imposed by limited memory, slow speed, short word-length, and noise-corrupted measurements available in the existing F-4E/G fire control computer. Two candidate filters are proposed, one based on a constant velocity dynamics model, and the other based on a Gauss-Markov target acceleration model. Both models are implemented as extended Kalman filters in a computer simulation and evaluated using Monte Carlo analysis. The results of the simulation studies provide the basis for the conclusions and recommendations presented in this chapter.

Conclusions

A 9-state reduced order Kalman filter algorithm can be implemented in the constrained memory of the LRU-1 fire control computer and can operate within the allowable measurement interval, providing that the requirement for on-line

numerical integration is avoided. This requirement is met by preserving linear, time-invariant dynamics in the filter model. Both the proposed CV and GMA models are satisfactory in this respect, since inherent nonlinearities in these models are confined to the measurement equations. The results obtained from the performance evaluations of these filters support the conclusion that the CV and GMA filters are feasible replacements for the existing Wiener-Hopf filter in the F-4E/G OFP. The GMA filter is emphasized for two reasons. First, its performance exceeds that of the CV filter when evaluated in LRI simulations. Second, variations of the GMA filter can be adapted to successfully perform estimation for the F-4E/G ACM function as well as for the LRI function (32). A single filter capable of satisfying the requirements of both the LRI and ACM functions is strongly motivated by the speed and memory limitations of the LRU-1 computer.

Although the performance results of the tuned GMA filter indicate that its velocity error has a standard deviation well below that of the Wiener-Hopf benchmark value of 30 fps on all trajectories tested, there are a number of unresolved issues which impact the ability of the GMA filter to achieve similar performance in an operational setting. These issues include the failure of the angle rate measurements to improve filter performance, the modelling of the dynamic lags in the sine angle measurements, and the presence of large vertical channel errors attributed to lack of

observability in the simulated trajectories. The need to address these issues before attempting any operational filter implementation motivates many of the recommendations in the next section.

Recommendations

The conclusions reached in this study lead to recommendations in two general areas, advanced testing and operational implementation. Recommendations concerning advanced testing are motivated by the existence of the unresolved issues discussed above and the need to critically examine their impact on an operational filter. Attention should be focused on aspects of both the filter and truth models. One primary recommendation is to expand the truth model to accommodate three dimensional aircraft trajectories. This would help resolve the question of observability in the vertical channel. Another valuable improvement is to model individual sources of error separately in the truth model. Examples of errors that need to be modelled are the glint noise error in radar measurements, the errors associated with INS attitude angles, and errors in the ownship velocity vector. These error models complement the previously modelled errors associated with dynamic lags in the gimbal angles and with rate gyro transients in the angle rate measurements. The capability to turn these different errors on or off in an error budget gives the filter designer a powerful tool for locating the areas in which filter design

improvements can achieve the greatest gains in filter performance.

The filter model should also be critically reexamined during advanced testing. The angle rate measurement equations in the filter model are not validated by performance results in this study. This could possibly stem from inappropriate angle rate equations in the filter model, misaligned geometry between the truth model and the filter model, or a combination of both. Another recommended improvement to the filter is to model the dynamic lags in the gimbal angles by augmenting extra states to the basic 9-state dynamics model. The dynamics equations for the extra states are based on the truth model equations for calculating the lags.

Finally, the advanced testing program should expand the filter tuning procedures followed in this study. For example, additional noise terms could be added to those dynamics equations requiring ownship velocity terms. This noise would account for the uncertainty in ownship velocity generated by coordinate transformantions using noise-corrupted INS angles. Another possibility is ad hoc tuning using nonzero off diagonal terms in the driving noise or measurement noise matrices. A third recommendation in this area is to investigate adaptive tuning techniques again. The method used in Chapter VI to increase gimbal angle measurement noise strength during ownship maneuver can be adapted to use a variable-strength noise value calculated as a function of

range dependent noise (glint) and roll rate dependent noise (angle lags).

In addition to continued testing, several recommendations can be made concerning filter implementation. These recommendations, based on the evaluation results obtained in this study are as follows:

(1) Minimize complexity by implementing a 9 to 12 state filter in the fire control computer.

(2) Preserve linearity in the filter dynamics model to avoid the computational burden of on-line numerical integration.

(3) Avoid observability problems by choosing a coordinate frame in which all modes will be excited regardless of the trajectory flown. The north, east, and down frame used in this study may not be adequate in this respect under some conditions.

(4) Implement the final design using a square root or U-D algorithm. The impact of short wordlength is not specifically evaluated in this study, but is a well known cause of numerical instabilities in conventional Kalman algorithms.

(5) Tune the final filter for several different trajectories to insure it performs adequately for the variable conditions of the air-to-air combat environment.

The above recommendations are not all inclusive. Many techniques are available to today's optimal filter designer and all cannot be examined in a work of this scope. This study has demonstrated the feasibility of a Kalman filter for the F-4E/G LRI function and identified several critical issues which will affect the success of any Kalman filter employed for that purpose. The models provided in this study are a suitable basis for experimental filters which can be further improved by augmented models and continued testing.

Appendix A: Binary Calculations

Maximum relative range: 182,400 feet

In binary: 1011001000100000000

8 foot precision: 10110010001000---- (14 digits required)

Maximum total range: 4,152,640 feet

In binary: 1111111010111010100000000

8 ft precision: 111111010111010100---- (18 digits required)

Maximum relative velocity: 1520 fps

In binary: 10111110000

4 fps precision: 10111110--- (8 digits required)

Maximum total velocity: 760 fps

In binary: 1011111000

4 fps precision: 1011111--- (7 digits required)

Appendix B: State Transition Matrices

For the CV model:

$$[sI-F] = \begin{bmatrix} s & -1 & 0 & 0 & 0 & 0 \\ 0 & s & 0 & 0 & 0 & 0 \\ 0 & 0 & s & -1 & 0 & 0 \\ 0 & 0 & 0 & s & 0 & 0 \\ 0 & 0 & 0 & 0 & s & -1 \\ 0 & 0 & 0 & 0 & 0 & s \end{bmatrix}$$

$$[sI-F]^{-1} = \begin{bmatrix} \frac{1}{s} & \frac{1}{s^2} & 0 & 0 & 0 & 0 \\ 0 & \frac{1}{s} & 0 & 0 & 0 & 0 \\ 0 & 0 & \frac{1}{s} & \frac{1}{s^2} & 0 & 0 \\ 0 & 0 & 0 & \frac{1}{s} & 0 & 0 \\ 0 & 0 & 0 & 0 & \frac{1}{s} & \frac{1}{s^2} \\ 0 & 0 & 0 & 0 & 0 & \frac{1}{s} \end{bmatrix}$$

Taking the Laplace transform inverse,

$$\Phi(\Delta t) = \begin{bmatrix} 1 & \Delta t & 0 & 0 & 0 & 0 \\ 0 & 1 & 0 & 0 & 0 & 0 \\ 0 & 0 & 1 & \Delta t & 0 & 0 \\ 0 & 0 & 0 & 1 & 0 & 0 \\ 0 & 0 & 0 & 0 & 1 & \Delta t \\ 0 & 0 & 0 & 0 & 0 & 1 \end{bmatrix}$$

For $\Delta t = 0.04$

$$\Phi(0.04) = \begin{bmatrix} 1 & 0.04 & 0 & 0 & 0 & 0 \\ 0 & 1 & 0 & 0 & 0 & 0 \\ 0 & 0 & 1 & 0.04 & 0 & 0 \\ 0 & 0 & 0 & 1 & 0 & 0 \\ 0 & 0 & 0 & 0 & 1 & 0.04 \\ 0 & 0 & 0 & 0 & 0 & 1 \end{bmatrix}$$

The input matrix, $B_d(t_i)$, is calculated using (4-15).

$$B_d(t_i) = \int \begin{bmatrix} 1 & \Delta t & 0 & 0 & 0 & 0 \\ 0 & 1 & 0 & 0 & 0 & 0 \\ 0 & 0 & 1 & \Delta t & 0 & 0 \\ 0 & 0 & 0 & 1 & 0 & 0 \\ 0 & 0 & 0 & 0 & 1 & \Delta t \\ 0 & 0 & 0 & 0 & 0 & 1 \end{bmatrix} \begin{bmatrix} -1 & 0 & 0 \\ 0 & 0 & 0 \\ 0 & -1 & 0 \\ 0 & 0 & 0 \\ 0 & 0 & -1 \\ 0 & 0 & 0 \end{bmatrix} d\tau$$

$$= \begin{bmatrix} -0.04 & 0 & 0 \\ 0 & 0 & 0 \\ 0 & -0.04 & 0 \\ 0 & 0 & 0 \\ 0 & 0 & -0.04 \\ 0 & 0 & 0 \end{bmatrix}$$

$Q_d(t_i)$ is calculated by evaluating (4-16), with

$$Q(\tau) = \begin{bmatrix} q_N & 0 & 0 \\ 0 & q_E & 0 \\ 0 & 0 & q_N \end{bmatrix}$$

Carrying out the indicated matrix multiplications in (4-16) and integrating over the 0.04 second update interval yields

$$Q_d = \begin{bmatrix} 0 & 0 & 0 & 0 & 0 & 0 \\ 0 & *_N & 0 & 0 & 0 & 0 \\ 0 & 0 & 0 & 0 & 0 & 0 \\ 0 & 0 & 0 & *_E & 0 & 0 \\ 0 & 0 & 0 & 0 & 0 & 0 \\ 0 & 0 & 0 & 0 & 0 & *_D \end{bmatrix}$$

where $*_i = 0.04q_i \quad (i=N,E,D)$

The same procedures apply for the GMA model. For example,

$$\Phi(\Delta t) = \begin{bmatrix} *_{3x3} & 0_{3x3} & 0_{3x3} \\ 0_{3x3} & *_{3x3} & 0_{3x3} \\ 0_{3x3} & 0_{3x3} & *_{3x3} \end{bmatrix}$$

where

$$*_{3x3} = \begin{bmatrix} 1 & t & \tau^2\left(\frac{t}{\tau} - 1 + \exp\left(-\frac{t}{\tau}\right)\right) \\ 0 & 1 & \left(1 - \exp\left(-\frac{t}{\tau}\right)\right) \\ 0 & 0 & \exp\left(-\frac{t}{\tau}\right) \end{bmatrix}$$

Evaluating at $\tau = 0.5$ and $\Delta t = 0.04$ yields the values listed in (4-25).

Appendix C: Coordinate Frames

The various coordinate frames used in this study are defined below. Positive rotations are illustrated except for the two degree fixed angle relating the body and radar reference l-axes, which is shown as a negative j-axis rotation. Notation is consistent with the sources listed.

Geographic (inertial) Frame:
Axes: N,E,D
Source: 10:3-425

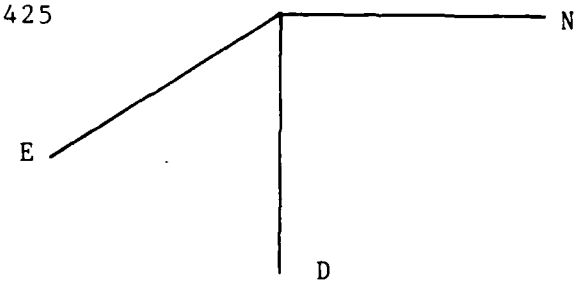

Space Frame:
Axes: x,y,z
Source: 10:3-425

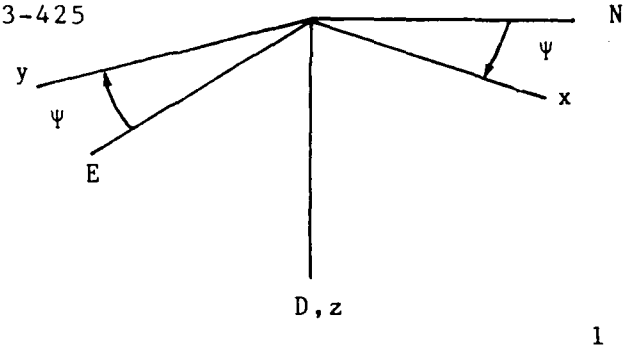

Body Frame:
Axes: 1,m,n (1=FRL)
Source: 10:3-111, 3-425

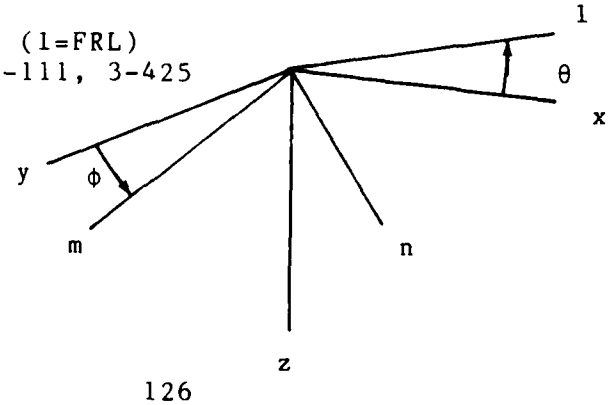

Radar Reference Frame:
Axes: i_o, j_o, k_o (i_o=RBL)
Source: 10:3-411

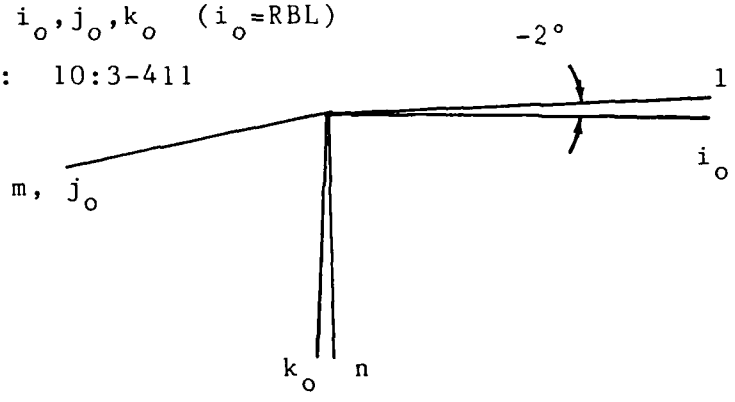

Antenna (tracker) Frame:
Axes: i,j,k (i ≈ los)
Source: 10:3-370

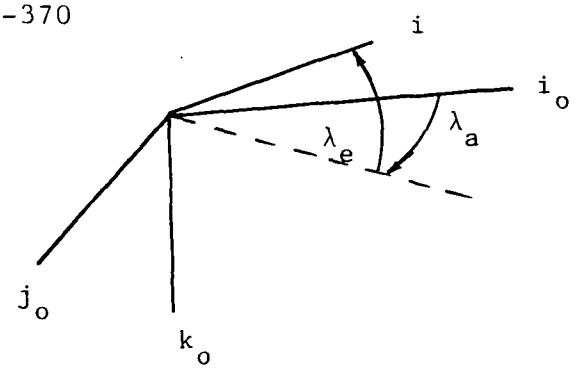

A windstream (TAS) reference is also related to the radar reference frame by angle-of-attack, α (10:3-411):

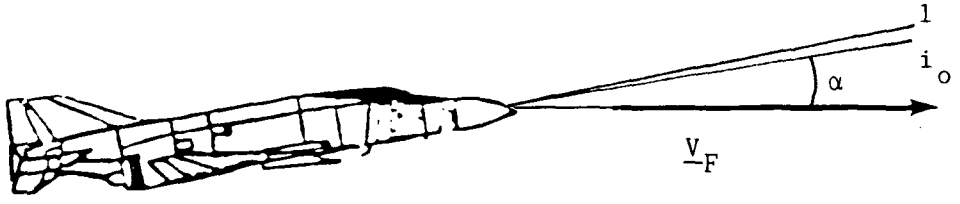

These coordinate references can related by standard, order dependent, Euler angle rotations. For instance, the

full transformation from geographic to antenna coordinates is represented by:

$$\begin{bmatrix} i \\ j \\ k \end{bmatrix} = [{}^{2}\lambda_e]\,[{}^{3}\lambda_a]\,[{}^{2}\text{-}2]\,[{}^{1}\phi]\,[{}^{2}\theta]\,[{}^{3}\psi] \begin{bmatrix} N \\ E \\ D \end{bmatrix} \qquad \text{(C-1)}$$

where $[{}^{n}A]$ are the following n-axis rotation matrices (38:20):

$$[{}^{1}A] = \begin{bmatrix} 1 & 0 & 0 \\ 0 & \cos A & \sin A \\ 0 & -\sin A & \cos A \end{bmatrix} \qquad \text{(C-2)}$$

$$[{}^{2}A] = \begin{bmatrix} \cos A & 0 & -\sin A \\ 0 & 1 & 0 \\ \sin A & 0 & \cos A \end{bmatrix} \qquad \text{(C-3)}$$

$$[{}^{3}A] = \begin{bmatrix} \cos A & \sin A & 0 \\ -\sin A & \cos A & 0 \\ 0 & 0 & 1 \end{bmatrix} \qquad \text{(C-4)}$$

The inverse transformation is

$$\begin{bmatrix} N \\ E \\ D \end{bmatrix} = [{}^{3}\psi]^{T}\,[{}^{2}\theta]^{T}\,[{}^{1}\phi]^{T}\,[{}^{2}\text{-}2]^{T}\,[{}^{3}\lambda_a]^{T}\,[{}^{2}\lambda_e]^{T} \begin{bmatrix} i \\ j \\ k \end{bmatrix} \qquad \text{(C-5)}$$

where superscript T indicates the transpose of the above rotation matrices. Specific transformations used in this study are calculated below.

TRANSFORMATION 1: F-4E/G velocity in radar reference coordinates can be calculated as

$$\begin{bmatrix} V_{F_{io}} \\ V_{F_{jo}} \\ V_{F_{ko}} \end{bmatrix} = [{}^{2}\alpha] \begin{bmatrix} TAS \\ 0 \\ 0 \end{bmatrix} \tag{C-6}$$

$$\underline{V}_F^R = \begin{bmatrix} \cos\alpha & 0 & -\sin\alpha \\ 0 & 1 & 0 \\ \sin\alpha & 0 & \cos\alpha \end{bmatrix} \begin{bmatrix} TAS \\ 0 \\ 0 \end{bmatrix} \tag{C-7}$$

$$\underline{V}_F^R = \begin{bmatrix} TAS\cos\alpha \\ 0 \\ TAS\sin\alpha \end{bmatrix} \tag{C-8}$$

TRANSFORMATION 2: Converting a vector from radar reference coordinates to geographic coordinates requires

$$\underline{V}_F^G = [T2]\ \underline{V}_F^R \tag{C-9}$$

where the transformation [T2] is given by

$$[T2] = [{}^{3}\psi]^T\ [{}^{2}\theta]^T\ [{}^{1}\phi]^T\ [{}^{2}-2]^T \tag{C-10}$$

Carrying out the indicated matrix multiplications yields the following matrix elements:

$$T2_{11} = \{\cos \Psi \cos \theta \cos -2 \} - \{\cos \Psi \sin \theta \cos \phi \sin -2\} - \{\sin \Psi \sin \phi \sin -2 \} \quad \text{(C-11)}$$

$$T2_{21} = \{\sin \Psi \cos \theta \cos -2 \} - \{\sin \Psi \sin \theta \cos \phi \sin -2\} + \{\cos \Psi \sin \phi \sin -2 \} \quad \text{(C-12)}$$

$$T2_{31} = \{-\sin \theta \cos -2\} - \{\cos \theta \cos \phi \sin -2\} \quad \text{(C-13)}$$

$$T2_{12} = \{\cos \Psi \sin \theta \sin \phi\} - \{\sin \Psi \cos \phi\} \quad \text{(C-14)}$$

$$T2_{22} = \{\sin \Psi \sin \theta \sin \phi\} + \{\cos \Psi \cos \phi\} \quad \text{(C-15)}$$

$$T2_{32} = \cos \theta \sin \phi \quad \text{(C-16)}$$

$$T2_{13} = \{\cos \Psi \cos \theta \sin -2\} + \{\cos \Psi \sin \theta \cos \phi \cos -2\} + \{\sin \Psi \sin \phi \cos -2\} \quad \text{(C-17)}$$

$$T2_{23} = \{\sin \Psi \cos \theta \sin -2\} + \{\sin \Psi \sin \theta \cos \phi \cos -2\} - \{\cos \Psi \sin \phi \cos -2\} \quad \text{(C-18)}$$

$$T2_{33} = \{-\sin \theta \sin -2\} + \{\cos \theta \cos \phi \cos -2\} \quad \text{(C-19)}$$

One possible simplification is the approximation

$$\cos -2 \simeq 1 \quad \text{(C-20)}$$

TRANSFORMATION 3: The inverse of transformation 2 above is given by

$$\begin{bmatrix} i_o \\ j_o \\ k_o \end{bmatrix} = [T3] \begin{bmatrix} N \\ E \\ D \end{bmatrix} \quad \text{(C-21)}$$

where $[T3] = [T2]^T$ due to the orthonormality of all rotation matrices.

TRANSFORMATION 4: The full transformation from geographic coordinates to antenna coordinates expressed in (C-1) can be obtained by applying two additional rotations to the result of transformation 3 above:

$$\begin{bmatrix} i \\ j \\ k \end{bmatrix} = [{}^{2}\lambda_{e}]\,[{}^{3}\lambda_{a}]\,[T3] \begin{bmatrix} N \\ E \\ D \end{bmatrix} \qquad \text{(C-22)}$$

The elements of this matrix are:

$$T4_{11} = \cos\lambda_e \cos\lambda_a T3_{11} + \cos\lambda_e \sin\lambda_a T3_{21} - \sin\lambda_e T3_{31} \qquad \text{(C-23)}$$

$$T4_{21} = -\sin\lambda_a T3_{11} + \cos\lambda_a T3_{21} \qquad \text{(C-24)}$$

$$T4_{31} = \sin\lambda_e \cos\lambda_a T3_{11} + \sin\lambda_e \sin\lambda_a T3_{21} + \cos\lambda_e T3_{31} \qquad \text{(C-25)}$$

$$T4_{12} = \cos\lambda_e \cos\lambda_a T3_{12} + \cos\lambda_e \sin\lambda_a T3_{22} - \sin\lambda_e T3_{32} \qquad \text{(C-26)}$$

$$T4_{22} = -\sin\lambda_a T3_{12} + \cos\lambda_a T3_{22} \qquad \text{(C-27)}$$

$$T4_{32} = \sin\lambda_e \cos\lambda_a T3_{12} + \sin\lambda_e \sin\lambda_a T3_{22} + \cos\lambda_e T3_{32} \qquad \text{(C-28)}$$

$$T4_{13} = \cos\lambda_e \cos\lambda_a T3_{13} + \cos\lambda_e \sin\lambda_a T3_{23} - \sin\lambda_e T3_{33} \qquad \text{(C-29)}$$

$$T4_{23} = -\sin \lambda_a \, T3_{13} + \cos \lambda_a \, T3_{23} \qquad \text{(C-30)}$$

$$T4_{33} = \sin \lambda_e \cos \lambda_a \, T3_{13} + \sin \lambda_e \sin \lambda_a \, T3_{23} + \cos \lambda_e \, T3_{33} \qquad \text{(C-31)}$$

Appendix D

Tuned CV Filter Performance (4 Measurements)

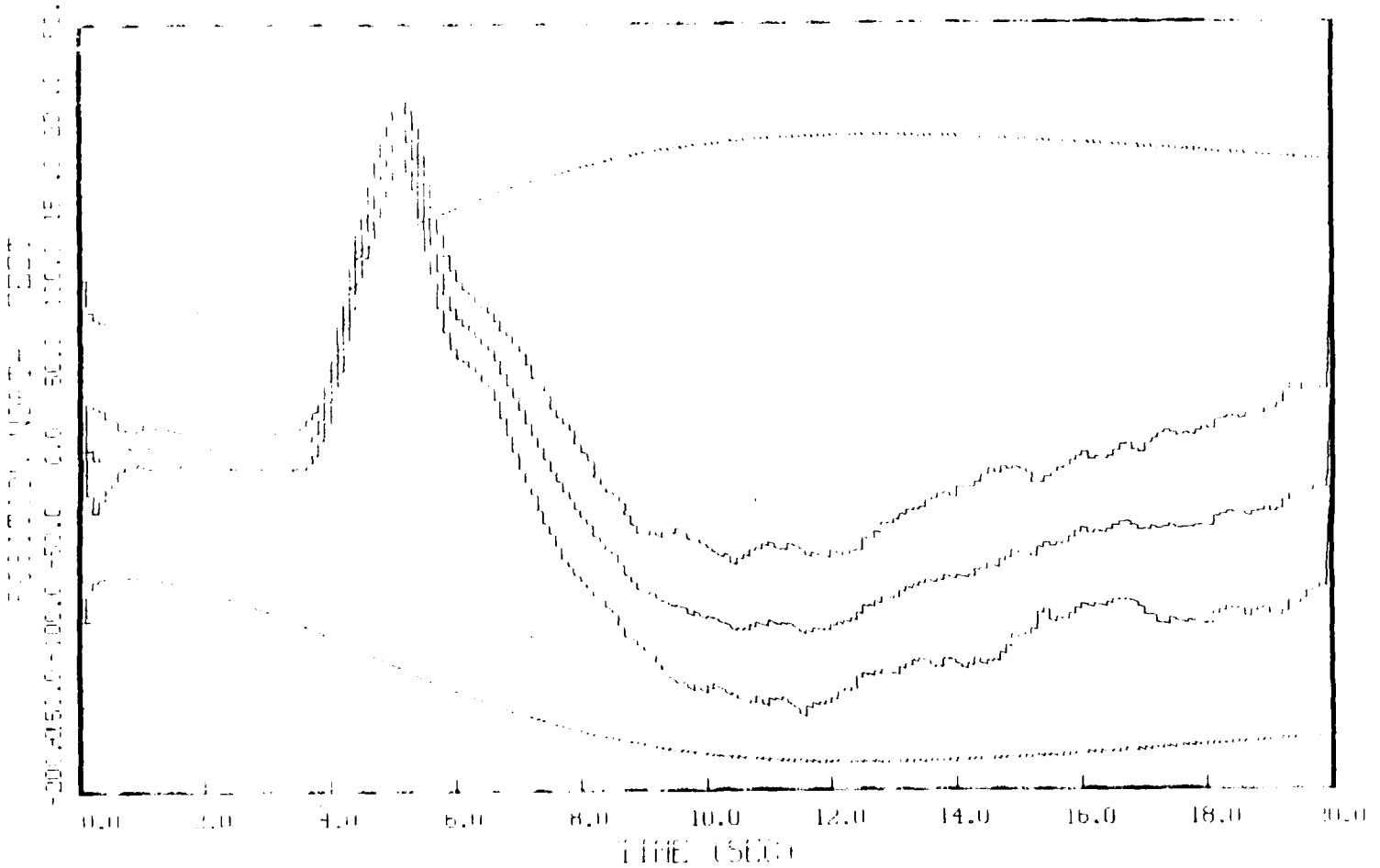

FIG. D.1: CONSTANT VELOCITY MODEL, STATE 1, 20 RUNS, 4 BEAMS
BEAM TRACE FOR 1, Q=100, DOUBLE RATE BEAMS, INHIBITED (R1

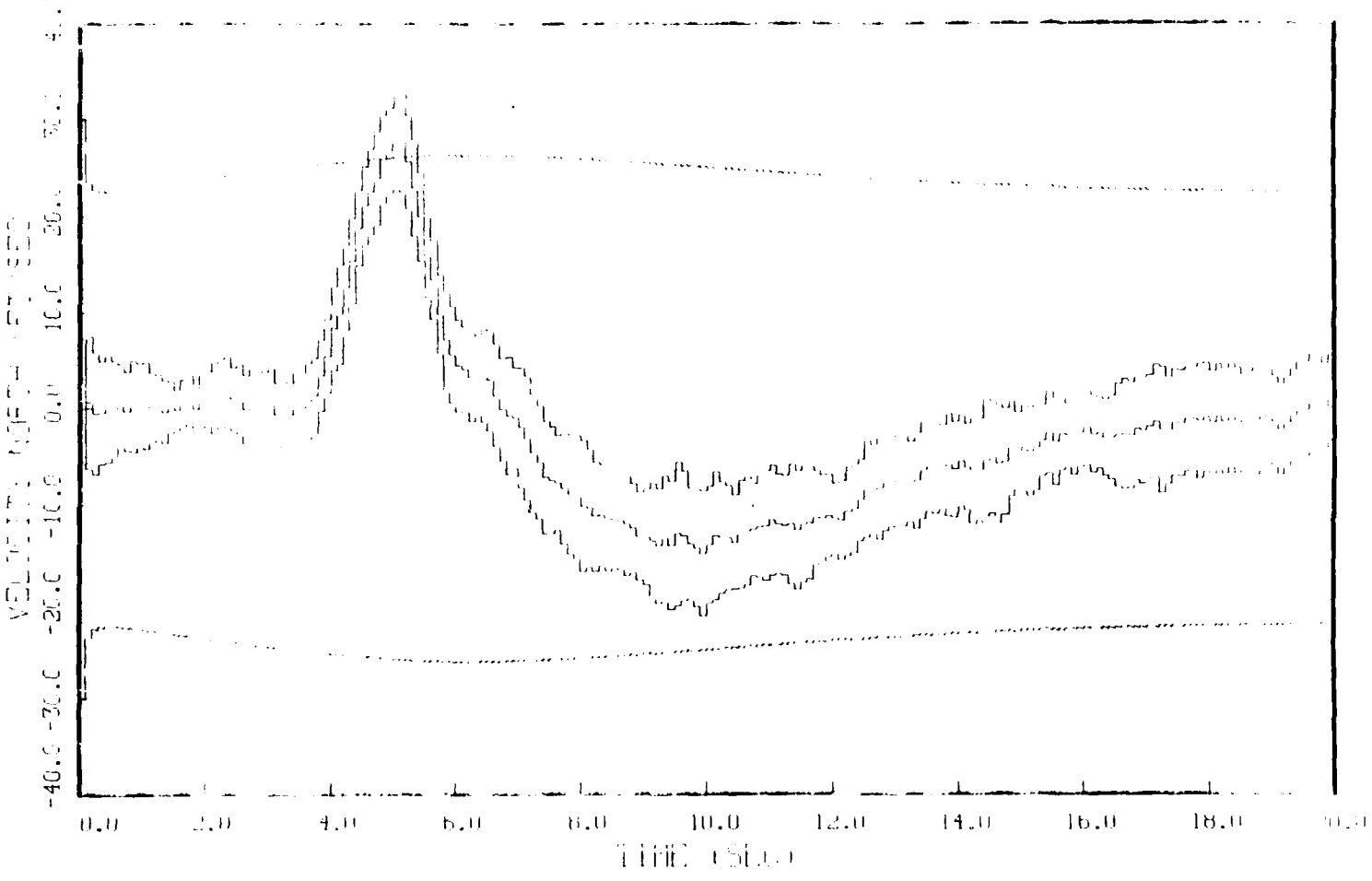

FIG. D.2: CONSTANT VELOCITY MODEL, STATE 2, 20 KNOT, 1 MILE
BEAM TRAJECTORY, 0-100, ANGLE RATE MEAS. INHIBITED

R1

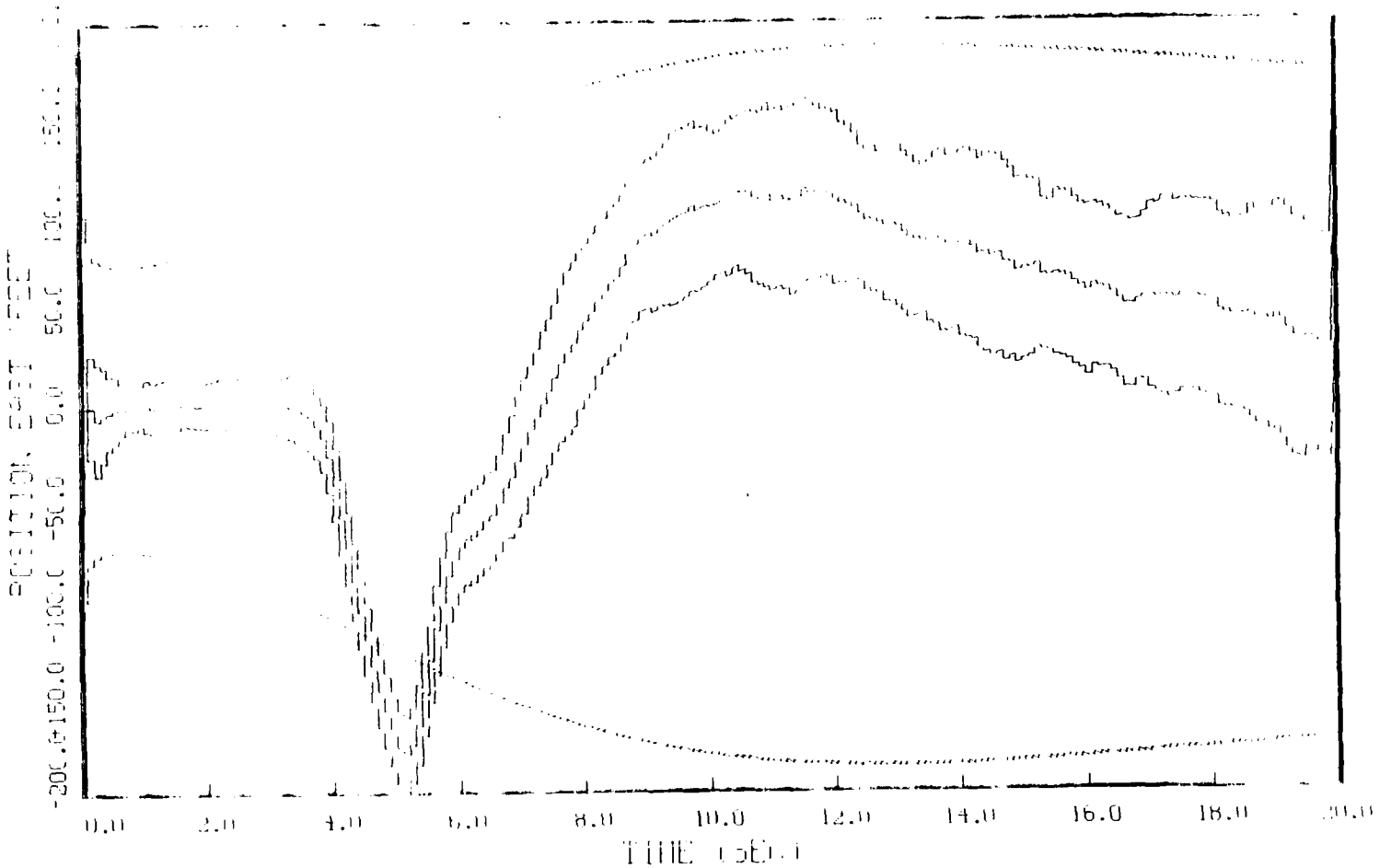

FIG. 6.3: CONSTANT VELOCITY MODEL, STATE 3, 20 RUNS, 4 BEAMS
BEAM TRANSITIONS, α=100, ANGLE RATE MEAS. INHIBITED (R1

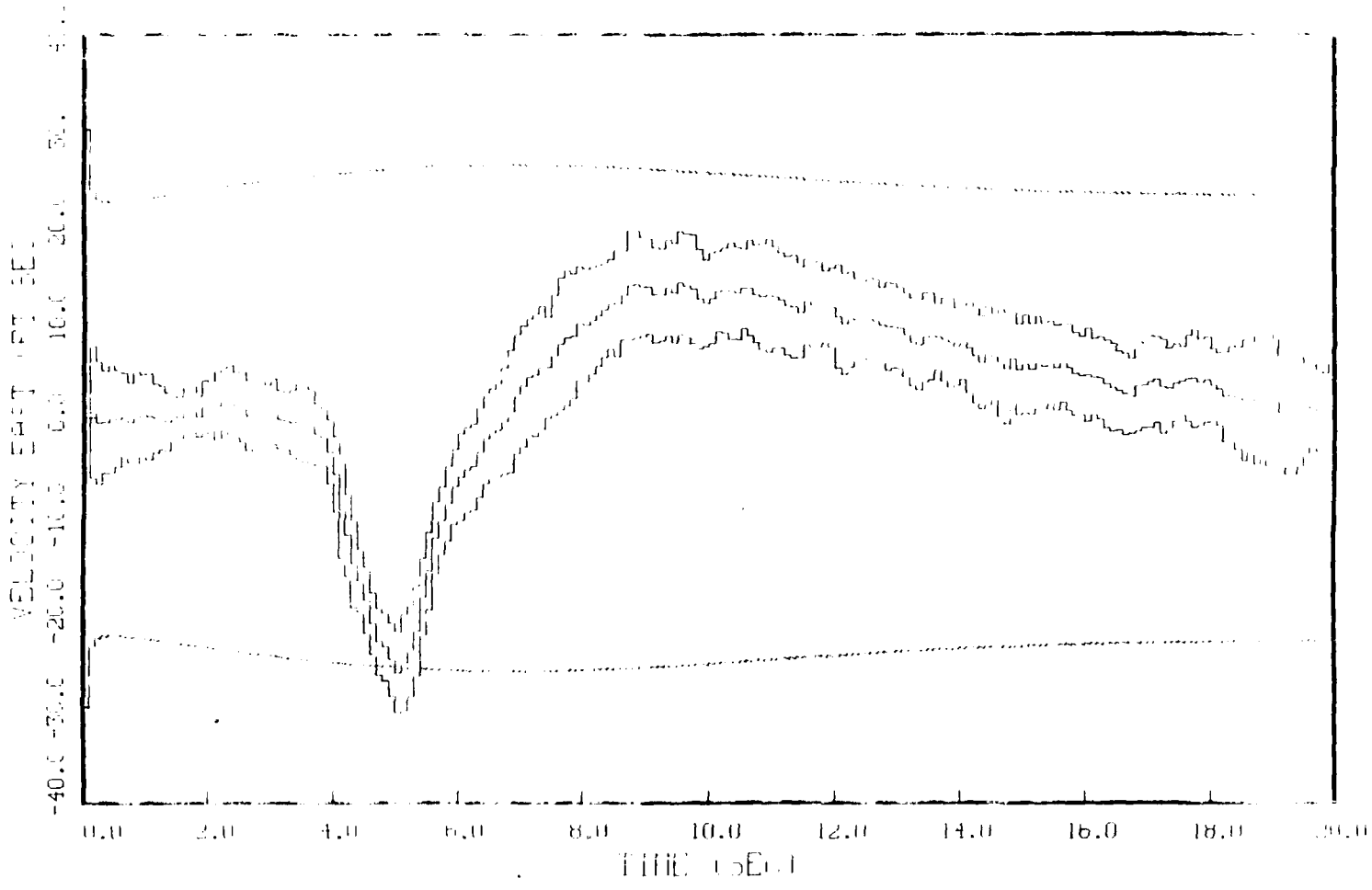

FIG. 6.4: CONSTANT VELOCITY MODEL, STATE 4, 20 RUNS, 4 MEMS
BEAM TRAJECTORY, U-TOT, ANGLE RATE MEAS. INHIBITED 1 R1

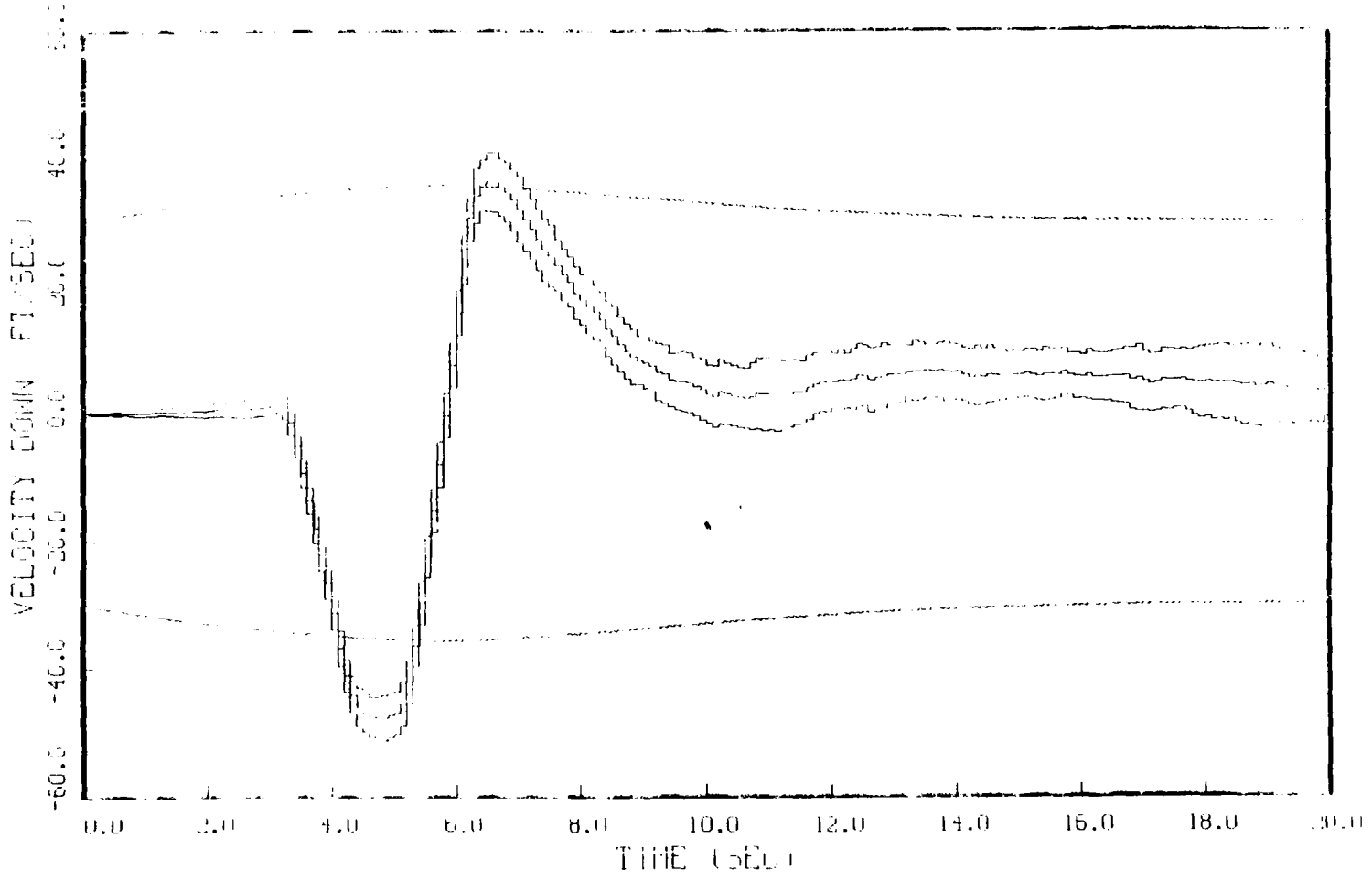

FIG. D.2a DOWNWARD VELOCITY MODEL, STATE 6, 30 RUNS, 4 MEAS
BEAM TRAJECTORY, D-100, ANGLE RATE MEAS. INHIBITED 1 R1

Appendix E

Baseline Comparisons of CV and GMA Filters

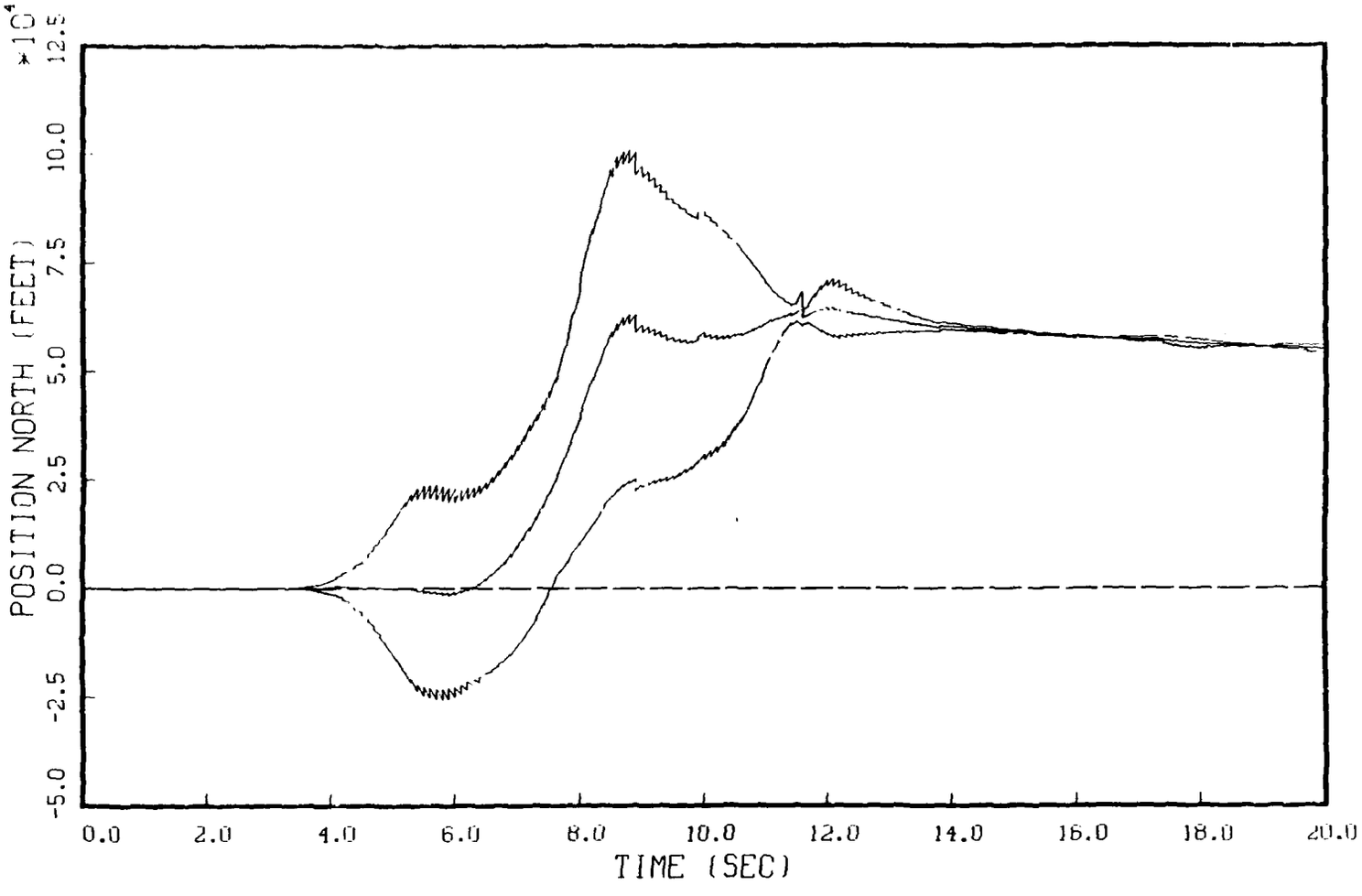

FIG. E.1: CONSTANT VELOCITY MODEL, STATE 1, 5 RUNS
BEAM TRAJECTORY, Q=5000, 6 MEAS (ORIGINAL R)

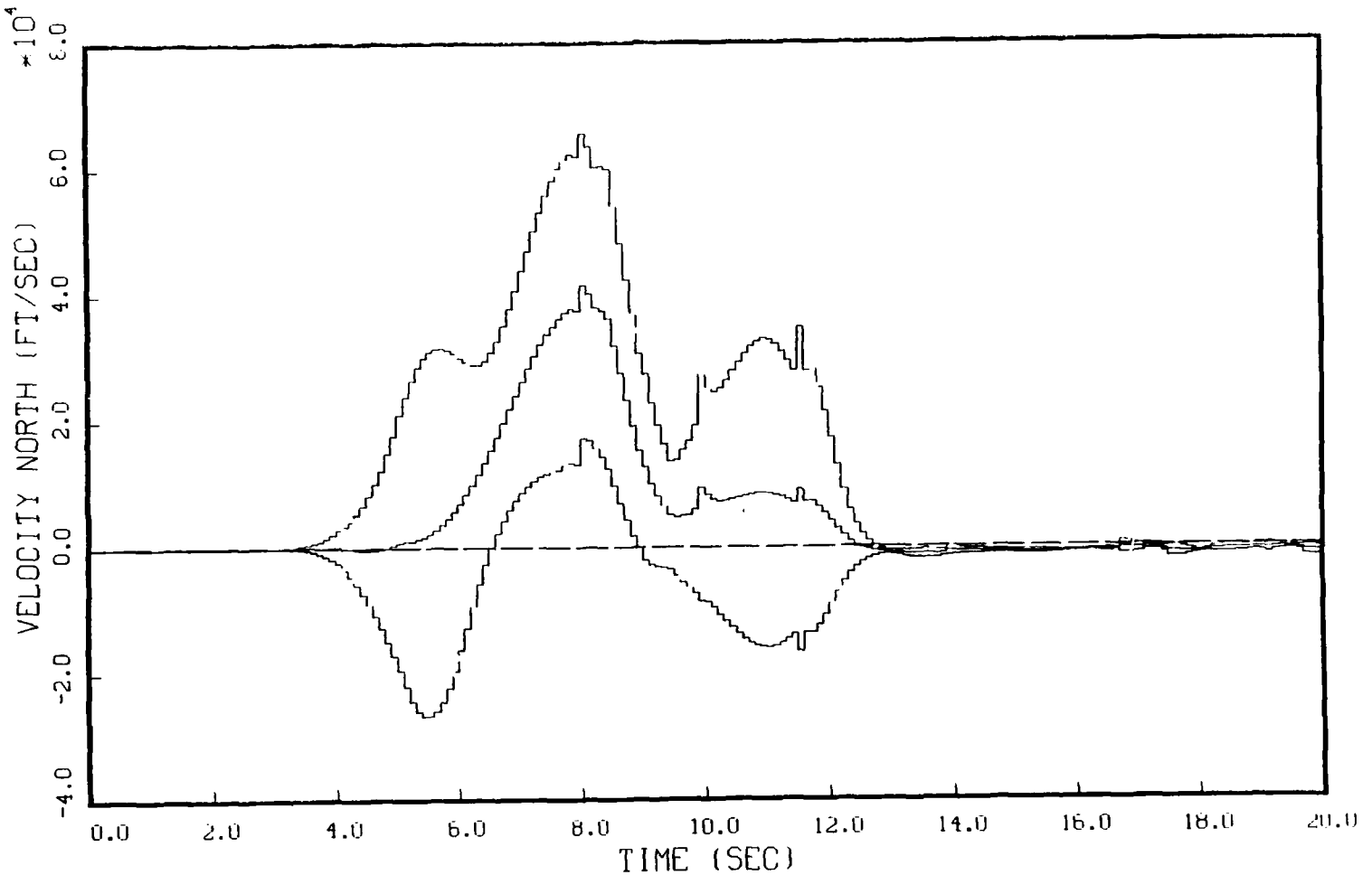

FIG. E.2: CONSTANT VELOCITY MODEL, STATE 2, 5 RUNS
BEAM TRAJECTORY, 0-5000, 6 MEAS (ORIGINAL R)

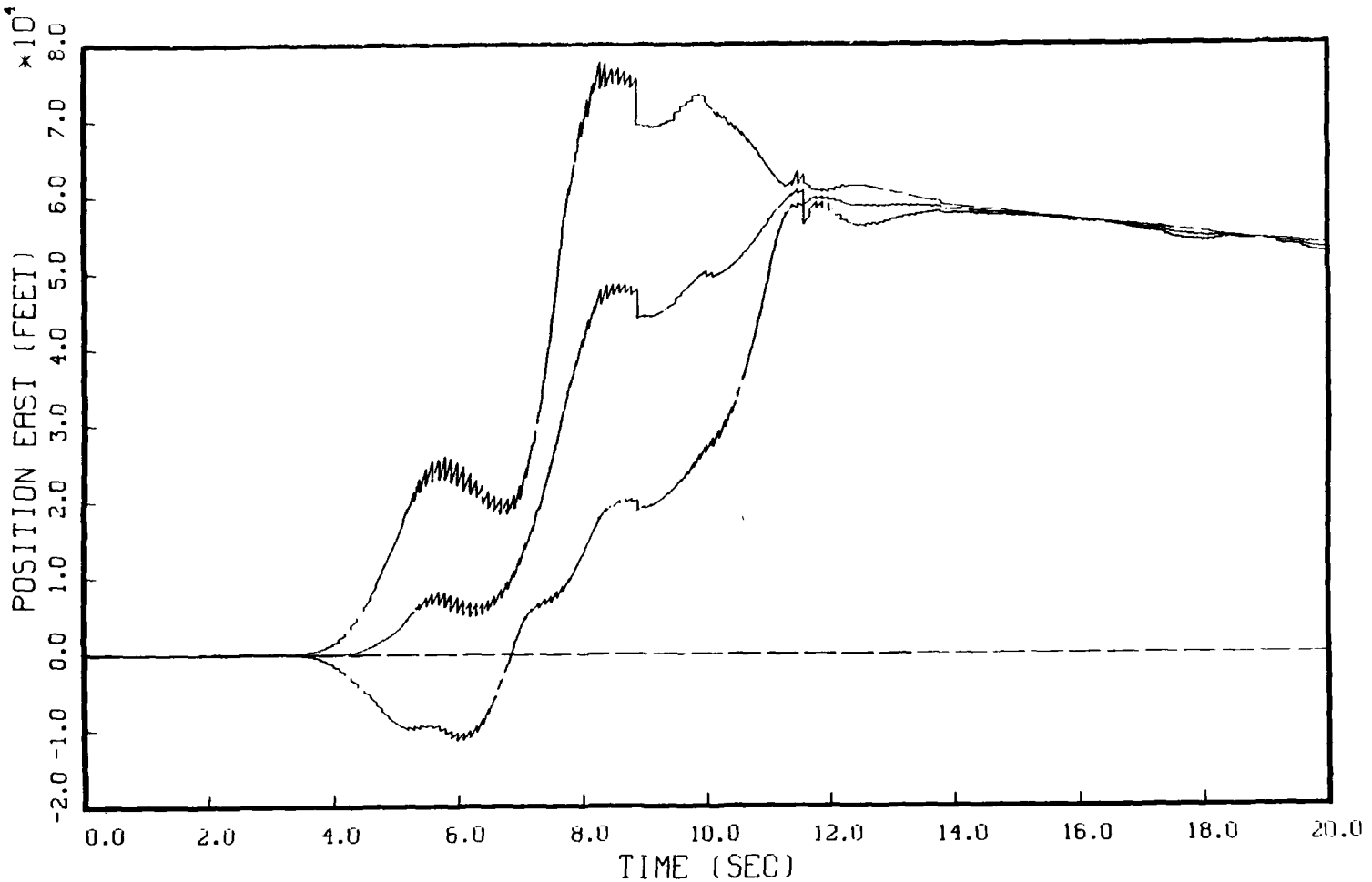

FIG. E.3: CONSTANT VELOCITY MODEL, STATE 3, 5 RUNS
BEAM TRAJECTORY, 0-5000, 6 MEAS (ORIGINAL R)

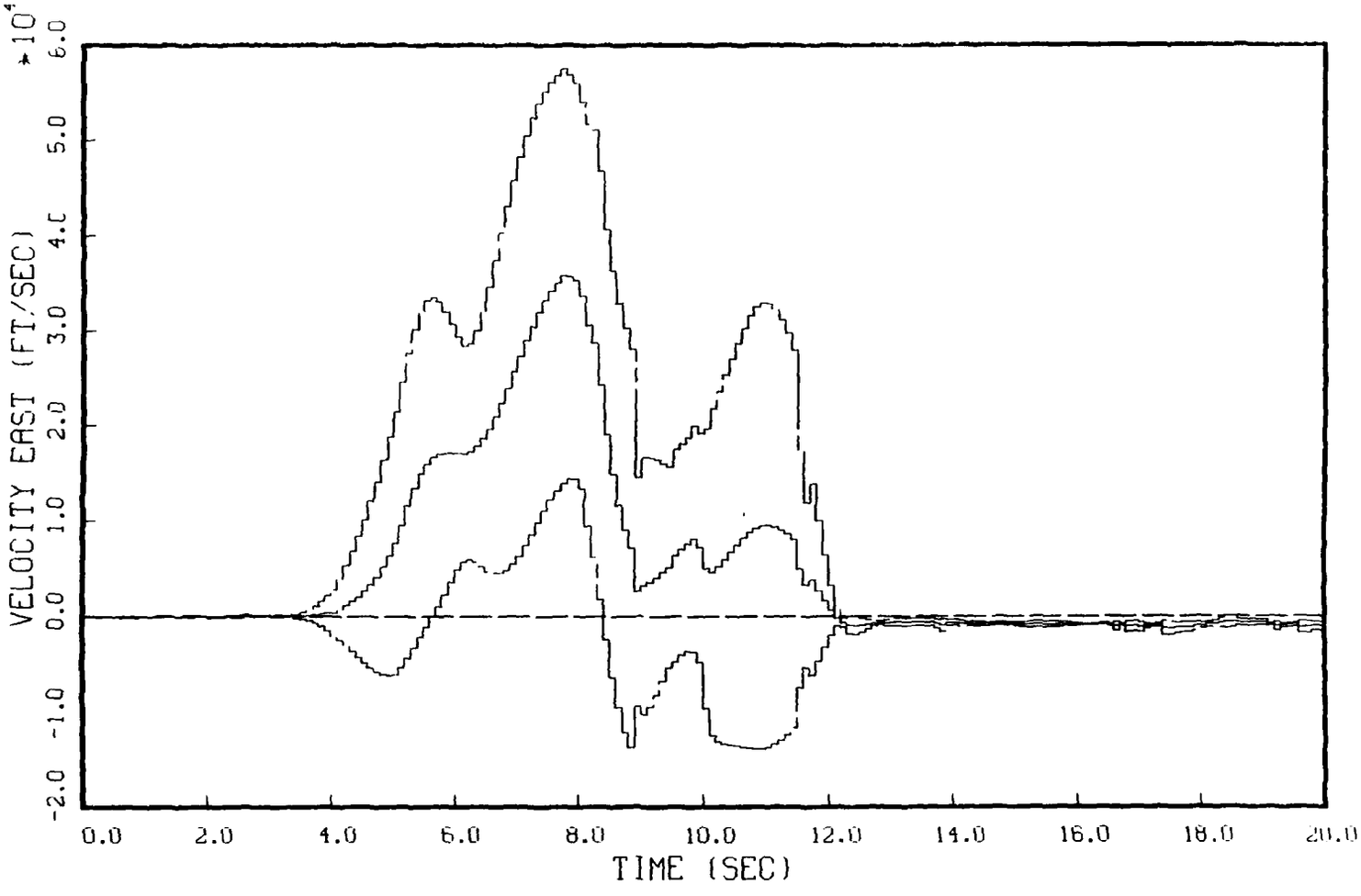

FIG. E.4: CONSTANT VELOCITY MODEL, STATE 4, 5 RUNS
BEAM TRAJECTORY, 0-5000, 6 MEAS (ORIGINAL R)

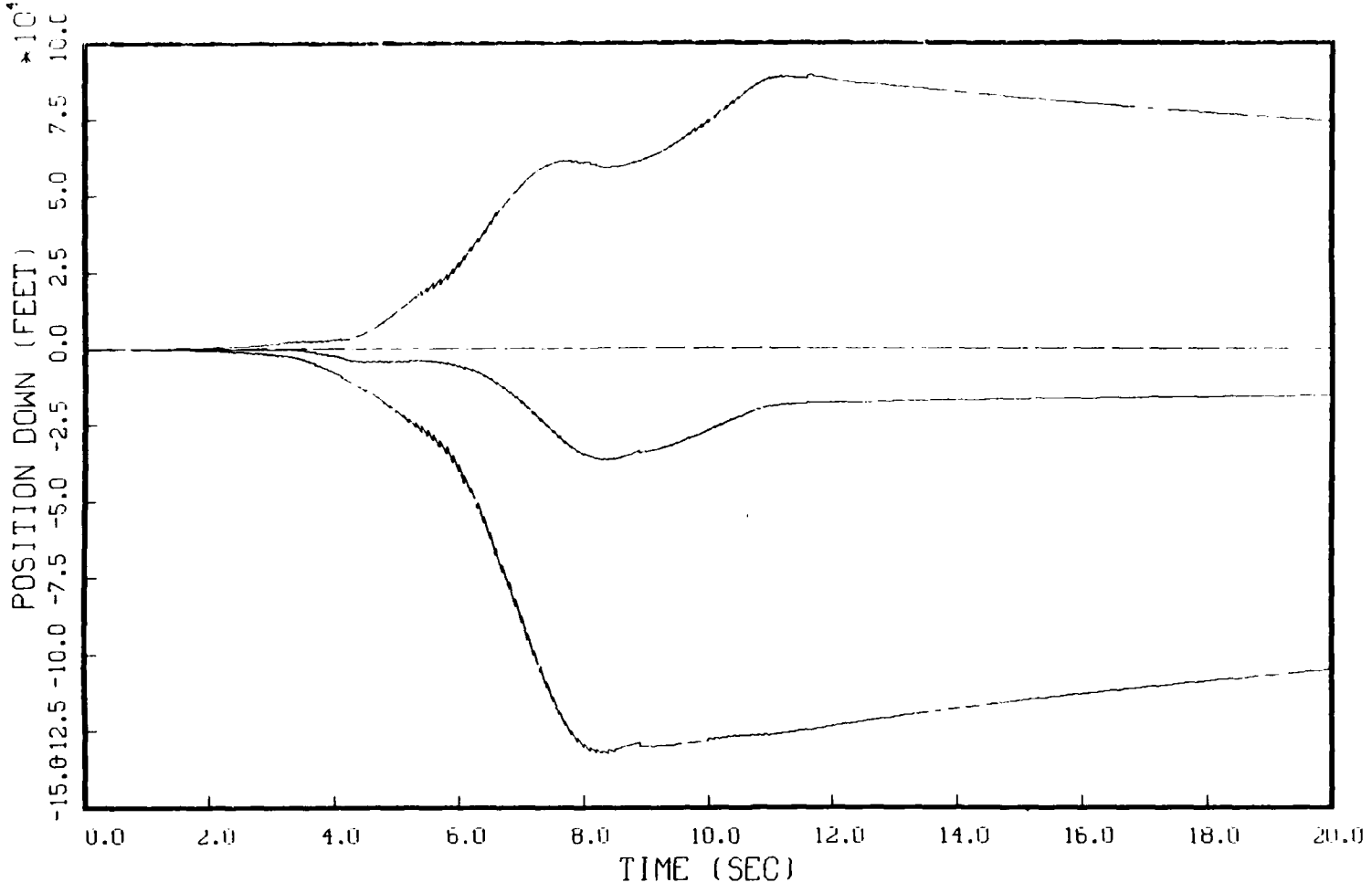

FIG. E.5: CONSTANT VELOCITY MODEL, STATE 5, 5 RUNS
BEAM TRAJECTORY, Q=5000, 6 MEAS (ORIGINAL R)

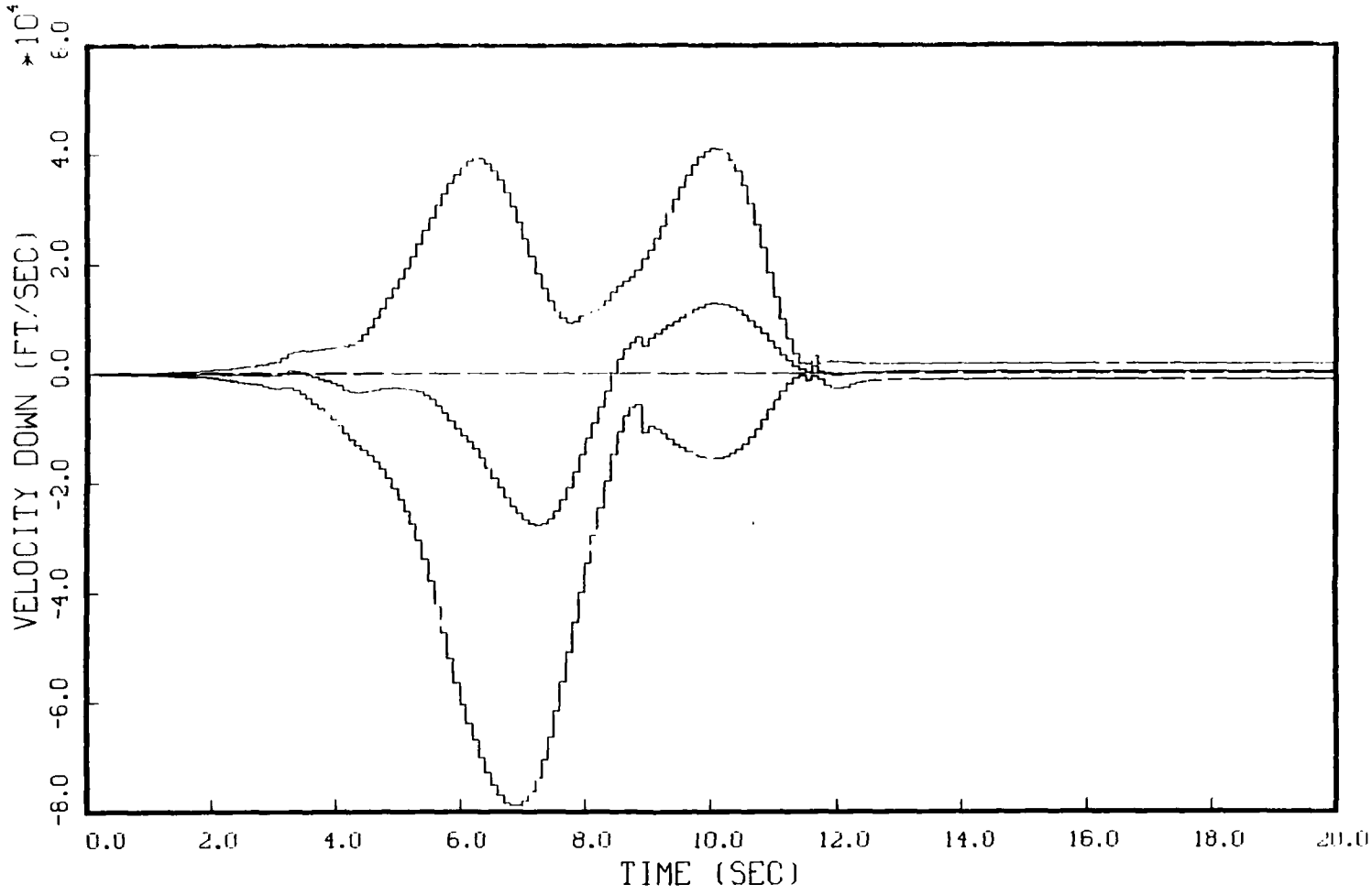

FIG. E.6: CONSTANT VELOCITY MODEL, STATE 6, 5 RUNS
BEAM TRAJECTORY, 0-5000, 6 MEAS (ORIGINAL R)

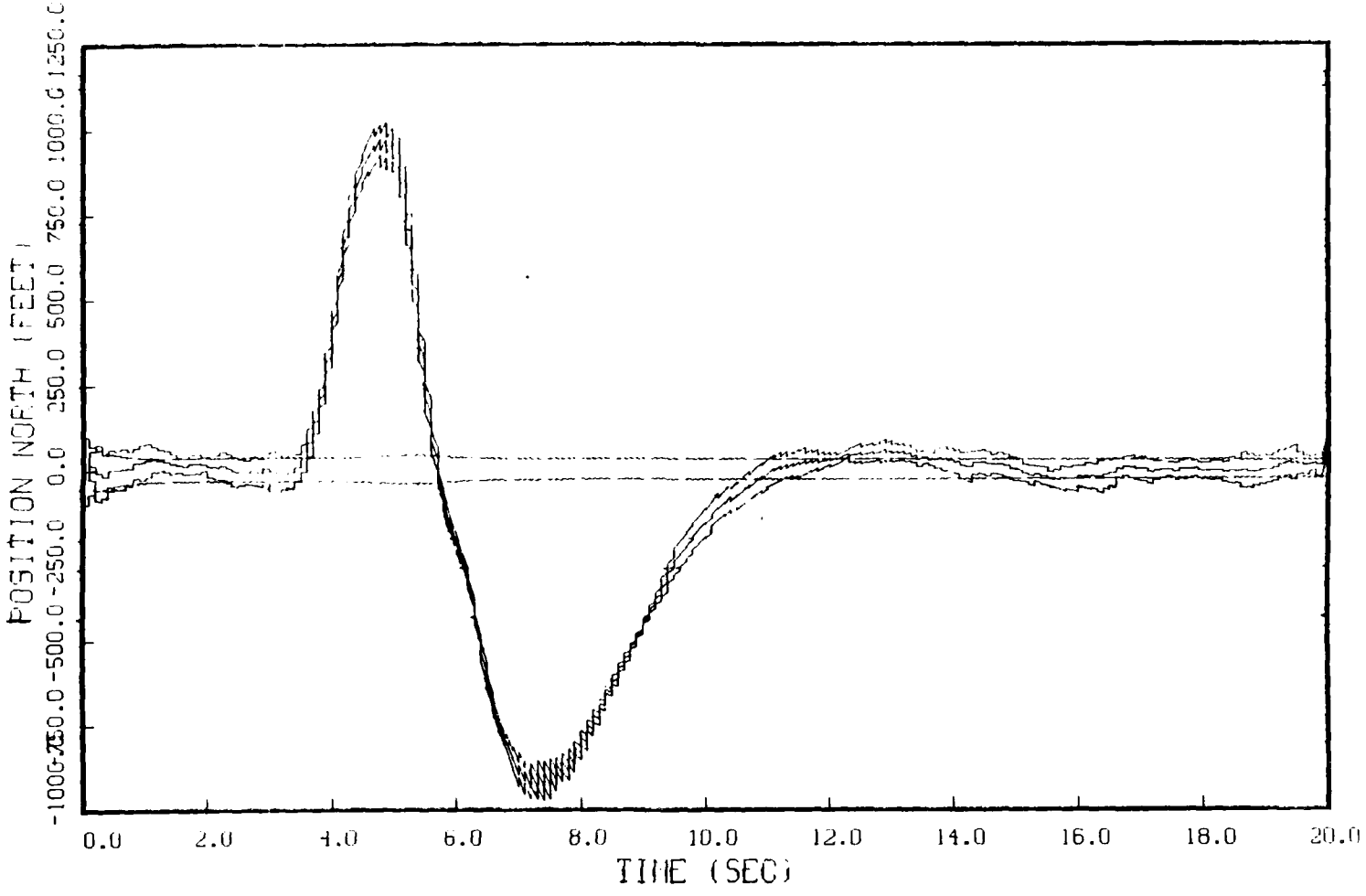

FIGURE E.7: GAUSS MARKOV MODEL, STATE 1, 5 RUNS
BEAM TRAJECTORY, 0-5000, 6 MEAS (ORIGINAL R)

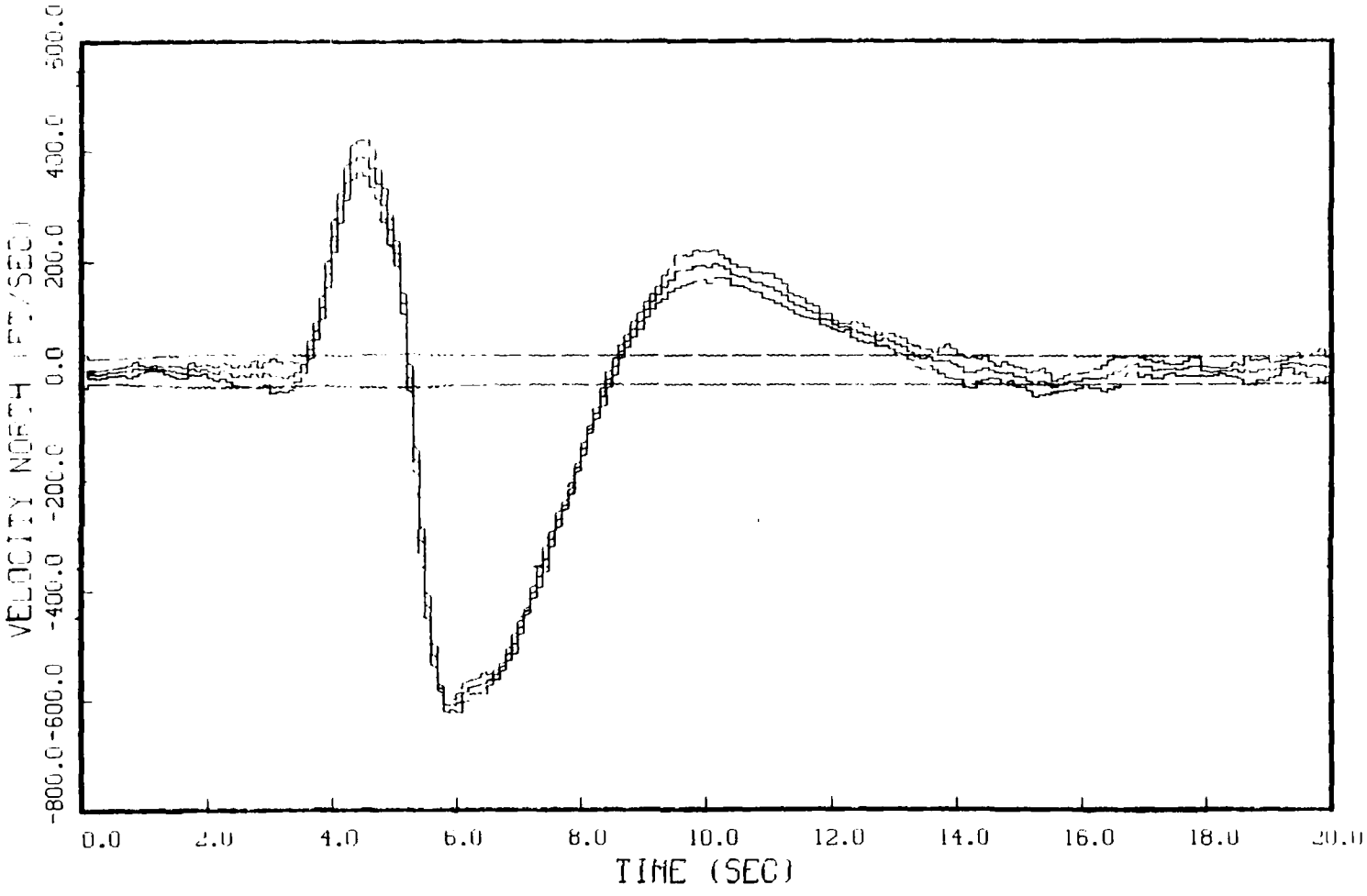

FIGURE E.8: GAUSS MARKOV MODEL, STATE 2, 5 RUNS
BEAM TRAJECTORY, Q=5000, 6 MEAS (ORIGINAL R)

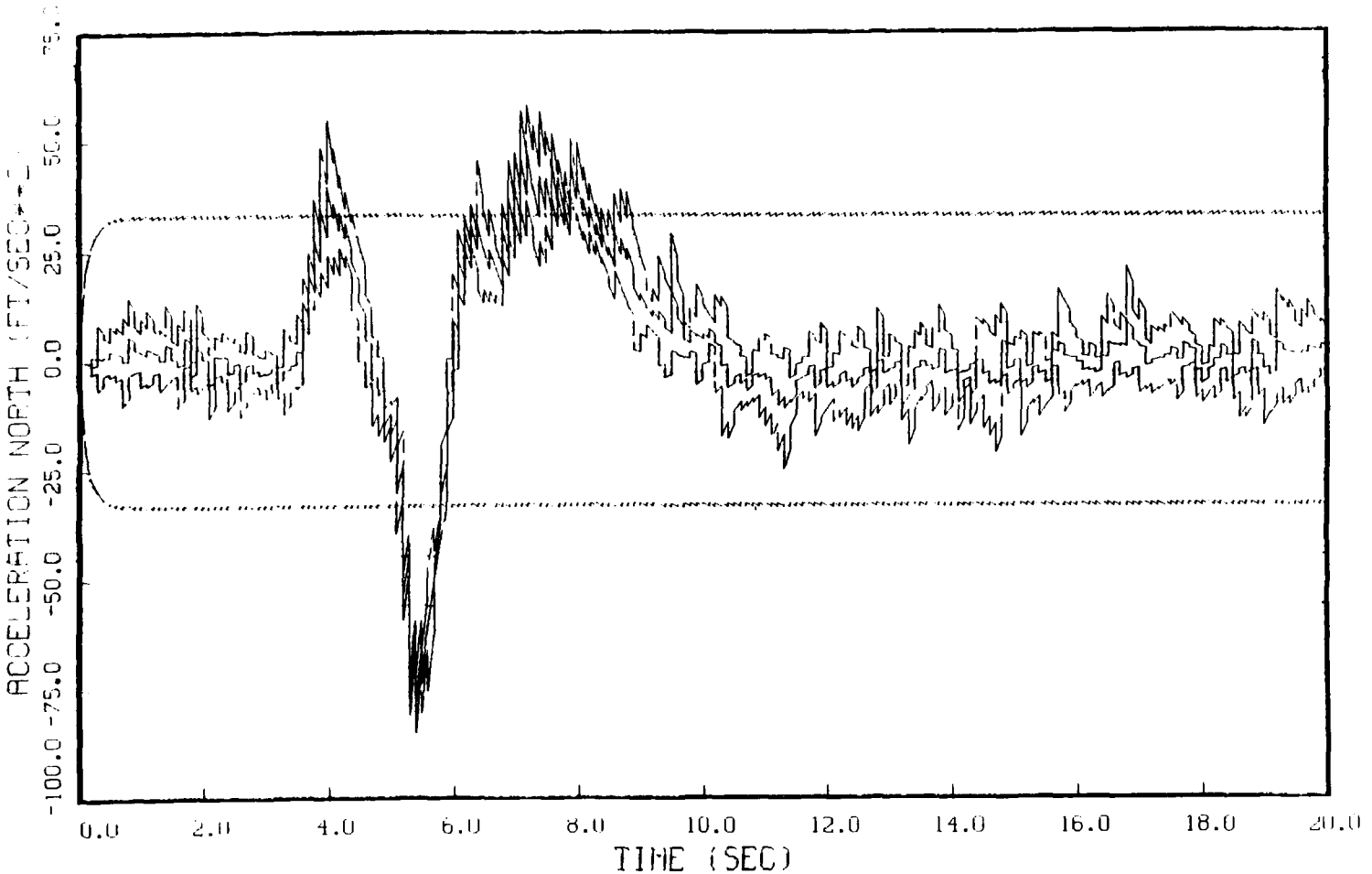

FIGURE E.9: GAUSS MARKOV MODEL, STATE 3, 5 RUNS
BEAM TRAJECTORY, 0-5000, 6 MEAS (ORIGINAL R)

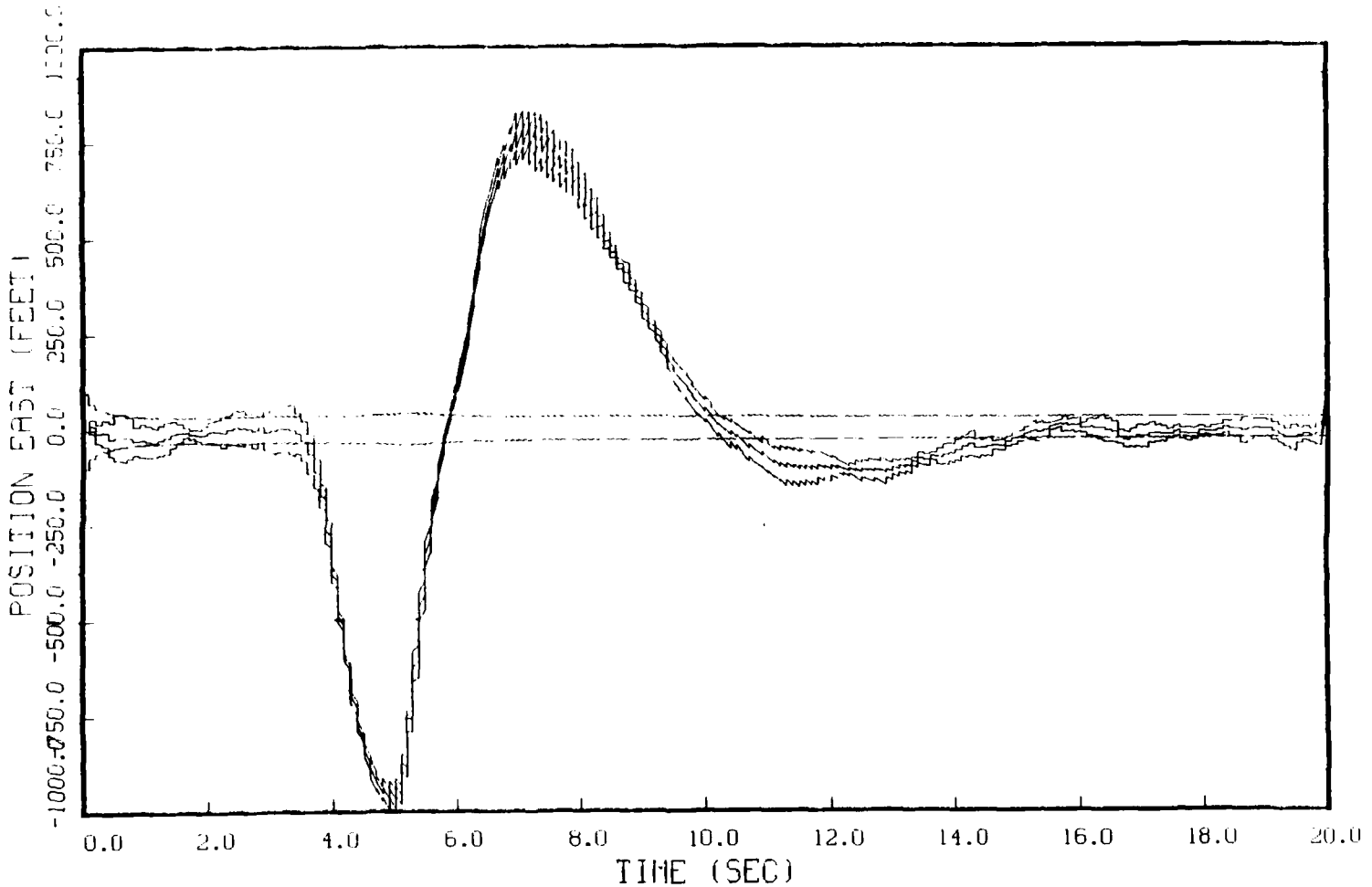

FIGURE E.10: GAUSS MARKOV MODEL, STATE 4, 5 RUNS
BEAM TRAJECTORY, Q=5000, 6 MEAS (ORIGINAL R)

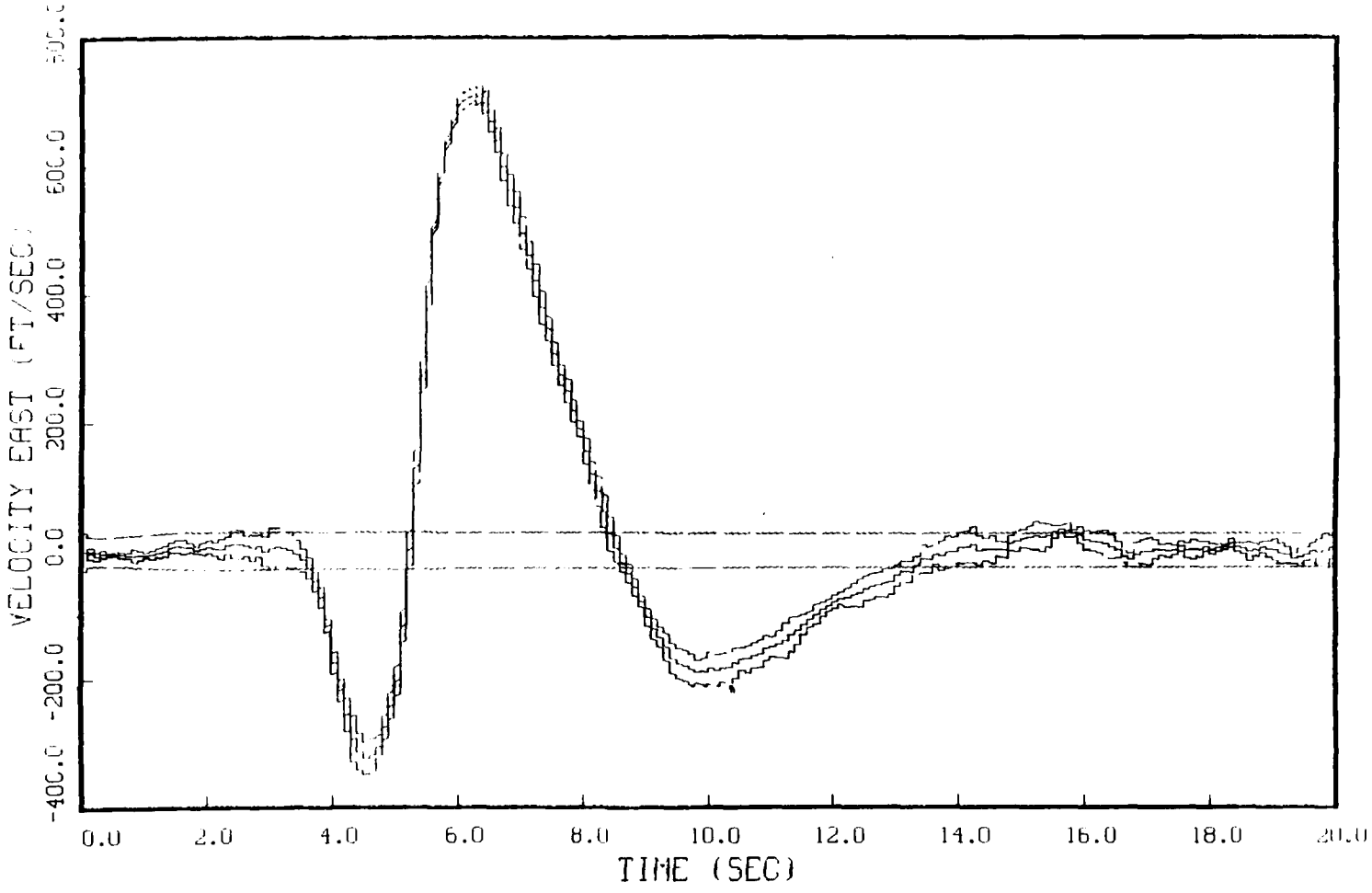

FIGURE E.11: GAUSS MARKOV MODEL, STATE 5, 5 RUNS
BEAM TRAJECTORY, Q=5000, 6 MEAS (ORIGINAL R)

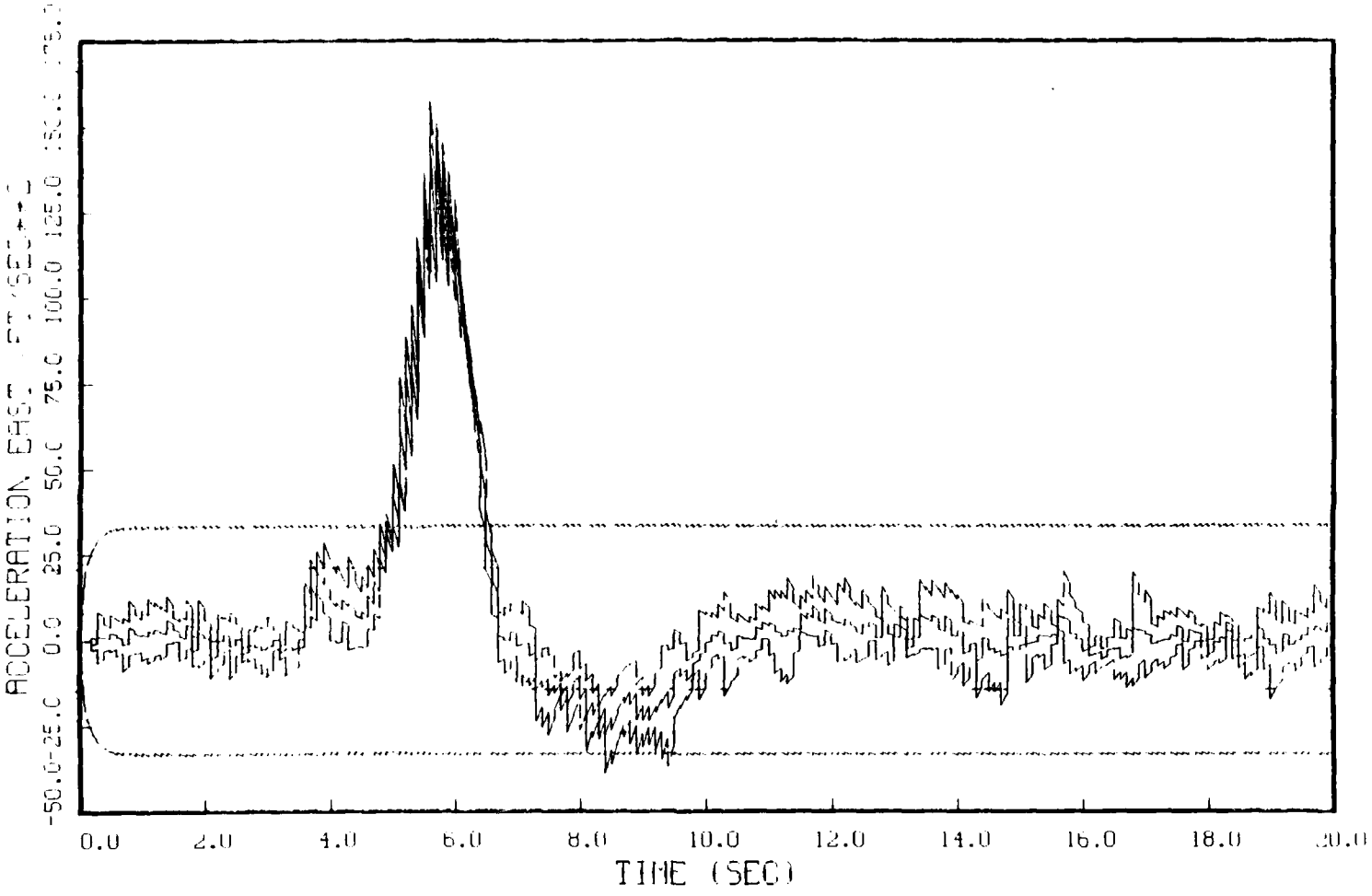

FIGURE E.12: GAUSS MARKOV MODEL, STATE 6, 5 RUNS
BEAM TRAJECTORY, D=5000, 6 MEAS (ORIGINAL R)

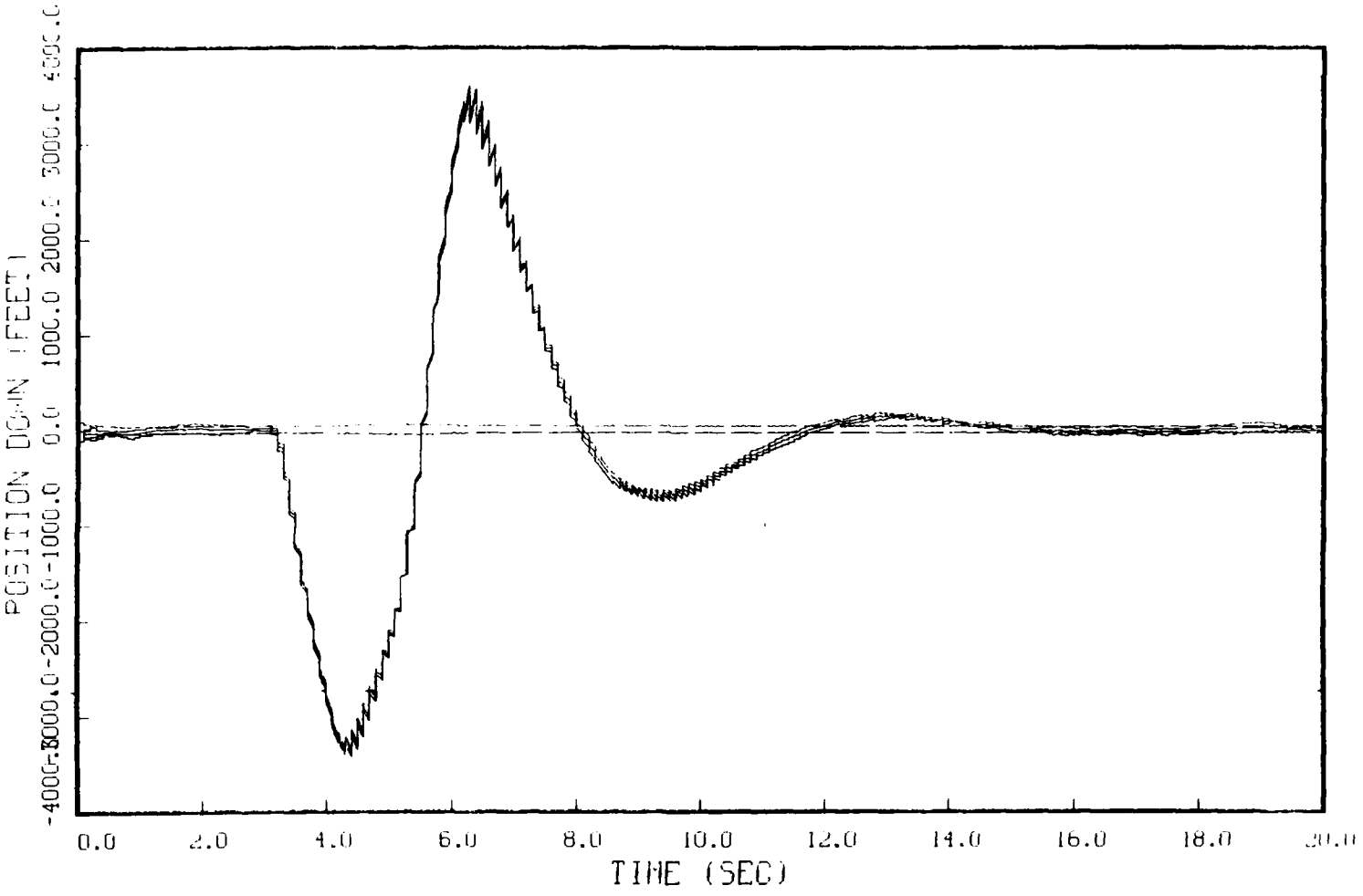

FIGURE E.13: GAUSS MARKOV MODEL, STATE 7, 5 RUNS
BEAM TRAJECTORY, 0-5000, 6 MEAS (ORIGINAL R)

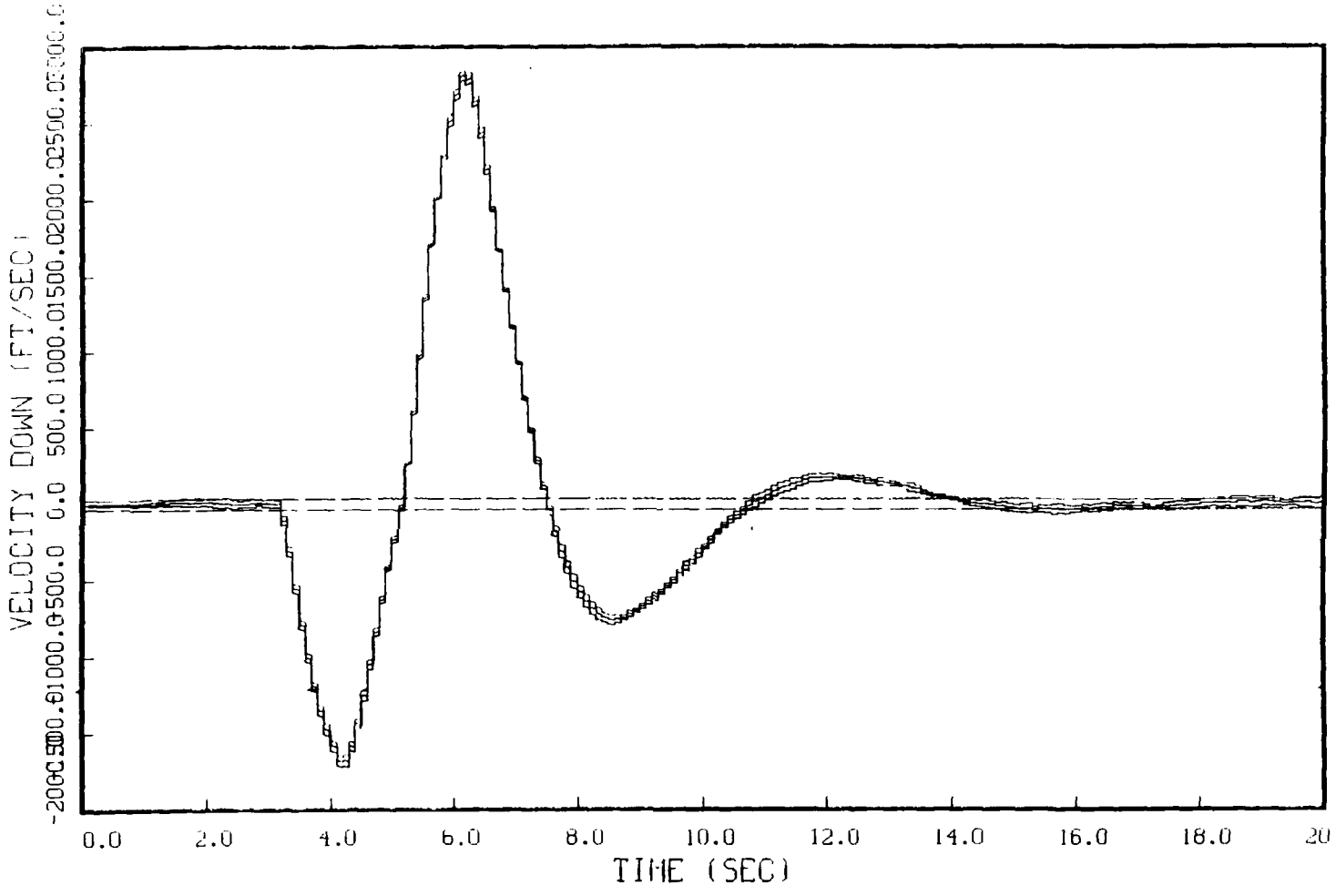

FIGURE E.14: GAUSS MARKOV MODEL, STATE 8, 5 RUNS
BEAM TRAJECTORY, 0-5000, 6 MEAS (ORIGINAL R)

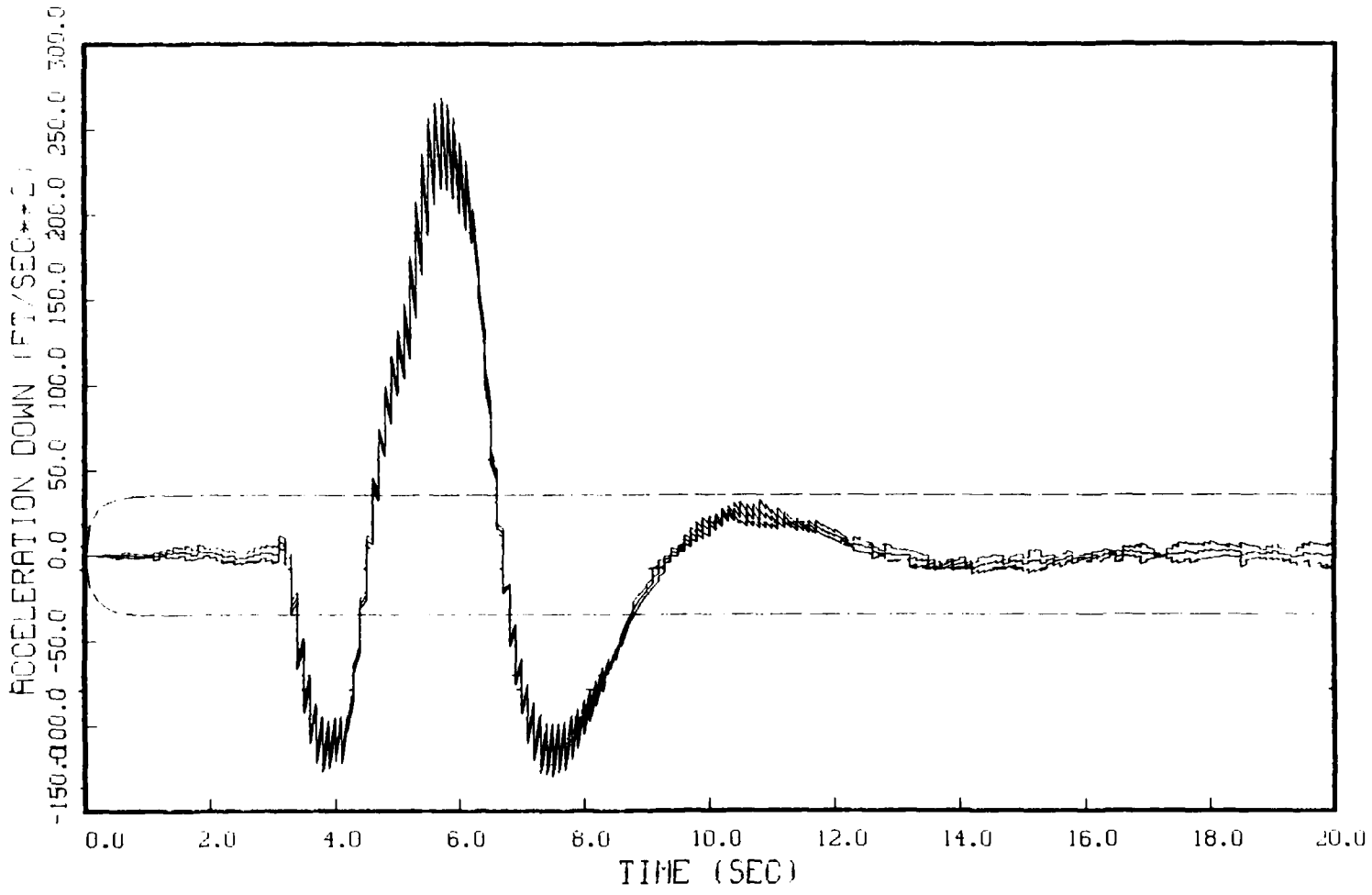

FIGURE E.15: GAUSS MARKOV MODEL, STATE 9, 5 RUNS
BEAM TRAJECTORY, 0-5000, 6 MEAS (ORIGINAL R)

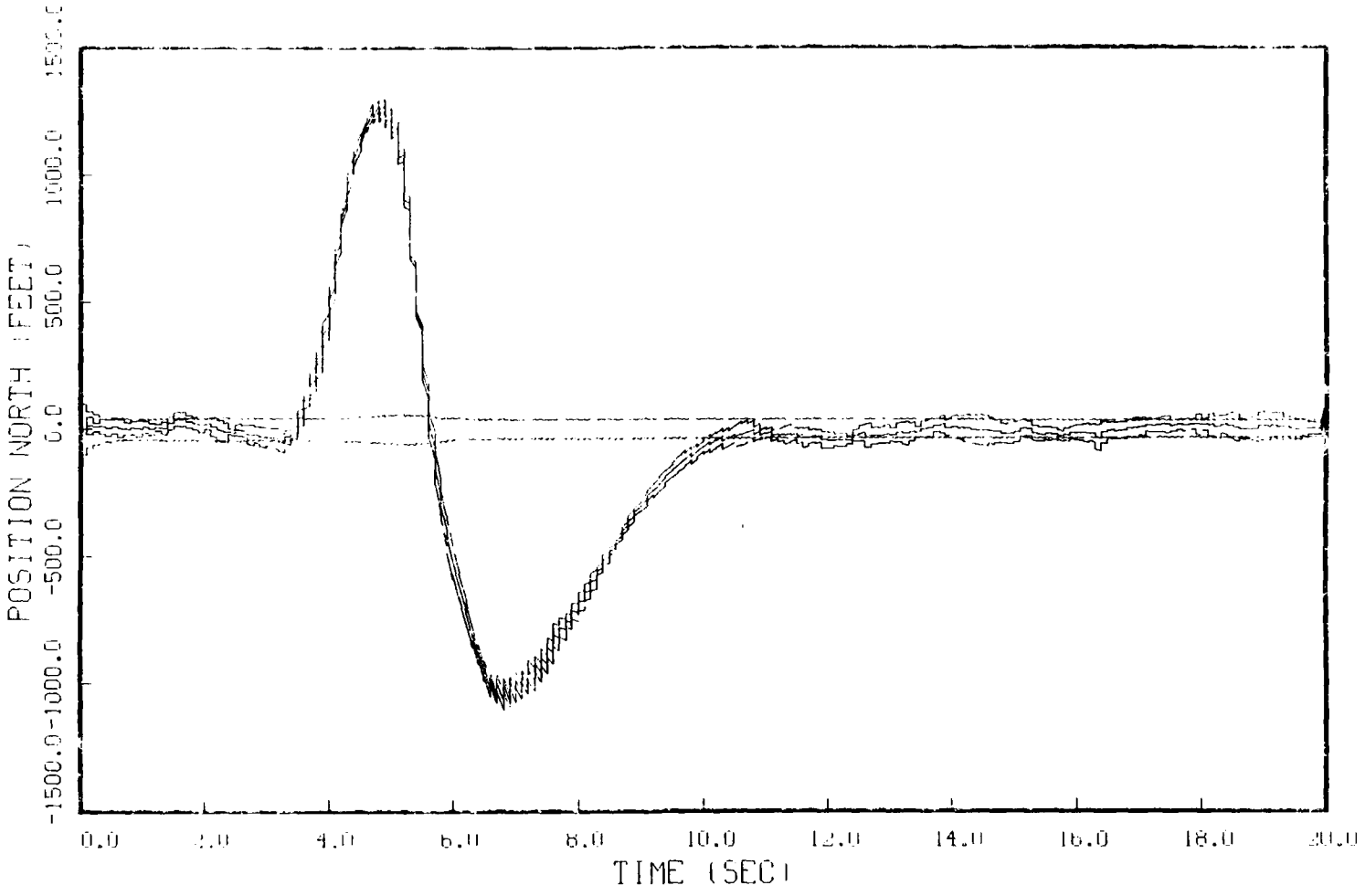

FIG. E.16: CONSTANT VELOCITY MODEL, STATE 1, 5 RUNS, 4 MEAS
BEAM TRAJECTORY, Q=5000, ANGLE RATE MEAS. INHIBITED (ORIGINAL R)

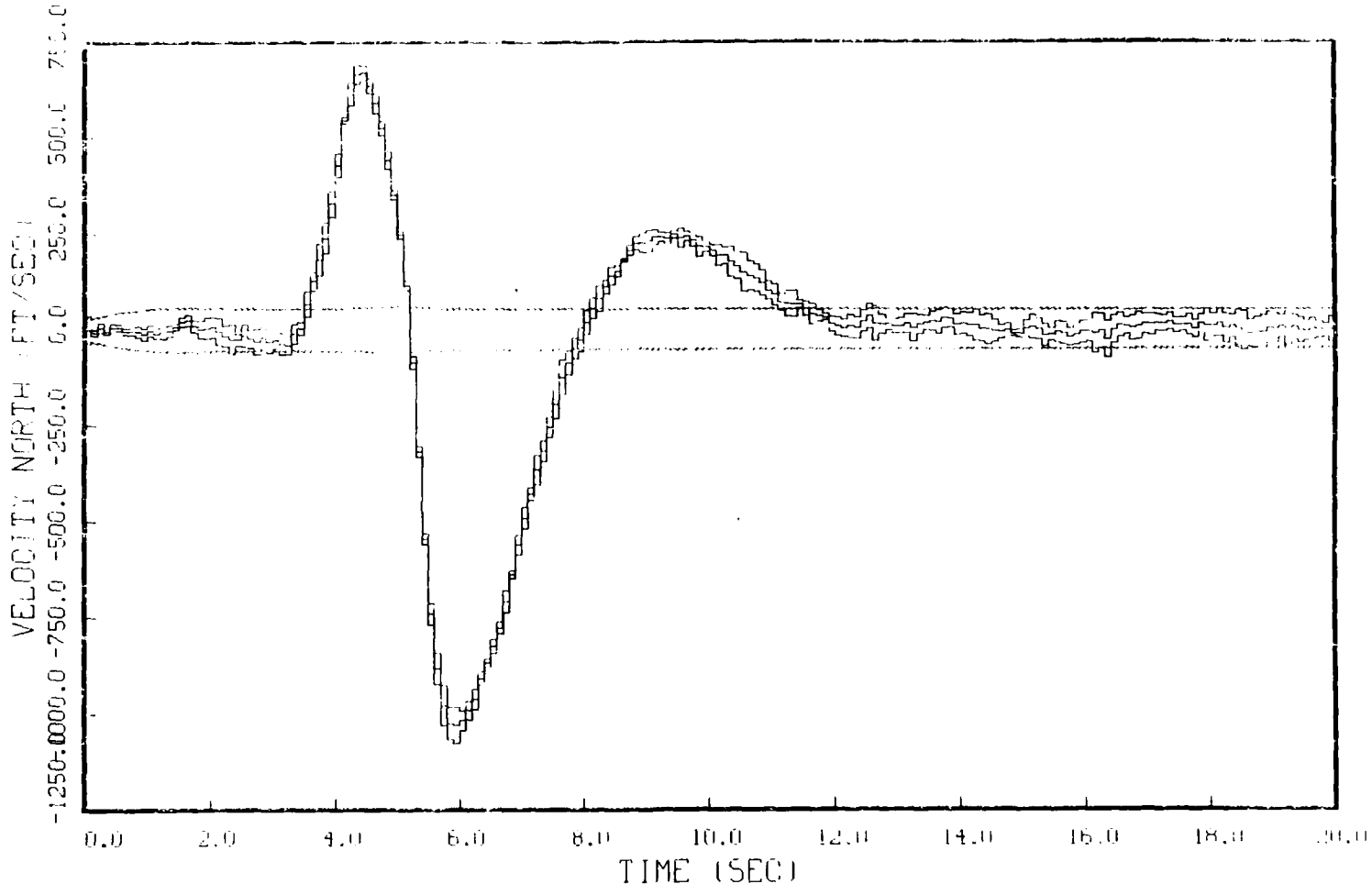

FIG. E.17: CONSTANT VELOCITY MODEL, STATE 2, 5 RUNS, 4 MEAS
BEAM TRAJECTORY, Q=5000, ANGLE RATE MEAS. INHIBITED (ORIGINAL R)

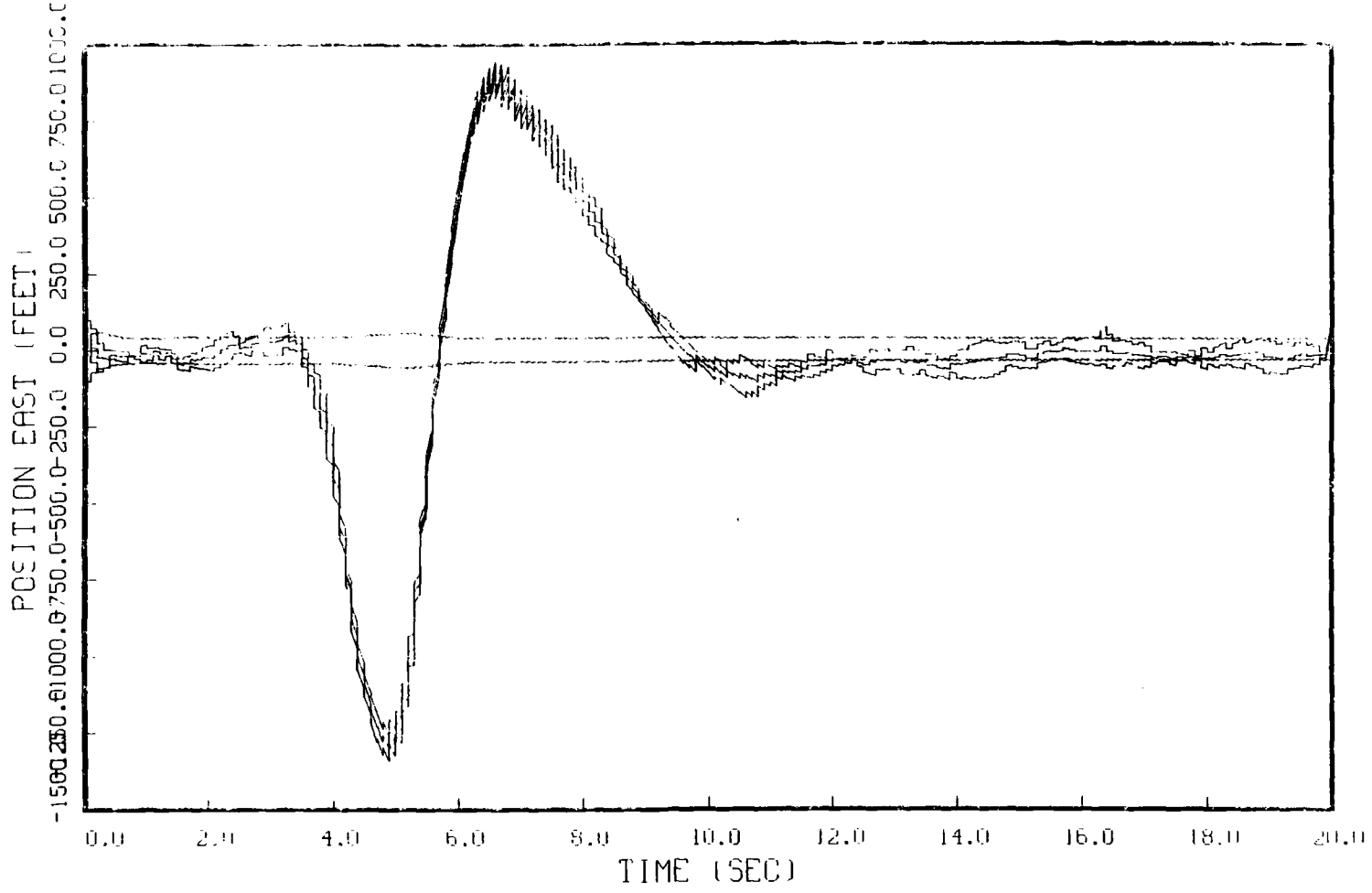

FIG. E.16: CONSTANT VELOCITY MODEL, STATE 3, 5 RUNS, 4 MEAS
BEAM TRAJECTORY, D=5000, ANGLE RATE MEAS. INHIBITED (ORIGINAL R)

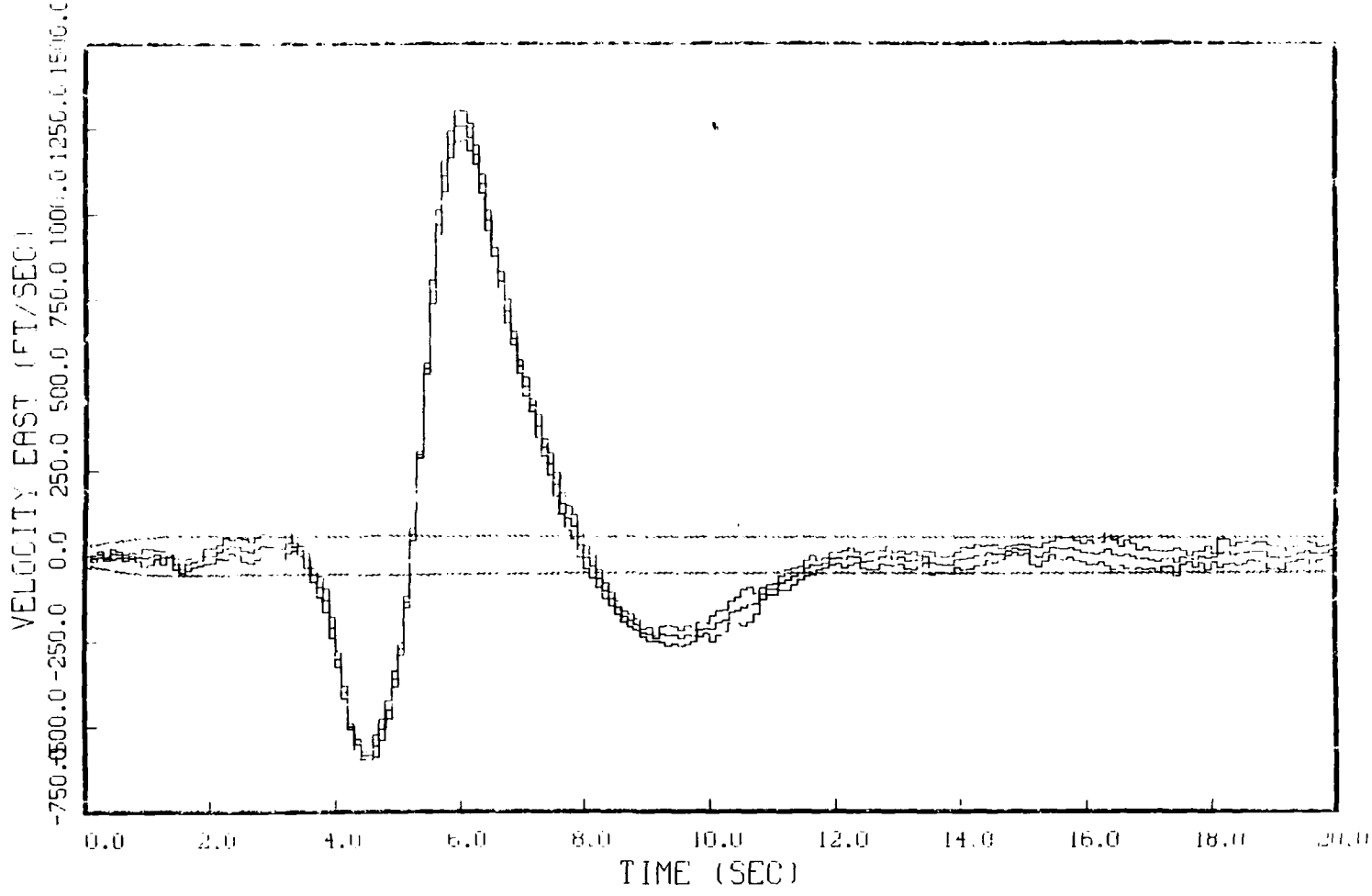

FIG. E.19: CONSTANT VELOCITY MODEL, STATE 4, 5 RUNS, 4 MEAS
BEAM TRAJECTORY, Q=5000, ANGLE RATE MEAS. INHIBITED (ORIGINAL R)

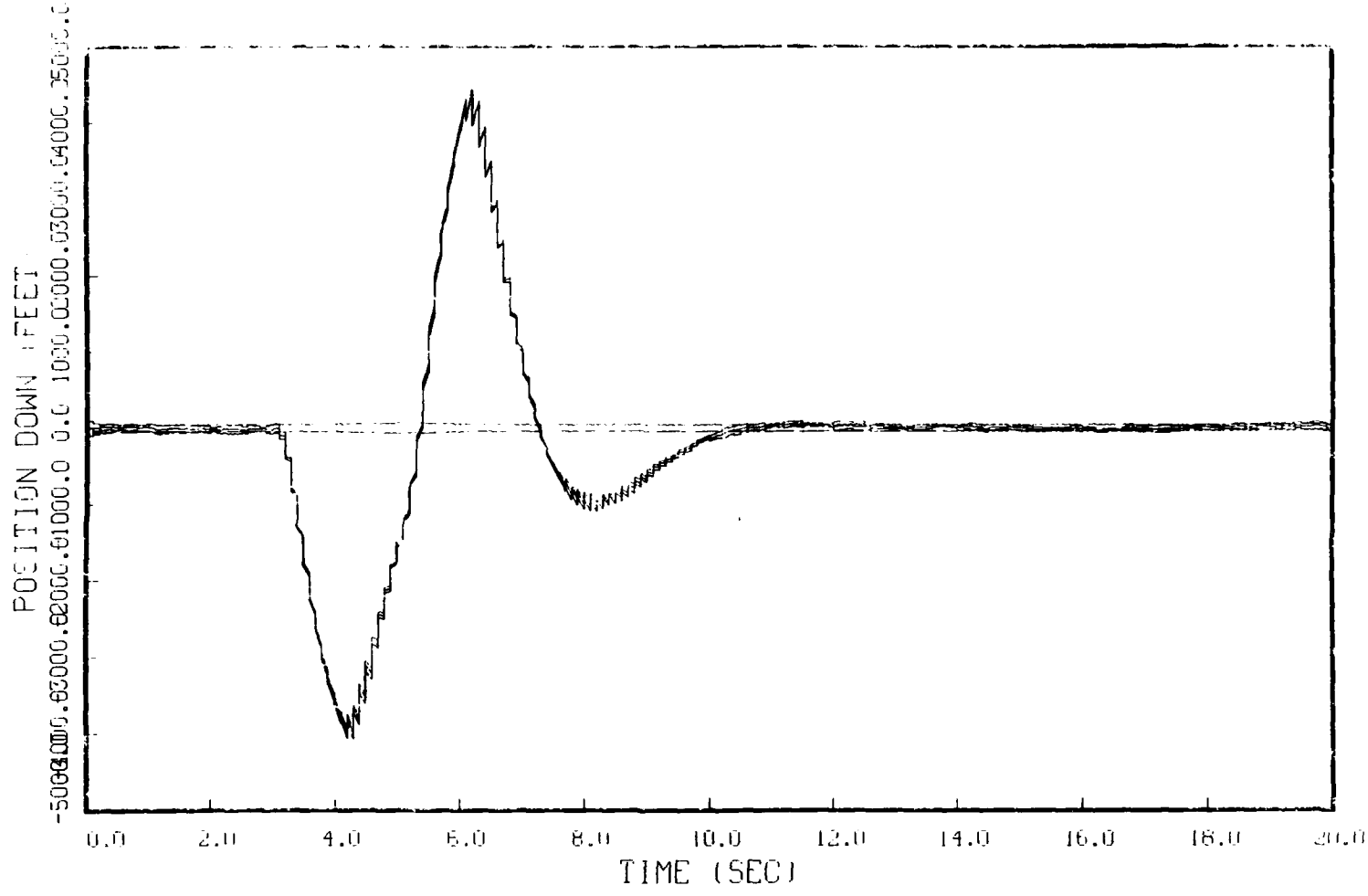

FIG. E.20: CONSTANT VELOCITY MODEL, STATE 5, 5 RUNS, 4 MEAS
BEAM TRAJECTORY, Q=5000, ANGLE RATE MEAS. INHIBITED (ORIGINAL R)

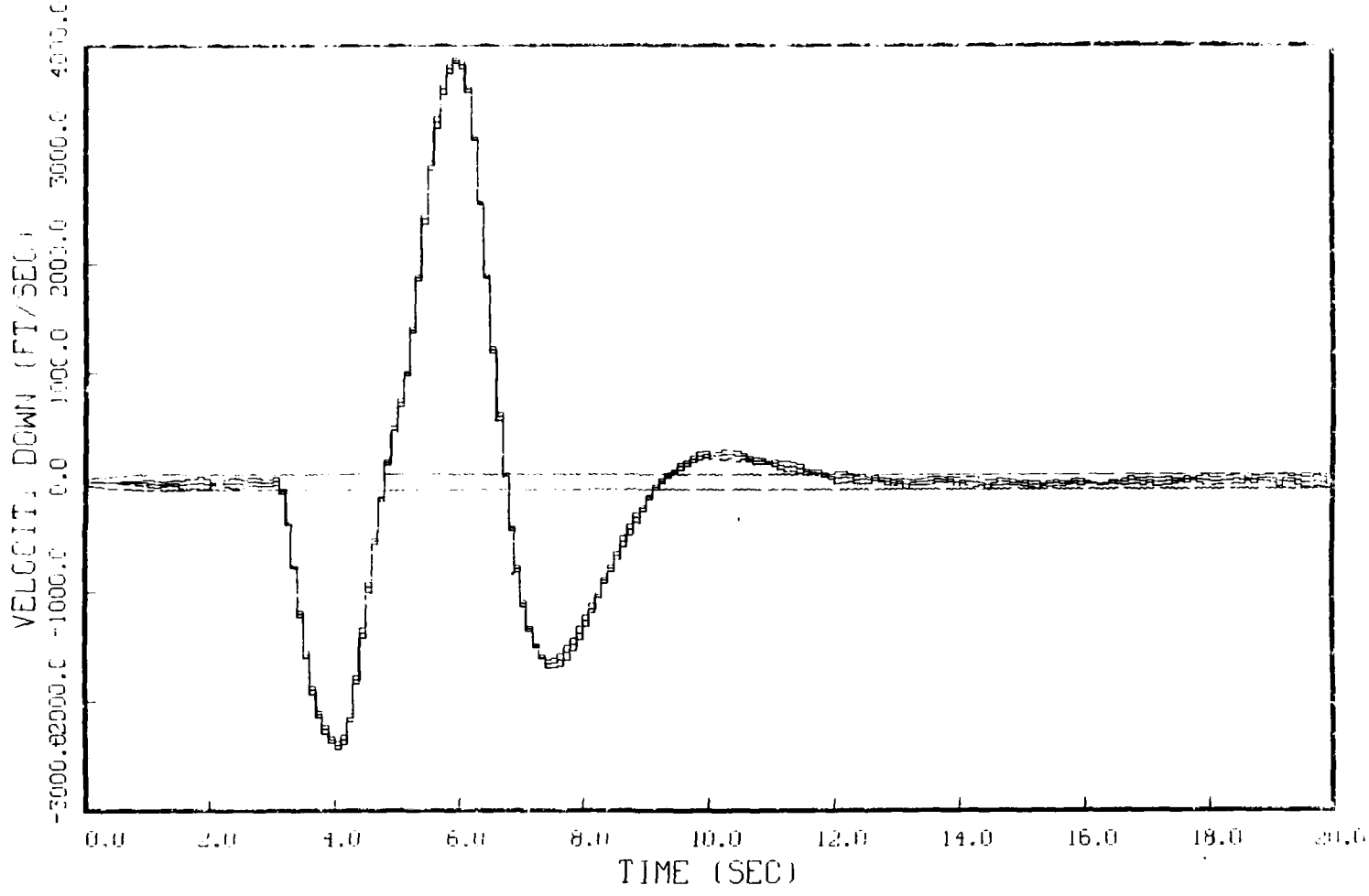

FIG. E.21: CONSTANT VELOCITY MODEL, STATE 6, 5 RUNS, 4 MEAS
BEAM TRAJECTORY, Q=5000, ANGLE RATE MEAS. INHIBITED (ORIGINAL R)

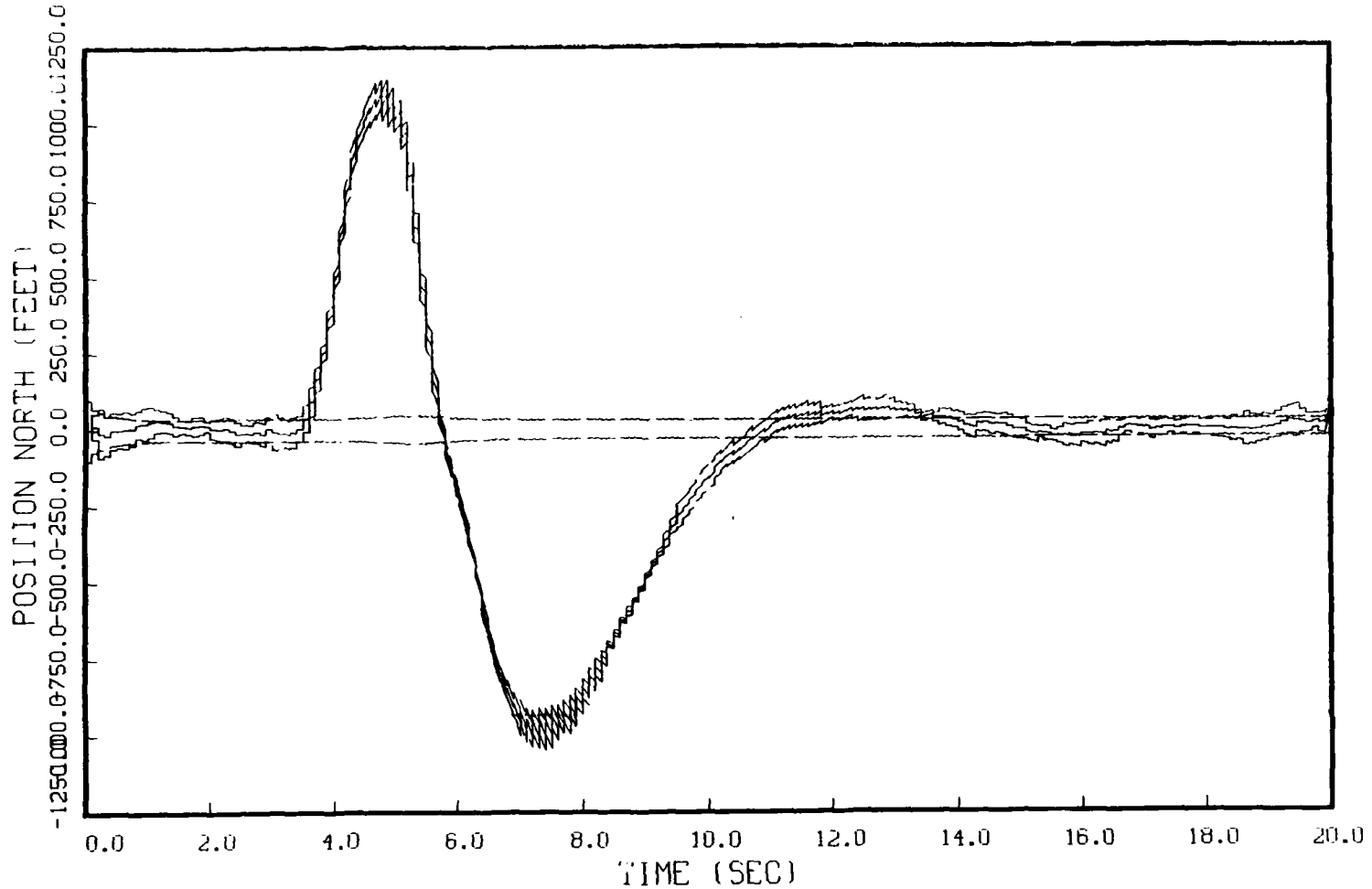

FIGURE E.22: GAUSS MARKOV MODEL, STATE 1, 5 RUNS
BEAM TRAJECTORY, Q=5000, ANGLE RATE MEAS. INHIBITED (ORIGINAL R)

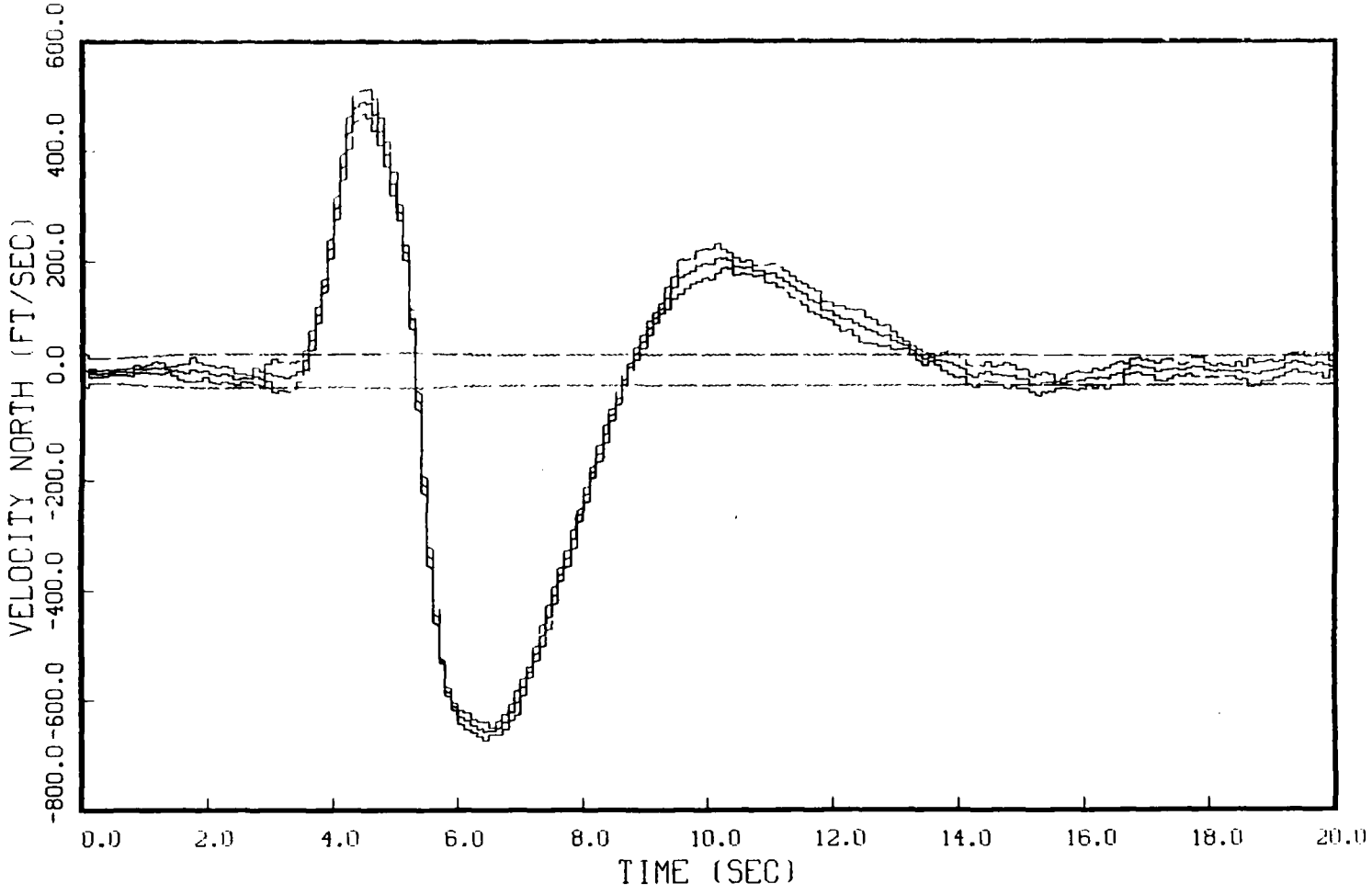

FIGURE E.23: GAUSS MARKOV MODEL, STATE 2, 5 RUNS
BEAM TRAJECTORY, Q-5000, ANGLE RATE MEAS. INHIBITED (ORIGINAL R)

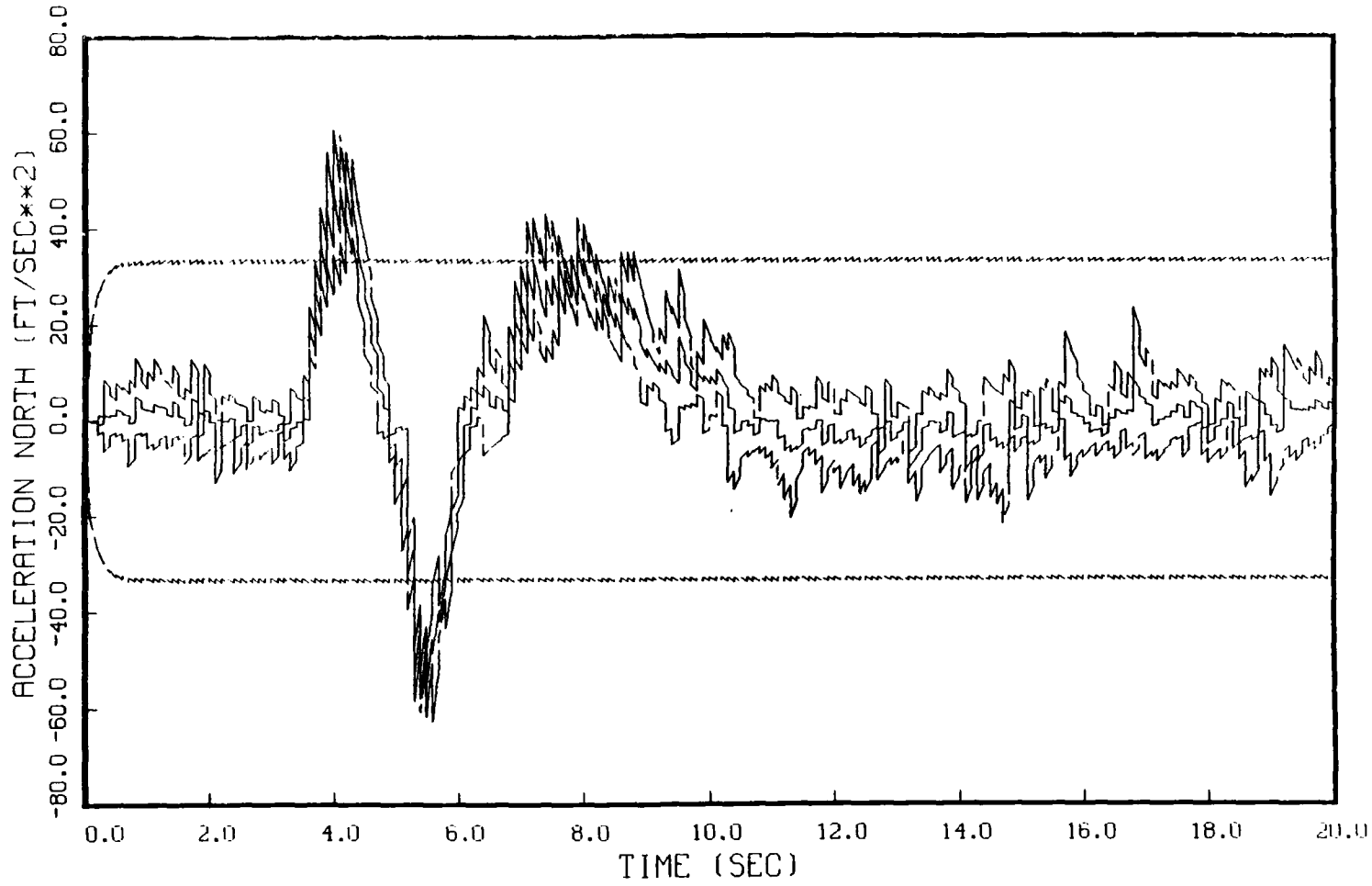

FIGURE E.24: GAUSS MARKOV MODEL, STATE 3, 5 RUNS
BEAM TRAJECTORY, Q=5000, ANGLE RATE MEAS. INHIBITED (ORIGINAL R)

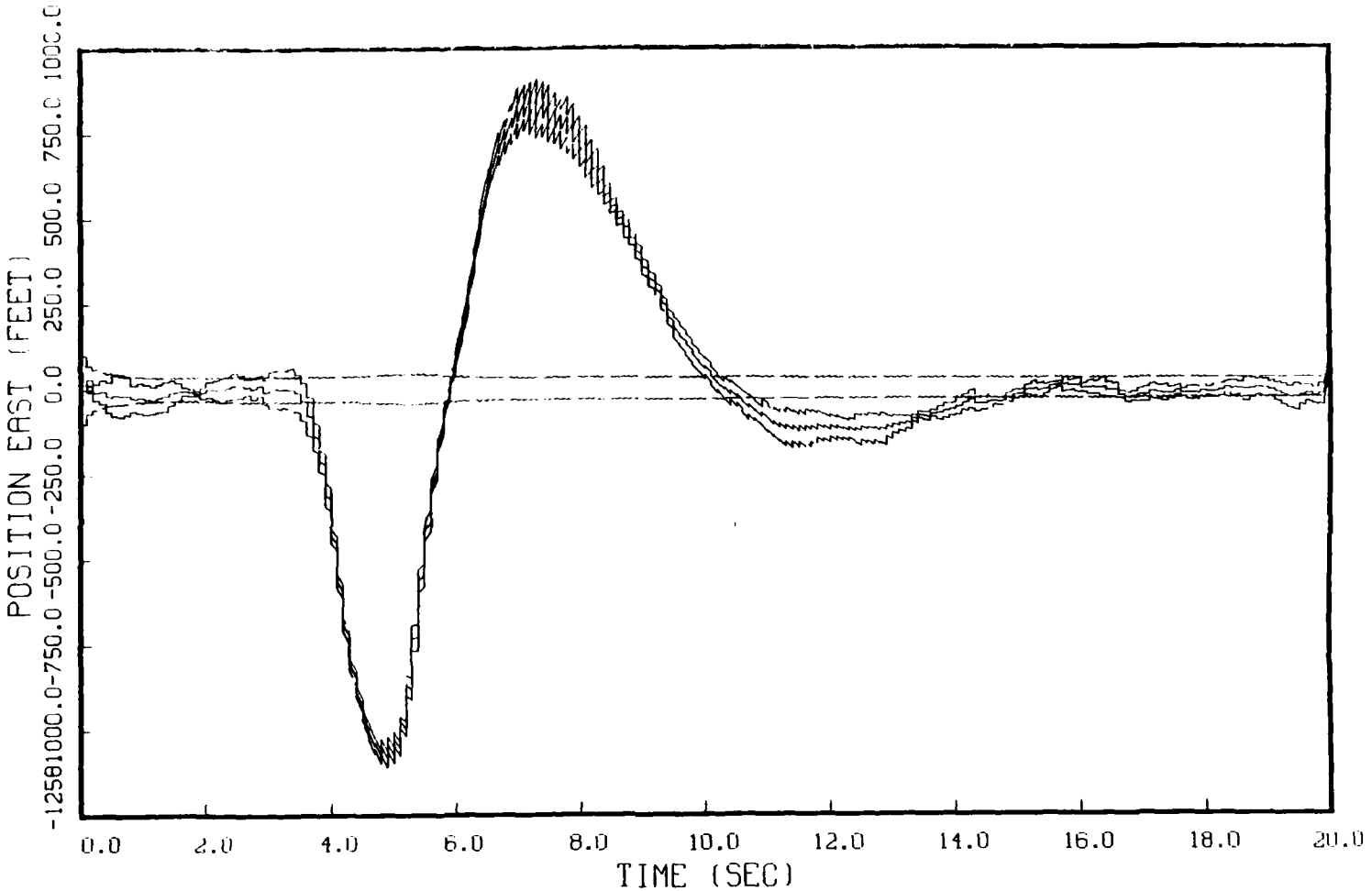

FIGURE E.25: GAUSS MARKOV MODEL, STATE 4, 5 RUNS
BEAM TRAJECTORY, 0-5000, ANGLE RATE MEAS. INHIBITED (ORIGINAL R)

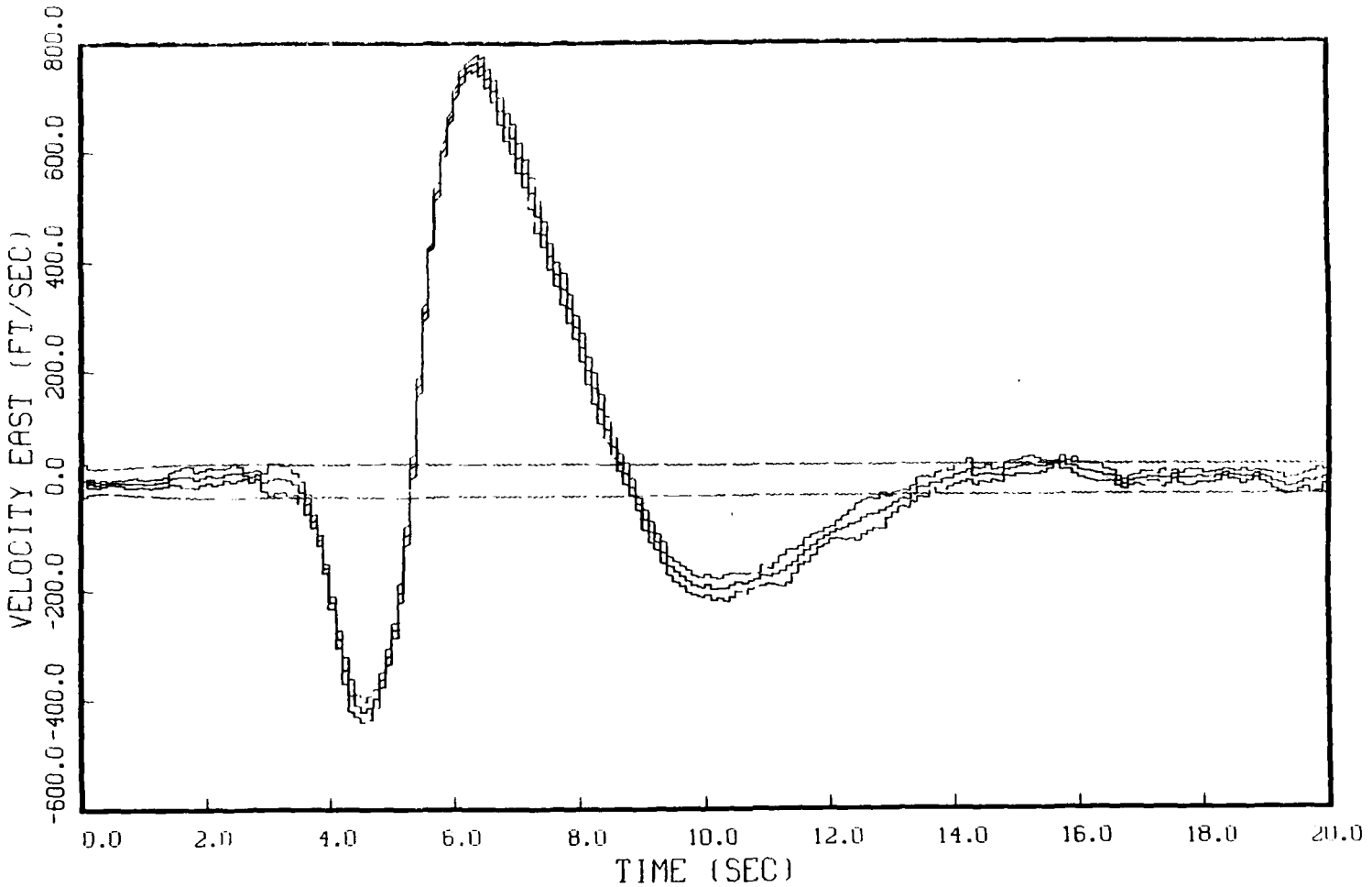

FIGURE E.26: GAUSS MARKOV MODEL, STATE 5, 5 RUNS
BEAM TRAJECTORY, Q=5000, ANGLE RATE MEAS. INHIBITED (ORIGINAL R)

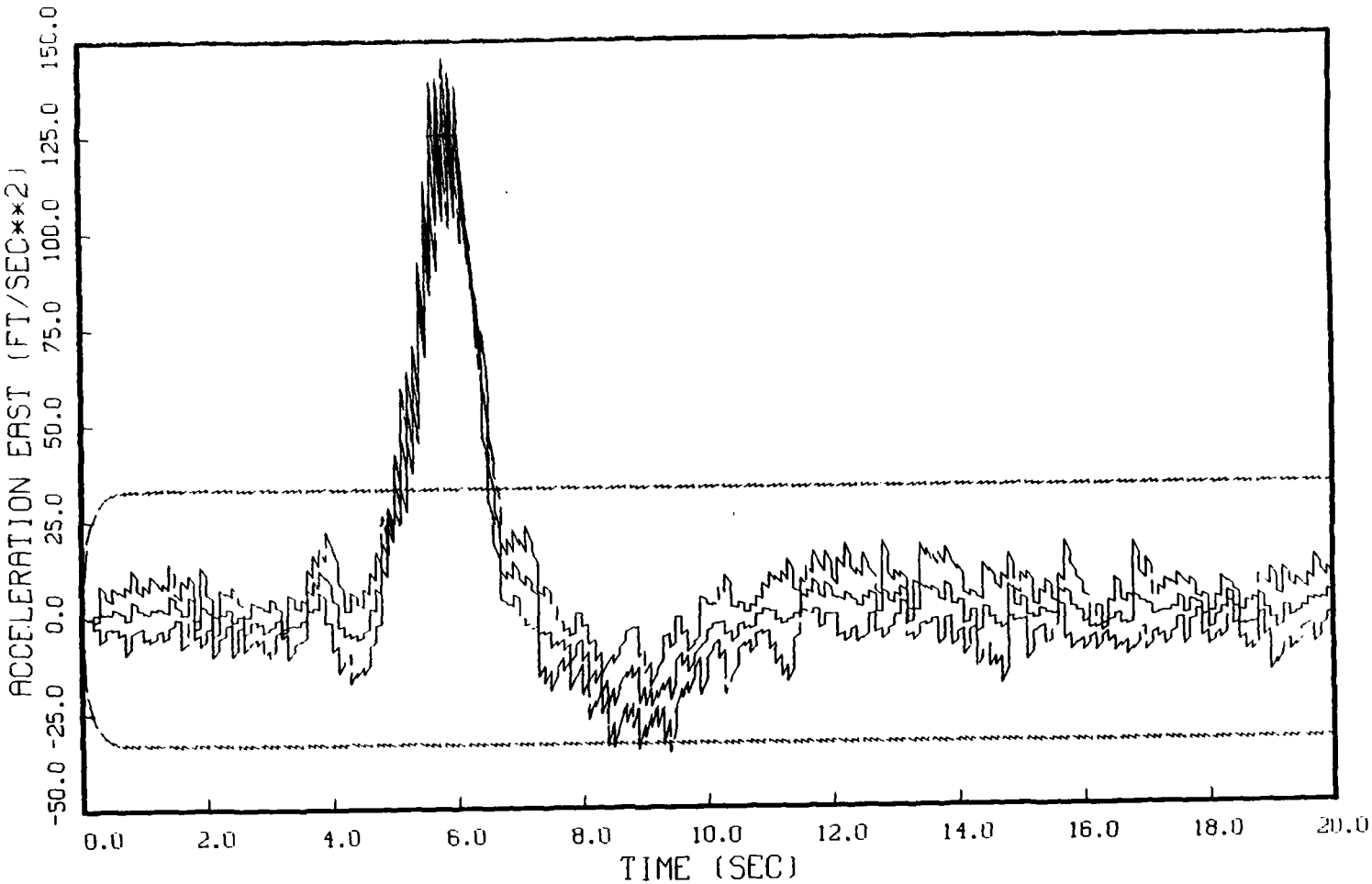

FIGURE E.27: GAUSS MARKOV MODEL, STATE 6, 5 RUNS
BEAM TRAJECTORY, 0-5000, ANGLE RATE MEAS. INHIBITED (ORIGINAL R)

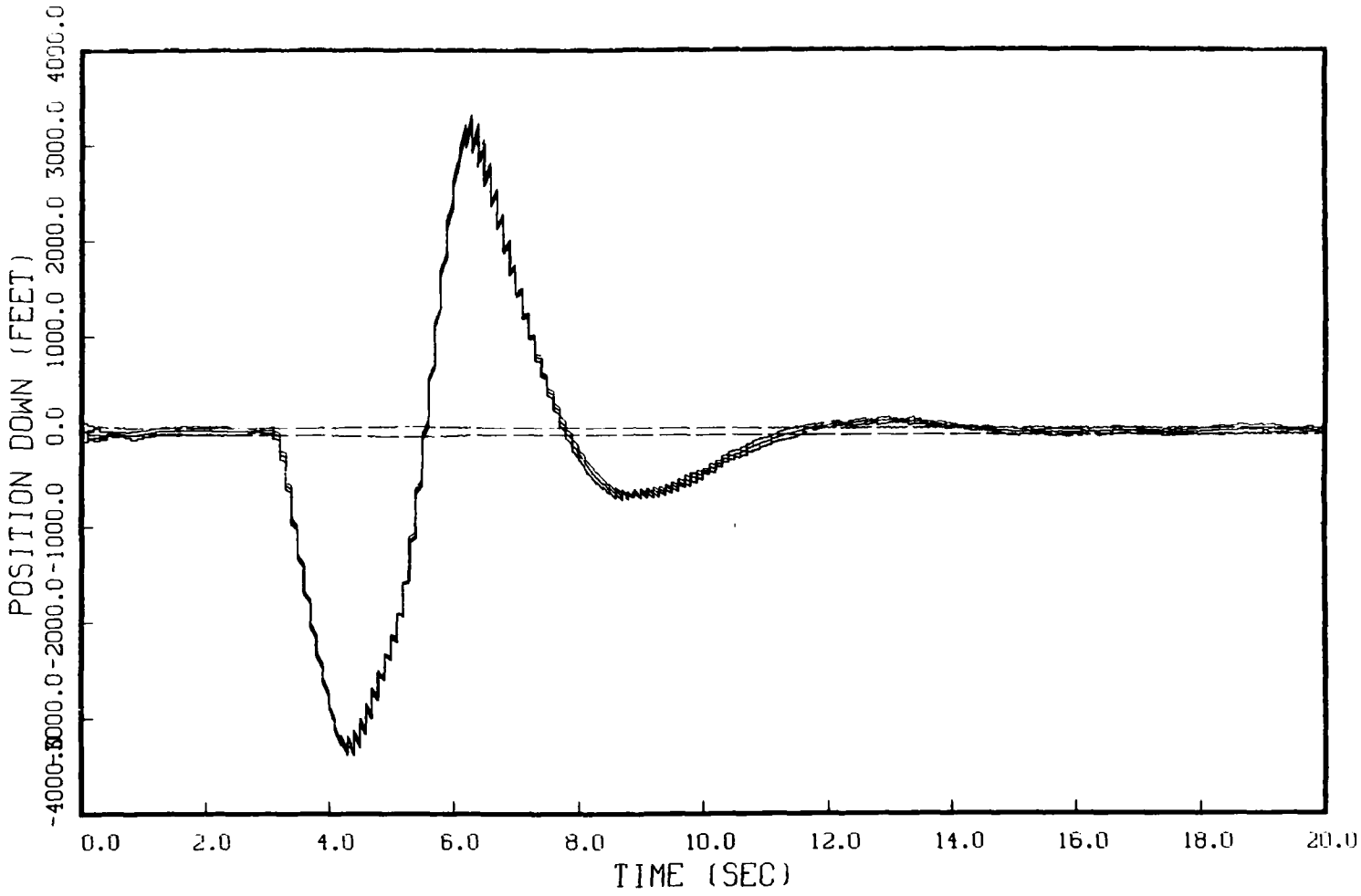

FIGURE E.28: GAUSS MARKOV MODEL, STATE 7, 5 RUNS
BEAM TRAJECTORY, 0-5000, ANGLE RATE MEAS. INHIBITED (ORIGINAL R)

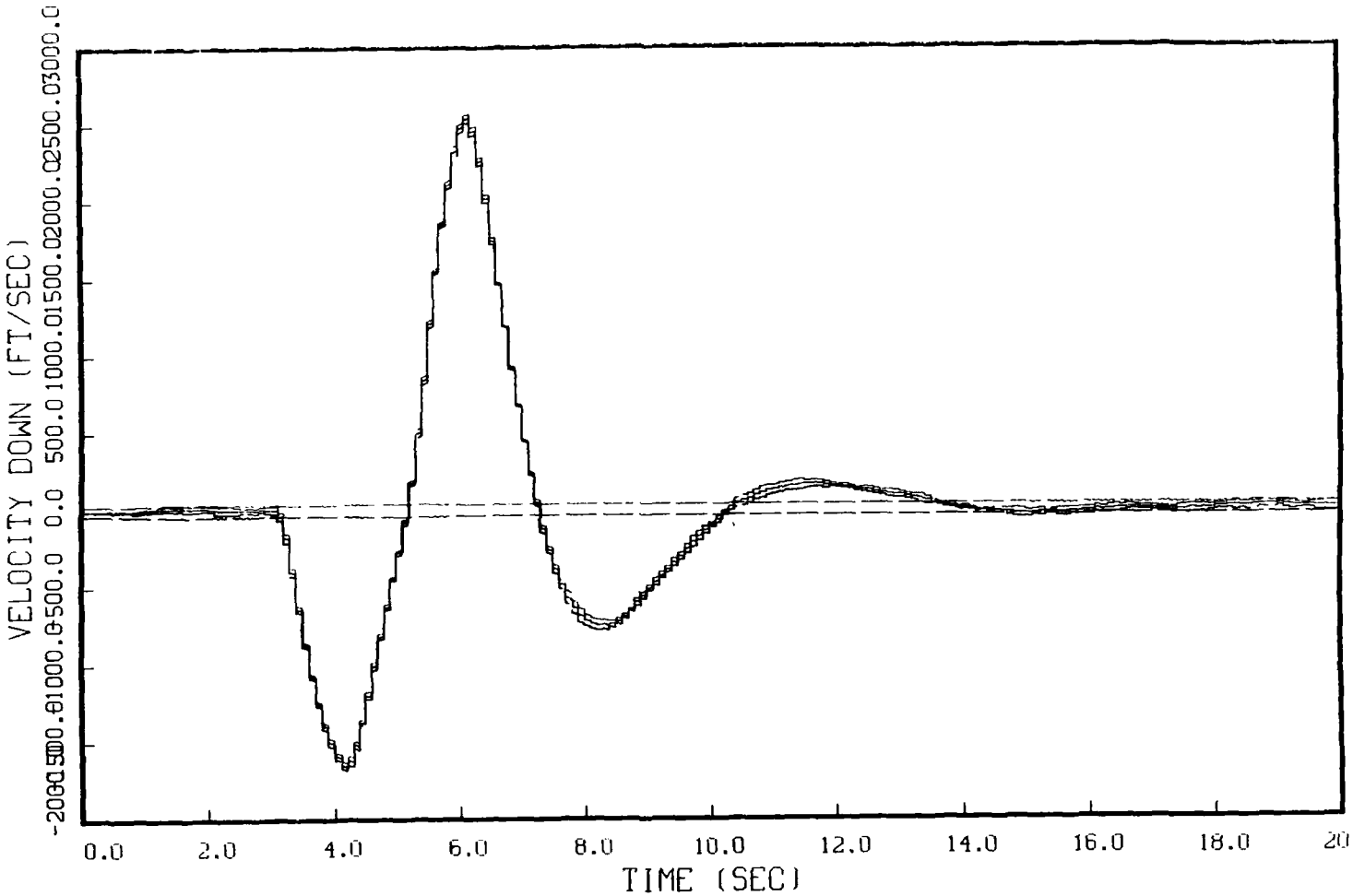

FIGURE E.29: GAUSS MARKOV MODEL, STATE 8, 5 RUNS
BEAM TRAJECTORY, 0-5000, ANGLE RATE MEAS. INHIBITED (ORIGINAL R)

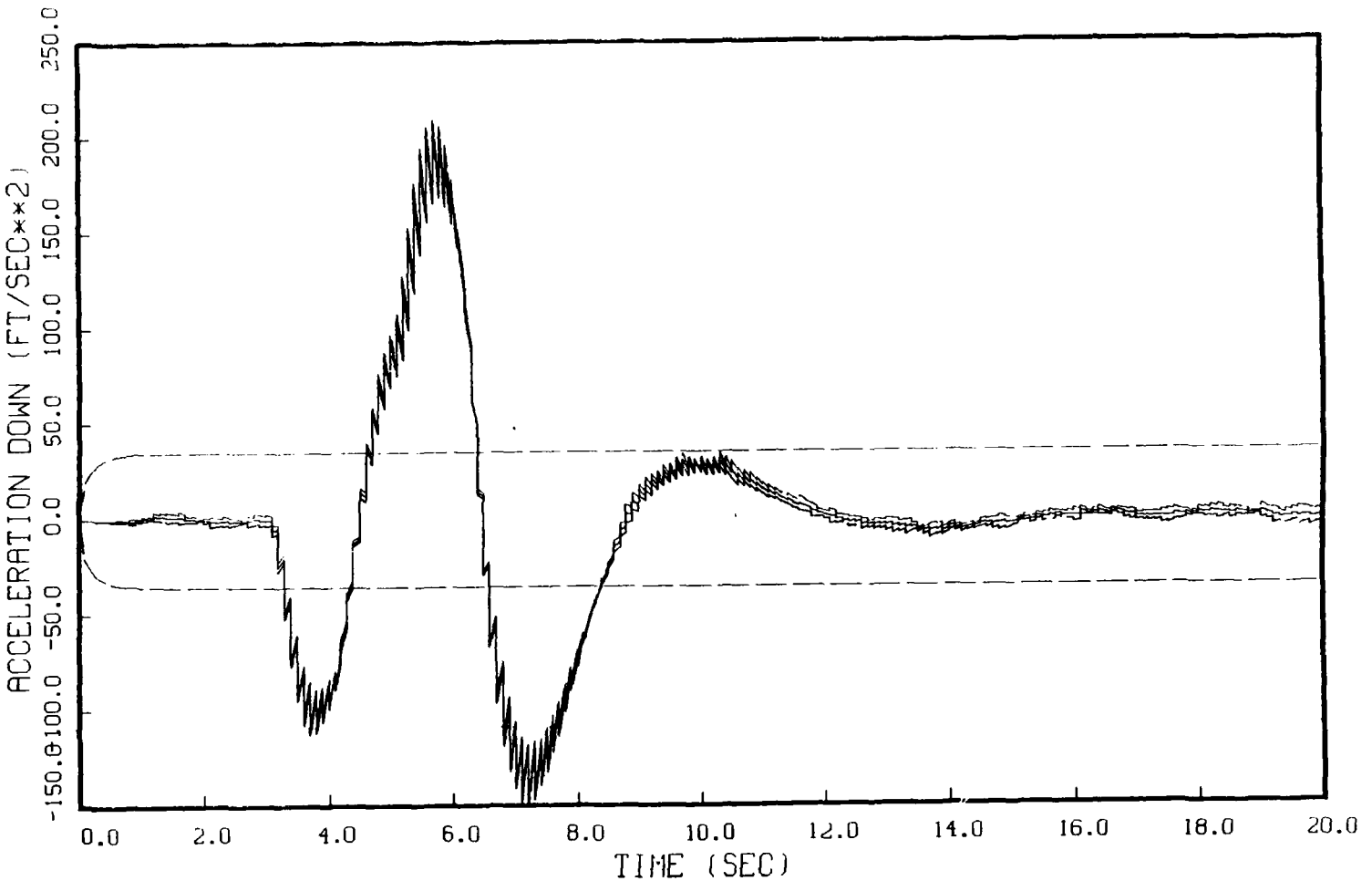

FIGURE E.30: GAUSS MARKOV MODEL, STATE 9, 5 RUNS
BEAM TRAJECTORY, 0-5000, ANGLE RATE MEAS. INHIBITED (ORIGINAL R)

Appendix F

Filter Tuning Using Driving Noise

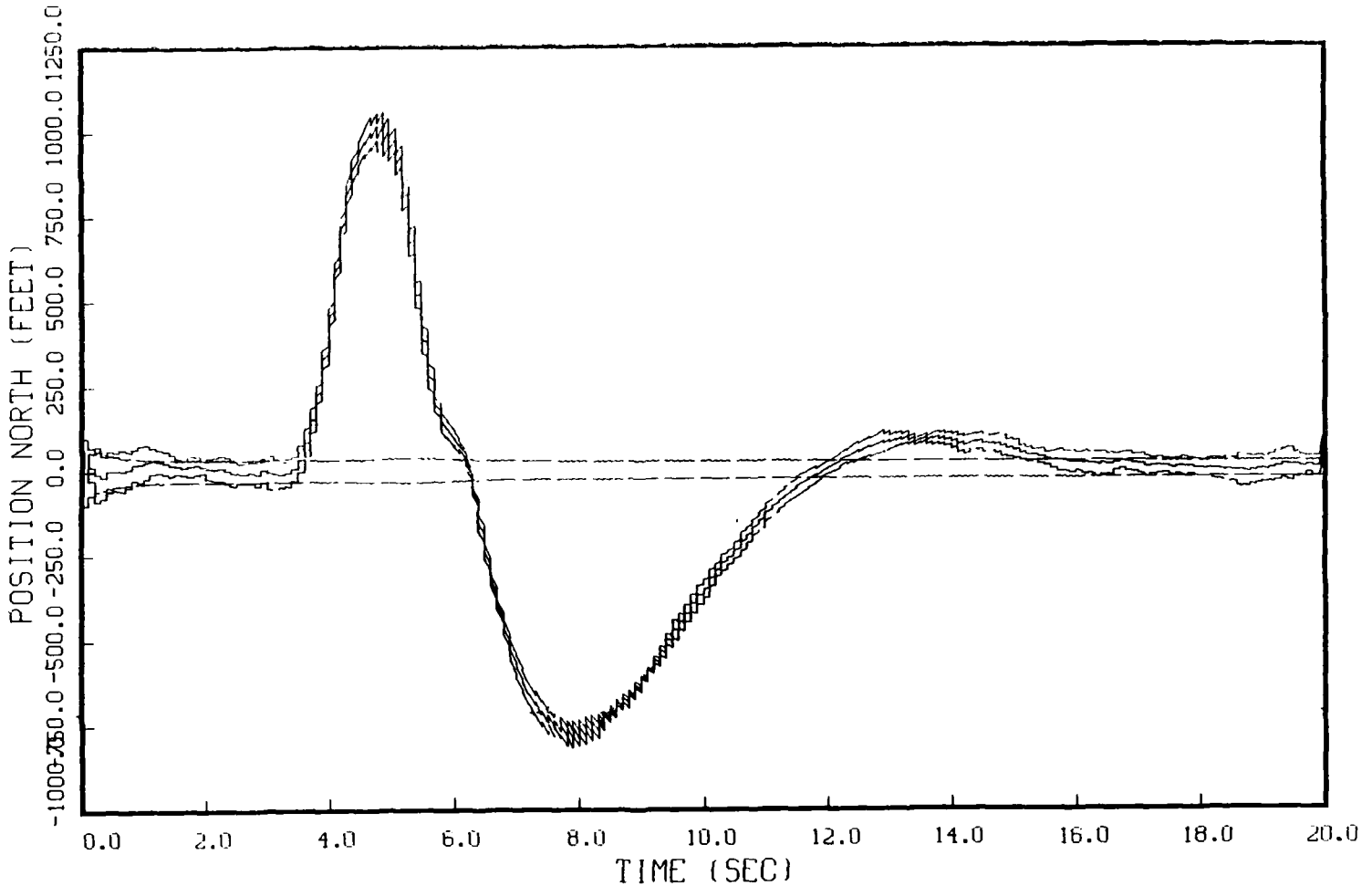

FIGURE F.1: GAUSS MARKOV MODEL, STATE 1, 5 RUNS
BEAM TRAJECTORY, Q=1000, ANGLE RATE MEAS. INHIBITED (ORIGINAL R)

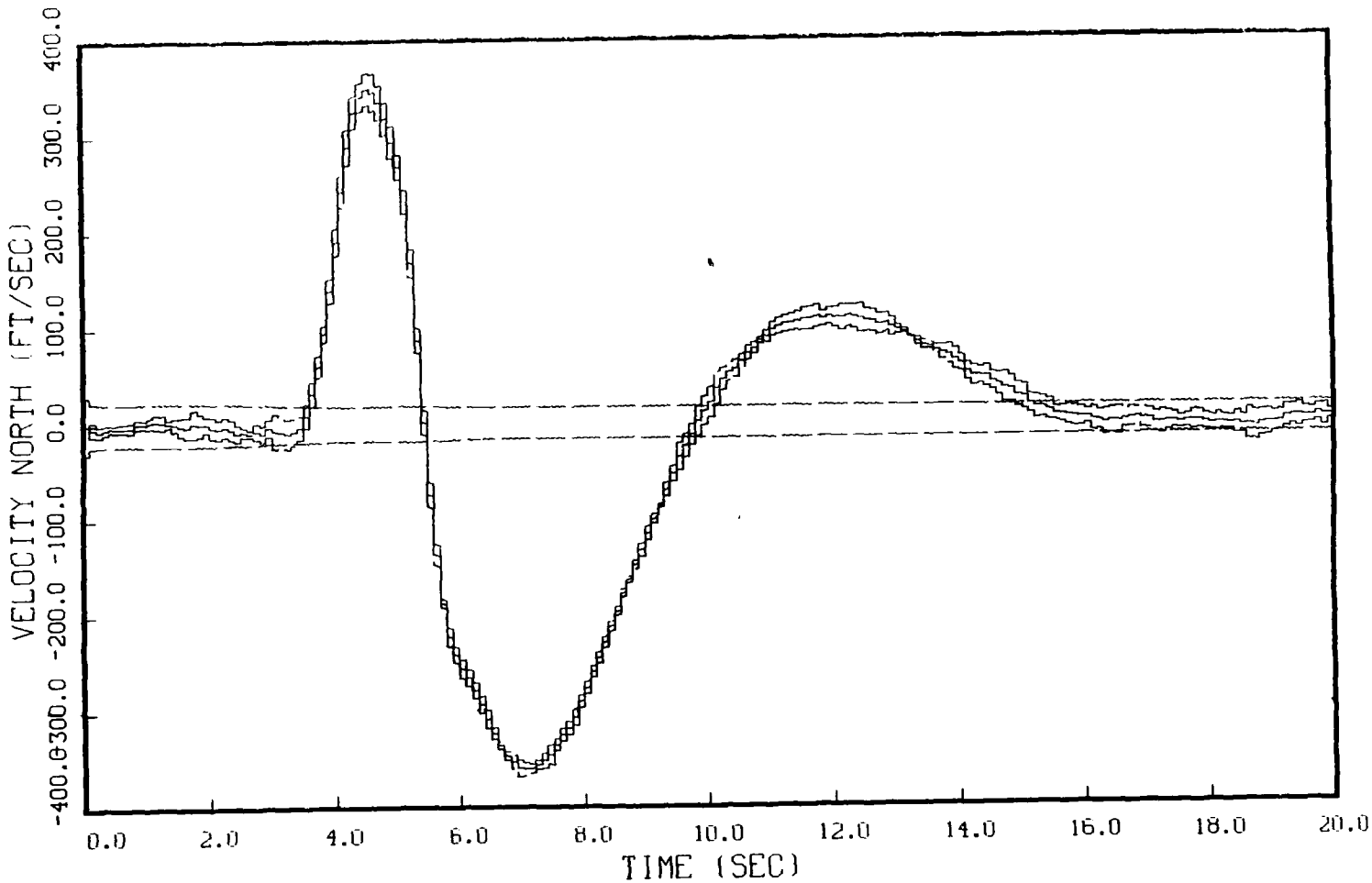

FIGURE F.2: GAUSS MARKOV MODEL, STATE 2, 5 RUNS
BEAM TRAJECTORY, 0-1000, ANGLE RATE MEAS. INHIBITED (ORIGINAL R)

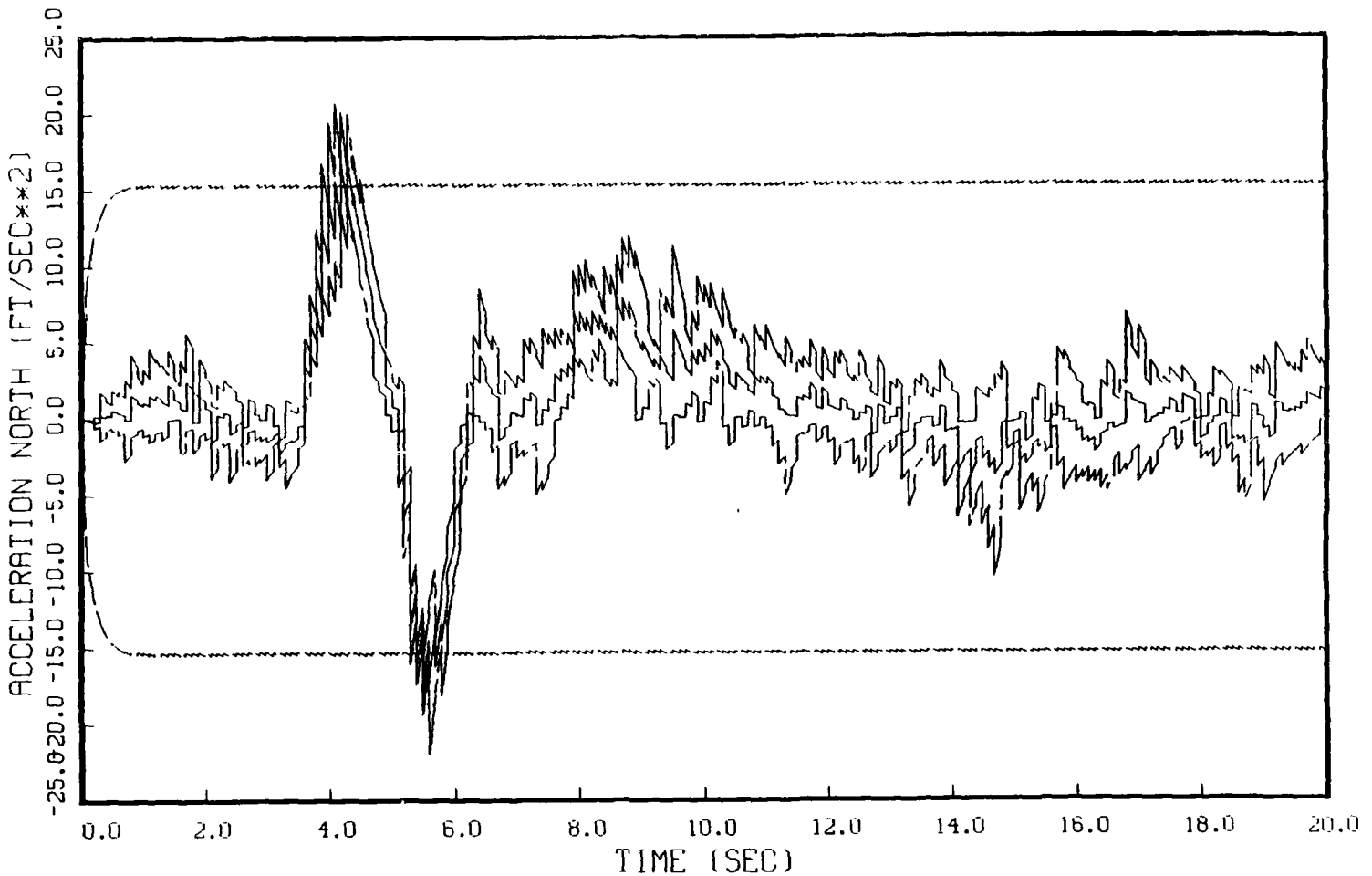

FIGURE F.3: GAUSS MARKOV MODEL, STATE 3, 5 RUNS
BEAM TRAJECTORY, 0-1000, ANGLE RATE MEAS. INHIBITED (ORIGINAL R)

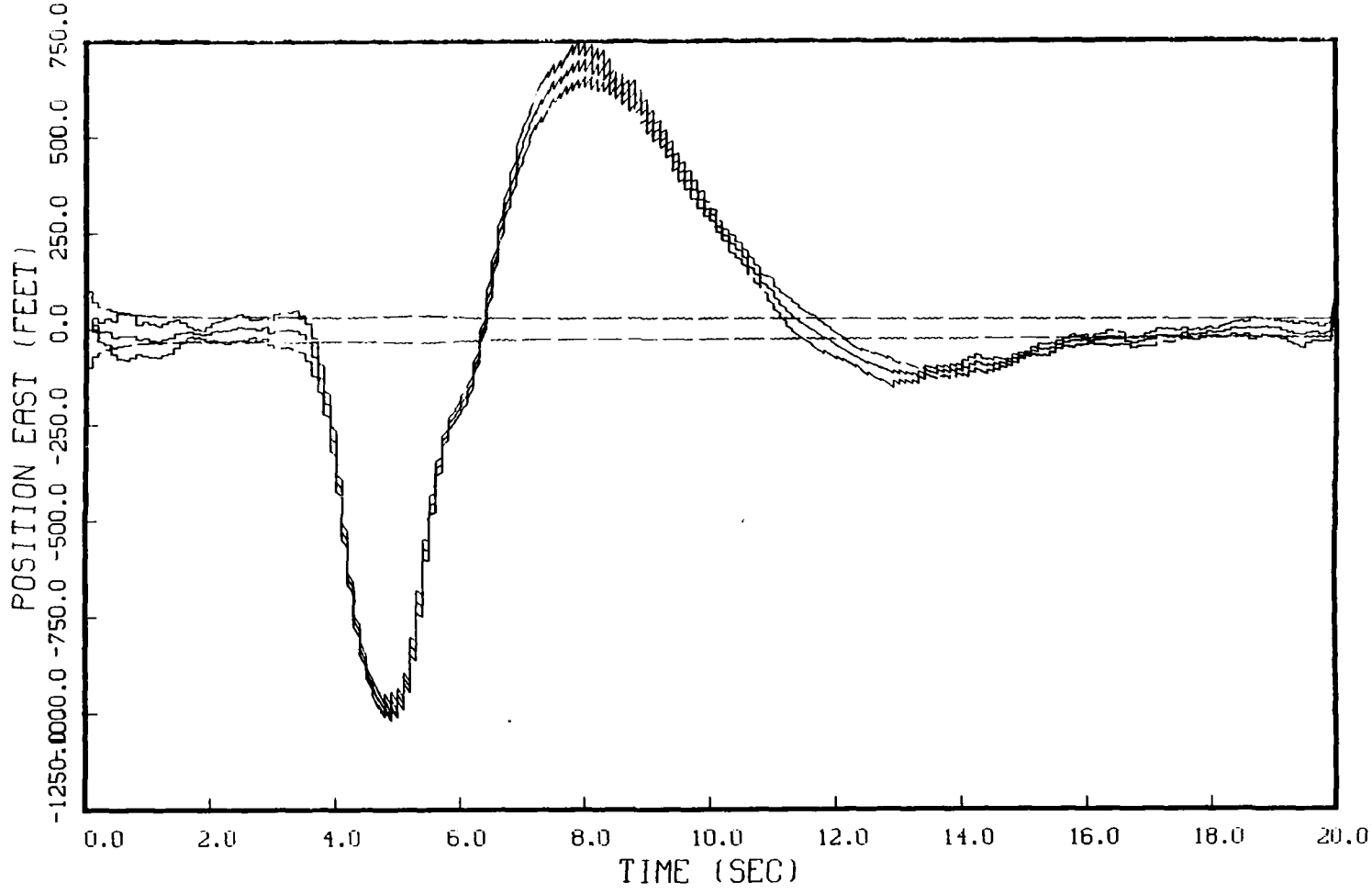

FIGURE F.4: GAUSS MARKOV MODEL, STATE 4, 5 RUNS
BEAM TRAJECTORY, 0-1000, ANGLE RATE MEAS. INHIBITED (ORIGINAL R)

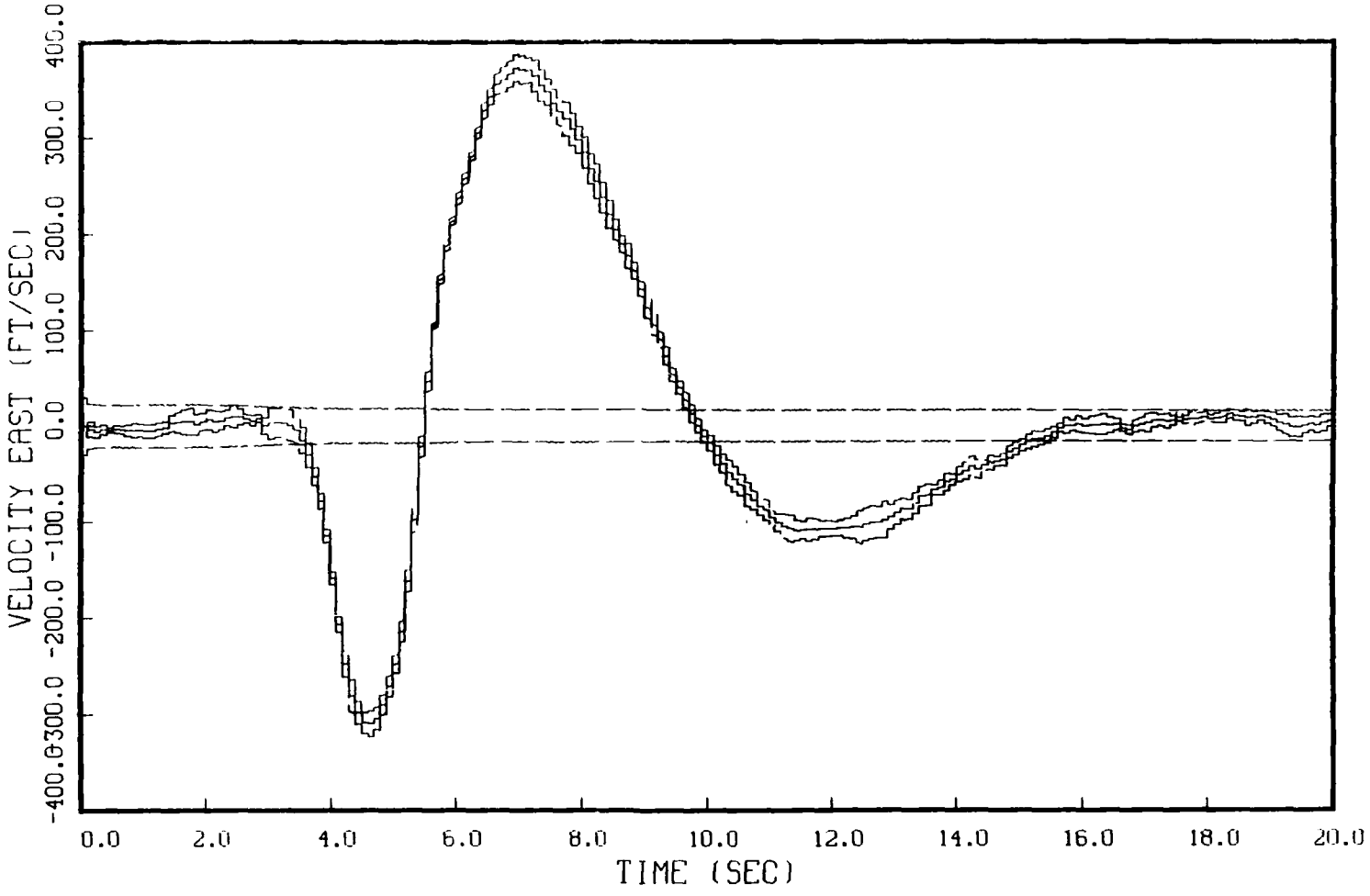

FIGURE F.5: GAUSS MARKOV MODEL, STATE 5, 5 RUNS
BEAM TRAJECTORY, 0-1000, ANGLE RATE MEAS. INHIBITED (ORIGINAL R)

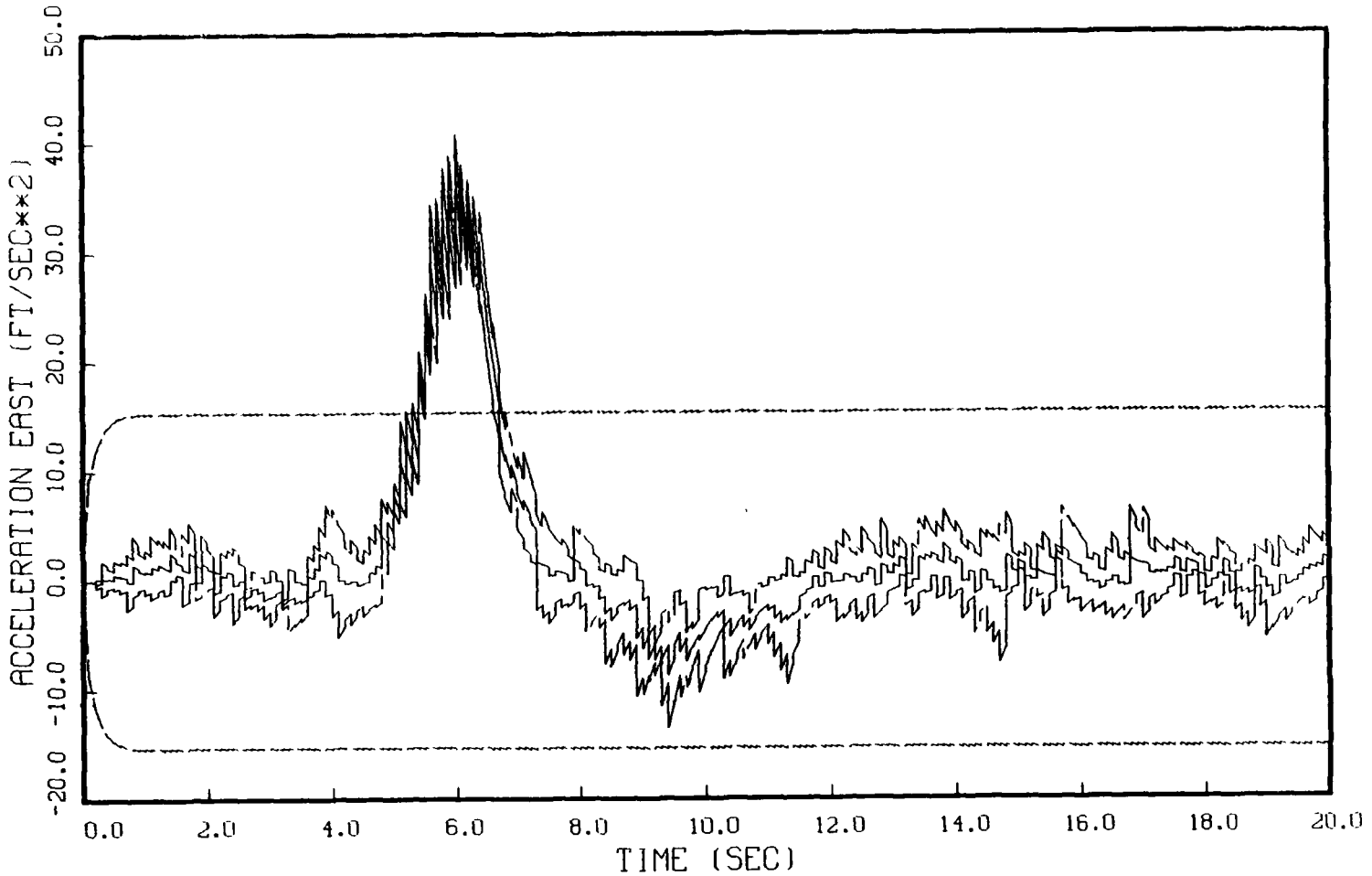

FIGURE F.6: GAUSS MARKOV MODEL, STATE 6, 5 RUNS
BEAM TRAJECTORY, 0-1000, ANGLE RATE MEAS. INHIBITED (ORIGINAL R)

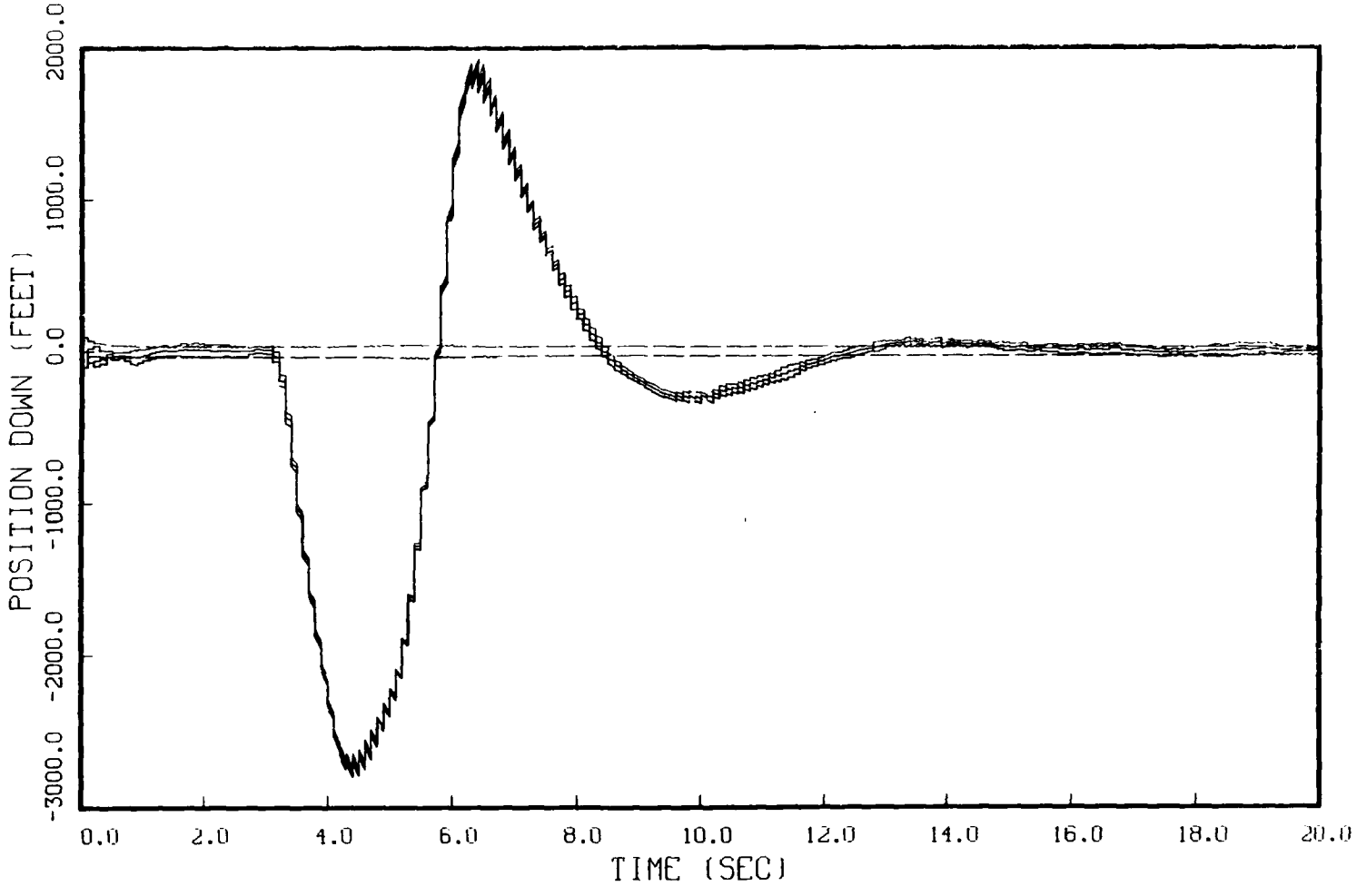

FIGURE F.7: GAUSS MARKOV MODEL, STATE 7, 5 RUNS
BEAM TRAJECTORY, Q-1000, ANGLE RATE MEAS. INHIBITED (ORIGINAL R)

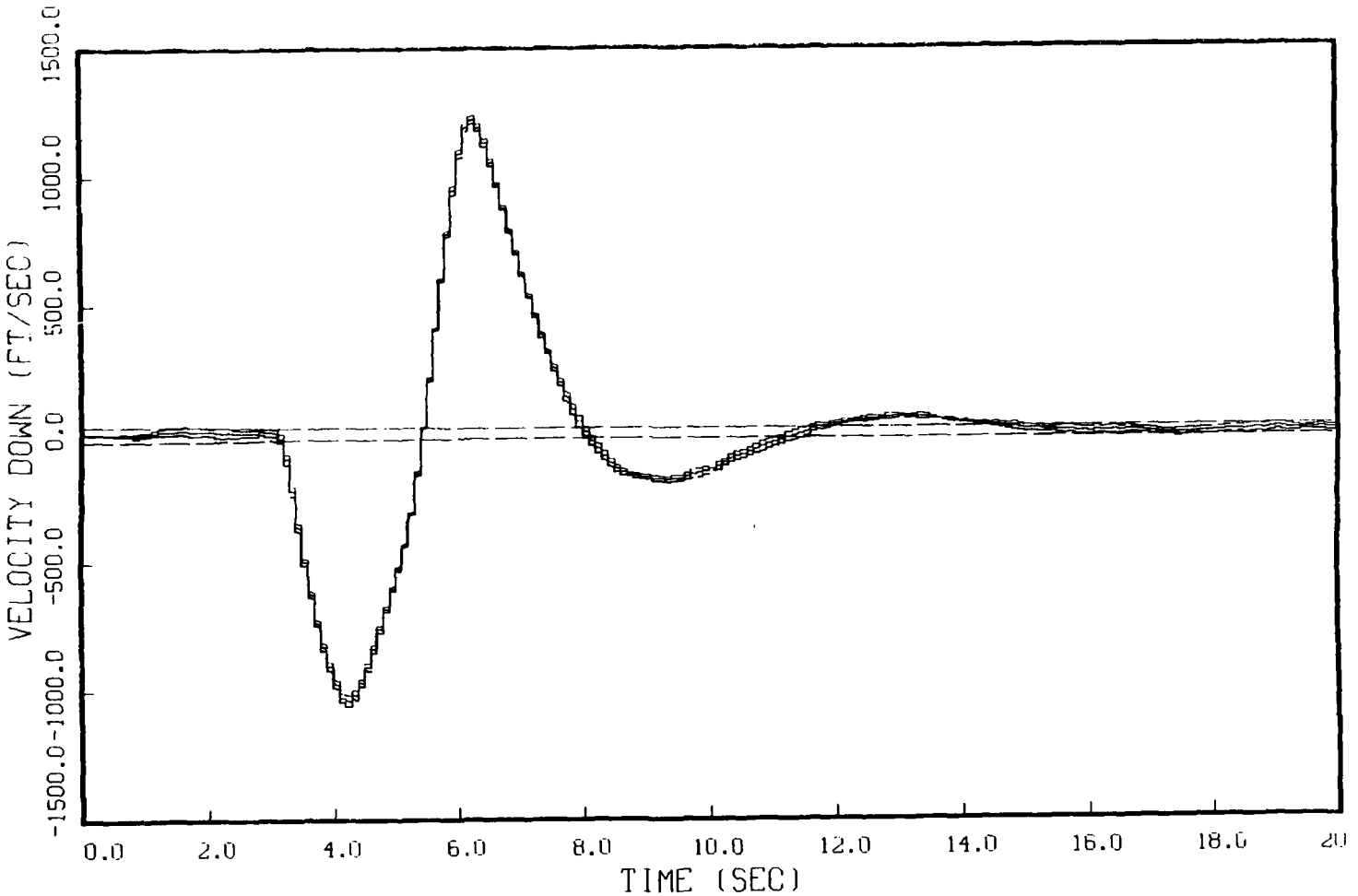

FIGURE F.8: GAUSS MARKOV MODEL, STATE 8, 5 RUNS
BEAM TRAJECTORY, Q=1000, ANGLE RATE MEAS. INHIBITED (ORIGINAL R)

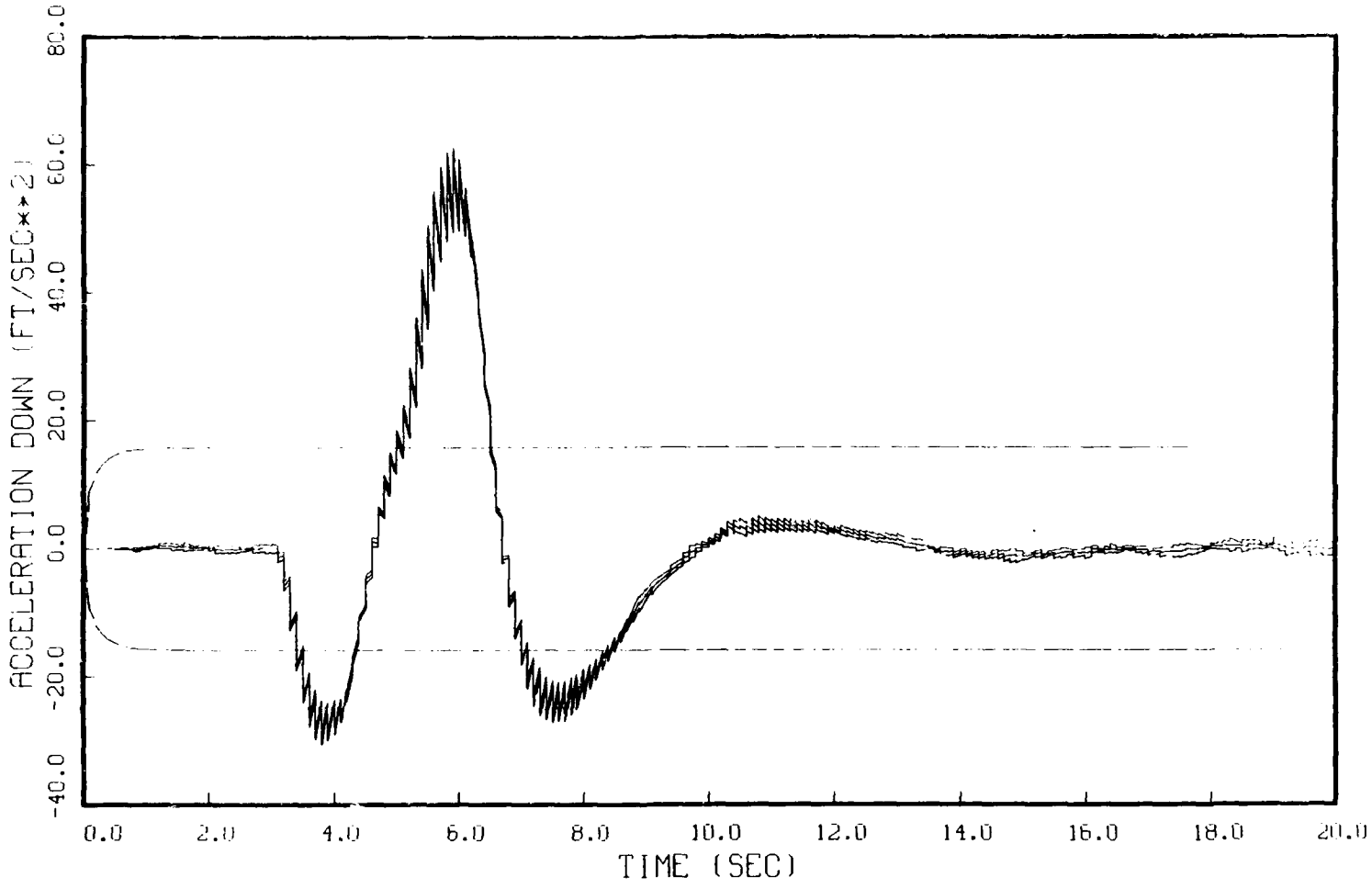

FIGURE F.9: GAUSS MARKOV MODEL, STATE 9, 5 RUNS
BEAM TRAJECTORY, Q=1000, ANGLE RATE MEAS. INHIBITED (ORIGINAL R)

AD-A164 205 KALMAN FILTER DESIGN FOR THE LONG RANGE INTERCEPT FUNCTION OF THE F-4E/G F.. (U) AIR FORCE INST OF TECH WRIGHT-PATTERSON AFB OH SCHOOL OF ENGI.. R C HALBERT

UNCLASSIFIED DEC 85 AFIT/GE/ENG/85D-20 F/G 17/9 NL

3/4

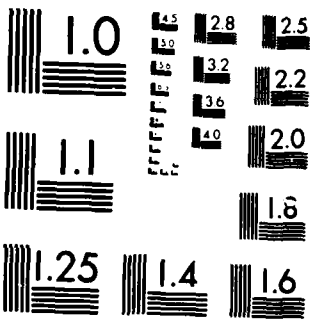

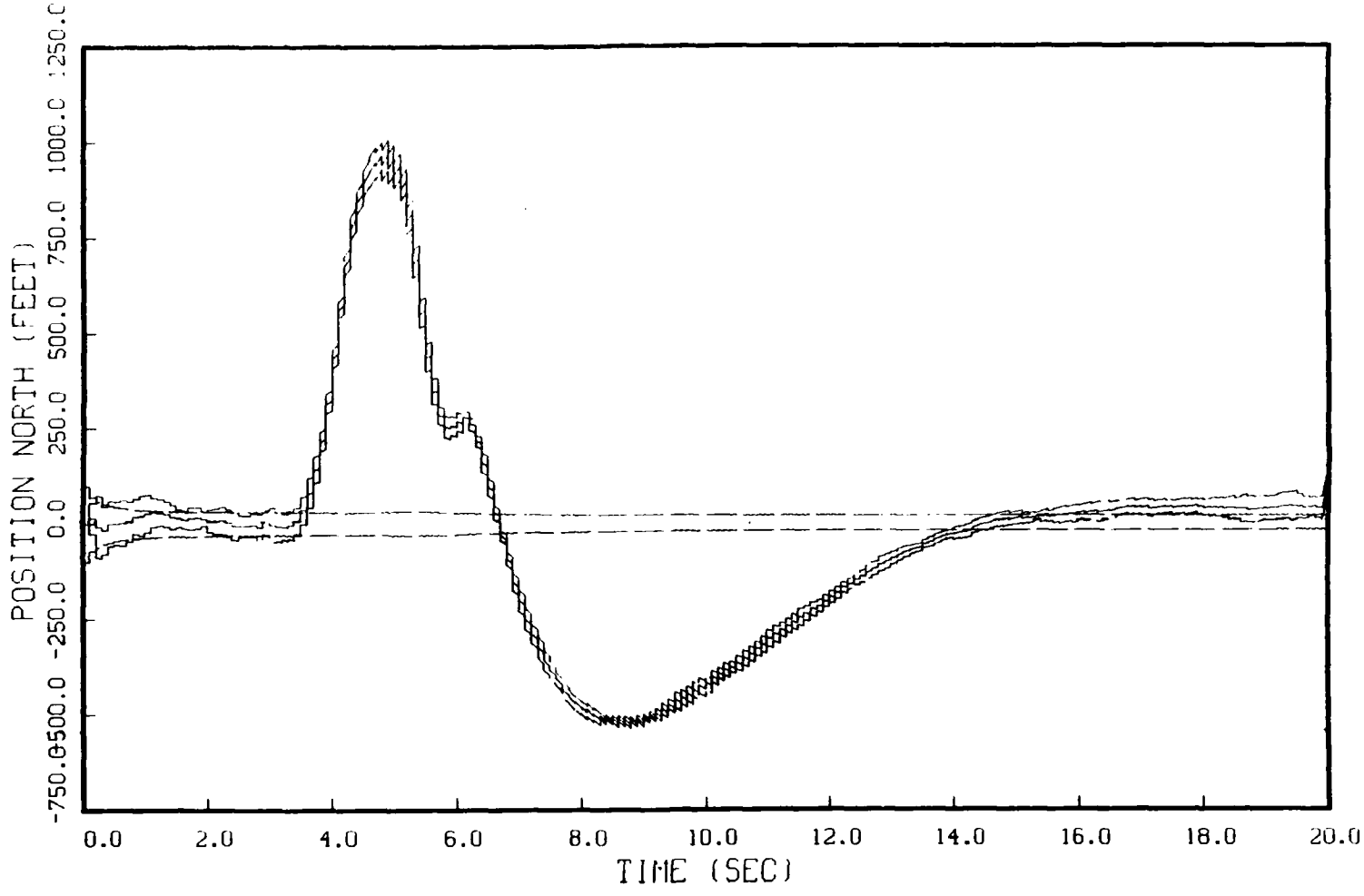

FIGURE F.10: GAUSS MARKOV MODEL, STATE 1, 5 RUNS
BEAM TRAJECTORY, 0-100, ANGLE RATE MEAS. INHIBITED (ORIGINAL R)

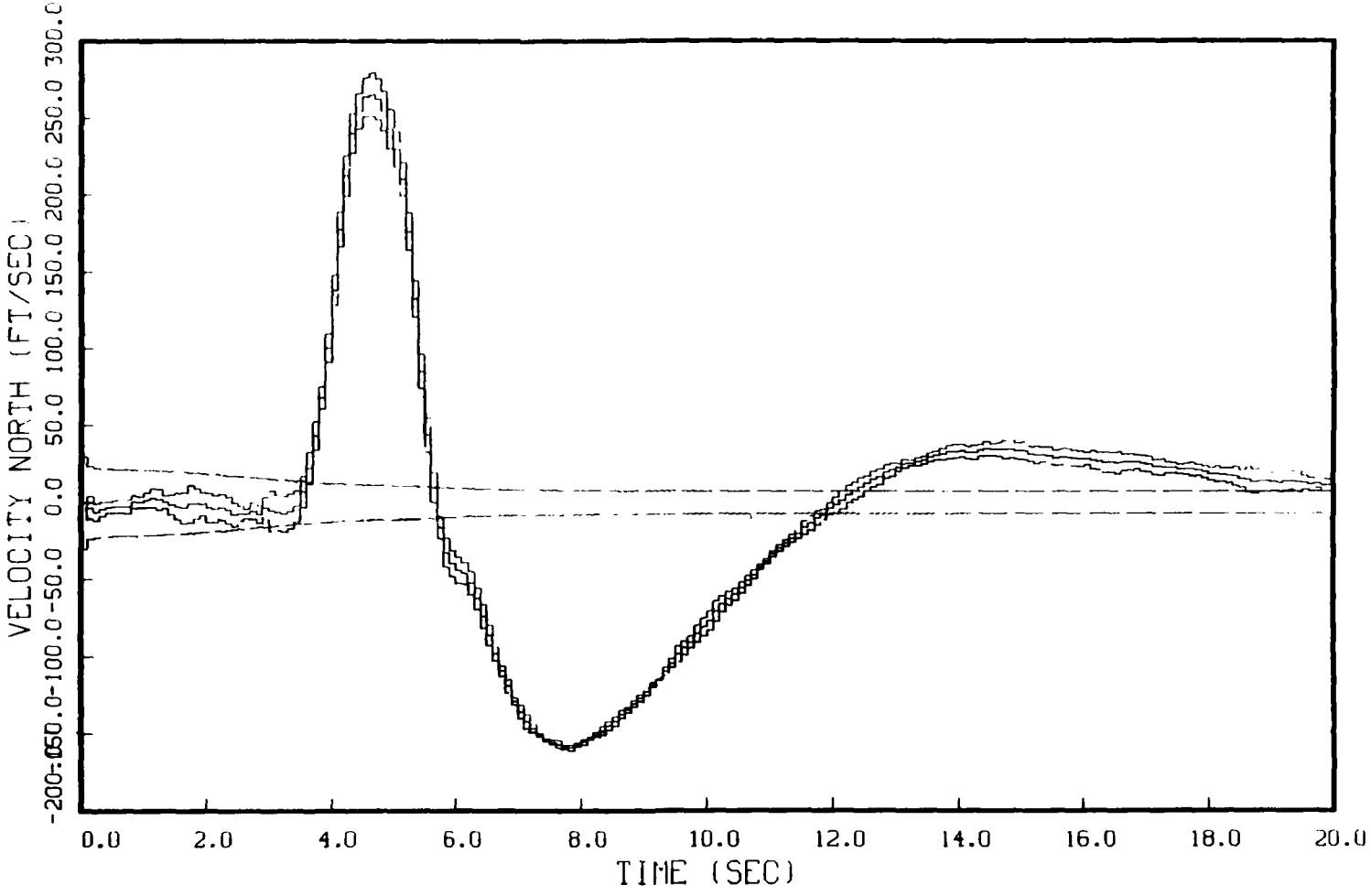

FIGURE F.11: GAUSS MARKOV MODEL, STATE 2, 5 RUNS
BEAM TRAJECTORY, 0-100, ANGLE RATE MEAS. INHIBITED (ORIGINAL R)

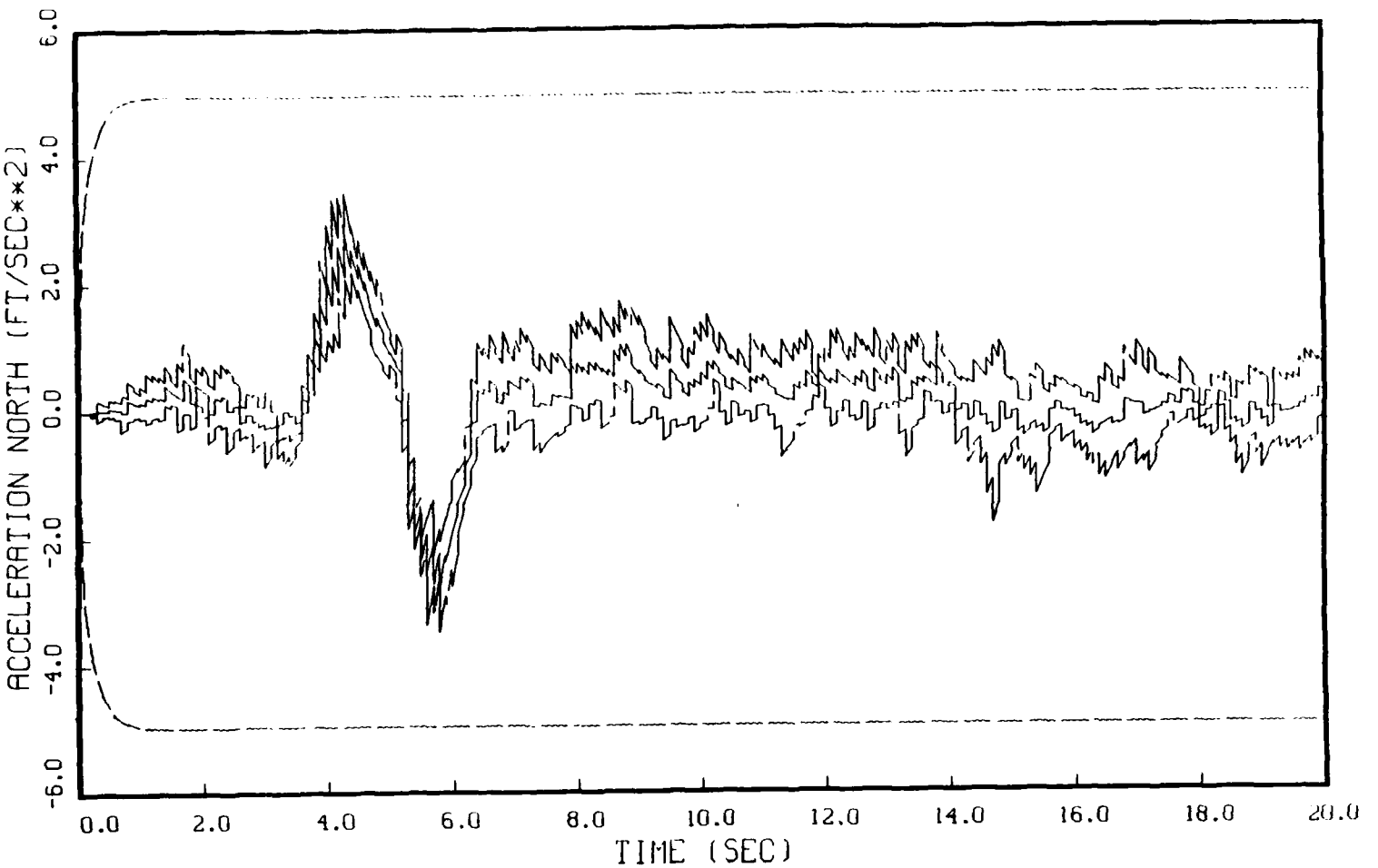

FIGURE F.12: GAUSS MARKOV MODEL, STATE 3, 5 RUNS
BEAM TRAJECTORY, 0-100, ANGLE RATE MEAS. INHIBITED (ORIGINAL R)

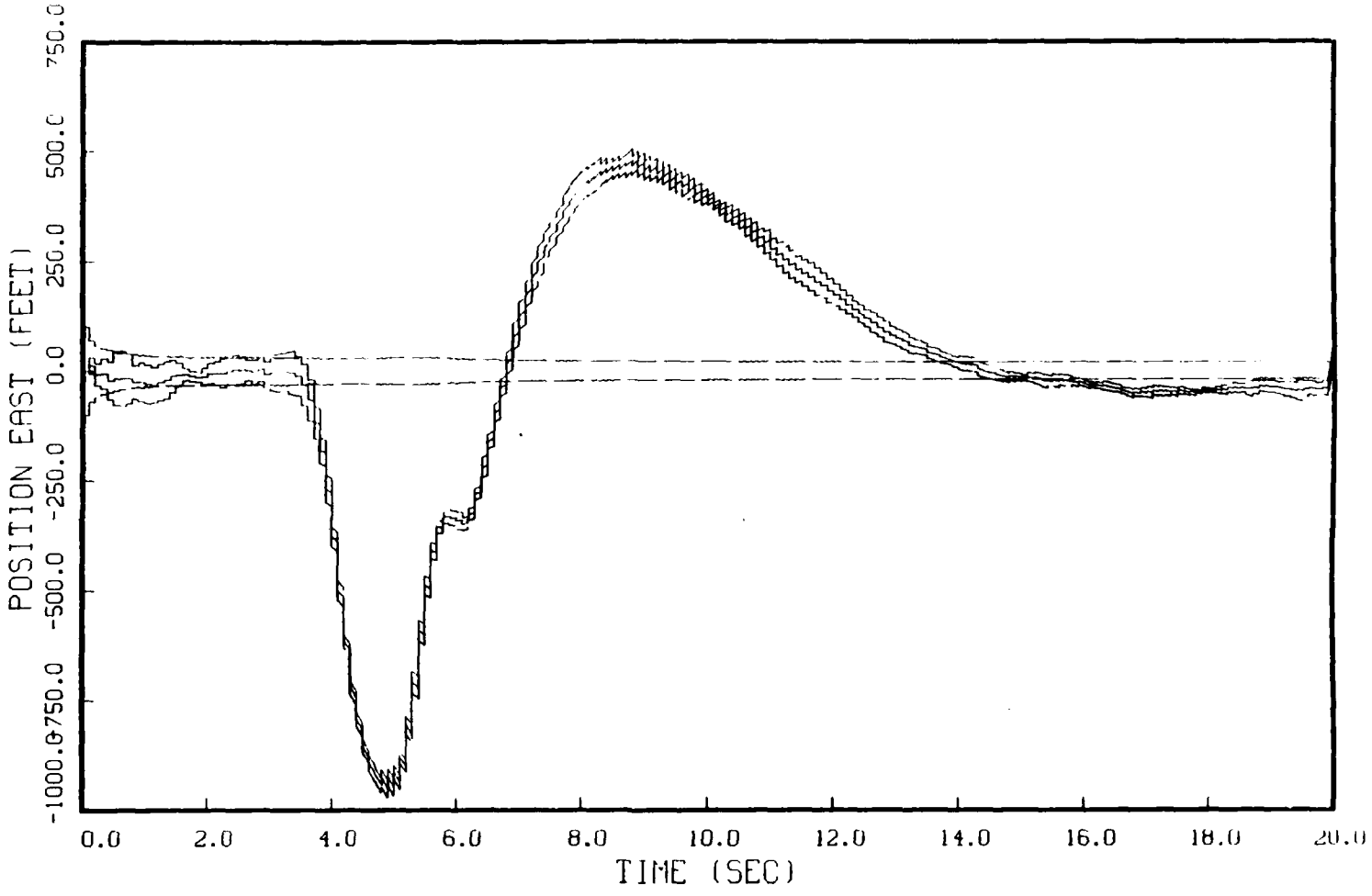

FIGURE F.13: GAUSS MARKOV MODEL, STATE 4, 5 RUNS
BEAM TRAJECTORY, Q-100, ANGLE RATE MEAS. INHIBITED (ORIGINAL R)

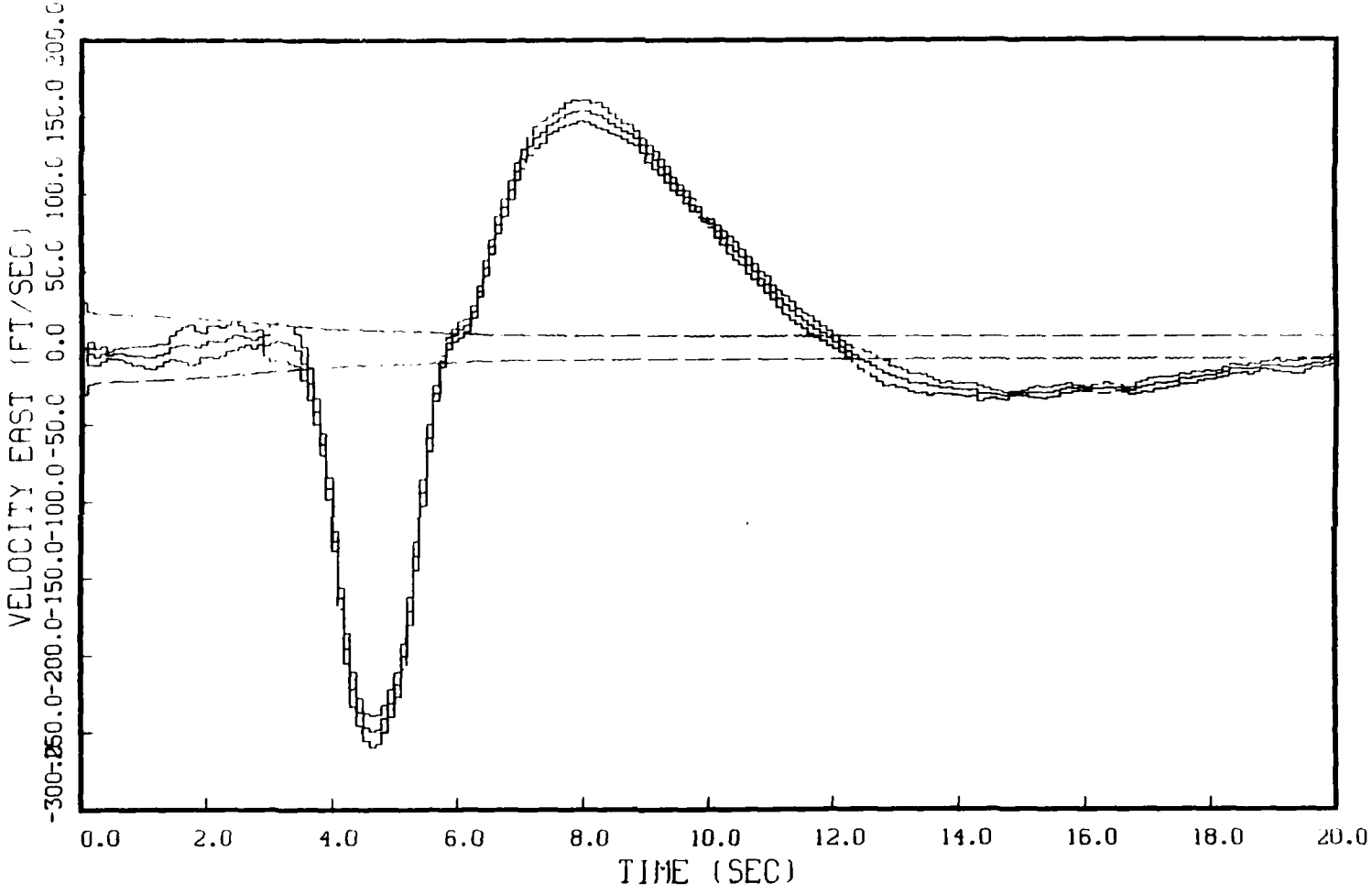

FIGURE F.14: GAUSS MARKOV MODEL, STATE 5, 5 RUNS
BEAM TRAJECTORY, 0-100, ANGLE RATE MEAS. INHIBITED (ORIGINAL R)

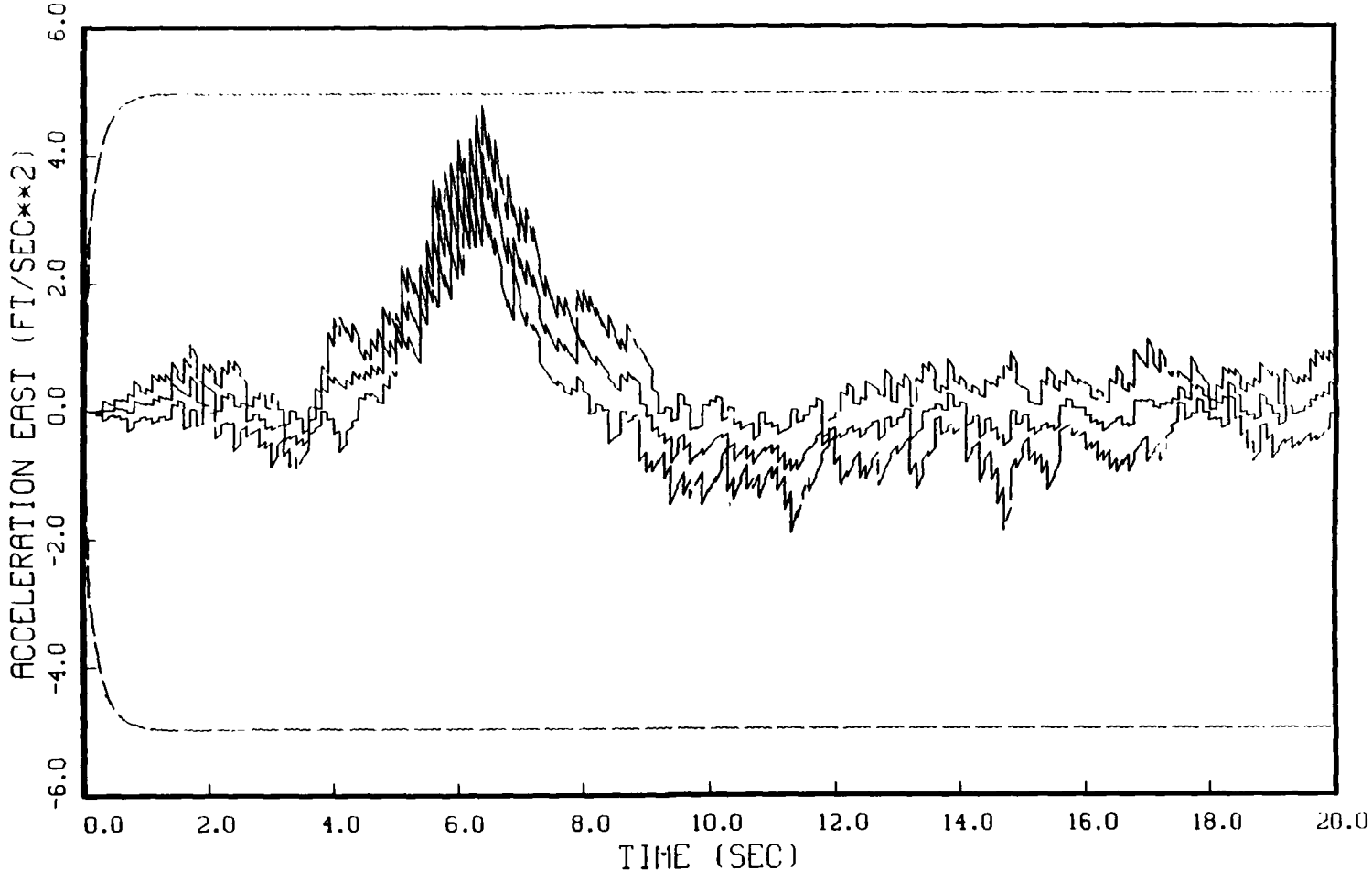

FIGURE F.15: GAUSS MARKOV MODEL, STATE 6, 5 RUNS
BEAM TRAJECTORY, 0-100, ANGLE RATE MEAS. INHIBITED (ORIGINAL R)

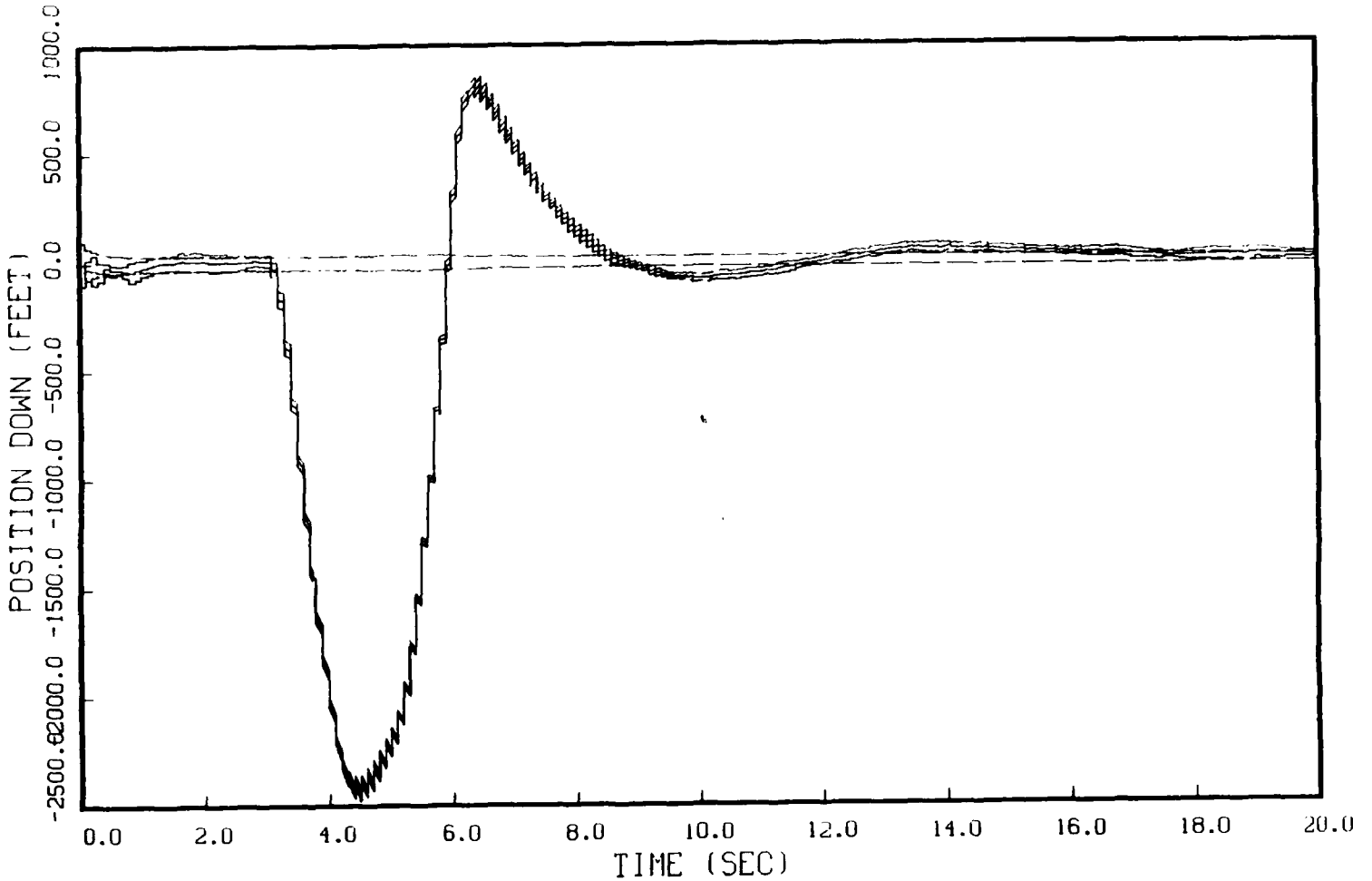

FIGURE F.16: GAUSS MARKOV MODEL, STATE 7, 5 RUNS
BEAM TRAJECTORY, 0-100, ANGLE RATE MEAS. INHIBITED (ORIGINAL R)

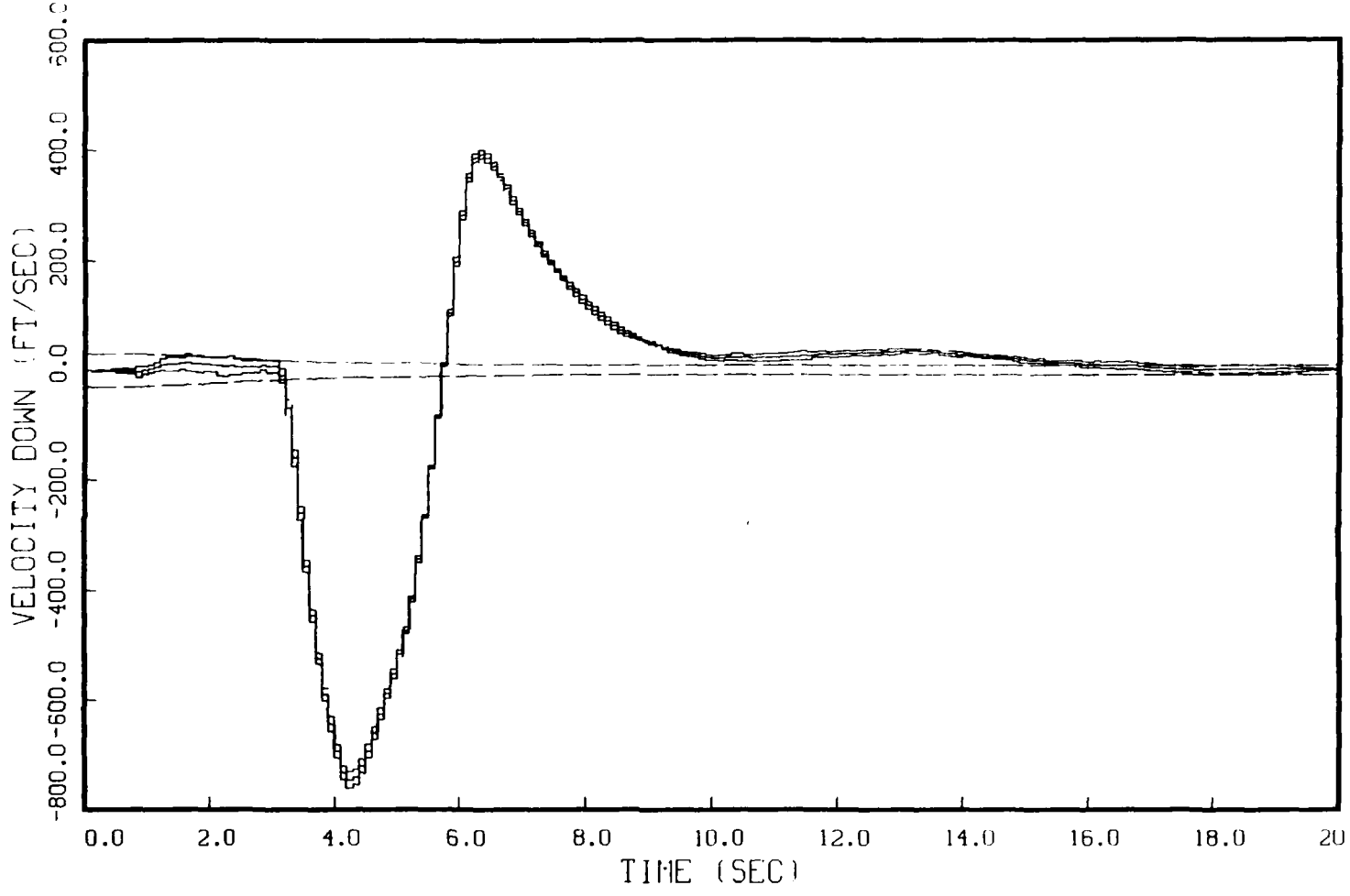

FIGURE F.17: GAUSS MARKOV MODEL, STATE 8, 5 RUNS
BEAM TRAJECTORY, 0-100, ANGLE RATE MEAS. INHIBITED (ORIGINAL P)

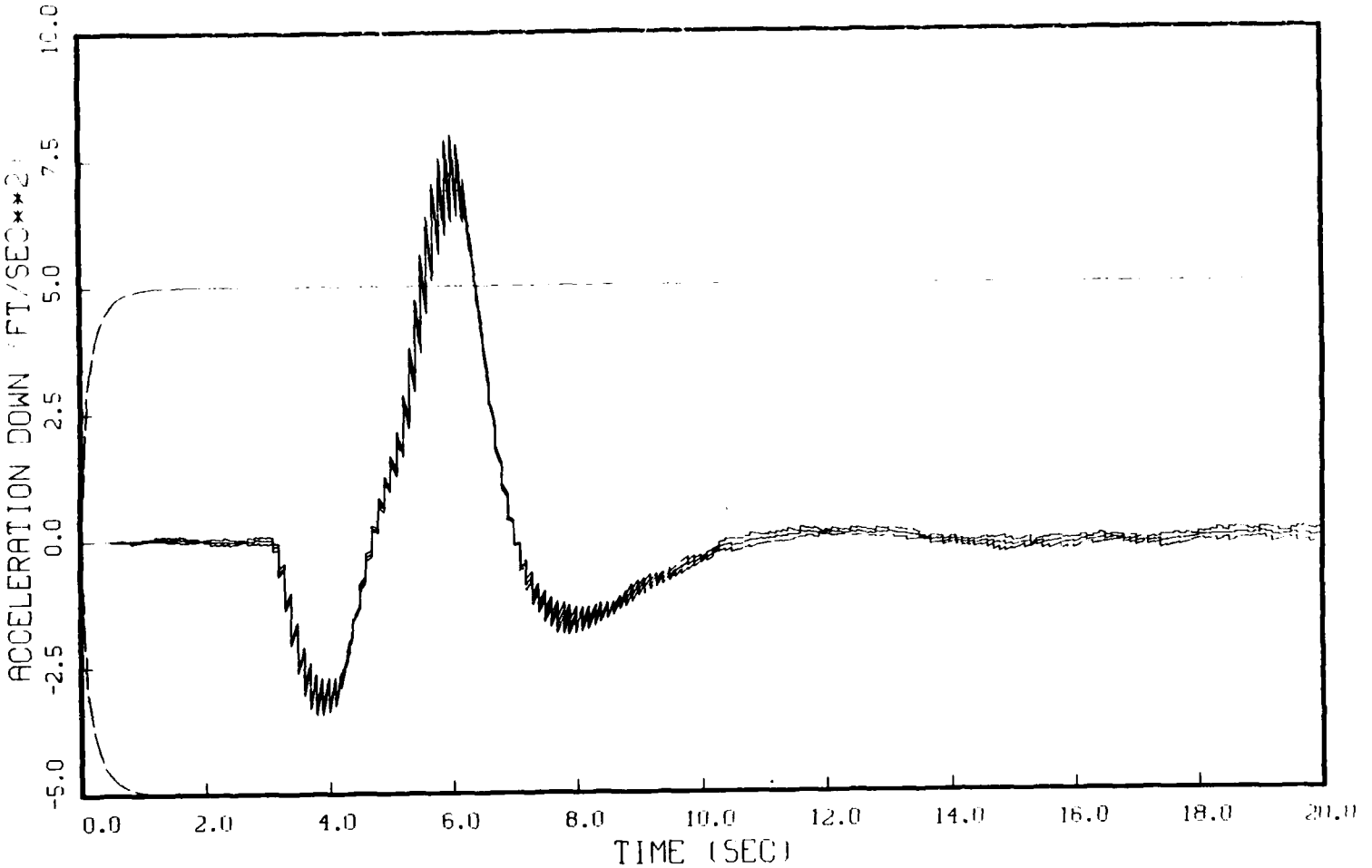

FIGURE F.18: GAUSS MARKOV MODEL, STATE 9, 5 RUNS
BEAM TRAJECTORY, O=100, ANGLE RATE MEAS. INHIBITED (ORIGINAL R)

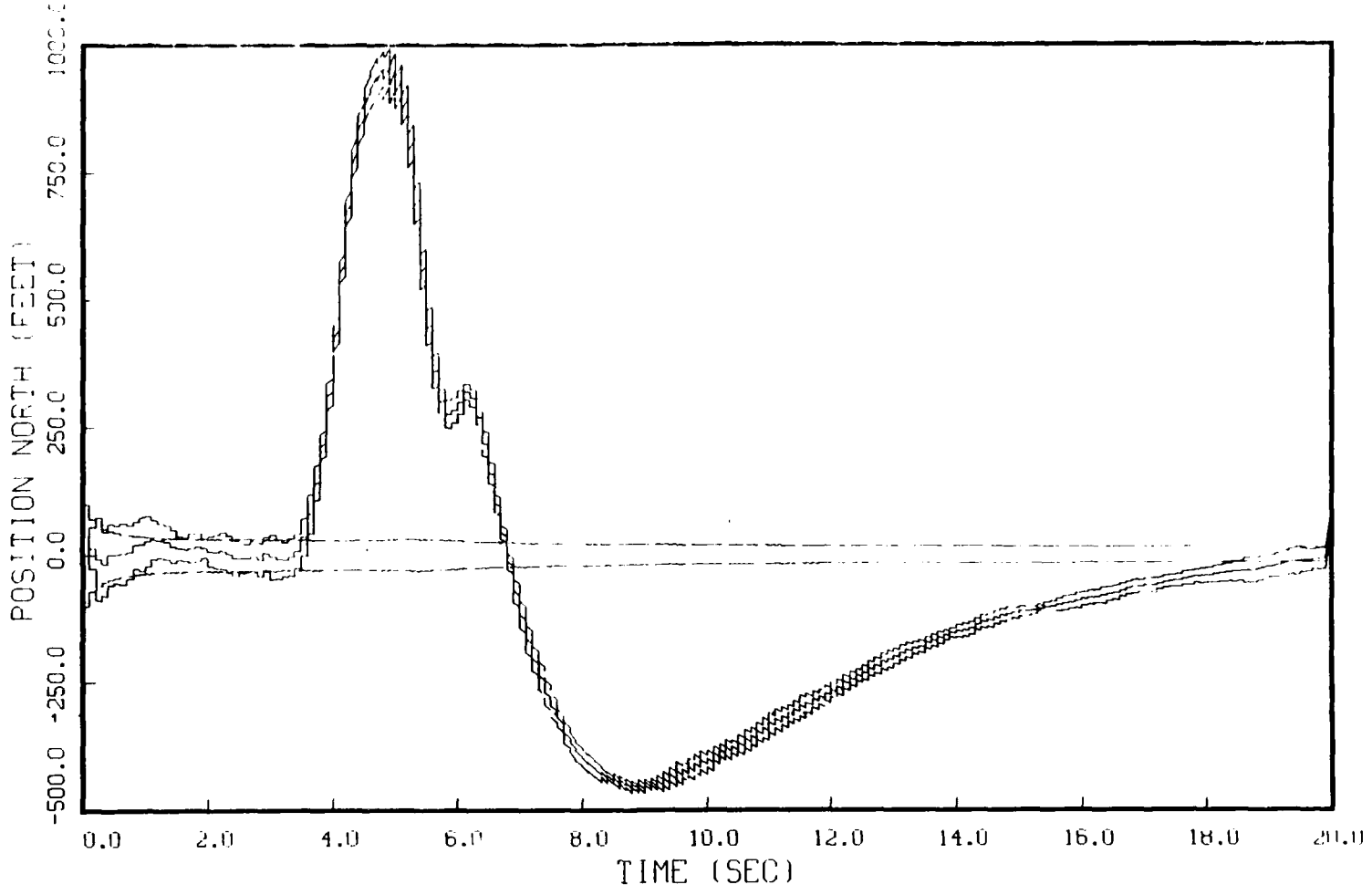

FIGURE F.19: GAUSS MARKOV MODEL, STATE 1, 5 RUNS
BEAM TRAJECTORY, Q-10, ANGLE RATE MEAS. INHIBITED (ORIGINAL R)

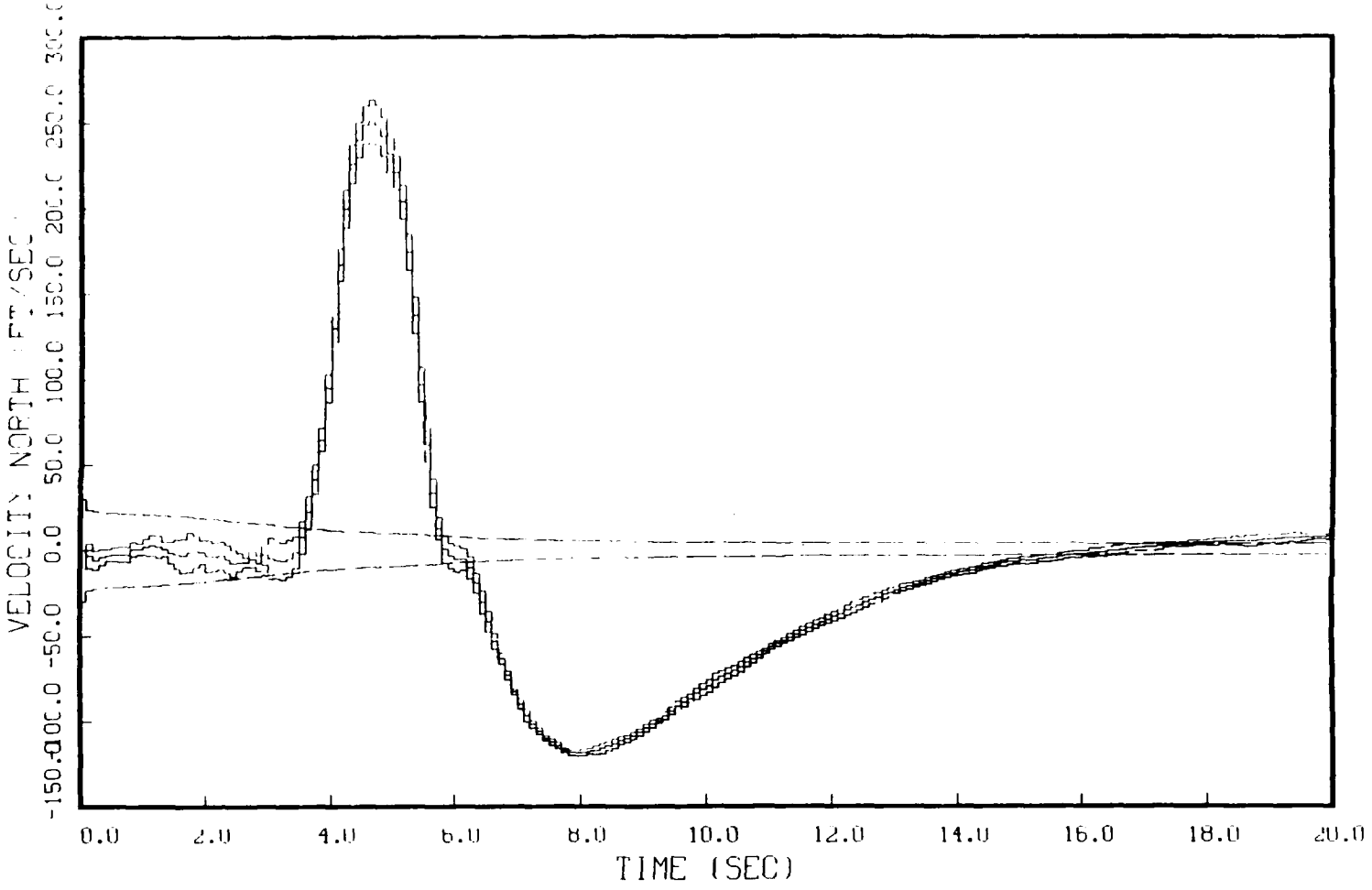

FIGURE F.20: GAUSS MARKOV MODEL, STATE 2, 5 RUNS
BEAM TRAJECTORY, 0-10, ANGLE RATE MEAS. INHIBITED (ORIGINAL R)

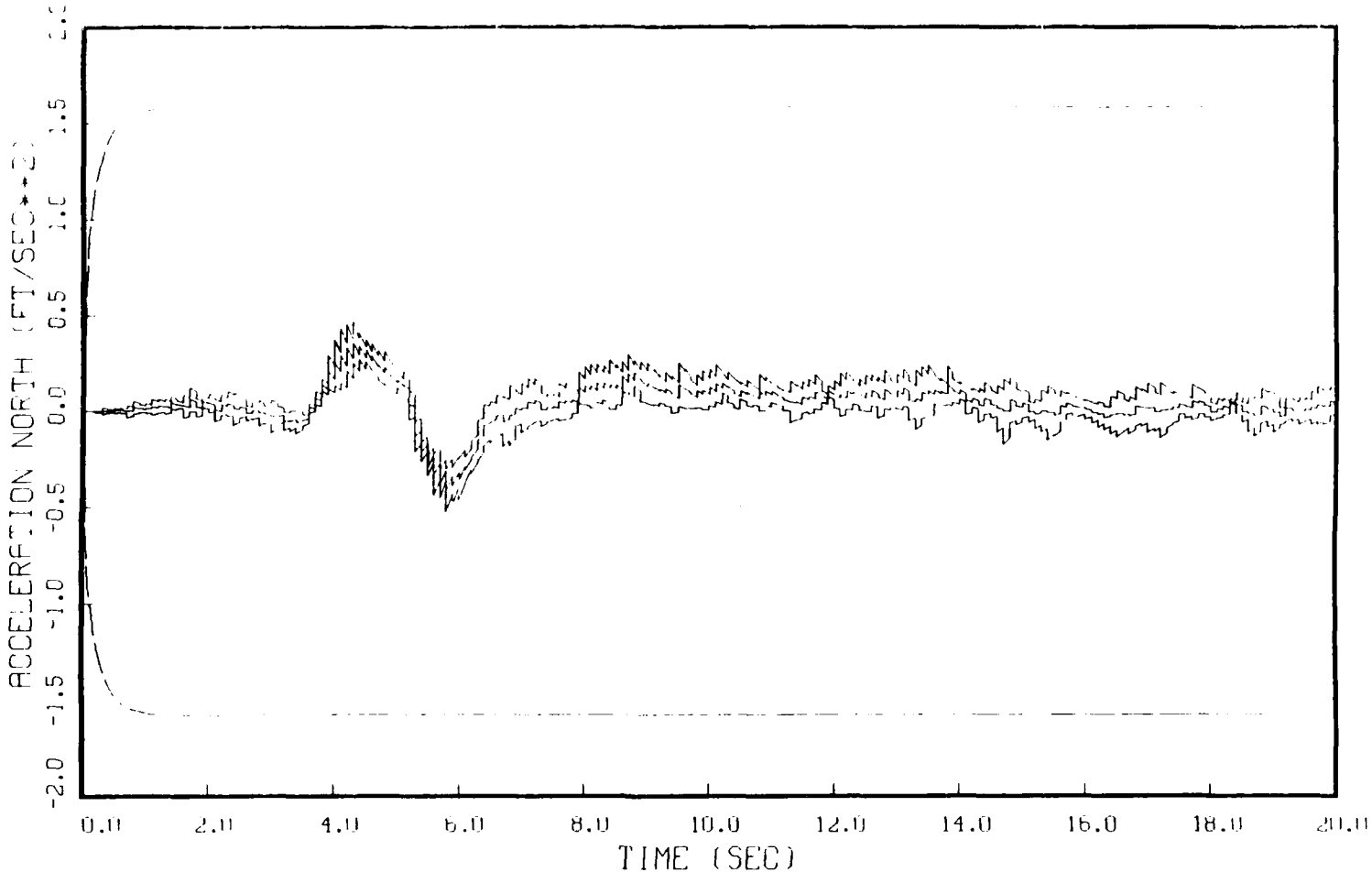

FIGURE F.21: GAUSS MARKOV MODEL, STATE 3, 5 RUNS
BEAM TRAJECTORY, 0-10, ANGLE RATE MEAS. INHIBITED (ORIGINAL R)

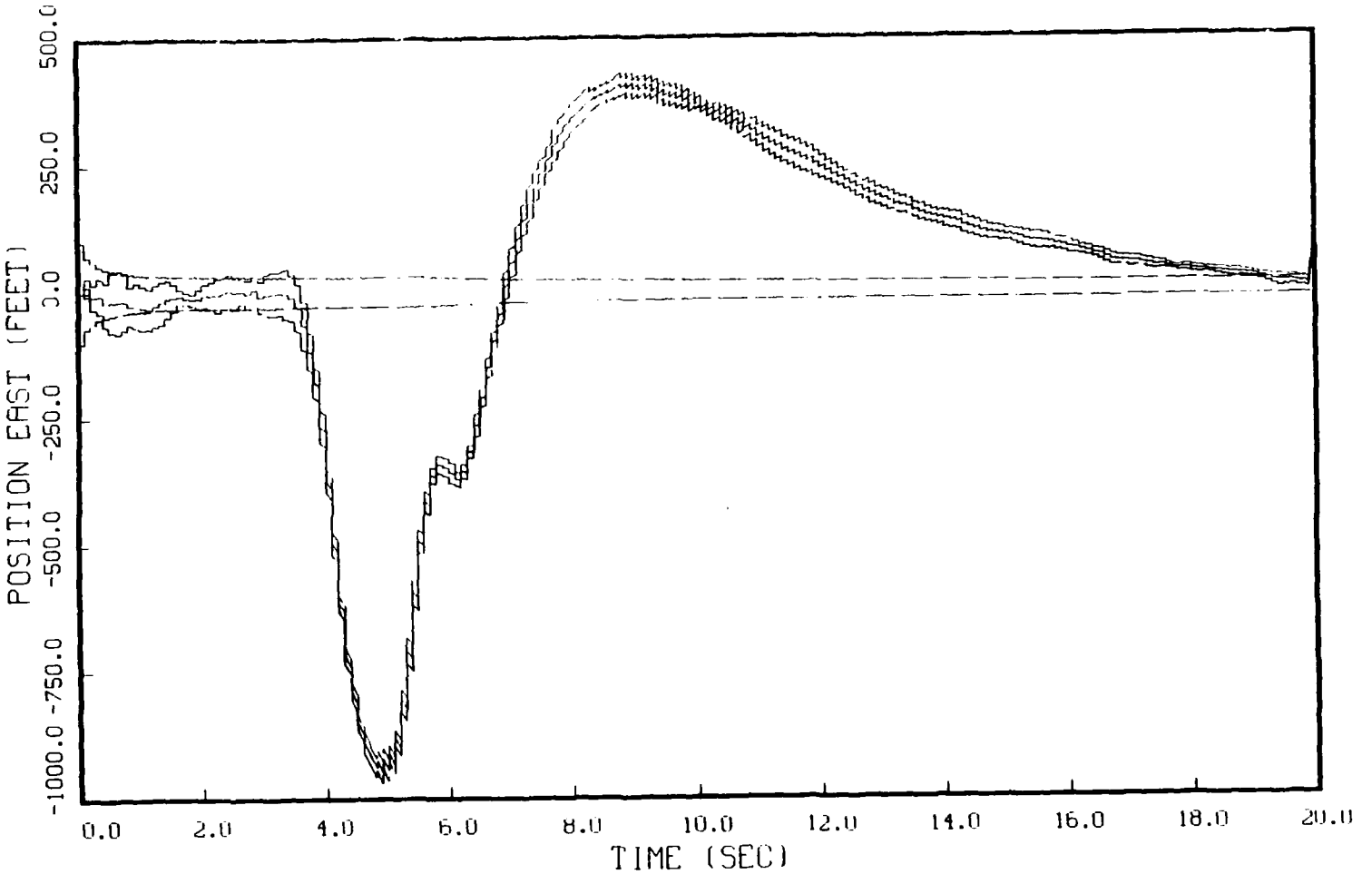

FIGURE F.22: GAUSS MARKOV MODEL, STATE 4, 5 RUNS
BEAM TRAJECTORY, 0-10, ANGLE RATE MEAS. INHIBITED (ORIGINAL R)

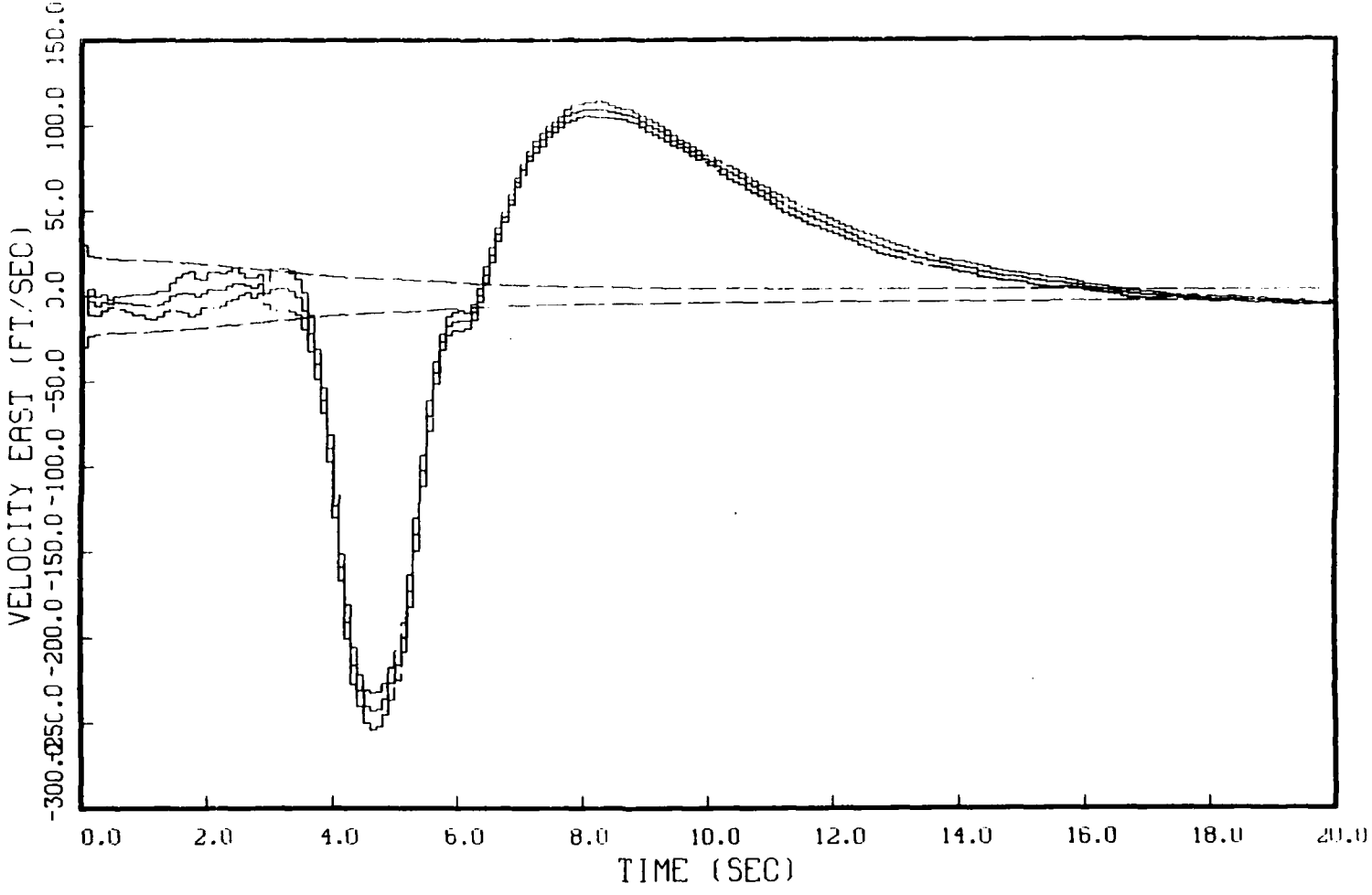

FIGURE F.23: GAUSS MARKOV MODEL, STATE 5, 5 RUNS
BEAM TRAJECTORY, 0-10, ANGLE RATE MEAS. INHIBITED (ORIGINAL R)

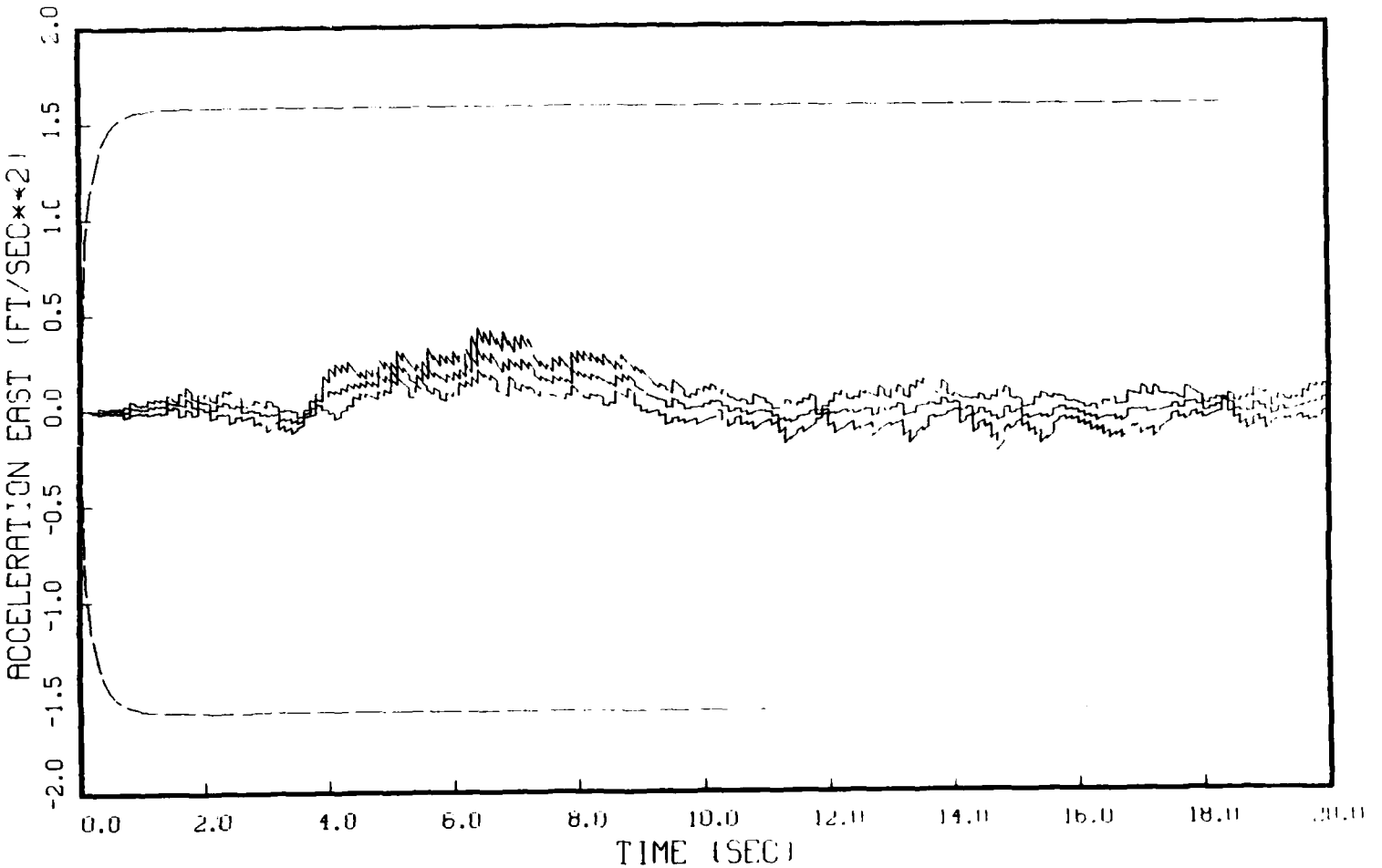

FIGURE F.24: GAUSS MARKOV MODEL, STATE 6, 5 RUNS
BEAM TRAJECTORY, 0-10, ANGLE RATE MEAS. INHIBITED (ORIGINAL R)

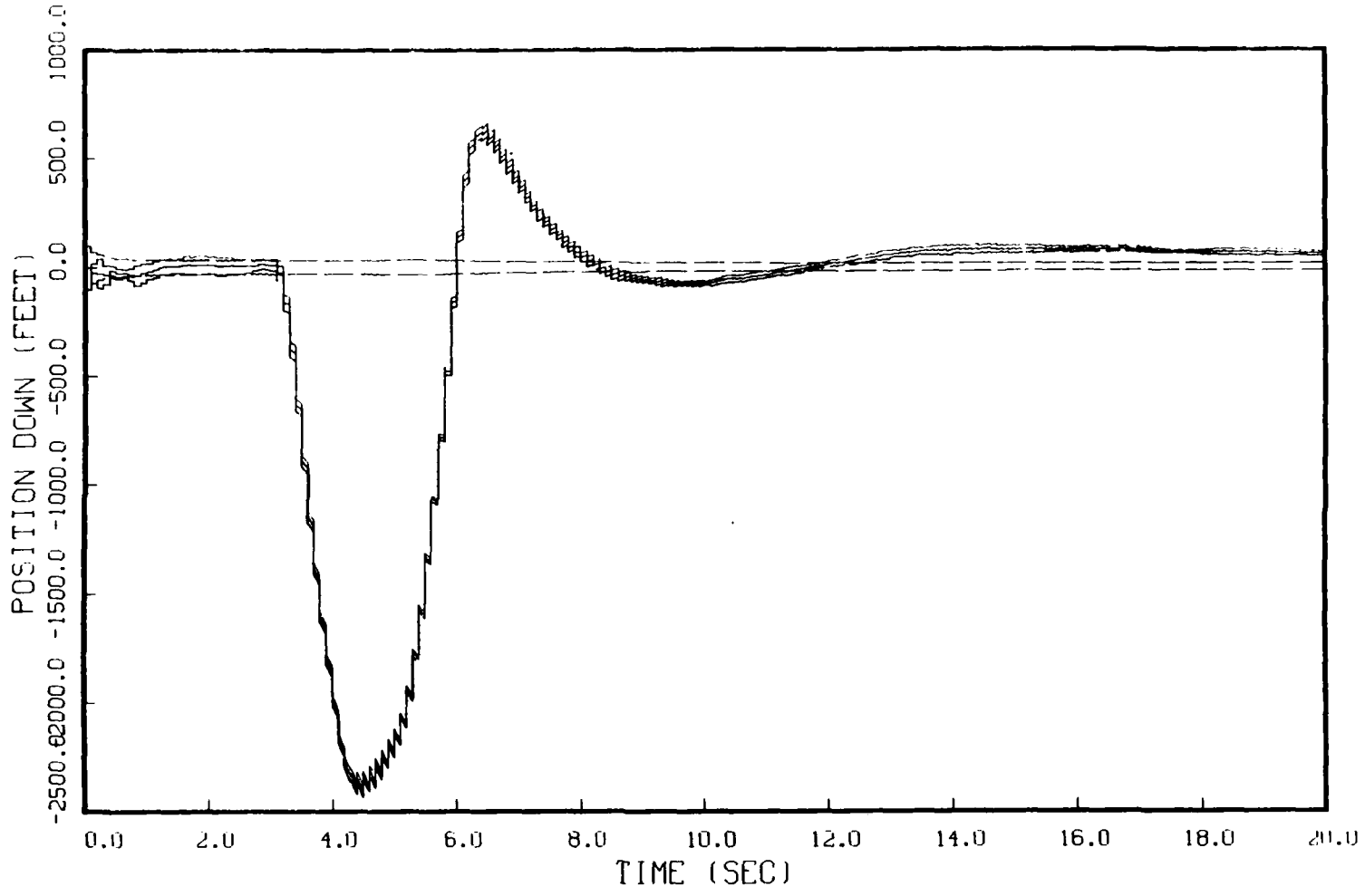

FIGURE F.25: GAUSS MARKOV MODEL, STATE 7, 5 RUNS
BEAM TRAJECTORY, 0-10, ANGLE RATE MEAS. INHIBITED (ORIGINAL R)

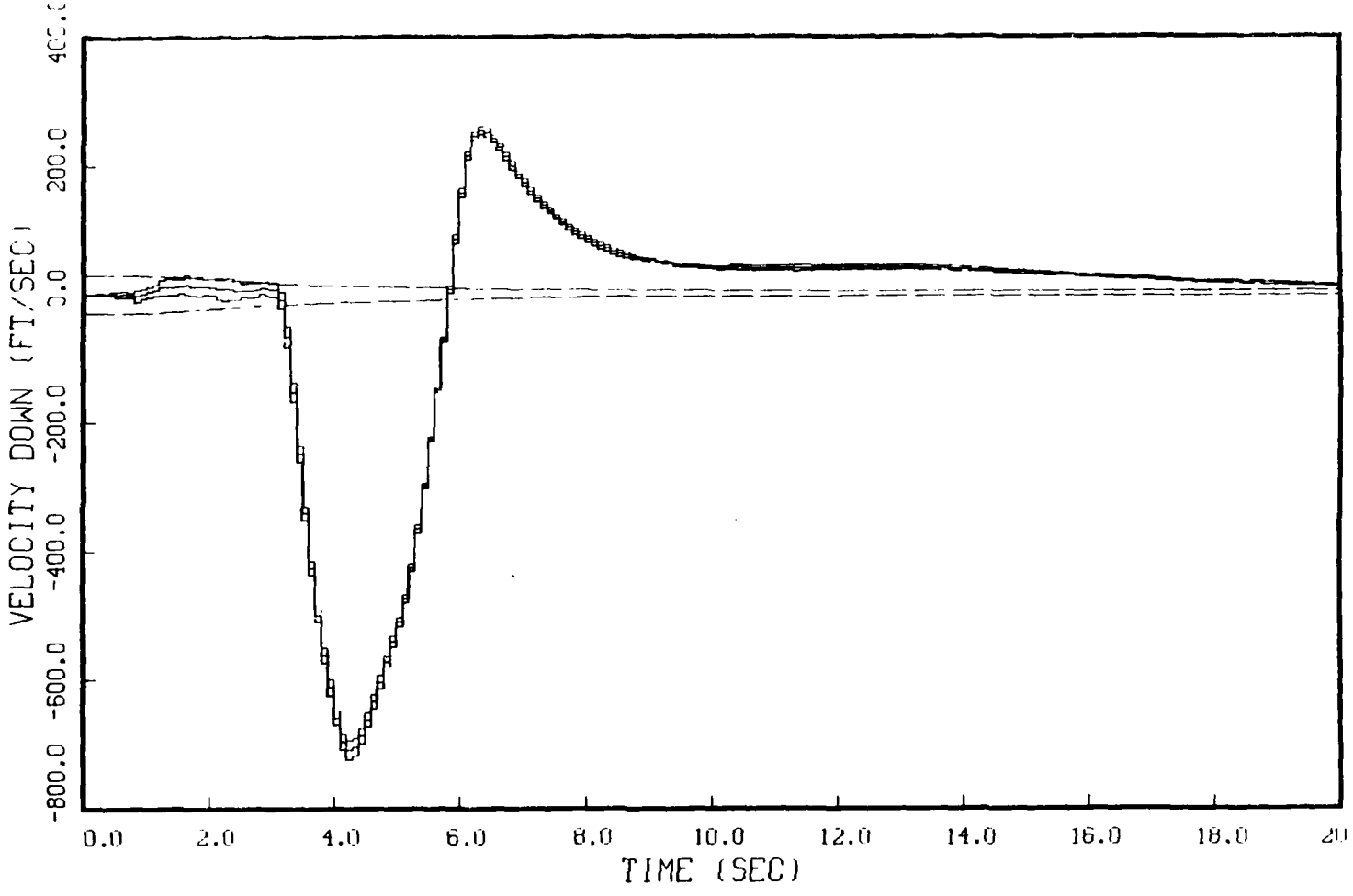

FIGURE F.26: GAUSS MARKOV MODEL, STATE 8, 5 RUNS
BEAM TRAJECTORY, 0-10, ANGLE RATE MEAS. INHIBITED (ORIGINAL R)

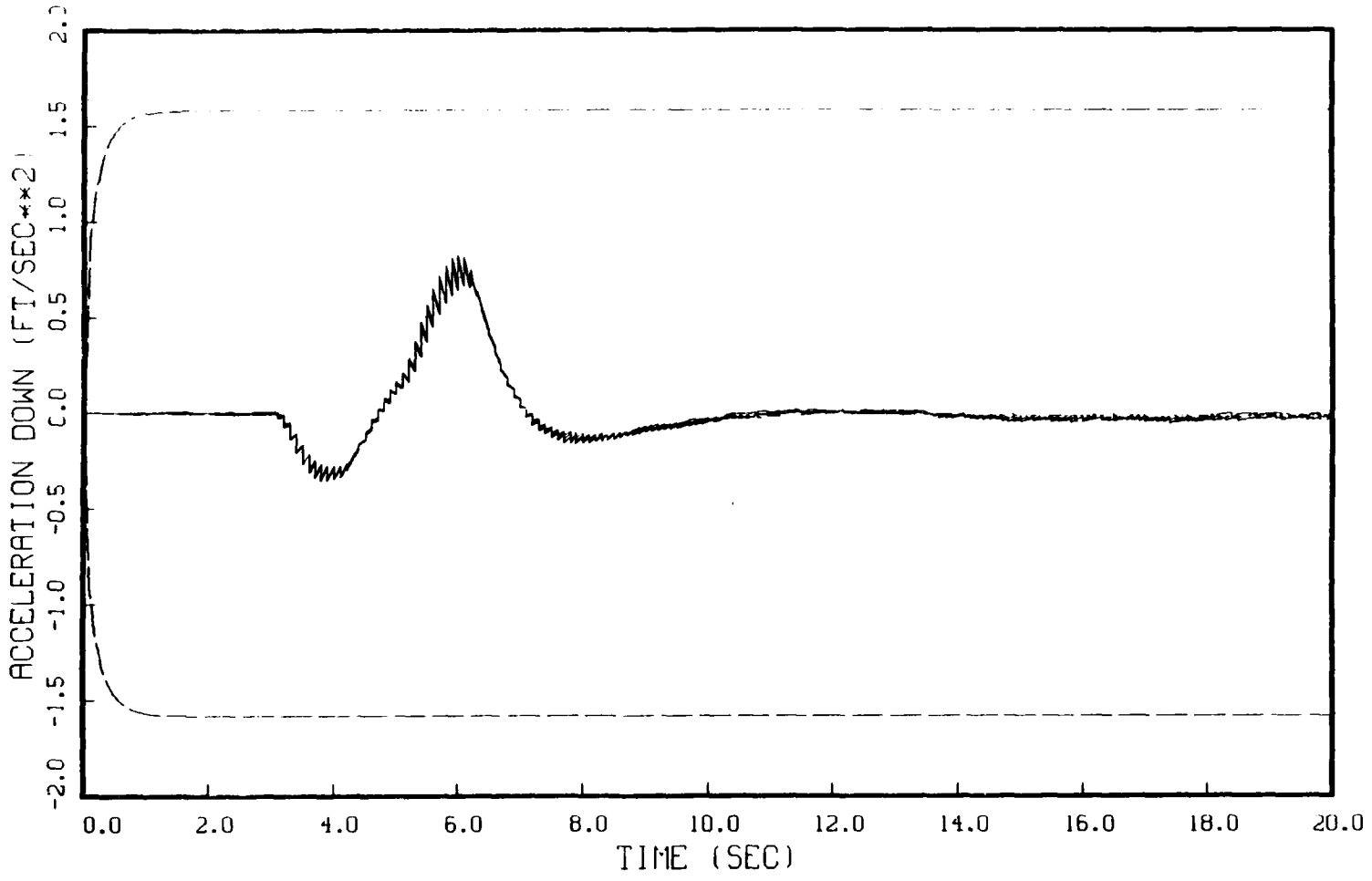

FIGURE F.27: GAUSS MARKOV MODEL, STATE 9, 5 RUNS
BEAM TRAJECTORY, Q-10, ANGLE RATE MEAS. INHIBITED (ORIGINAL R)

Appendix G

Error Budget Studies

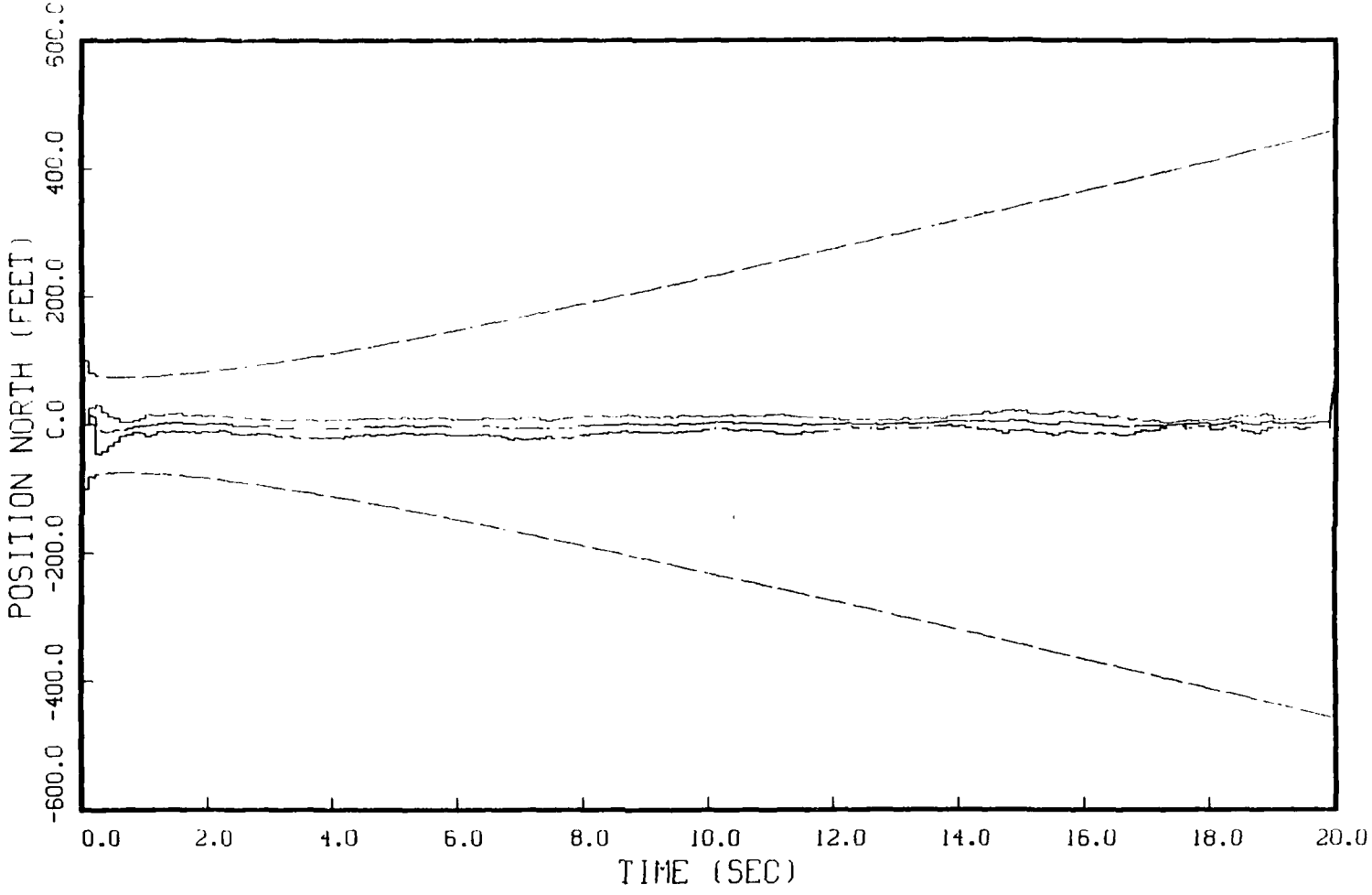

FIGURE G.1: GAUSS MARKOV MODEL, STATE 1, 5 RUNS
BEAM TRAJECTORY, 0-100, 2 MEAS: RNG & RNG RATE (ORIGINAL R)

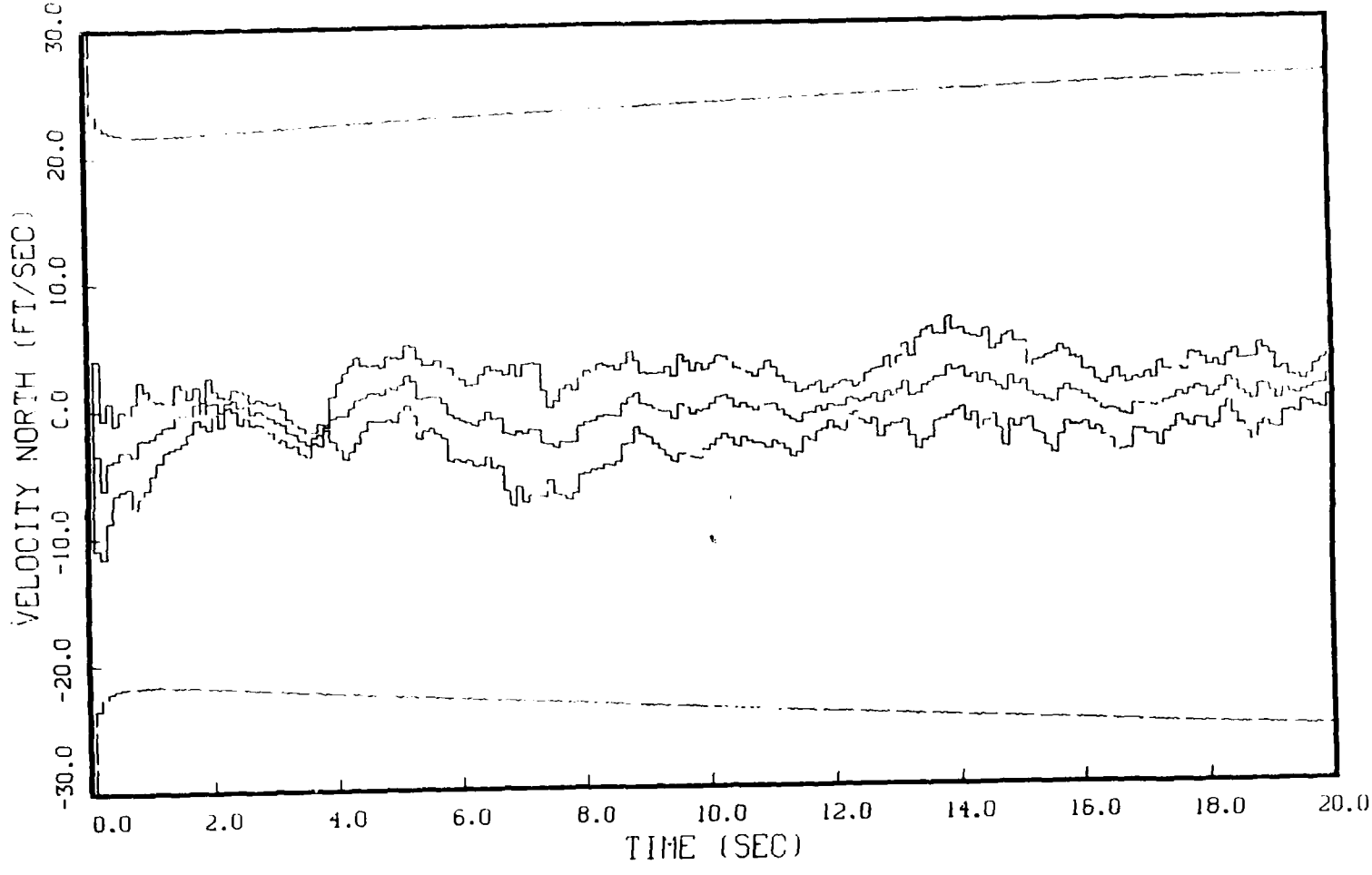

FIGURE 6.2: GAUSS MARKOV MODEL, STATE 2, 5 RUNS
BEAM TRAJECTORY, 0-100, 2 MEAS: RNG & RNG RATE (ORIGINAL R)

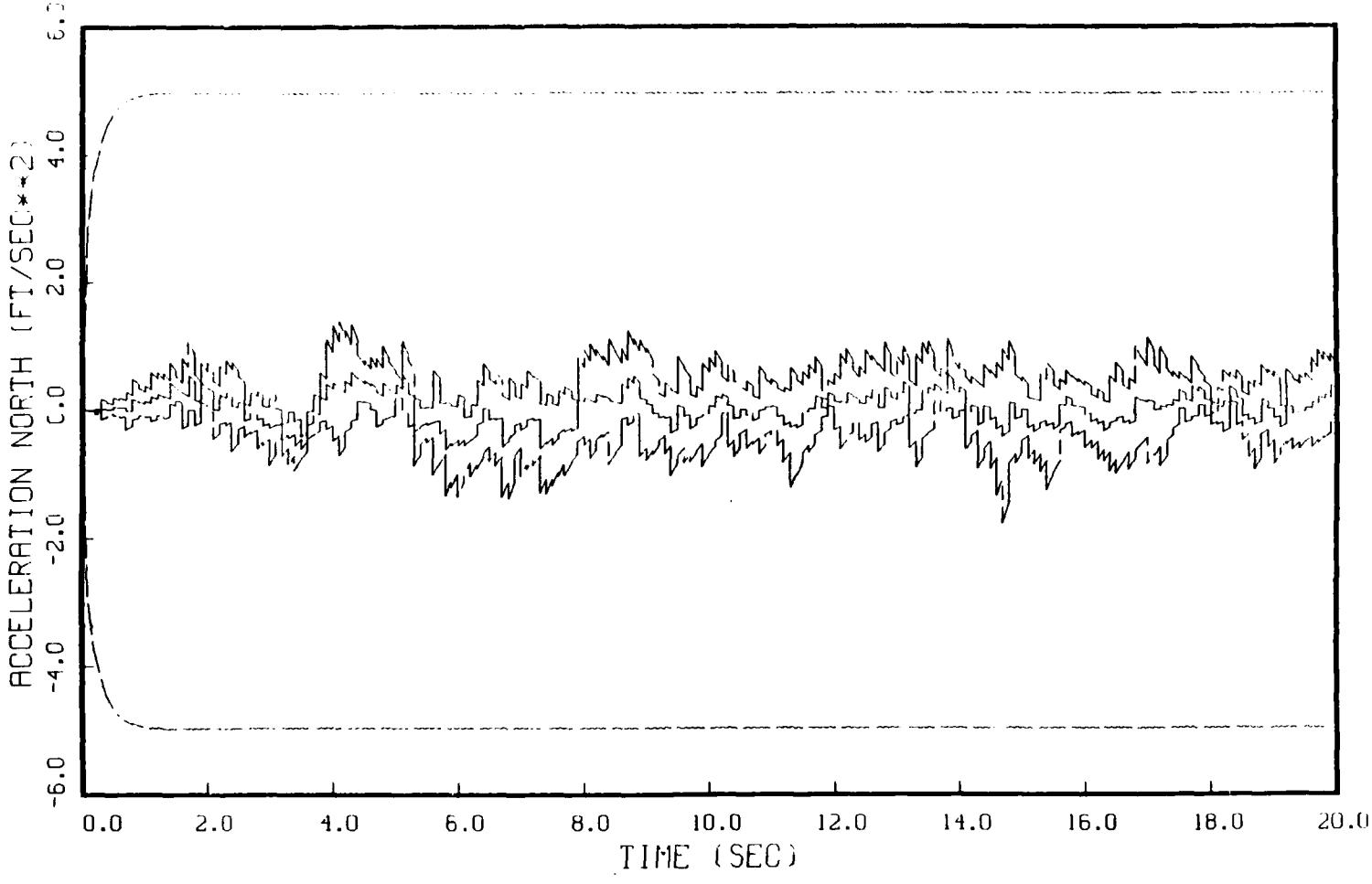

FIGURE 6.3: GAUSS MARKOV MODEL, STATE 3, 5 RUNS
BEAM TRAJECTORY, 0-100, 2 MEAS: RNG & RNG RATE (ORIGINAL R)

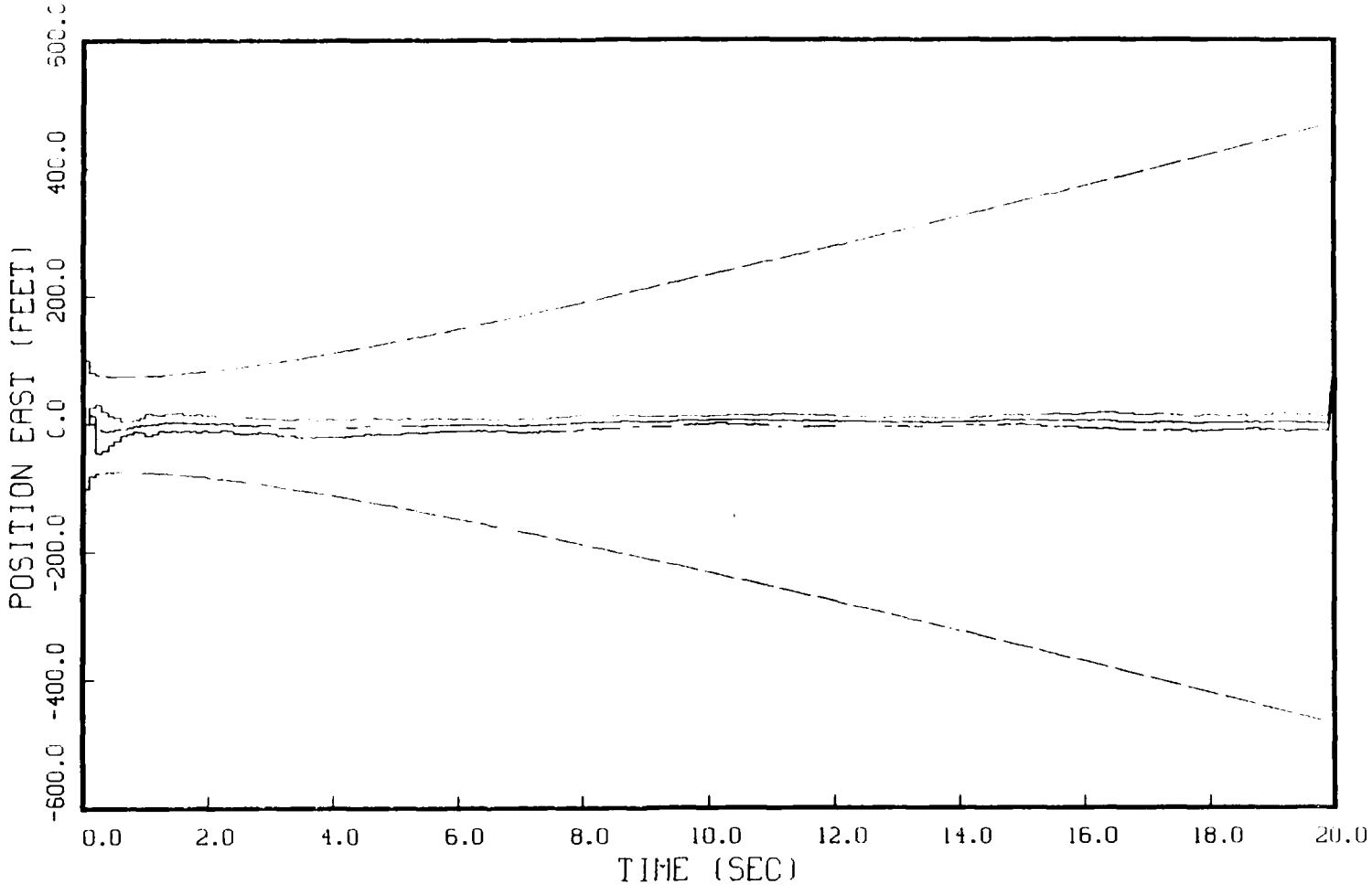

FIGURE G.4: GAUSS MARKOV MODEL, STATE 4, 5 RUNS
BEAM TRAJECTORY, 0-100, 2 MEAS: RNG & RNG RATE (ORIGINAL R)

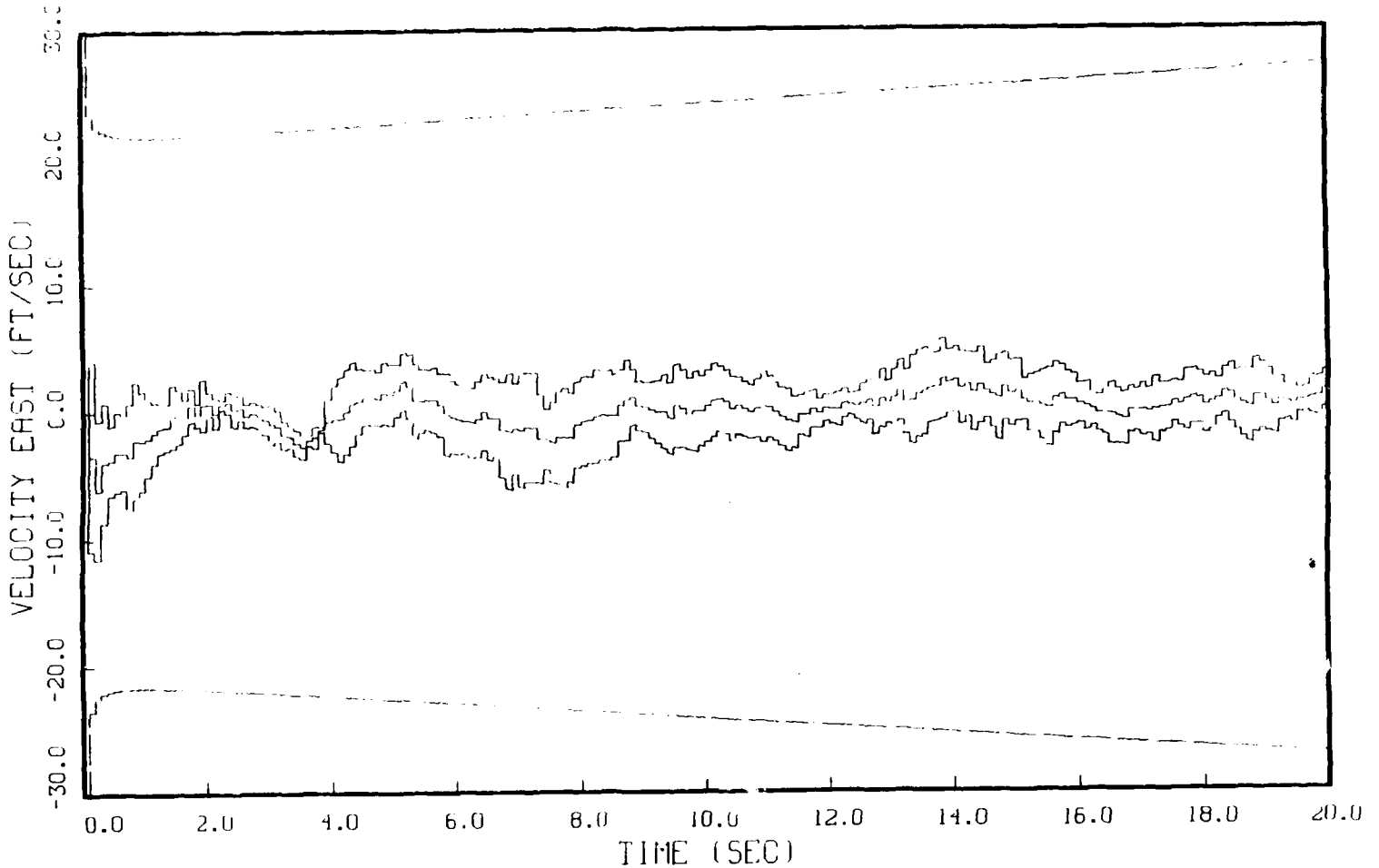

FIGURE 6.5: GAUSS MARKOV MODEL, STATE 5, 5 RUNS
BEAM TRAJECTORY, 0-100, 2 MEAS: RNG & RNG RATE (ORIGINAL R)

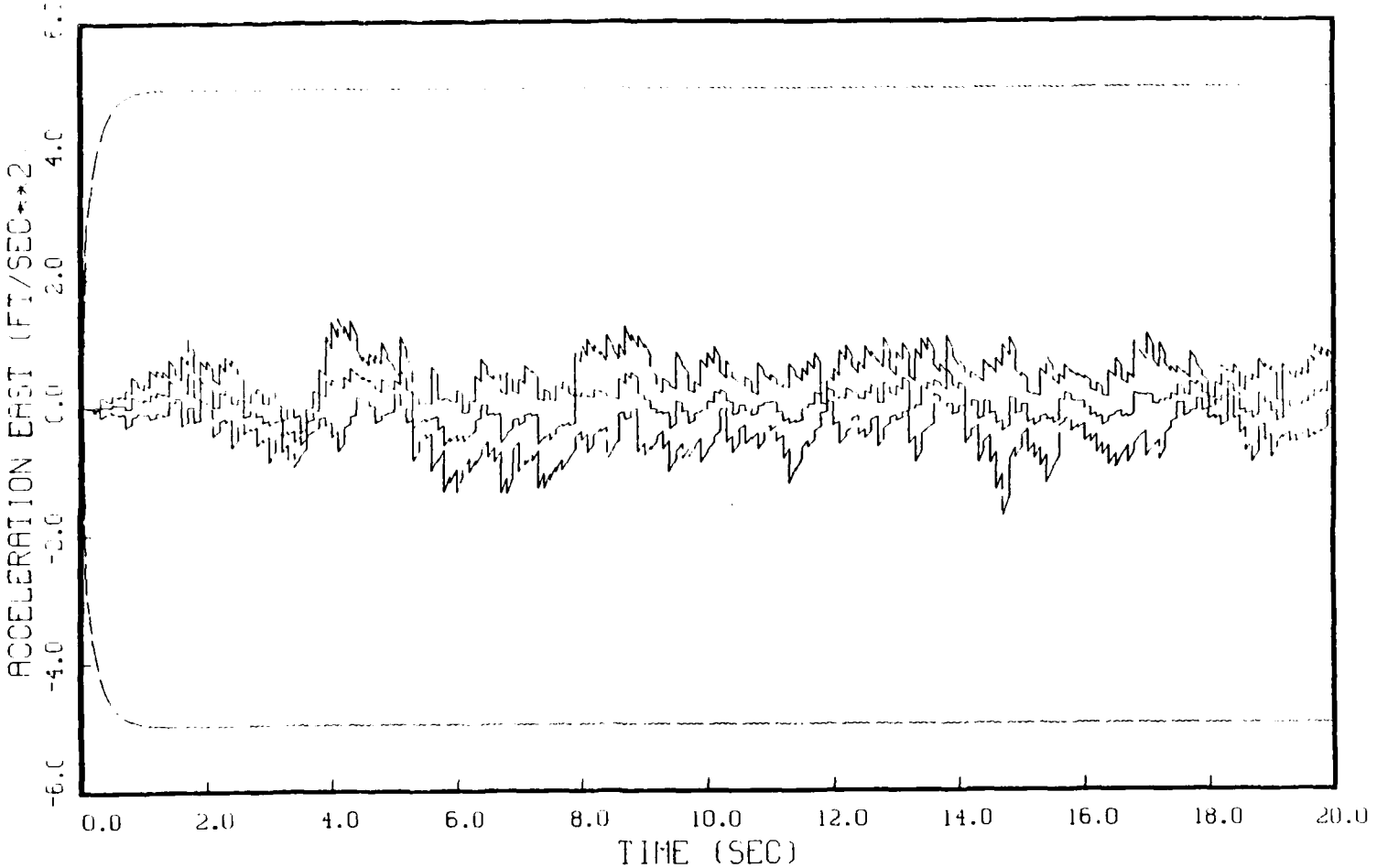

FIGURE G.6: GAUSS MARKOV MODEL, STATE 6, 5 RUNS
BEAM TRAJECTORY, 0-100, 2 MEAS: RNG & RNG RATE (ORIGINAL R)

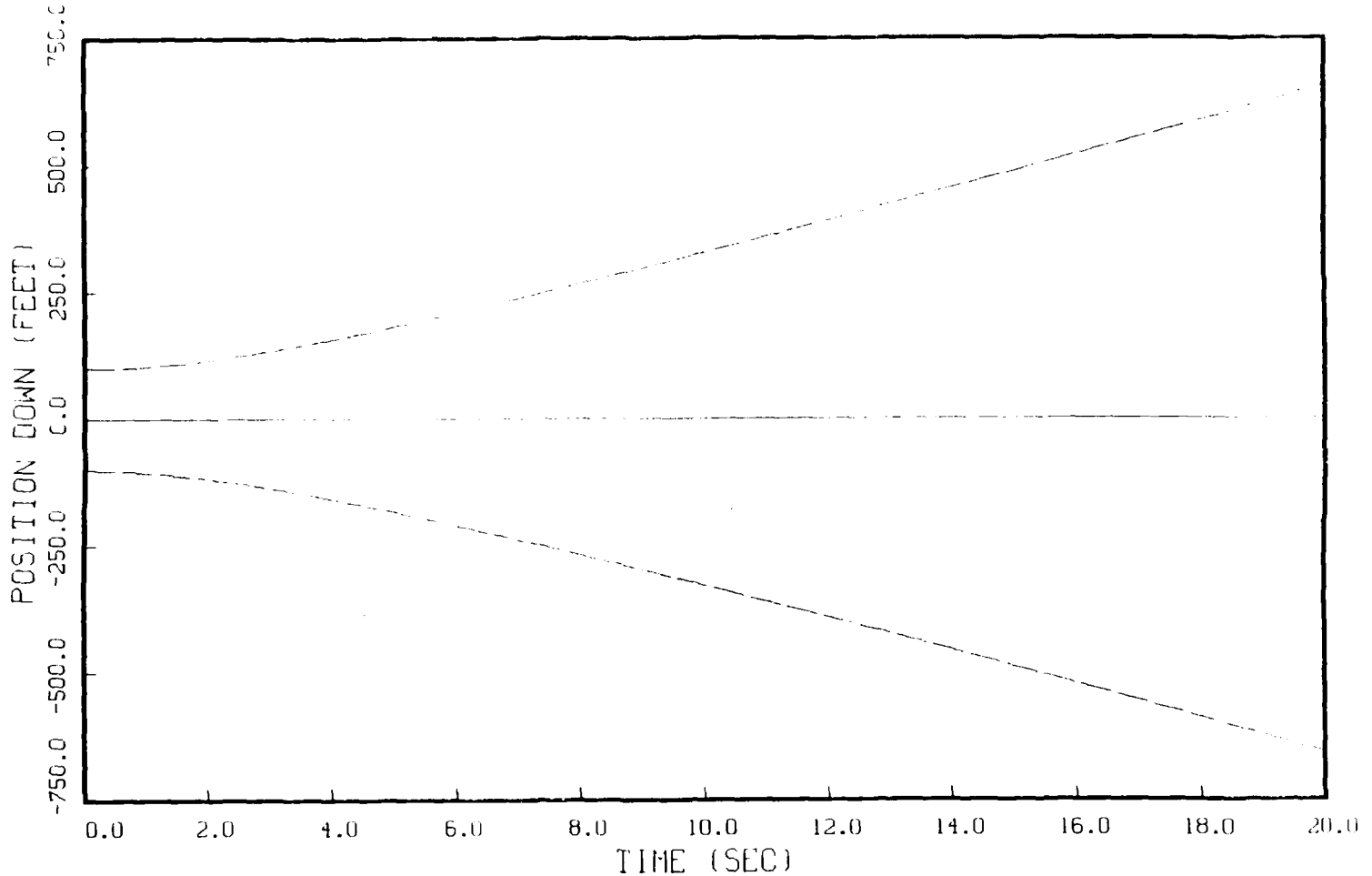

FIGURE 6.7: GAUSS MARKOV MODEL, STATE 7, 5 RUNS
BEAM TRAJECTORY, Q=100, 2 MEAS: RNG & RNG RATE (ORIGINAL R)

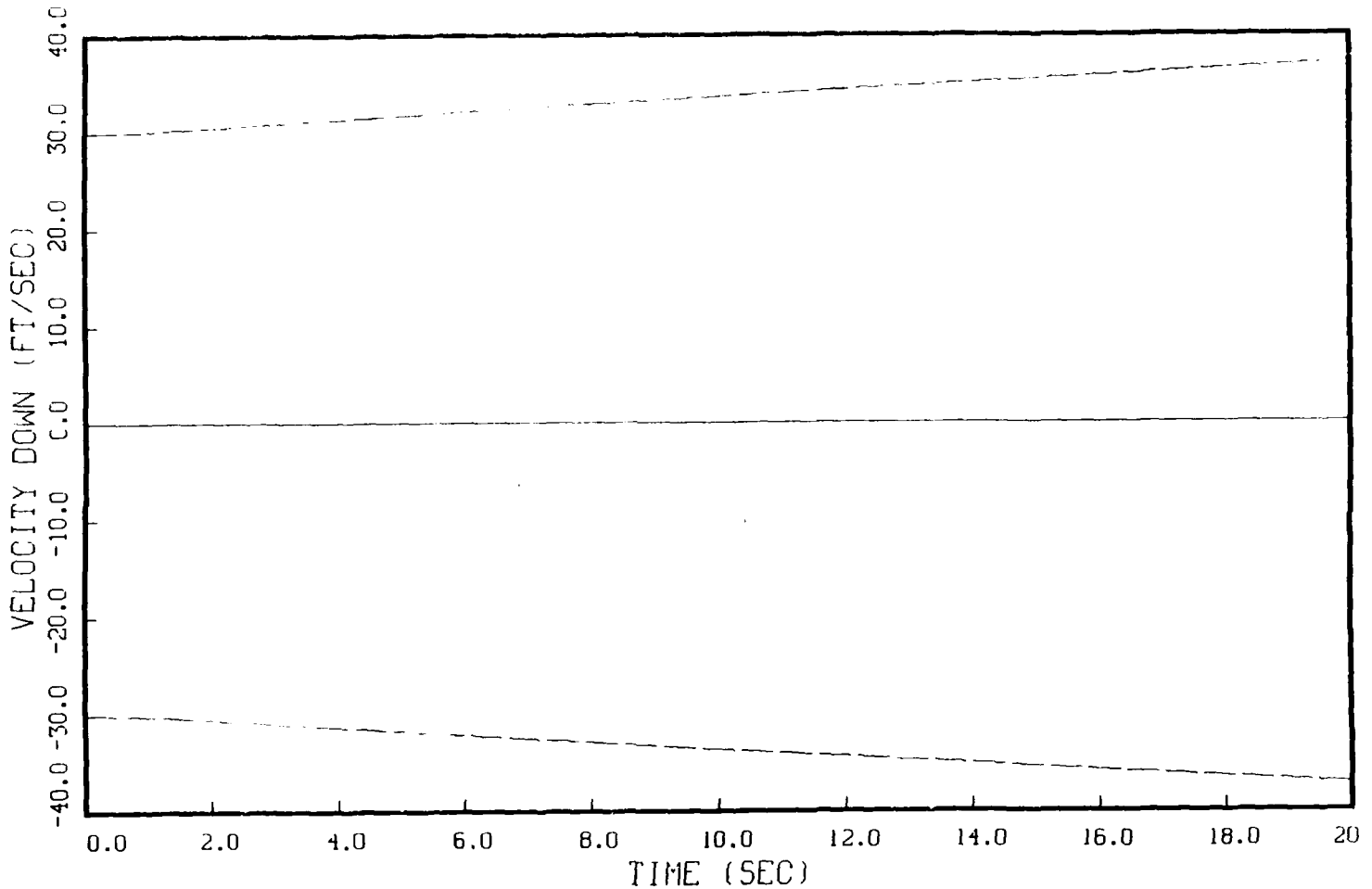

FIGURE 6.8: GAUSS MARKOV MODEL, STATE 8, 5 RUNS
BEAM TRAJECTORY, 0-100, 2 MEAS: RNG & RNG RATE (ORIGINAL R)

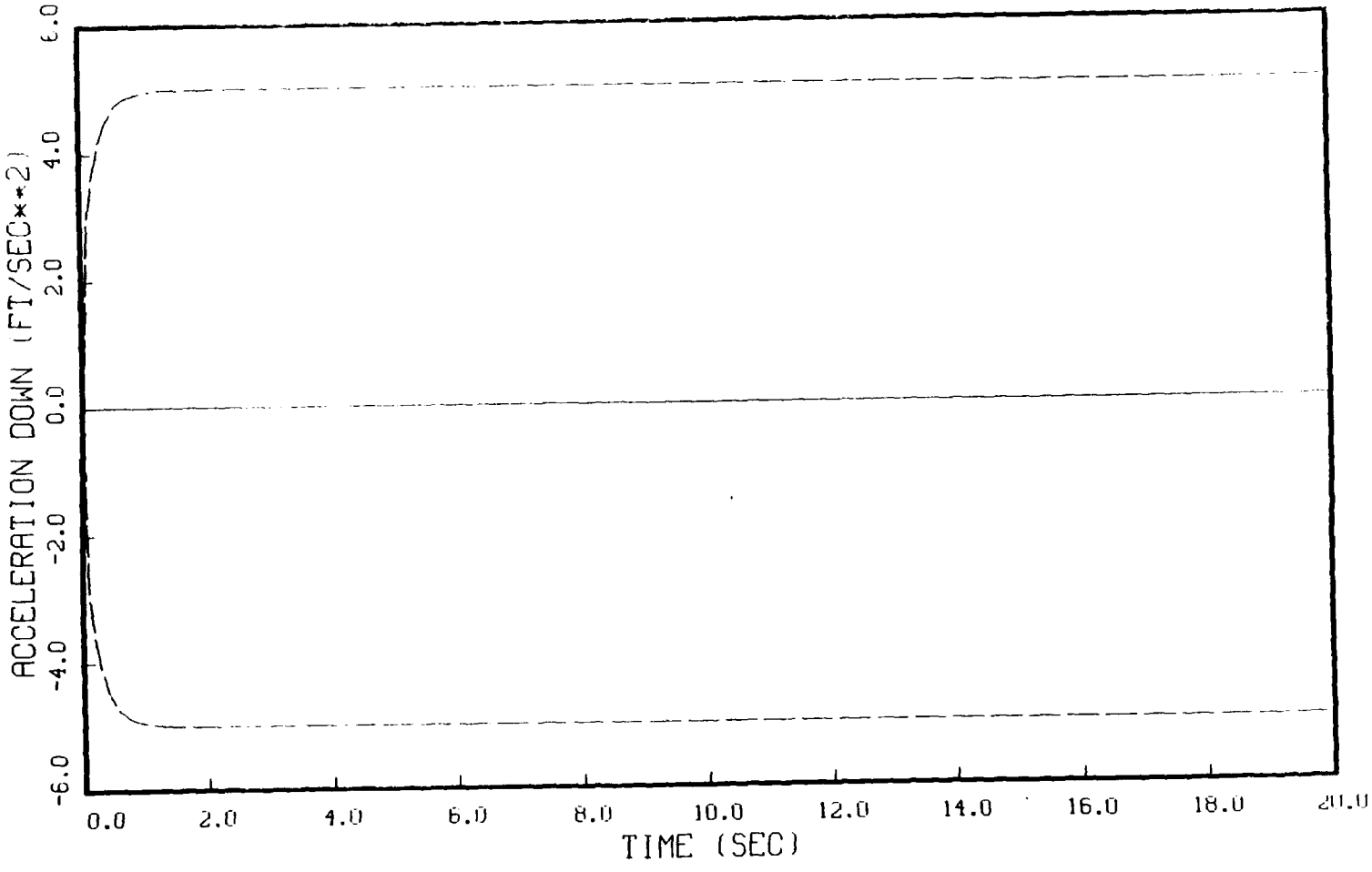

FIGURE 6.9: GAUSS MARKOV MODEL, STATE 9, 5 RUNS
BEAM TRAJECTORY, 0-100, 2 MEAS: RNG & RNG RATE (ORIGINAL R)

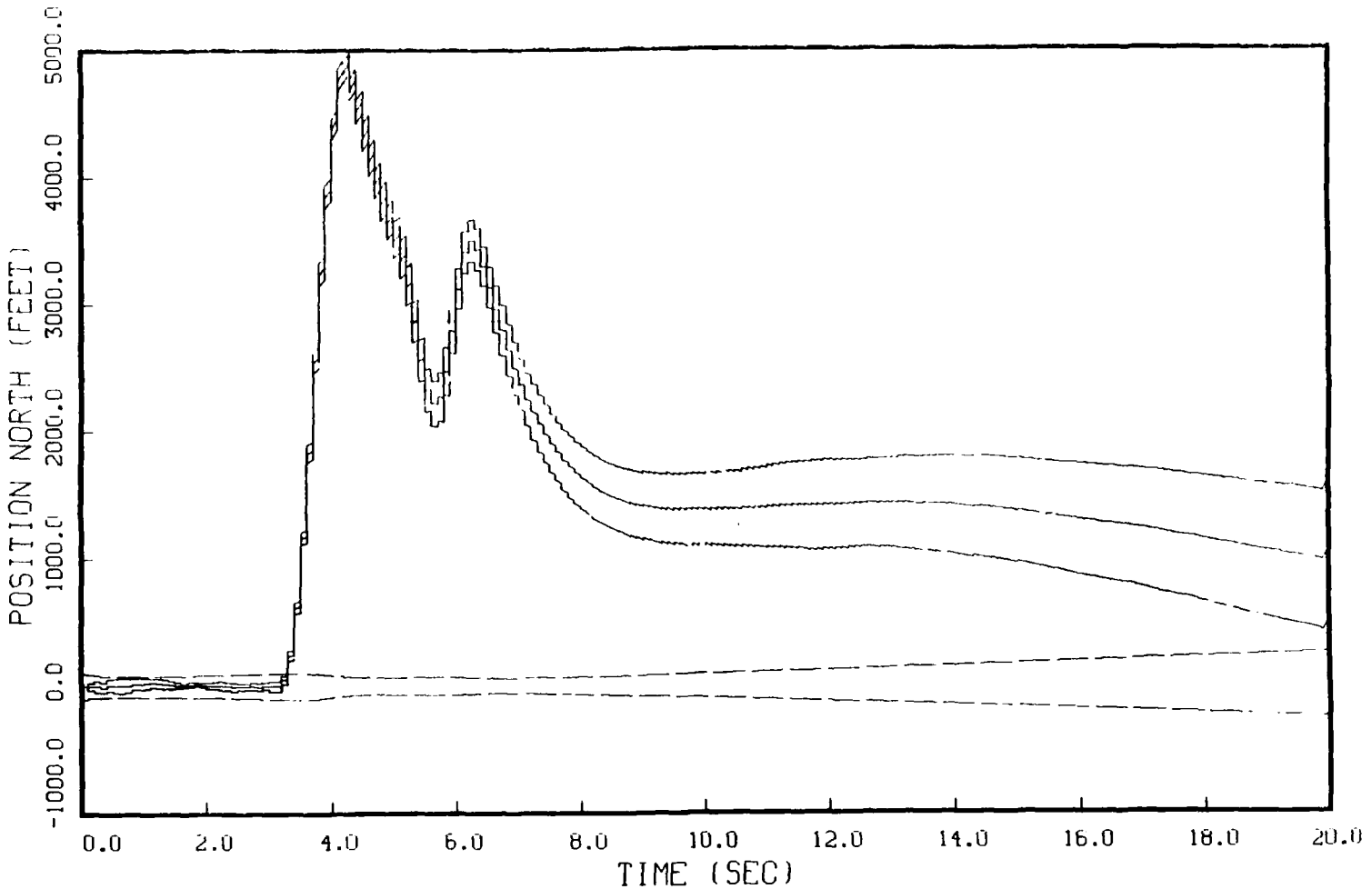

FIGURE 6.10: GAUSS MARKOV MODEL, STATE 1, 5 RUNS
BEAM TRAJECTORY, 0-100, 2 MEAS: SIN AZ & SIN EL (ORIGINAL R)

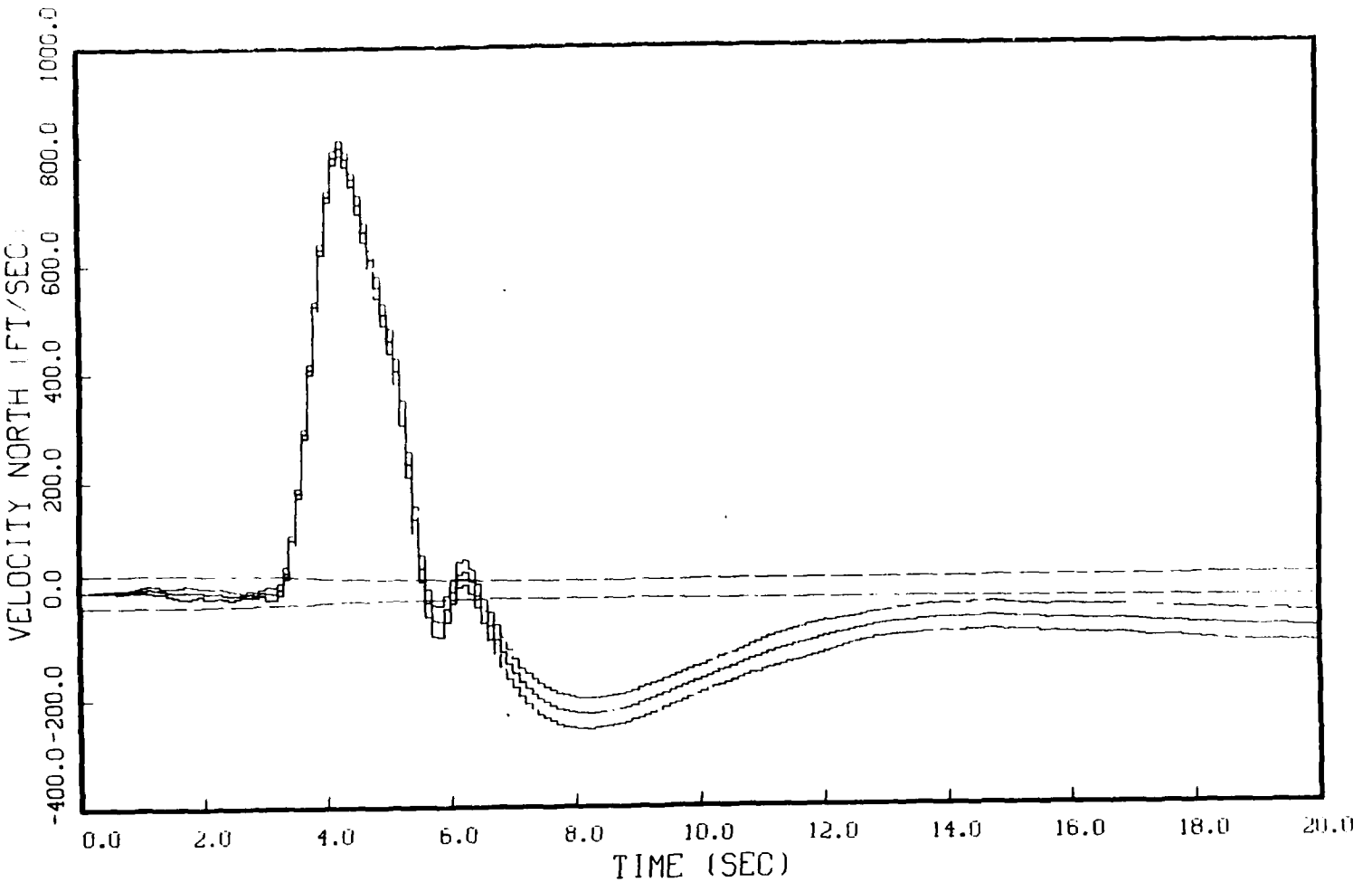

FIGURE 6.11: GAUSS MARKOV MODEL, STATE 2, 5 RUNS
BEAM TRAJECTORY, 0-100, 2 MEAS: SIN AZ & SIN EL (ORIGINAL R)

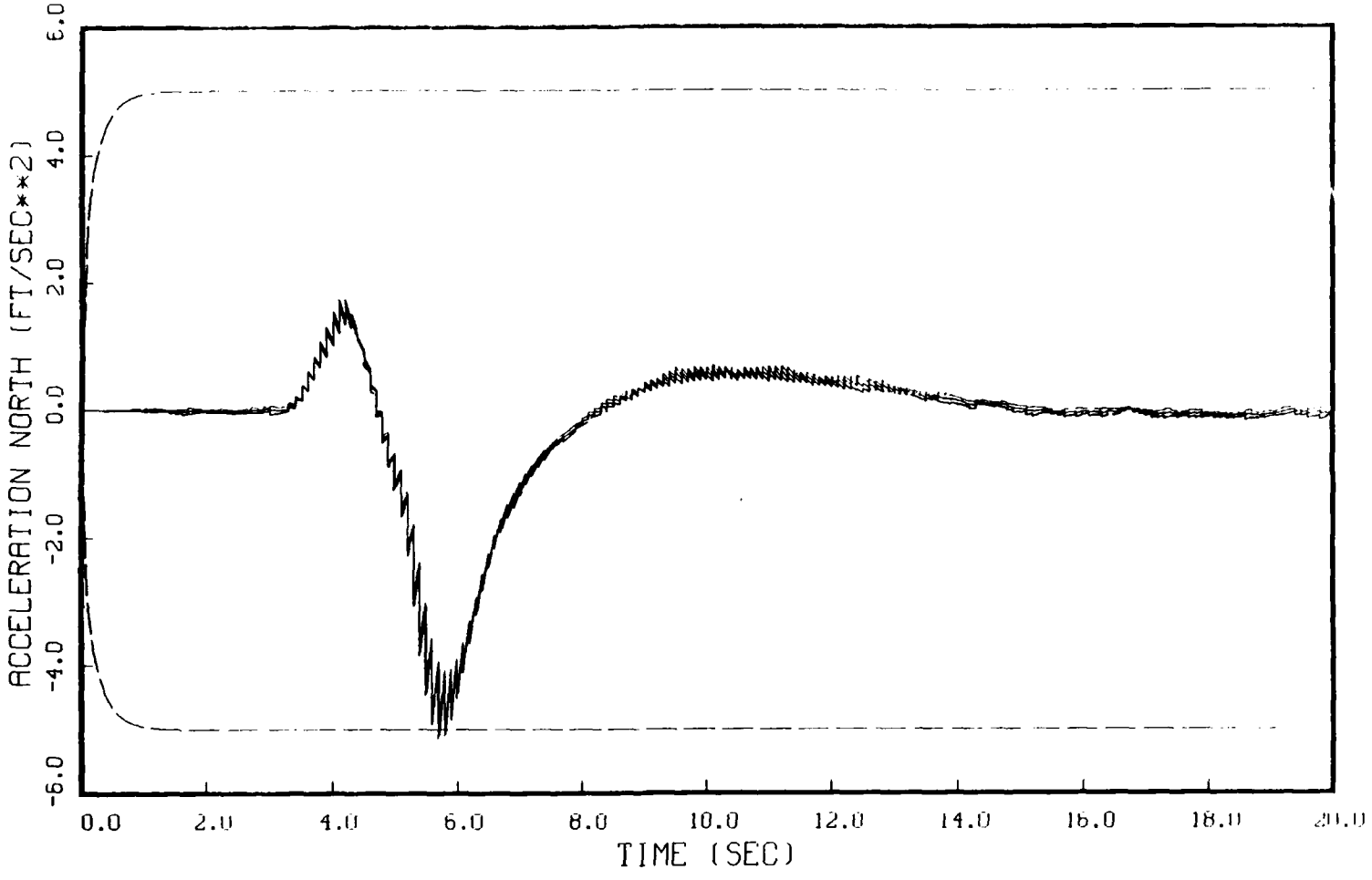

FIGURE 6.12: GAUSS MARKOV MODEL, STATE 3, 5 RUNS
BEAM TRAJECTORY, 0-100, 2 MEAS: SIN AZ & SIN EL (ORIGINAL R)

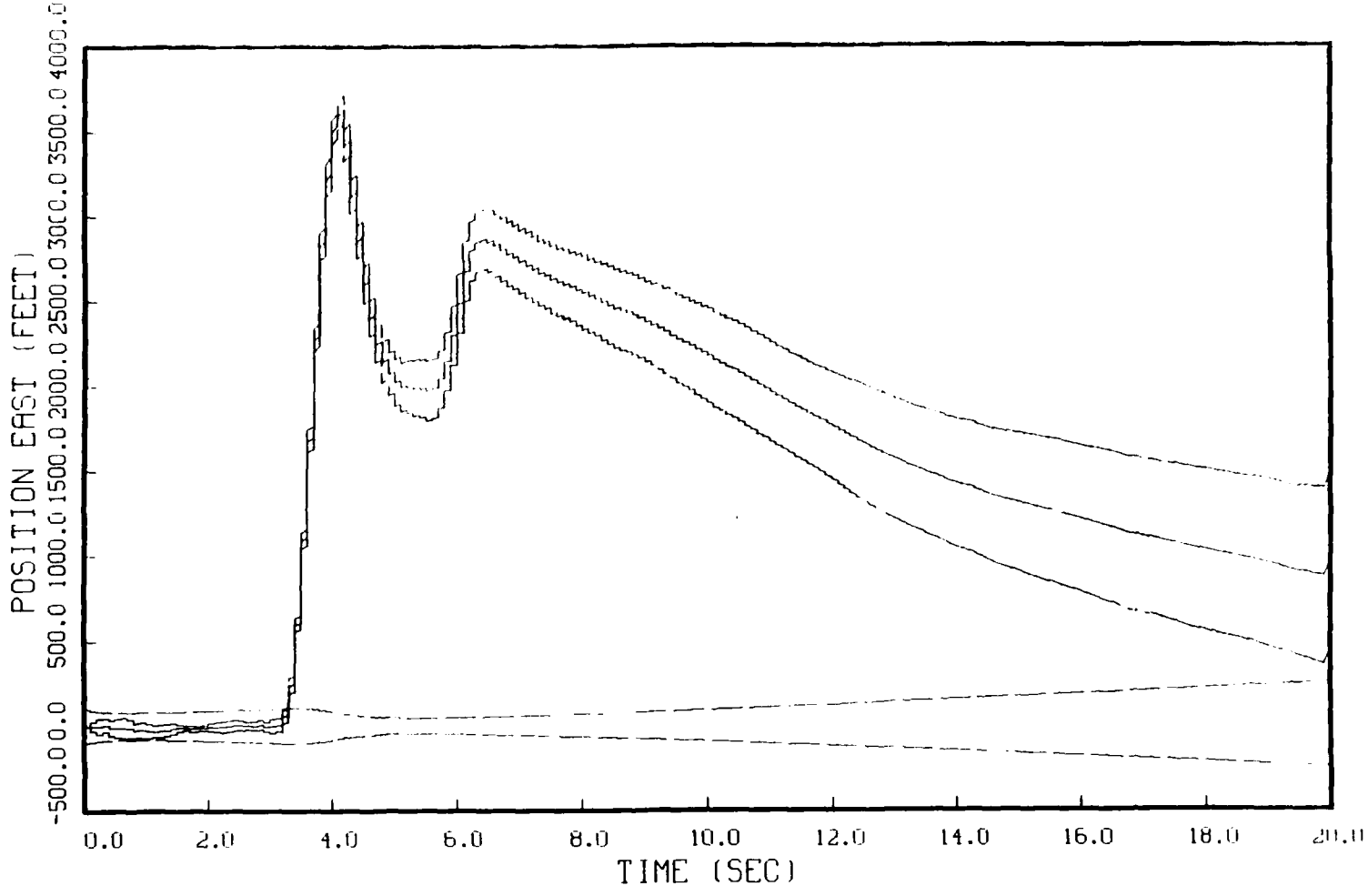

FIGURE 6.13: GAUSS MARKOV MODEL, STATE 4, 5 RUNS
BEAM TRAJECTORY, Q=100, 2 MEAS: SIN AZ & SIN EL (ORIGINAL R)

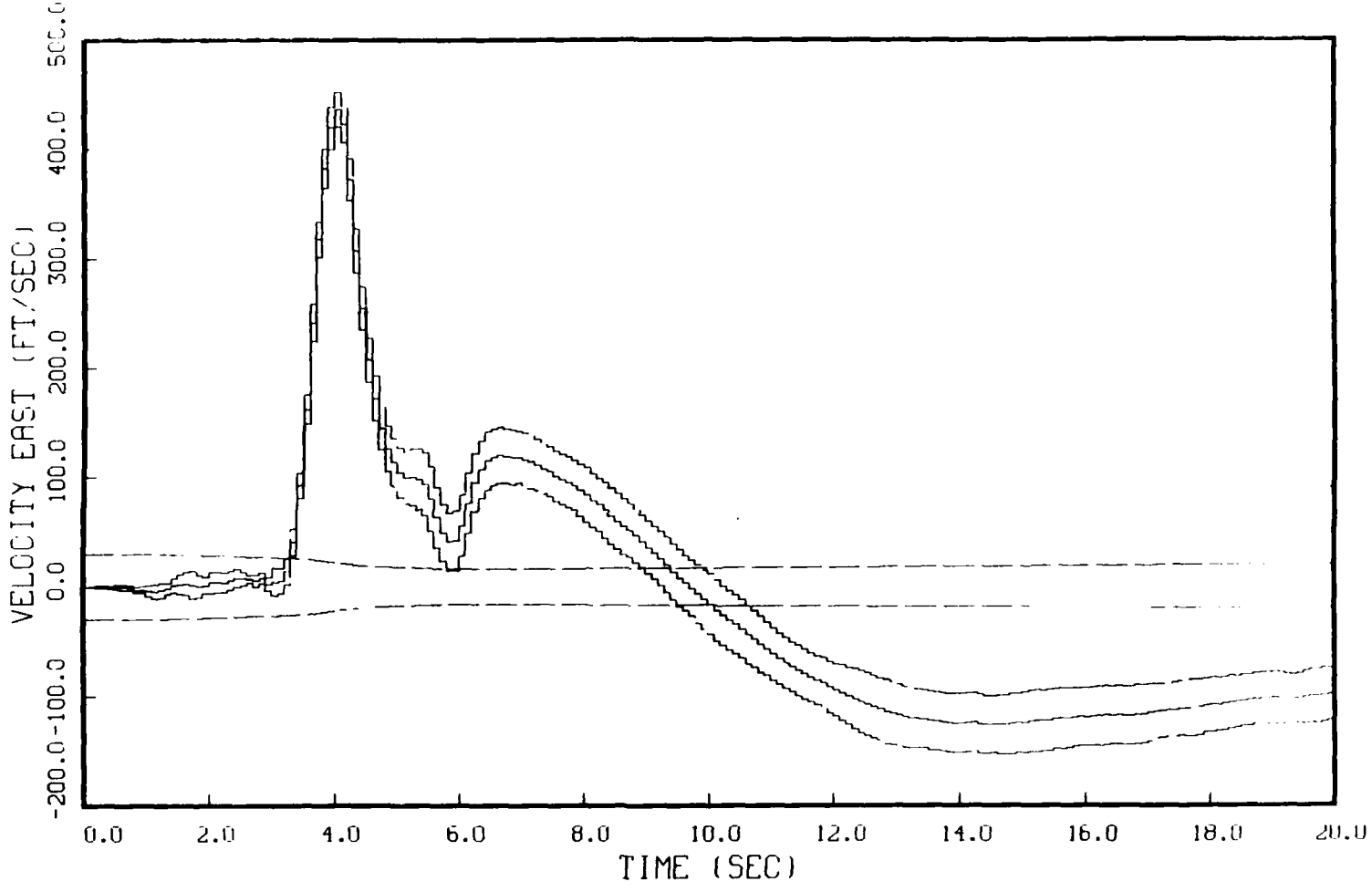

FIGURE 6.14: GAUSS MARKOV MODEL, STATE 5, 5 RUNS
BEAM TRAJECTORY, 0-100, 2 MEAS: SIN AZ & SIN EL (ORIGINAL R)

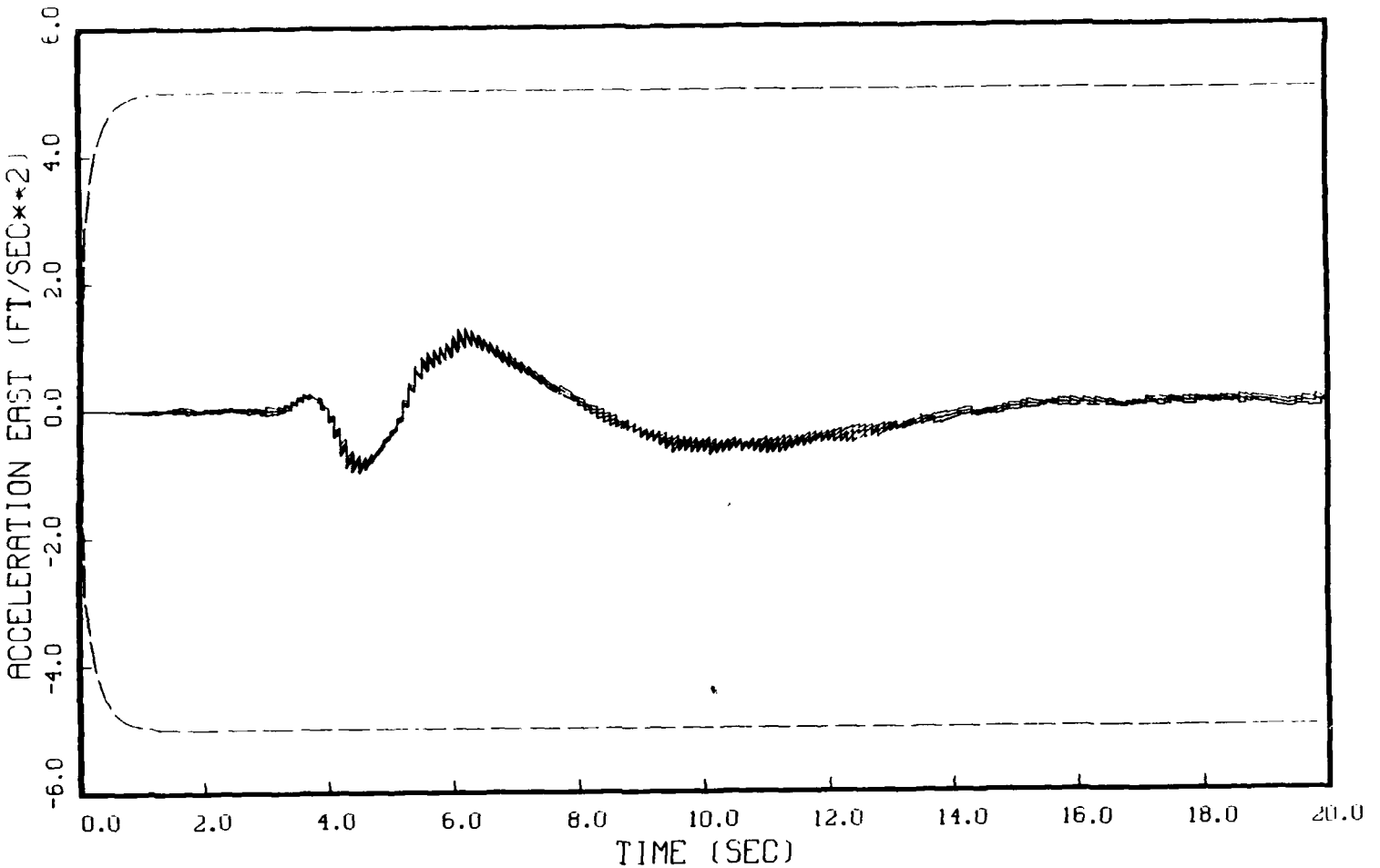

FIGURE 6.15: GAUSS MARKOV MODEL, STATE 6, 5 RUNS
BEAM TRAJECTORY, Q=100, 2 MEAS: SIN AZ & SIN EL (ORIGINAL R)

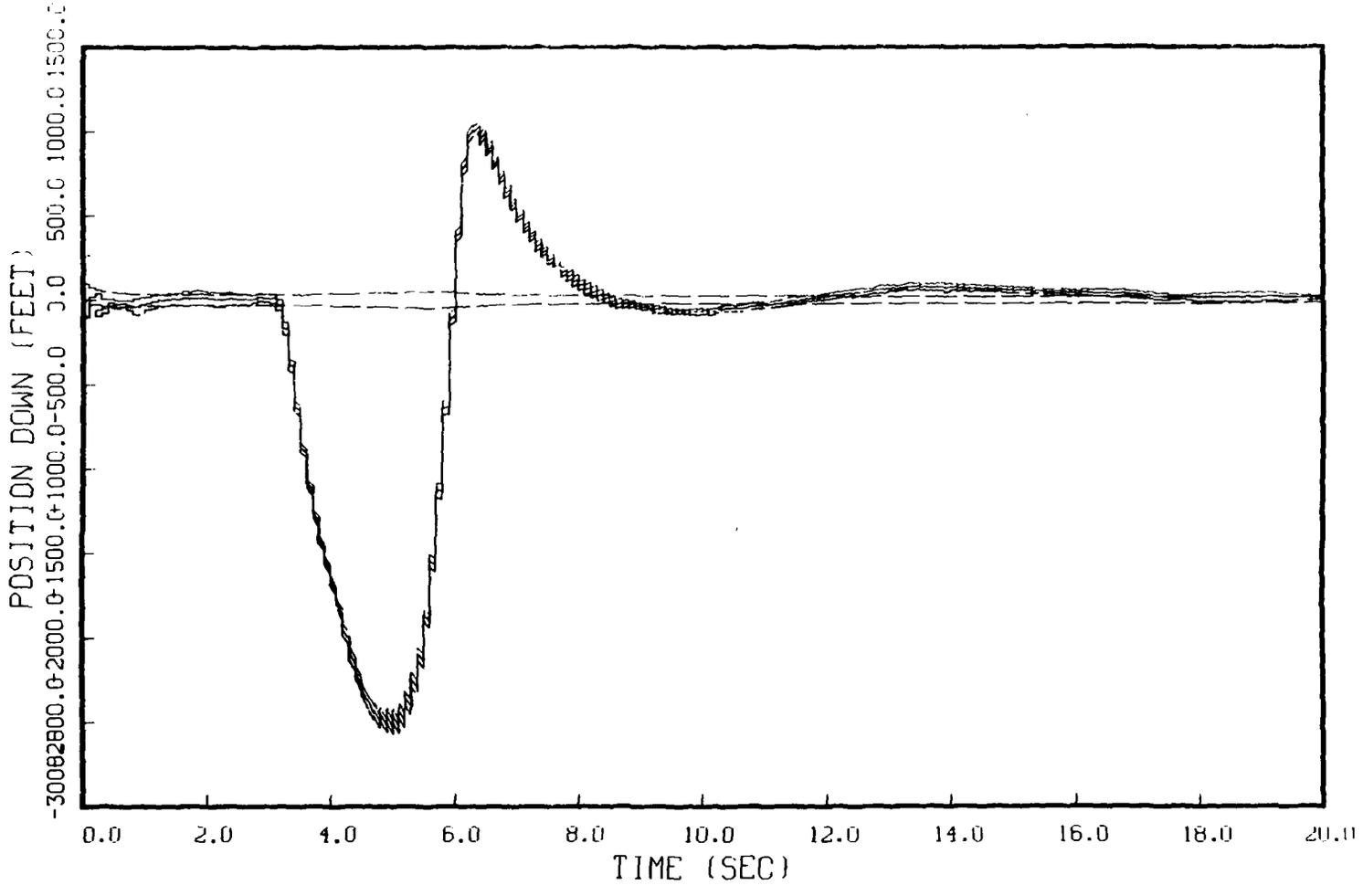

FIGURE 6.16: GAUSS MARKOV MODEL, STATE 7, 5 RUNS
BEAM TRAJECTORY, 0-100, 2 MEAS: SIN AZ & SIN EL (ORIGINAL R)

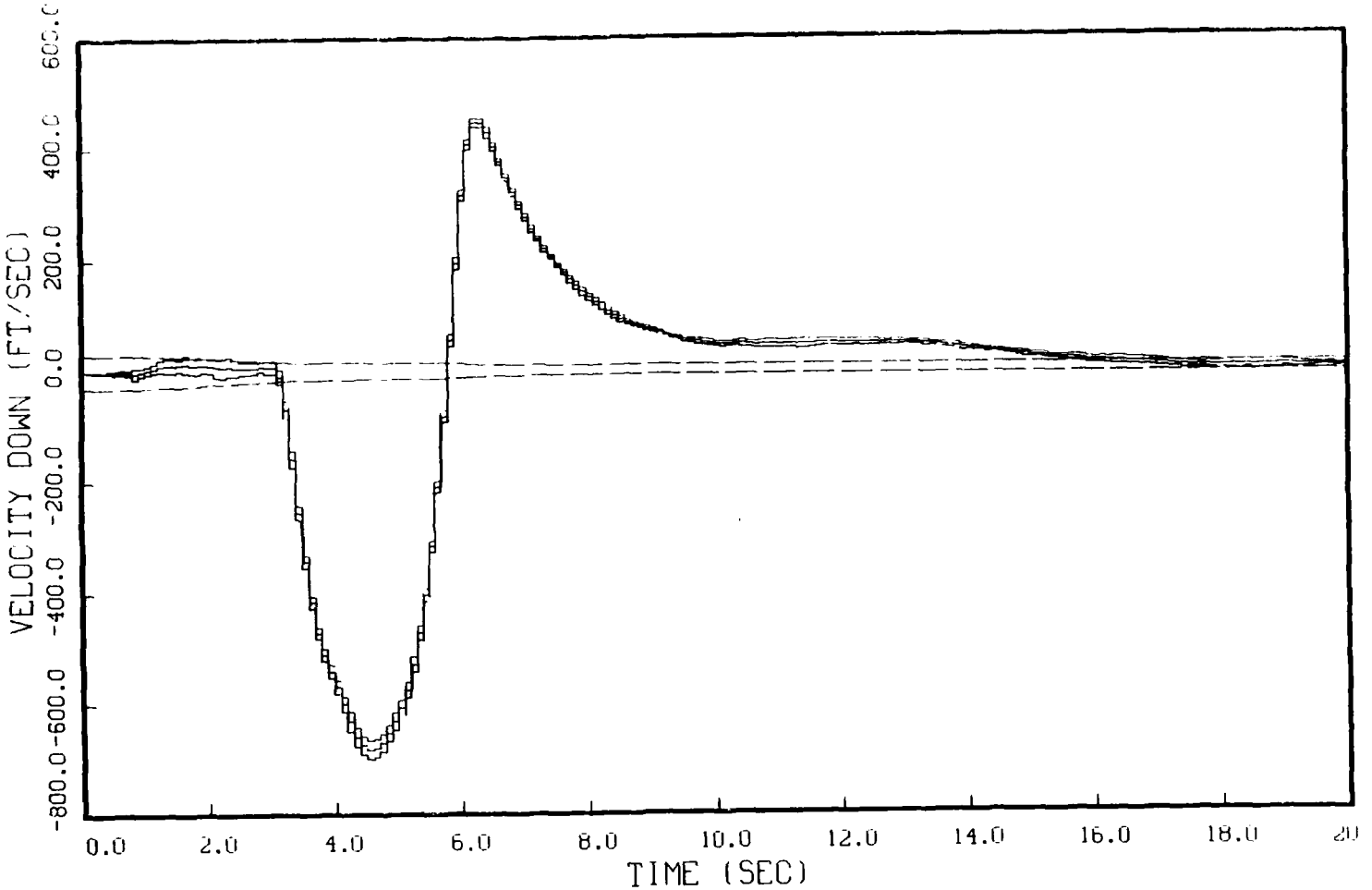

FIGURE 6.17: GAUSS MARKOV MODEL, STATE 8, 5 RUNS
BEAM TRAJECTORY, 0-100, 2 MEAS: SIN AZ & SIN EL (ORIGINAL R)

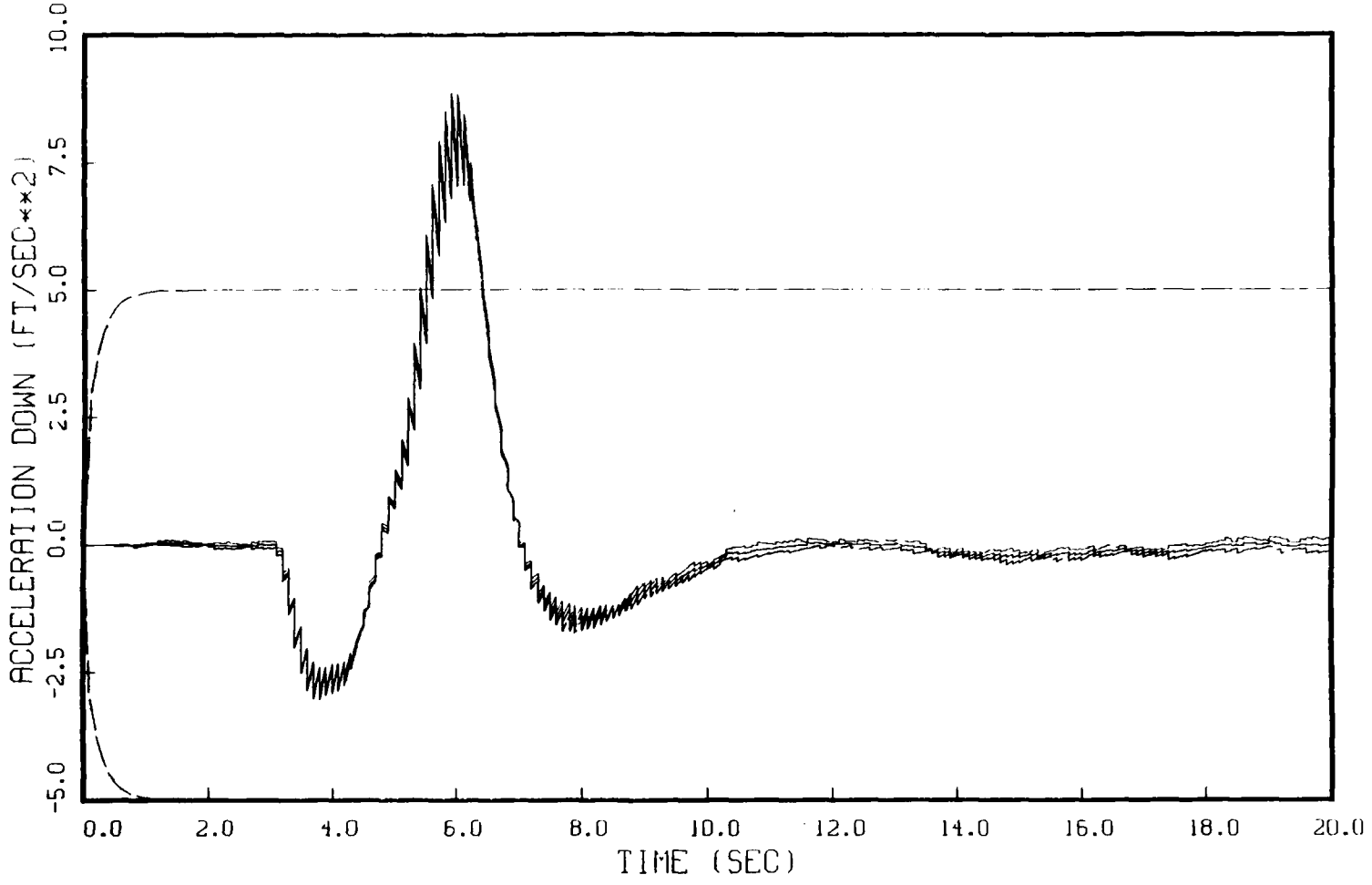

FIGURE G.18: GAUSS MARKOV MODEL, STATE 9, 5 RUNS
BEAM TRAJECTORY, 0-100, 2 MEAS: SIN AZ & SIN EL (ORIGINAL R)

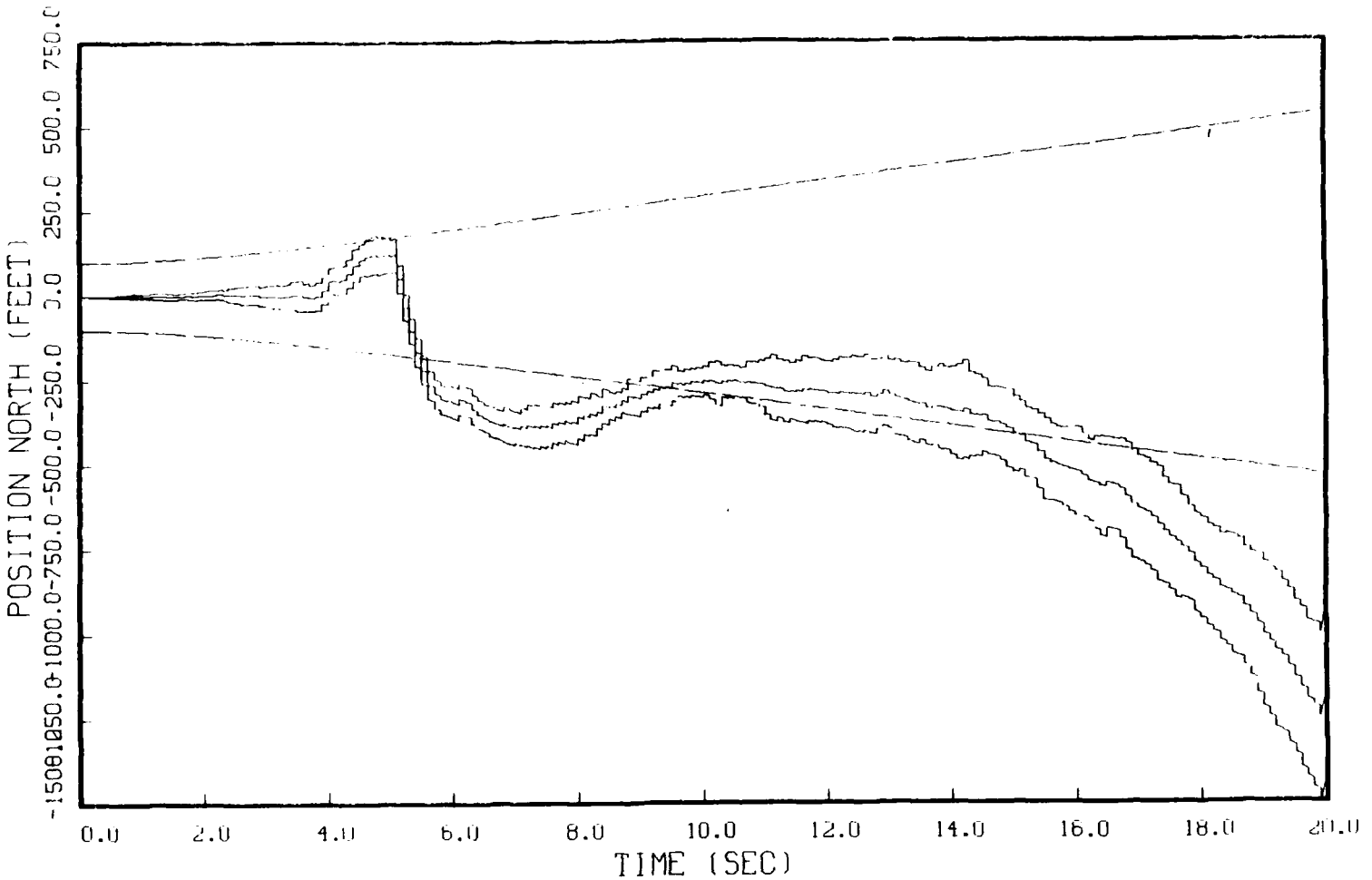

FIGURE 6.19: GAUSS MARKOV MODEL, STATE 1, 5 RUNS
BEAM TRAJECTORY, Q=100, 2 MEAS: OMEGA J & OMEGA K (ORIGINAL R)

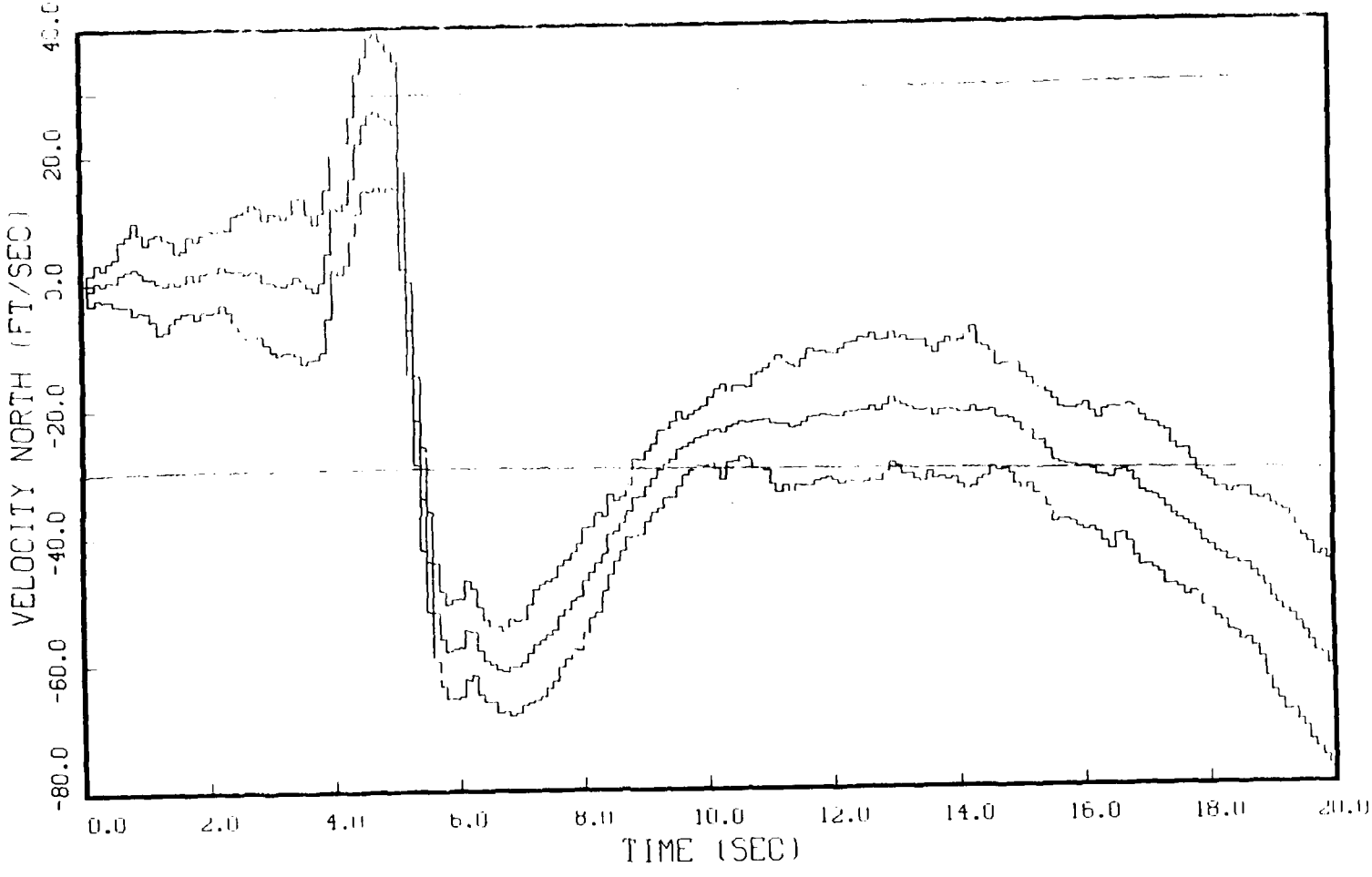

FIGURE 6.20: GAUSS MARKOV MODEL, STATE 2, 5 RUNS
BEAM TRAJECTORY, Q=100, 2 MEAS: OMEGA J & OMEGA K (ORIGINAL R)

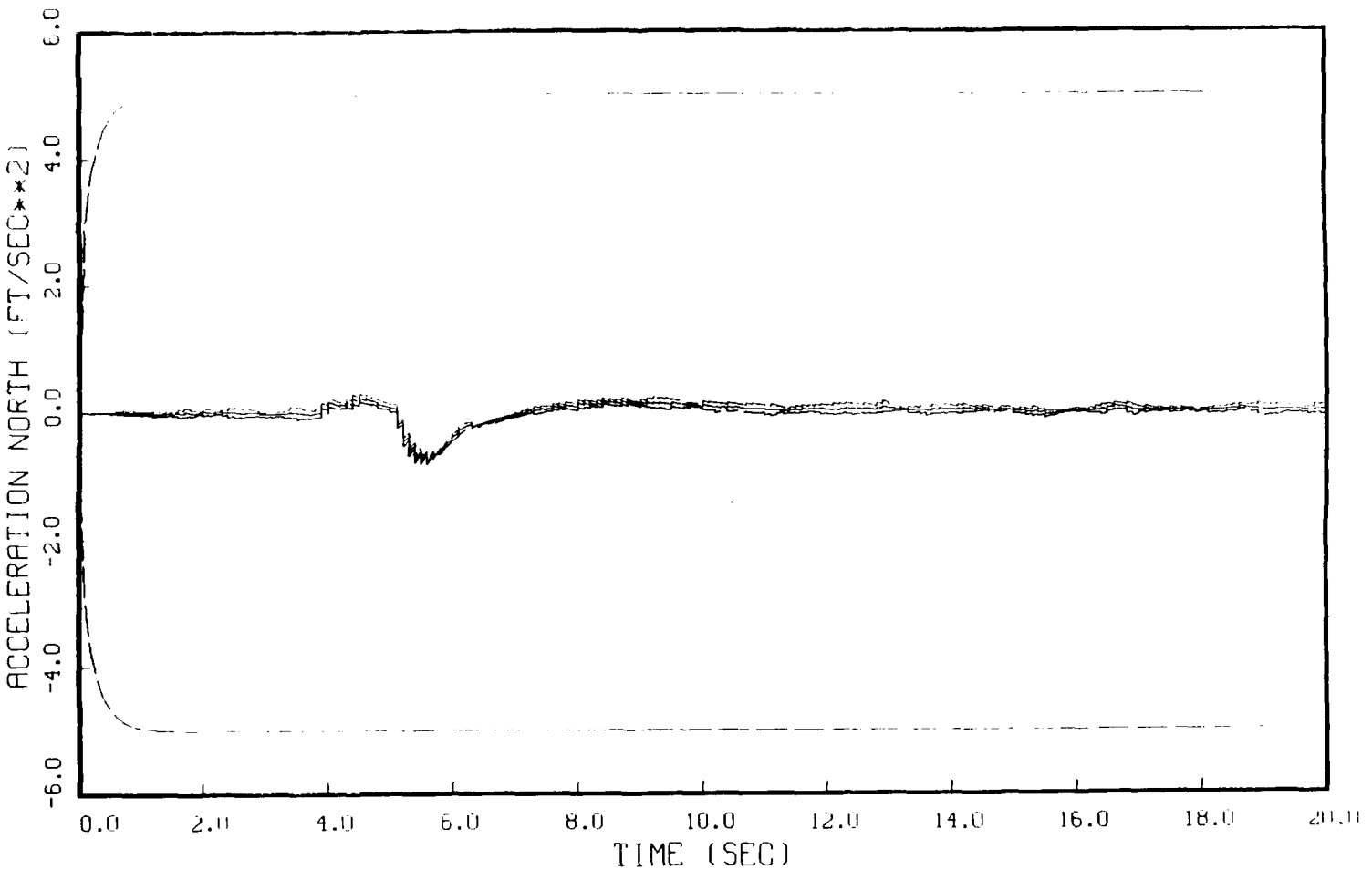

FIGURE 6.21: GAUSS MARKOV MODEL, STATE 3, 5 RUNS
BEAM TRAJECTORY, 0-100, 2 MEAS: OMEGA J & OMEGA K (ORIGINAL R)

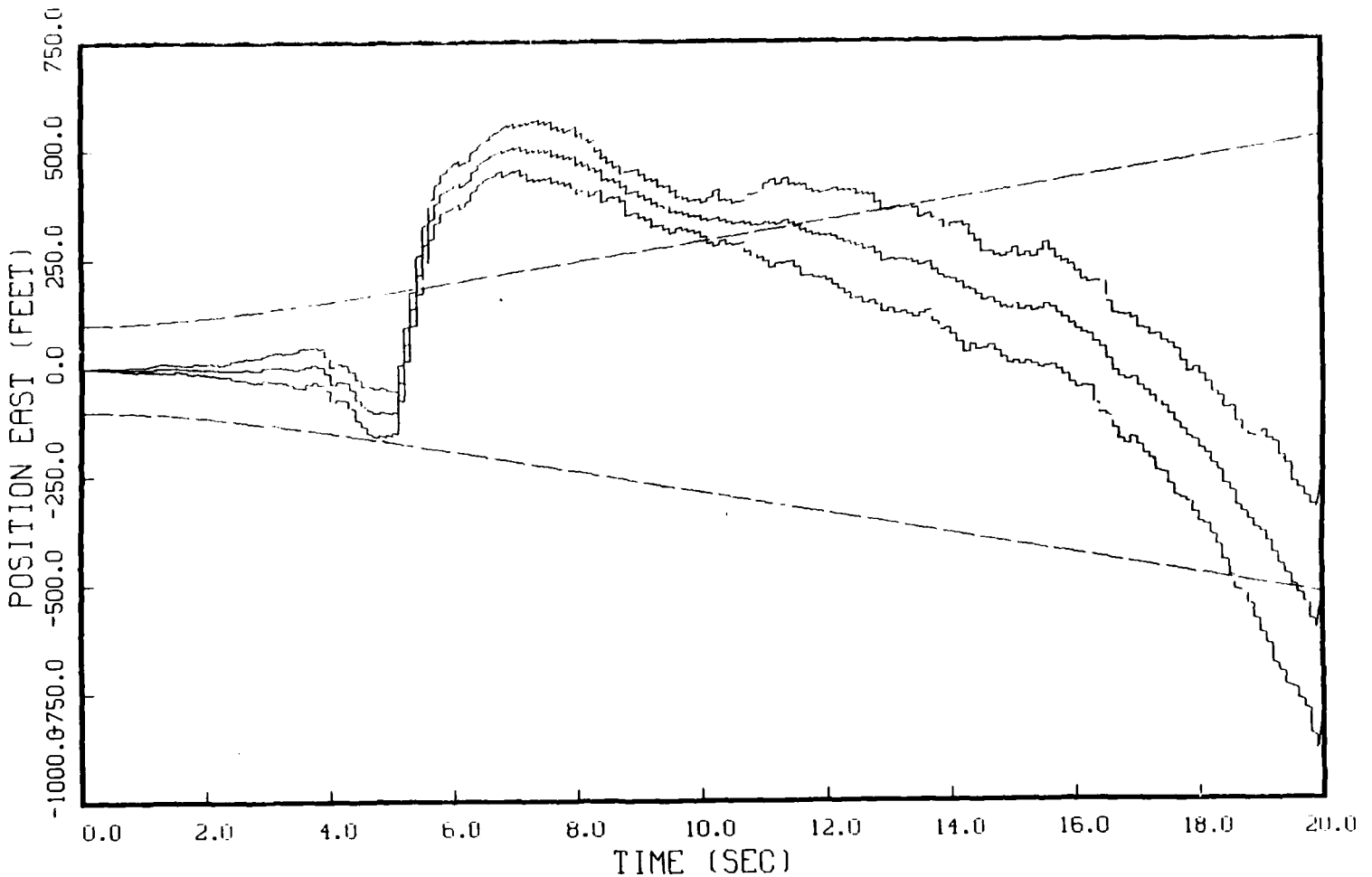

FIGURE 6.22: GAUSS MARKOV MODEL, STATE 4, 5 RUNS
BEAM TRAJECTORY, Q=100, 2 MEAS: OMEGA J & OMEGA K (ORIGINAL R)

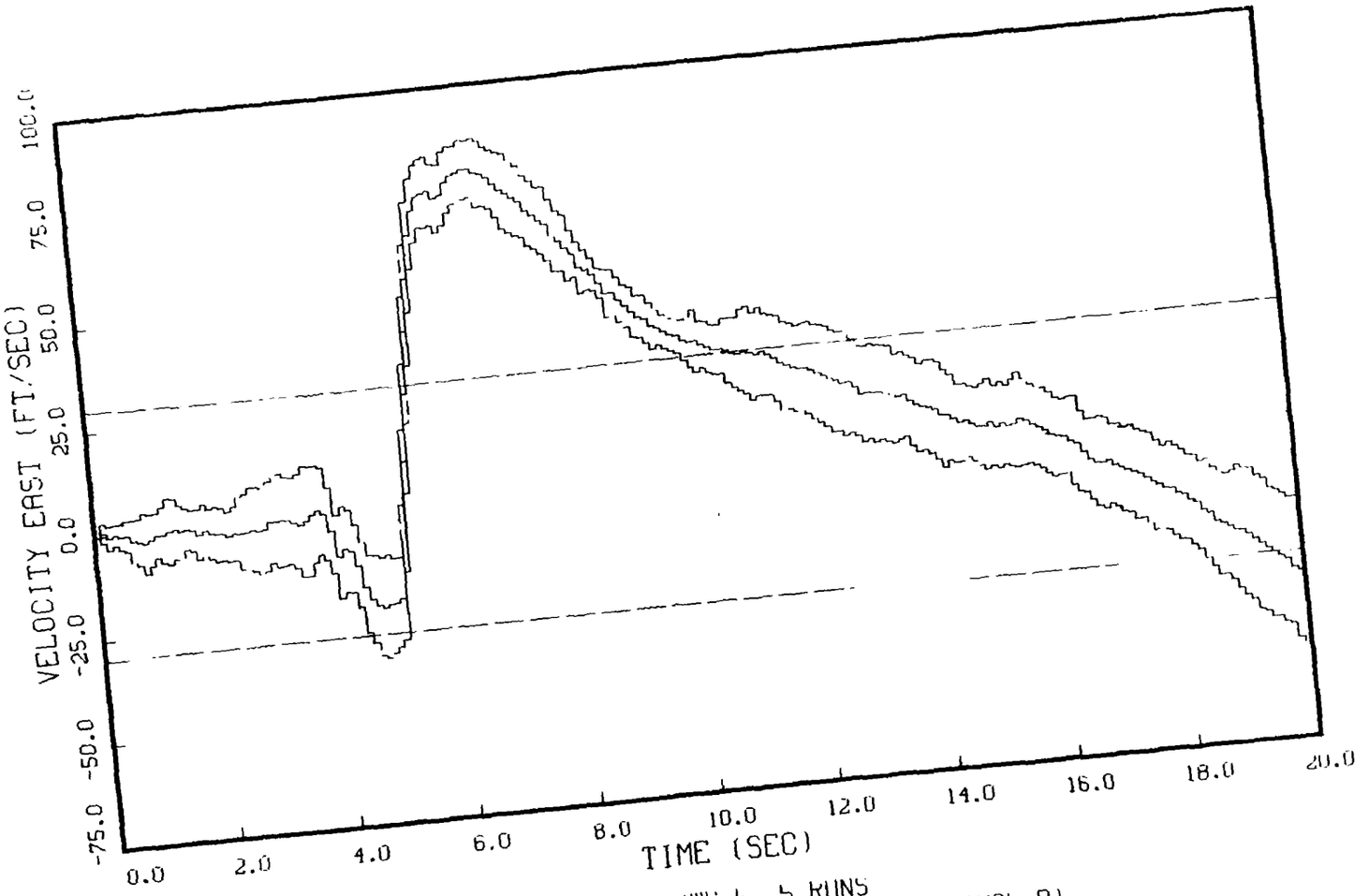

FIGURE 6.23: GAUSS MARKOV MODEL, STATE 5, 5 RUNS
BEAM TRAJECTORY, Q=100, 2 MEAS: OMEGA J & OMEGA K (ORIGINAL R)

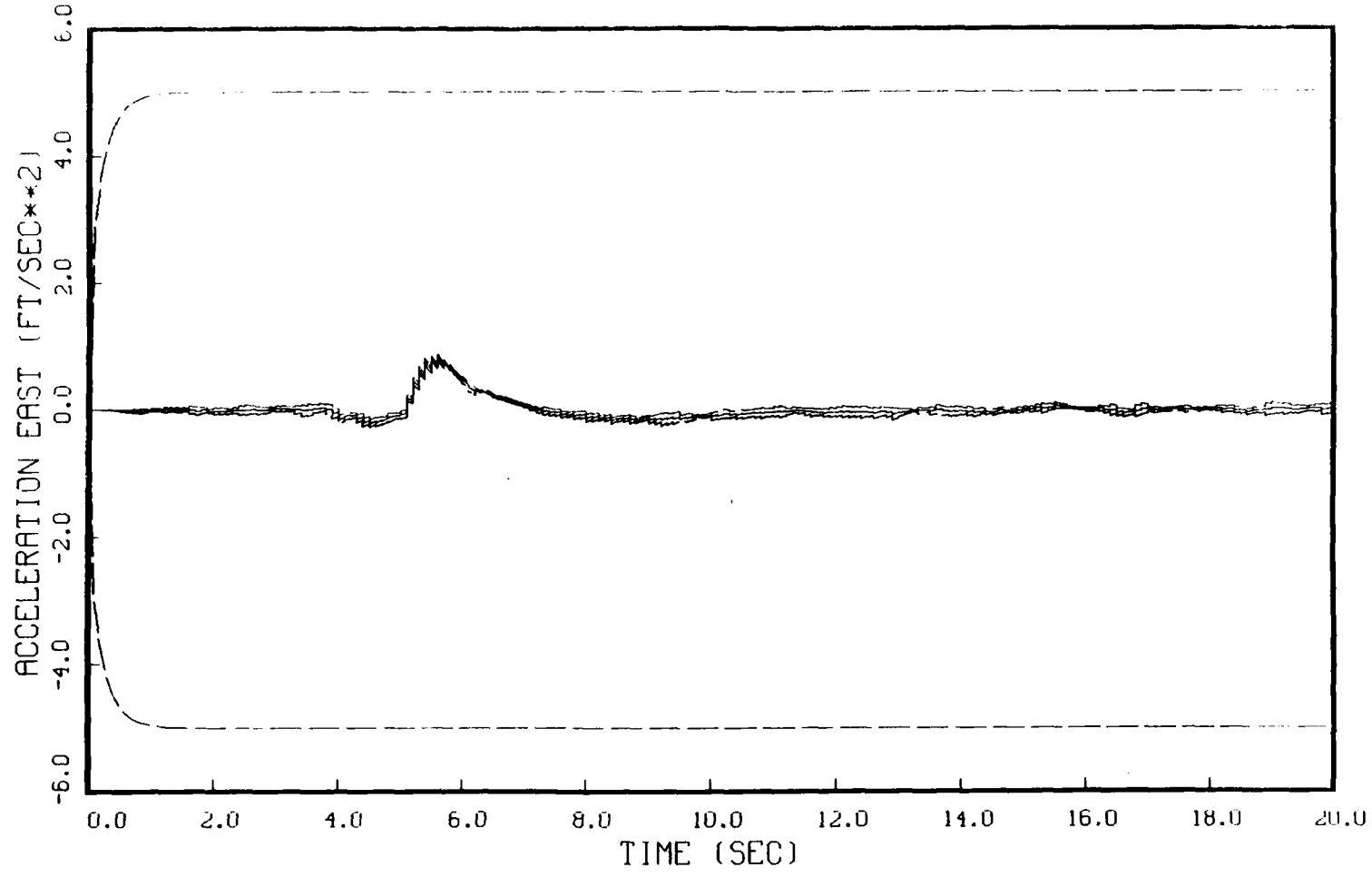

FIGURE 6.24: GAUSS MARKOV MODEL, STATE 6, 5 RUNS
BEAM TRAJECTORY, 0-100, 2 MEAS: OMEGA J & OMEGA K (ORIGINAL R)

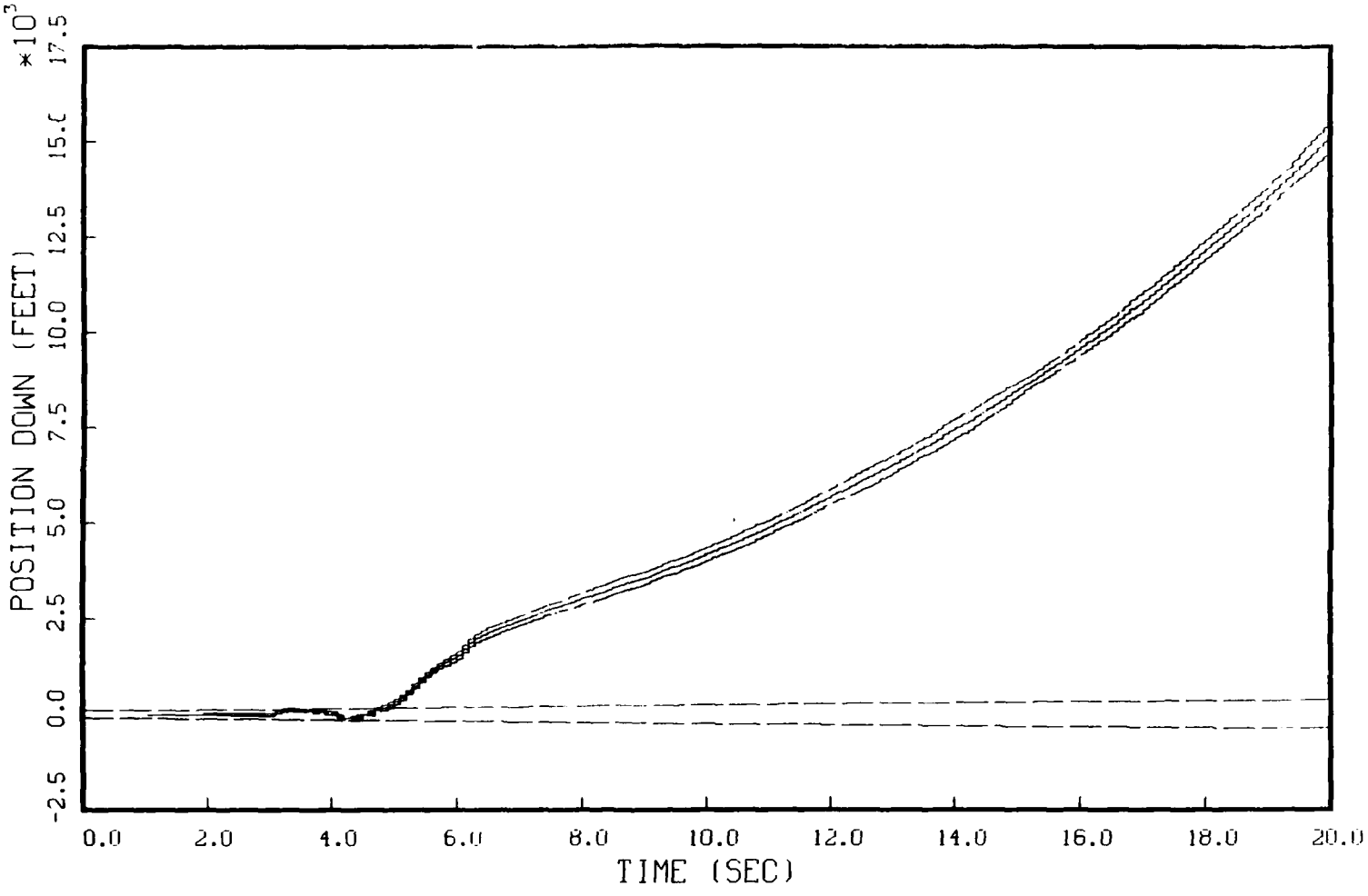

FIGURE 6.25: GAUSS MARKOV MODEL, STATE 7, 5 RUNS
BEAM TRAJECTORY, 0-100, 2 MEAS: OMEGA J & OMEGA K (ORIGINAL R)

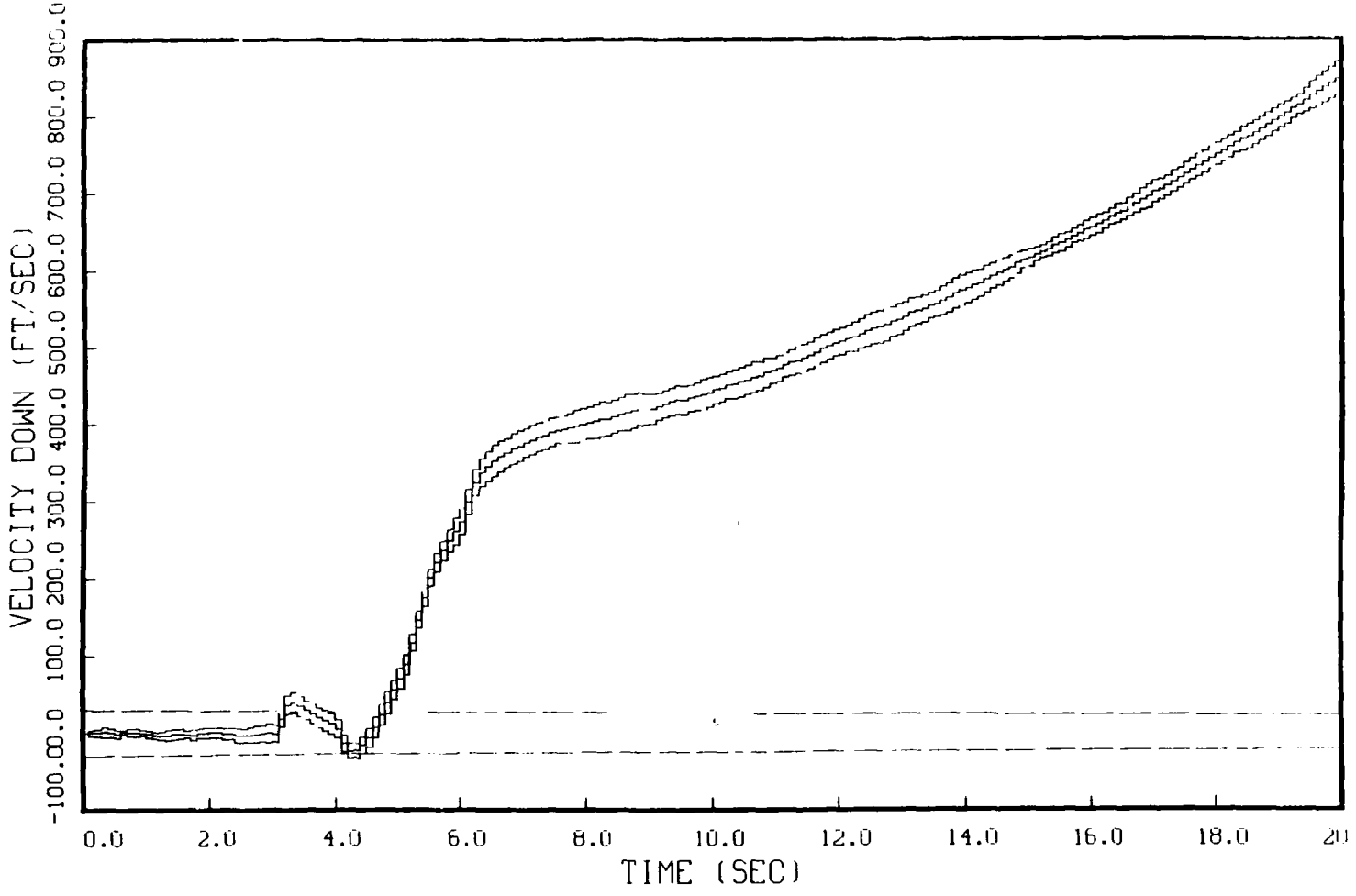

FIGURE 6.26: GAUSS MARKOV MODEL, STATE 8, 5 RUNS
BEAM TRAJECTORY, Q=100, 2 MEAS: OMEGA J & OMEGA K (ORIGINAL R)

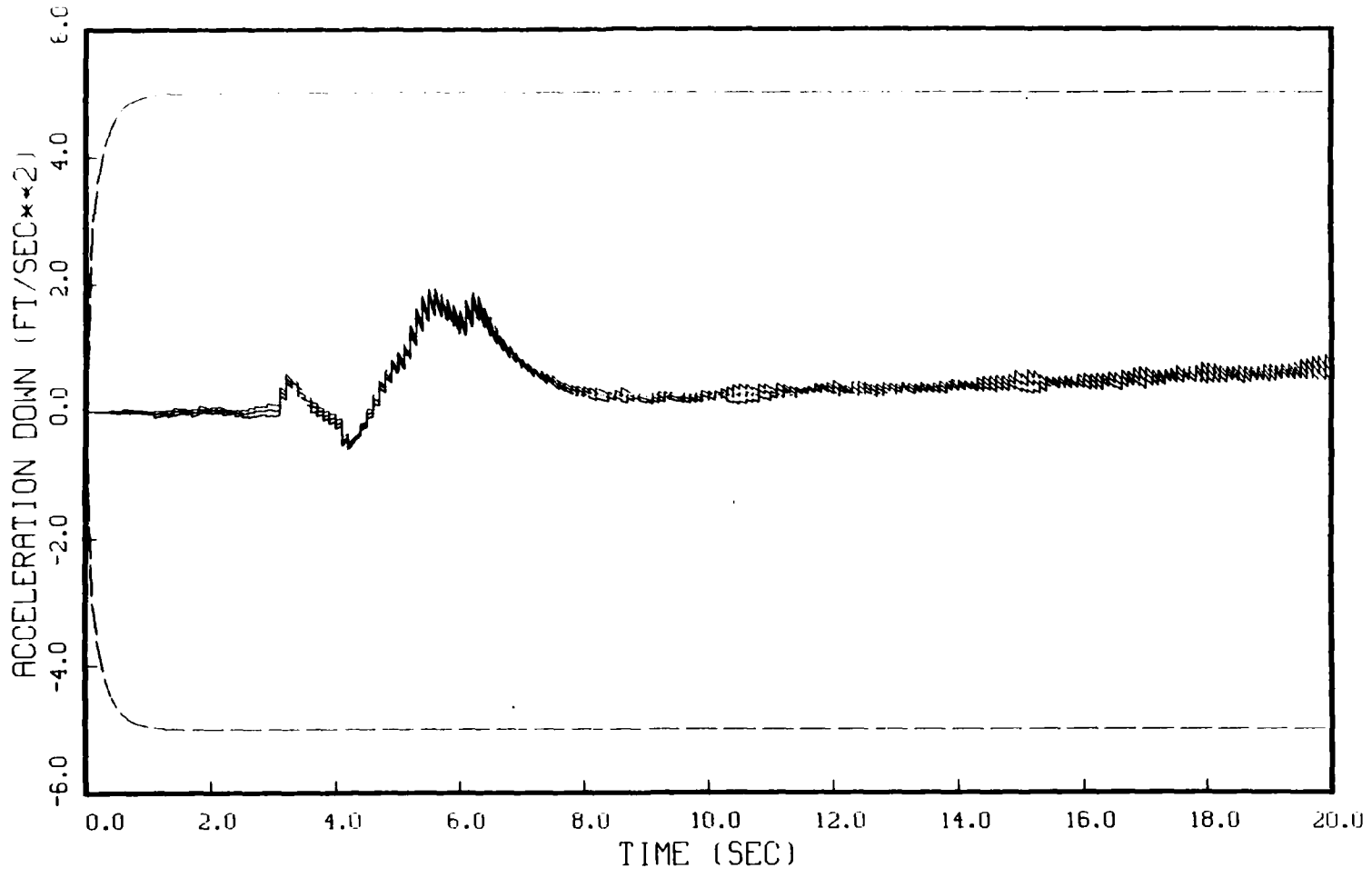

FIGURE 6.27: GAUSS MARKOV MODEL, STATE 9, 5 RUNS
BEAM TRAJECTORY, Q=100, 2 MEAS: OMEGA J & OMEGA K (ORIGINAL R)

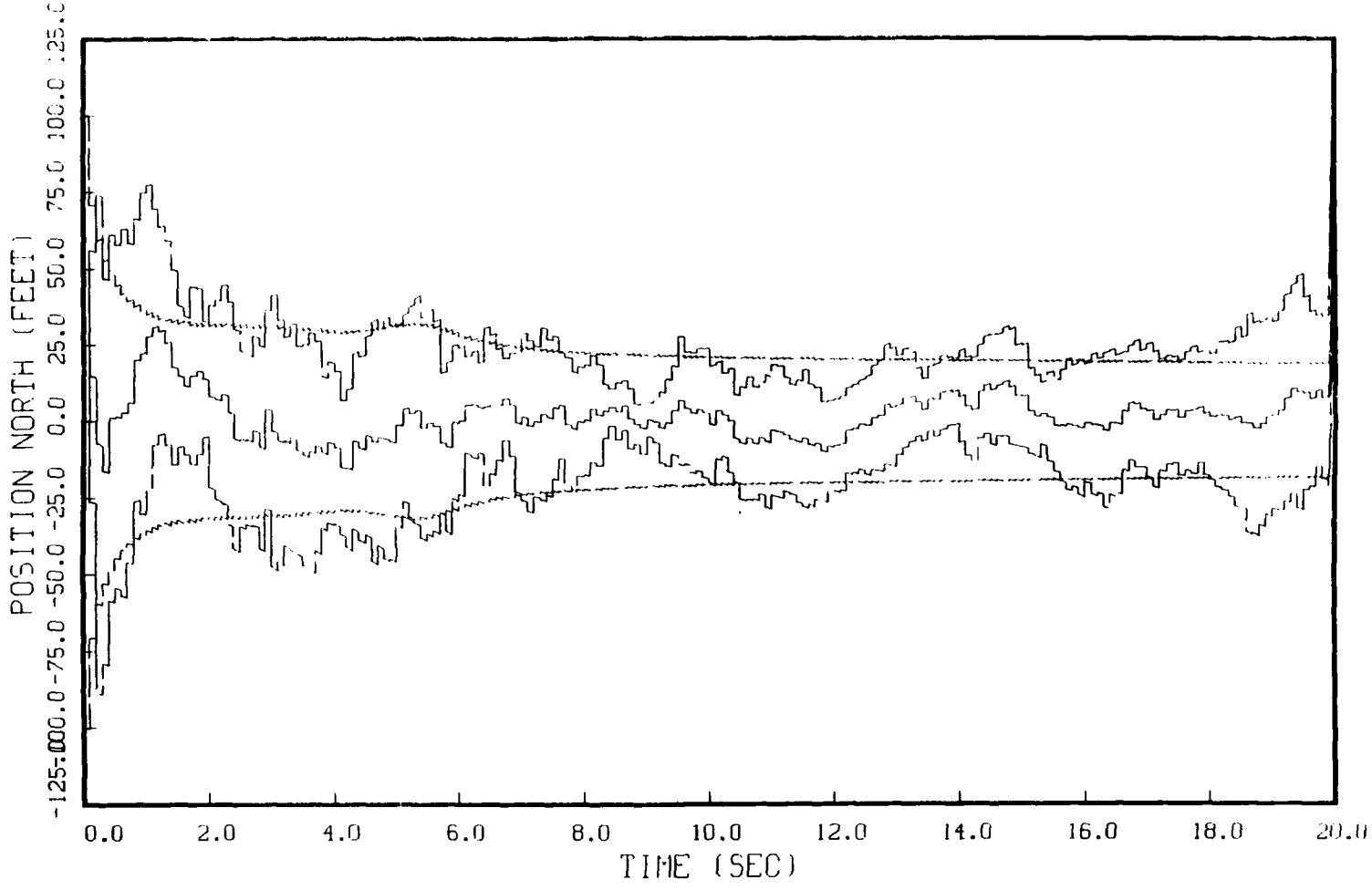

FIGURE G.28: GAUSS MARKOV MODEL, STATE 1, 5 RUNS, Q=100, 4 MEAS-ORIG R
BEAM TRAJECTORY WITH ANTENNA LAG ERROR REMOVED FROM TRUTH MODEL

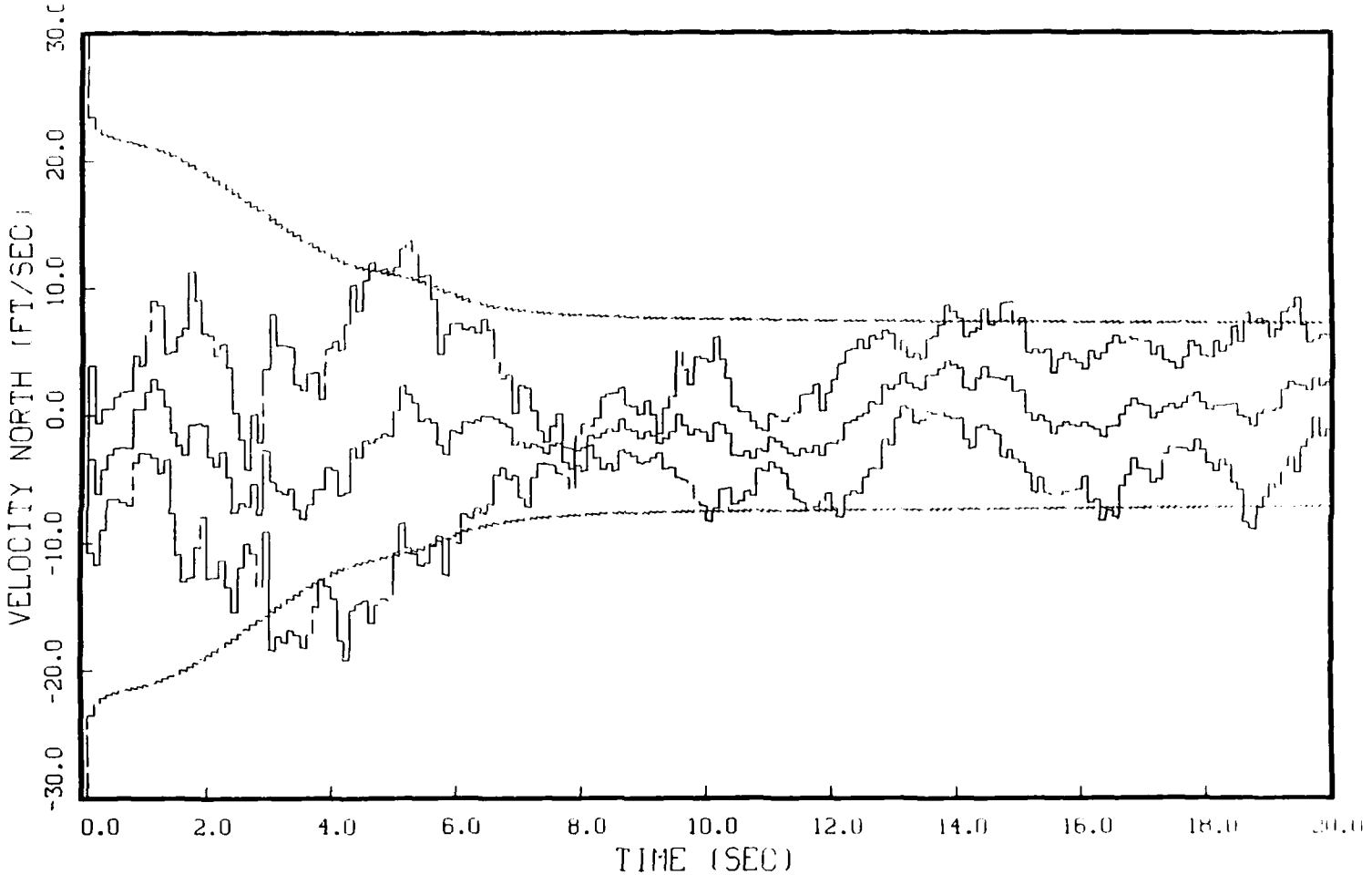

FIGURE G.29: GAUSS MARKOV MODEL, STATE 2, 5 RUNS, Q=100, 4 MEAS UPTO K
BEAM TRAJECTORY WITH ANTENNA LAG ERROR REMOVED FROM TRUTH MODEL

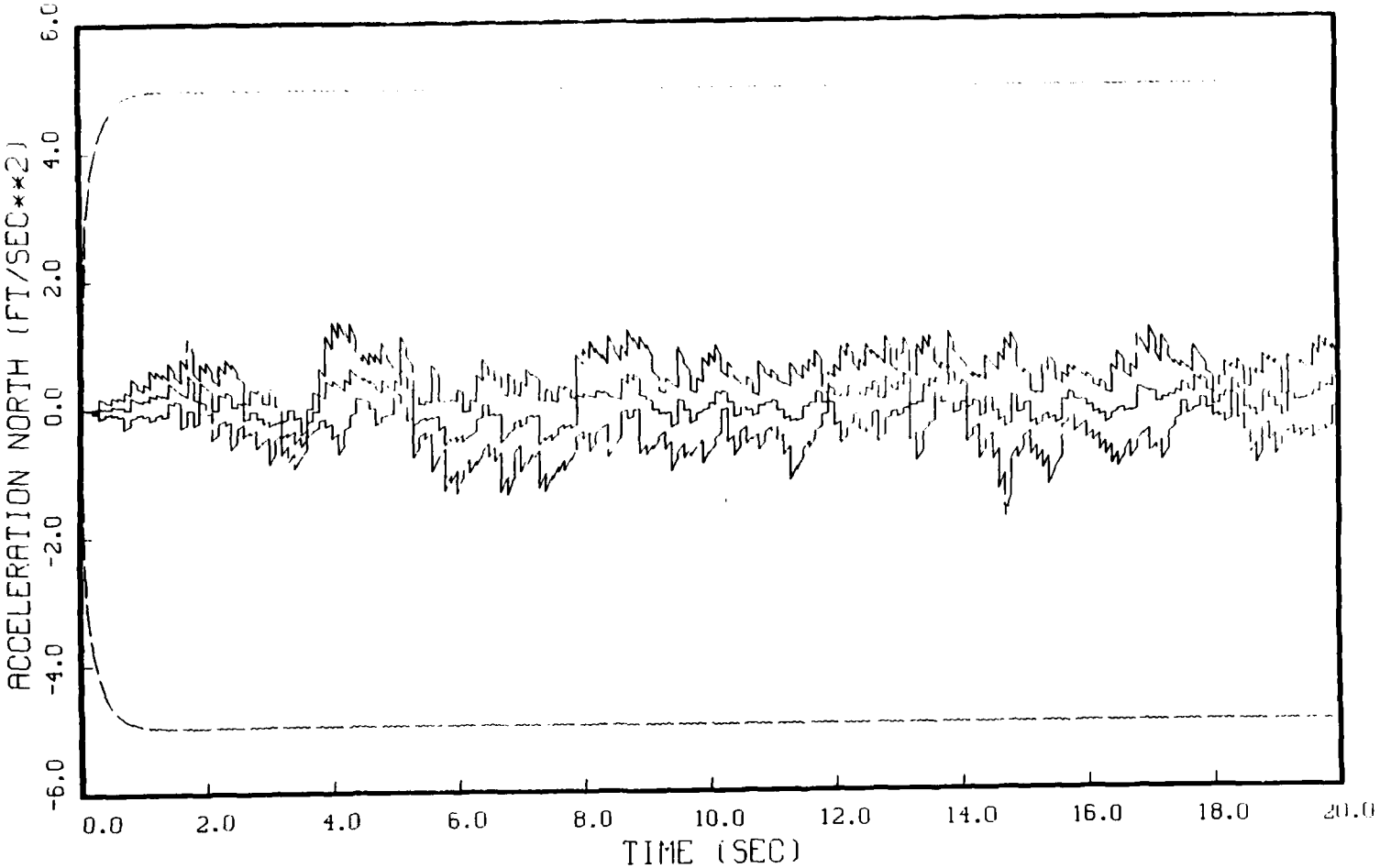

FIGURE G.30: GAUSS MARKOV MODEL, STATE 3, 5 RUNS, 0-100, 4 MEAS-ORIG R BEAM TRAJECTORY WITH ANTENNA LAG ERROR REMOVED FROM TRUTH MODEL

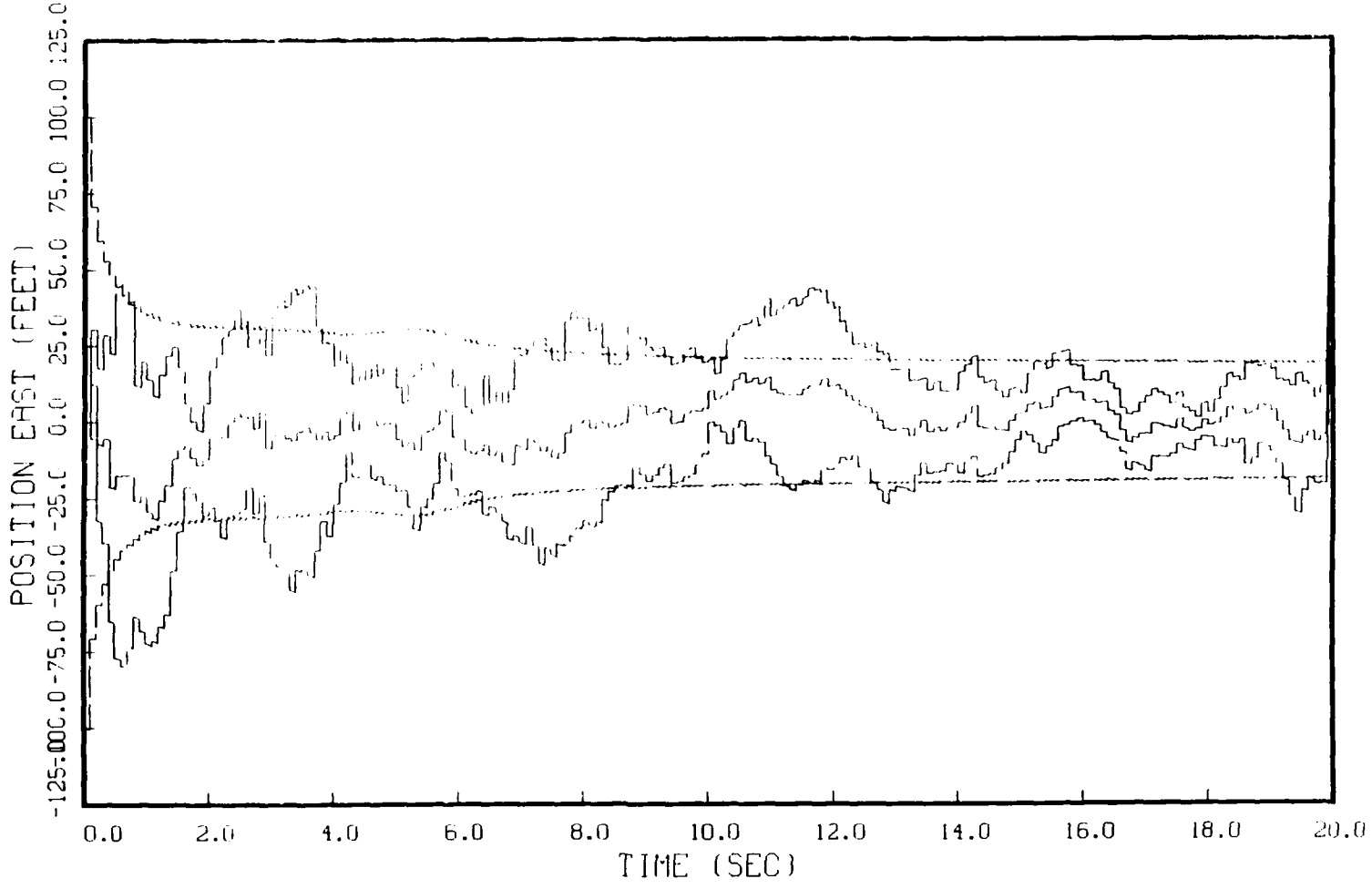

FIGURE G.31: GAUSS MARKOV MODEL, STATE 4, 5 RUNS, Q=100, 4 MEAS-ORIG R
BEAM TRAJECTORY WITH ANTENNA LAG ERROR REMOVED FROM TRUTH MODEL

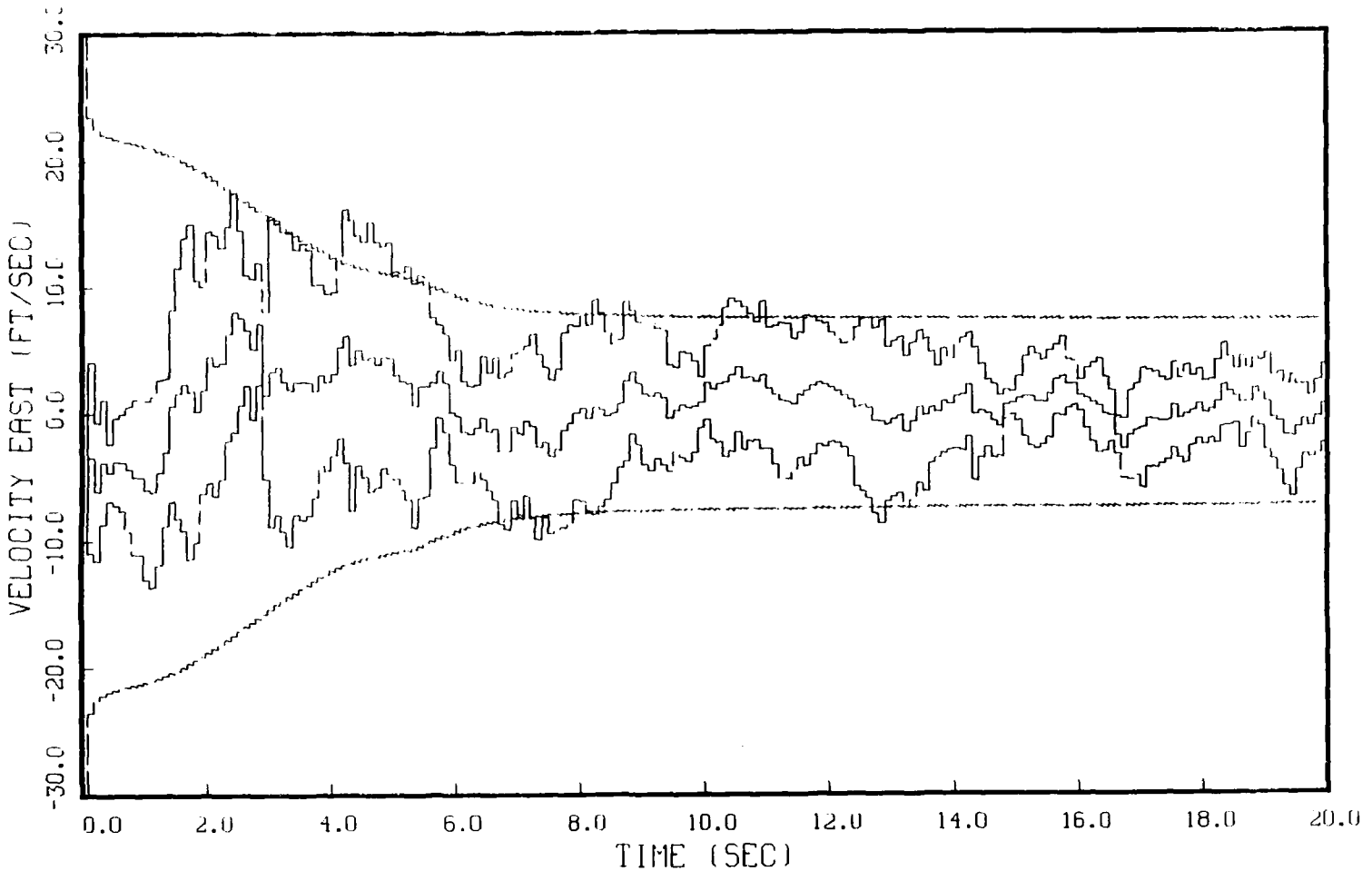

FIGURE G.32: GAUSS MARKOV MODEL, STATE 5, 5 RUNS, 0-100, 4 MEAS-ORIG R
BEAM TRAJECTORY WITH ANTENNA LAG ERROR REMOVED FROM TRUTH MODEL

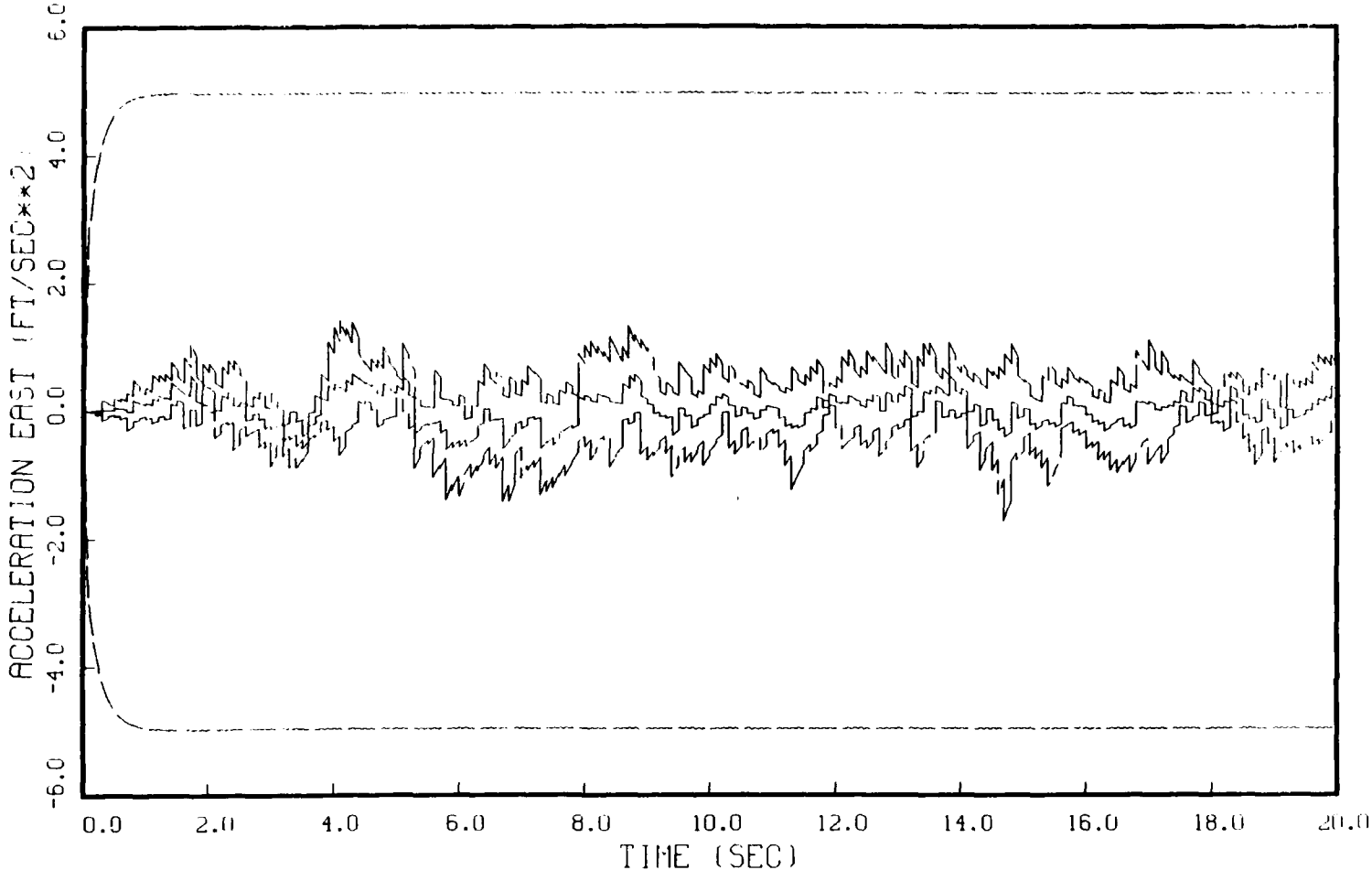

FIGURE G.33: GAUSS MARKOV MODEL, STATE 6, 5 RUNS, Q=100, 4 MEAS-ORIG R
BEAM TRAJECTORY WITH ANTENNA LAG ERROR REMOVED FROM TRUTH MODEL

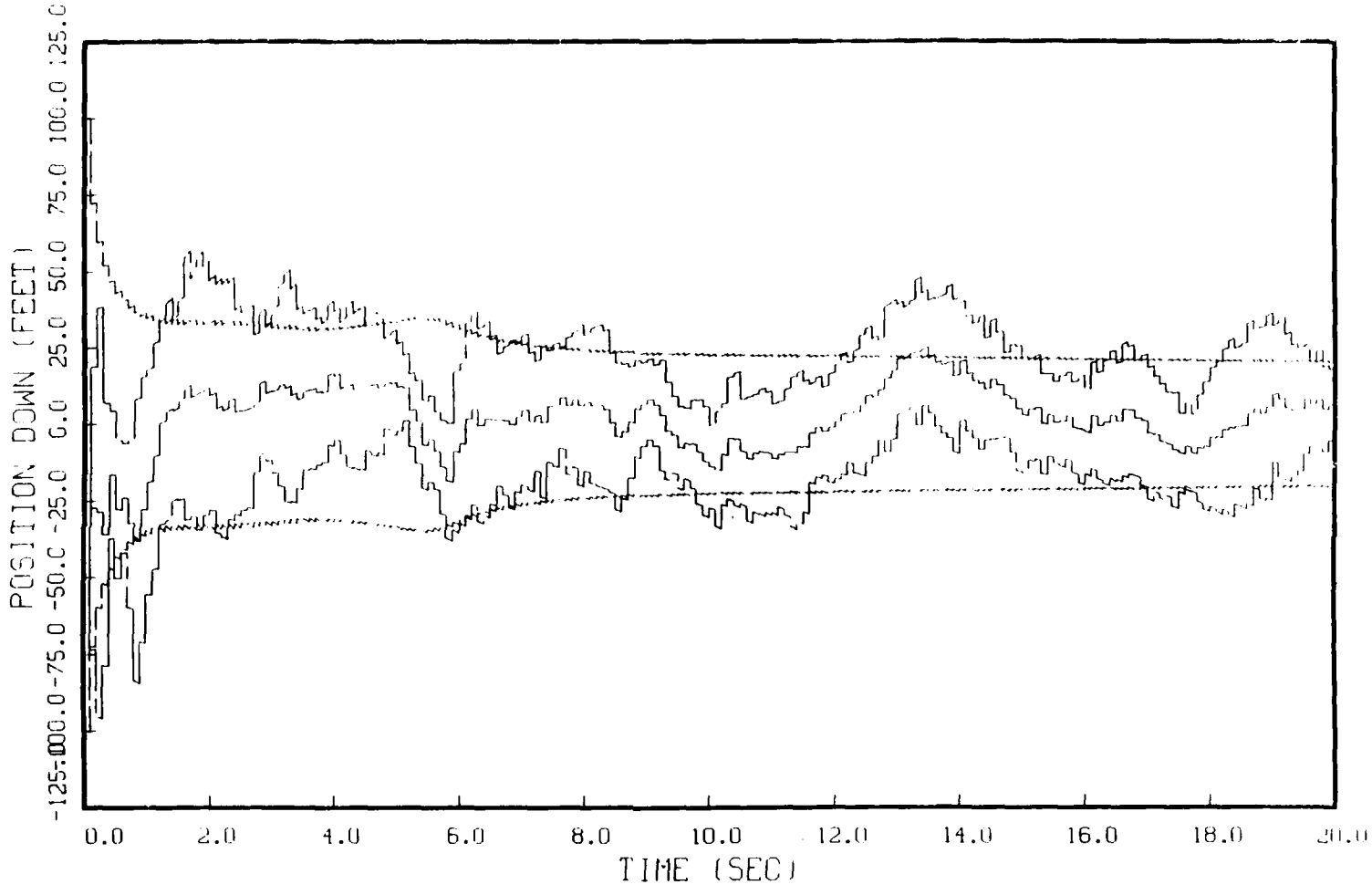

FIGURE G.34: GAUSS MARKOV MODEL, STATE 7, 5 RUNS, U=100, 4 MEAS ORIG R
BEAM TRAJECTORY WITH ANTENNA LAG ERROR REMOVED FROM TRUTH MODEL

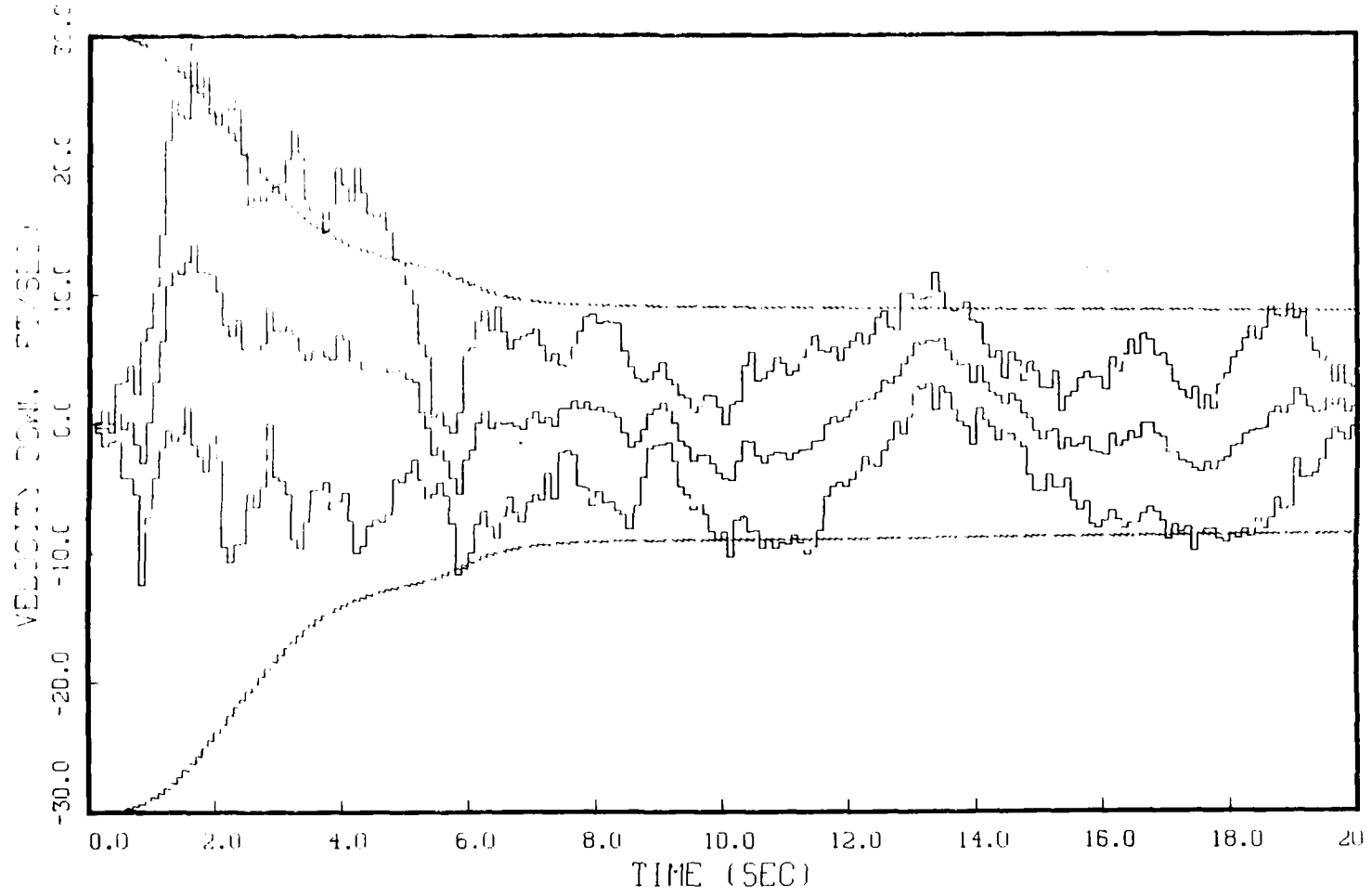

FIGURE G.35: GAUSS MARKOV MODEL, STATE 8, 5 RUNS, Q=100, 4 MEAS-ORIG R
BEAM TRAJECTORY WITH ANTENNA LAG ERROR REMOVED FROM TRUTH MODEL

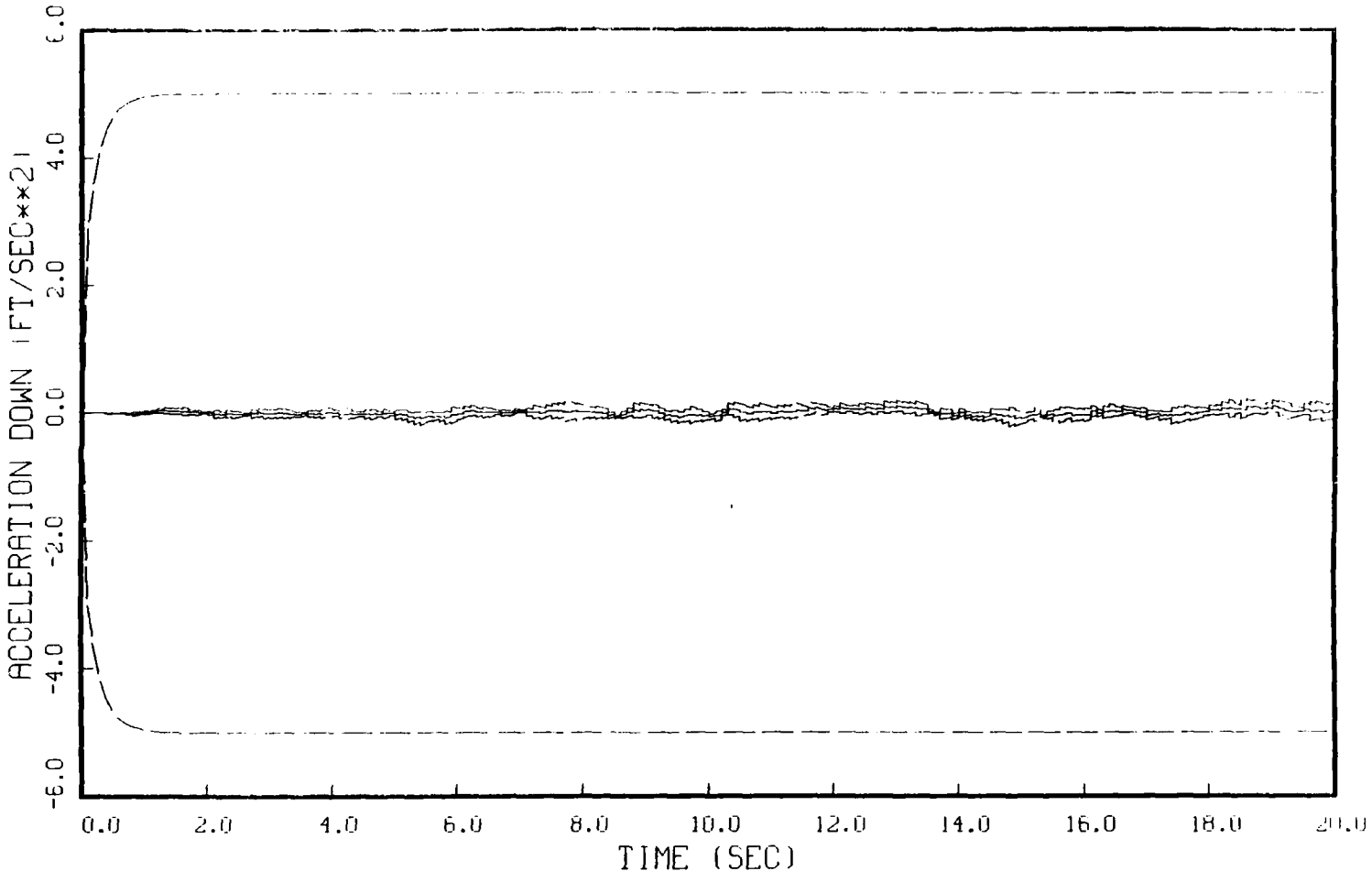

FIGURE G.36: GAUSS MARKOV MODEL, STATE 9, 5 RUNS, 0-100, 4 MEAS-ORIG R BEAM TRAJECTORY WITH ANTENNA LAG ERROR REMOVED FROM TRUTH MODEL

Appendix H

Filter Tuning Using Measurement Noise

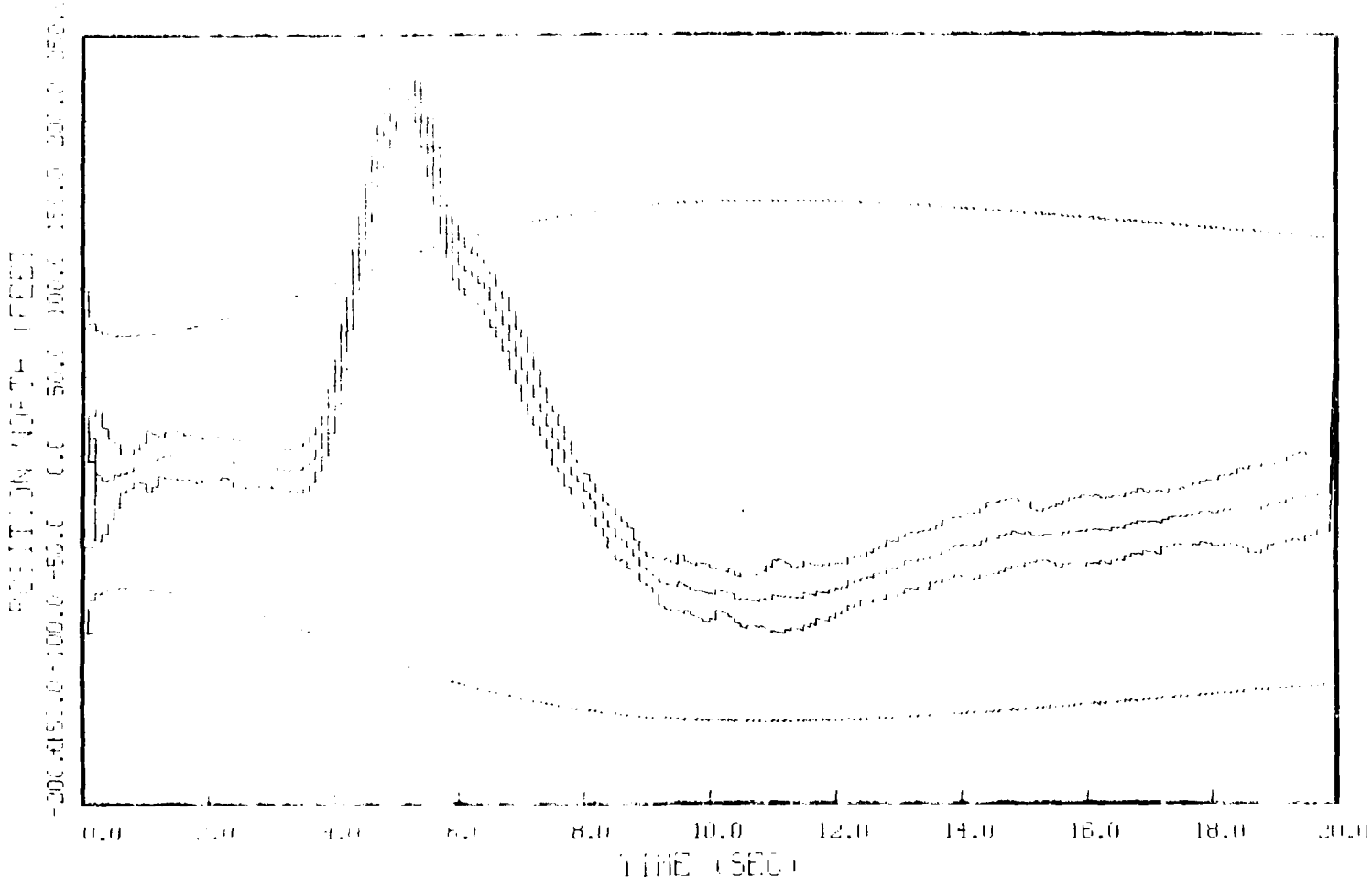

FIGURE B.1: [illegible] TARGET, STATE 1, 5 RUNS, Q-10D1, MEAS NOISE INCREASED
BEAM TRAJECTORY, [illegible] MEAS, RNG RATE, SIM AZ & EL QP=2.0E-4 FOR AZ & EL

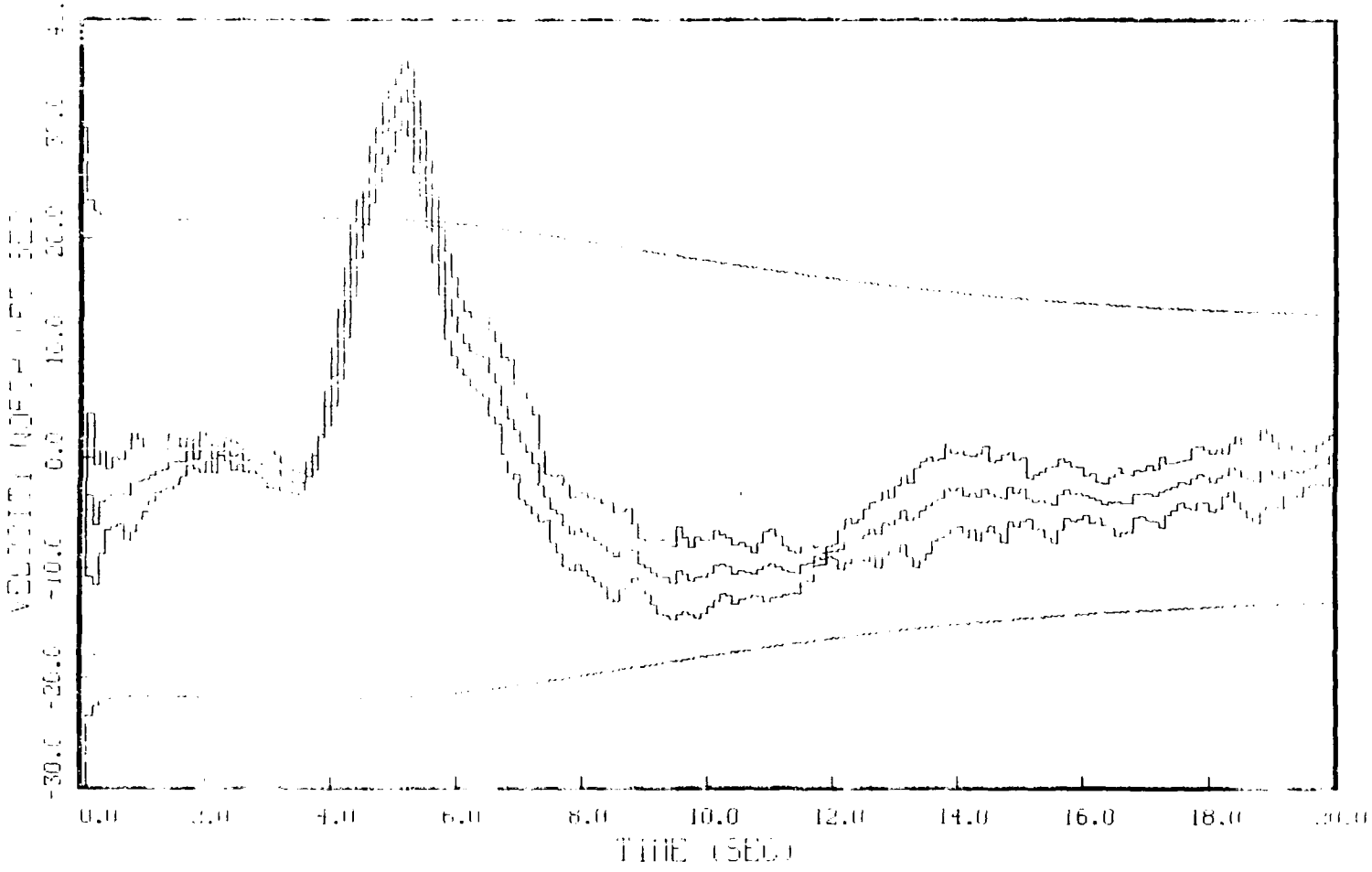

FIGURE [illegible]: SMALL BANTOV MODEL, STATE 2, 5 RUNS, U-100, MEAS NOISE INCREASED
BENT TRAJECTORY, 4 MEAS: 100, 100 RATE, SIN AZ & EL (R=2.0E-4 FOR AZ & EL)

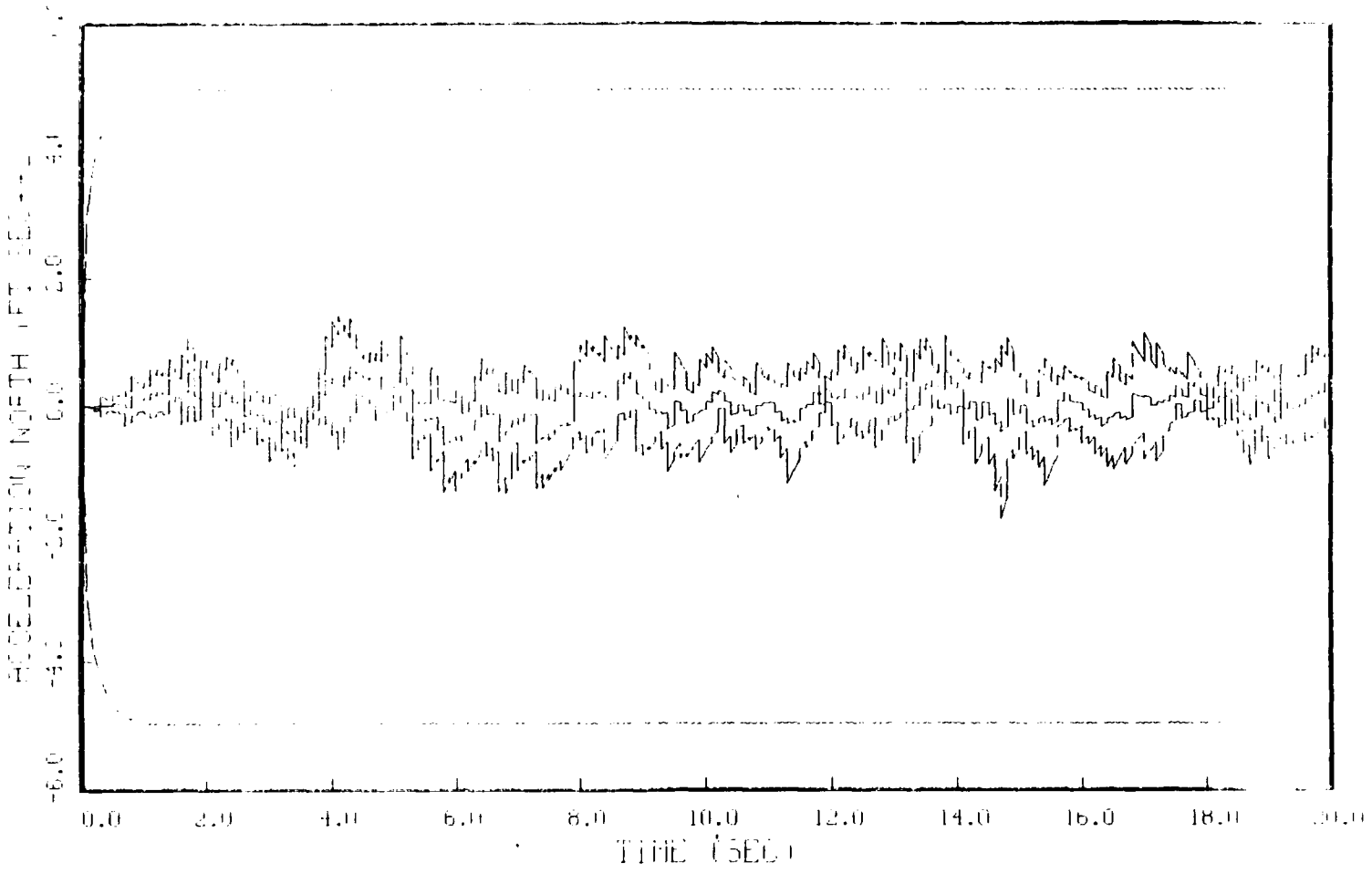

FIGURE H.3: [illegible] MODEL, STATE 3, 5 RUNS, U-DOT, MEAS NOISE INCREASED
BEAM TRAJECTORY, 4 DEM : RNG, RNG RATE, SIN AZ & EL (R=2.0E-4 FOR AZ & EL

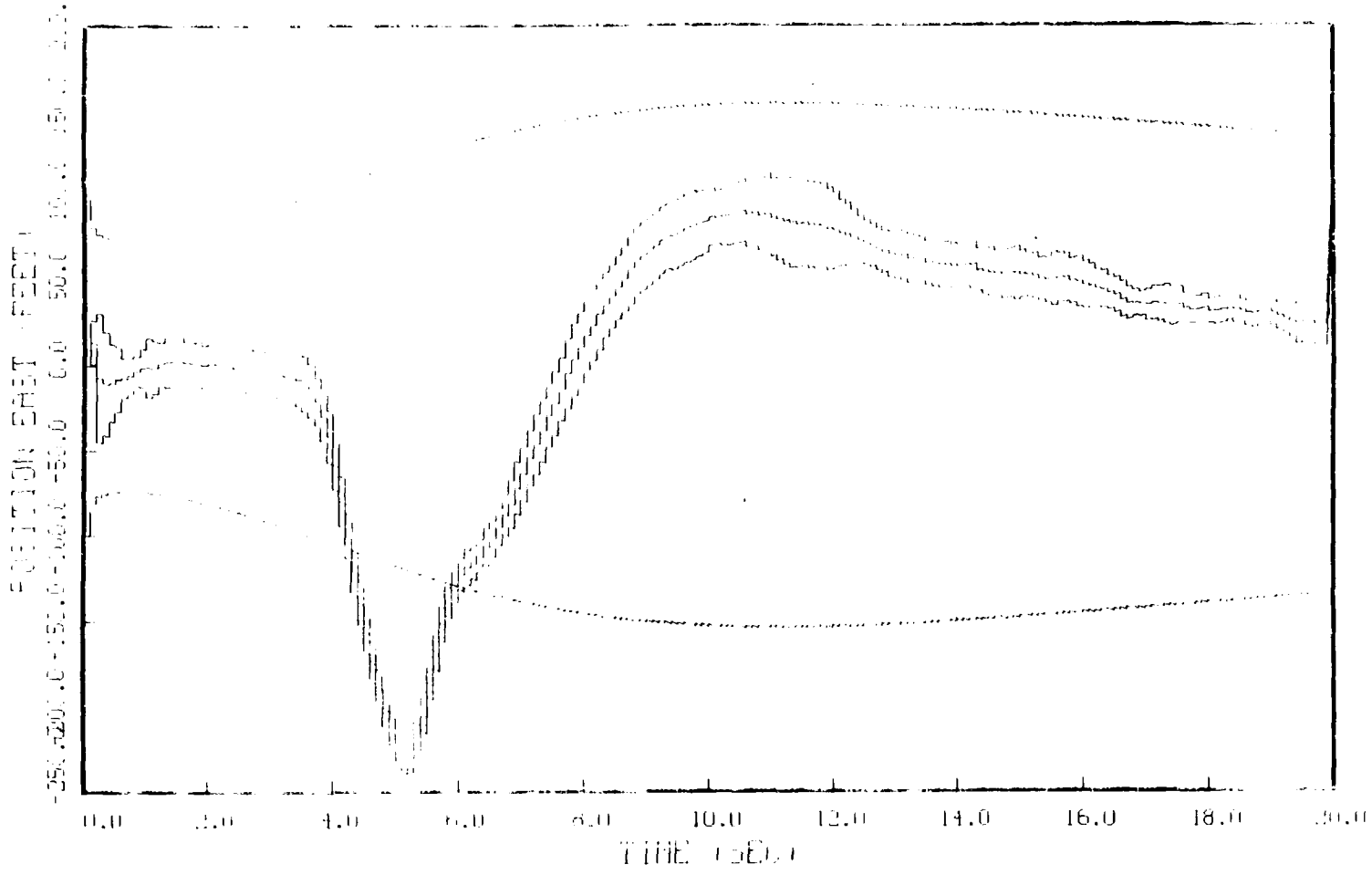

FIGURE II.1: [illegible] MODEL, STATE 4, 5 RUNS, 0-100, MEAS NOISE INCREASED
BEAM TRANSITIONS, 4 BEAMS: AZ&EL, AZ&EL RATE, SIN AZ & EL [illegible] FOR AZ & EL

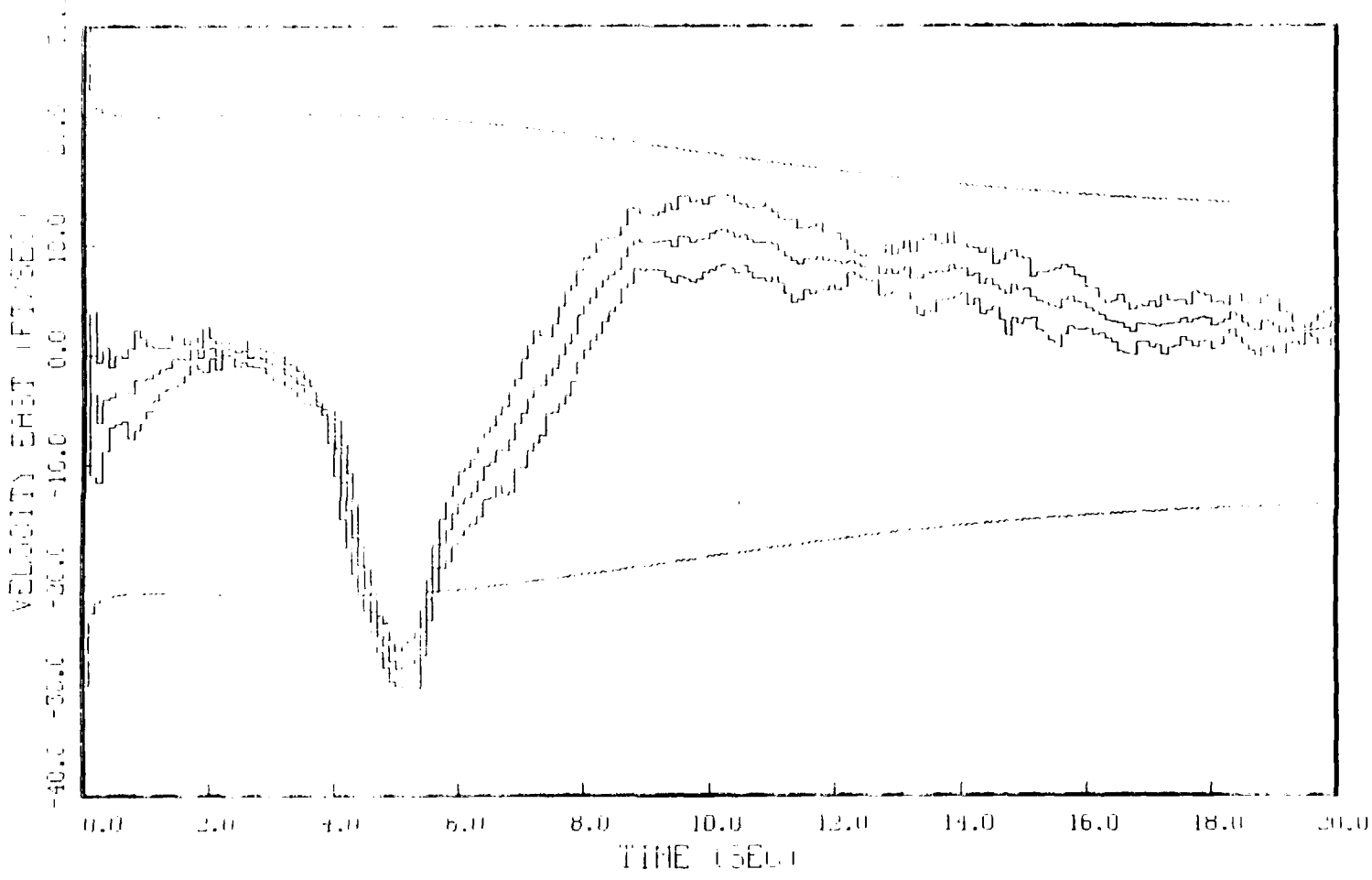

FIGURE II.5: GENESIS TRAJECTORY MODEL, STATE 5, 5 RUNS, 0-1000, MEAS NOISE INCREMENTED
BEAM TRAJECTORY, 4 MEAS: RNG, RNG RATE, SIN AZ & EL IR=2.0E-4 FOR AZ & EL

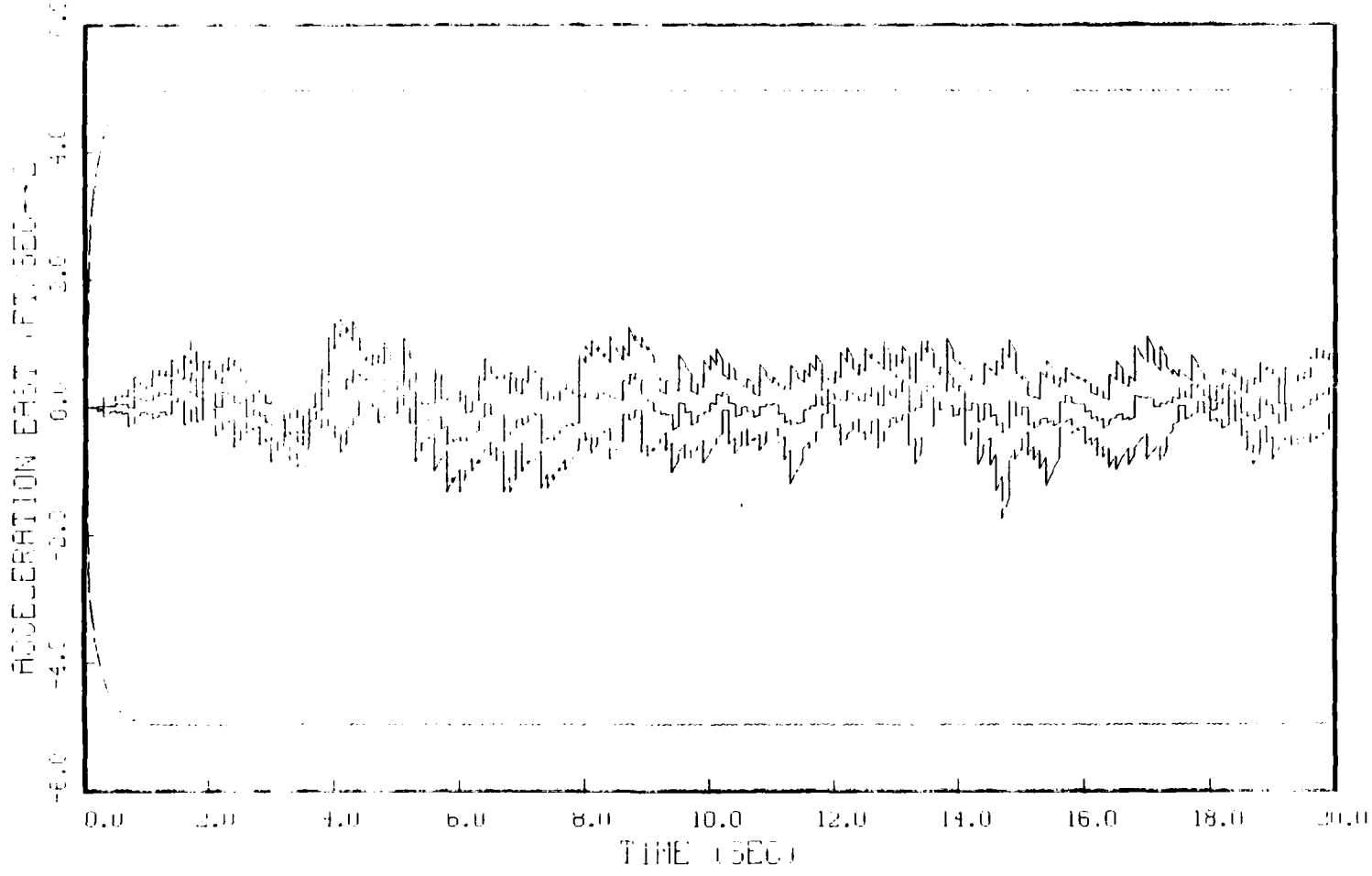

FIGURE II.6: GAUSS MARKOV MODEL, STATE 6, 5 RUNS, 0-100, MEMS NOISE INCREMENTED
BEAM TRANSMITTED, 4 MEMS: RNG, RNG RATE, SIN AZ & EL (R=3.0E+4 FOR AZ & EL)

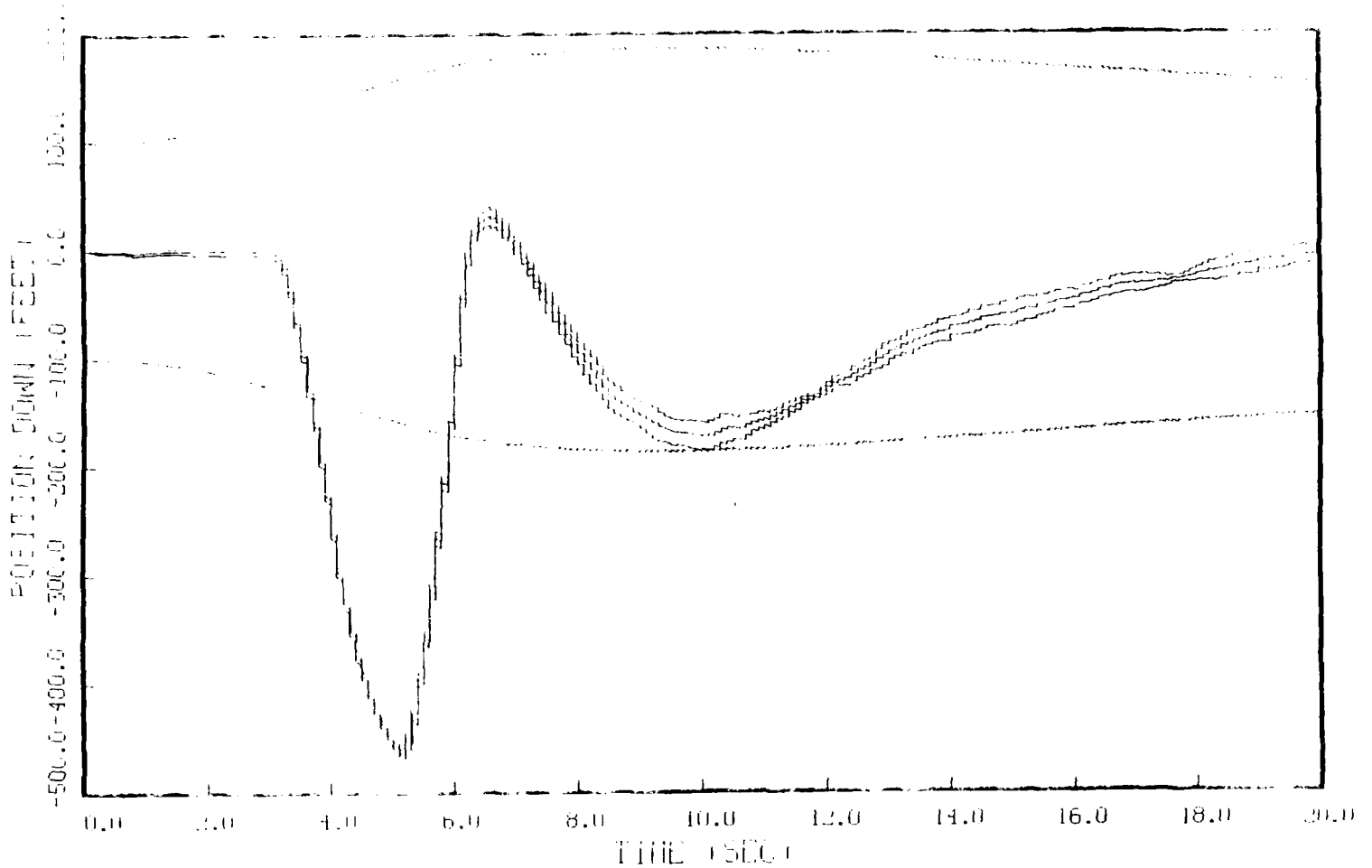

FIGURE 11. . GAUSS MARKOV MODEL, STATE 7, 5 RUNS, D=100, MEMS NOISE INCREMENTED
BEAM TRACKER TEST, 4 MEMS: RNG, RNG RATE, SIN AZ & EL TR=1.0E 4 FOR AZ & EL

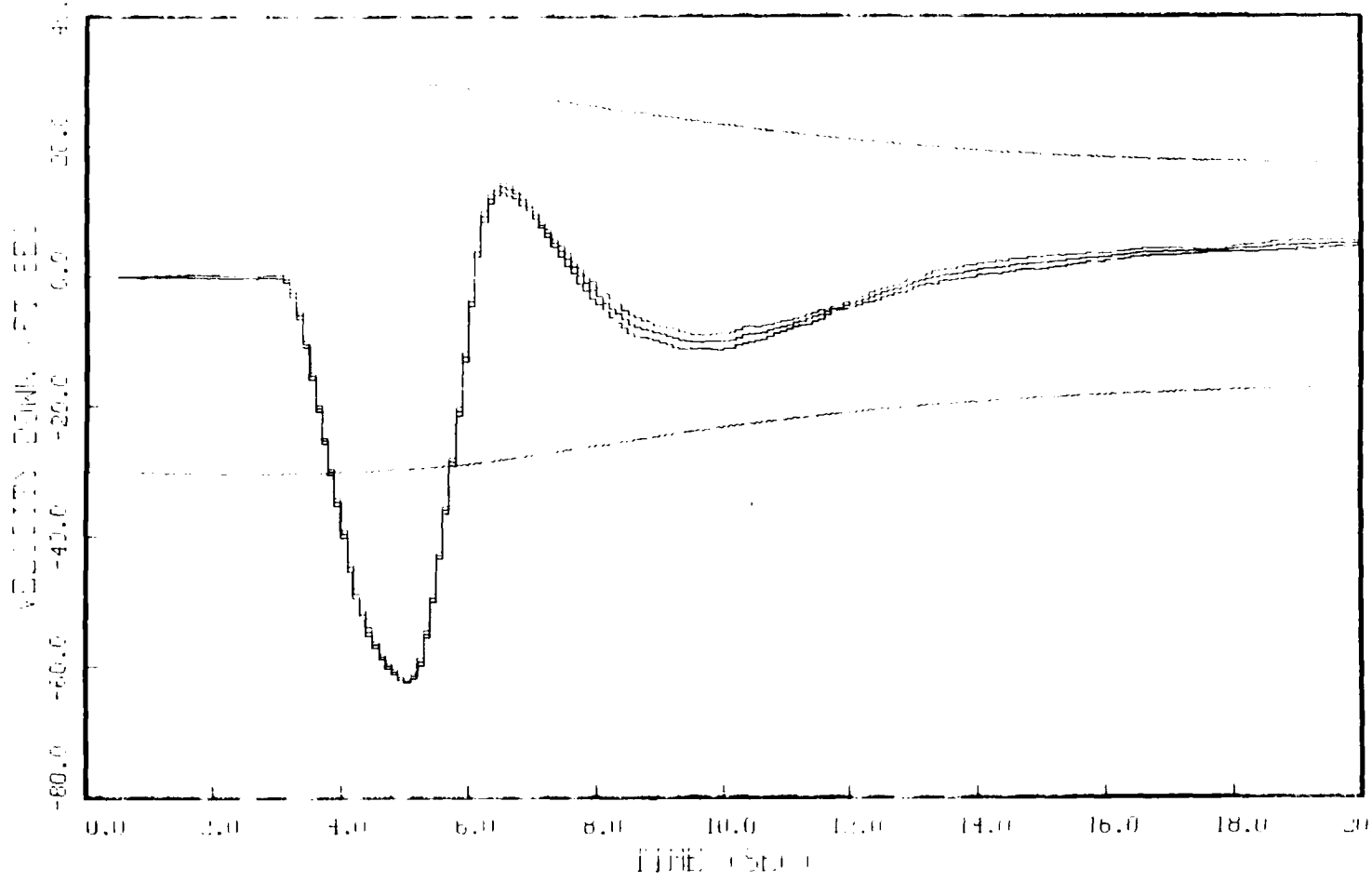

FIGURE II.6: [illegible] BEAM TRAJECTORY, 4 BEAMS: [illegible]

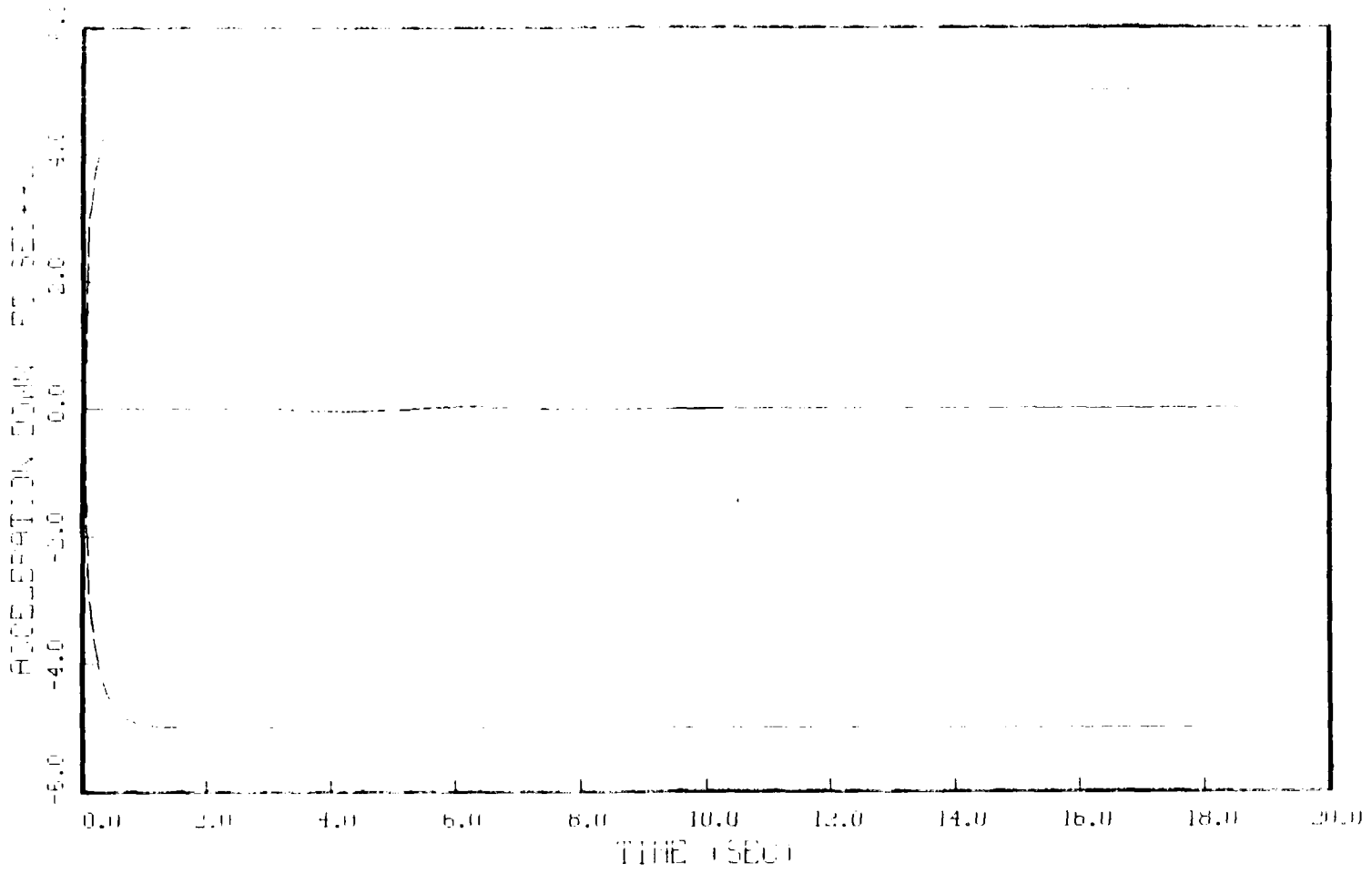

FIGURE II.9: GAUSS MARKOV MODEL, STATE 9, 5 RUNS, Q=100, MEAS NOISE INCREASED
BEAM TRAJECTORY, 4 MEAS: RNG, RNG RATE, SIN AZ & EL (R=3.0E 4 FOR AZ & EL)

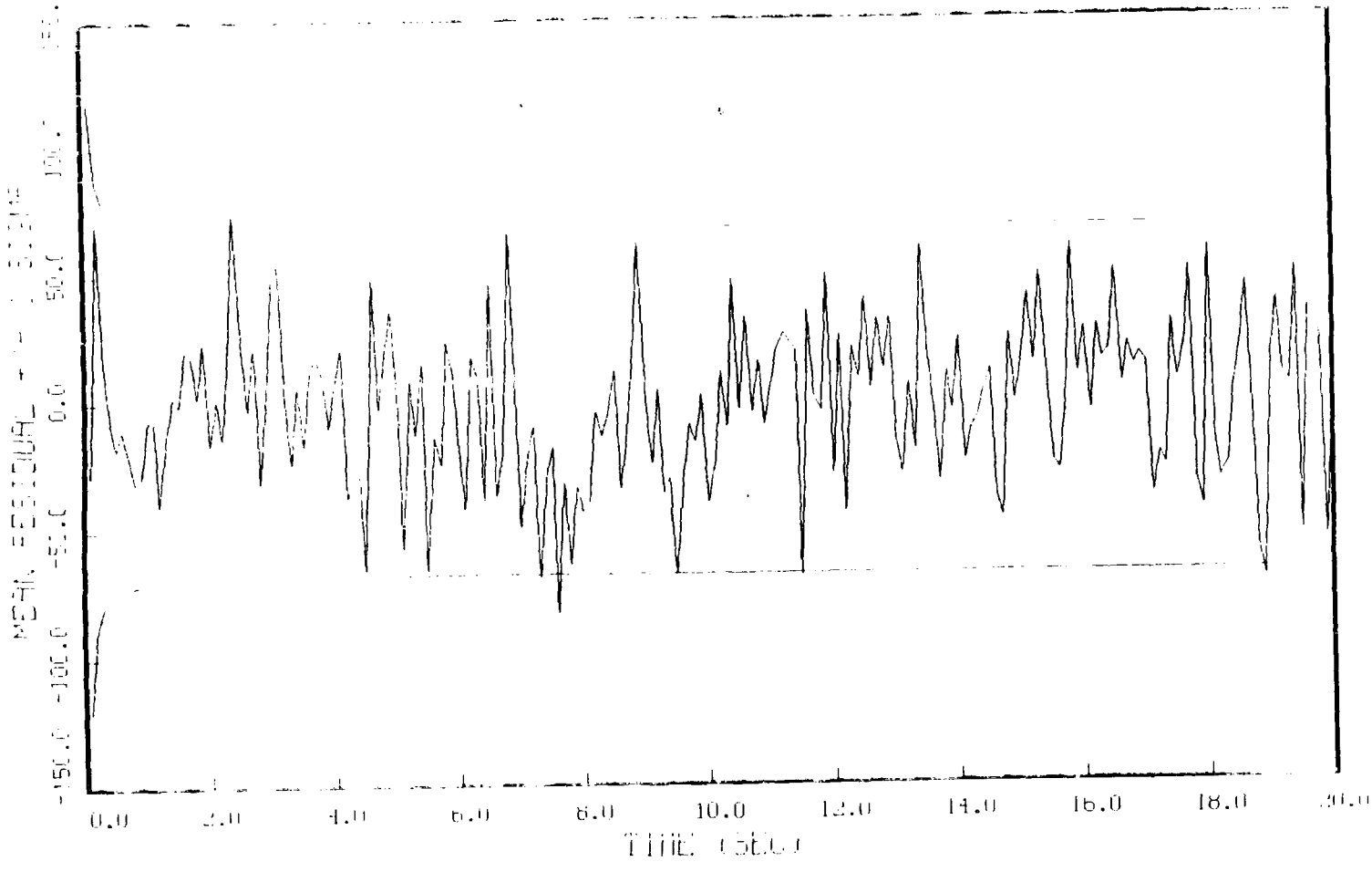

FIGURE B.11a: BASIS HARTLEY MODEL, RANGE RESIDUAL, 5 KNOTS
BEAM TRACKED DOPPLER, Q=100, R=4.0

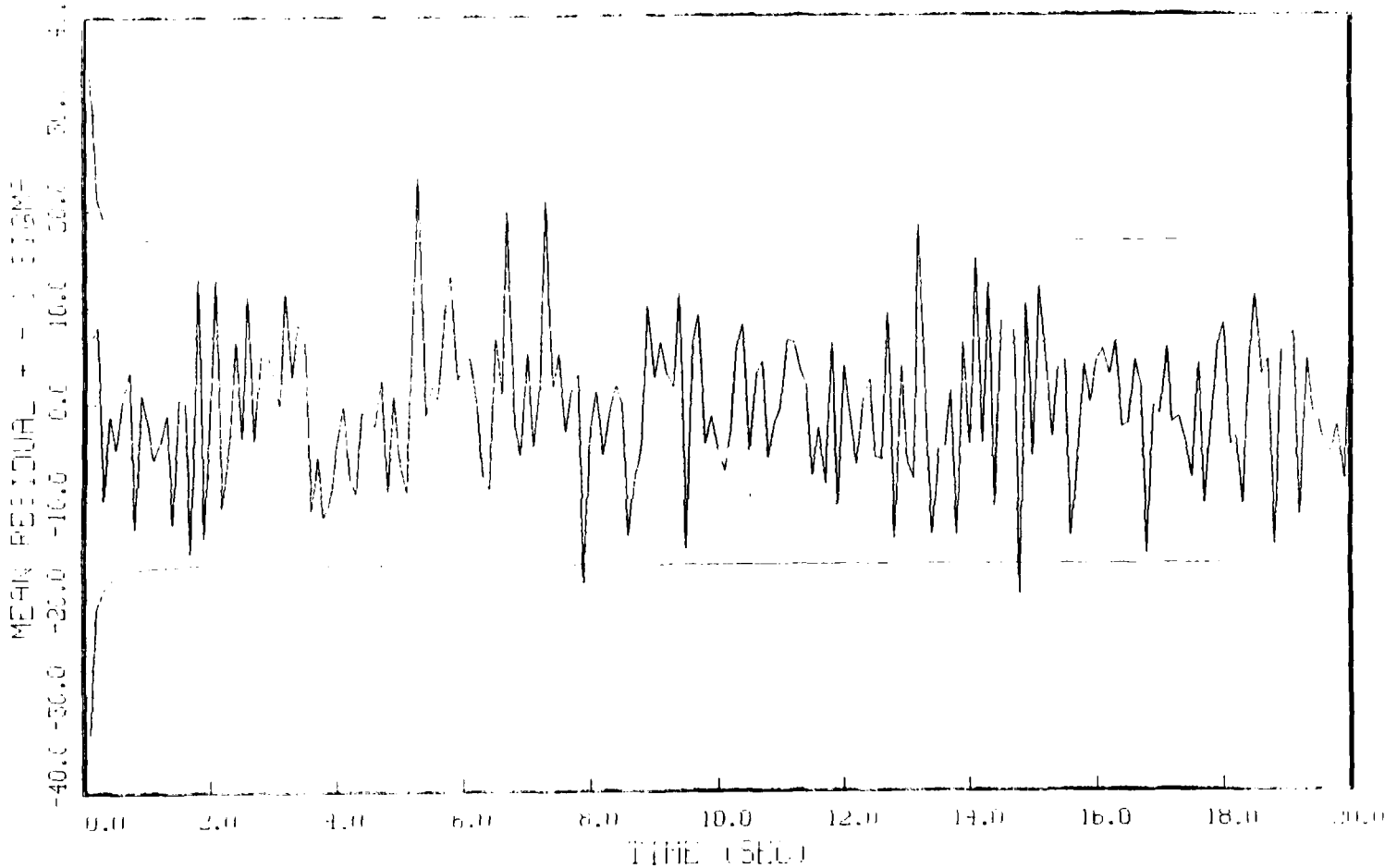

FIGURE H.11: CROSS RANGE VS. RANGE, RANGE RATE RESIDUAL, 5 POINT BEAM TRAJECTORY, S-100, R-250

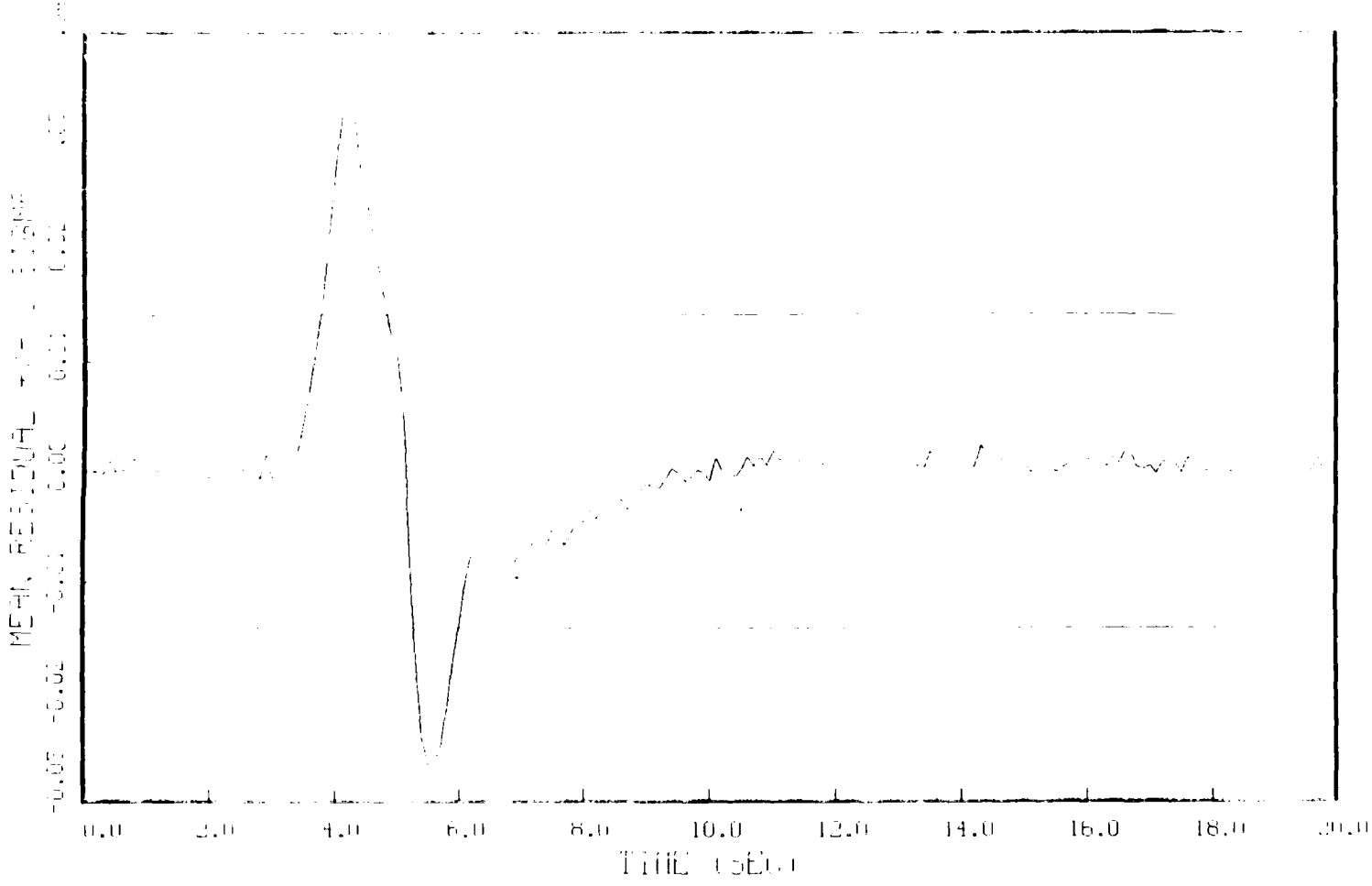

FIGURE B.12: [illegible] MODEL, SINE AZIMUTH RESIDUAL, 5 RUNS
BEAM TRAJECTORY, D-100, R=2.0E 04 (TRUE WHITE COMPONENT: R=1.1E 06)

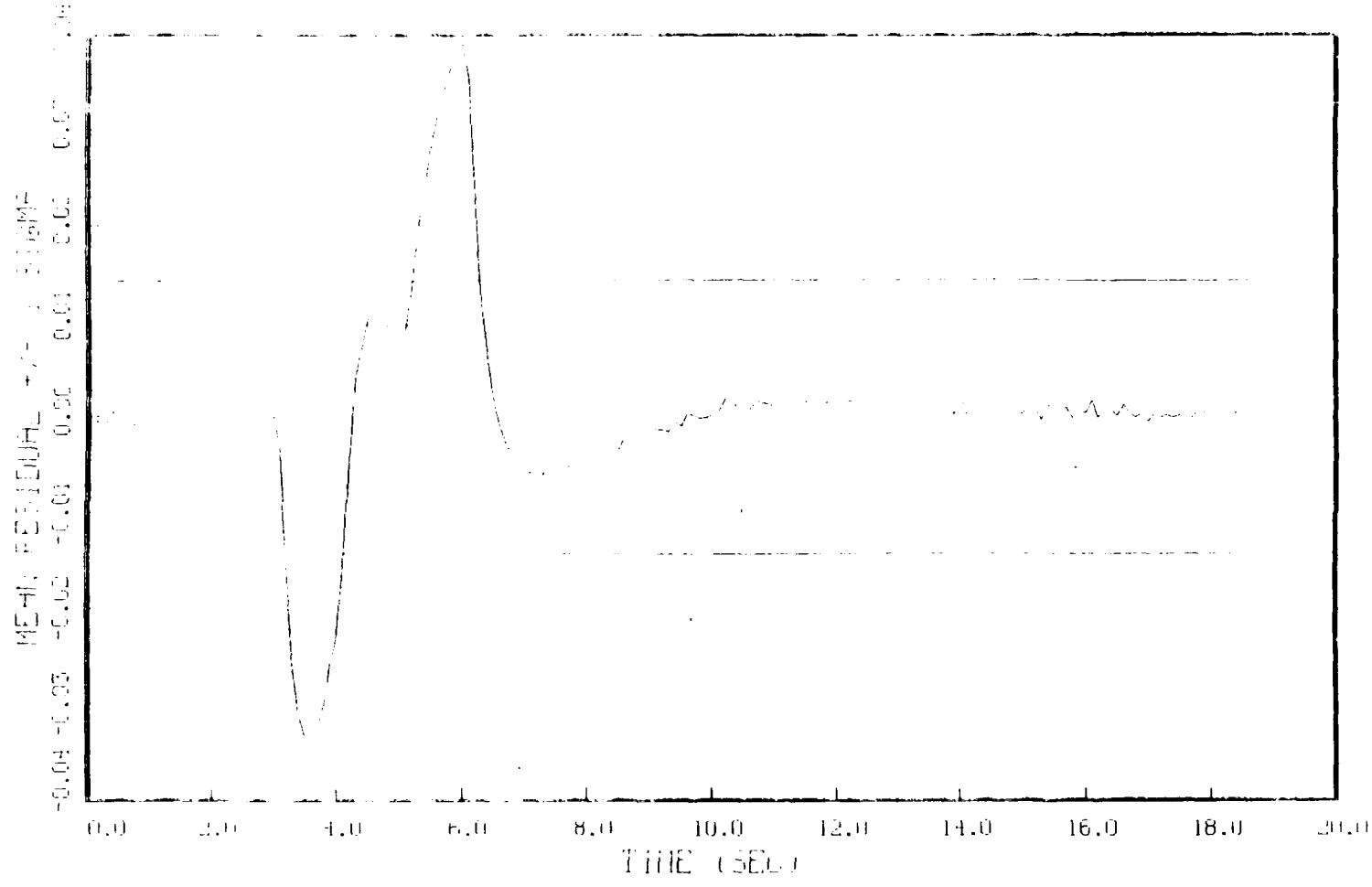

FIGURE [illegible]: [illegible] TRACK, SINE ELEVATION RESIDUAL, 5 RUNS
BEAM TEMPERATURE, 0-100, E-2.10E-04 TRUE WHITE COMPONENT: R-1.1E-06]

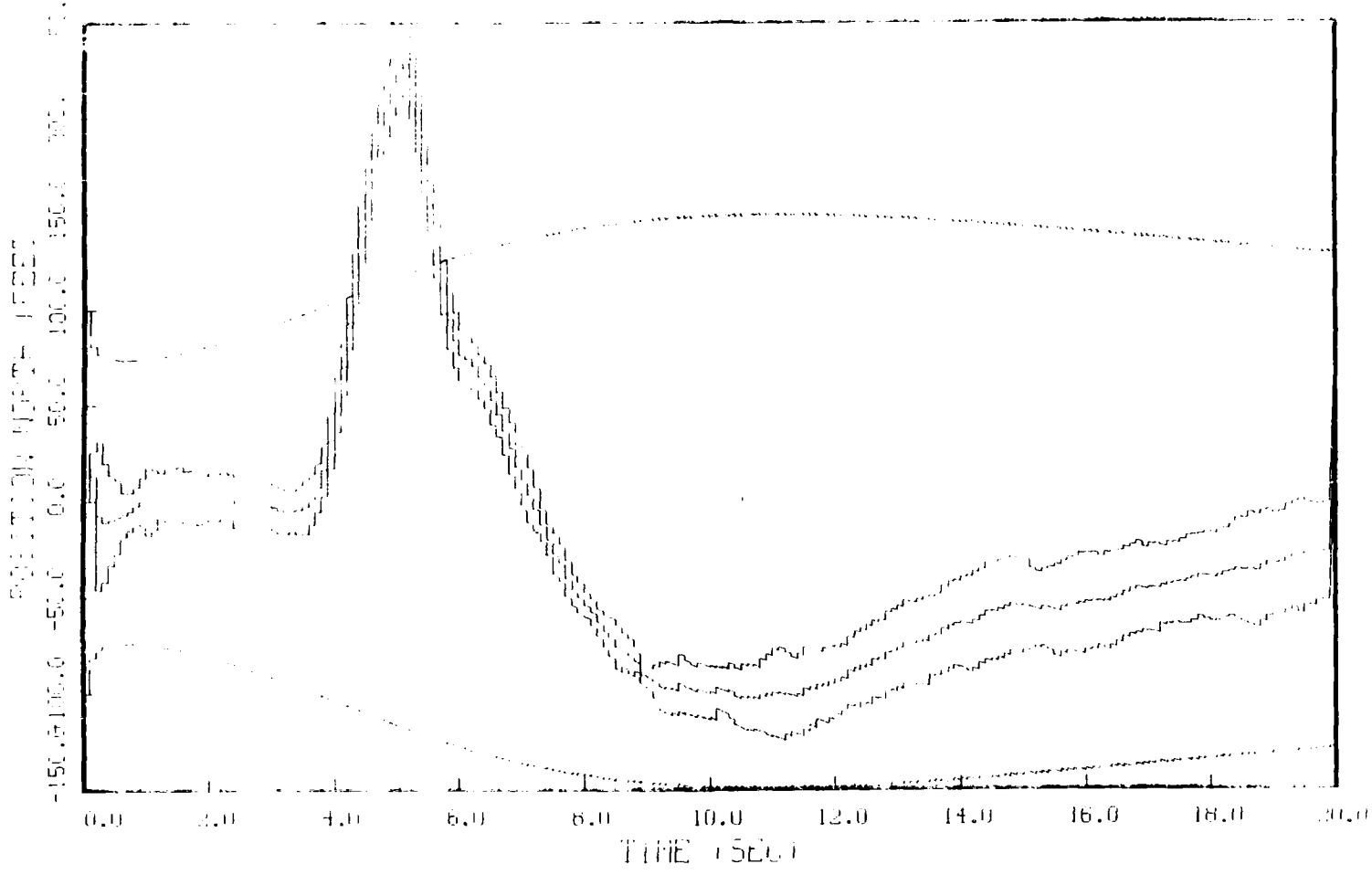

FIGURE II.11: SHUTTLE TRAJECTORY MODEL, STATE 1, 5 RUNS, Q=100, MEAS NOISE INCREASED
BEAM TRACKED OBJECT, 6 MEAS: DT=2.0E-4 FOR AZ & EL, R=1.E+04 FOR OMEGA DOT

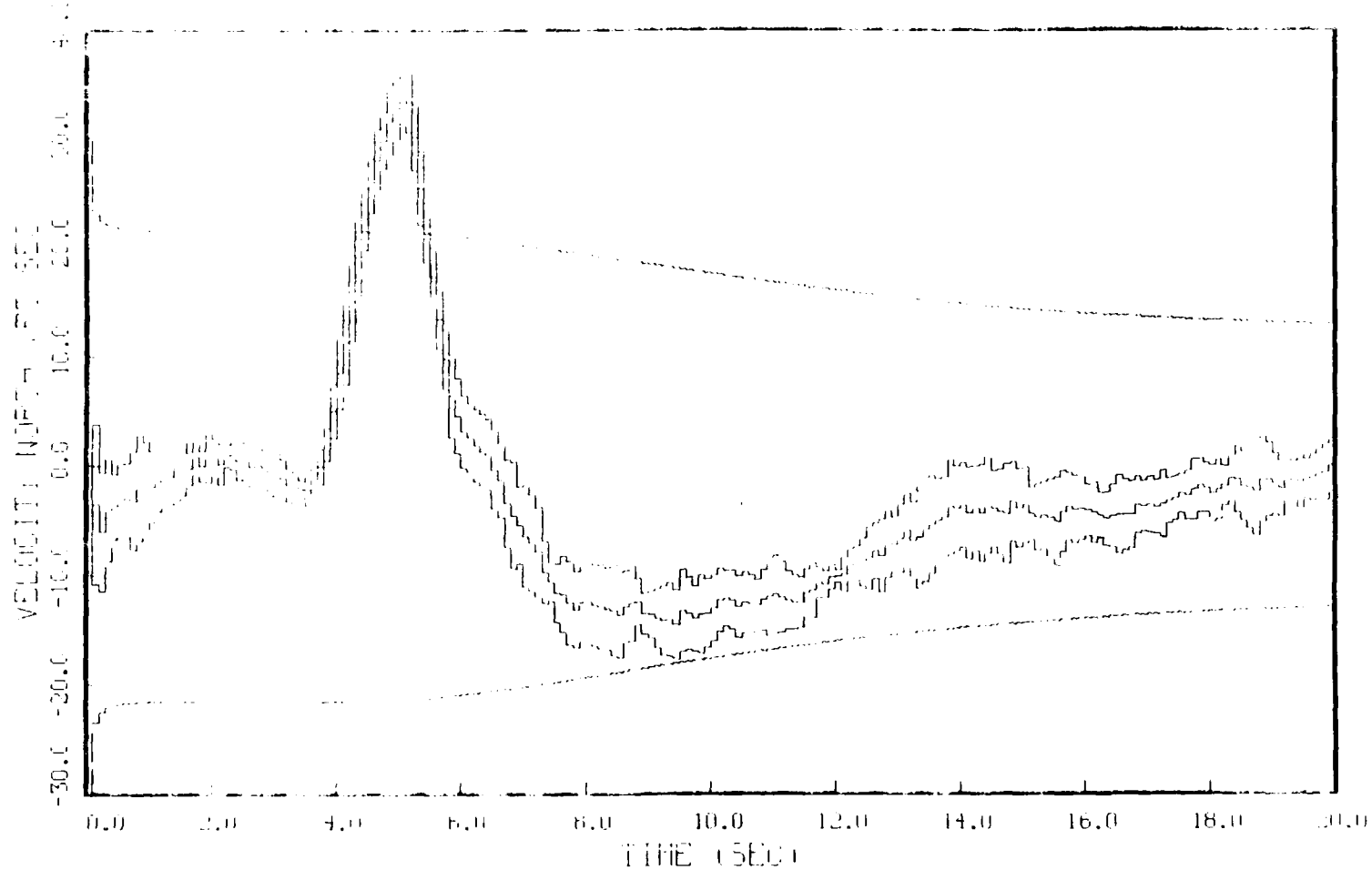

FIGURE B.1: [illegible] MODEL, STATE 2, 5 RUNS, Q=100, MEMS NOISE INCLUDED
BEAM TRACKER [illegible], G MEMS: Q=2.0E-4 FOR AZ & EL, R=1.2E-04 FOR OMEGA [illegible]

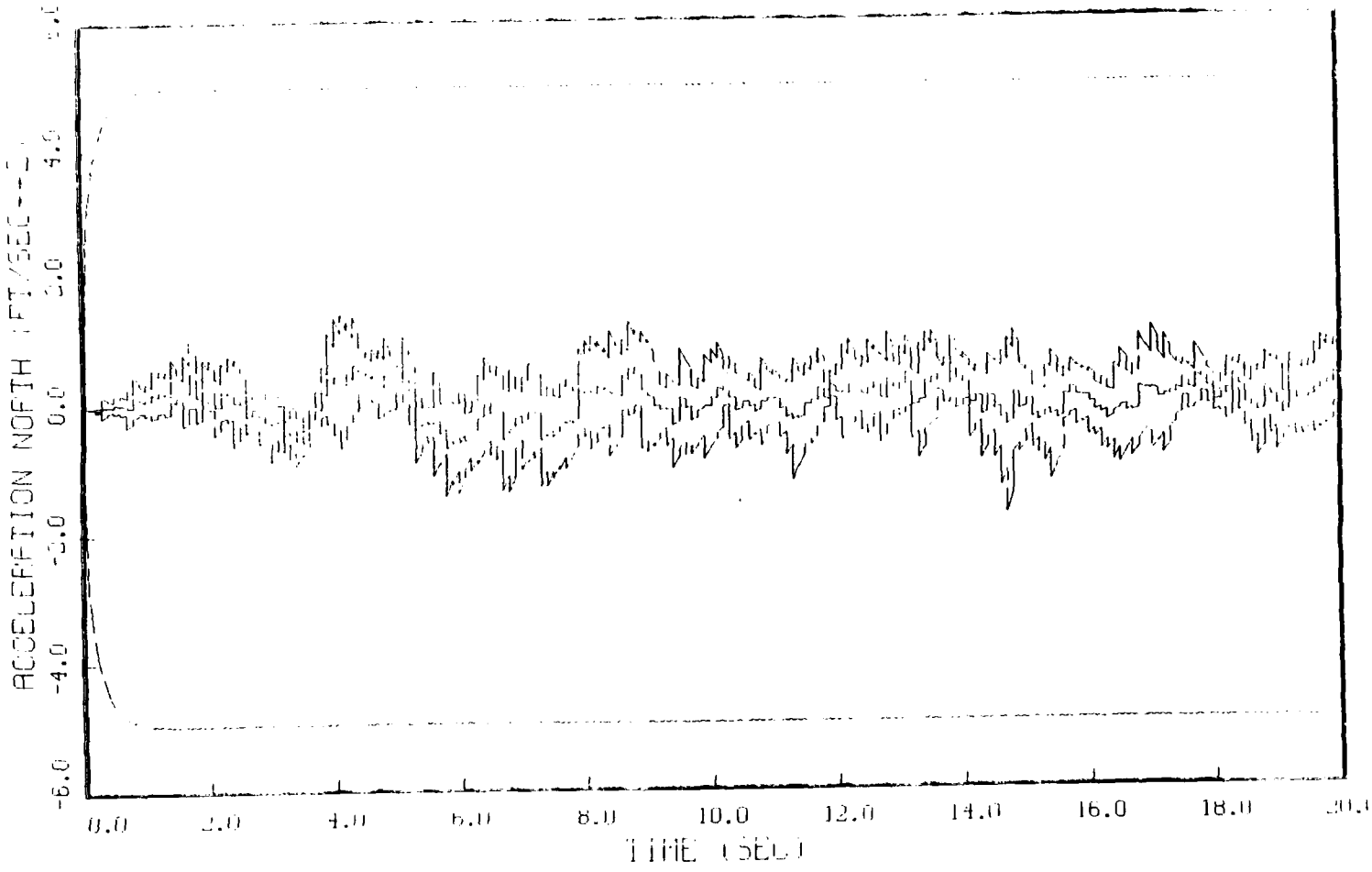

FIGURE B.16: GAUSS MARKOV MODEL, STATE 3, 5 RUNS, U=100, MEMS NOISE INCLUDED
BEAM TRAJECTORY, 6 BEAMS: TR=2.0E-4 FOR AZ & EL, R=1.2E-04 FOR OMEGA J & K

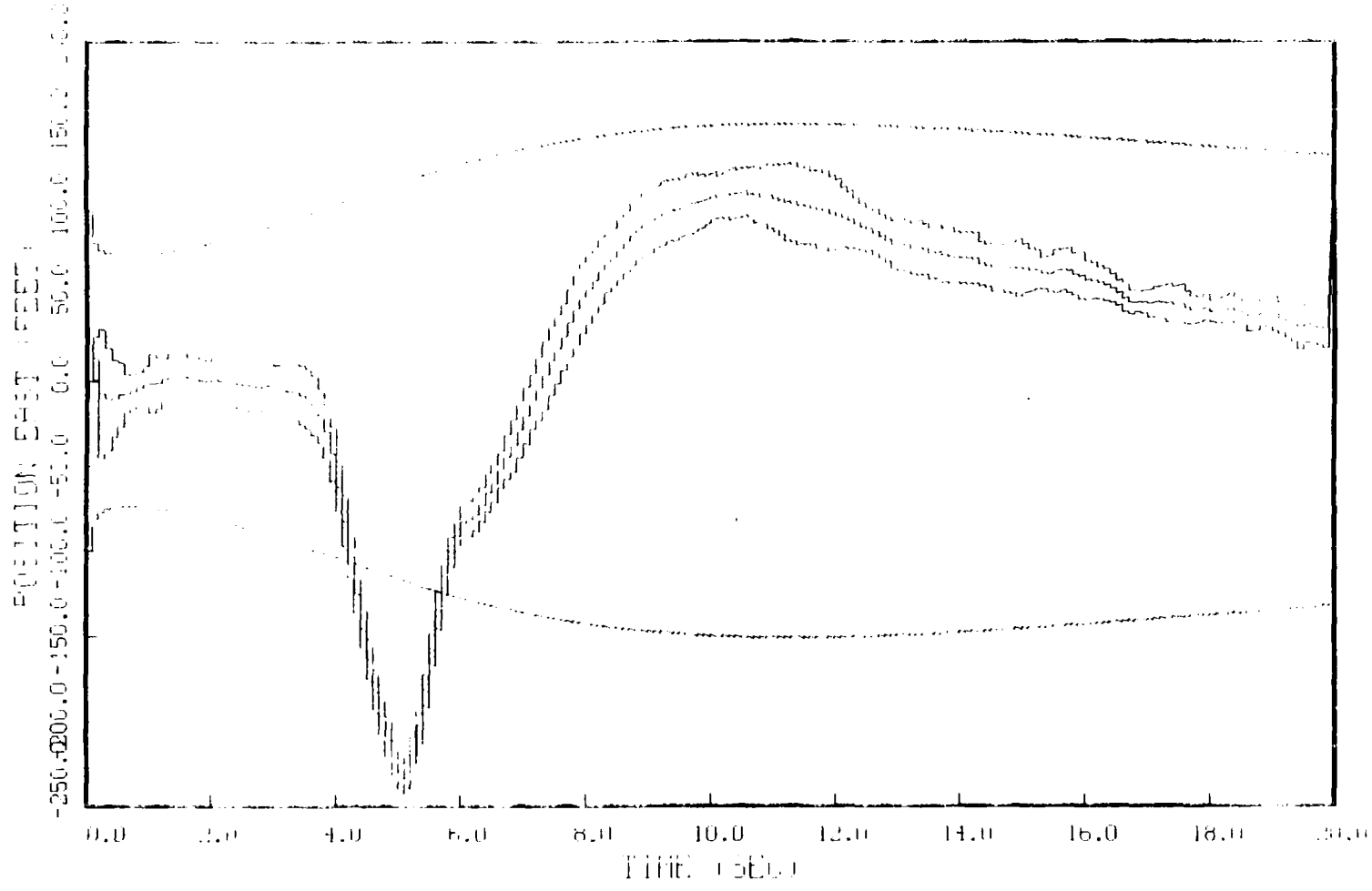

FIGURE H.1: GROUND TARGET MODEL, STATE 4, 5 RUNS, Q=100, NEAR NOISE INCLUDED
BEAM TRAJECTORY, Q ERROR: QR=2.0E-4 FOR AZ & EL, R=1.2E-04 FOR OMEGA

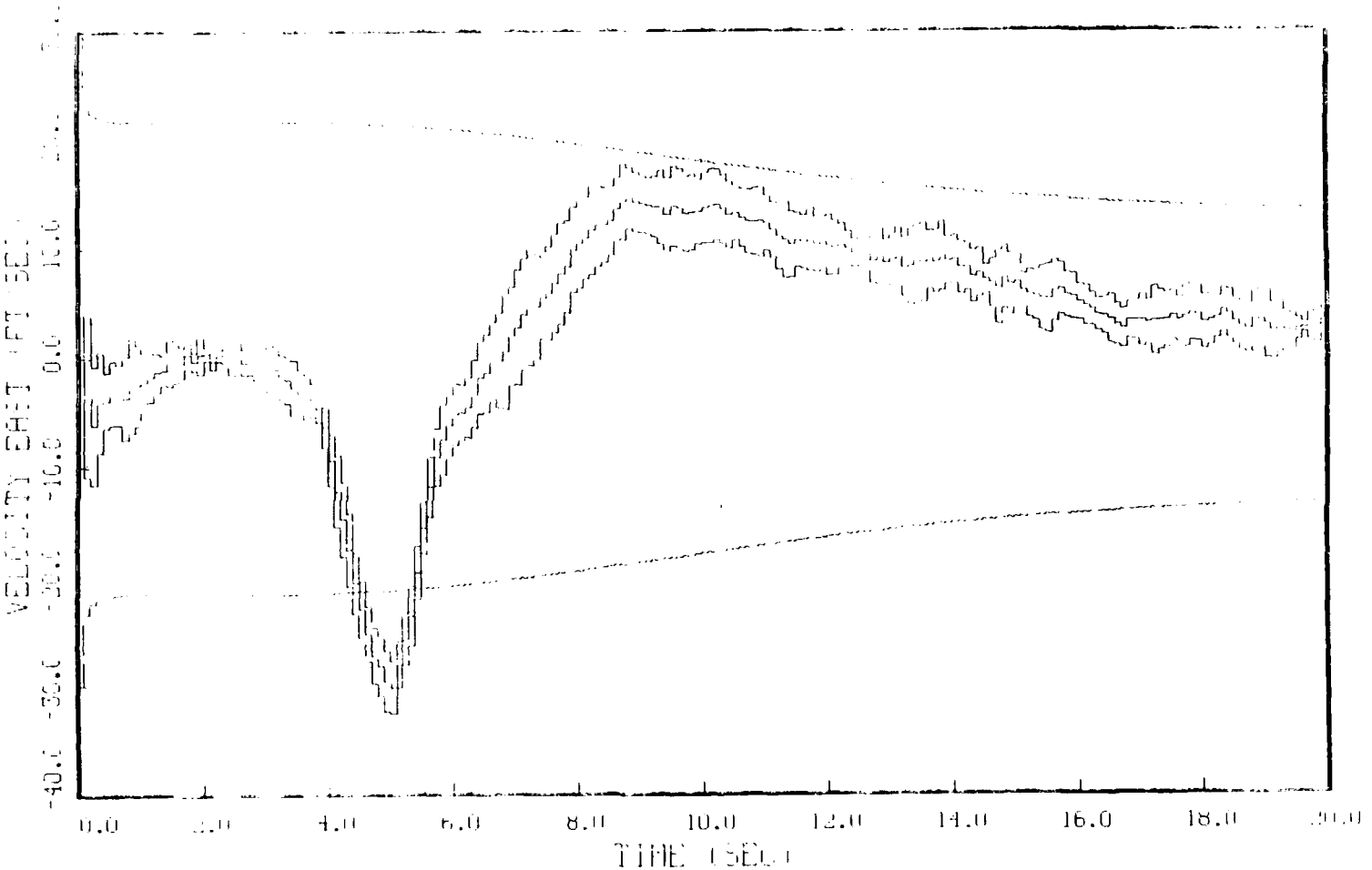

FIGURE H.15: CROSS TARGET MODEL, STATE 5, 5 RUNS, Q=100, MEMS NOISE INCLUDED
ECHO TRAJECTORY, 6 MEMS: QR=2.0E-4 FOR AZ & EL, R=1.2E-04 FOR OMEGA Y & Z

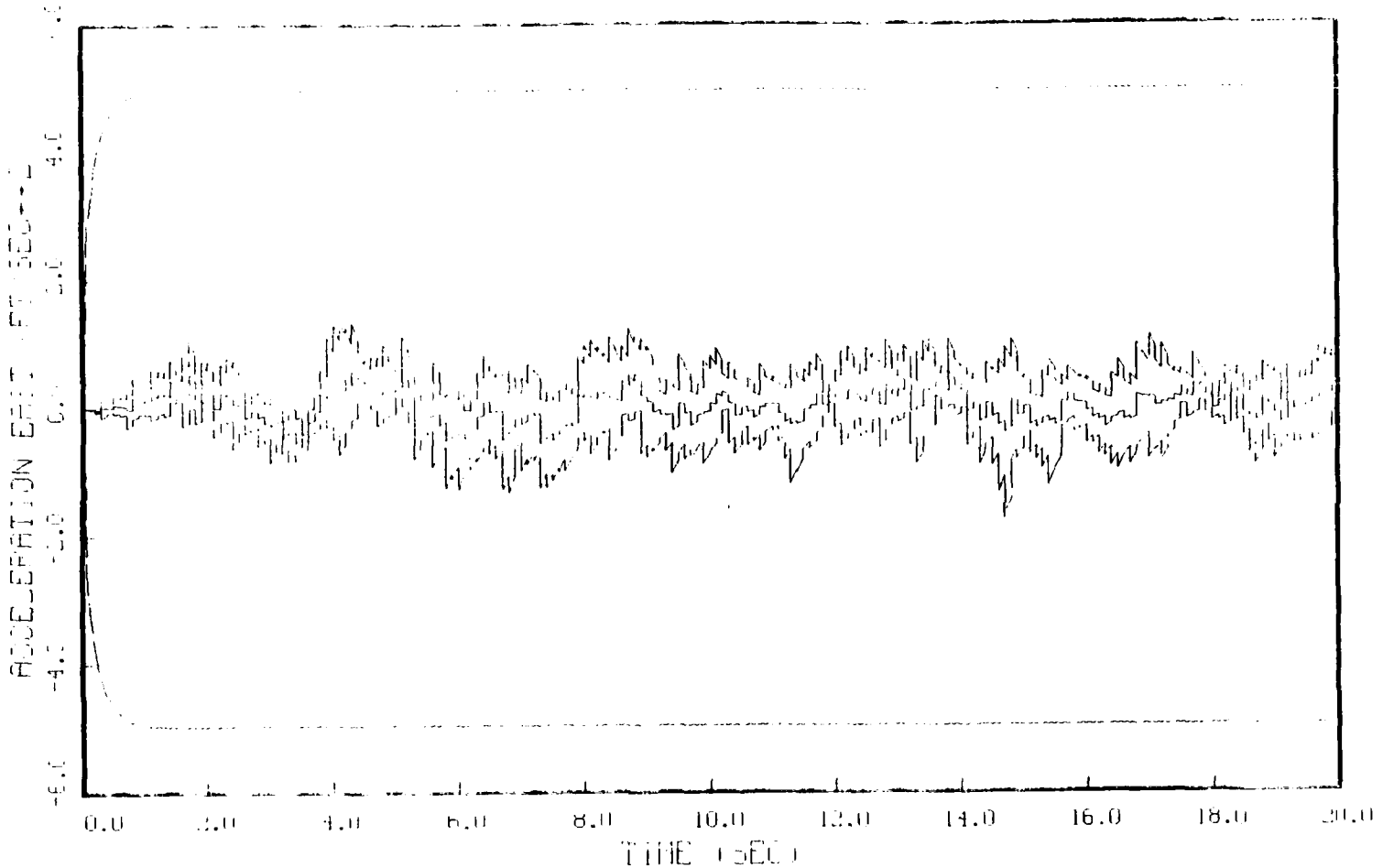

FIGURE II.20: [illegible] MODEL, STATE 6, 5 RUNS, 0-100, MEAS NOISE INCREASED
BEAM TRAJECTORY, 6 MEAS: [illegible] FOR AZ & EL, R=1.2E-04 FOR OMEGA 1 & 11

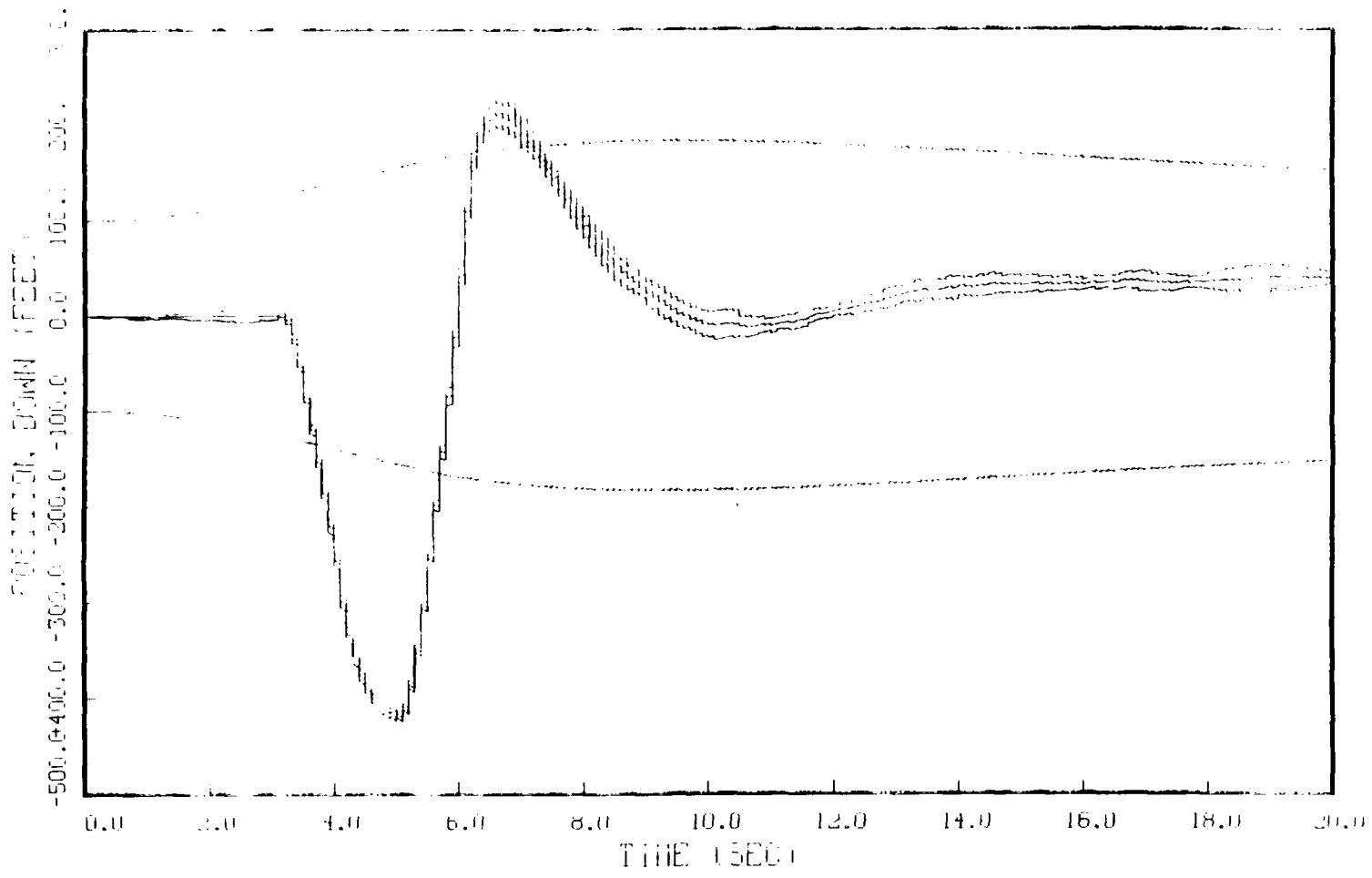

FIGURE 11.3: GAUSS MARKOV MODEL, STATE 7, 5 RUNS, Q=100, MEMS NOISE INCREMENTED
BEAM TRAJECTORY, 6 MEMS: TR=2.0E-4 FOR AZ & EL, K=1.2E-04 FOR OMEGA Z & Y

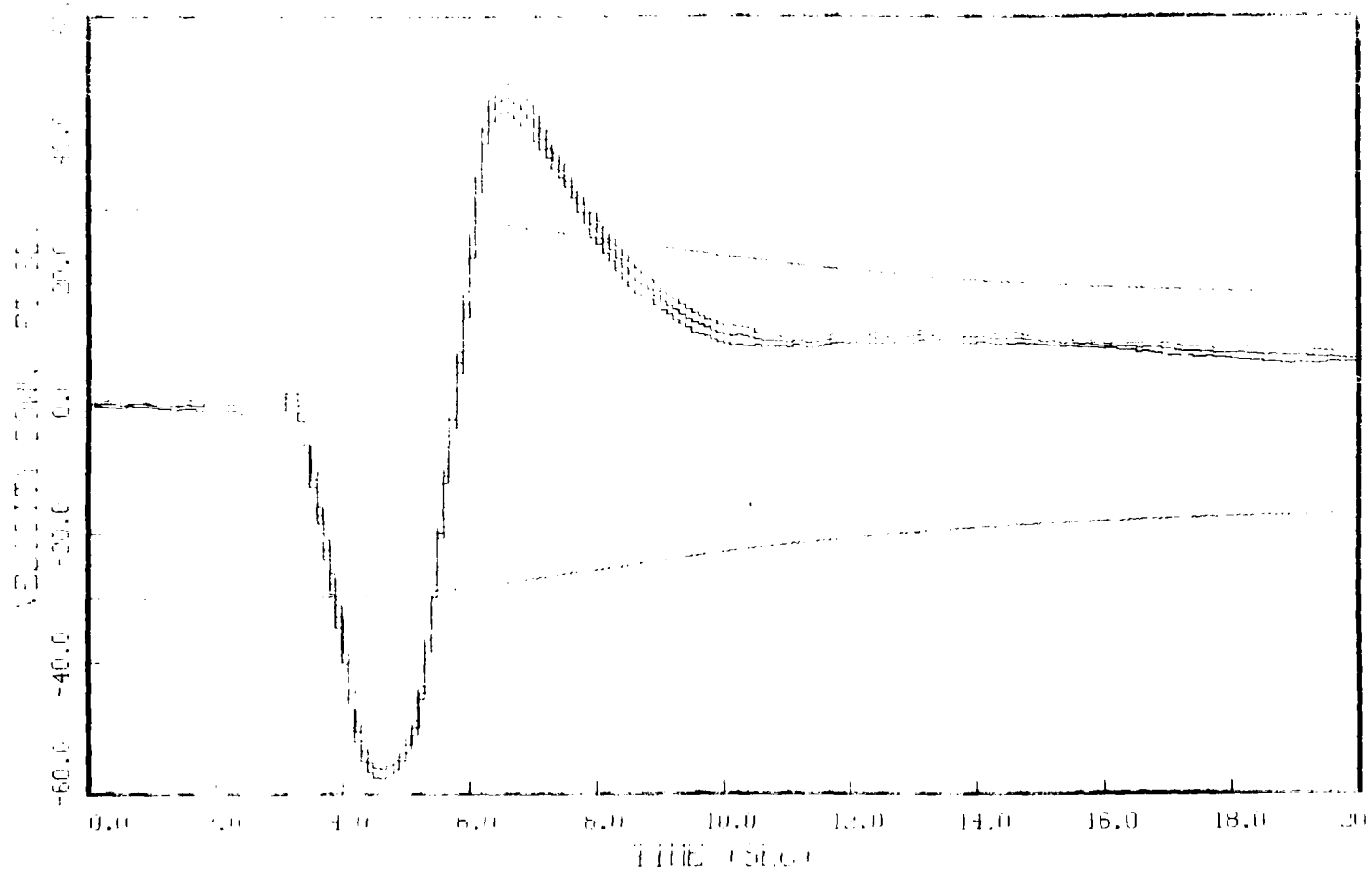

FIGURE [illegible]. [illegible] DOUBLE, STATE 6, 5 RUNS, 0-180, MEAS NOISE INCREASED
BEAM TRACK DATA, 5 RUNS: [illegible] FOR AZ & EL, [illegible] FOR OMEGA X & Y

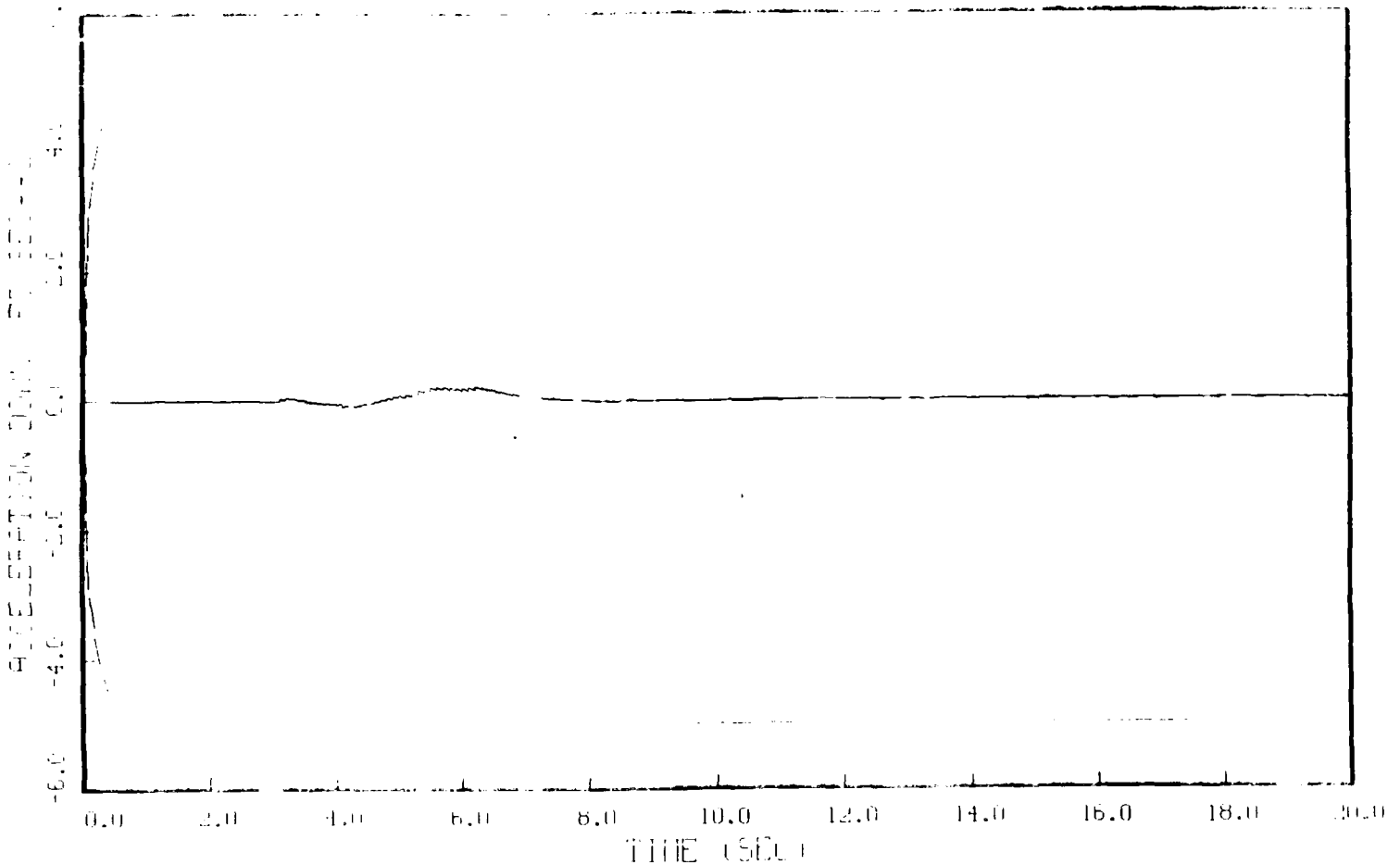

FIGURE B.23. [illegible] STATE 9, 5 RUNS, 0-100, MEAS NOISE INCLUDED
BEAM TRAJECTORY, 6 DEGS: [illegible] FOR AZ & EL, [illegible] FOR OMEGA

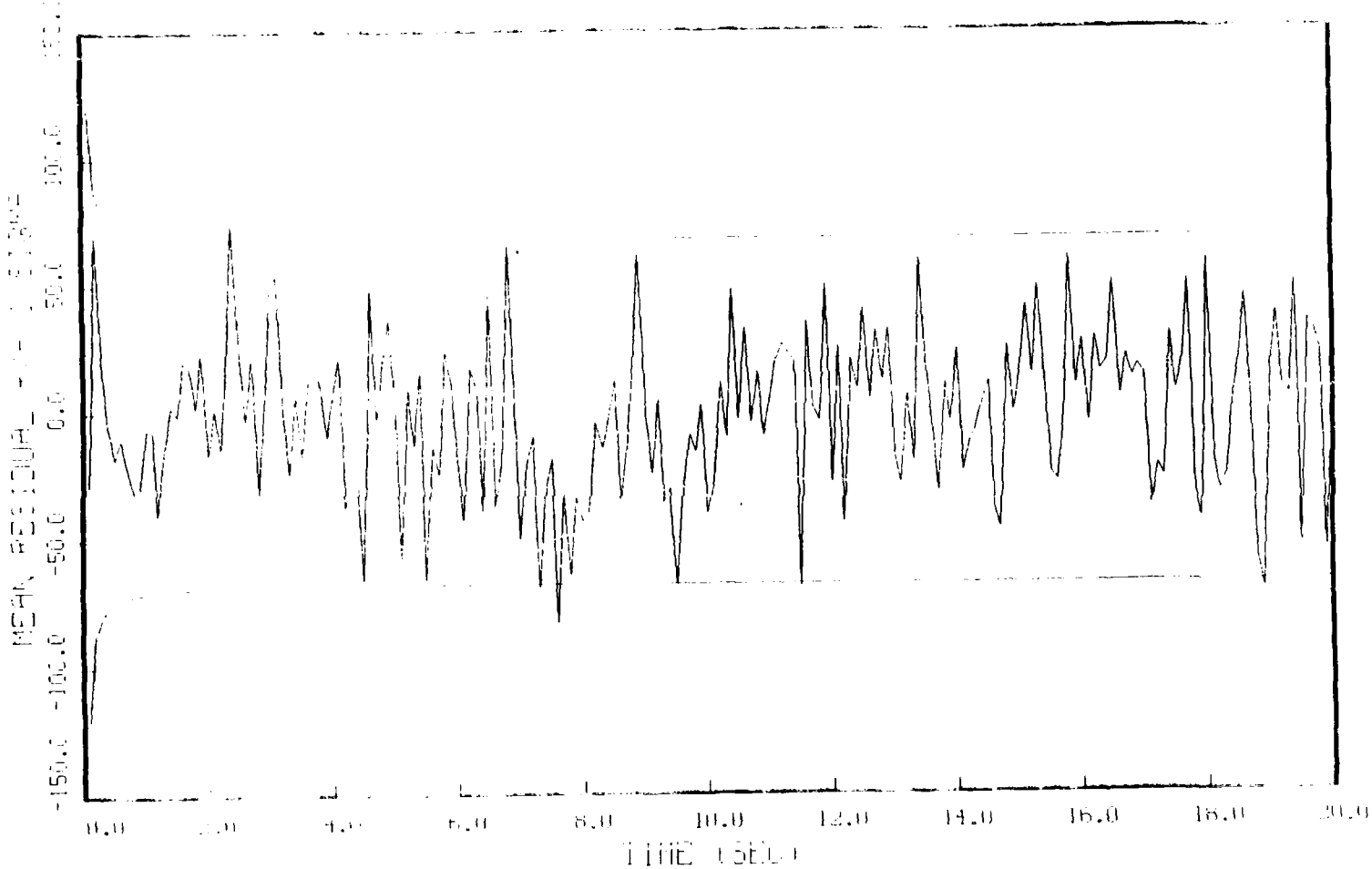

FIGURE [illegible]. [illegible] MODEL, RANGE RESIDUAL, 5 RUNS
BOEING TRANSPORT SIM., D-1001, R-14859

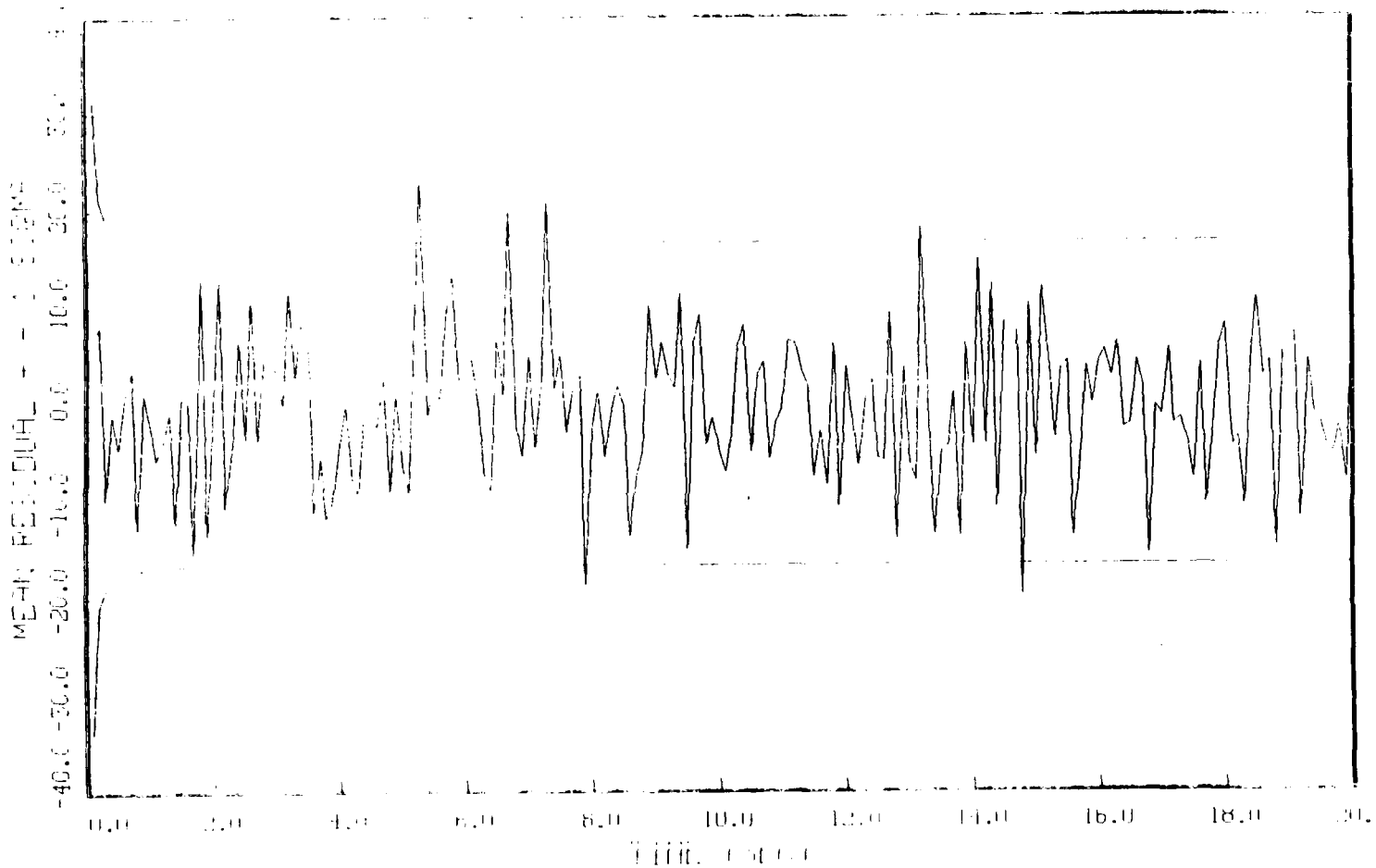
-40.0
-30.0
-20.0
-10.0
0.0
10.0
20.0
0.0
2.0
4.0
6.0
8.0
10.0
12.0
14.0
16.0
18.0
20.0

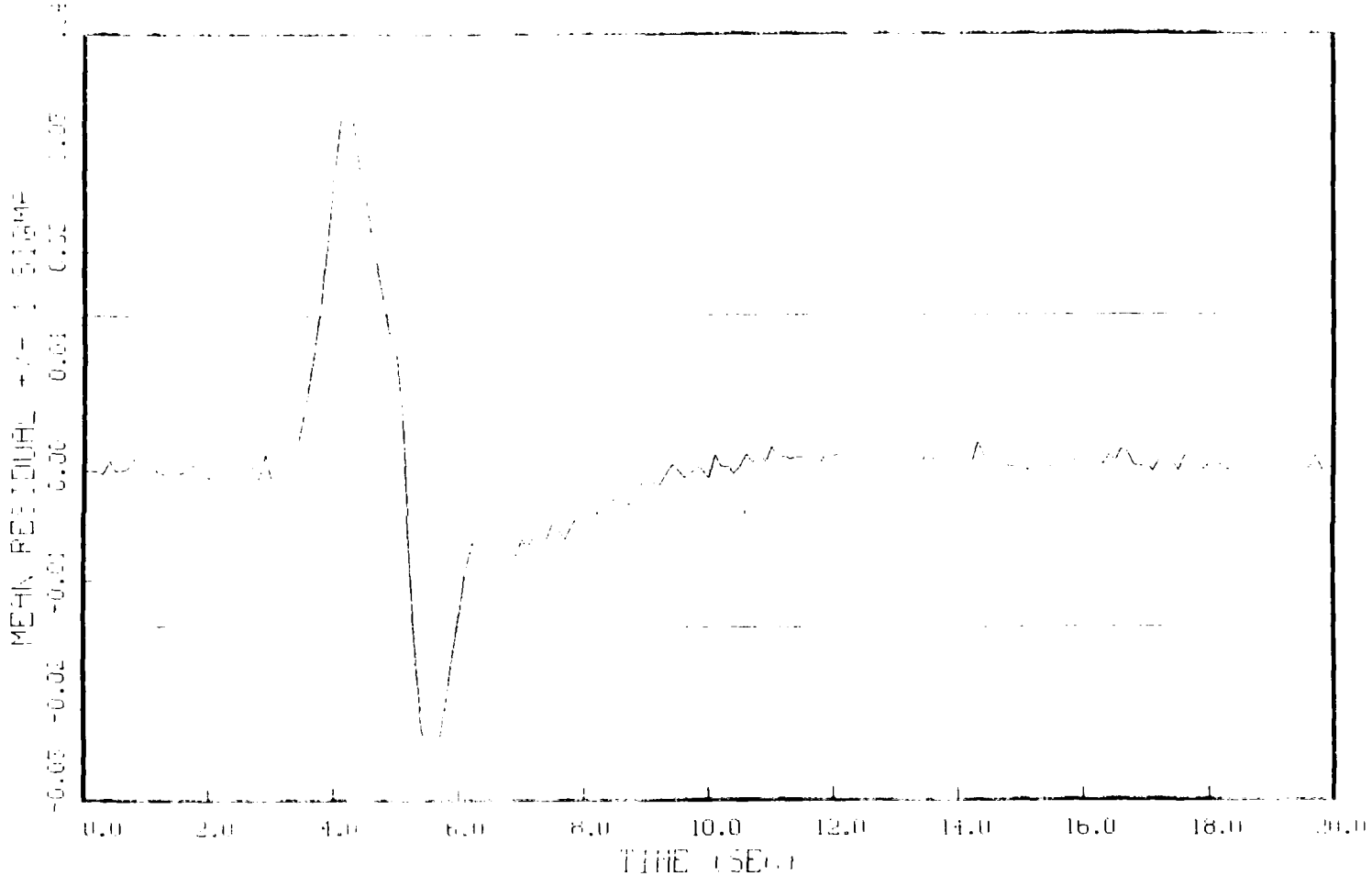

FIGURE B.2a: GAUSS-MARKOV MODEL, SINE AZIMUTH RESIDUAL, 5 RUNS
BEAM TRAJECTORY, Q=100, R=2.0E-11 TRUE WHITE COMPONENT: R=1.1E-06

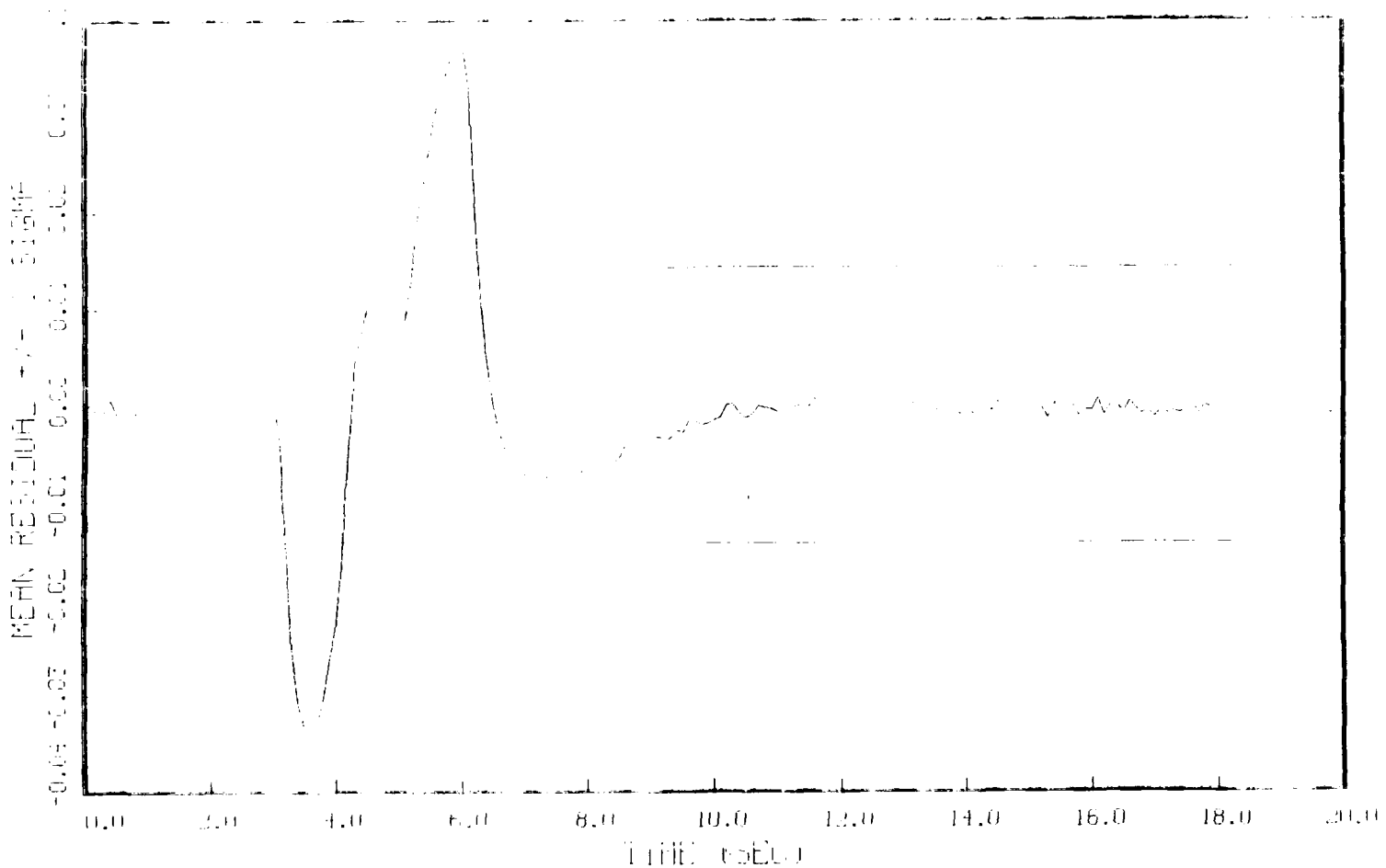

FIGURE H.[illegible] BEAM TRAJECTORY, D=100, P=2.0E-04 TORR, WHITE COMPONENT: R=1.1E-05

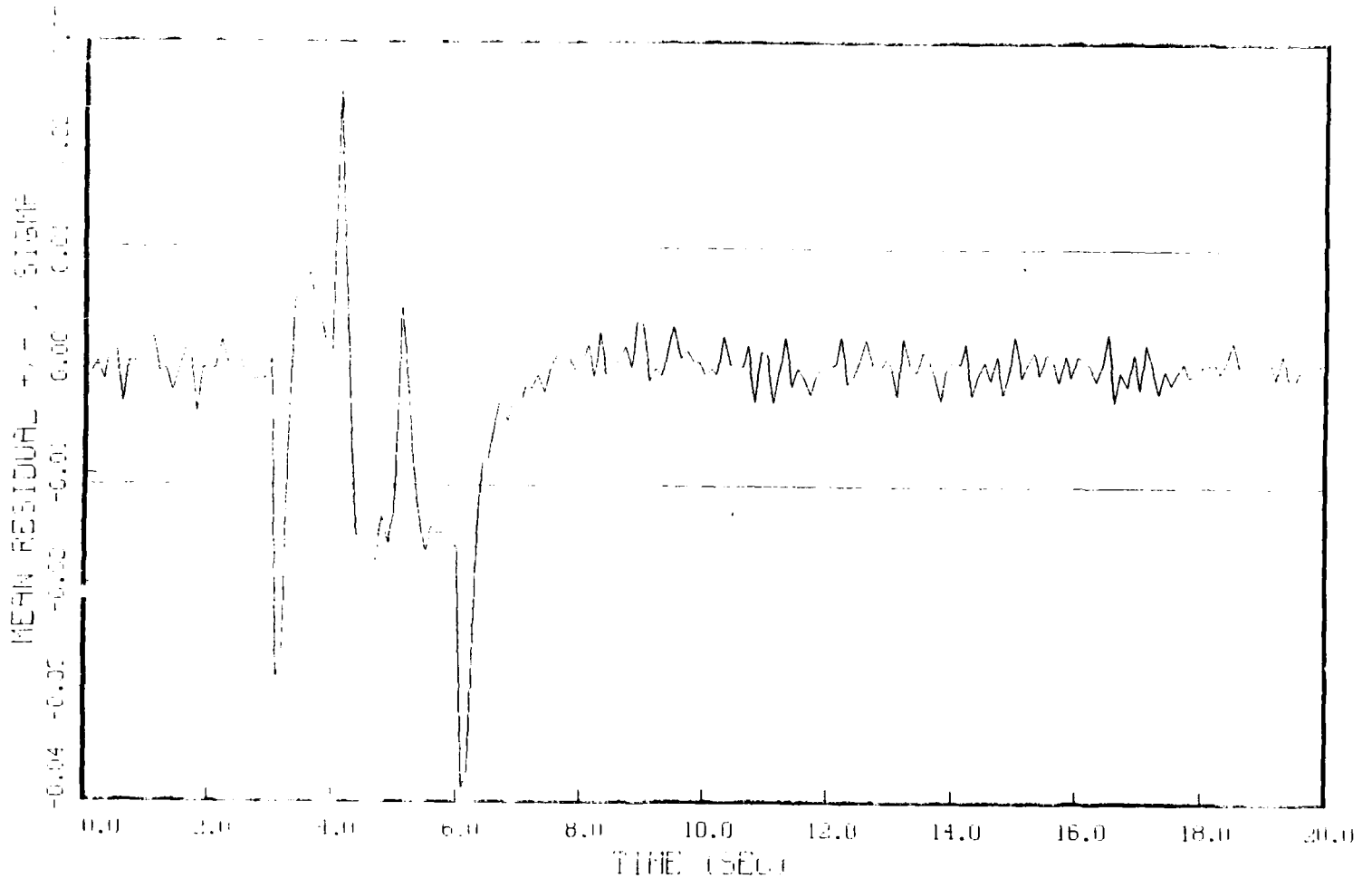

FIGURE II.2 : SOURCE TRACKING MODEL, GREEN 3 RESIDUAL, 5 RUNS
BEAM TRUE TOPT: 0-100, I-1.2E-04 CTRUE WHITE COMPONENT: R-1.2E-05)

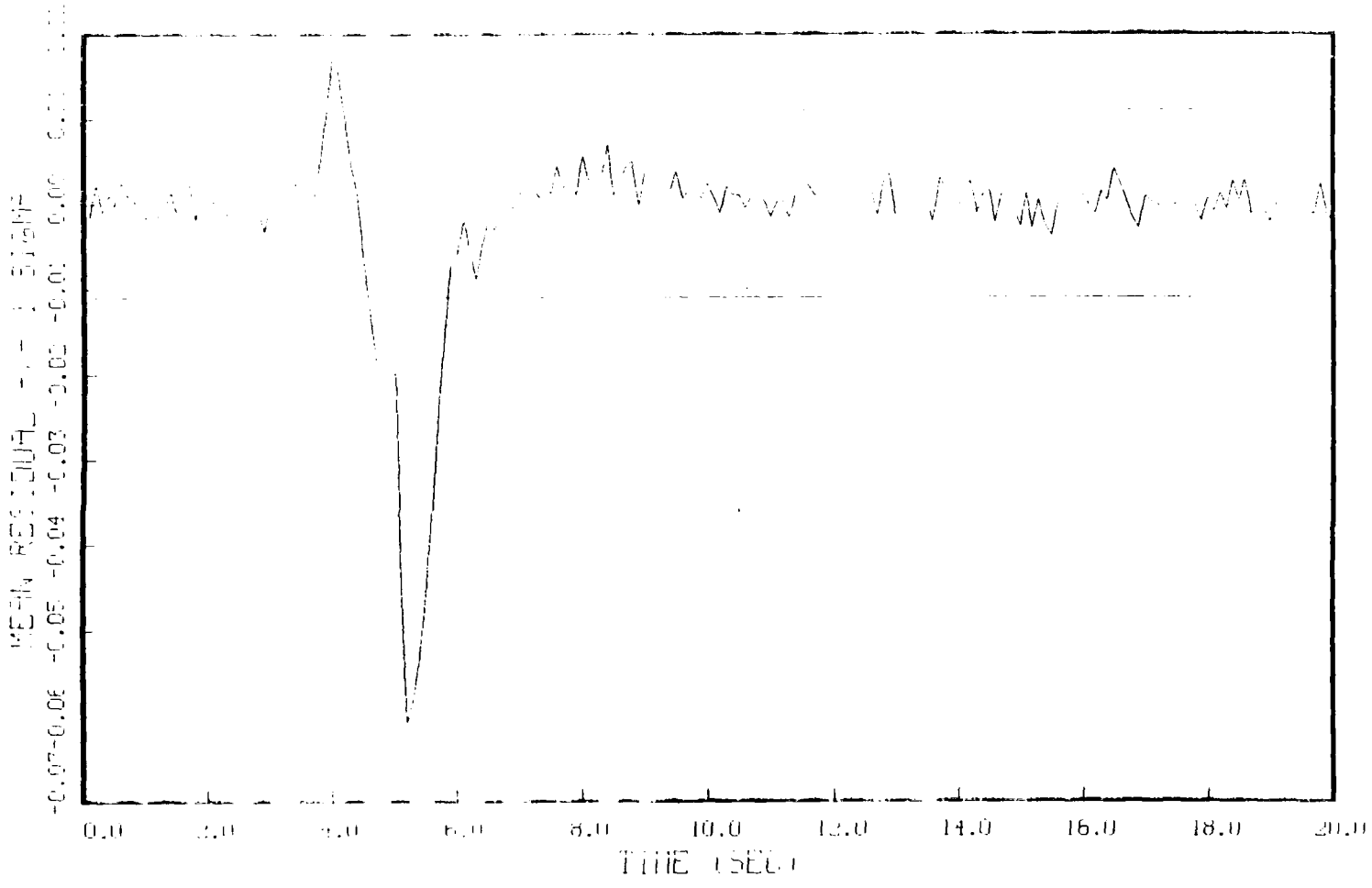

FIGURE II.... [illegible] MODEL, OMEGA K RESIDUAL, 5 RUNS
BEAM TRAJECTORY 1, U=100, R=1.2E 04 (TRUE WHITE COMPONENT: R=1.2E-05)

Appendix I

Filter Adaptation to F-4E/G Roll Rate

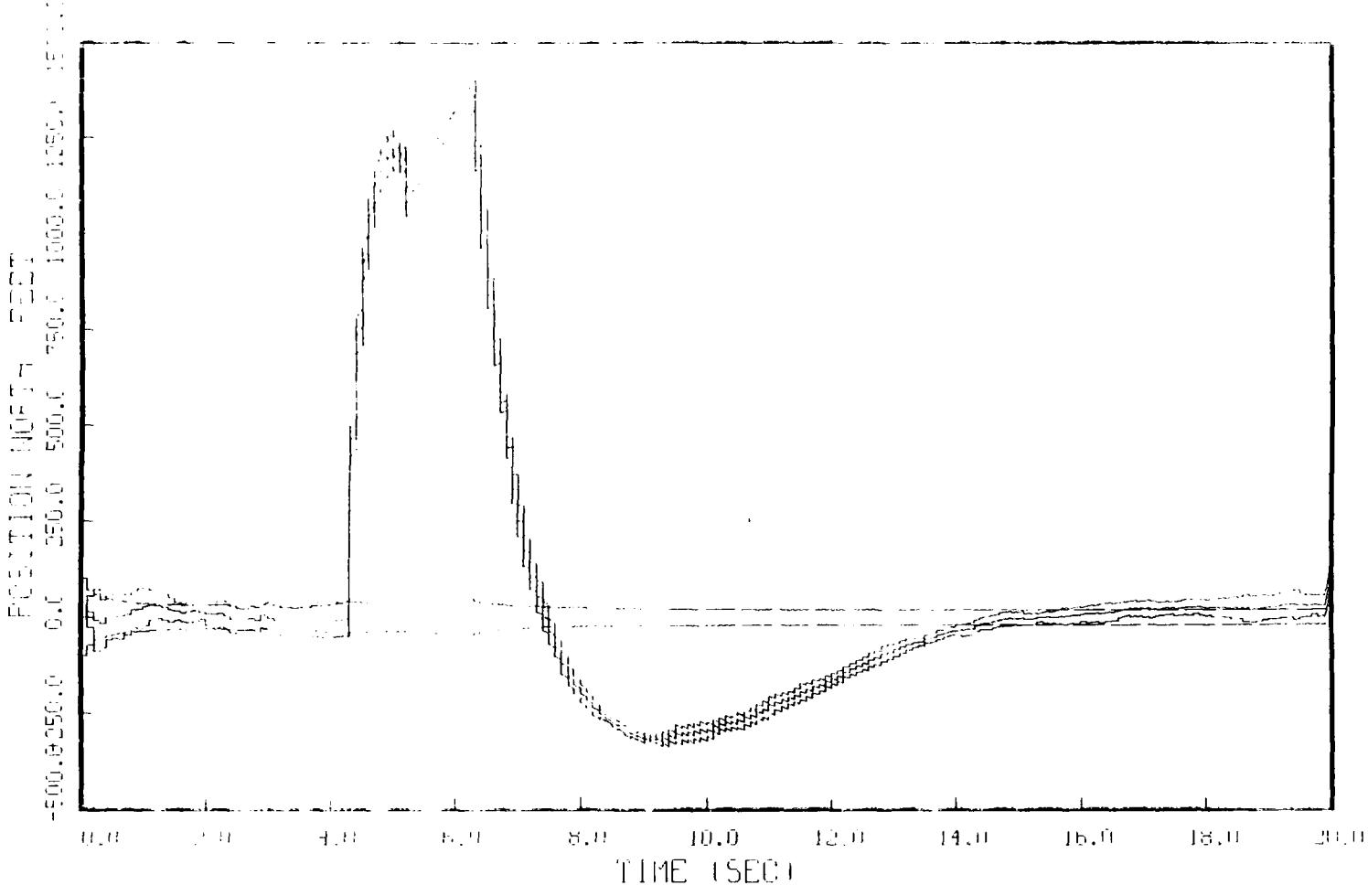

FIGURE I.1: GAUSS MARKOV MODEL, STATE 1, 5 RUNS, Q=100, ADAPTIVE R
BEAM TRACK TEST. NEAS: CK=5.0E-4 FOR AZ & EL DURING ROLL, ELSE 1.1E-06

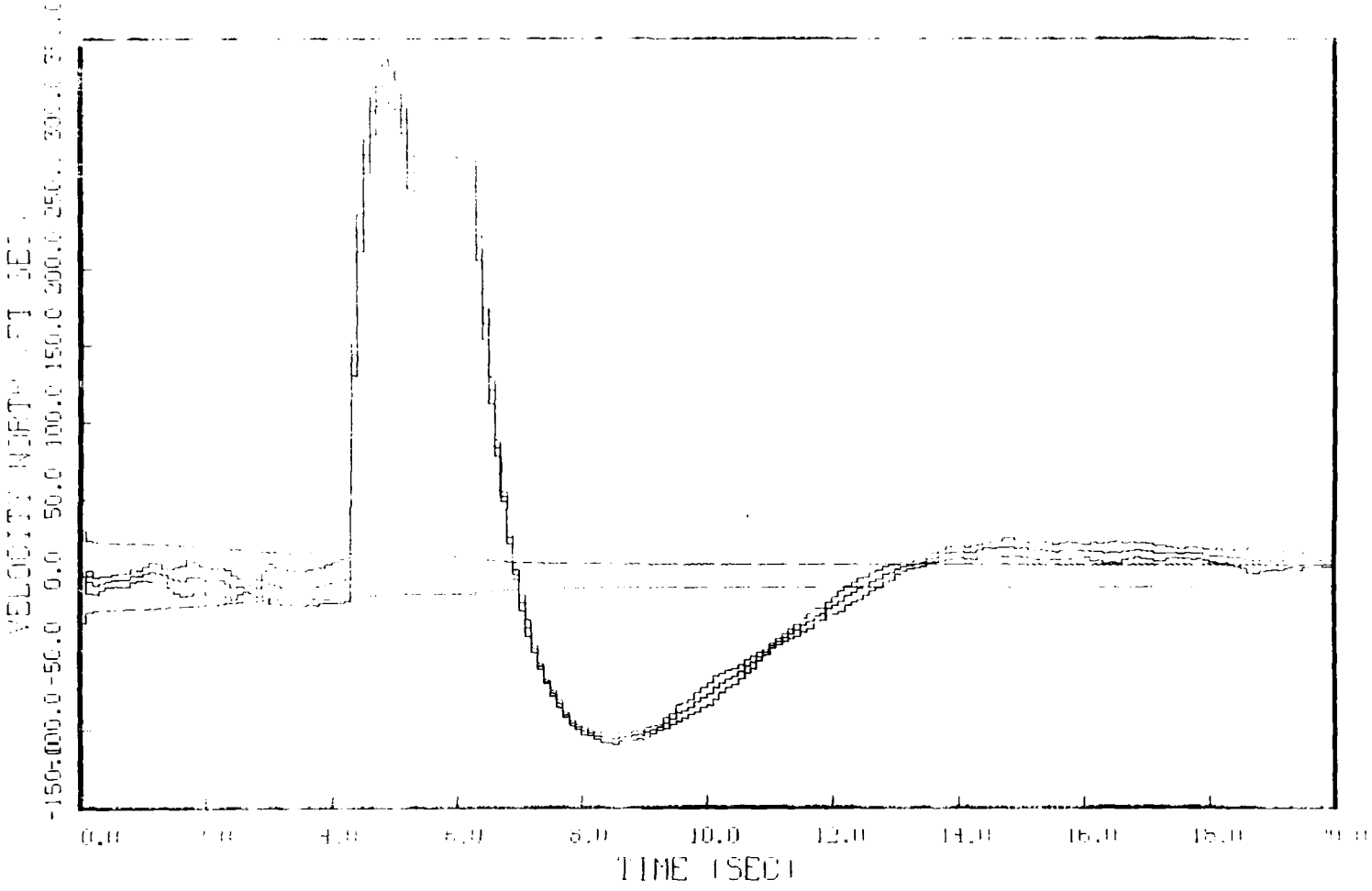

FIGURE I.2: [illegible] MARKOV MODEL, STATE 2, 5 RUNS, 0-100, ADAPTIVE R
BEAM TRACKING. NOTE: [illegible]K=3.0E-4 FOR AZ & EL DURING MODEL, ELSE 1.1E-07

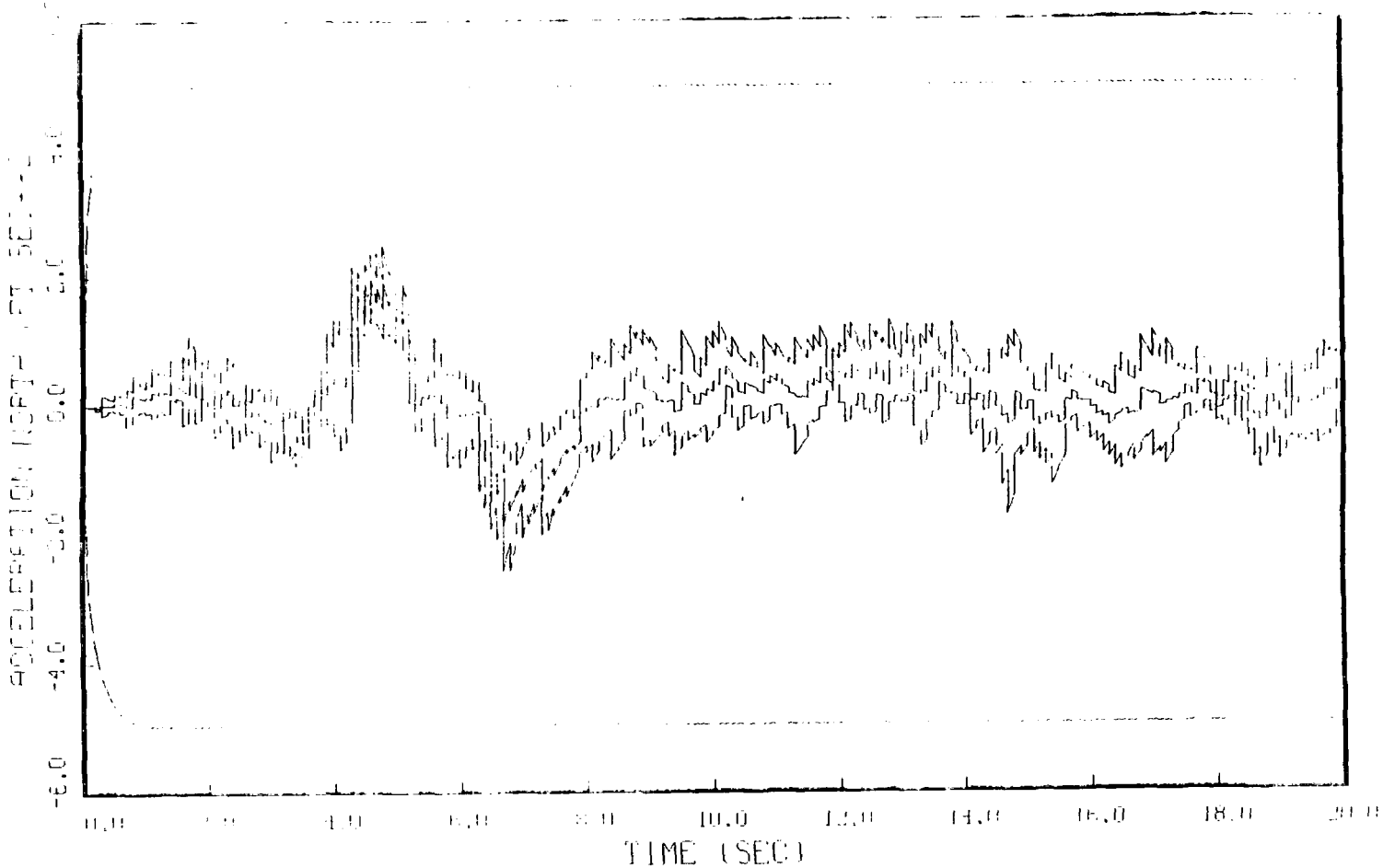

FIGURE I.3: BATOS BARLOW MODEL, STATE 3, 5 RUNS, U-TOT, ADAPTIVE R
BEAM TRANSMITTED. BEAM: U-3.0E-4 FOR AZ & EL DURING ROLL, ELSE 1.1E-06

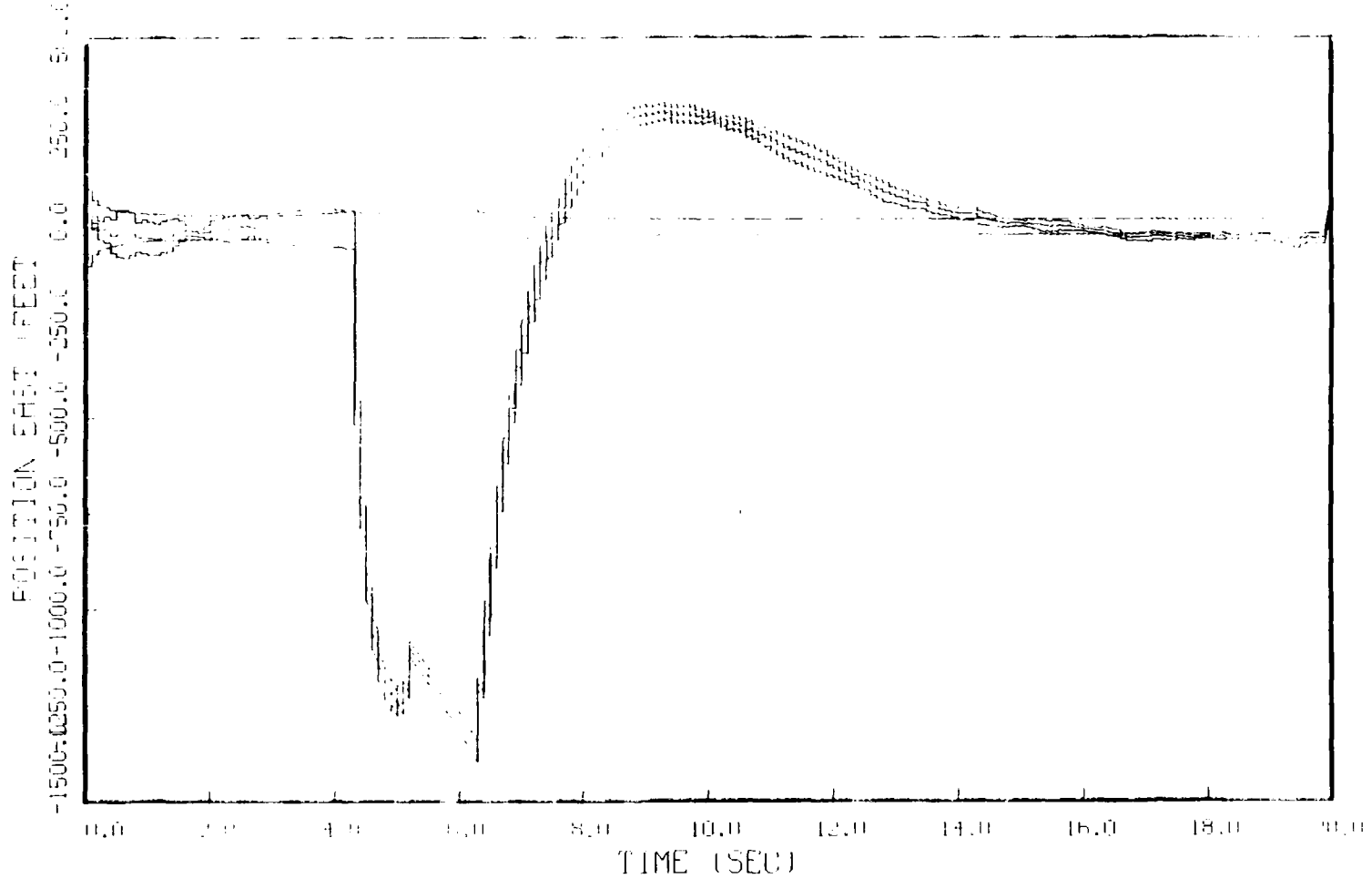

FIGURE I.4: GAUSS MARKOV MODEL, STATE 4, 5 RUNS, Q=100, ADAPTIVE R
BEAM TRAJECTORIES. NOTE: QR 5.0E-4 FOR AZ & EL DURING ROLL, ELSE 1.1E-01

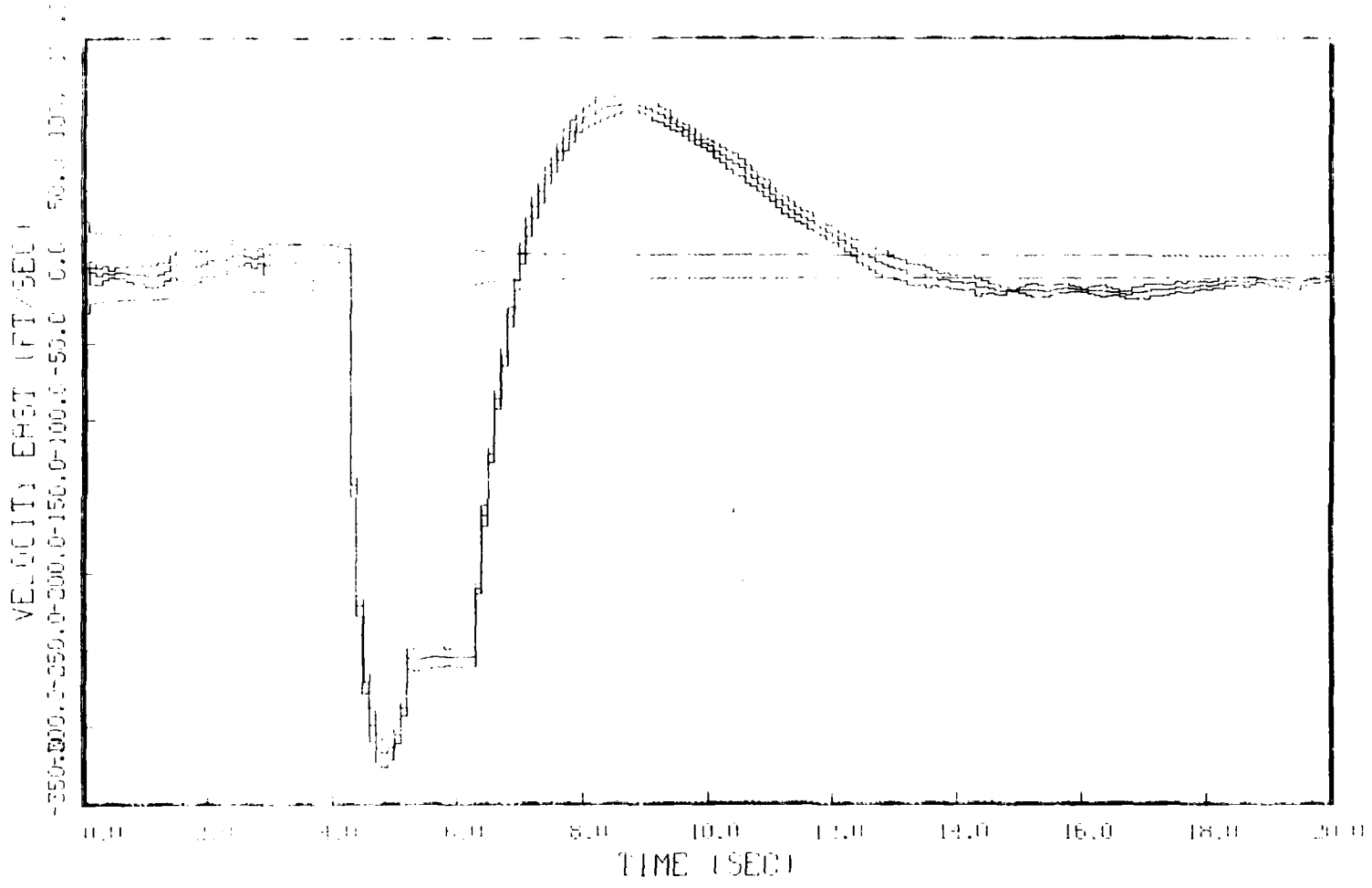

FIGURE 1.5: GAUSS MARKOV MODEL, STATE 5, 5 RUNS, D=100, ADAPTIVE R
BEAM TRAJECTORY. MEAS: DR=3.0E-4 FOR AZ & EL DURING ROLL, ELSE 1.0E-03

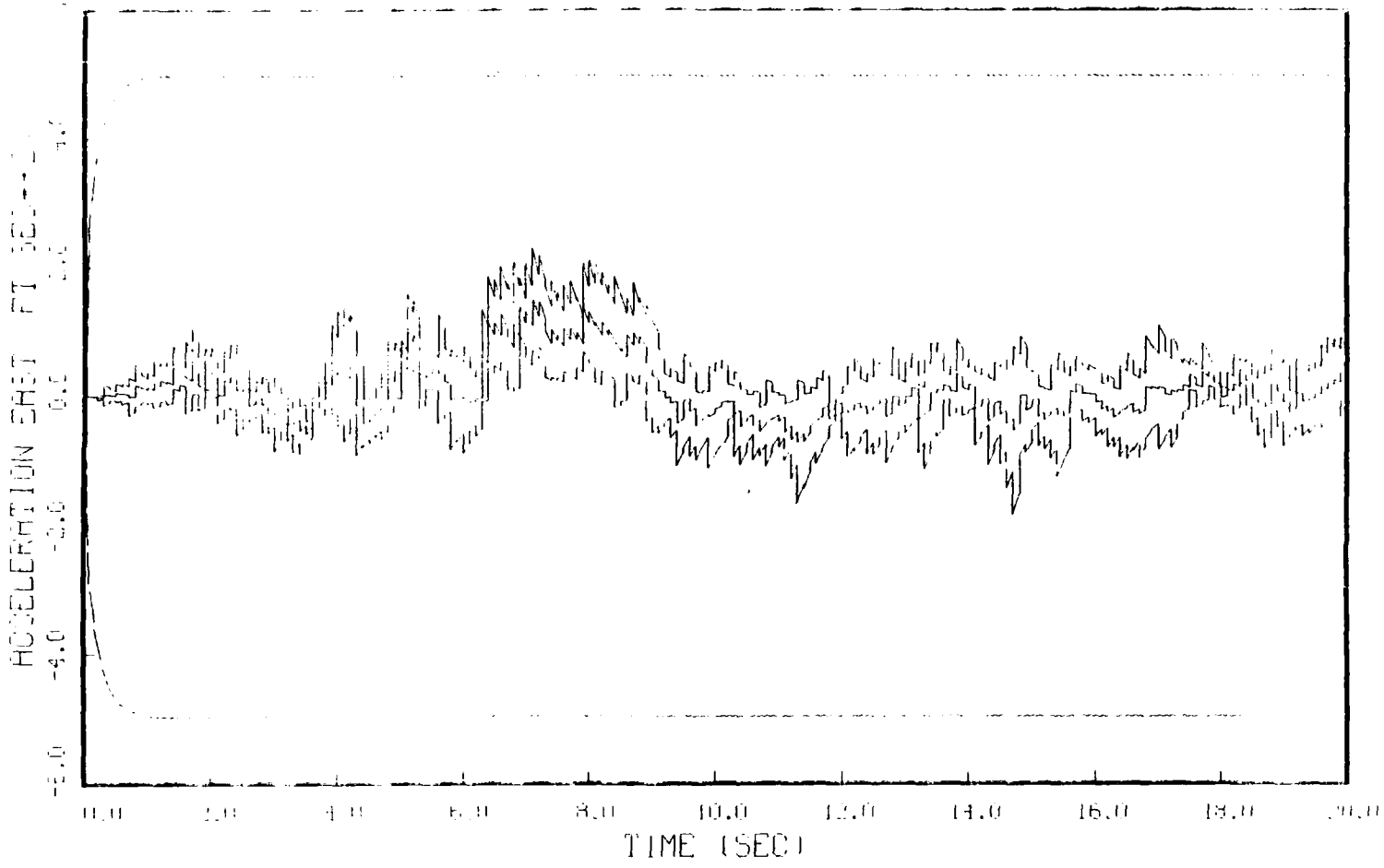

FIGURE I.6: GAUSS MARKOV MODEL, STATE 6, 5 RUNS, Q=100, ADAPTIVE R
BEAM TRAJECTORY. NEAS: (R=5.0E-4 FOR AZ & EL DURING ROLL, ELSE 1.1E-06)

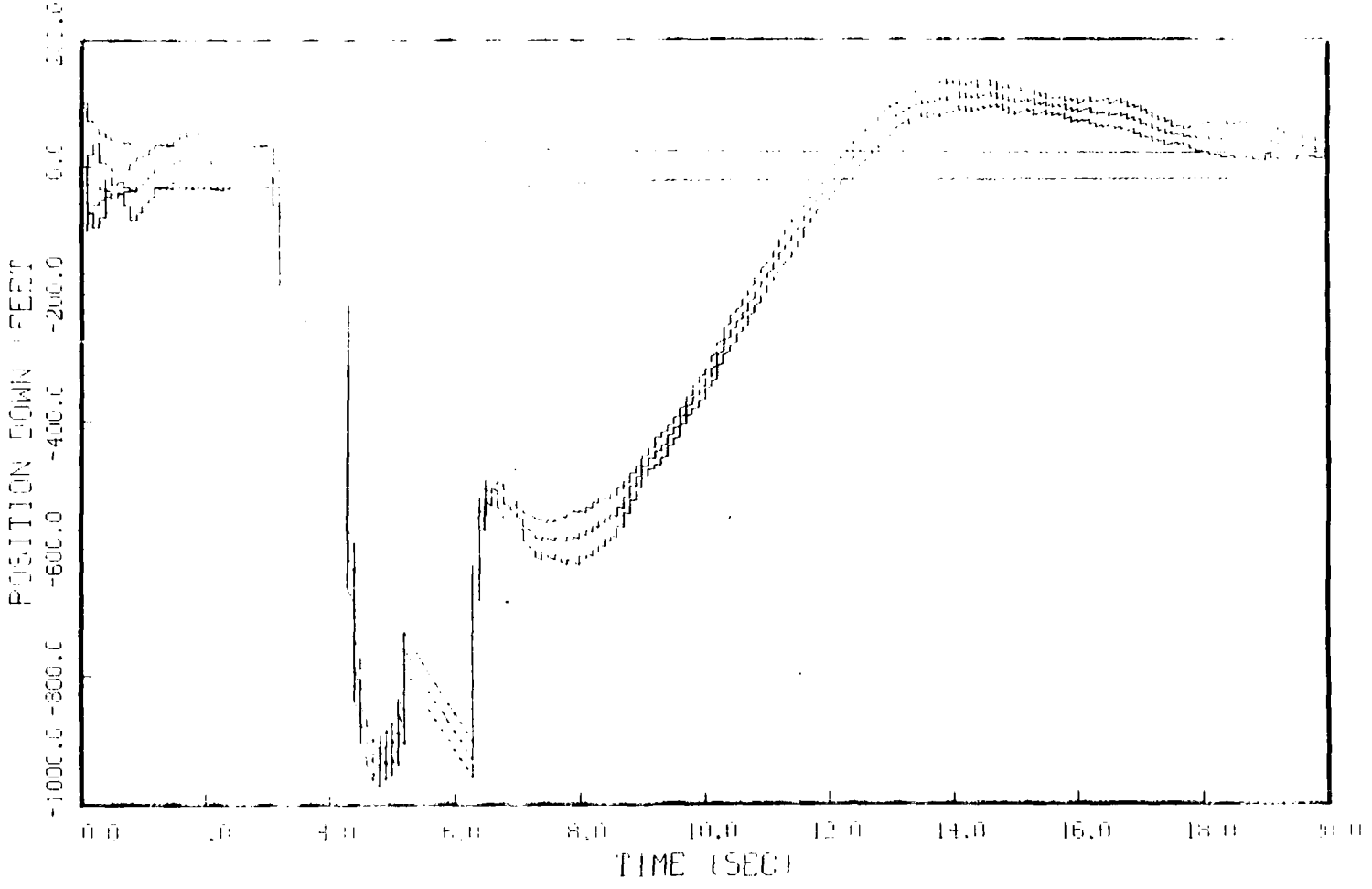

FIGURE I.2: GAUSS MANEUV MODEL, STATE 7, 5 RUNS, 0-100, ADAPTIVE R
BEAM TRACK PHASE. NOTE: DR=5.0E-4 FOR AZ & EL DURING ROLL, ELSE 1.0E-06

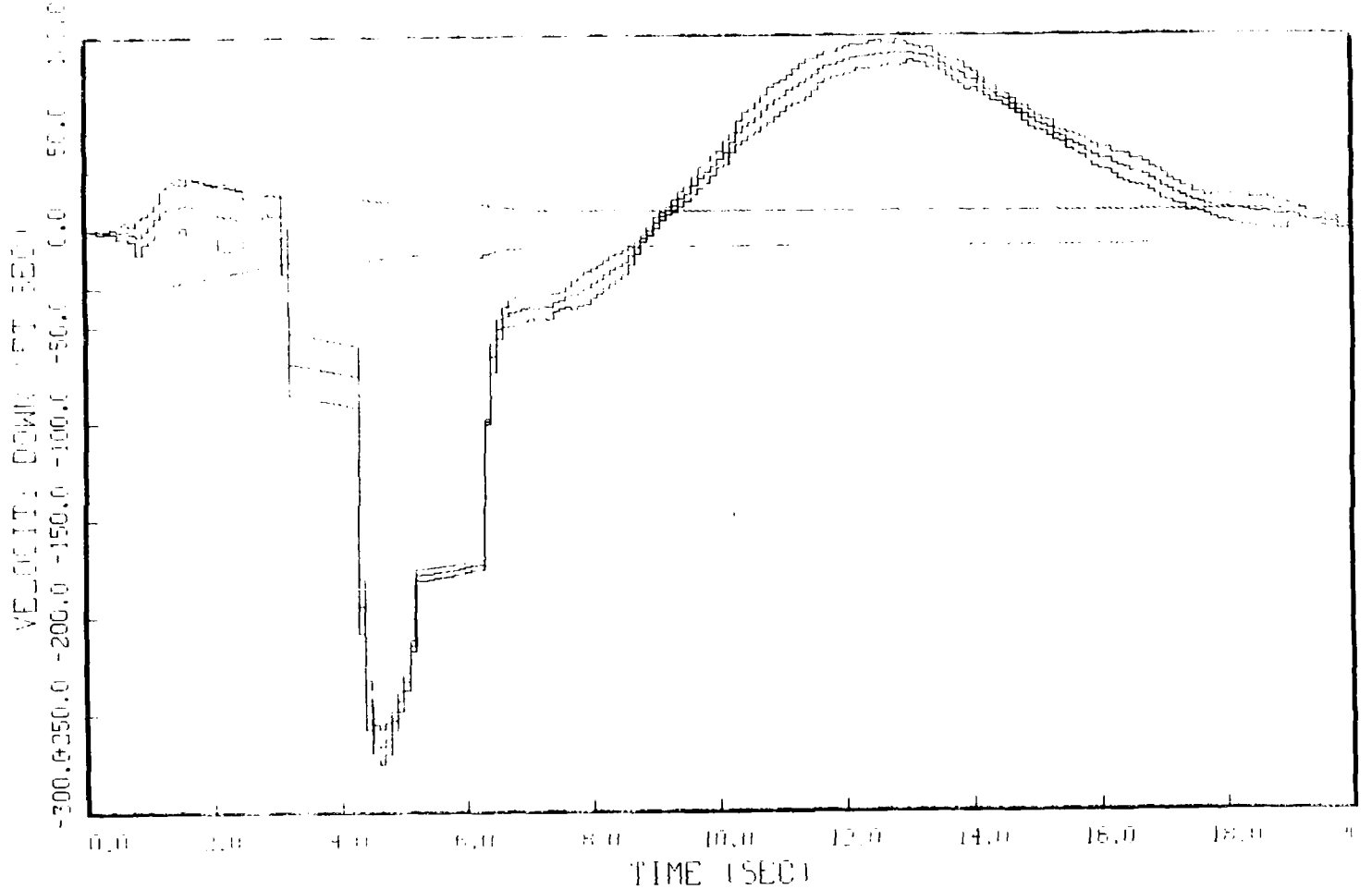

FIGURE I.6a: GAUSS MARKOV MODEL, STATE 8, 5 RUNS, Q=100, ADAPTIVE R
BEAM TRACKING, NOISE: QR=5.0E-4 FOR AZ & EL DURING ROLL, ELSE 1.0E-06

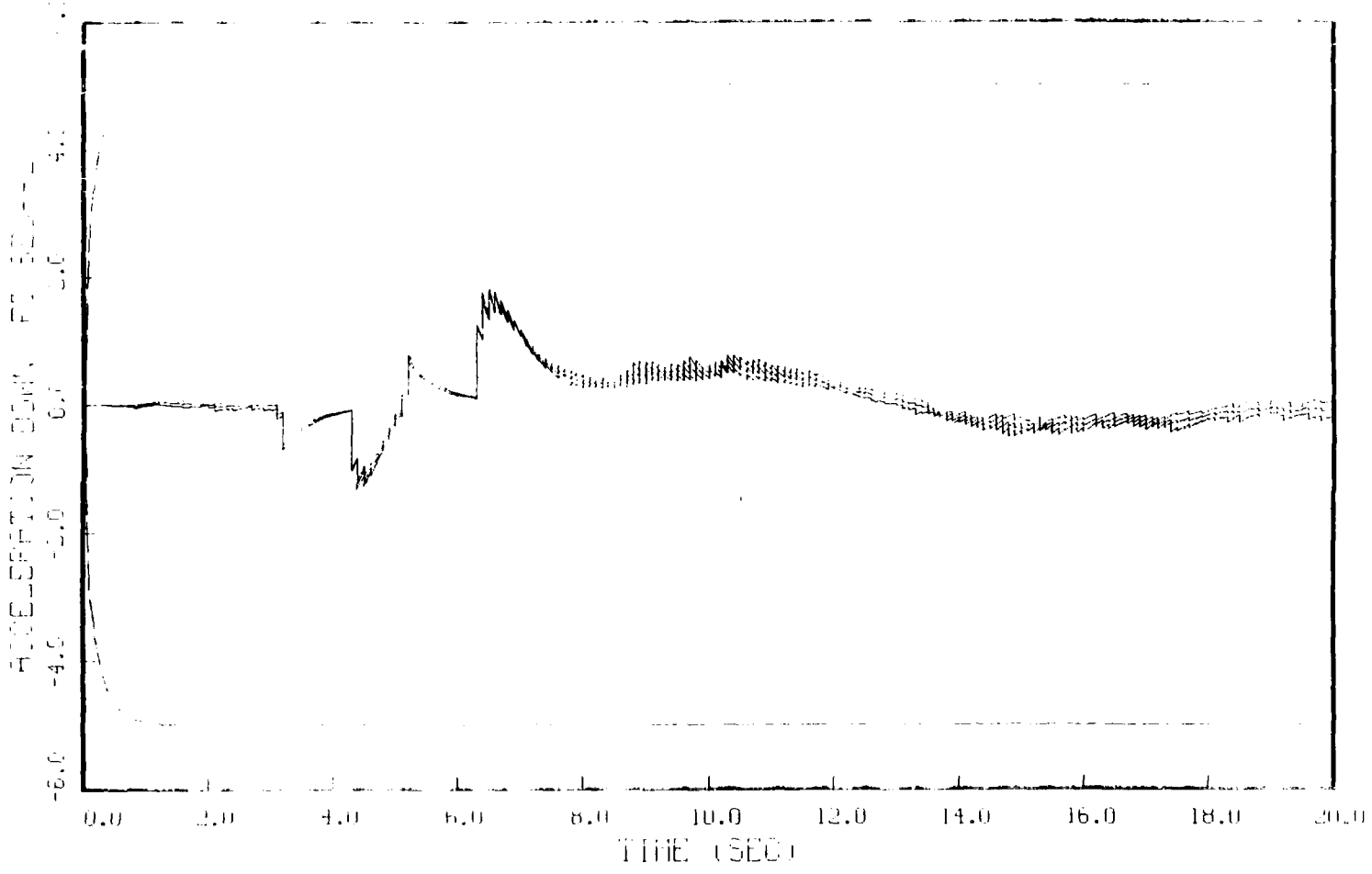

FIGURE I.3: [illegible] MODEL, STATE 9, 5 RUNS, 0-100, ADAPTIVE R
BEAM TRAJECTORY. NOTE: DR=3.0E 4 FOR AZ & EL DURING ROLL, ELSE 1.1E [illegible]

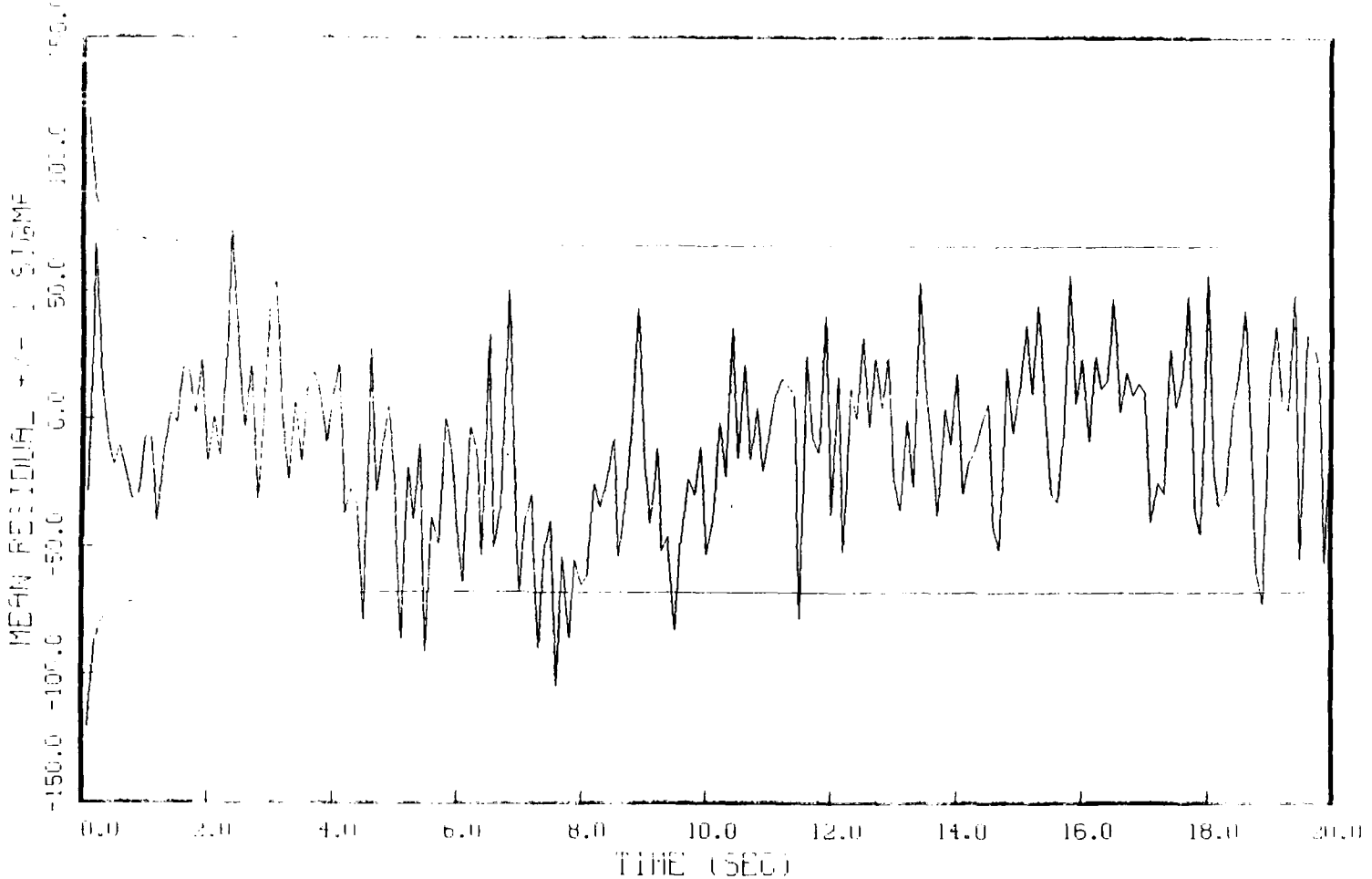

FIGURE 7.10: BASIC RANGE MODEL, RANGE RESIDUAL, 5 RUNS
BEAM TRACKING, U-100, R-1489

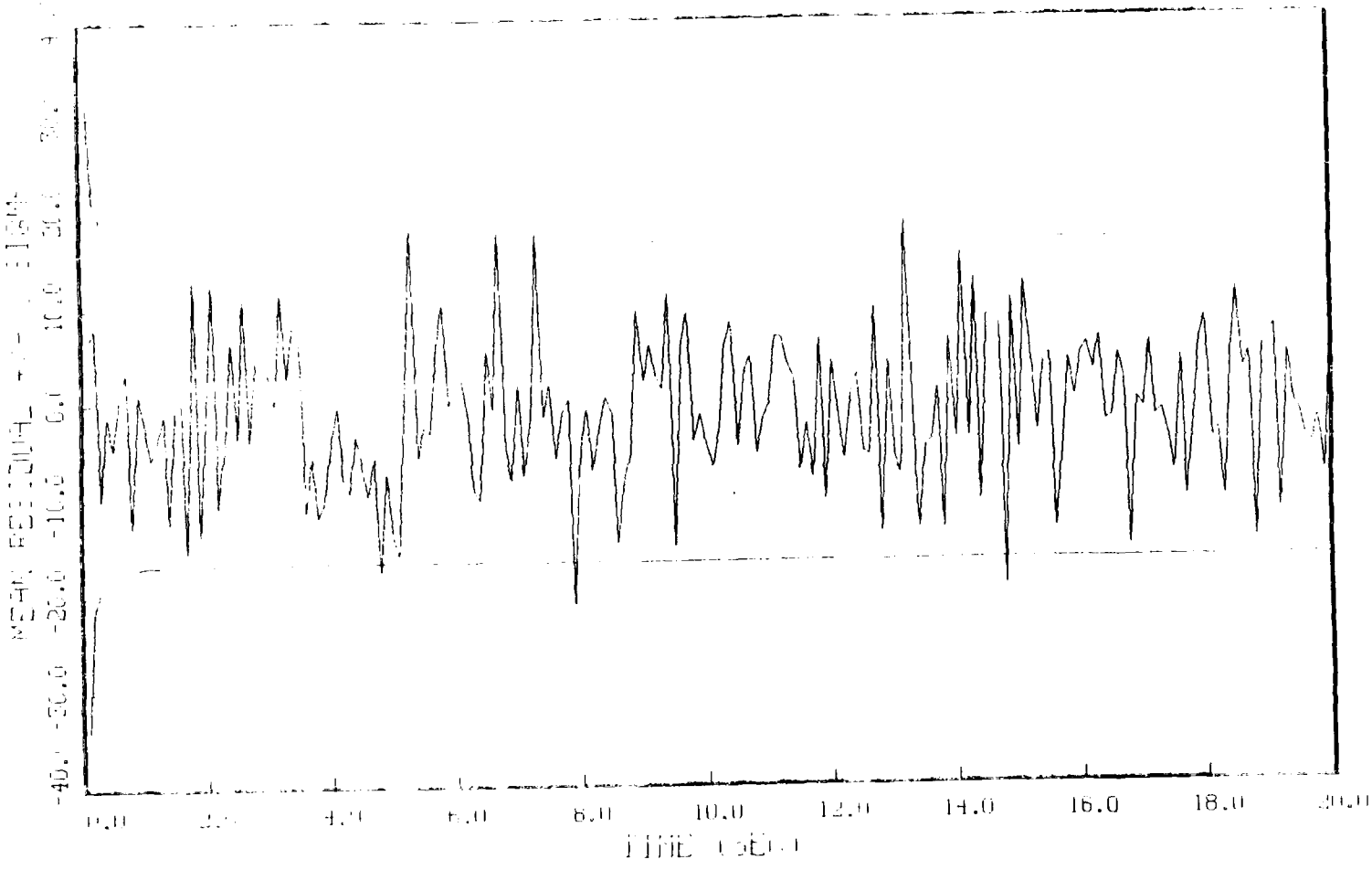

FIGURE 5.11: GAUSS-MARKOV MODEL, RANGE RATE RESIDUAL, 5 RUNS
BEAM TRACKING, Q=100, R=250

AD-A164 205 KALMAN FILTER DESIGN FOR THE LONG RANGE INTERCEPT FUNCTION OF THE F-4E/G F.. (U) AIR FORCE INST OF TECH WRIGHT-PATTERSON AFB OH SCHOOL OF ENGI.. R C HALBERT

4/4

UNCLASSIFIED DEC 85 AFIT/GE/ENG/85D-20 F/G 17/9 NL

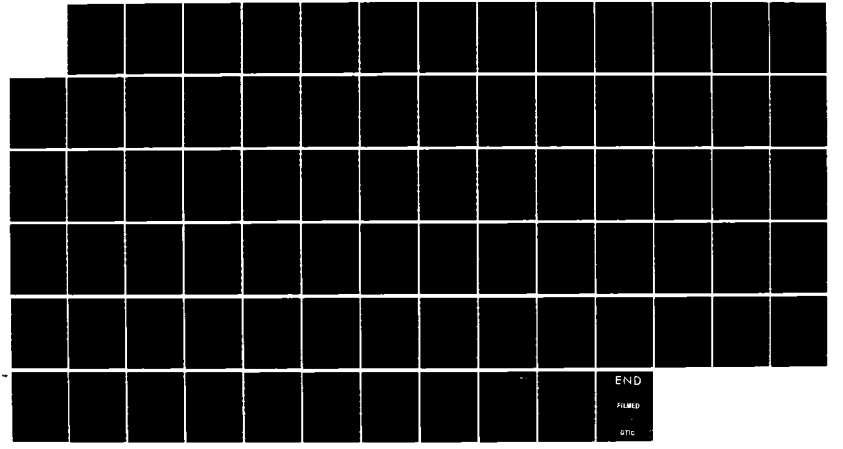

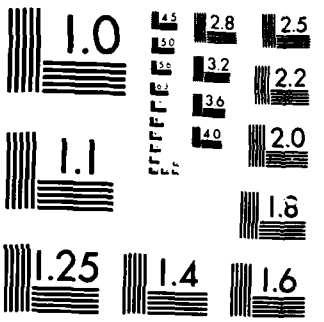

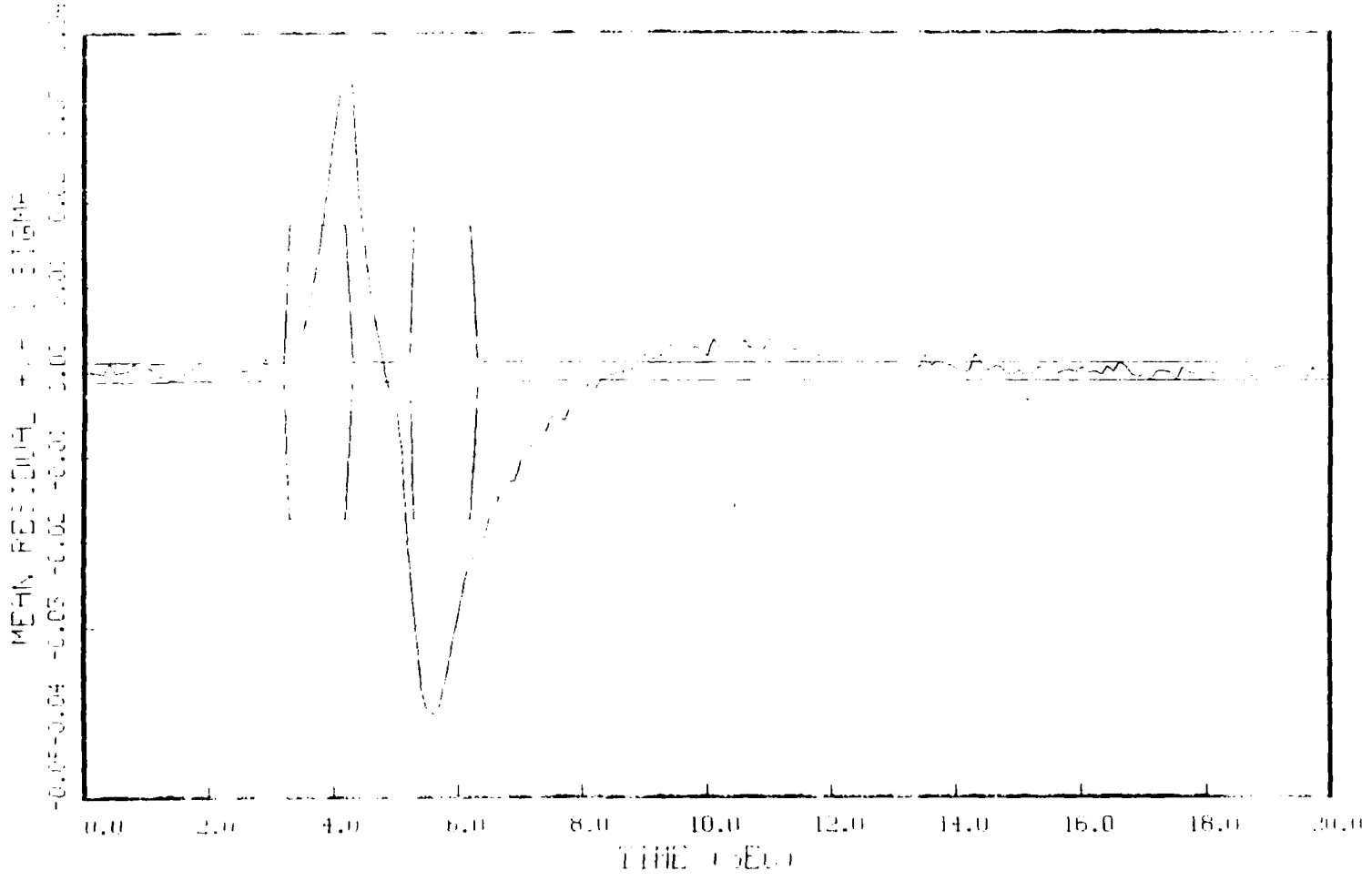

FIGURE [illegible] [illegible], [illegible], SIDE AZIMUTH RESIDUAL, 5 RUNS
BEAM TRAJECTORY, 0.000, R=2.0E 01 FOR ROLL STRUT TILTTE COMPONENT: R=1.1E 00

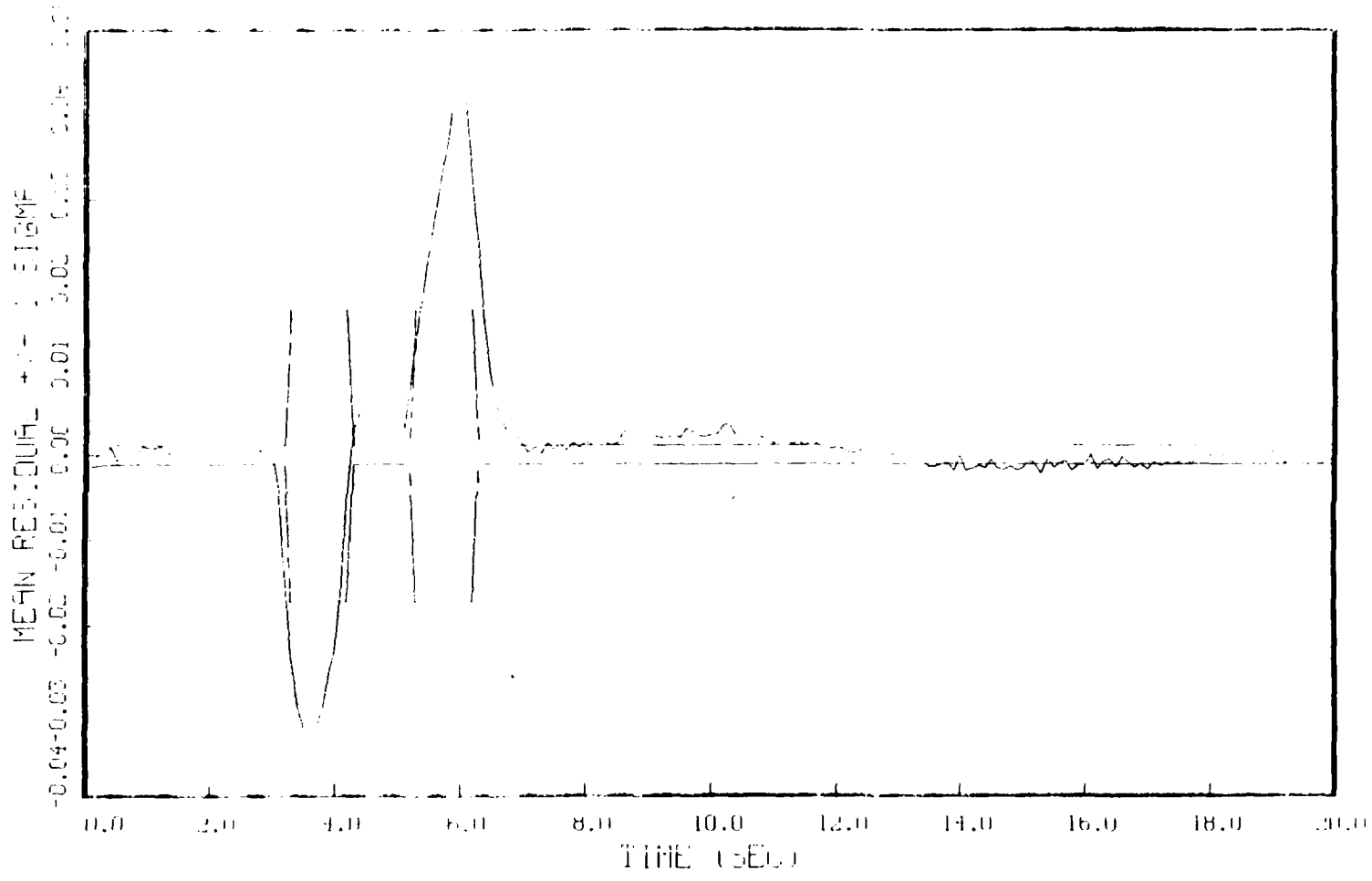

FIGURE I.13: GHOST THREAT MODEL, SINE ELEVATION RESIDUAL, 5 RUNS
BEAM TRAJECTORY, Q=100, R=5.0E-04 FOR ROLL (TRUE WHITE COMPONENT: R=1.1E-03

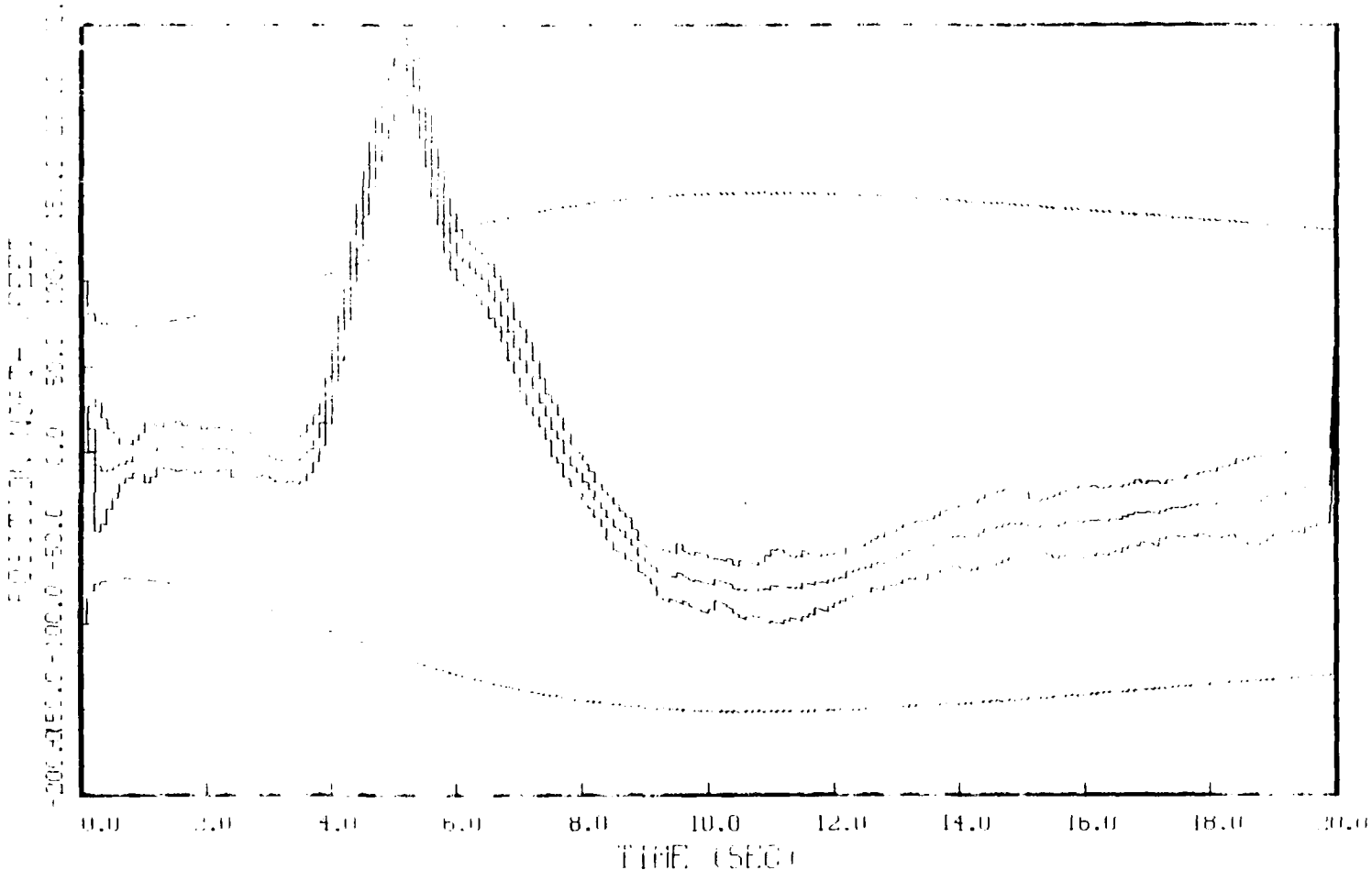

FIGURE I.11: GAMES RUNTIME MODEL, STATE 1, 5 RUNS, D=100, ADAPTIVE D
BEAM TRACKED TGT 1, 4 DEAD: DB=2.0E-4 FOR AZ & EL; D=1 DURING ROLL

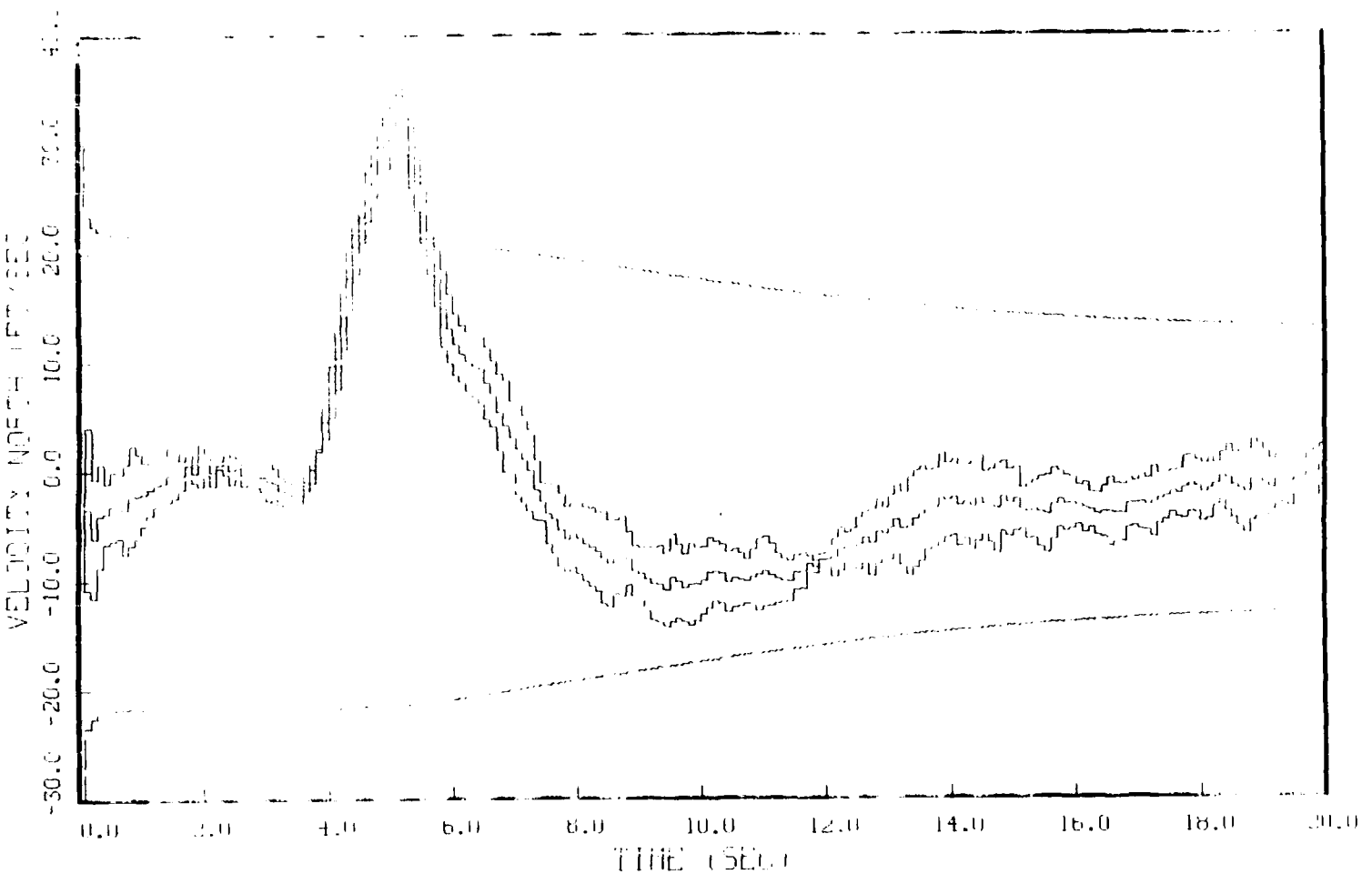

FIGURE 1.15: GAUSS MARKOV MODEL, STATE 2, 5 RUNS, Q=100, ADAPTIVE Q
BEAM TRAJECTORY, 4 MEAS: 1R-2.0E 4 FOR AZ & EL Q=1 DURING ROLL

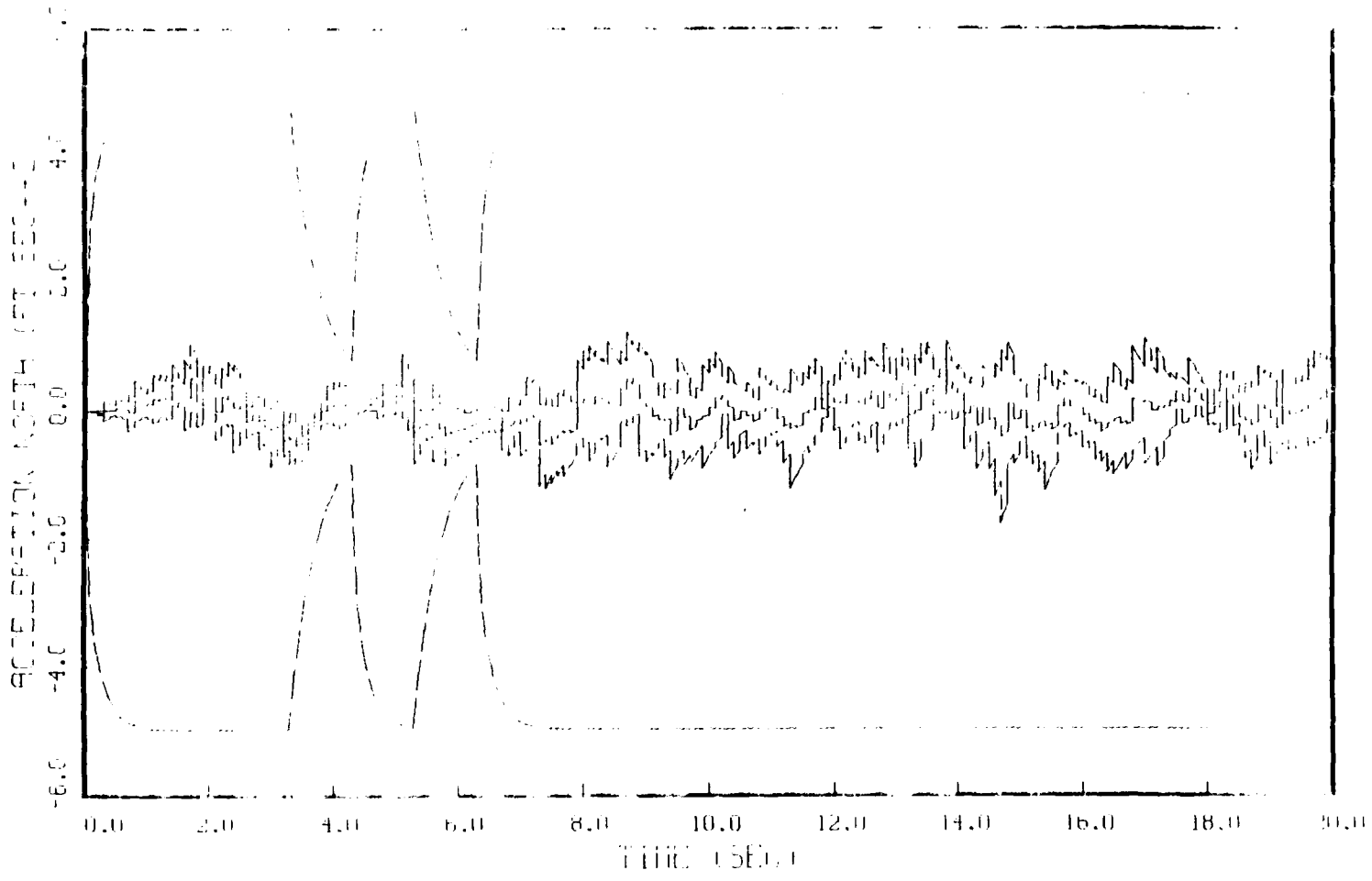

FIGURE I.16a CHUCK TURBULENCE MODEL, STATE 3, 5 RUNS, 0 TGT, ADAPTIVE 0
BEAM TRACED TGPL, 4 BEAMS IN-2.0E-4 FOR AZ & EL 0-1 DURING ROLL

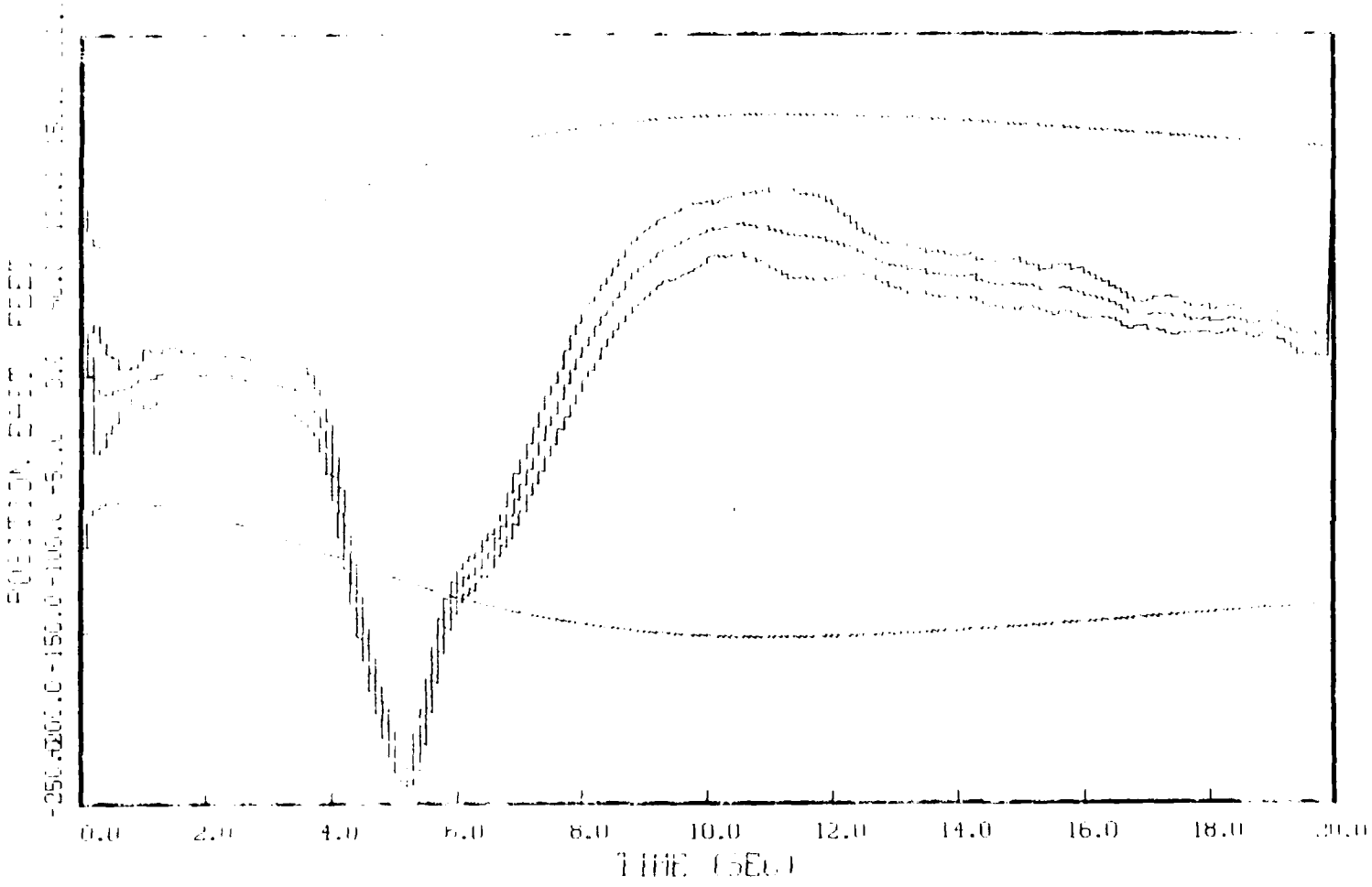

FIGURE I.1: GAUSS MARKOV MODEL, STATE 4, 5 RUNS, Q 100, ADAPTIVE Q
DEAD TRACKING, R MEAS: TF=2.0E-4 FOR AZ & EL1 Q=1 DURING ROLL

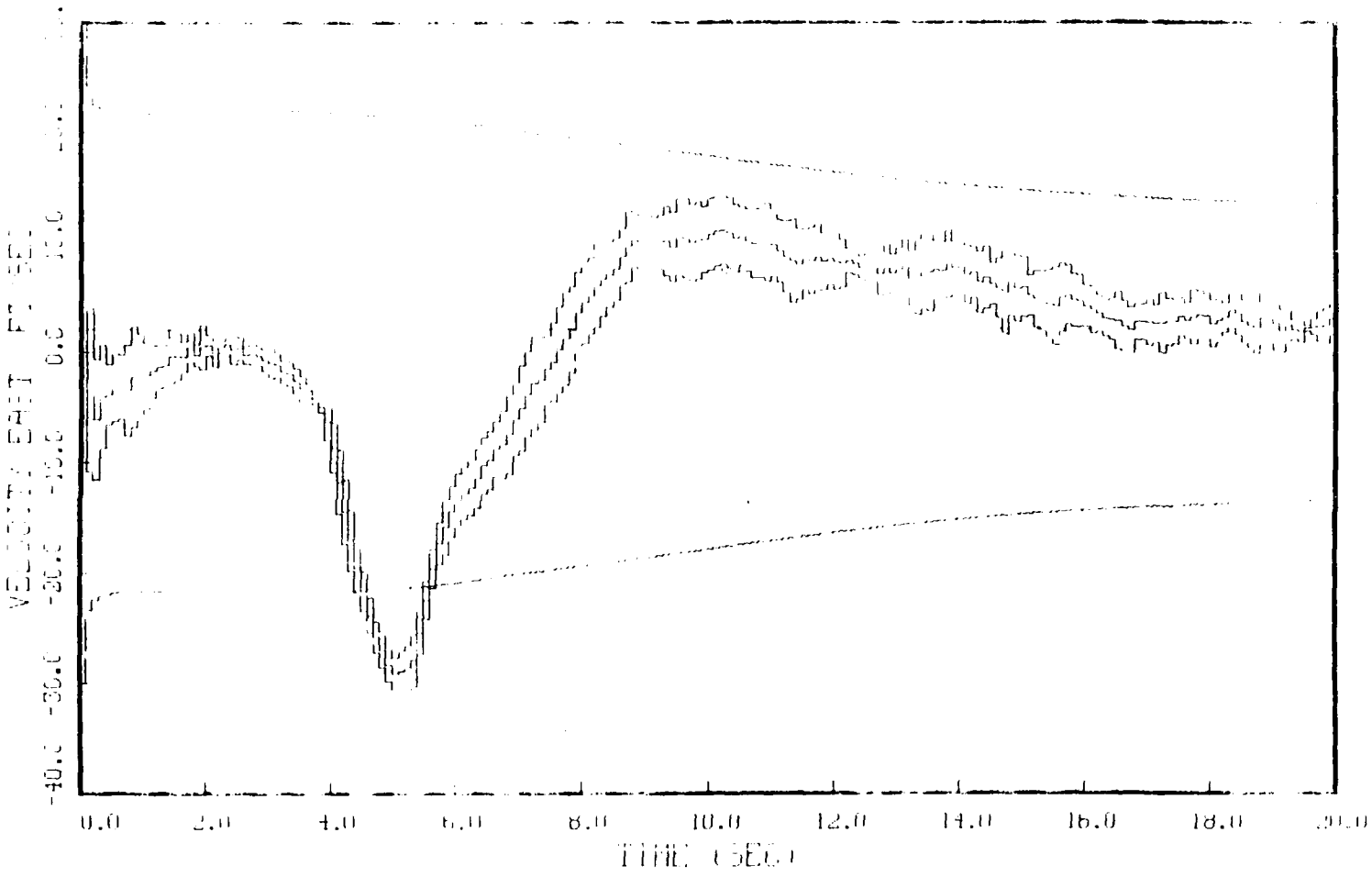

FIGURE I.16: [illegible] MODEL, STATE 5, 5 RUNS, 0-100, NOMINAL 0 BOMB TRAJECTORY, 4 METERS [illegible] FOR AZ & EL 0-1 TUMBLING BALL

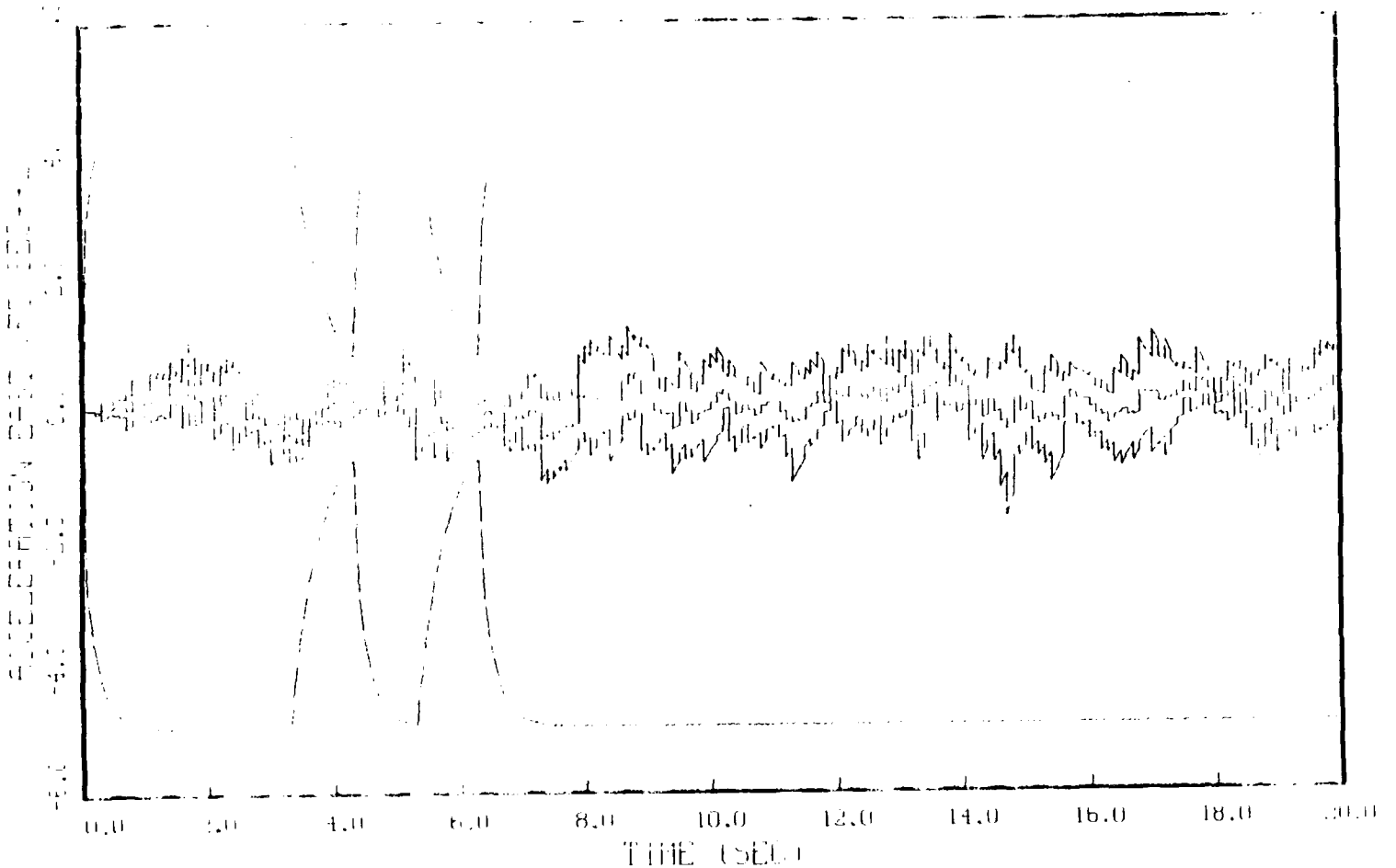

FIGURE 1.1a: GAUSS-MARKOV MODEL, STATE 6, 5 RUNS, Q=100, ADAPTIVE Q
BEAM THROW TORQUE, 4 MEAS: QF= 2.0E-4 FOR AZ & EL Q=1 DURING ROLL

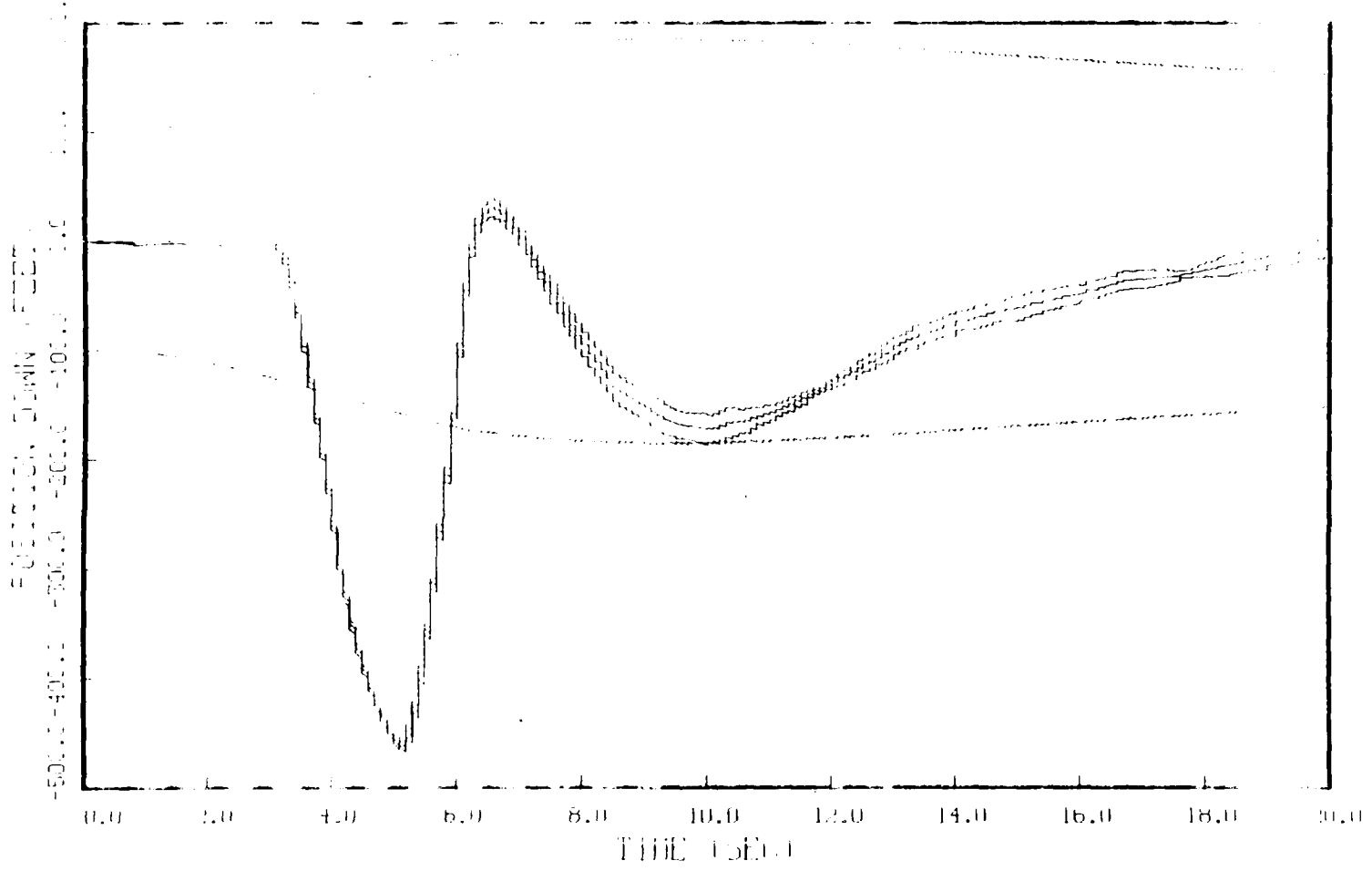

FIGURE 1.30: GRAY THUNDER MODEL, STATE 7, 5 RUNS, G=100, ADAPTIVE G
BEAM TRACKING, 4 ITEMS: G=2.0 F FOR AZ & EL G=1 DURING ROLL

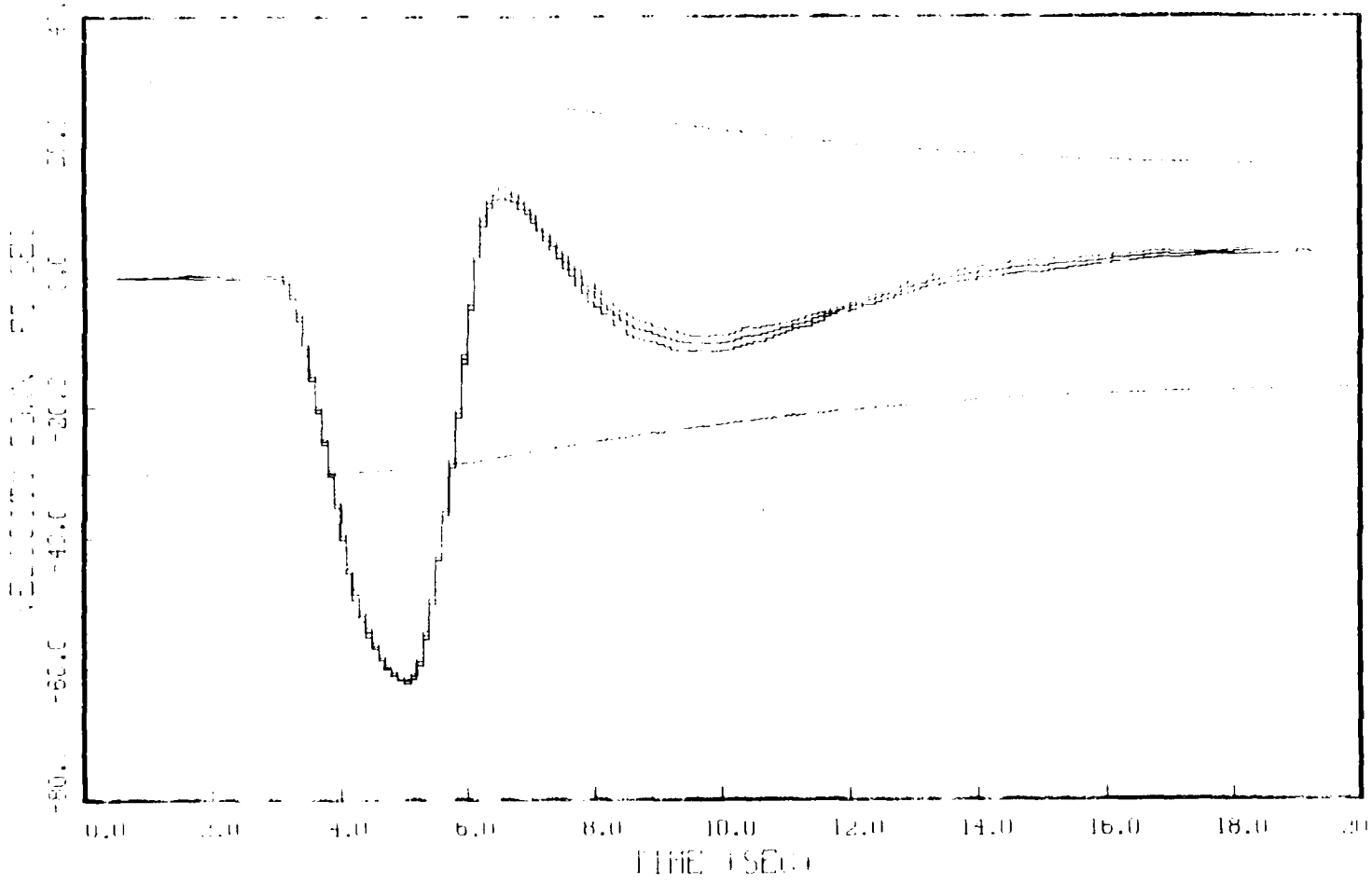

FIGURE 1.21: [illegible] MODEL, STATE 8, 5 RUNS, 0-100, ADAPTIVE 0
BEAM TRACED DATA, 4 DEM : [illegible] FOR AZ & EL 0-1 DURING ROLL

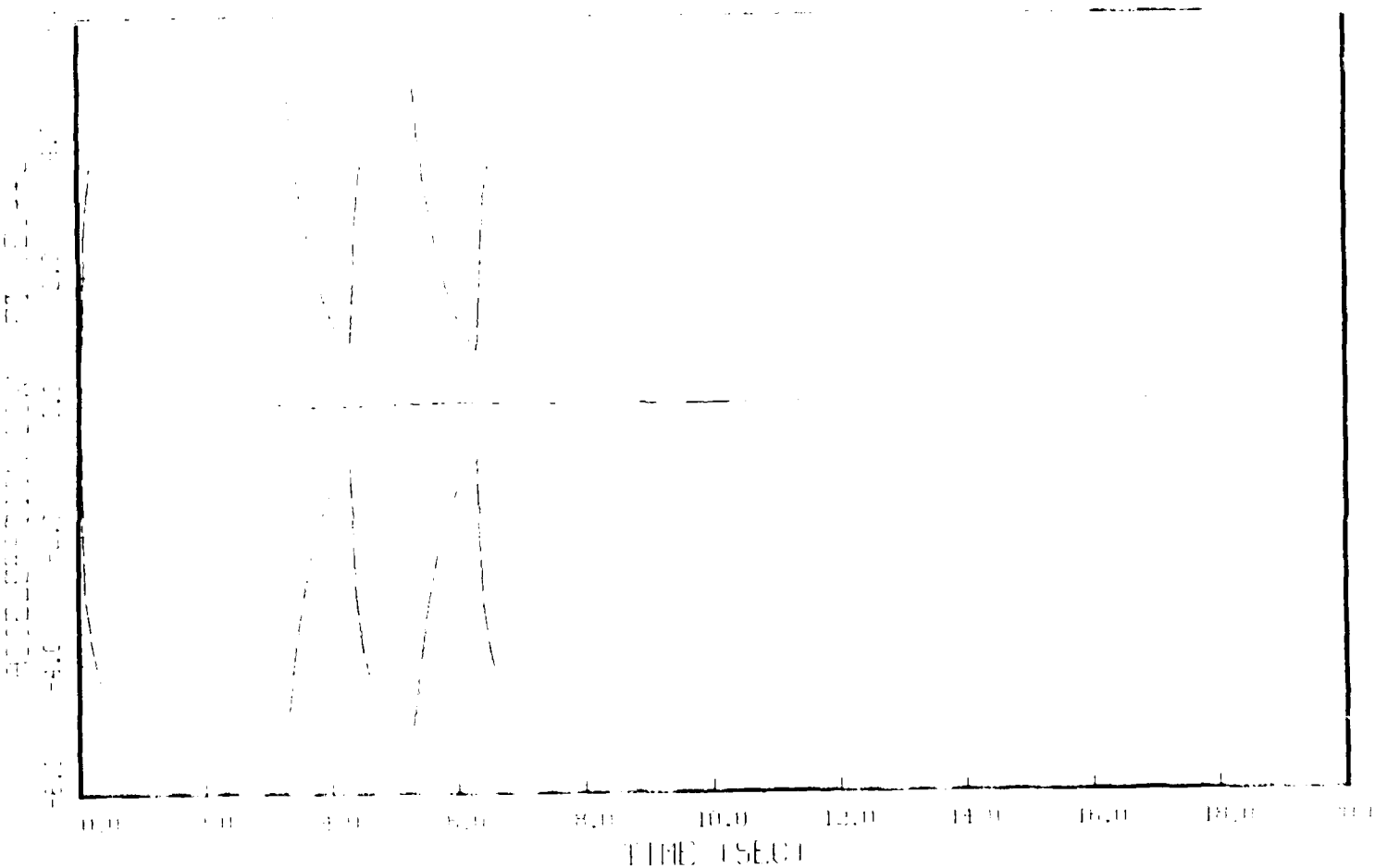

FIGURE [illegible]

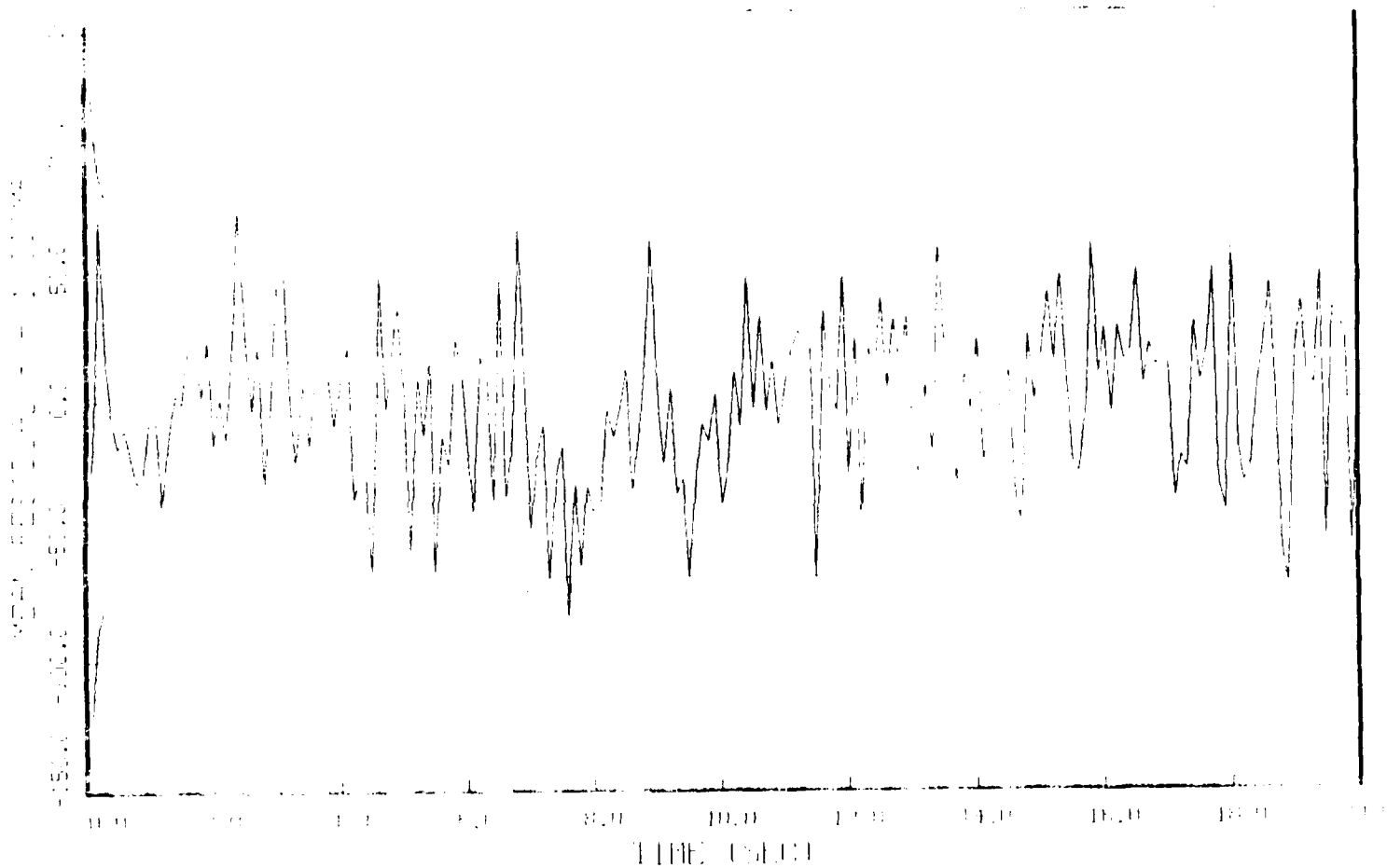

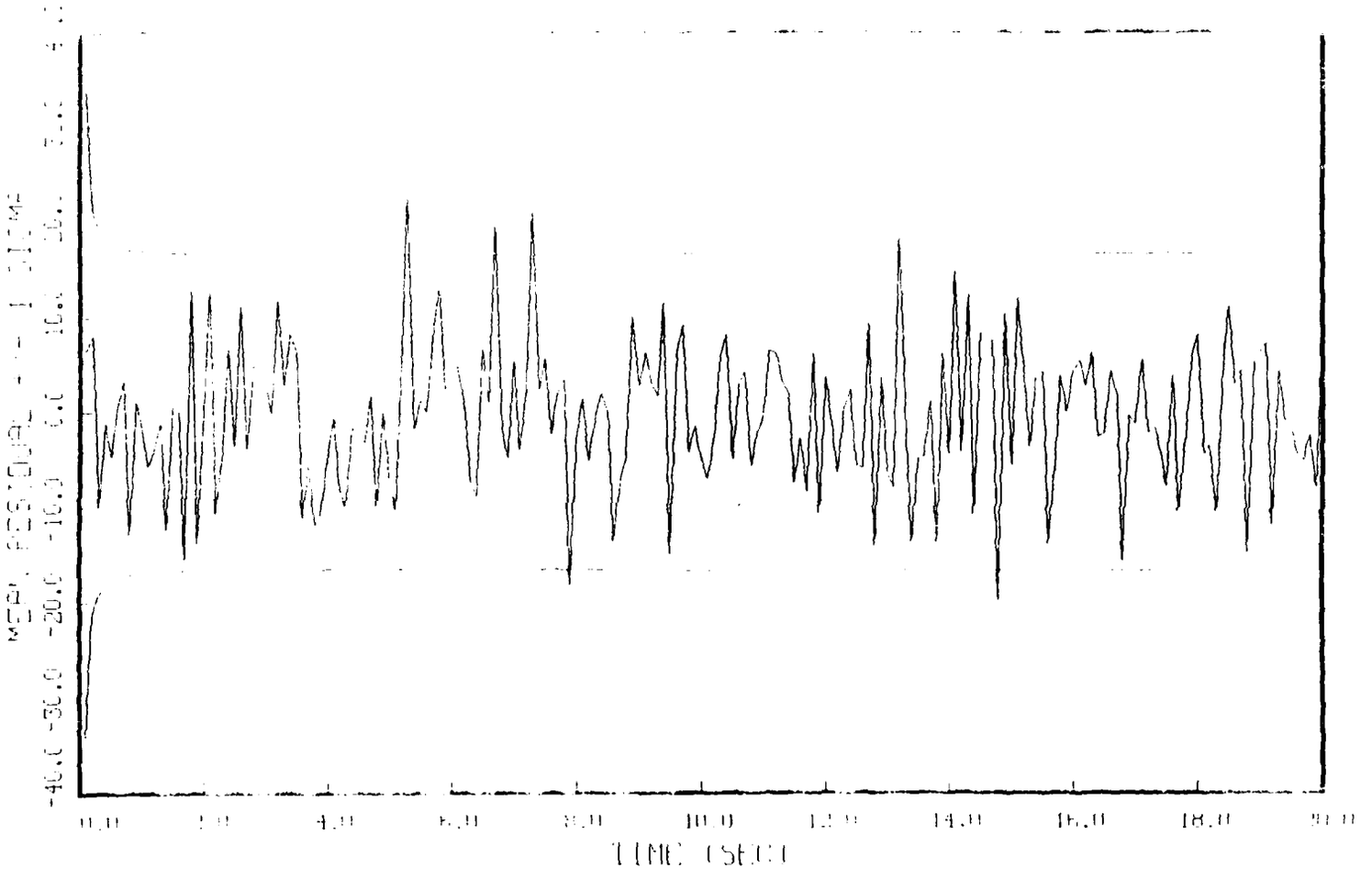

FIGURE I.24: CROSS DIRECTIV MODEL, RANGE RATE RESIDUAL, 5 RUNS
BEAM TRAJECTORY, 0-DAT OR 0-1 DIRECTION ROLL, R=2.0

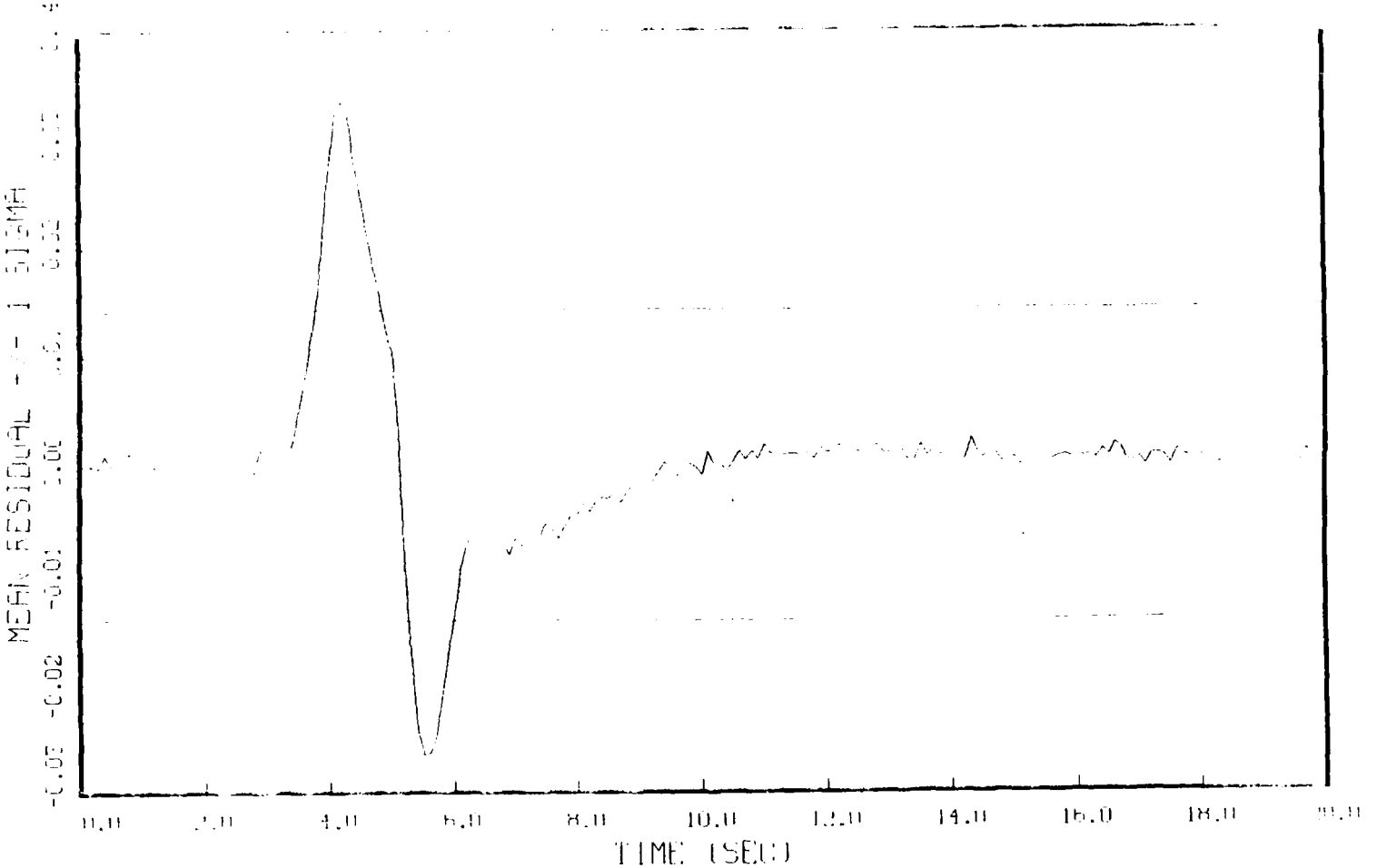

FIGURE 1.25: GAUSS MARKOV MODEL, SINE AZIMUTH RESIDUAL, 5 RUNS
GEAR INTEGRATION, R=2.0E 6 (TRUE UNITE COMPONENT: R=1.1E 06)

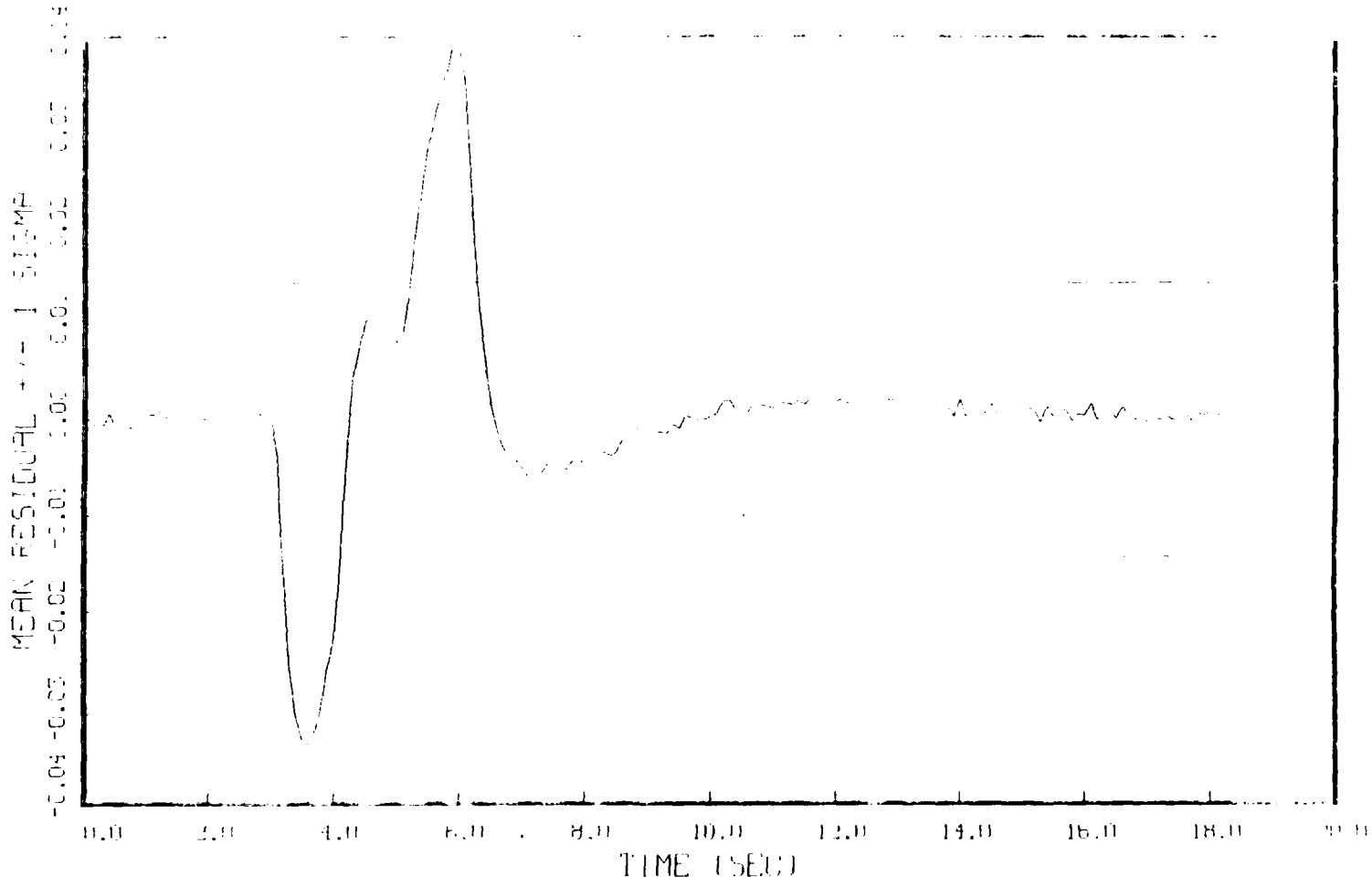

FIGURE I.26: GAUSS MARKOV MODEL, SINE ELEVATION RESIDUAL, 5 RUNS
BEAM TRAJECTORY, R=2.1E 6 STRUE RANGE COMPONENT: R 1.1E 06

Appendix J

Filter Comparisons on Three Trajectories

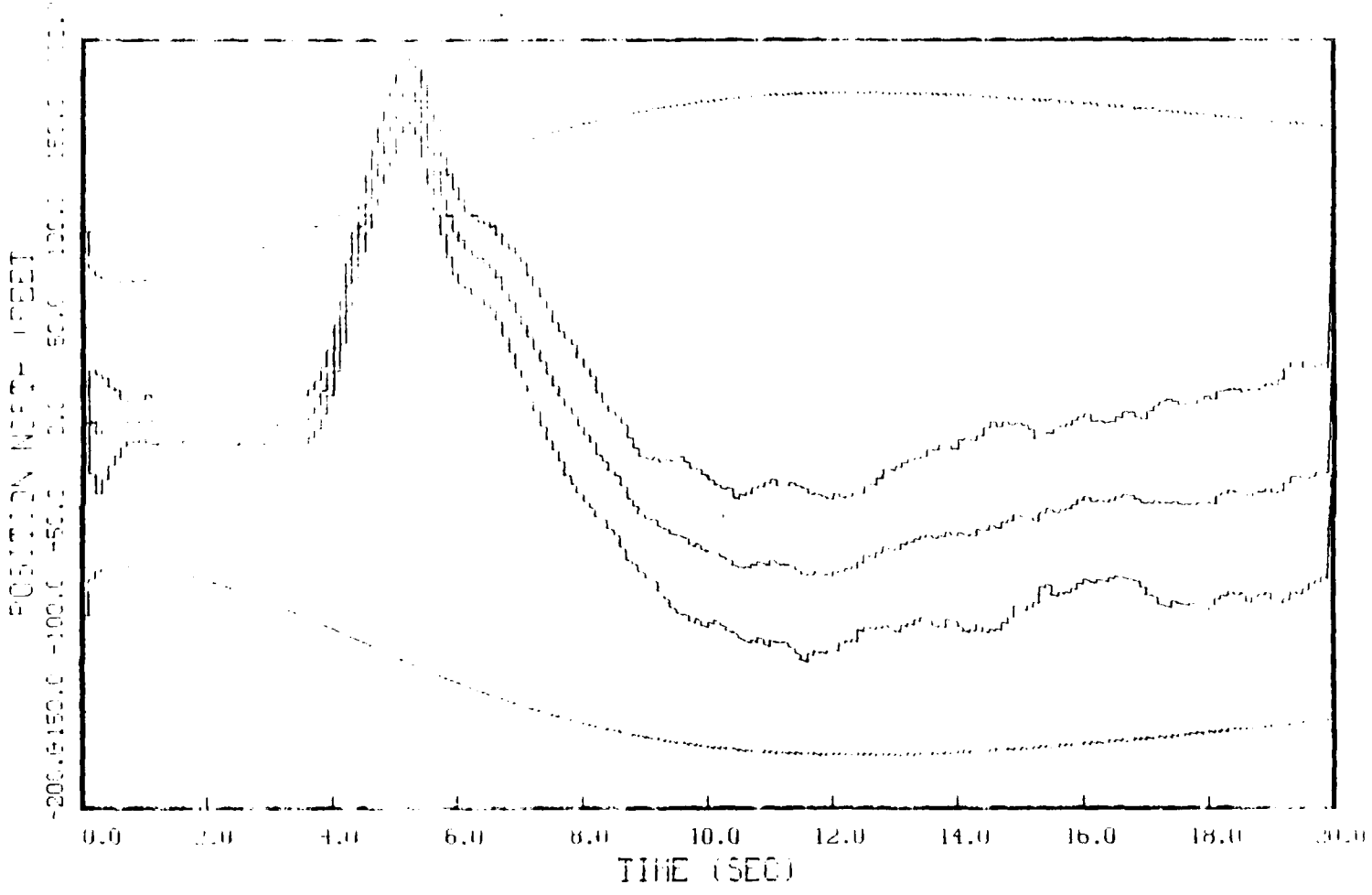

FIGURE 1.1: GAUSS MARKOV MODEL, STATE 1, 20 RUNS, 0-100, FULL STATE
BEAM TRACKING, 4 MEAS: RNG, RNG RATE, SIN AZ & EL (R=3.0E 4 FOR AZ & EL)

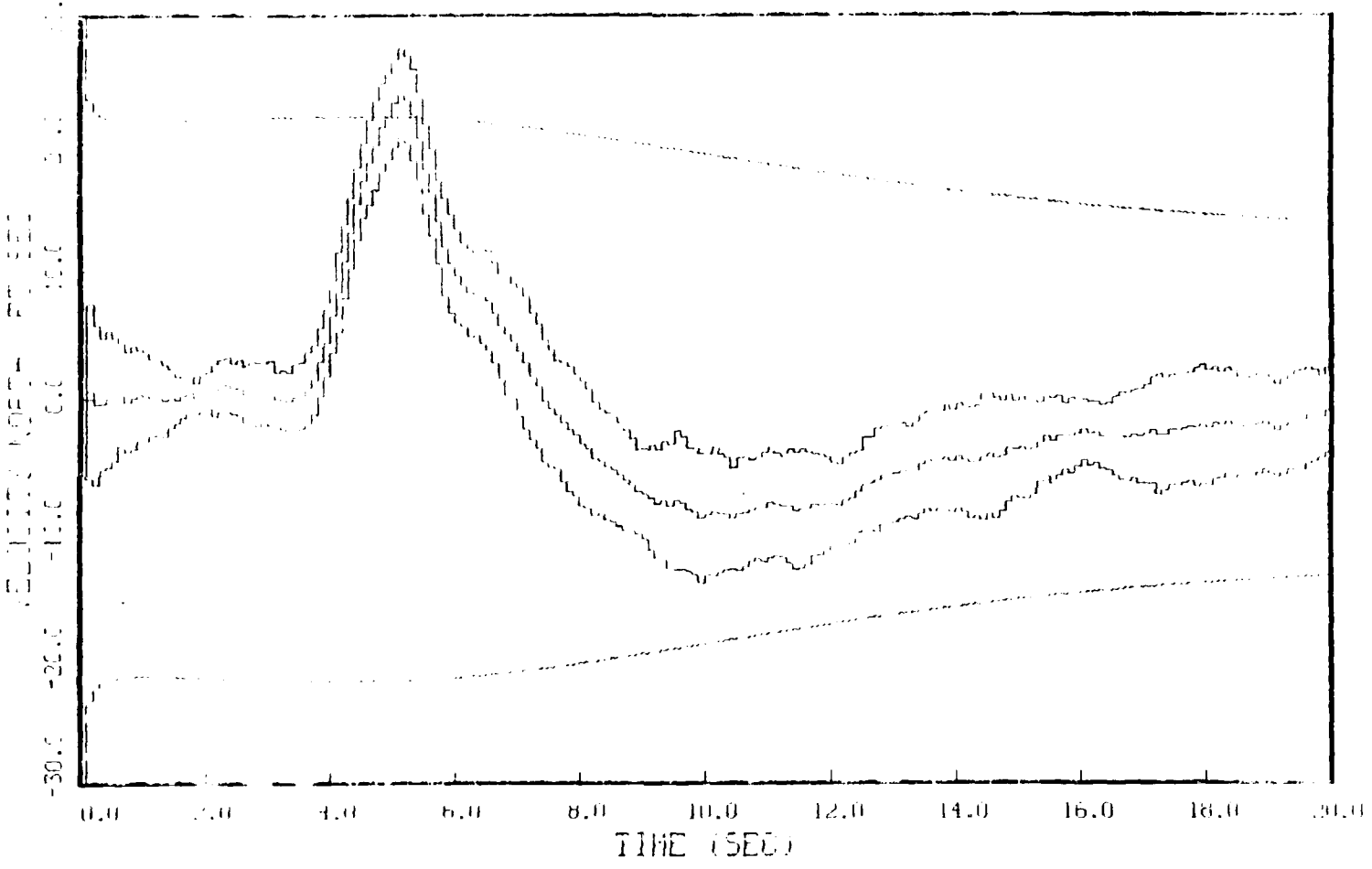

FIGURE 4.2: GAUSS MARKOV MODEL, STATE 2, 30 RUNS, Q=100, FULL STATE
BEAM TRAJECTORY, 4 BEAMS: RNG, RNG RATE, STN AZ & EL (R=3.0E 4 FOR AZ & EL)

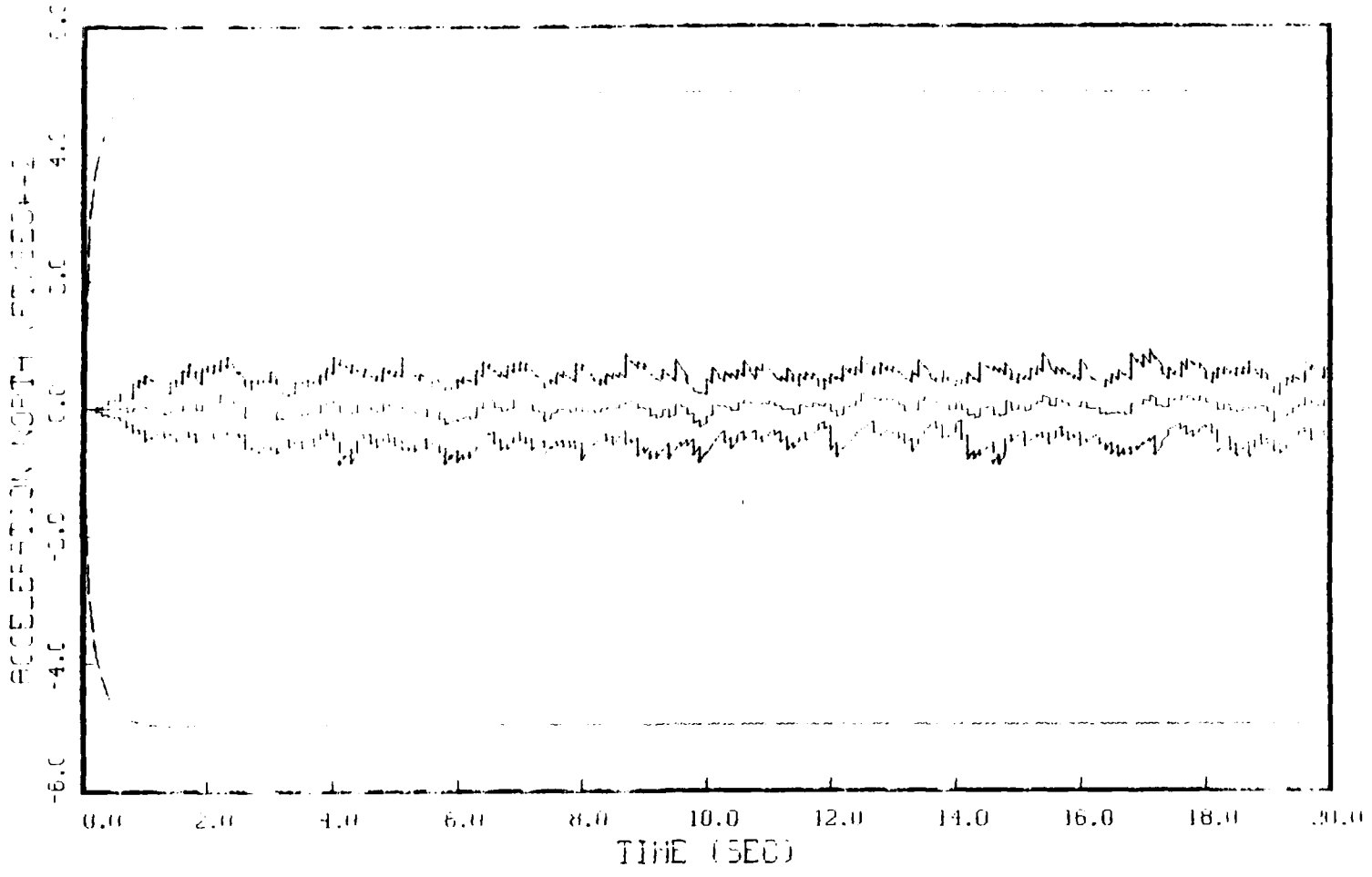

FIGURE J.3: GAUSS MARKOV MODEL, STATE 3, 20 RUNS, Q=100, FULL STATE
BEAM TRAJECTORY, 4 DEAD: RNG, RNG RATE, SIN AZ & EL (R=3.0E 4 FOR AZ & EL)

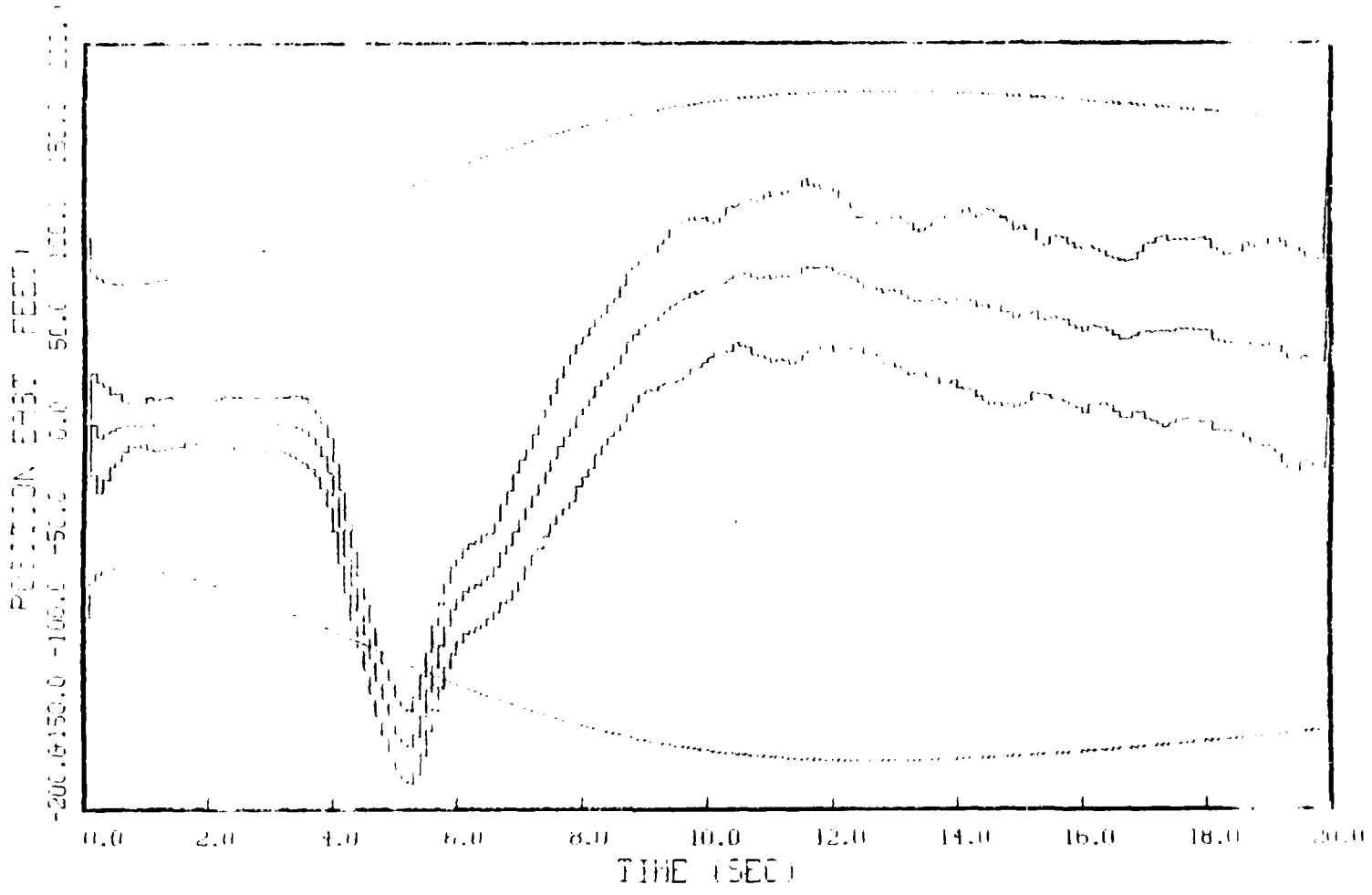

FIGURE 3.4: GROSS MANEUVER MODEL, STATE 4, 20 RUNS, U=100, FULL STATE
BEAM TRACKING TURN, 3 MEAS: RNG, RNG RATE, SIN AZ & EL OR=5.0E-4 FOR AZ & EL

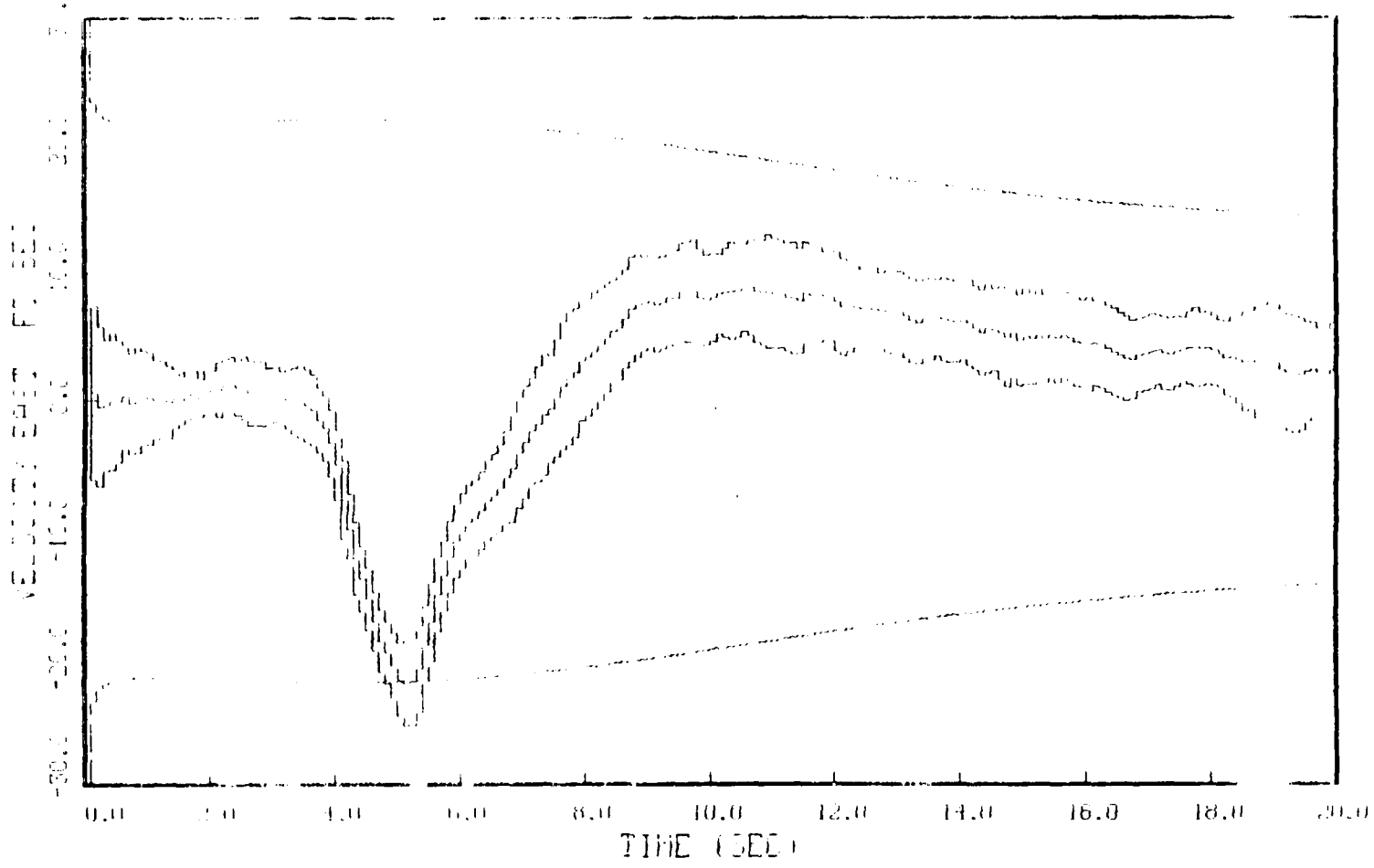

FIGURE 1.5: GAUSS-MARKOV MODEL, STATE 5, 20 RUNS, Q=100, FULL STATE
BEAM TRACKER (HZ), 3 MEAS., FUL, MID RATE, SIN HZ & EL ER=SLOE 4 FOR HZ & EL

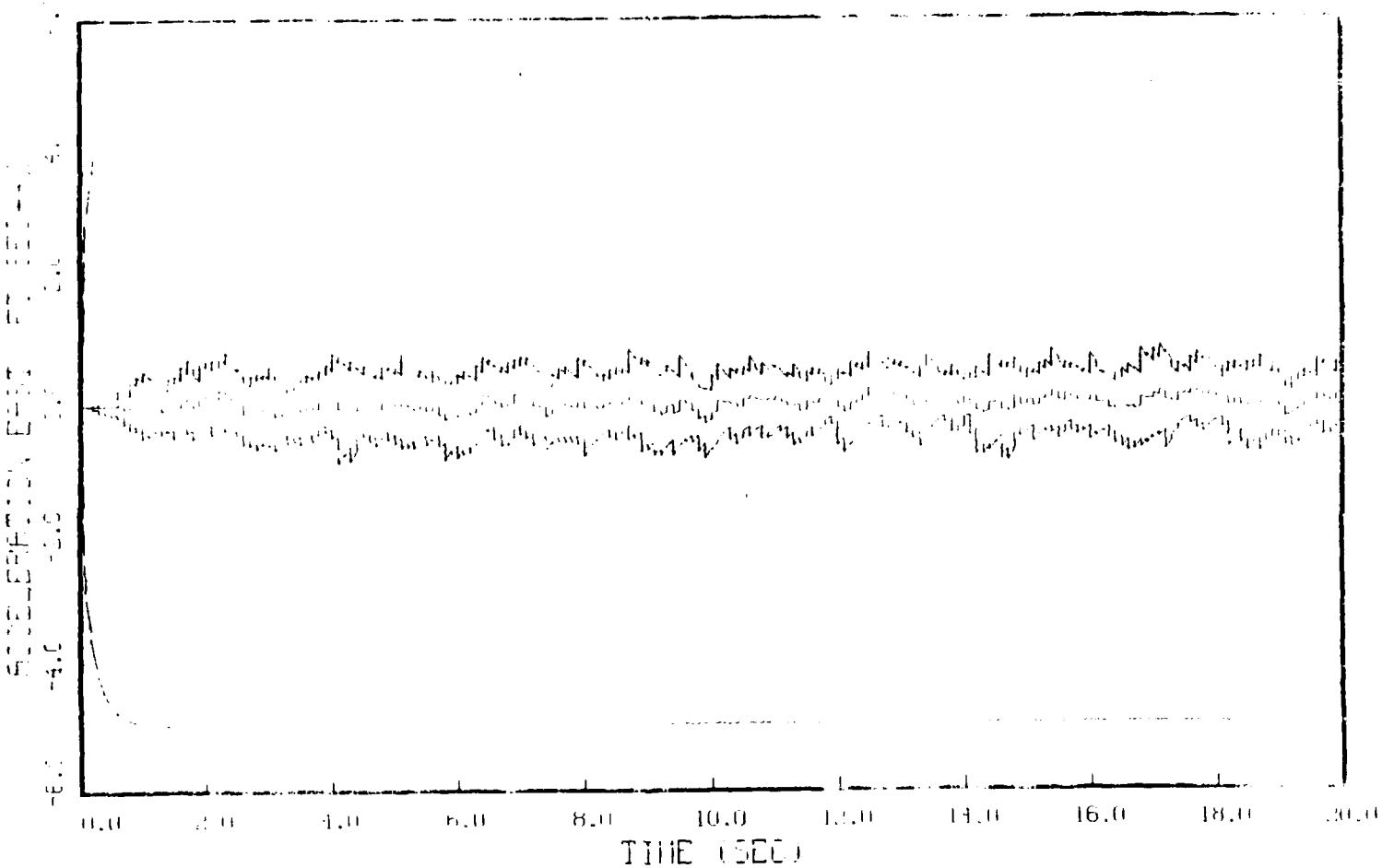

FIGURE J.6: GAUSS MARKOV MODEL, STATE 6, 20 RUNS, U-100, FULL STATE
BEAM TRACKER TORQUE, 4 DEGS: PSD, ROLL RATE, SIN HZ [illegible] 4 COS HZ [illegible]

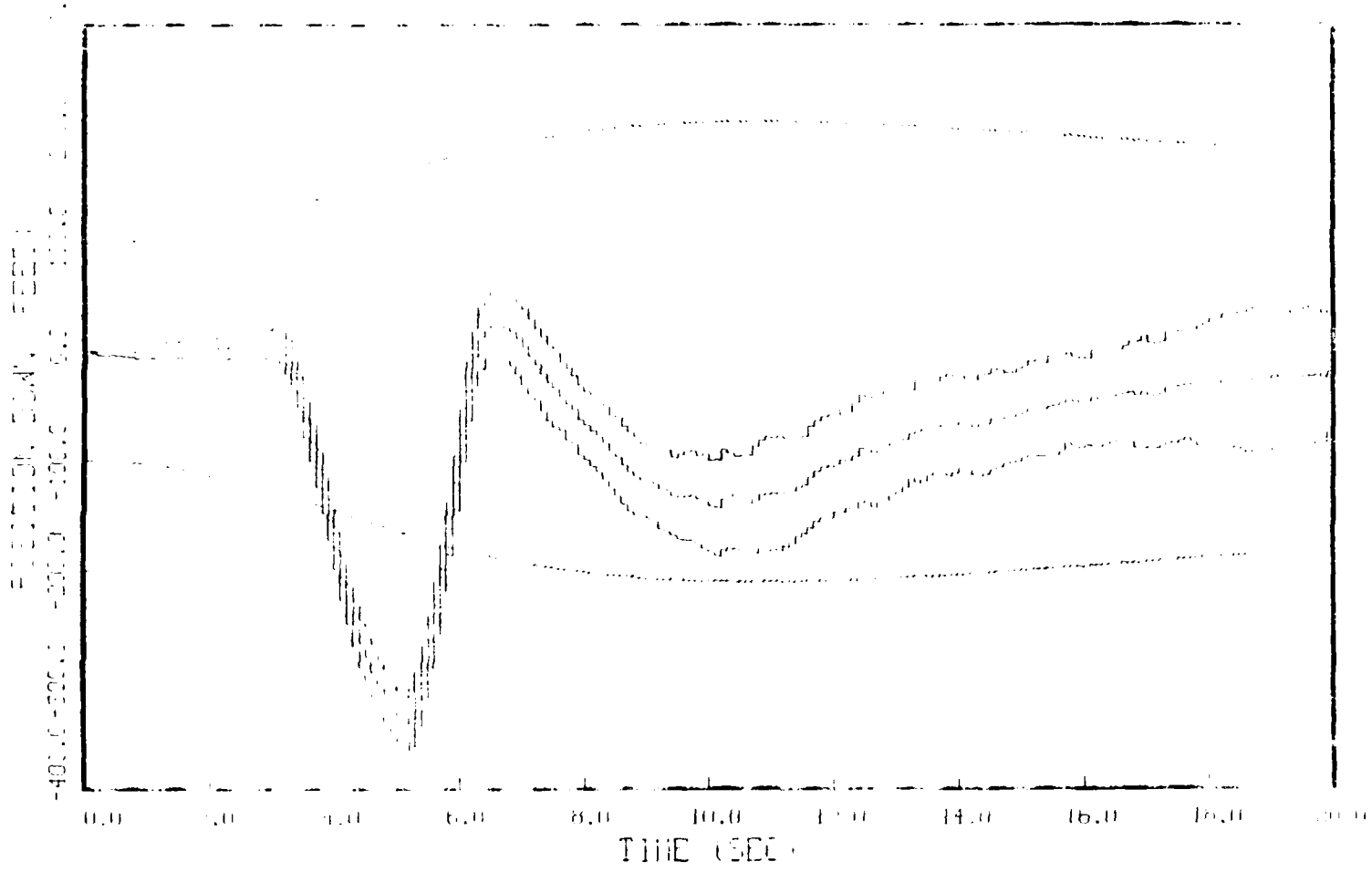

FIGURE 3.7 : [illegible]

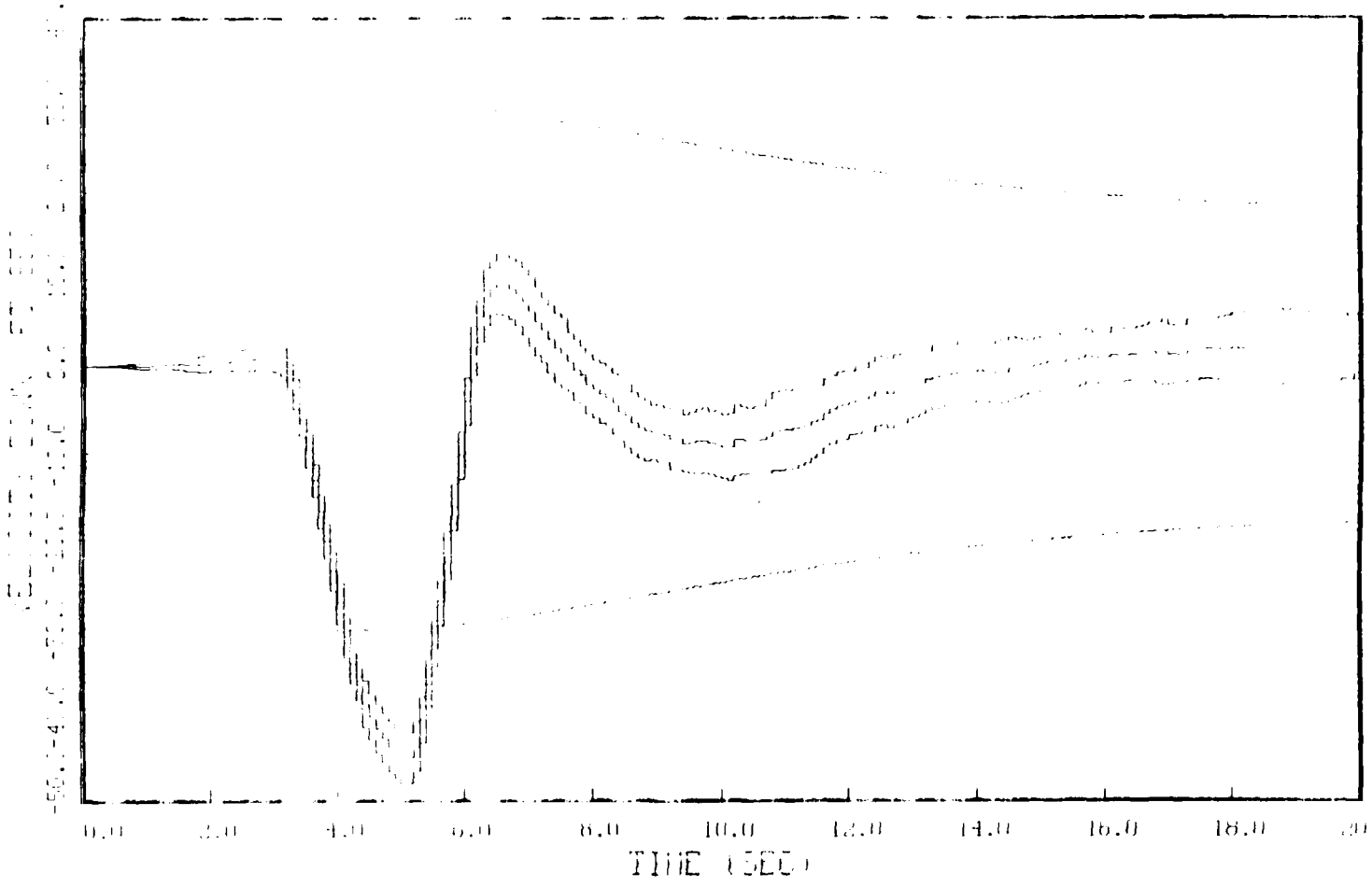

FIGURE J.6: [illegible]

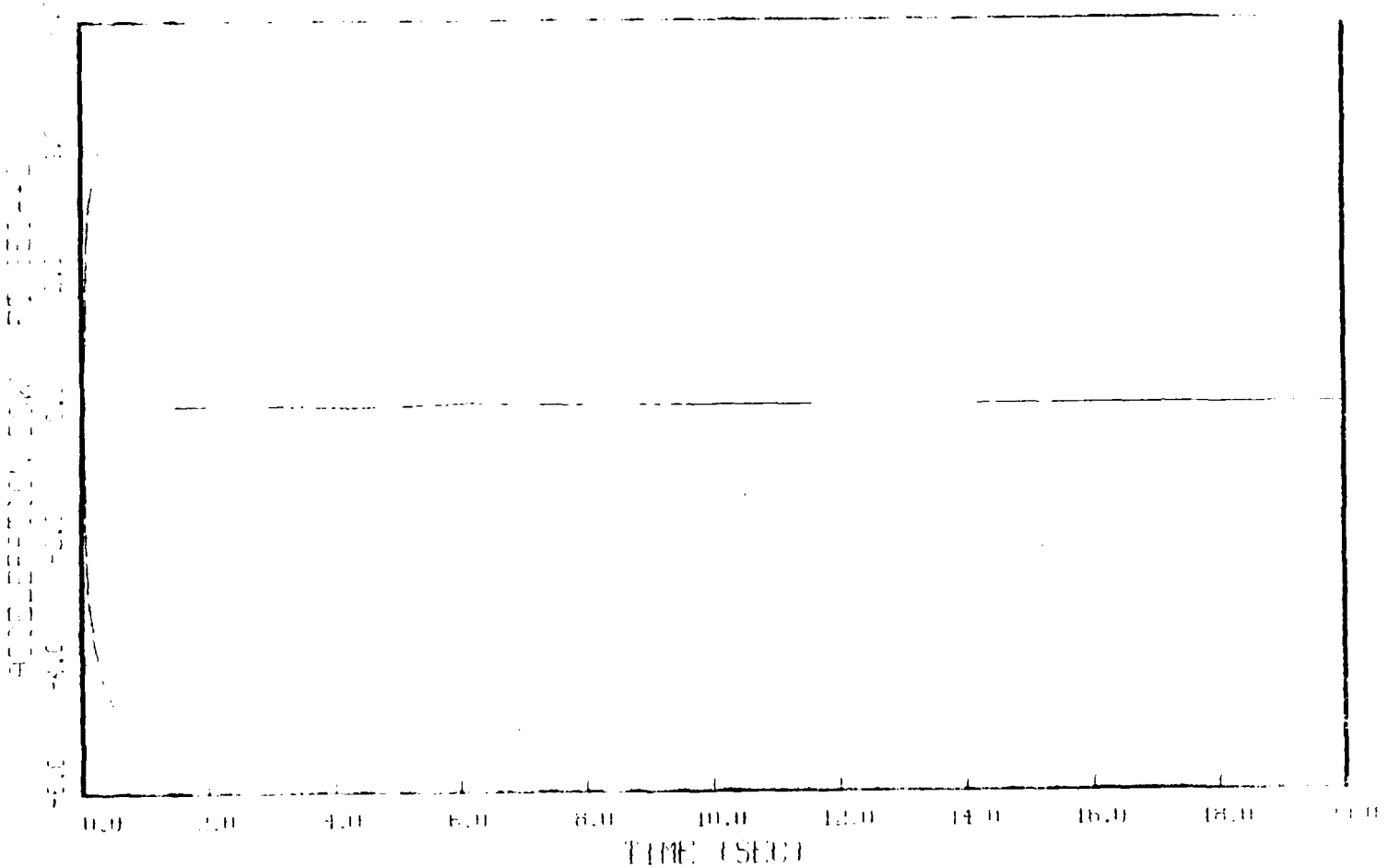

FIGURE 1.9: [illegible] MARKOV MODEL, STATE 9, 20 RUNS, D=100, FULL STATE
[illegible]

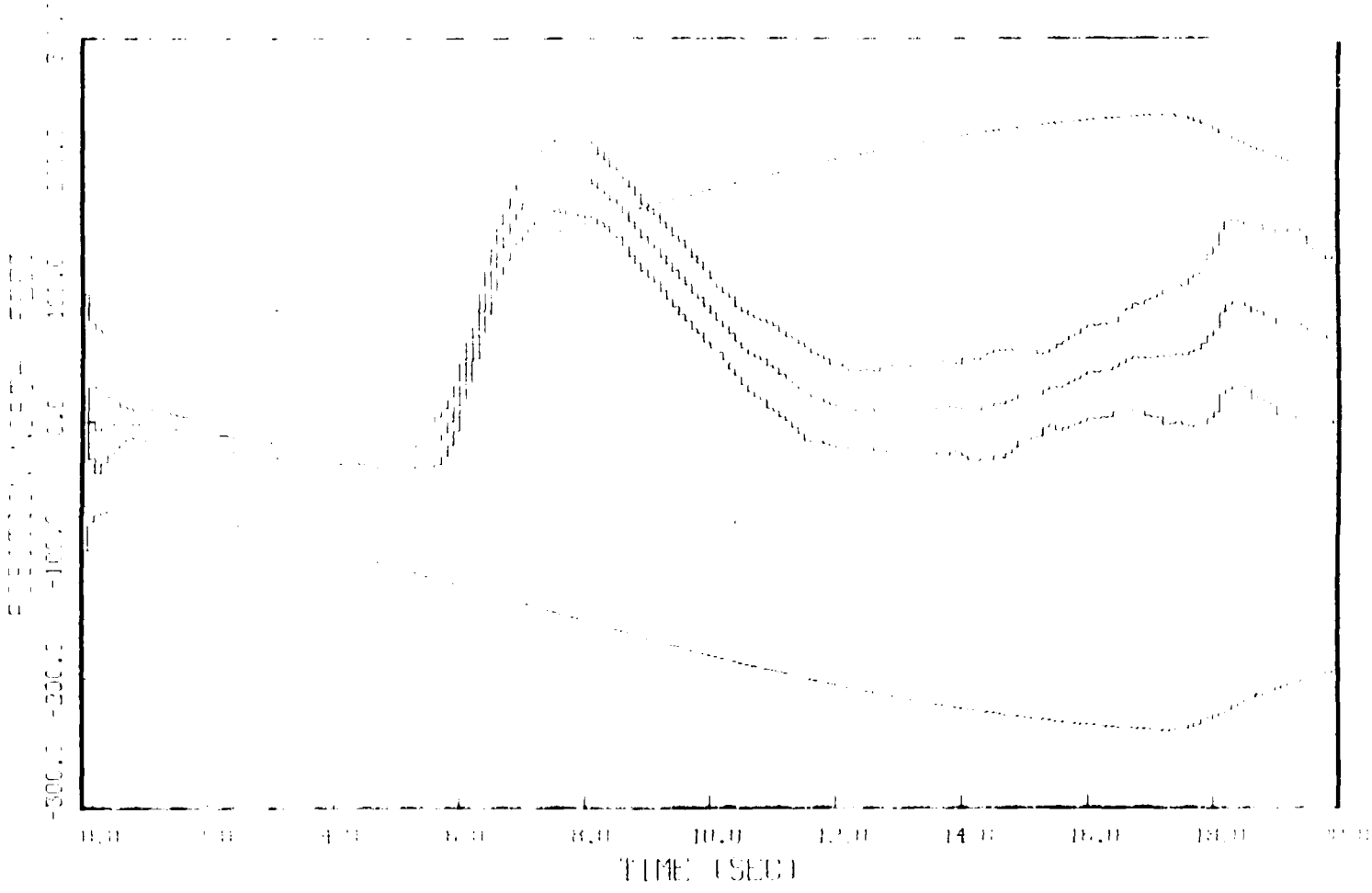

FIGURE 4.10: [illegible] MODEL, STATE 1, 20 RUNS, 0 100, FULL STATE
[illegible]

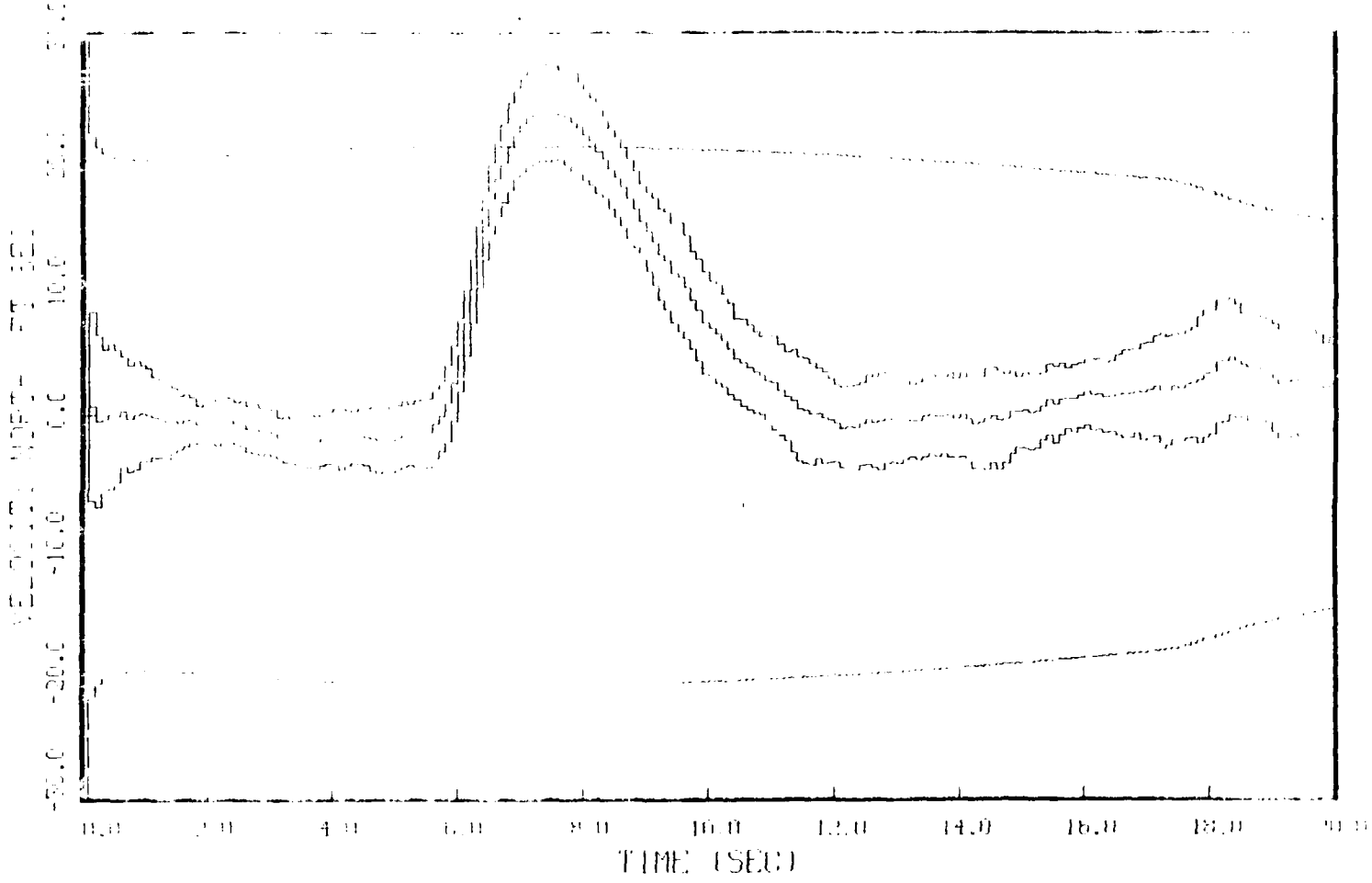

FIGURE 5.11: GROSS MARTIN MODEL, STATE 2, 20 RUNS, 0-100, FULL STATE
INITIALIZED, 4 GUNS: 1&2, 1&3 RATE, SIN AZ & EL GR=3.0E-4 FOR AZ & EL

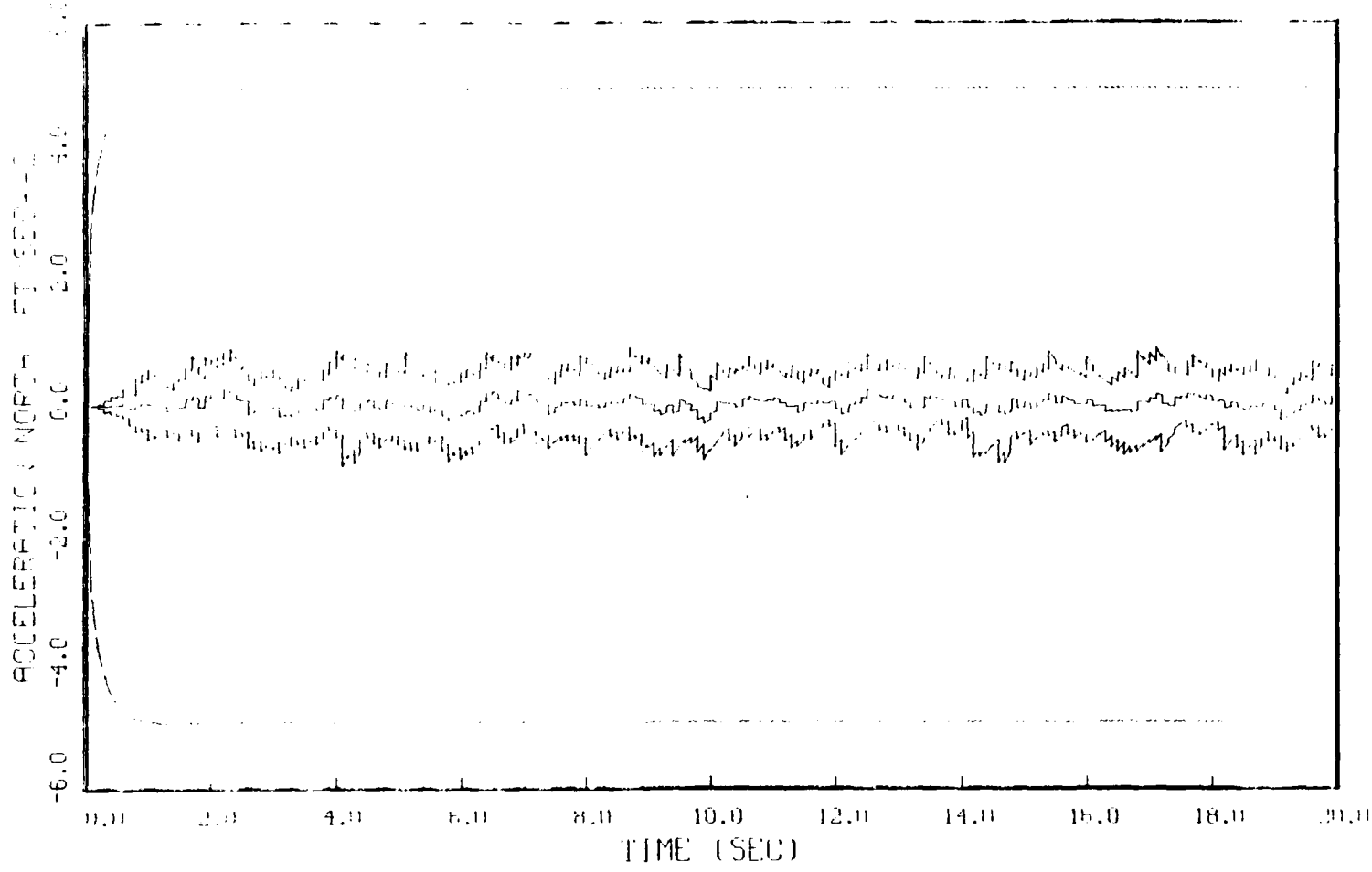

FIGURE 3.12: GAUSS MARKOV MODEL, STATE 3, 20 RUNS, Q=100, FULL STATE TAILCHASE, 4 MEAS: RNG, RNG RATE, SIN AZ & EL (R=3.0E-4 FOR AZ & EL)

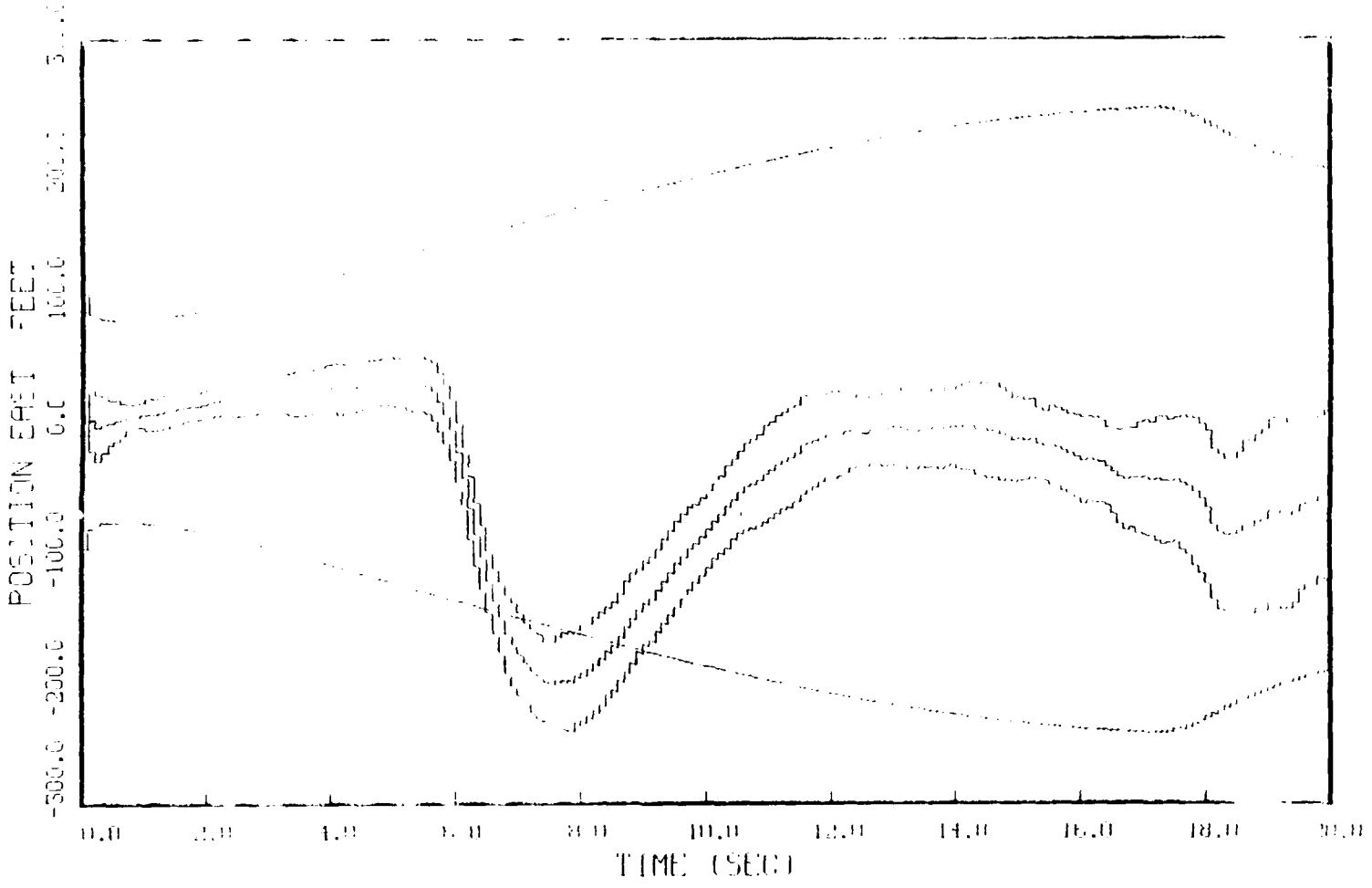

FIGURE 3.13: GAUSS MARKOV MODEL, STATE 4, 20 RUNS, Q=100, FULL STATE
INTEGRATOR, 4 MEAS: RNG, RNG RATE, SIN HZ & EL (R=3.0E-4 FOR HZ & EL)

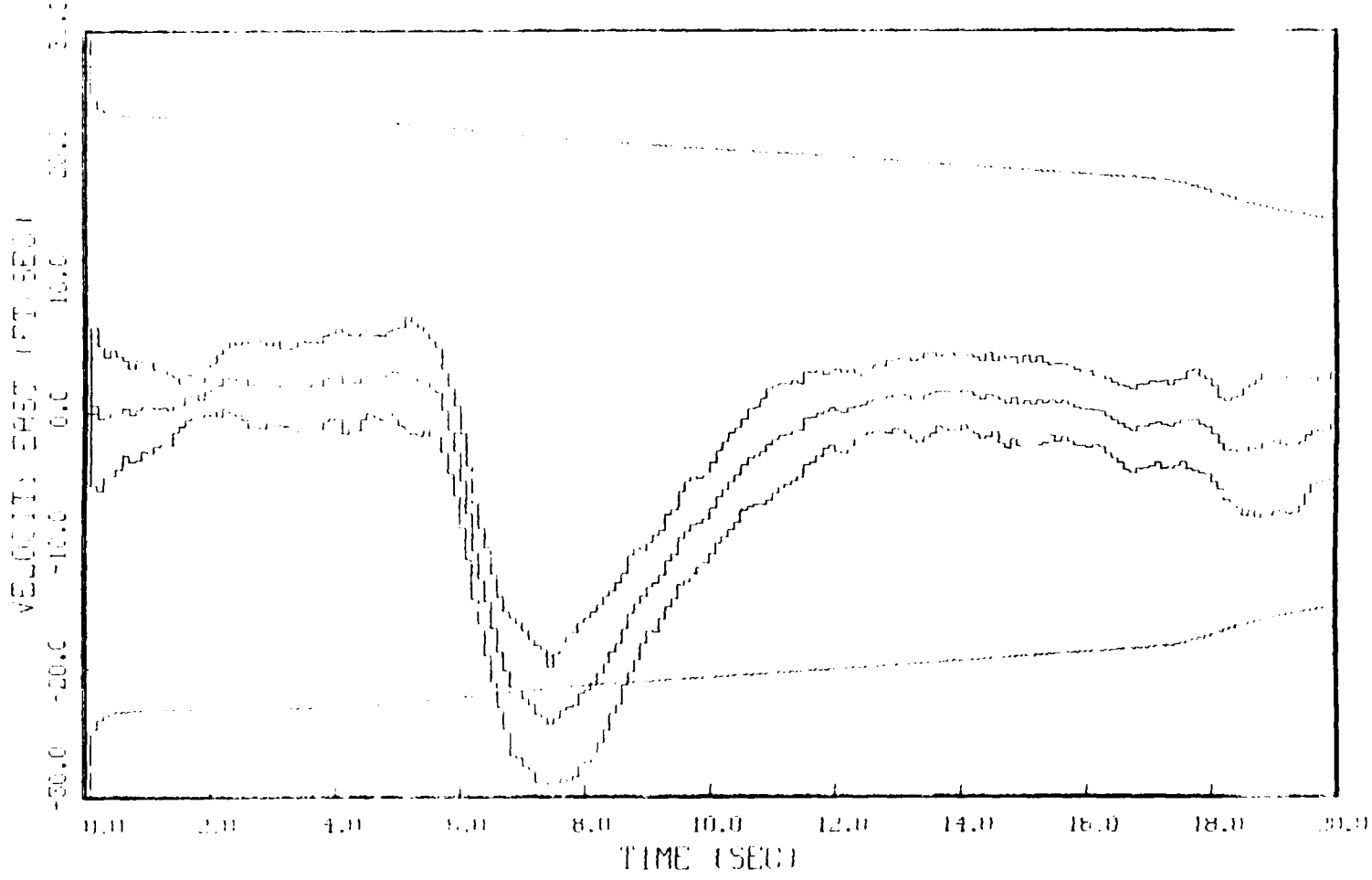

FIGURE 6.14: CROSS-MARKOV MODEL, STATE 5, 20 RUNS, D=100, FULL STATE
INTERCHANGE, 4 ITER = 100, 100 STEP, 5TH HZ & EL (R=5.0E-4 FOR HZ & EL)

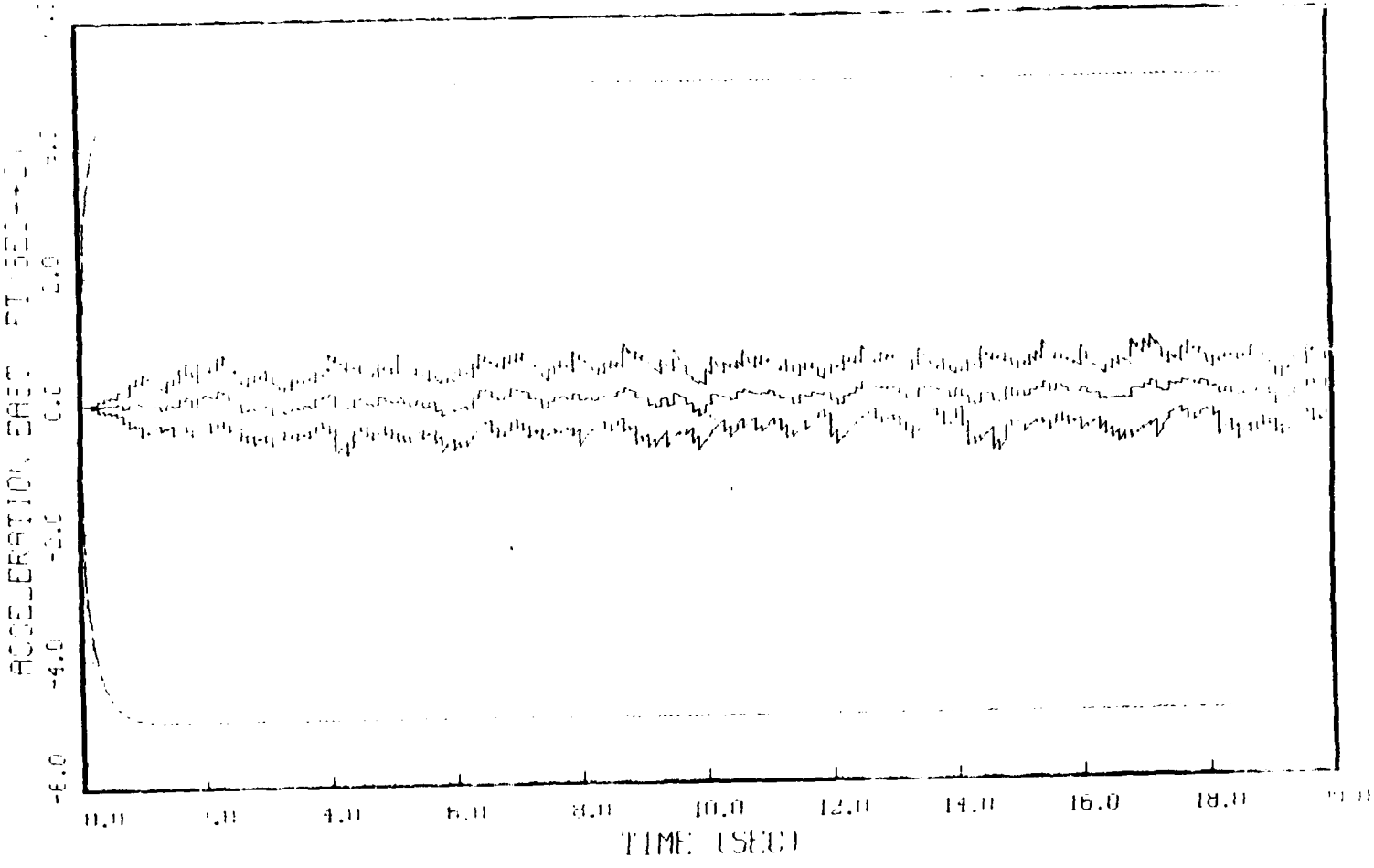

FIGURE 4.15: GAUSS MARKOV MODEL, STATE 6, 20 RUNS, U=100, FULL STATE
INTERCHANGE, 4 MEANS: RNG, RNG RATE, SIN AZ & EL (R=5.0) & COS AZ & EL

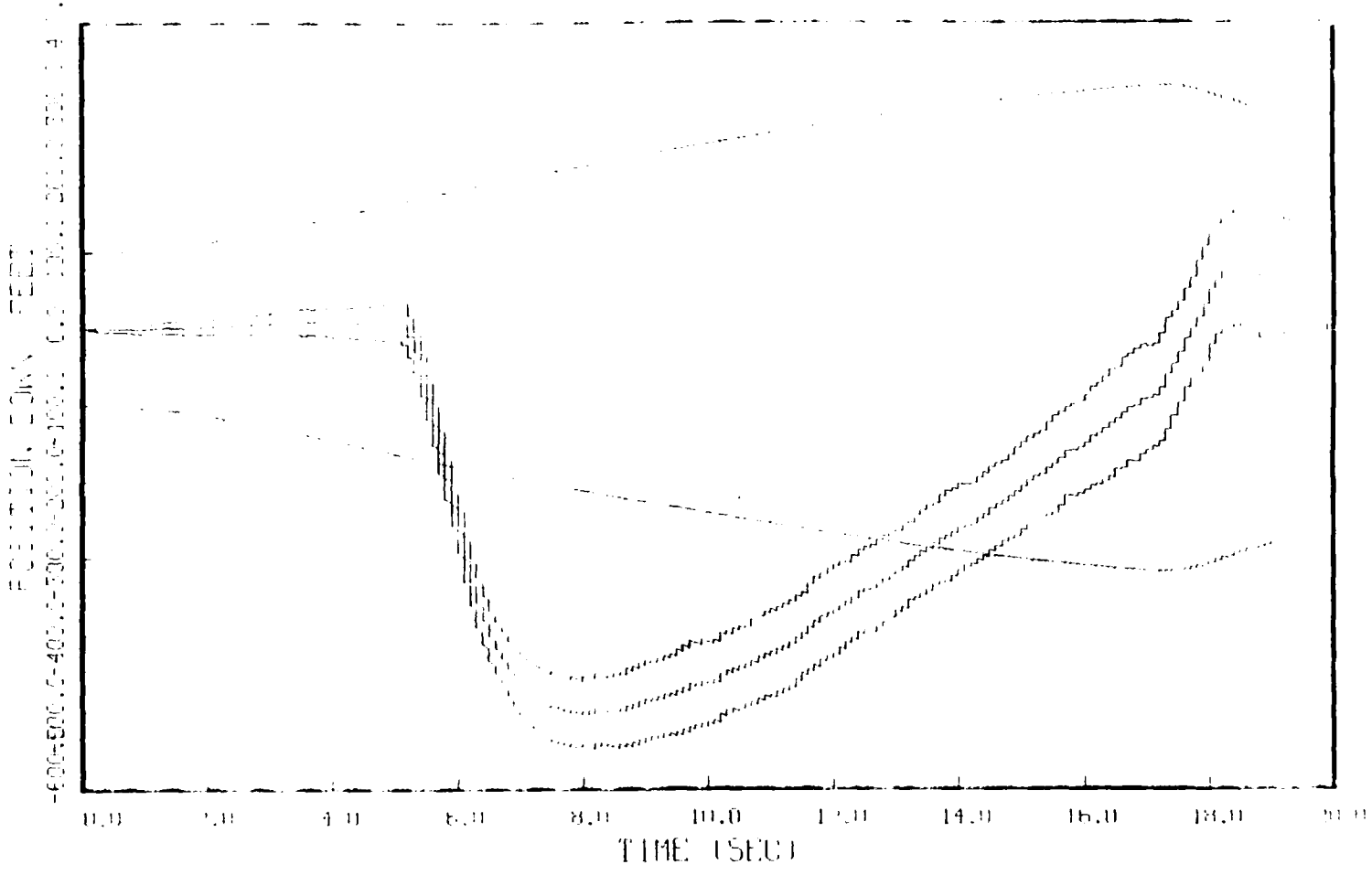

FIGURE 5.1a: GAUSS MARKOV MODEL, STATE 7, 20 RUNS, 0-100, FULL STATE
INIT. ANGLE, 4 MEAS.: RNG, RNG RATE, SIN AZ & EL (R=3.0E-4 FOR AZ & EL)

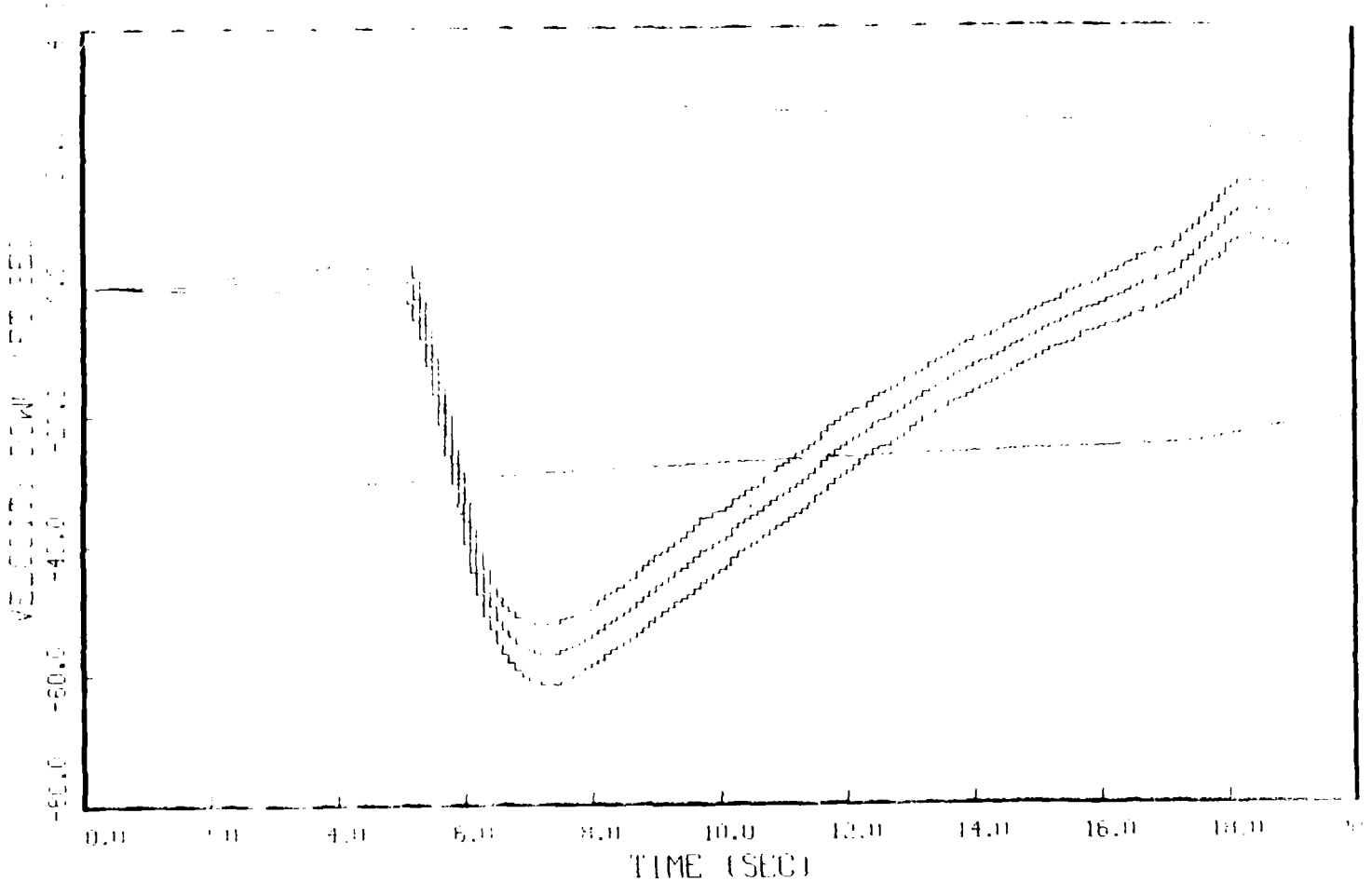

FIGURE 4.1*: GAUSS MARKOV MODEL, STATE 8, 20 RUNS, 0-100, FULL STATE
TRIGGERED, 4 LEAD: RNG, RNG RATE, SIN HZ & EL TE-SLOPE 4 FOR HZ & EL

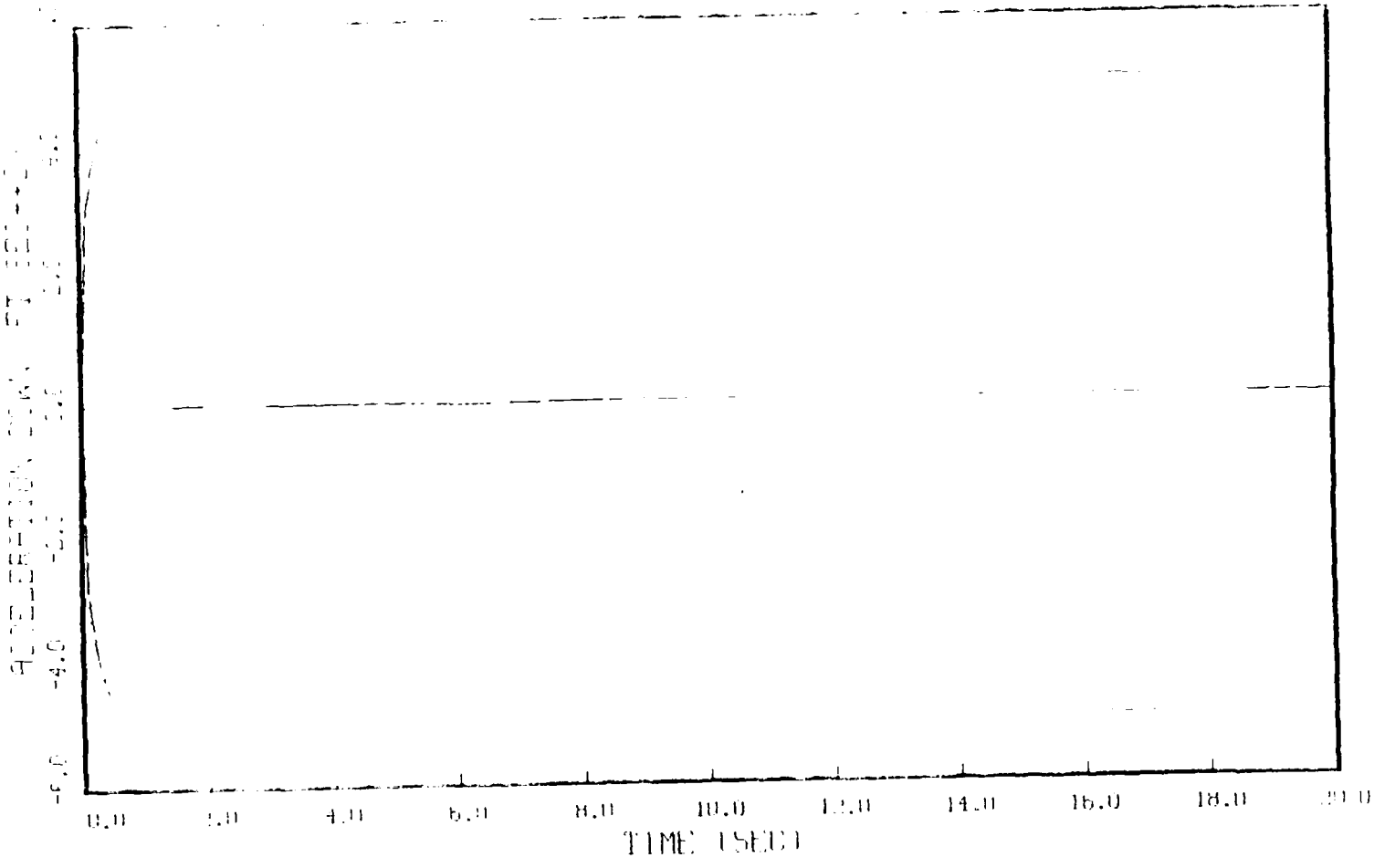

FIGURE J.16: GAUSS MARKOV MODEL, STATE 9, 20 RUNS, DT=100, FULL STATE
INTEGRATE, 4 MODES: RK5, FULL RATE, SIN HZ & EL DT=.01 4 FOR HZ & EL

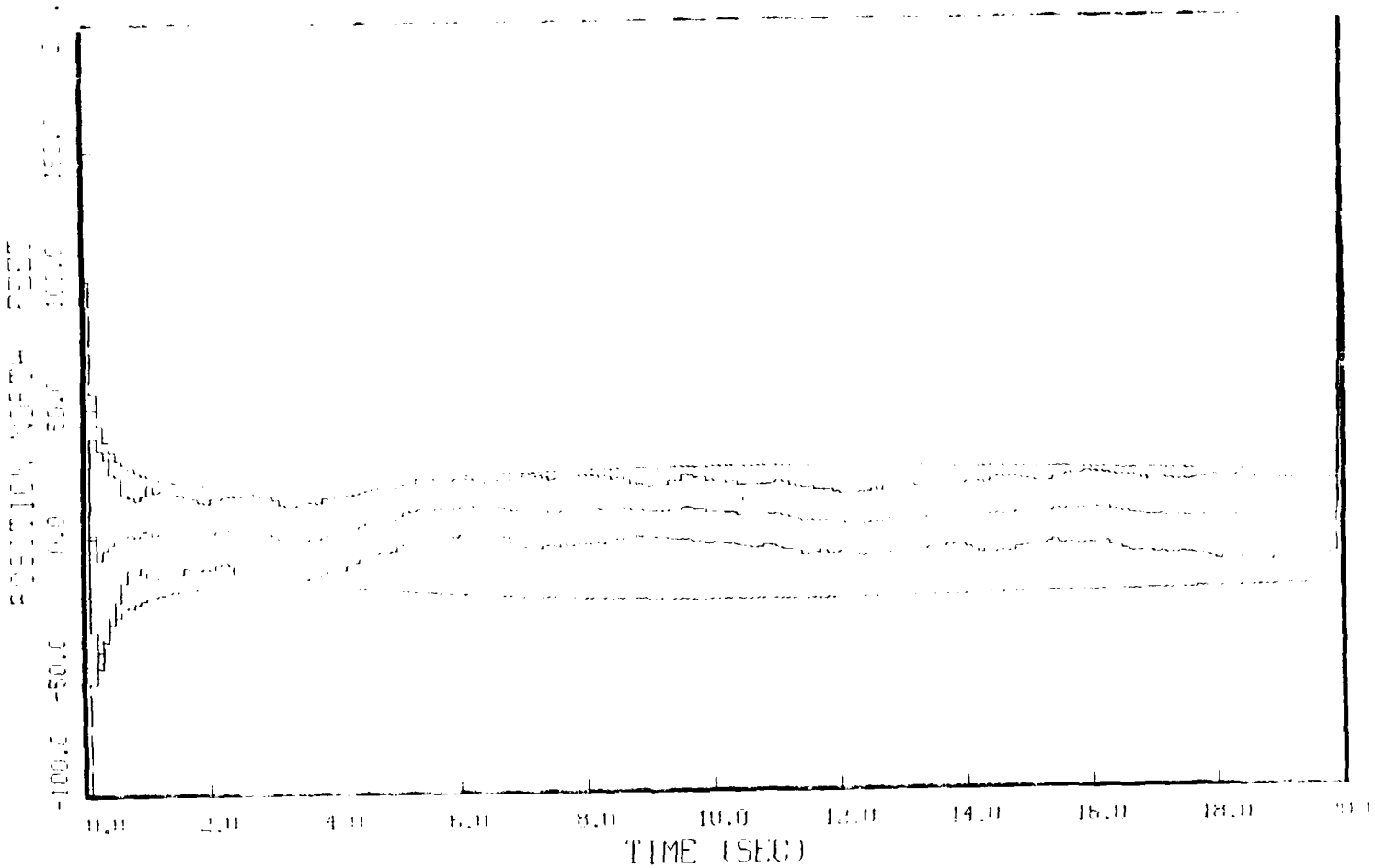

FIGURE 3.19: GAUSS MARKOV MODEL, STATE 1, 20 RUNS, Q=100, FULL STATE
MEASUREMENTS, 1 SIGMA: RNG, RNG RATE, SIN AZ & EL (R=3.0E-4 FOR AZ & EL)

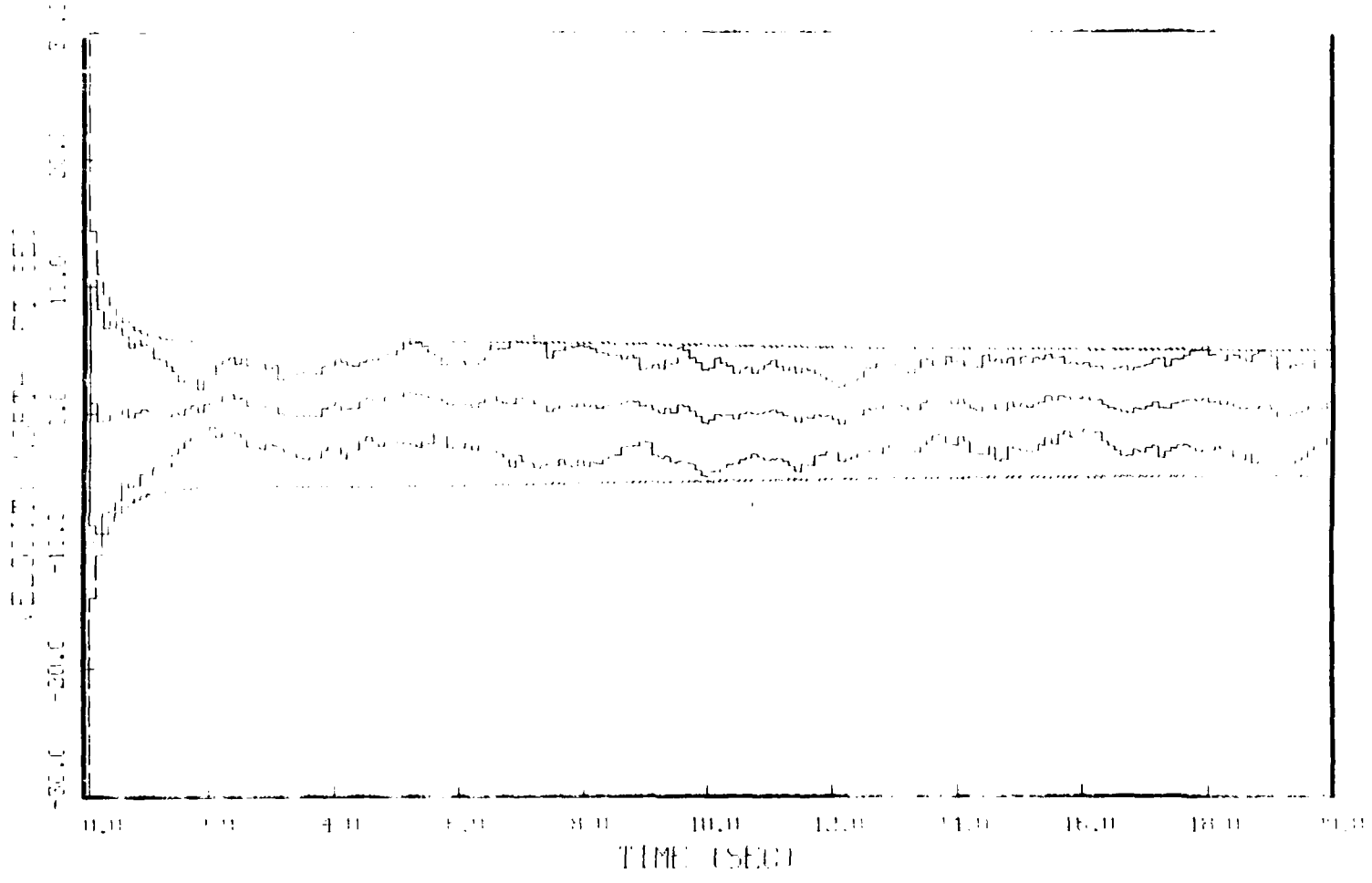

FIGURE 3.30: GAUSS MARKOV MODEL , STATE 2, 20 RUNS, [illegible], [illegible] STATE
[illegible] , 4 [illegible] RMS, RMS RATE, SIM RMS , [illegible] RMS, [illegible]

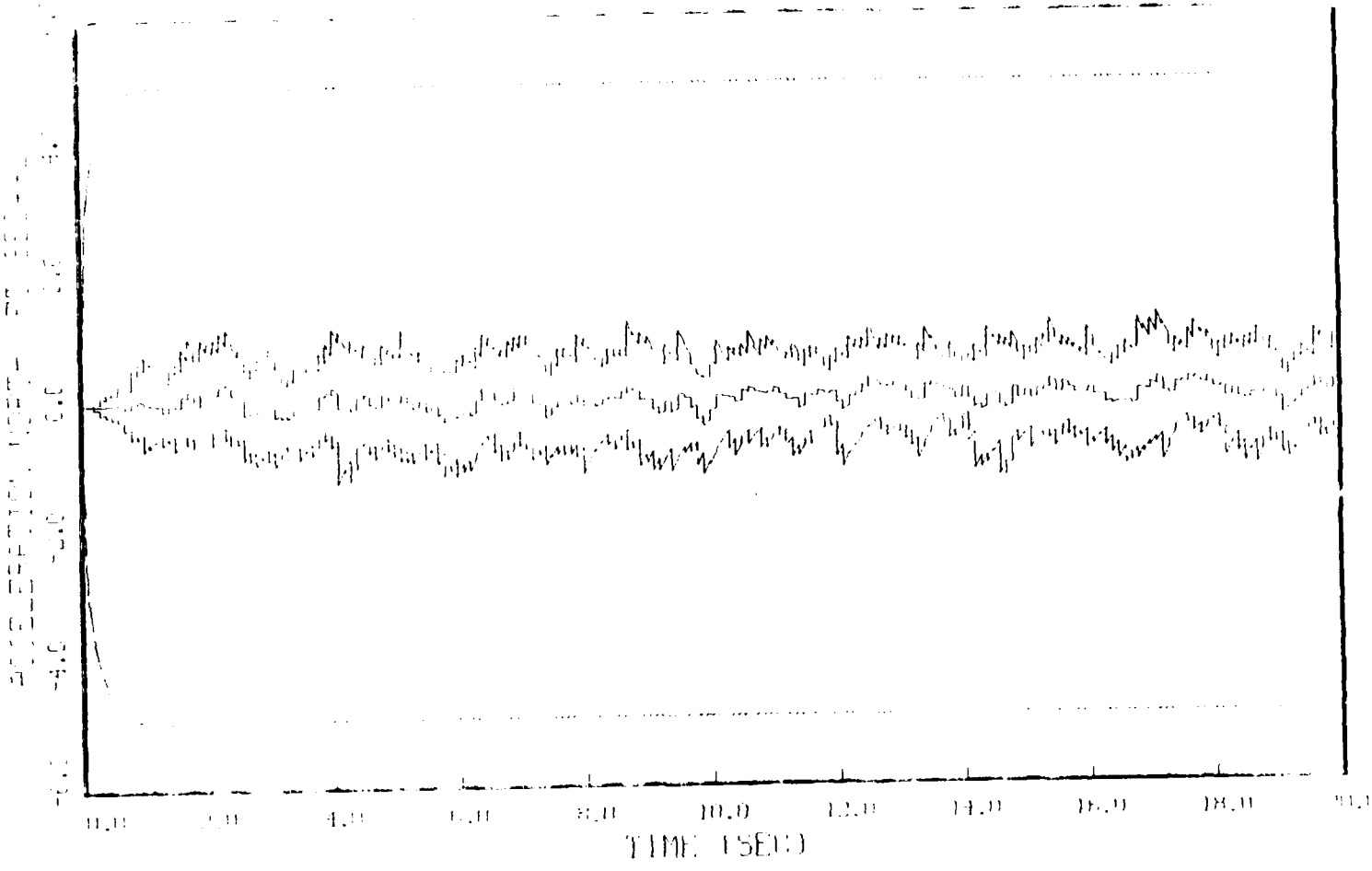

FIGURE [illegible]: CHOI-WILLIAMS MODEL, STATE 3, 20 RUNS, 6-TAU, FULL STATE [illegible]

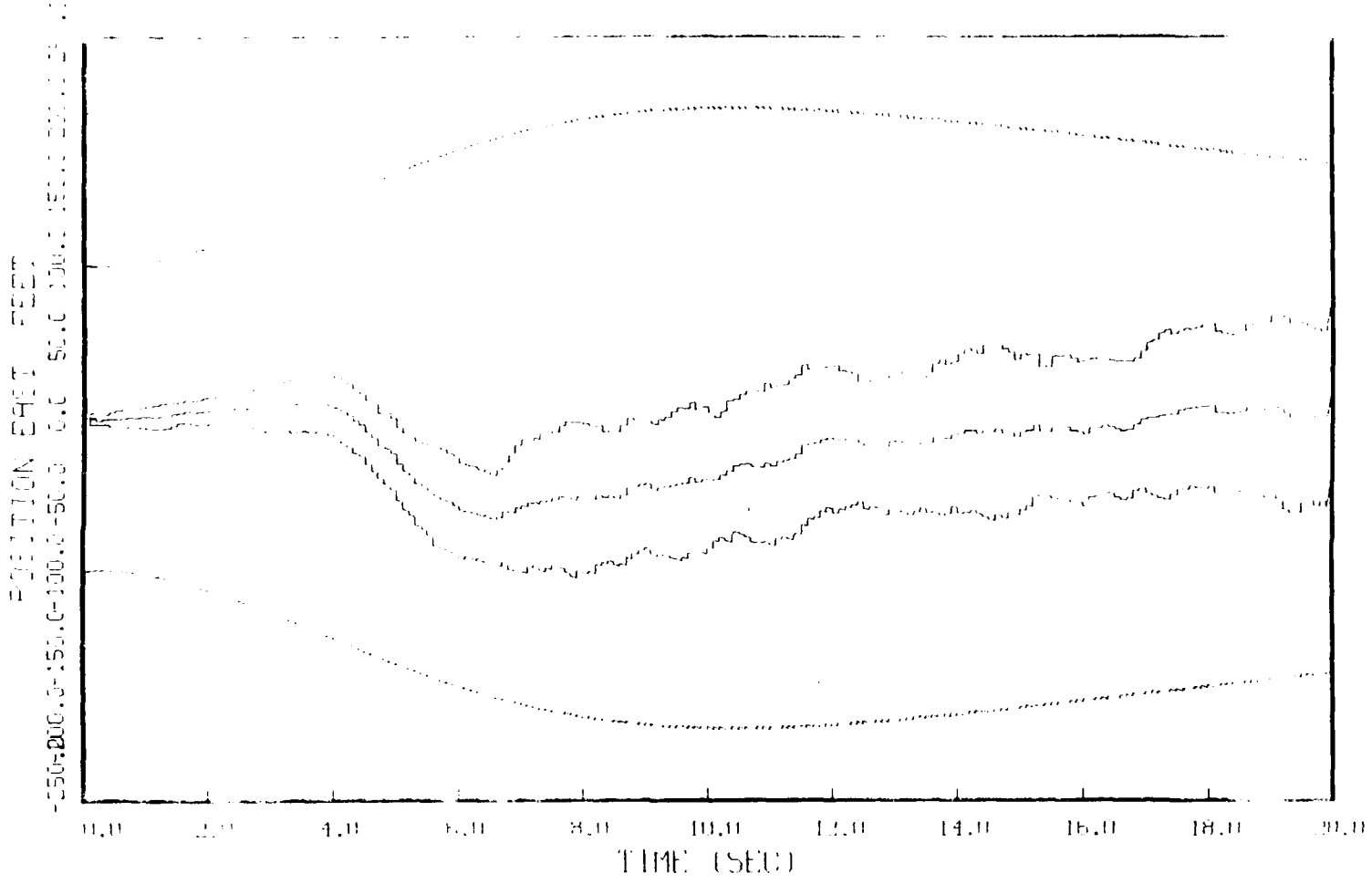

FIGURE [illegible] GROSS MAHEFUV MODEL, STATE 4, 20 RUNS, D=100, FULL STATE
[illegible], 1 HERTZ [illegible], SIN HZ & EL IN 5.0E-4 FOR HZ & EL

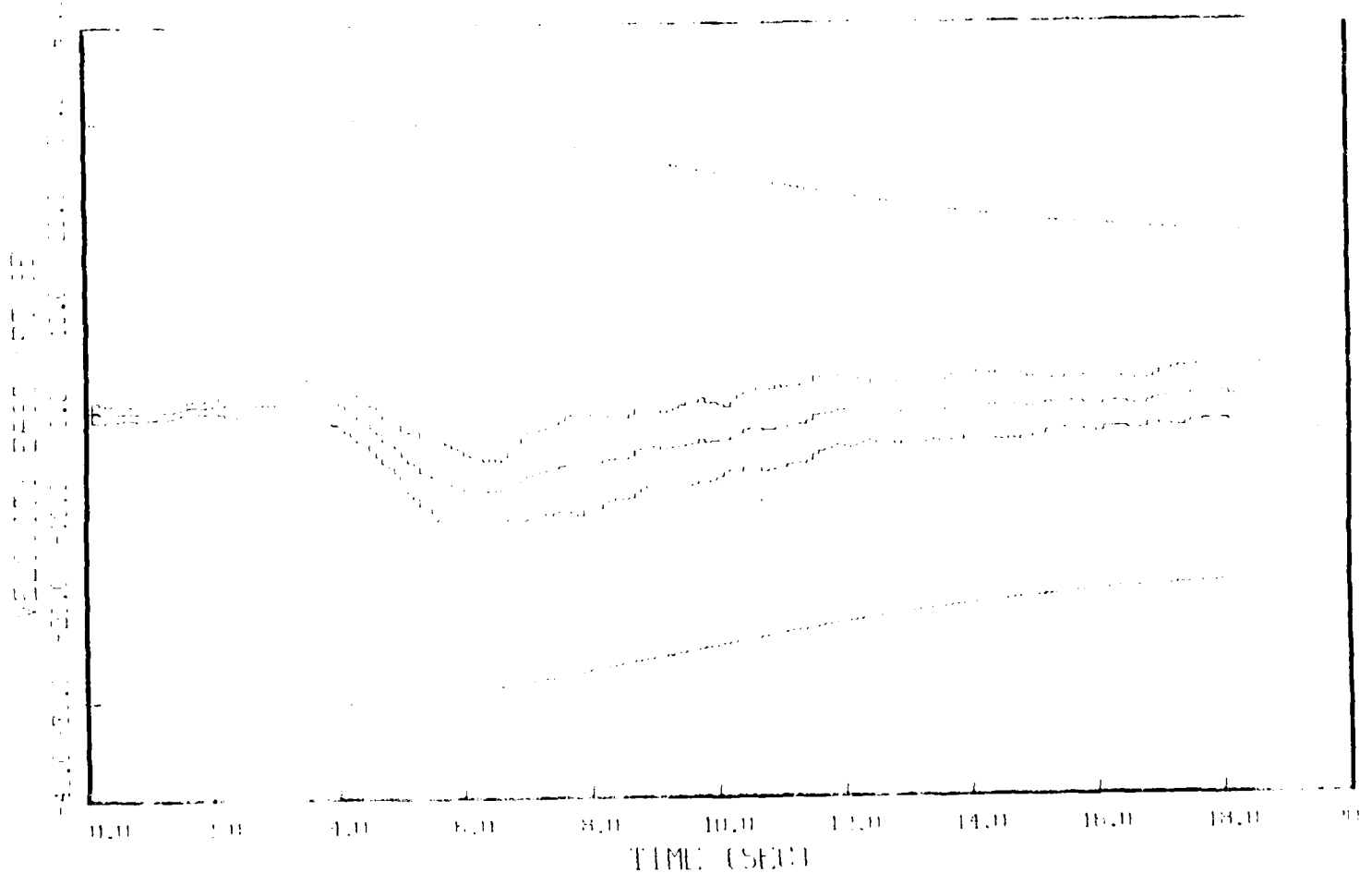

FIGURE [illegible]: [illegible] MOBILITY MODEL, STATE 5, 20 RUNS, [illegible], FULL STATE [illegible], [illegible] FIG, RMS RATE, STATE RX & EL [illegible] FOR RX & EL

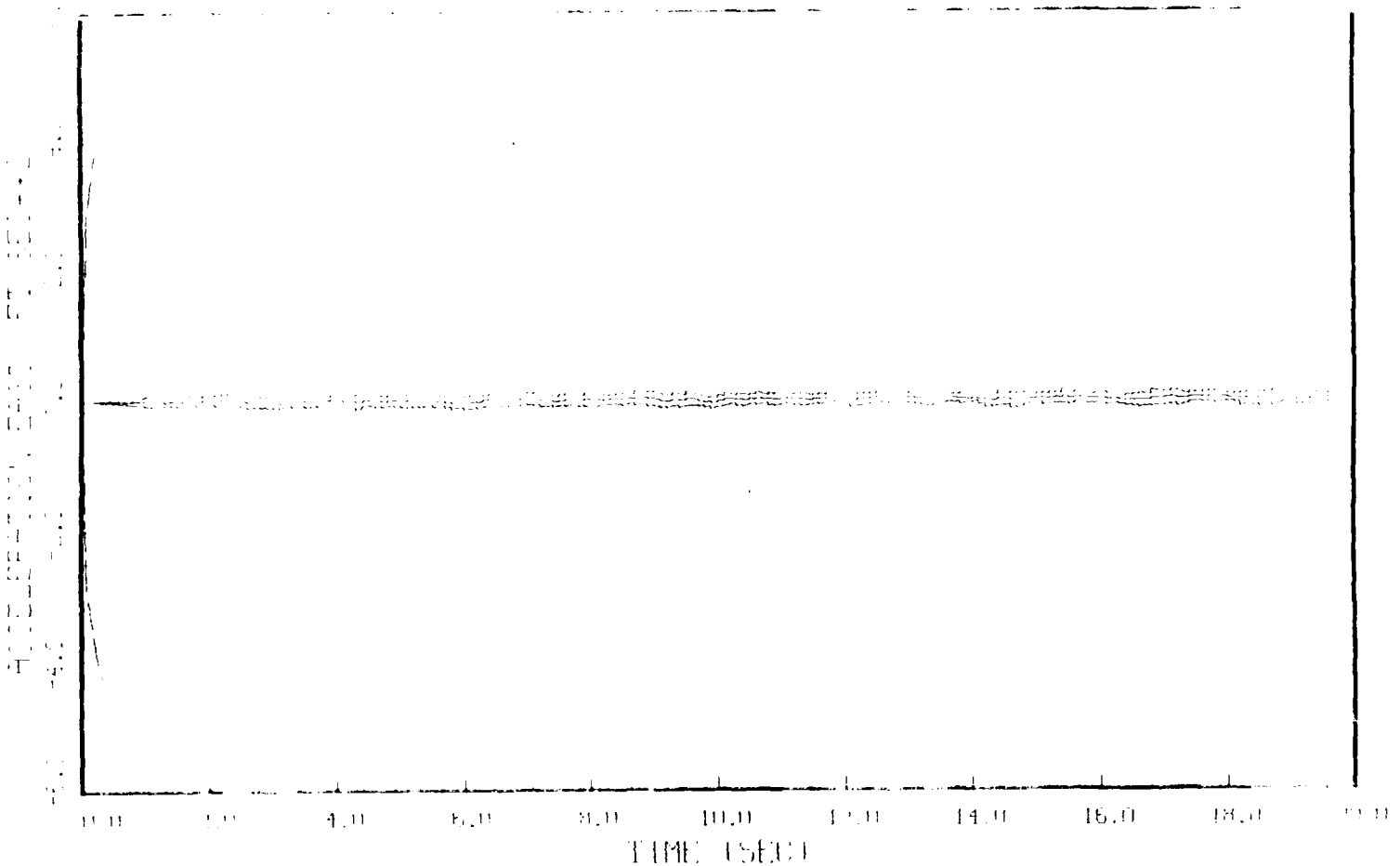

FIGURE [illegible]: GAUSS MARKOV MODEL, STATE 6, 20 RUNS, 0 100, FULL STATE
RECOVERY, [illegible] BIAS, BIAS RATE, STATE [illegible] 0.00E-4 FOR RE & [illegible]

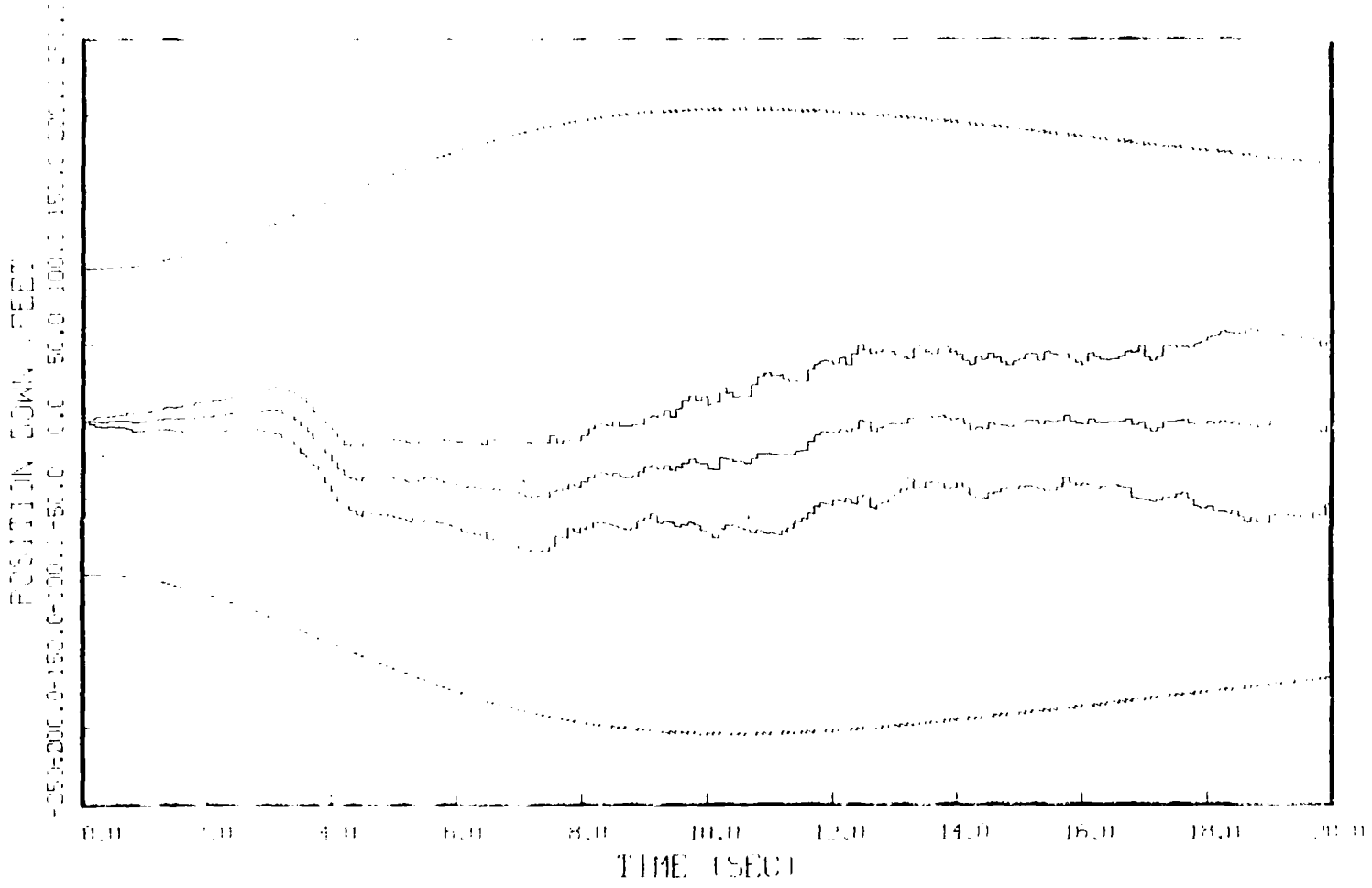

FIGURE [illegible]: [illegible] MARKOV MODEL, STATE 7, 20 RUNS, 0-100, FULL STATE
HEAD ON ATTACK, [illegible] RNG, RNG RATE, STN AZ & EL [illegible] FOR AZ & EL

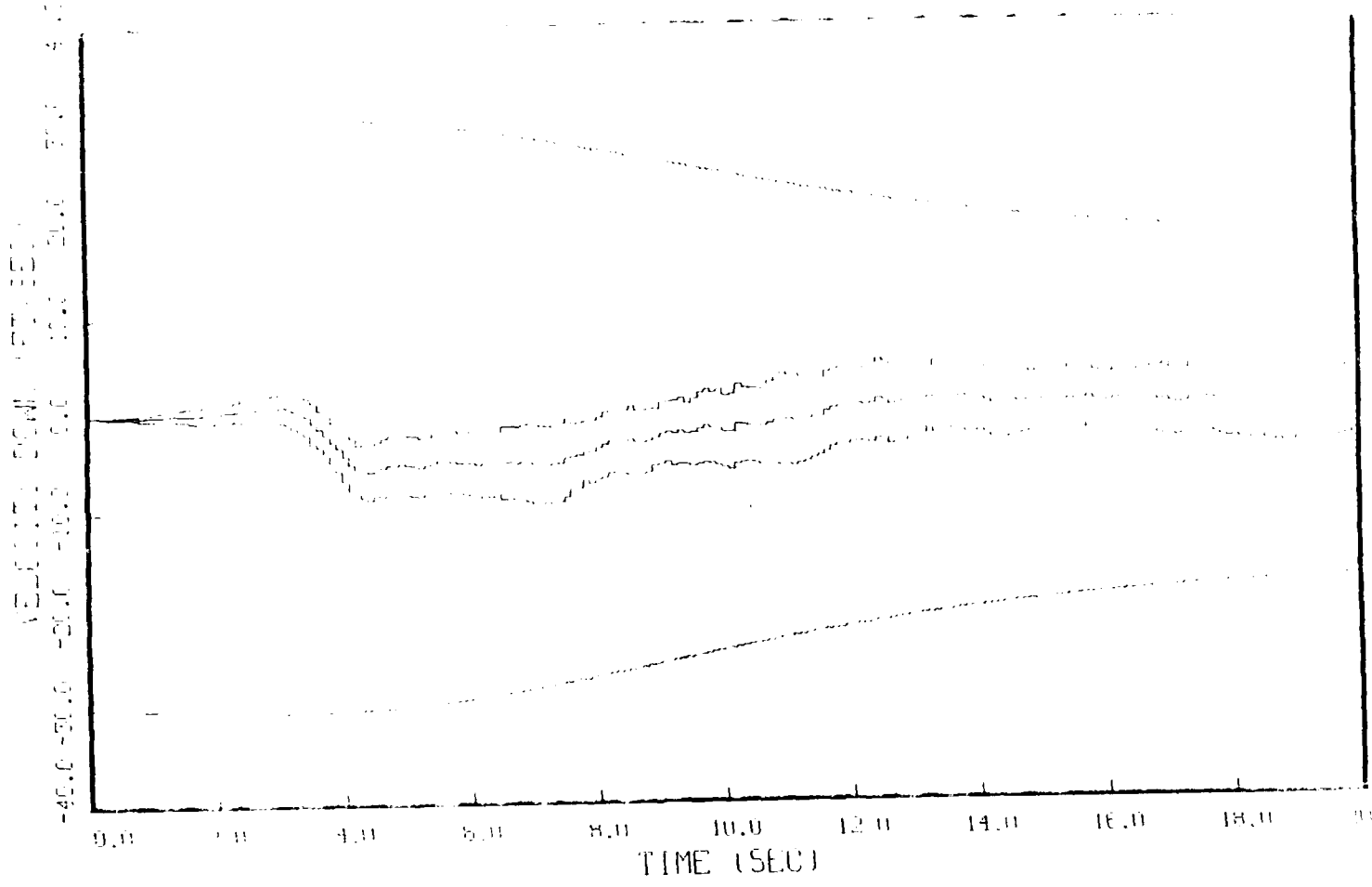

FIGURE 1.26: GAUSS MARKOV MODEL, STATE 8, 20 RUNS, 0-100, FULL STATE
HEAD ON ATTACK, 4 TERMS: ENG, ROG RATE, SIN HZ & CL TR= 3.0E 1 FOR HZ & CL

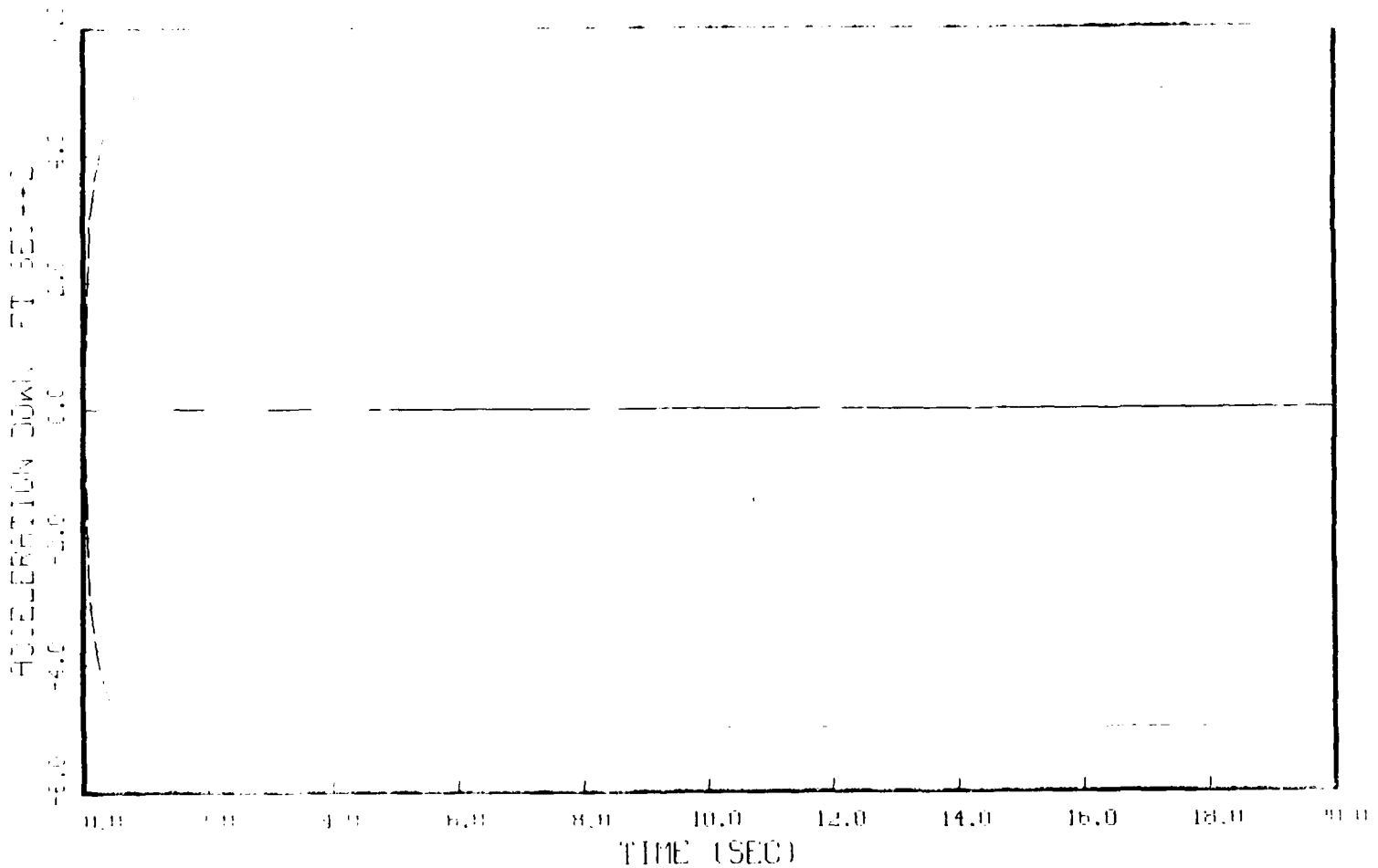

FIGURE [illegible] : [illegible] DYNAMIC MODEL, STATE 9, 20 RUNS, 0=100, FULL STATE
[illegible], [illegible] STD, LOG RATE, STD HZ & LL OK 3.0E-1 FOR HZ & LL

Appendix K

Ad Hoc Suppression of the Vertical Channel

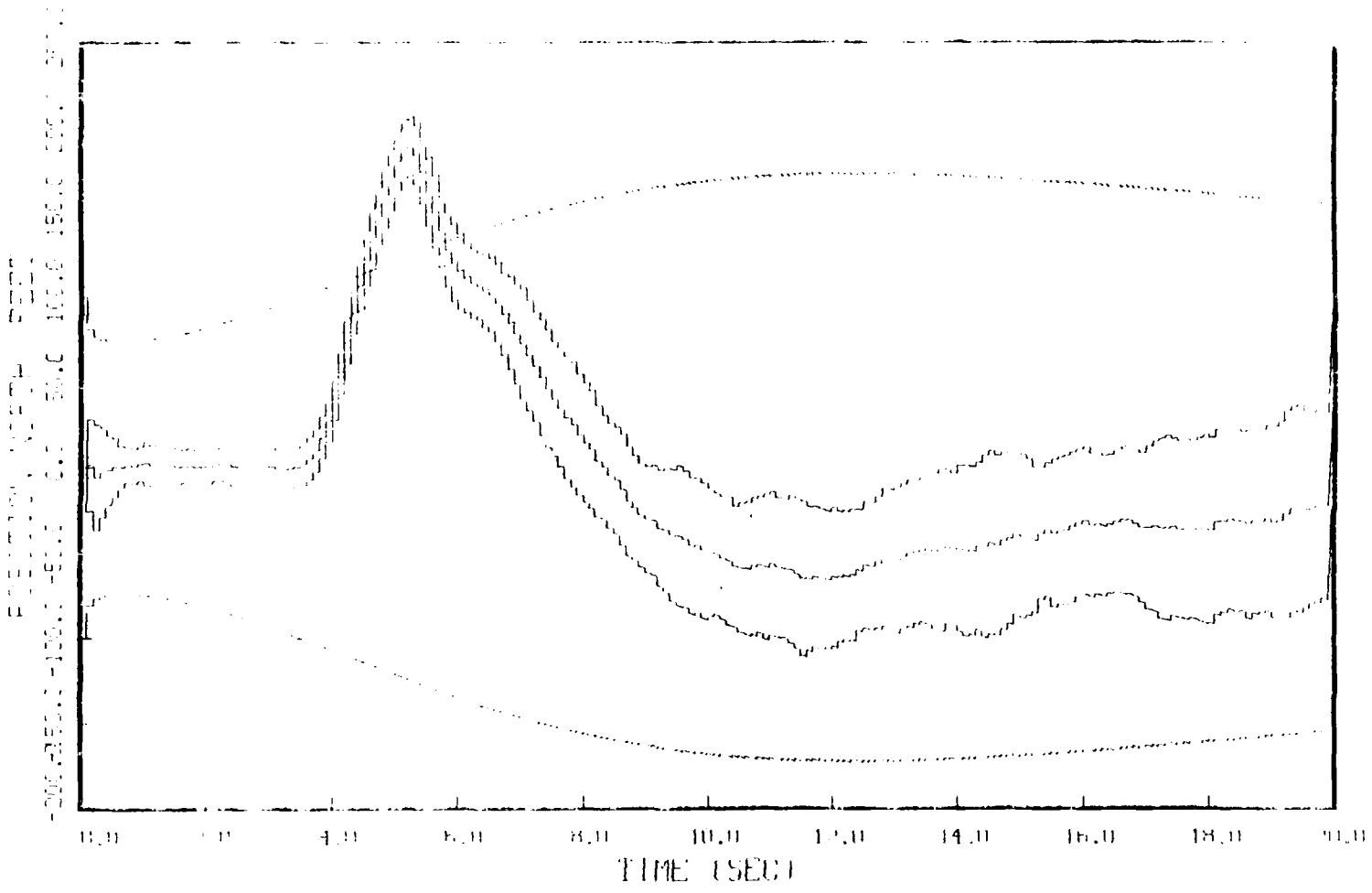

FIGURE [illegible]: GHIOTA CHARTOV MODEL, STATE 1, 20 RUNS, D=100, VERT CHAN SUPERIMPOSED
ON 3 TRIAXIAL RUNS, 4 [illegible] RMS, RMS RATE, STD HZ & EL IN SCALE 4 FOR HZ & EL

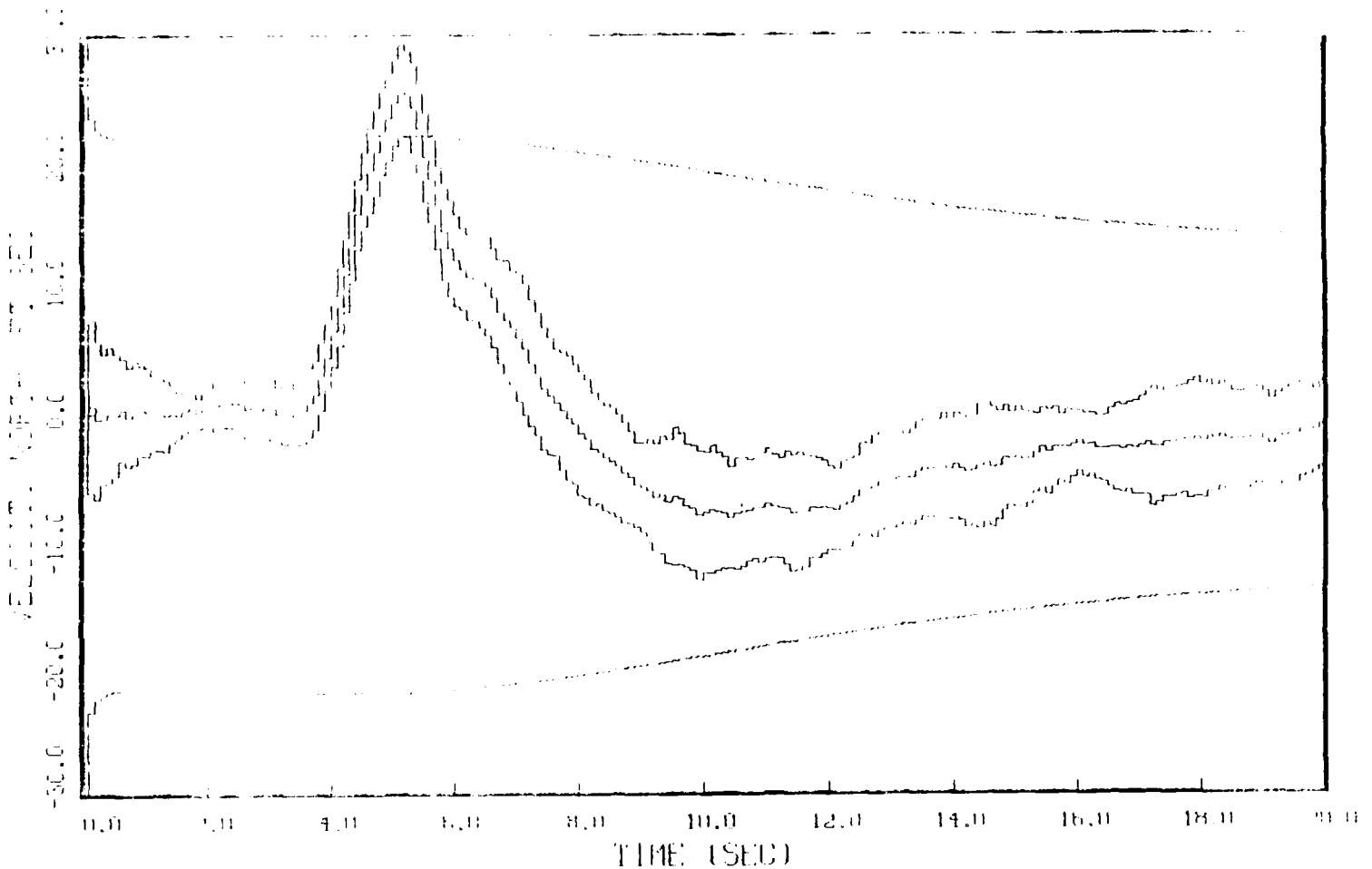

FIGURE [illegible]: [illegible] MARKOV MODEL, STATE 2, 20 RUNS, U=100, VERT CHAN SUPERIMPOSED
BEAM Trans: [illegible], [illegible] : NNS, 0.05 RATE, STD HZ & EL DS=5.0E-4 FOR HZ & EL

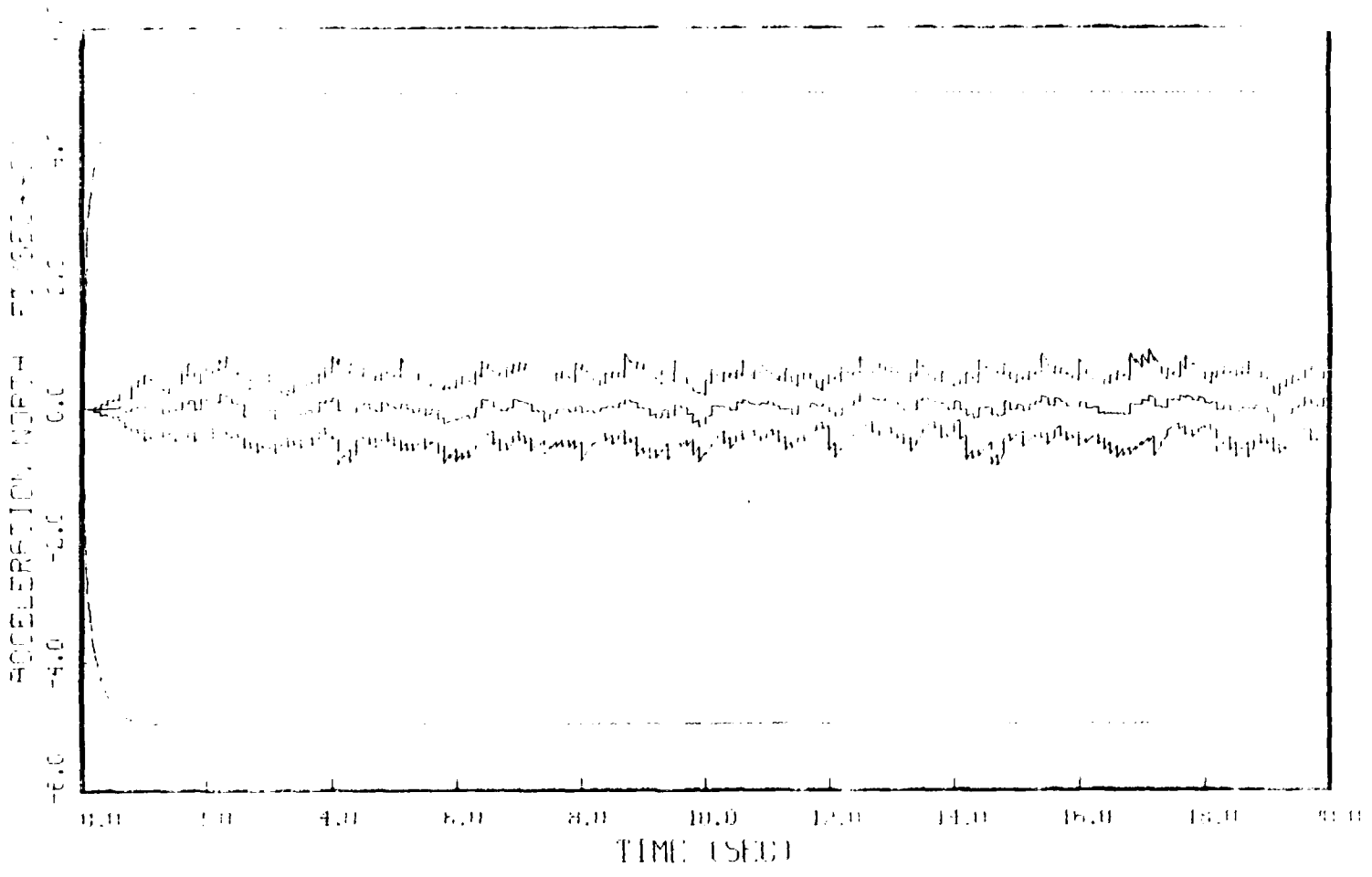

FIGURE F.3: GAUSS MARKOV MODEL, STATE 3, 20 RUNS, [illegible], VERT CHAN SUPPRESSED
SEAT TRANSMISSIBILITY, 4 FILES: RMS, RMS RATE, STD HZ & EL. OF 3.0E 4 FOR HZ & EL

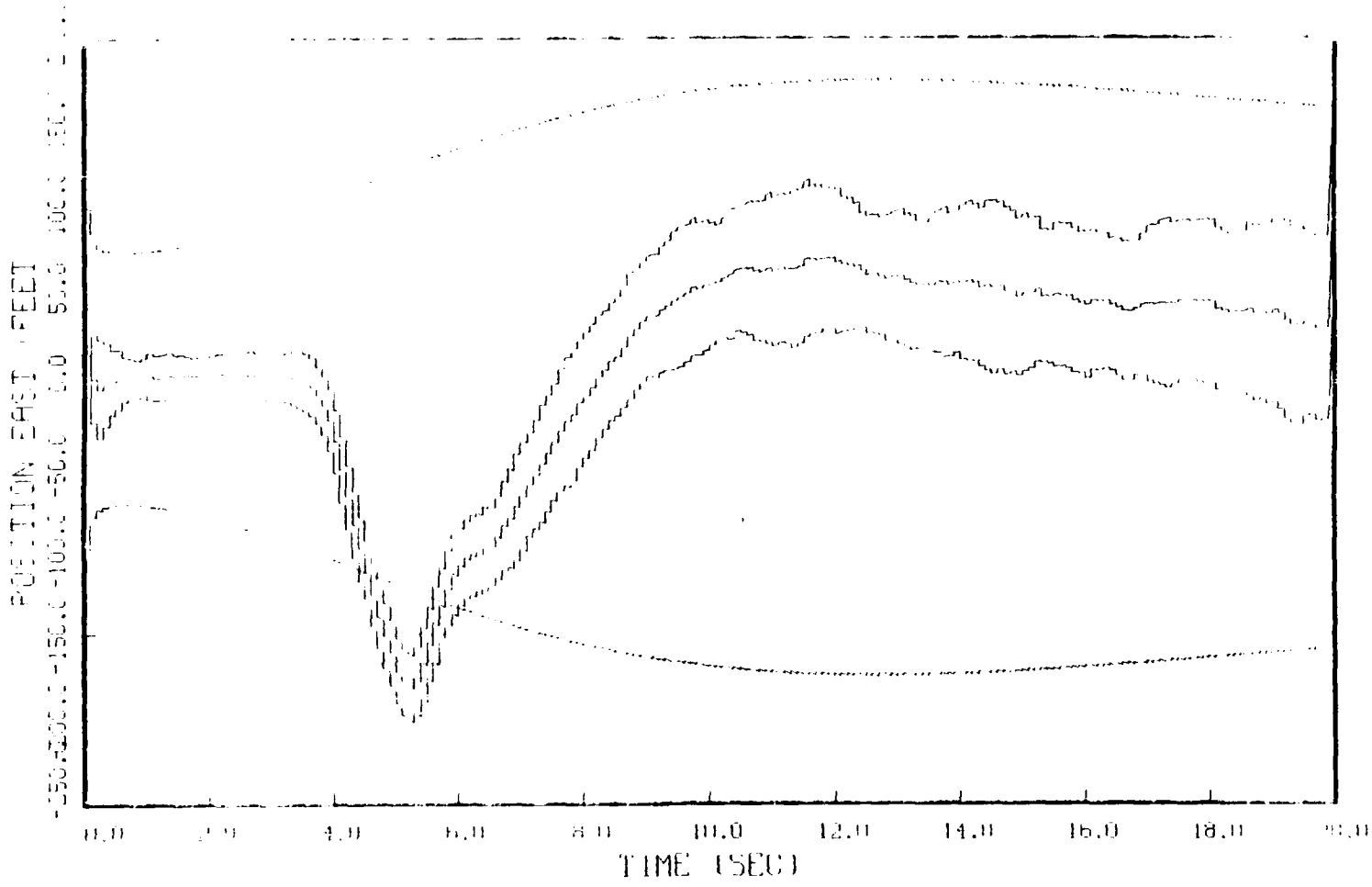

FIGURE F.4: GAINS ADAPTIV MODEL, STATE 4, 20 RUNS, U=100, VERT CHAN SUPPRESSED
BASE INFORMATION, 1 RUNS: RMS, MDG RATE, STD RZ & EL ER=3.0E-4 FOR RZ & EL

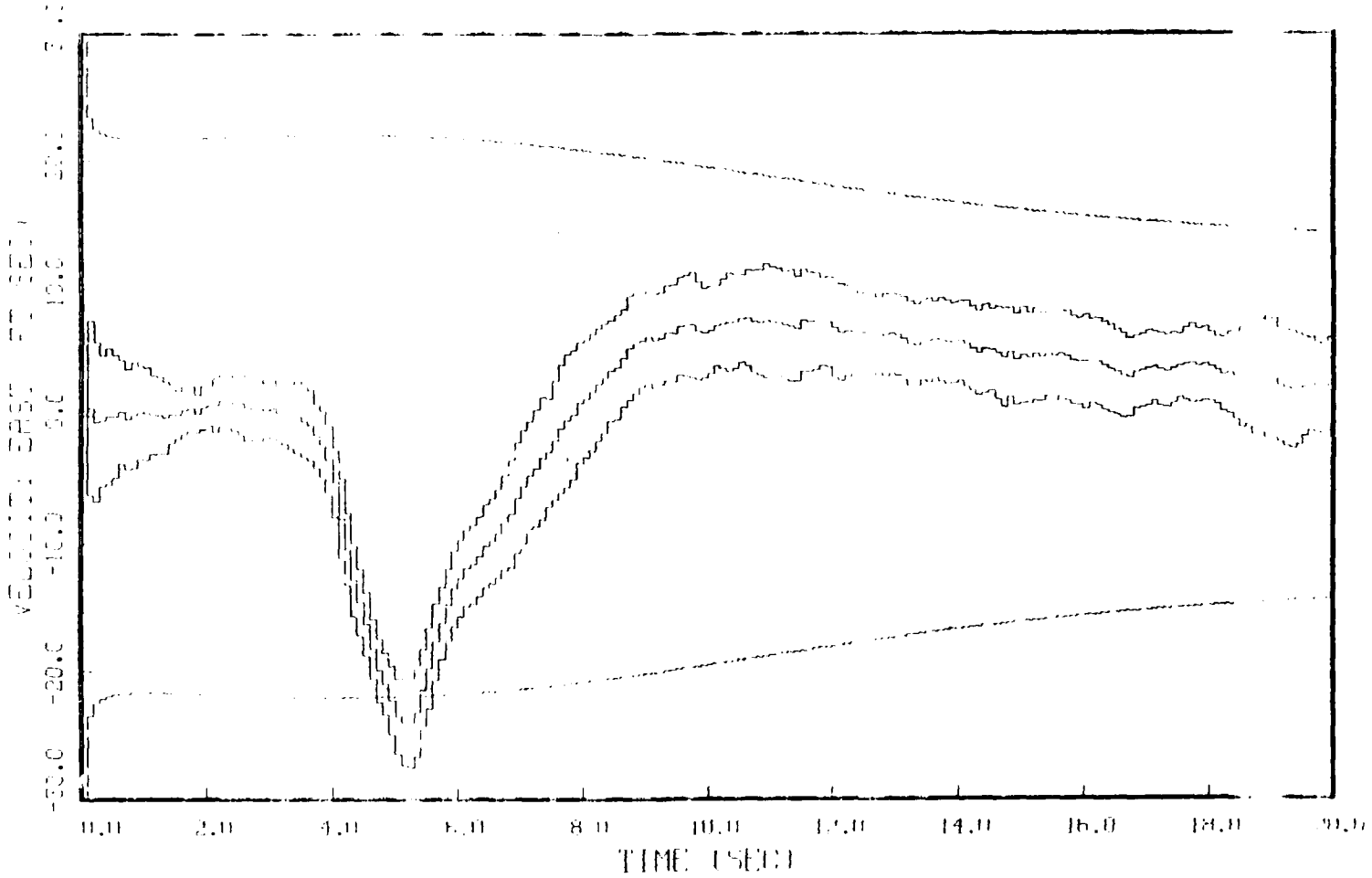

FIGURE K.5: GAUSS MARKOV MODEL, STATE 5, 20 RUNS, Q=100, VERT CHAN SUPPRESSED
BOND TEMPERATURE, 4 HERTZ, BIAS RATE, SIGMA BZ & EL DS=3.0E-4 FOR BZ & EL

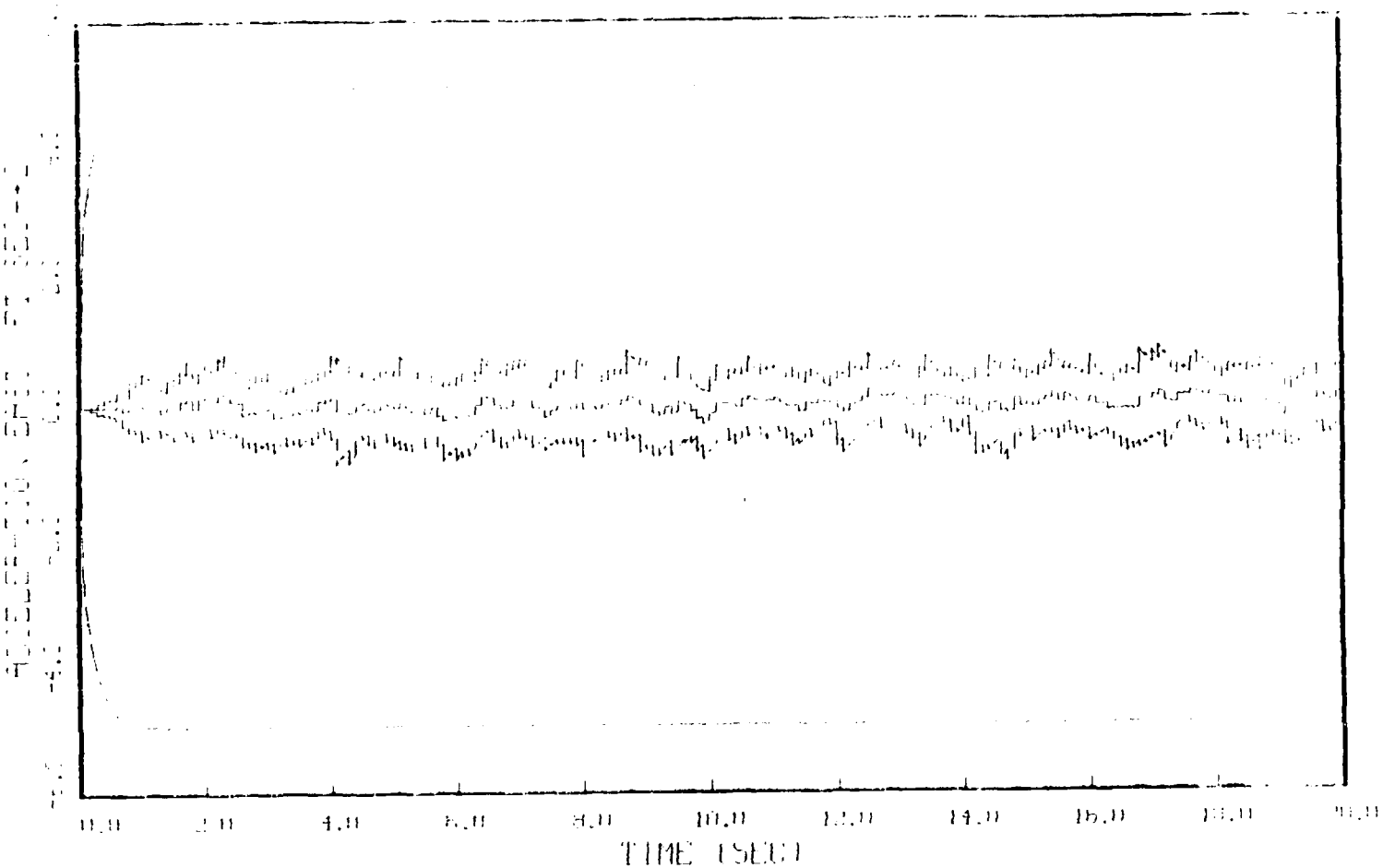

FIGURE F.6: GROSS MARKOV MODEL, STATE 6, 20 RUNS, D=100, VERT CHAN SUBSET OF
INERT TRAJECTORY, 4 RESP: RMS, RMS RATE, STD DEV & EL (RMS=5.0E-4 FOR DEG & EL)

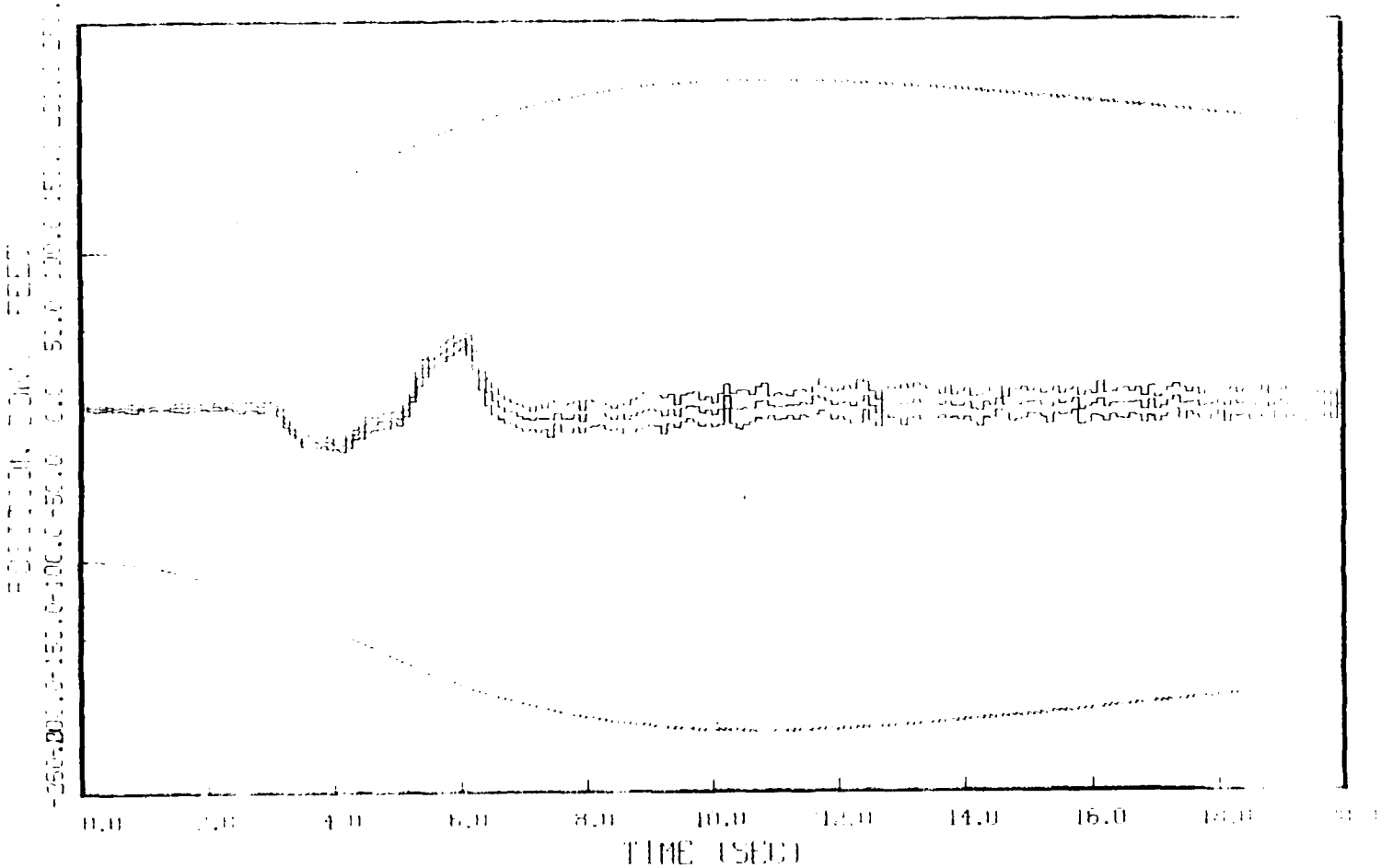

FIGURE E.2 : [illegible] MARKOV MODEL, STATE 7, 20 RUNS, D-[illegible], VERT CHAN SUBJECT [illegible] [illegible], 1 SECOND, 60HZ, 60HZ RATE, STD DEV = [illegible] E-3.0E-4 FOR HZ = [illegible]

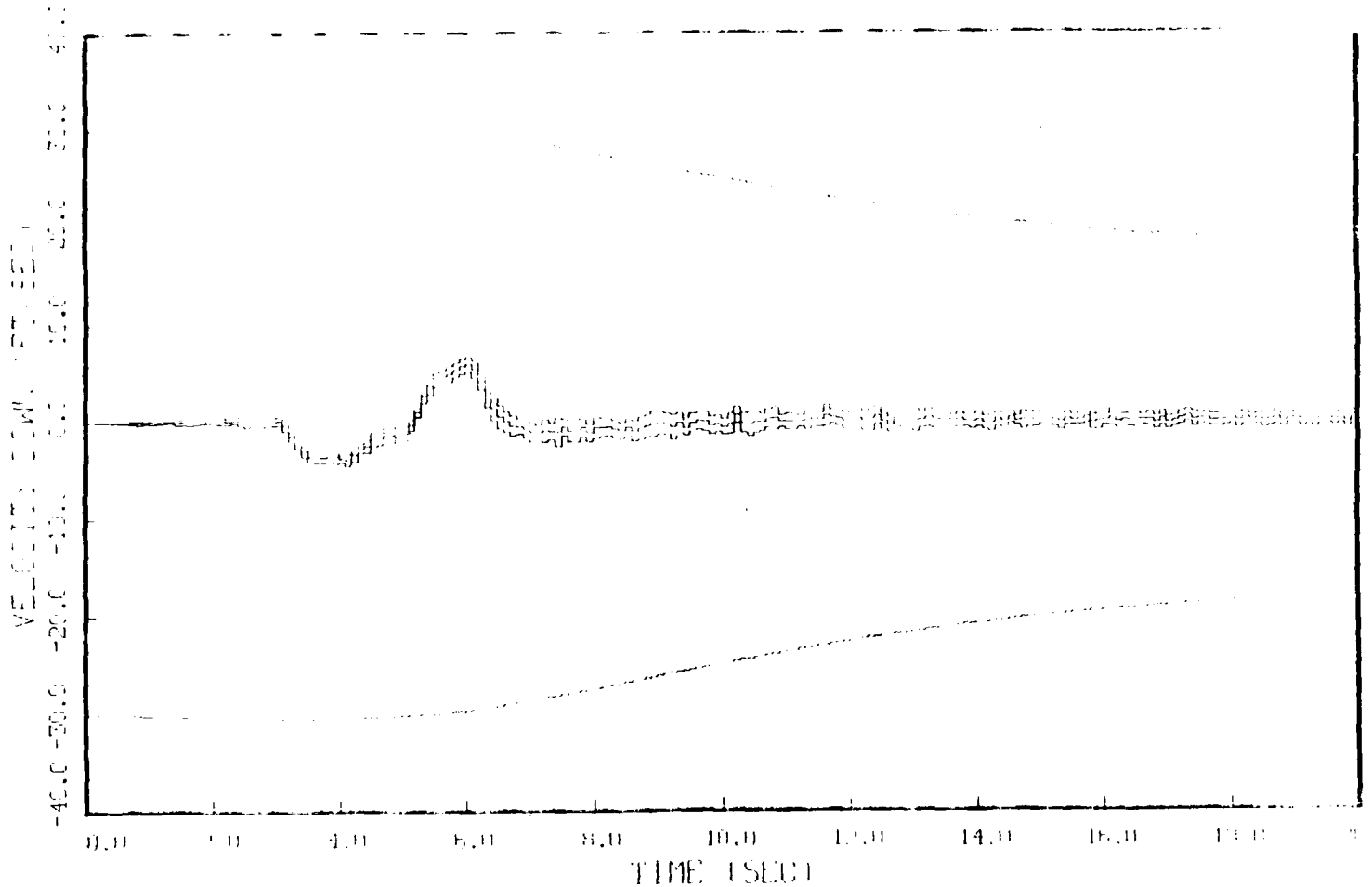

FIGURE 4.28: GRUMMAN MARTIN MODEL, STATE 8, 30 RUNS, U=100, VERT GUST VELOCITY VS TIME
BEAM TRAJECTORY, 4 VIEWS: RMS, ENS RATE, STN #2 & EL U=-5.0E-4 FOR #2 & #3

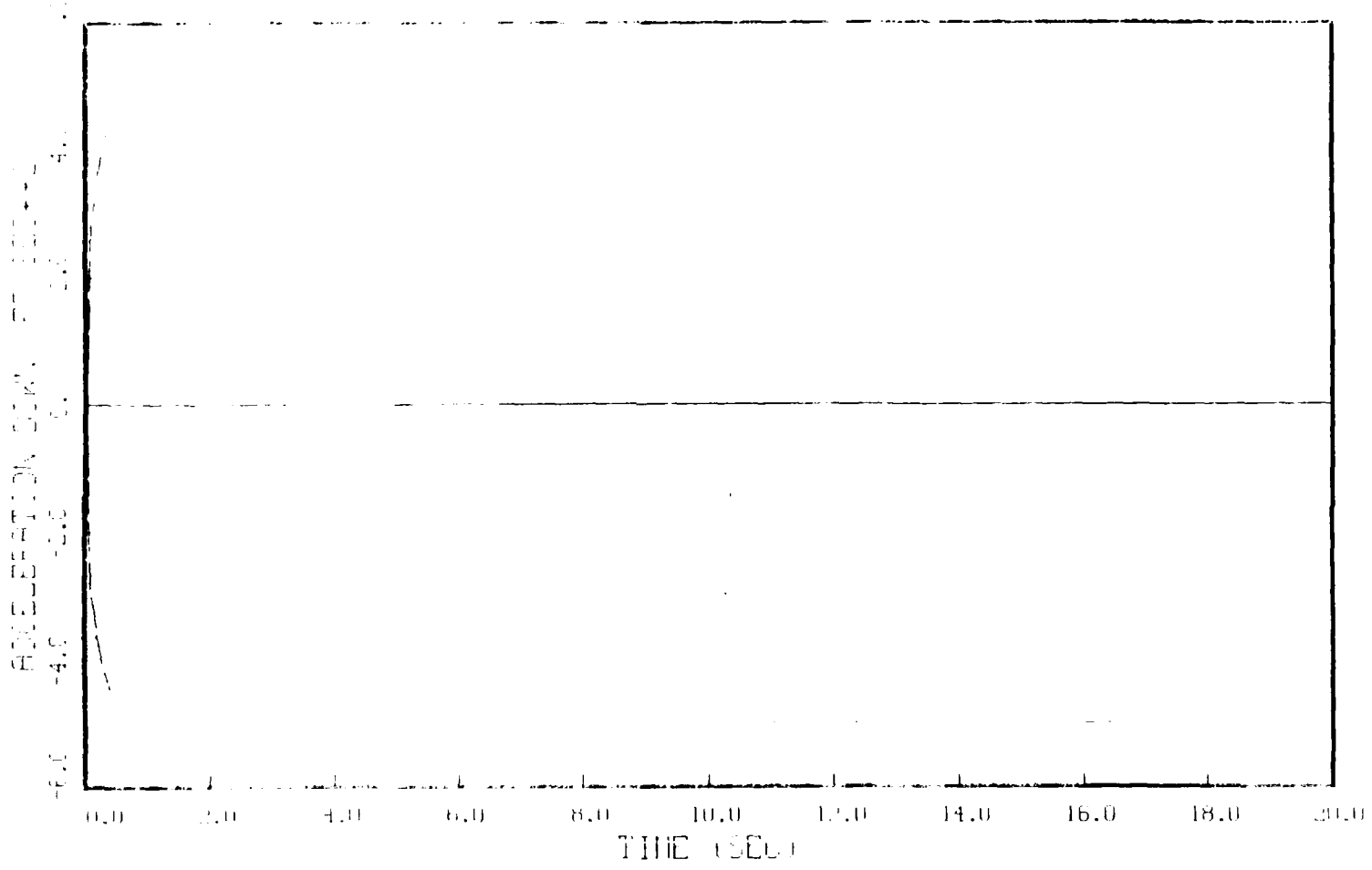

FIGURE [illegible] DIRECTIVE MODEL, STATE 9, 20 RUNS, 0 TRIM, VERT CHAN SUPERPOSED
BEAM RIDER COMMAND, 4 DEGREE RMS, RMS RATE, SIN HZ & EL (3-5.0E 4 FOR HZ & EL)

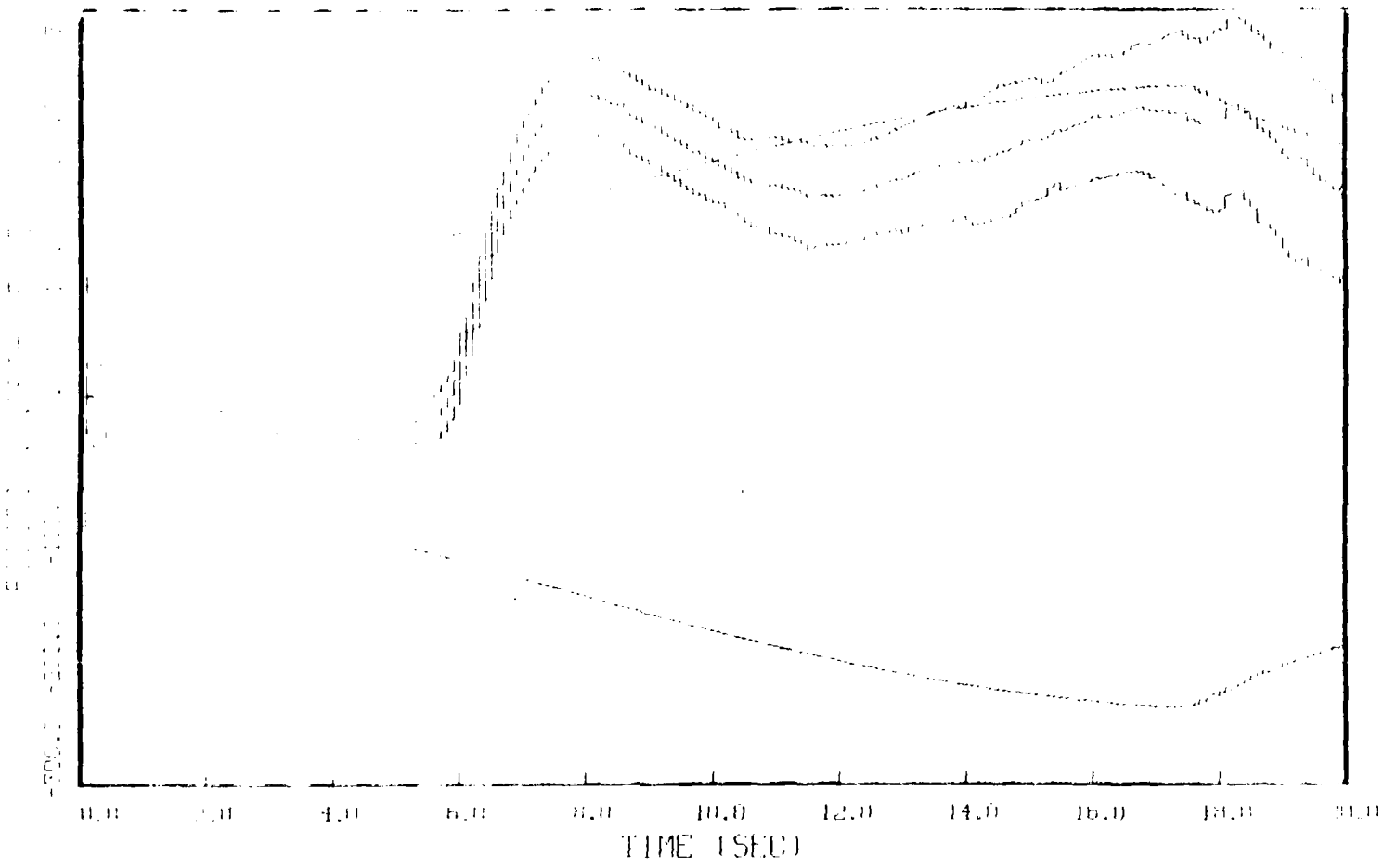

FIGURE F.10: GAUSS MARKOV MODEL, STATE 1, 20 RUNS, Q=100, VERT CHAN SUPPRESS.
INTEGRATED, 4 TERMS: RNG, RNG RATE, SIN AZ & EL (K=5.0E-4 FOR AZ & EL)

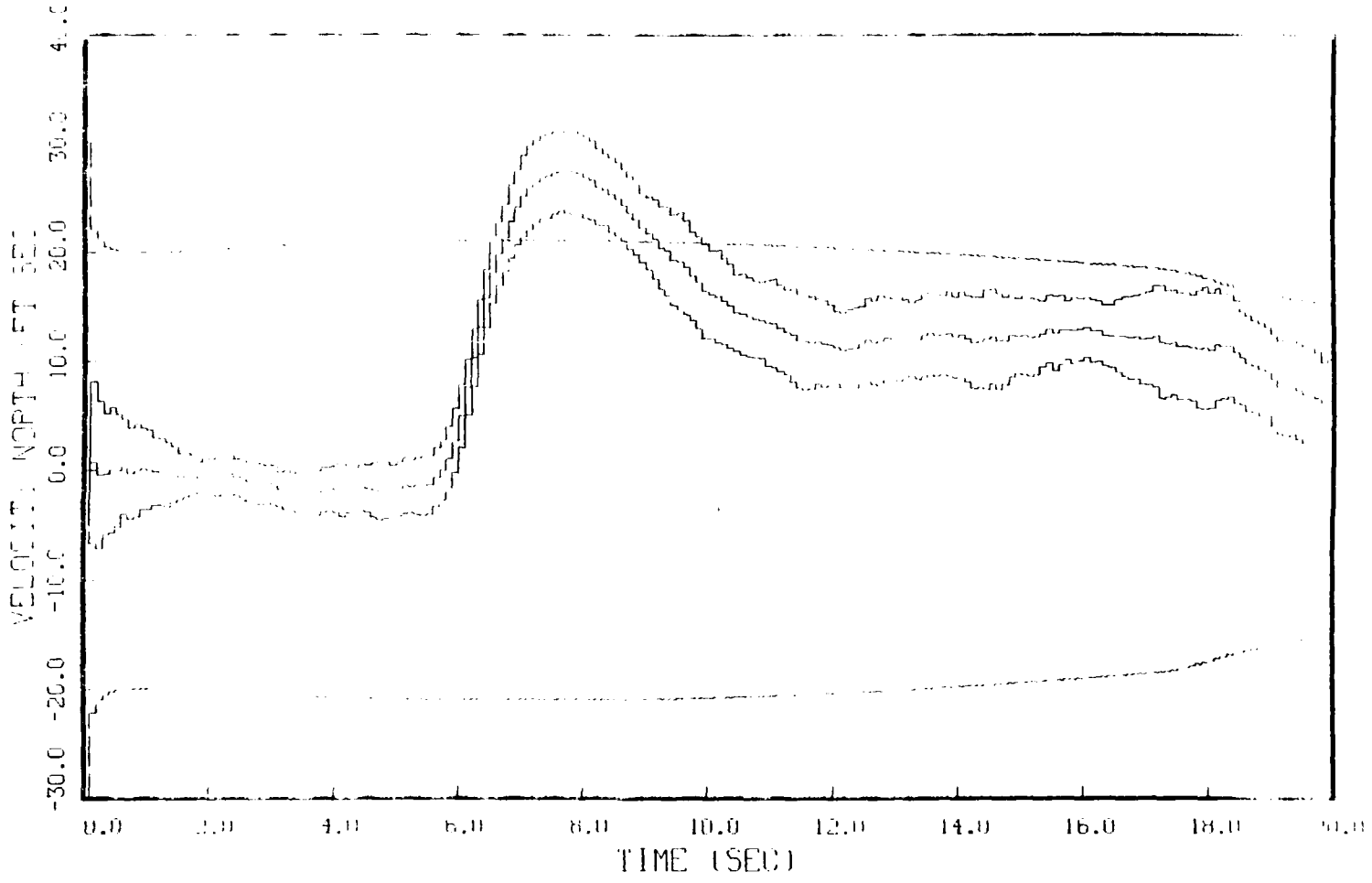

FIGURE F.11: GAUSS MARKOV MODEL, STATE 2, 20 RUNS, Q=100, VERT CHAN SUPPRESSED, THILCHANGE, 1 TECH: NAG, FOG RATE, SIN HZ & EL (R=3.0E-4 FOR HZ & EL)

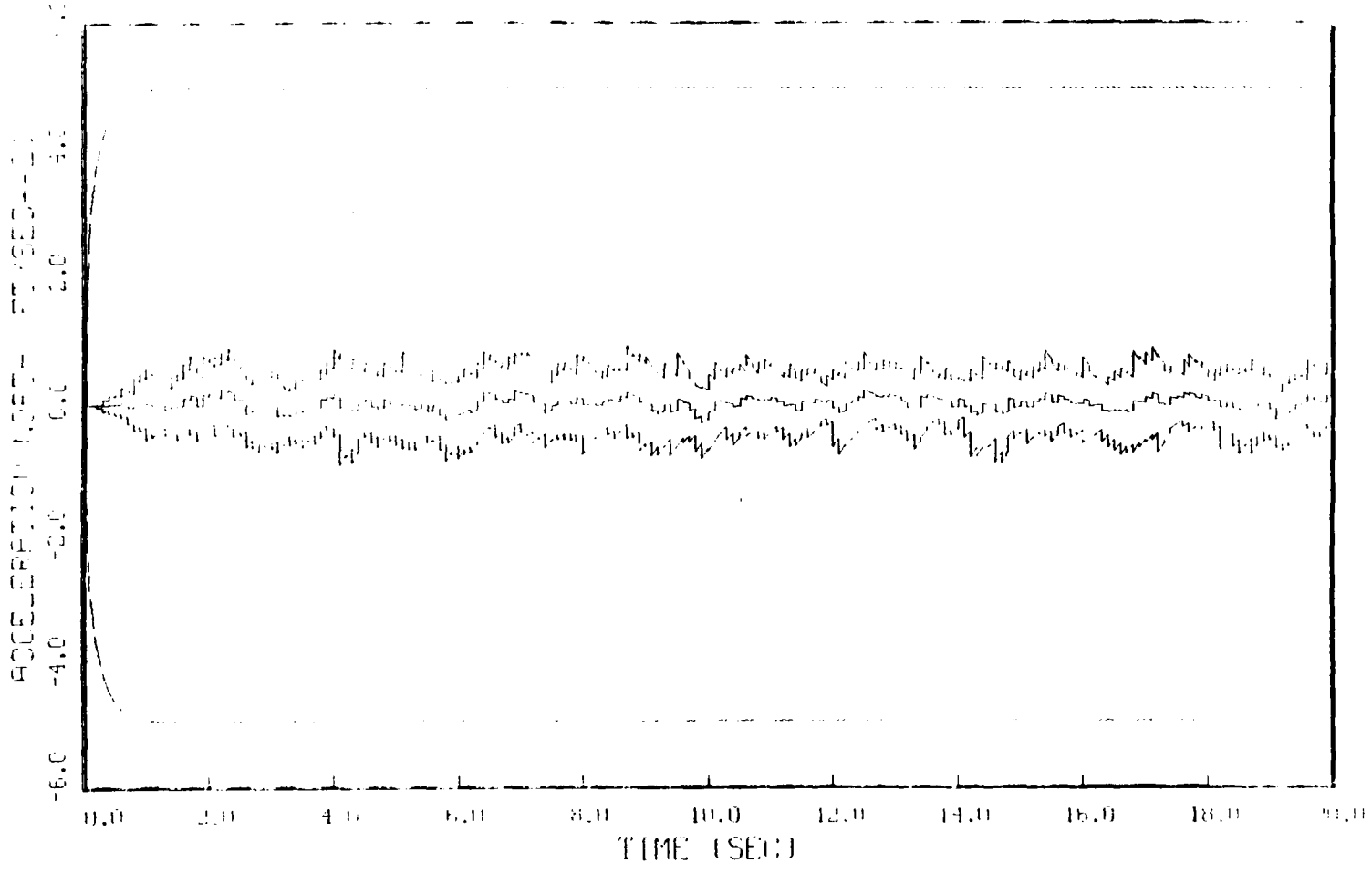

FIGURE F.12: GAUSS MARKOV MODEL, STATE 3, 20 RUNS, 0-100, VERT CHAN SUPPRESSED, TATECHNEL, 1 REMS: RMS, RMS ERROR, SIM HZ & EL ON-SCOPE 1 FOR HZ & EL?

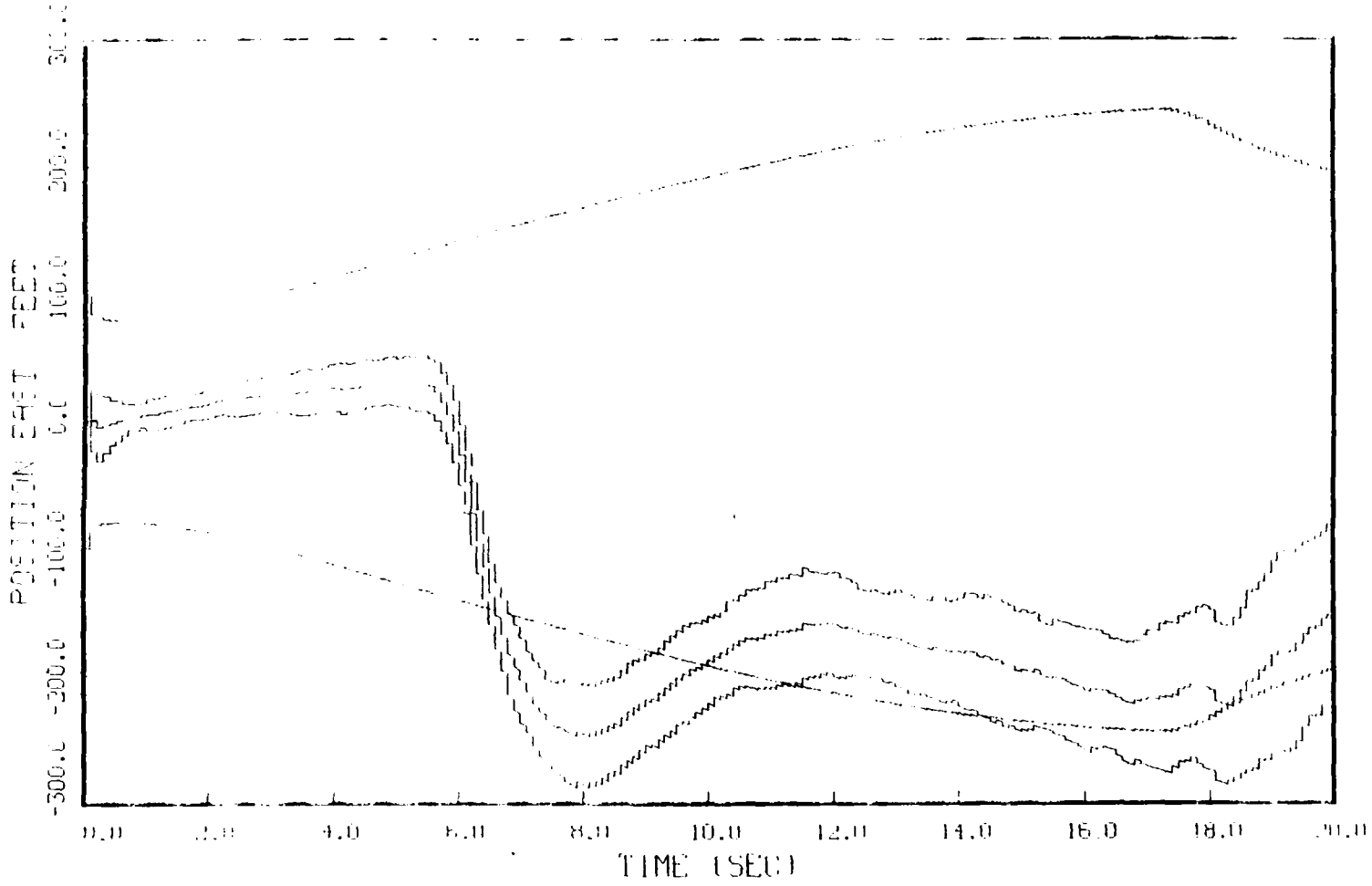

FIGURE 5.13: GAUSS MARKOV MODEL, STATE 4, 20 RUNS, U=100, VERT CHAN SUPPRES.
TAILCHASE, 4 MEAS: RNG, RNG RATE, SIN AZ & EL (R=3.0E-4 FOR AZ & EL)

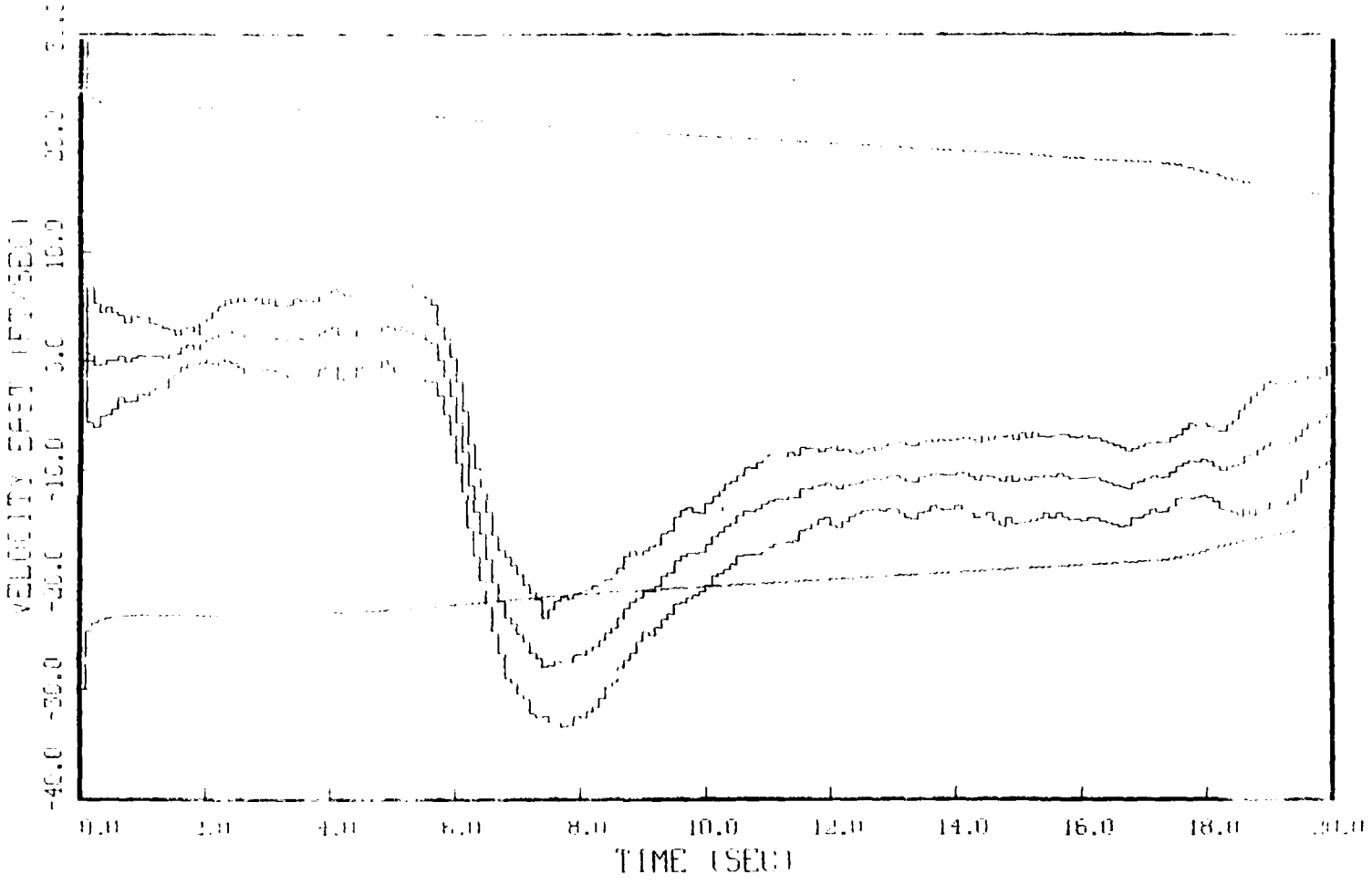

FIGURE I.14: [illegible] MODEL, STATE 5, 20 RUNS, U=100, VERT CHAN SUPPR = [illegible], 4 HERTZ: ROS, RMS RATE, SIN HZ & EL IN-SYNC 4 FOR HZ & EL)

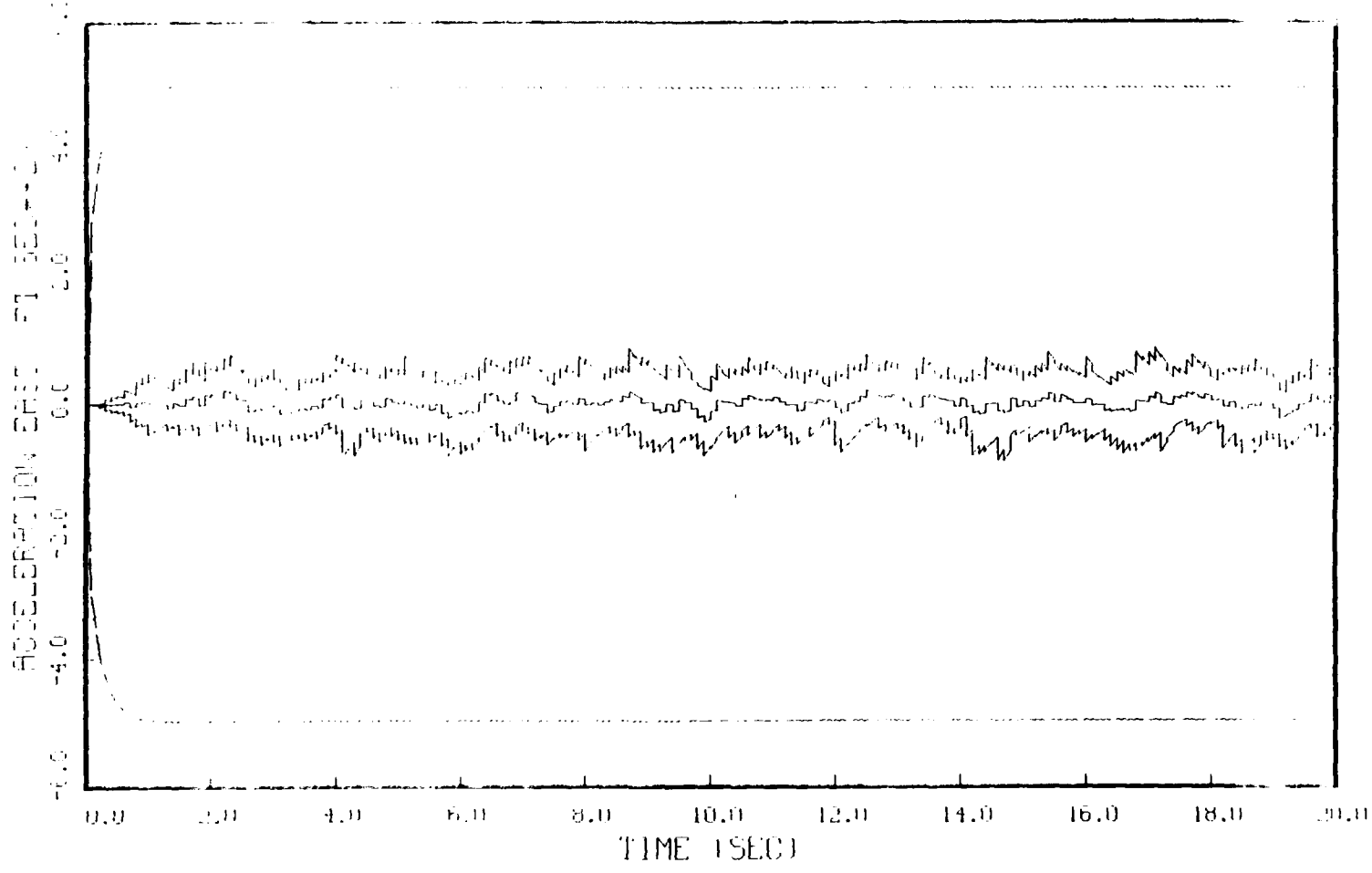

FIGURE 4.15: GAUSS MARKOV MODEL, STATE 6, 20 RUNS, Q=100, VERT CHAN SUPPRE...
INTLCHANGE, 4 MEMS: RNG, RNG RATE, SIN AZ & EL (R=3.0E 4 FOR AZ & EL)

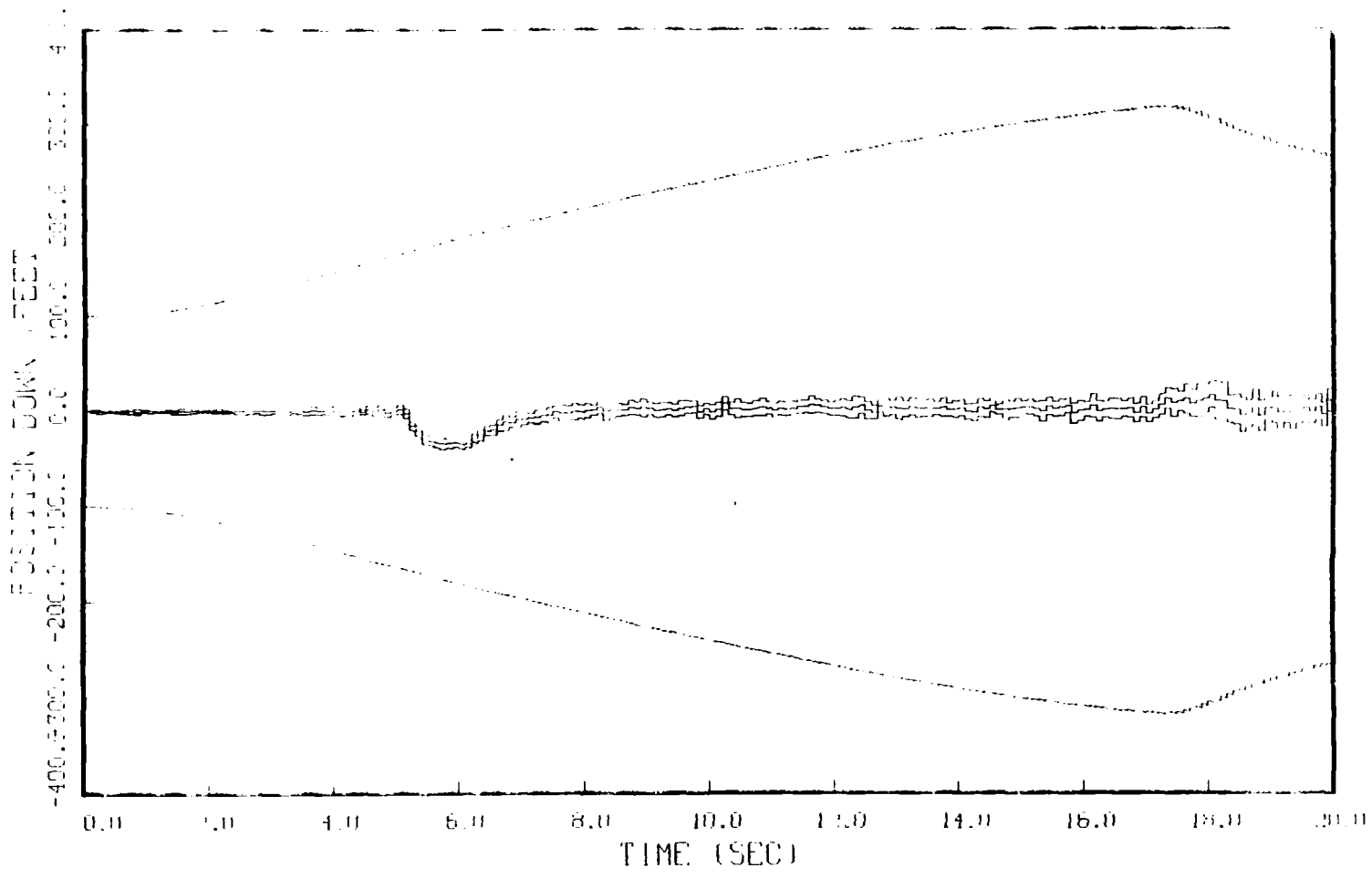

FIGURE 1.16: GAUSS MARKOV MODEL, STATE 7, 20 RUNS, D=100, VERT CHAN SUPPRESS, TAILCHASE, 4 MEAS: RNG, RNG RATE, SIN AZ & EL (R=3.0E-4 FOR AZ & EL)

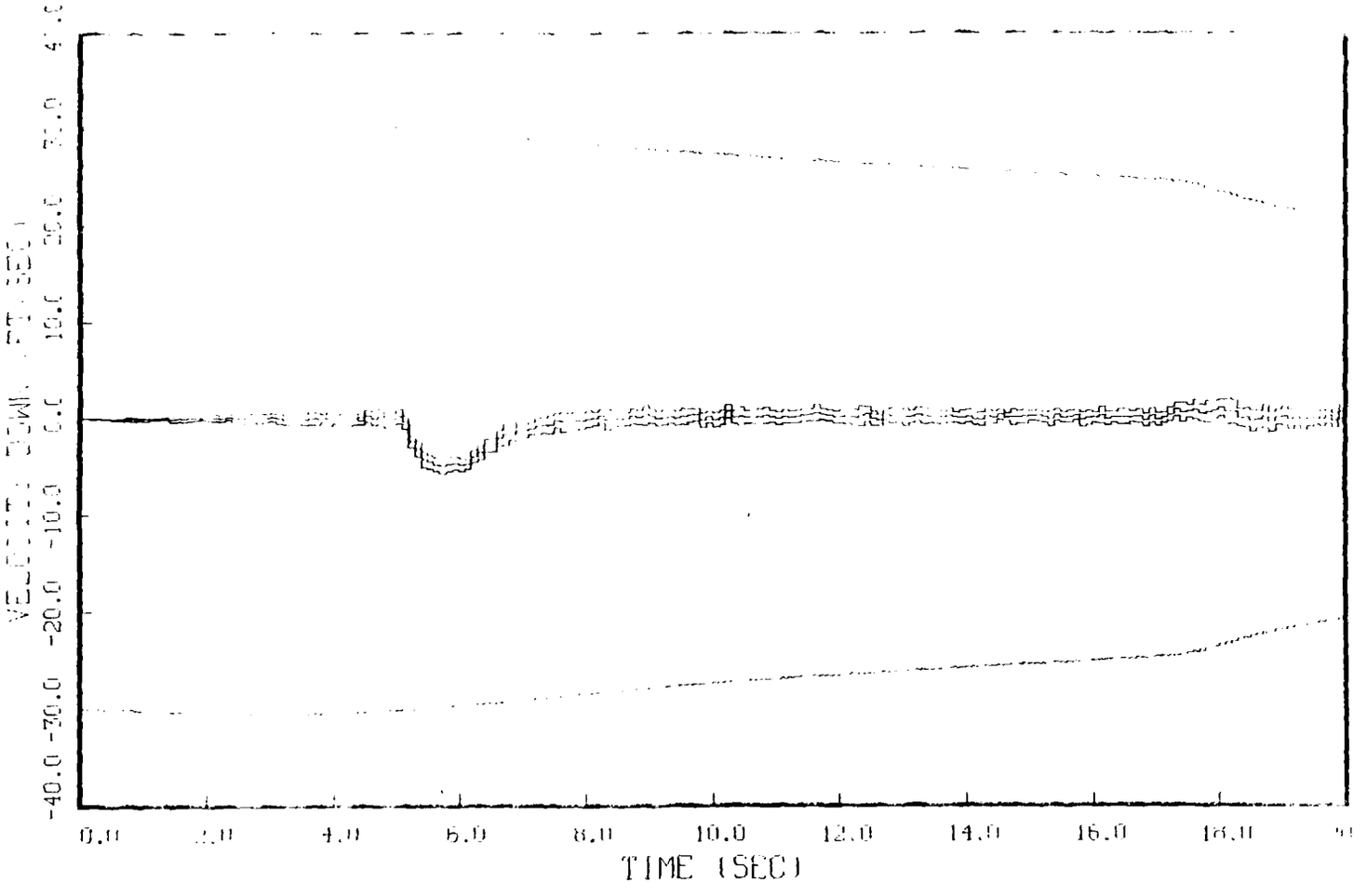

FIGURE 1.1%: GAUSS MARKOV MODEL, STATE 8, 20 RUNS, Q=100, VERT CHAN SUPPRESS.
THEORETICAL, 4 TERMS: RNG, RNG RATE, SIN AZ & EL (R=3.0E 4 FOR AZ & EL)

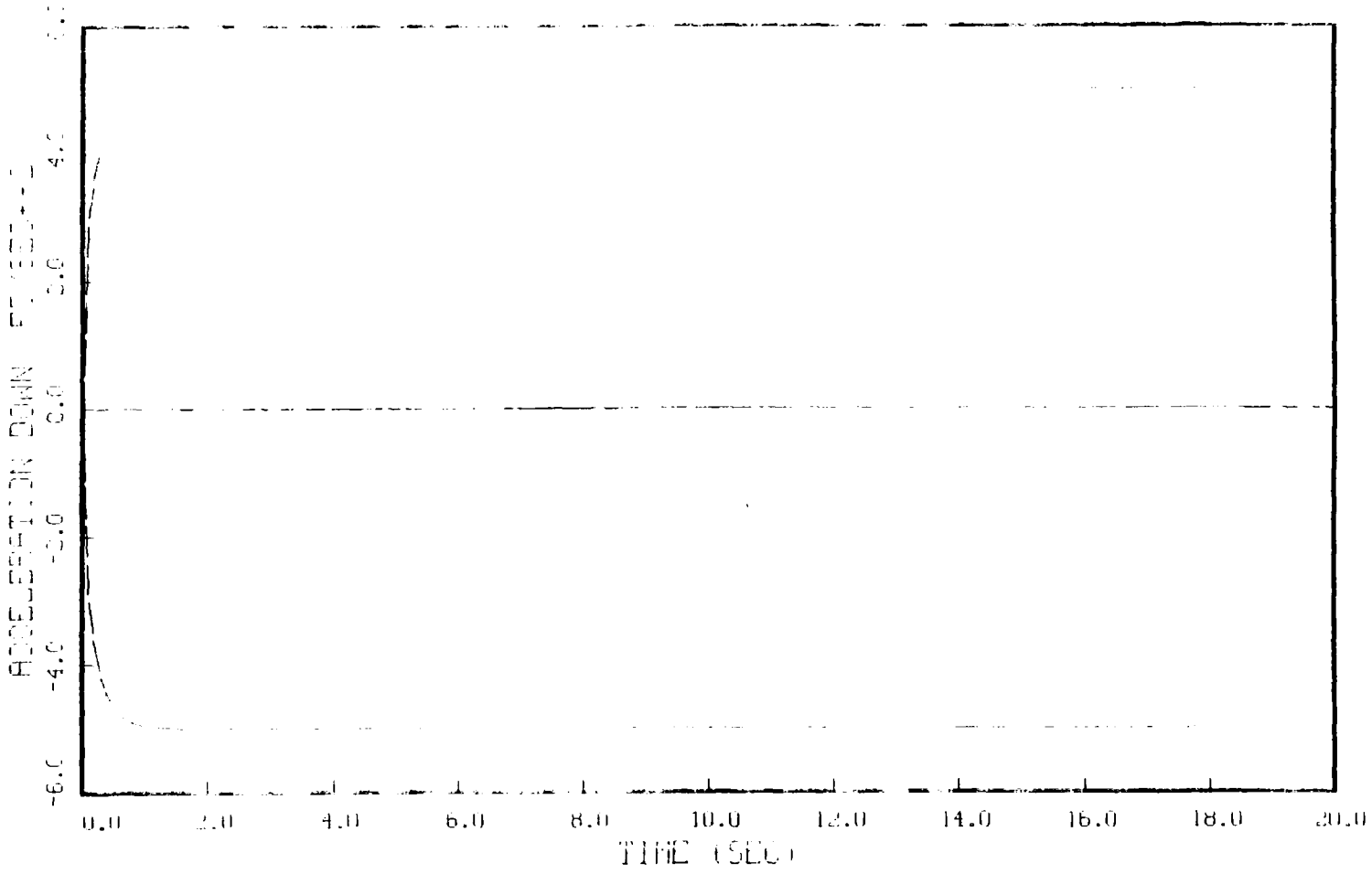

FIGURE F.13: GAUSS MARKOV MODEL, STATE 9, 20 RUNS, D=100, VERT CHAN SUPPRES.
THILCHANG, 4 MEAS: RNG, RNG RATE, SIN AZ & EL (R=3.0E-4 FOR AZ & EL)

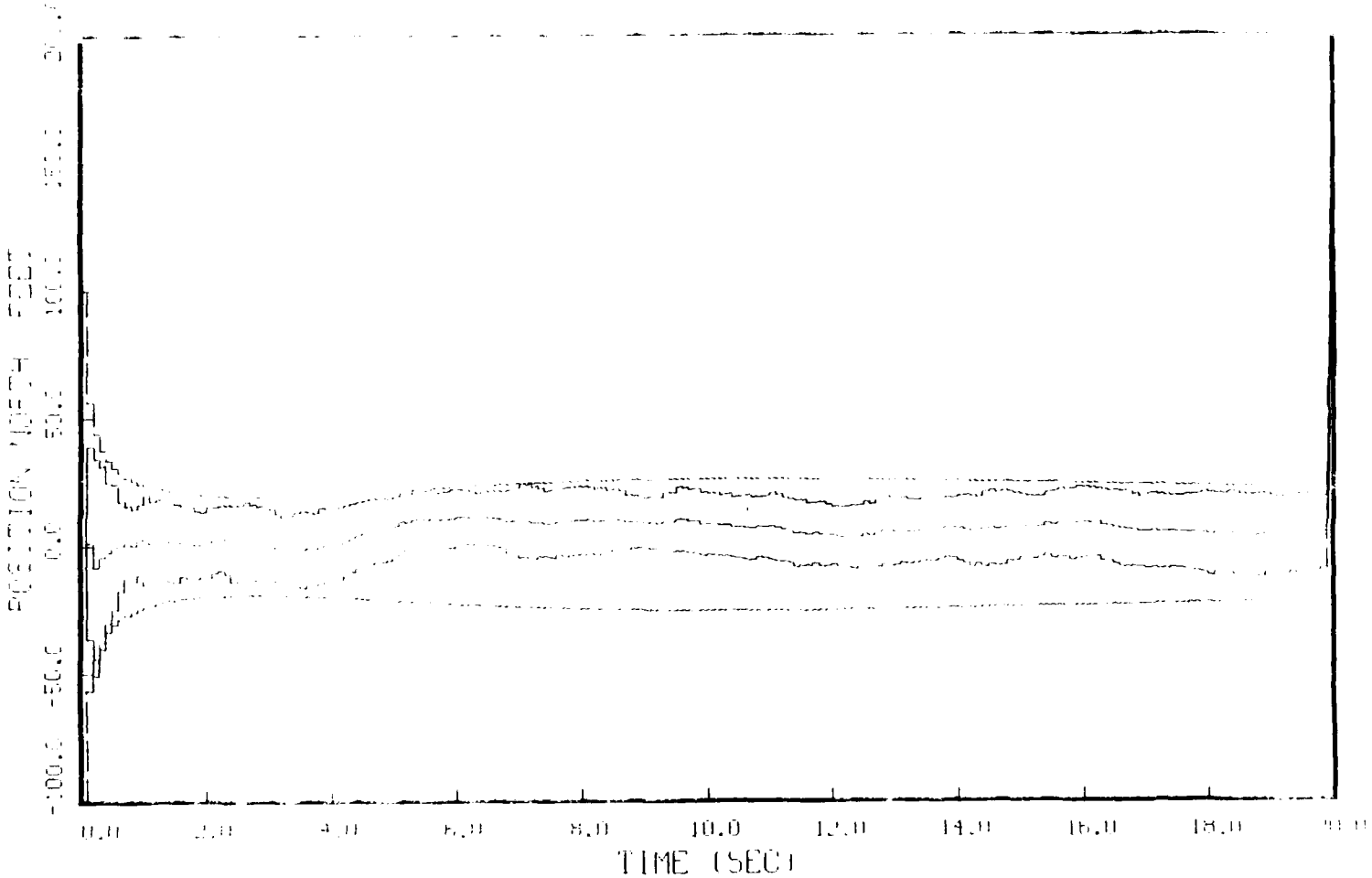

FIGURE F.19: GAUSS MARKOV MODEL, STATE 1, 20 RUNS, Q=100, VERT CHAN SUPPRES.
HEAD-ON ATTACK, 4 MEAS: RNG, RNG RATE, SIN AZ & EL (R=3.0E-4 FOR AZ & EL)

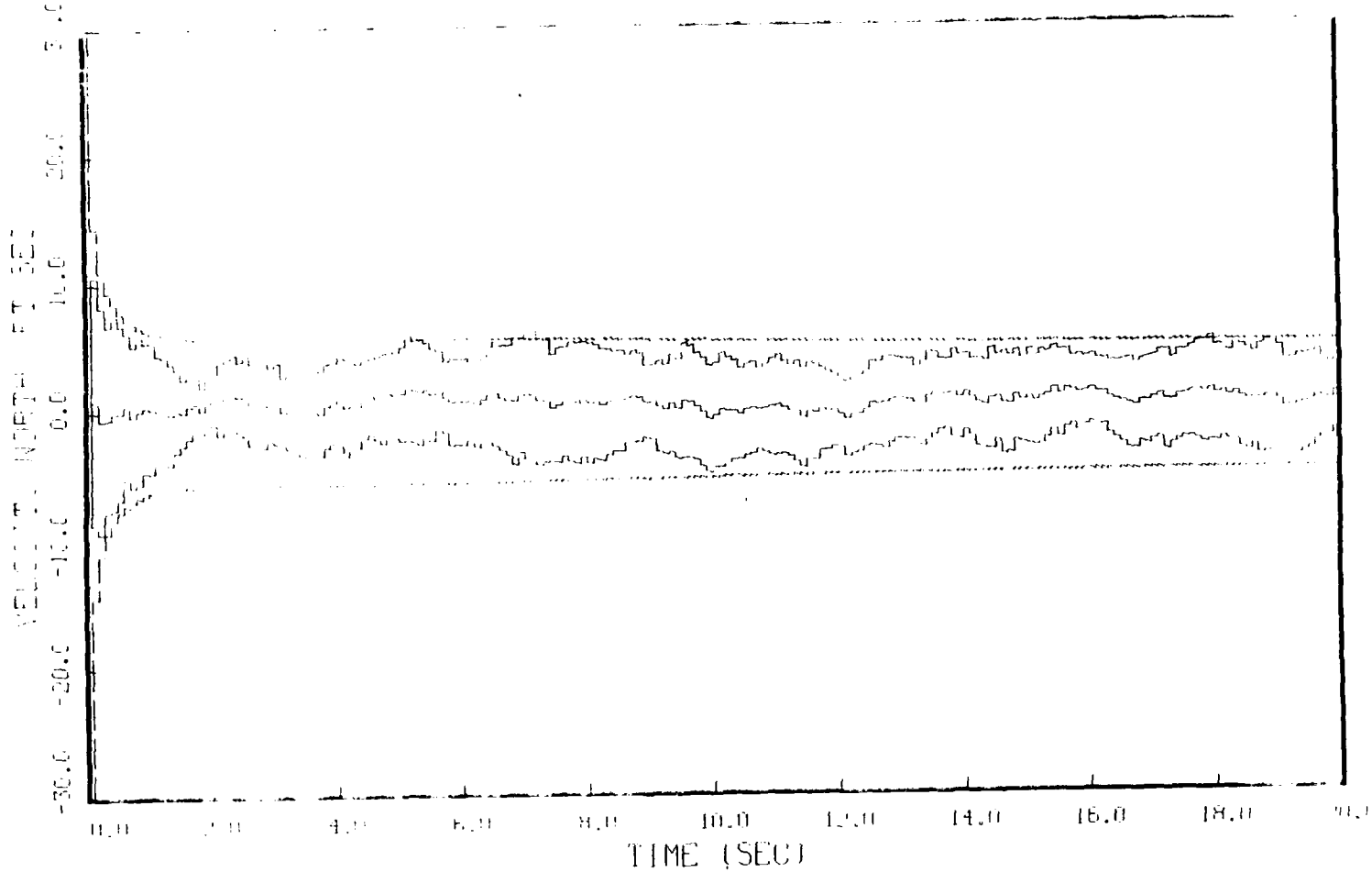

FIGURE I.20: GAUSS MARKOV MODEL, STATE 2, 20 RUNS, Q=100, VERT CHAN SUPPRESS.
HEAD ON ATTACK, 4 MEAS: RNG, RNG RATE, SIN AZ & EL TR=5.0E-4 FOR AZ & EL

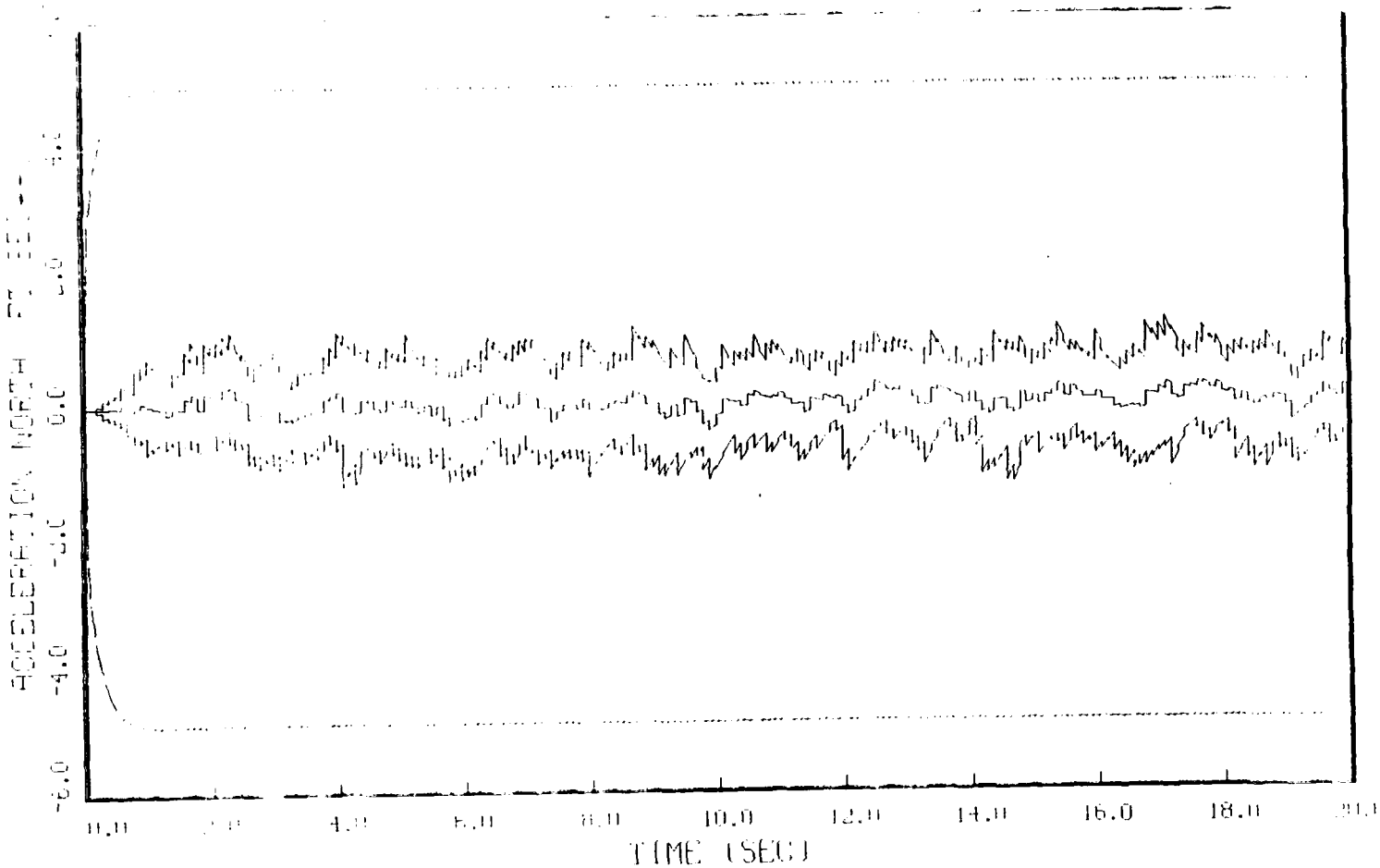

FIGURE [illegible]: GAUSS MARKOV MODEL, STATE 3, 20 RUNS, Q=100, VERT CHAN SUPPRESS. HEMP-ON METHOD, 4 DEMOS: RNG, RNG RATE, SIN AZ & EL IR 3.0E-4 FOR AZ & EL

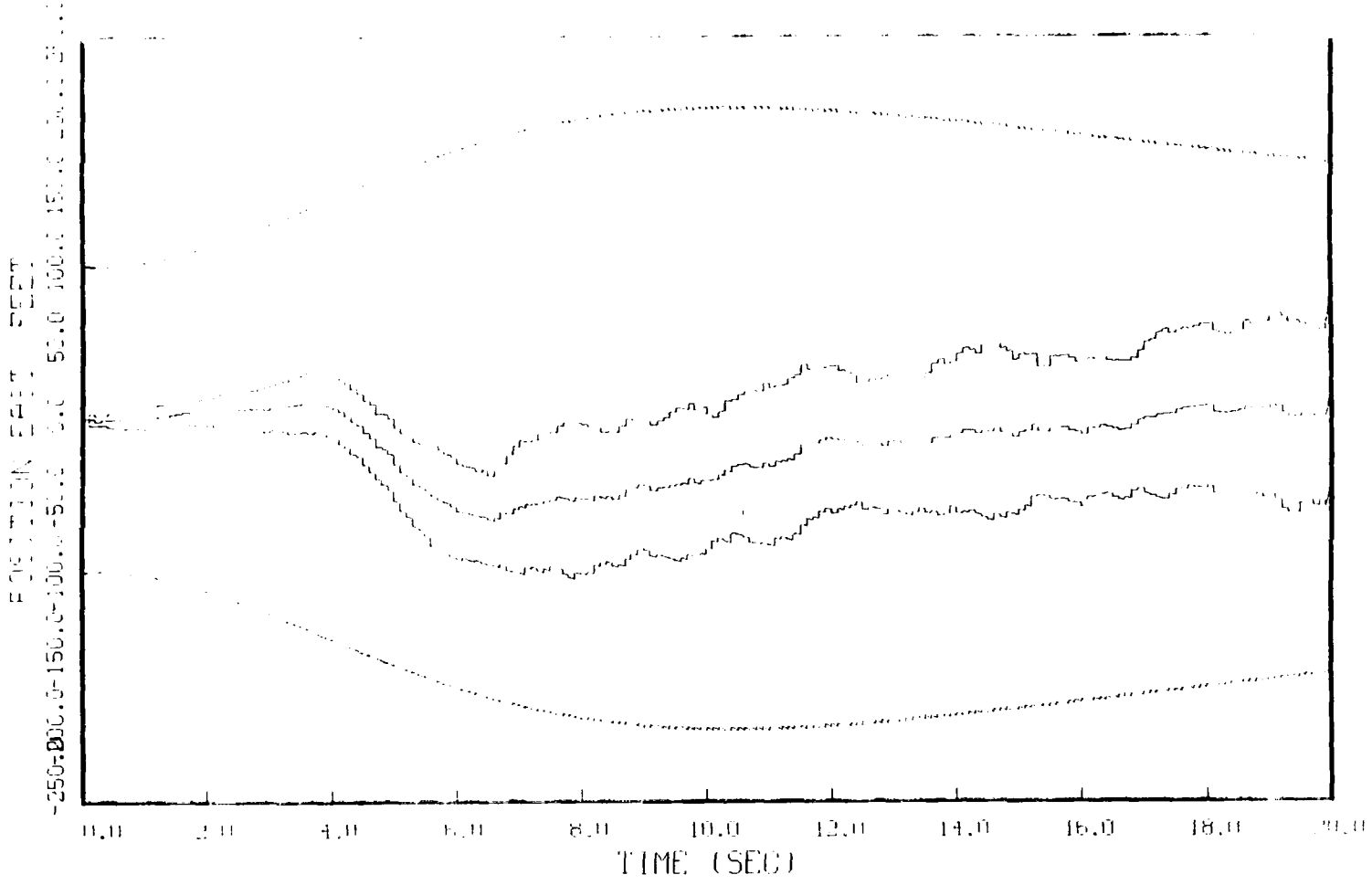

FIGURE 4.22: GAUSS MARKOV MODEL, STATE 4, 20 RUNS, Q=100, VERT CHAN SUPPRES.
NEAR-OPTIMAL, 4 MEAS: RNG, RNG RATE, SIN AZ & EL (R=5.0E-4 FOR AZ & EL)

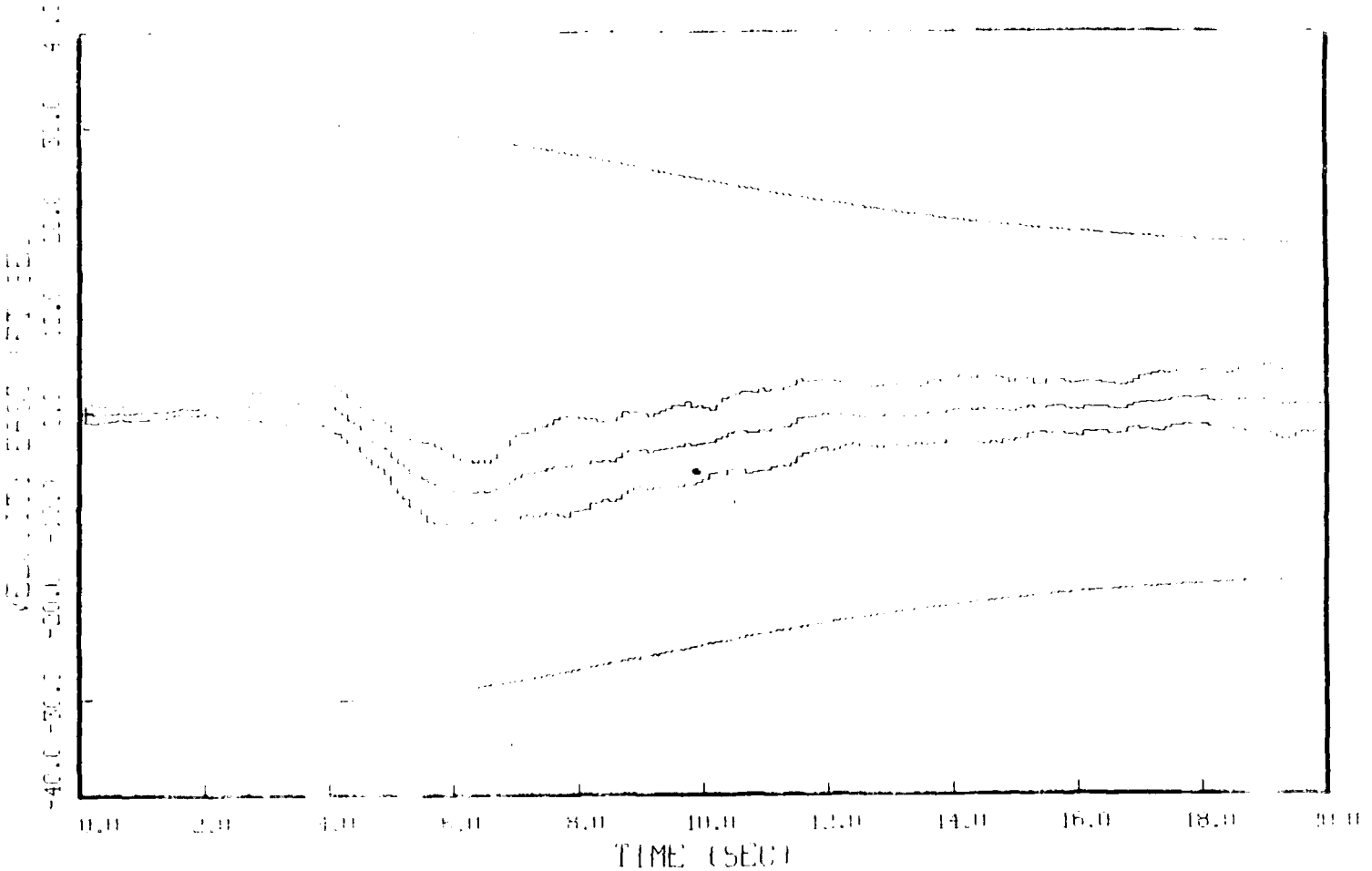

FIGURE 1.25: GAUSS-MARKOV MODEL, STATE 5, 20 RUNS, Q=100, VERT CHAN SUPPRES.
HEAD-ON ATTACK, 1 MEAS: RNG, RNG RATE, SIN AZ & EL ER=5.0E-4 FOR AZ & EL

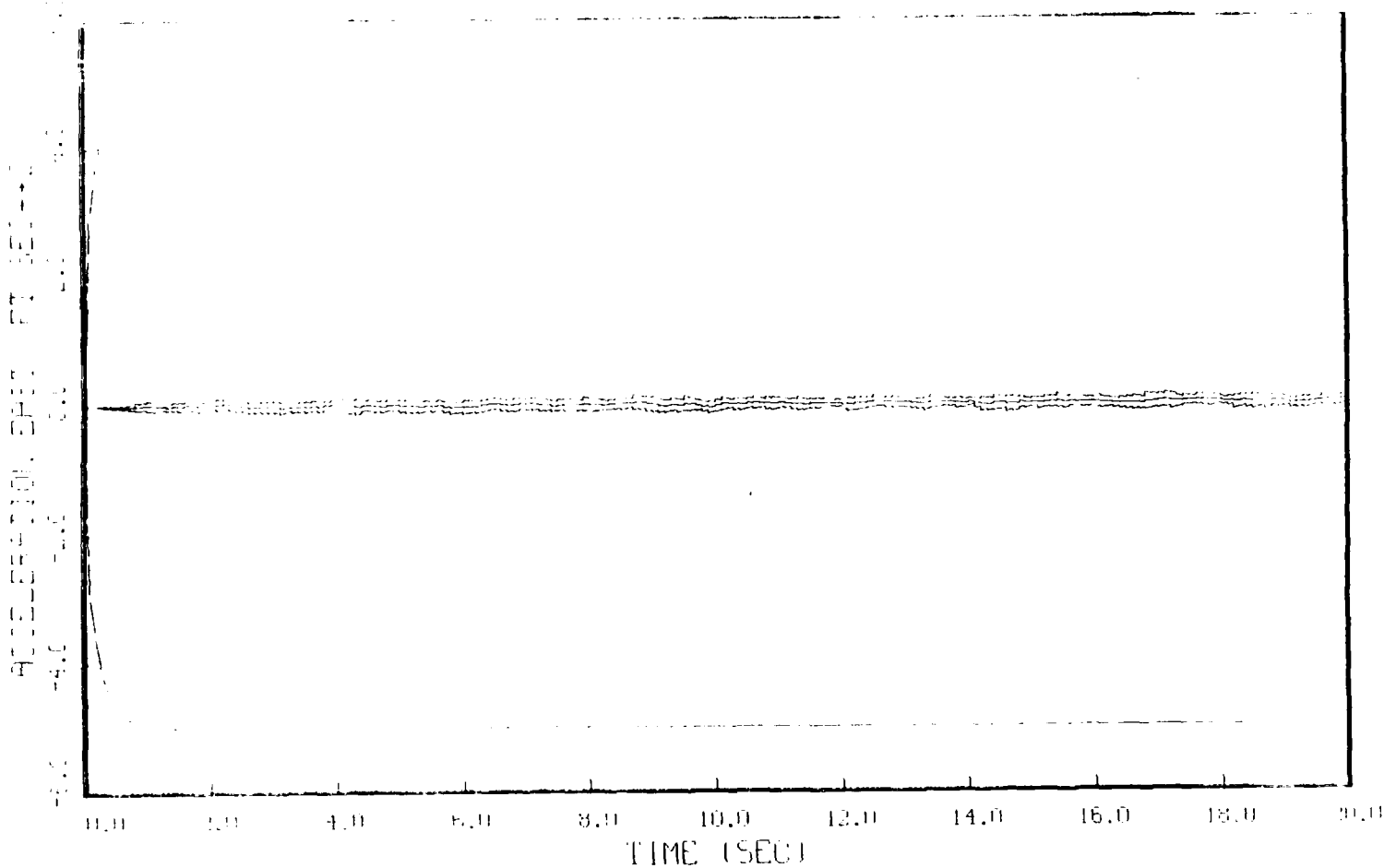

FIGURE F.24: GAUSS MARKOV MODEL, STATE 6, 20 RUNS, Q=100, VERT CHAN SUPPRESS.
HOMER ON ATTMEA , 1 MEAS: RNG, RNG RATE, SIN AZ & EL (R=3.0E-4 FOR AZ & EL)

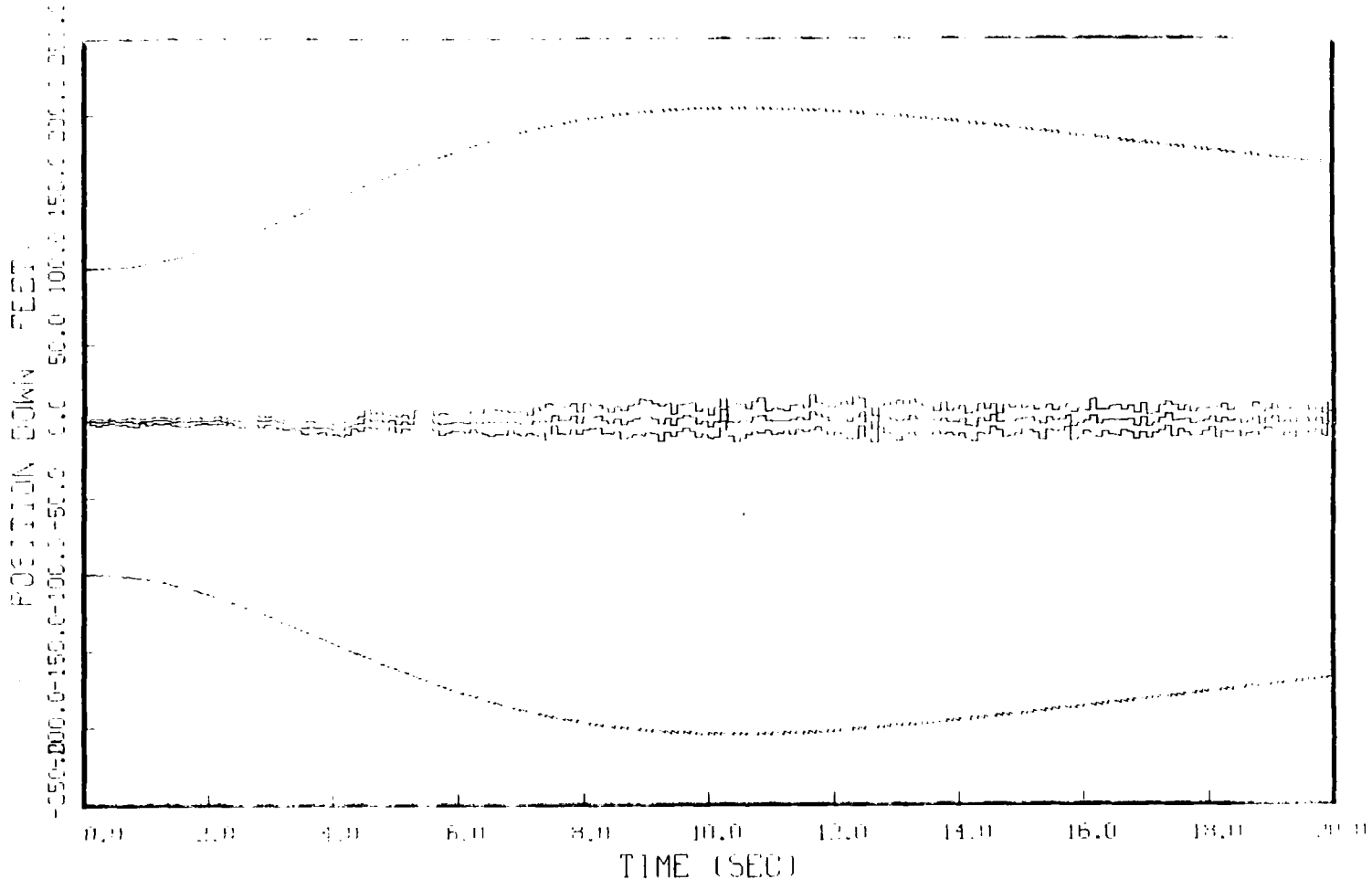

FIGURE [illegible]: GAUSS MARKOV MODEL, STATE 7, 20 RUNS, 0-100, VERT CHAN SUPPRESS, HEAD-ON ATTACK, 4 DEMOS: PNG, RNG RATE, SIN AZ & EL (R=3.0E 4 FOR AZ & EL)

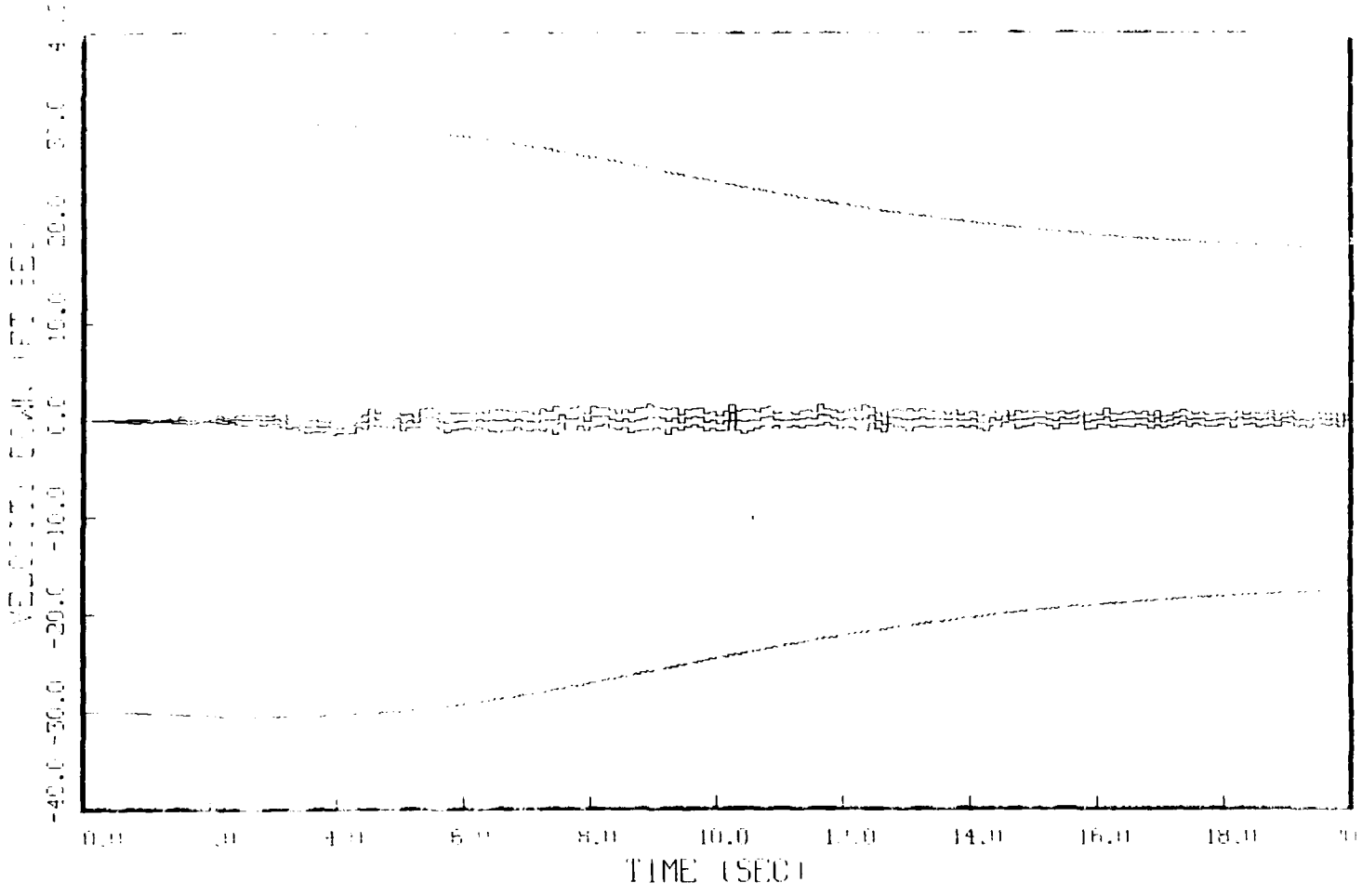

FIGURE I.2e: GAUSS MARKOV MODEL, STATE 8, 20 RUNS, 0-100, VERT CHAN SUPPRESS, HEAD-ON ATTACK, 1 DEAD: LNG, EOG RATE, SIM AZ & EL (K=3.0E-4 FOR AZ & EL)

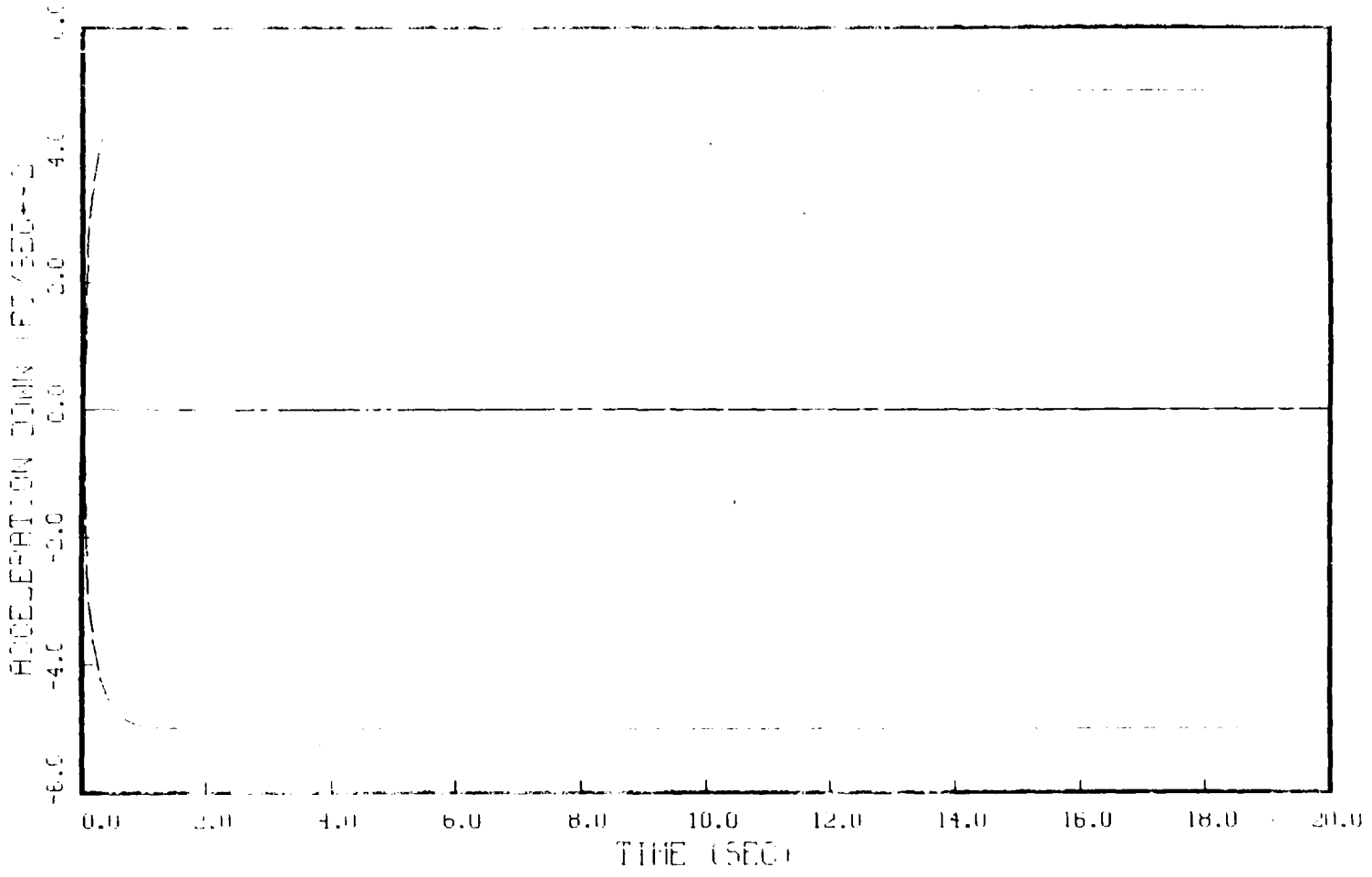

FIGURE [illegible]: GAUSS MARKOV MODEL, STATE 9, 20 RUNS, Q=100, VERT CHAN SUPPRES.
HEAD-ON ATTACK, 4 MEAS: RNG, RNG RATE, SIN AZ & EL (R=3.0E 4 FOR AZ & EL)

Bibliography

1. Maybeck, Peter S. Stochastic Models, Estimation, and Control, Volume 1. New York: Academic Press, Inc., 1979.

2. Maybeck, Peter S. Stochastic Models, Estimation, and Control, Volume 2. New York: Academic Press, Inc., 1982.

3. Maybeck, Peter S. Stochastic Models, Estimation, and Control, Volume 3. New York: Academic Press, Inc., 1982.

4. Chang, Chaw-Bing and John A. Tabaczynski. "Application of State Estimation to Target Tracking," IEEE Transactions on Automatic Control, AC-29 (2): 98-109 (February 1984).

5. Hougaard, Hugh, Sponsoring Engineer. "Steering Dot Stability." Report accompanying research request by OO-ALC/MMECB, Hill AFB, UT, January 1985.

6. Farrell, James L. and others. "Dynamic Scaling for Air-to-Air Tracking," IEEE Proceedings of the National Aerospace Electronics Conference, NAECON 1975, Dayton, Ohio, May 1975.

7. Avionics Branch, F-16 Program Office. Telephone interview. Wright-Patterson AFB, OH, 5 March 1985.

8. Hougaard, Hugh, Robert Beale, and Charles Strickler. OO-ALC/MMECB software engineers. Personal interviews. Hill AFB, UT, 13-15 March 1985. Follow up interviews conducted by telephone, May-October 1985.

9. Hougaard, Hugh. "Proposed AFIT Thesis Topic," Research request by OO-ALC/MMECB, Hill AFB, UT, January 1985.

10. OO-ALC/MMECB. F-4E/G Operational Flight Program Description, P004 Update. Hill AFB, UT, 27 January 1984.

11. Department of the Air Force. Aircrew Weapons Delivery Manual (Nonnuclear) T.O. 1F-4E-34-1-1. Ogden ALC/MMEDT, Hill AFB, UT, 15 April 1979 (change 17, 15 September 1984).

12. Worsley, William H. Comparison of Three Extended Kalman Filters for Air-to-Air Tracking. MS thesis, GAE/AA/805-2, School of Engineering, AFIT (AU), Wright-Patterson AFB, OH, December 1980. (AD A094 767)

13. Musick, Stanton H. SOFE: A Generalized Digital Simulation for Optimal Filter Evaluation, User's Manual, AFWAL-TR-80-1108, Wright-Patterson AFB, OH, October 1980.

14. Department of the Air Force. Antenna Control (Servo Assy.) (LRU 7). T.O. 12P2-2APQ120-2-3-7. Ogden ALC/MMEDT, Hill AFB, UT, 1 February 1973 (change 13, 1 October 1984).

15. Worsley, William H. Lecture notes for EE 738, Digital Avionics Fire Control. School of Engineering, Air Force Institute of Technology (AU), Wright-Patterson AFB, OH, April 1985.

16. Landau, Mark I. "Radar Tracking of Airborne Targets," IEEE Proceedings of the National Aerospace Electronics Conference, NAECON 1976, Dayton, Ohio, May 1976.

17. Bryson, Arthur E. Jr. "New Concepts in Control Theory, 1959-1984," Journal of Guidance, Control, and Dynamics, 8 (4): 417-425 (July-August 1985)

18. Bryan, Ralph S. Cooperative Estimation of Targets by Multiple Aircraft. MS thesis, GE/EE/80-5. School of Engineering, Air Force Institute of Technoloy (AU), Wright-Patterson AFB, OH, June 1980 (AD A085799).

19. Bryan, Ralph S. Personal interviews. May-June 1985.

20. Department of the Air Force. Air Combat Maneuver Digital Computer (LRU 1). T. O. 12P2-2APQ120-2-3-28. Ogden ALC/MMEDT, Hill AFB,UT, 22 August 1978 (change 11, 1 August 1983).

21. Department of the Air Force. Fire Control System, USAF F-4E Series Aircraft. T. O. 1F-4E-2-19. Ogden ALC/MMEDT, Hill AFB, UT, 1 June 1980 (change 24, 15 October 1984).

22. Taylor, John W. R., editor. Jane's All the World's Aircraft, 1978-79. New York: Franklin Watts, Inc., 1978.

23. Ogden ALC, Air Force Logistics Command. F-4E Improved Air-to-Air Missile Program, Contract No. F42600-76-C-0236 (Revision B), with Westinghouse Defense and Electronic Systems Center, Aerospace Division. Hill AFB, UT, 20 December 1978.

24. OO-ALC/MMECB. Radar flight test data. Hill AFB, UT, 22 July, 1985.

25. Skolnik, Merrill I. Introduction to Radar Systems. New York: McGraw-Hill Book Co., 1980.

26. Singer, Robert A. "Estimating Optimal Tracking Filter Performance for Manned Maneuvering Targets," IEEE Transactions on Aerospace and Electronic Systems, AES-6, (4): 473-483 (July 1970).

27. Weston, Andrew C. Dual-Seeker Measurement Processing for Tactical Missile Guidance. MS Thesis, GE/EE/82D-70, School of Engineering, AFIT (AU), Wright-Patterson AFB, OH, December 1982 (AD A124725).

28. Musick, Stanton H. SOFEPL: A Plotting Postprocessor for 'SOFE', User's Manual, AFWAL-TR-80-1109, Wright-Patterson AFB, OH, November 1981.

29. Musick, Stanton H. Personal interviews. June-September, 1985.

30. Musick, Stanton H. "SOFE - A Computer Program for Kalman Filter Design," IEEE Proceedings of the National Aerospace Electronics Conference, NAECON 1981, 2: 742-749, Dayton, Ohio, May 1981.

31. Musick, Stanton H. FORTRAN source code for SOFE. Avionics Laboratory, Wright-Patterson AFB, OH 45433, August 1985.

32. Anderson, Ross B. Preliminary Kalman Filter Design to Improve Air Combat Maneuvering Target Estimation for the F-4E/G Fire Control System.

33. Maybeck, Peter S. and others. "Invest gation of Constant Turn-Rate Dynamics Models in Filters for Airborne Vehicle Tracking," IEEE Proceedings of the National Aerospace Electronics Conference, NAECON 1982, 896-903, Dayton, Ohio, May 1982.

34. Fitts, John M. "Aided Tracking ad Applied to High Accuracy Pointing Systems," IEEE Transactions on Aerospace and Electronic Systems, AES-9, (3): 350-368 (May 1973).

35. Pearson, John B. and Edwin B. Stear. "Kalman Filter Applications in Airborne Radar Tracking," IEEE Transactions on Aerospace and Electronic Systems, AES-10, (3): 319-329 (May 1974).

36. Kendrick, J. D. and others. "Estimation of Aircraft Target Motion Using Orientation Measurements," IEEE Transactions on Aerospace and Electronic Systems, AES-17, (2): 254-260 (March 1981).

37. Kendrick, J. D. Estimation of Aircraft Target Motion Using Pattern Recognition Orientation Measurements. PhD dissertation. School of Engineering, Air Force Institute of Technology (AU), Wright-Patterson AFB, OH, 1978.

38. D'Souza, A. Frank and Vijay K. Garg. Advanced Dynamics, Modeling and Analysis. Englewood Cliffs, New Jersey: Prentice-Hall, Inc., 1984.

VITA

Captain Robert C. Halbert was born on 28 September 1954 in Kountze, Texas. He graduated from high school in Ranger, Texas in 1973 and entered the United States Air Force Academy that same year. He received the degree of Bachelor of Science in Electrical Engineering in 1977 and following graduation, entered USAF pilot training at Reese AFB, Texas. He received his wings in August 1978 and served as a KC-135 pilot with the 92nd Air Refueling Squadron, Fairchild AFB, Washington until entering the School of Engineering, Air Force Institute of Technology, in June 1984.

Permanent address: 120 Homer St
Ranger, Texas 76470

UNCLASSIFIED
SECURITY CLASSIFICATION OF THIS PAGE

AD-A164 205

REPORT DOCUMENTATION PAGE

1a. REPORT SECURITY CLASSIFICATION: UNCLASSIFIED	1b. RESTRICTIVE MARKINGS
2a. SECURITY CLASSIFICATION AUTHORITY	3. DISTRIBUTION/AVAILABILITY OF REPORT: Approved for public release; distribution unlimited.
2b. DECLASSIFICATION/DOWNGRADING SCHEDULE	
4. PERFORMING ORGANIZATION REPORT NUMBER(S): AFIT/GE/ENG/85D-20	5. MONITORING ORGANIZATION REPORT NUMBER(S)
6a. NAME OF PERFORMING ORGANIZATION: School of Engineering; 6b. OFFICE SYMBOL (If applicable): AFIT/ENG	7a. NAME OF MONITORING ORGANIZATION
6c. ADDRESS (City, State and ZIP Code): Air Force Institute of Technology, Wright-Patterson AFB, Ohio 45433	7b. ADDRESS (City, State and ZIP Code)
8a. NAME OF FUNDING/SPONSORING ORGANIZATION: Air Force Logistics Cmd; 8b. OFFICE SYMBOL (If applicable): OO-ALC/MMECB	9. PROCUREMENT INSTRUMENT IDENTIFICATION NUMBER: Unfunded
8c. ADDRESS (City, State and ZIP Code): OO-ALC/MMECB, Hill AFB, Utah 84056	10. SOURCE OF FUNDING NOS. — PROGRAM ELEMENT NO. / PROJECT NO. / TASK NO. / WORK UNIT NO.
11. TITLE (Include Security Classification): See Box 19	
12. PERSONAL AUTHOR(S): Robert C. Halbert, B. S. Capt, USAF	
13a. TYPE OF REPORT: MS Thesis; 13b. TIME COVERED: FROM _____ TO _____; 14. DATE OF REPORT (Yr., Mo., Day): 1982 December; 15. PAGE COUNT: 362	
16. SUPPLEMENTARY NOTATION	Approved for public release: IAW AFR 190-17. LYNN E. WOLAVER 16 Jan 86 Dean for Research and Professional Development Air Force Institute of Technology (AFIT) Wright-Patterson AFB OH 45433
17. COSATI CODES: FIELD 09; GROUP 03; SUB. GR.	18. SUBJECT TERMS (Continue on reverse if necessary and identify by block number): Kalman Filtering, F-4E/G Fire Control System, Radar Tracking and Signal Processing, Monte Carlo Analysis

19. ABSTRACT (Continue on reverse if necessary and identify by block number)

Title: KALMAN FILTER DESIGN FOR THE LONG RANGE INTERCEPT FUNCTION OF THE F-4E/G FIRE CONTROL SYSTEM

This study examines reduced-order Kalman filters designed to improve performance of the F-4E/G long range air-to-air capability (LRI function). Operational requirements dictate a high degree of accuracy and constraints imposed by existing hardware mandate minimal complexity. Two linear dynamics models are proposed, one based on constant target velocity, and the other based on time-correlated target acceleration. A nonlinear model is developed for measurements available in the existing F-4E/G hardware, including range, range rate, radar antenna gimbal angles, and radar antenna rates. The models are implemented in extended Kalman filter formulations employing linear propagation equations to avoid on-line numerical integration. Performance evaluations are performed on three test trajectories using Monte Carlo analysis. (cont.)

20. DISTRIBUTION/AVAILABILITY OF ABSTRACT: UNCLASSIFIED/UNLIMITED ☒ SAME AS RPT. ☐ DTIC USERS ☐	21. ABSTRACT SECURITY CLASSIFICATION: UNCLASSIFIED
22a. NAME OF RESPONSIBLE INDIVIDUAL: William H. Worsley, Major, USAF	22b. TELEPHONE NUMBER (Include Area Code): 513-255-3576; 22c. OFFICE SYMBOL: AFIT/ENG

DD FORM 1473, 83 APR — EDITION OF 1 JAN 73 IS OBSOLETE.

UNCLASSIFIED
SECURITY CLASSIFICATION OF THIS PAGE

19. Abstract (continued)

Filter tuning, error budgets, adaptive techniques, and observability issues are addressed during filter evaluation. Results of the evaluation indicate the filter designs can meet the requirements of the F-4E/G fire control system. Recommendations are made for continued testing and for operational implementation.

END

FILMED

DTIC